

CHEMIA

STUDIA UNIVERSITATIS BABEȘ-BOLYAI CHEMIA

4/2022

ISSN (print): 1224-7154;
ISSN (online): 2065-9520; ISSN-L: 2065-9520
©2022 STUDIA UBB CHEMIA
Published by Babeș-Bolyai University

EDITORIAL BOARD OF STUDIA UNIVERSITATIS BABEȘ-BOLYAI CHEMIA

ONORARY EDITOR:

IONEL HAIDUC – Member of the Romanian Academy

EDITOR-IN-CHIEF:

LUMINIȚA SILAGHI-DUMITRESCU

EXECUTIVE EDITOR:

CASTELIA CRISTEA

GUEST EDITOR:

CLAUDIA CIMPOIU

EDITORIAL BOARD:

PAUL ȘERBAN AGACHI, Babeș-Bolyai University, Cluj-Napoca, Romania

LIVAIN BREAU, UQAM University of Quebec, Montreal, Canada

HANS JOACHIM BREUNIG, Institute of Inorganic and Physical
Chemistry, University of Bremen, Bremen, Germany

JEAN ESCUDIE, HFA, Paul Sabatier University, Toulouse, France

ION GROSU, Babeș-Bolyai University, Cluj-Napoca, Romania

EVAMARIE HEY-HAWKINS, University of Leipzig, Leipzig, Germany

FLORIN DAN IRIMIE, Babeș-Bolyai University, Cluj-Napoca, Romania

FERENC KILAR, University of Pecs, Pecs, Hungary

BRUCE KING, University of Georgia, Athens, Georgia, USA

ANTONIO LAGUNA, Department of Inorganic Chemistry, ICMA,
University of Zaragoza, Zaragoza, Spain

JURGEN LIEBSCHER, Humboldt University, Berlin, Germany

KIERAN MOLLOY, University of Bath, Bath, UK

IONEL CĂTĂLIN POPESCU, Babeș-Bolyai University, Cluj-Napoca,
Romania

CRISTIAN SILVESTRU, Babeș-Bolyai University, Cluj-Napoca, Romania

[http://chem.ubbcluj.ro/~studiachemia/;](http://chem.ubbcluj.ro/~studiachemia/)
http://www.studia.ubbcluj.ro/serii/chemia/index_en.html

YEAR
MONTH
ISSUE

Volume 67 (LXVII) 2022
DECEMBER
4

PUBLISHED ONLINE: 2022-12-30
PUBLISHED PRINT: 2022-12-30
ISSUE DOI: 10.24193/subbchem.2022.4

S T U D I A

UNIVERSITATIS BABEȘ–BOLYAI

CHEMIA

4

CONTENT/ SOMMAIRE/ INHALT/ CUPRINS

Claudia CIMPOIU, In Memoriam Prof. <u>Teodor Hodișan</u> PhD, 1942 - 2012	7
Anamaria HOSU, Claudia CIMPOIU, A Cost-Effective and Rapid Method Base on High-Performance Thin-Layer Chromatography in Evaluating the Roasted Coffee Adulteration.....	11
Cristian Ionuț CIUCANU, Ionel CIUCANU, Sorin OLARIU, Derivatization of Rosuvastatin as Methyl Ester for Its Analysis by Gas Chromatography-Mass Spectrometry in Plasma	19
Alina FILIP, Zsófia BATA, Anca Elena ANGHEL, László POPPE, László Csaba BENCZE, Production of Recombinant, Non-Tagged Phenylalanine Ammonia-Lyases Employing TEV Protease-Removable Affinity Tags	27
Izabella IRSAI, Szilárd Zoltán PESEK, Radu SILAGHI-DUMITRESCU, Polylactic Acid Inter-Chain Interactions	47

Lorentz JÄNTSCHI, Modelling of Acids and Bases Revisited	73
Niloofar Soltani AHMADI, Farhoush KIANI, Seyed-Ahmad SHAHIDI, Azade GHORBANI-HASANSARAEI, Fatemeh ZABIHI, Fardad KOOHYAR, The Effect of Solvent and Temperature on Protonation Constants of DL-Phenylalanine in Different Aqueous Solutions of Methanol at Different Temperatures	93
Andrada MAICANEANU, Cerasella INDOLEAN, Investigation on the Potential Usage of Lignocellulosic Wastes for Cd(II) Removal.....	109
Kah-Tong CHAN, Siew-Teng ONG, Optimization of Methylene Blue Dye Removal by Peanut Husk Using Plackett-Burman Design and Response Surface Methodology.....	121
Ildiko LUNG, Adina STEGARESCU, Ocsana OPRIȘ, Maria-Loredana SORAN, Testing MWCNT-COOH/Fe ₃ O ₄ Nanocomposite for the Removal of Ampicillin from Synthetic Aqueous Solutions.....	141
Saken ABDIMOMYN, Azhar ATCHABAROVA, Dinara ABDUAKHYTOVA, Rustam TOKPAYEV, Kanagat KISHIBAYEV, Tamina KHAVAZA, Andrey KURBATOV, Graziella Liana TURDEAN, Mikhail NAURYZBAYEV, Investigation of the Functional Layer Formation on the Surface of Carbon Material.....	151
Arnella NECHITA ROTTA, Cristina BOTA, Balázs BRÉM, Dan Ioan PORUMB, Emese GÁL, Analysis of Products from the Pyrolysis of Plastics Waste from a Printing Plant: a Pilot Scale Study	169
Adrian PATRUT, Victor BOCOS-BINTINTAN, Roxana T. PATRUT, Doriana PARTILA, Ileana-Andreea RATIU, Laszlo RAKOSY, Karl F. VON REDEN, Radiocarbon Dating of the Historic Emperor's Beech from Muncel, Baia de Aries, Romania	187
Ebru AKKEMİK, Mehmet FİDAN, Merve BALABAN, Behcet İNAL, Icp-Oes and LC-ESI-MS/MS Analyses, Enzyme Inhibition and DNA Protection Potential of <i>Pelargonium Quercetorum</i> Agnew	197
Norbert MUNTEAN, Tiberiu FRENȚIU, Gábor RÁKOS, Enikő COVACI, The Influence of the Distillation Process on the Content of Metals in Home- and Industrially-Brewed Alcoholic Beverages – Risk Assessment to Human Health.....	215

Dorina CASONI, Ileana Maria SIMION, Simona Codruța Aurora COBZAC, Alexandra-Gabriela KIRALY, Development of a New Micro-HPTLC Protocol for Total Antioxidant Potential Determination of Redox-Active Drugs	235
Liana Maria COSTEA, Raluca RAD, Claudia CIMPOIU, Adela MEGHESAN, Determination of 2,4-Dichlorophenoxyacetic Acid (2,4-D) from Tomatoes by Lc-Ms/Ms Analysis.....	249
Julia BOTH, Gabriella SZABÓ, Liana-Maria MUREȘAN, Study on the Corrosion Inhibition Efficiency of Aluminum Tripolyphosphate on Zinc Substrate	261
Mihaela VLASSA, Miuța FILIP, Virginia COMAN, Vlad PĂNESCU, Cătălina HERGHELEGIU, Simion BELDEAN-GALEA, Glyphosate and Aminomethylphosphonic Acid Levels in Water and Soil Samples From Transylvanian Roma Community Analyzed by HPLC-FLD Method	273
Vlad Alexandru PĂNESCU, Robert BEGY, Gheorghe ROȘIAN, Maria Concetta BRUZZONITI, Mihail Simion BELDEAN-GALEA, Historical Assessment of Atmospheric Persistent Organic Polutants Depositions in Muntinu Glacial Lake, Southern Romanian Carpathians, Based on Radionuclide-Dated Sediments.....	287
Melinda GAL, Alexandru TURZA, Bianca STOEAN, Luiza GAINA, Castelia CRISTEA, Emese GAL, Tamas LOVASZ, Dan PORUMB, Luminita SILAGHI-DUMITRESCU, Alternative Procedures for the Green Synthesis of 3,7-bis(<i>n,n</i> -(2-hydroxyethyl)amino)phenothiazinium Dye.....	303
Csaba VÁRHELYI Jr., Roland SZALAY, György POKOL, János MADARÁSZ, Laura MARINCAS, Raluca-Anca MEREU, Judith MIHÁLY, Judit PAPP, Melinda SIMON-VÁRHELYI, Róbert TÖTÖS, Maria TOMOAI-COTIȘEL, Synthesis of Pt(II)-Complexes With Symmetrical and Unsymmetrical Glyoximes, Their Physical-Chemical and Biological Study.....	315
Carmen SACALIS, Sara JAHIJ, Alexandra AVRAM, Synthesis and Investigations of γ -L-Glutamyl-Cyclohexyl Amide and Its Transition Metal Complexes	337
Sorin HODISAN, Ramona POP MAGHIAR, Alina GROZE, Mariana GANEA, Oana STANASEL, Characterisation of <i>Origanum Vulgare</i> Extracts	353

Studia Universitatis Babes-Bolyai Chemia has been selected for coverage in Thomson Reuters products and custom information services. Beginning with V. 53 (1) 2008, this publication is indexed and abstracted in the following:

- Science Citation Index Expanded (also known as SciSearch®)
- Chemistry Citation Index®
- Journal Citation Reports/Science Edition

I n M e m o r i a m

**Prof. Teodor Hodişan Ph.D.
1942 - 2012**



Professor Teodor Hodisan graduated the Faculty of Chemistry of "Babeş-Bolyai" University from Cluj-Napoca in 1966 and was assigned as a scientific researcher at the Institute of Chemistry of the Romanian Academy from Cluj-Napoca. On February 1, 1968, he was appointed by competition as an assistant at the Department of Analytical Chemistry, Faculty of Chemistry, "Babeş-Bolyai" University in Cluj-Napoca. Afterwards, he ascended through all the steps of the university hierarchy: lecturer (1975), associated professor (1990) and professor (1997). In 1973, he defended his doctoral thesis under the scientific supervision of the renowned emeritus scientist Prof. Docentus Candin Liteanu.

From the beginning he worked under the guidance of eminent professor Candin Liteanu in the field of analytical chemistry, specialization chromatographic analysis, a field in full expansion at that time. Thus, the research directions approached were focused on the development and application of chromatographic methods and he became a follower of the illustrious professor, managing to preserve the reputation of the Cluj chromatography school along with his colleague Prof. Simion Gocan.

The research carried out resulted in the elaboration, as author or co-author, of 8 published books and 2 treatises on chromatographic analysis. He elaborated a number of 80 scientific works, published in renowned journals from the country and abroad. He was co-author of 3 invention patents and 5 innovator certificates. He participated in most of the analytical chemistry scientific events organized in the country as well as abroad.

He participated to the finalization of 10 scientific research contracts with various industrial and research units, as grant director or co-participant, in the field of liquid chromatography.

He guided numerous students in the preparation of their doctoral theses and contributed to the training of many researchers and teaching staff members.

During the period 2002-2007, he was the head of the Analytical Chemistry department. Also, he was a member of the Analytical Chemistry Society, and he was the president of this society, Transylvanian subsidiary between 1992 and 1994.

The research carried out by professor Hodisan became a fundamental basis for many of us who are currently working in the field of chromatography and in the name of all colleagues who had the opportunity to work along with

him, I want to address my special thanks for everything he did and for imparting inspirations with a positive impact on our scientific careers.

22.12.2022

Prof. dr. Claudia Cimpoiu
"Babeş-Bolyai" University
Faculty of Chemistry and Chemical Engineering

A COST-EFFECTIVE AND RAPID METHOD BASE ON HIGH-PERFORMANCE THIN-LAYER CHROMATOGRAPHY IN EVALUATING THE ROASTED COFFEE ADULTERATION

Anamaria HOSU^{a,b}, Claudia CIMPOIU^{a,b,*}

ABSTRACT. Coffee is rich in phytochemicals that give its fingerprint and differentiate it from other plant based food. Due to its widespread use and high cost price, it happens that some manufacturers counterfeit it with various additions of cheaper products. This study exhibits a new approach in evaluating of roasted coffee based on high-performance thin-layer chromatography (HPTLC) method. The separation of compounds was performed on silica gel 60 F254 HPTLC plates using a mixture of chloroform – methanol – acetonitrile, 6 : 1.5 : 2.5 v/v/v as mobile phase. The images of the plate were statistically analysed in order to find the most representative featurings for each samples.

Keywords: coffee, adulteration, HPTLC, UV-Vis spectrophotometry, chicory, soybean, wheat

INTRODUCTION

Together with tea, coffee is the most important beverage worldwide, with great social and commercial importance. Also, from an economic point of view, coffee is the most traded and valuable product worldwide after oil [1]. Despite being consumed in large quantities, coffee is still quite expensive compared to other food products found in the market. Due to its high price, various cheaper substitutes have been added to it over the years, especially

^a Babeş-Bolyai University, Faculty of Chemistry and Chemical Engineering, 11 Arany Janos str., RO-400028, Cluj-Napoca, Romania

^b Research Center for Advanced Chemical Analysis, Instrumentation and Chemometrics, 11 Arany Janos, 400028 Cluj-Napoca, Romania

* Corresponding author: claudia.cimpoi@ubbcluj.ro



to the ground coffee. Theoretically, any plant material that contains sufficient soluble carbohydrates has the potential to be added to coffee [2]. The main materials with which coffee is adulterated are roasted and unroasted coffee pods, twigs, barley, soy, wheat, chicory, malt, starch, corn, maltodextrins, glucose syrup and caramelized sugar [3].

Visually, a difference cannot be made between genuine and counterfeit coffee, which is why several analytical methods have been developed in order to detect counterfeit coffee. The modern methods of evaluating fakes have replaced the old organoleptic and empirical tests and are constantly updated because food falsification is carried out constantly and new problems always appear. Thus, techniques such as mid-infrared Fourier transform spectroscopy (FT-MIR) technique [4], high-performance liquid chromatography (HPLC) [5], mass spectroscopy, gas chromatography, capillary electrophoresis [6] are used. All these techniques are sensitive and precise, but they need the sample preparation that can be take extremely large time and also, they can be performed only by trained personnel. That is why we considered that using thin-layer chromatography (TLC) can be a quick and simple alternative.

The objective of this paper is to develop a new cheap and fast method for the evaluation of the adulteration of coffee.

RESULTS AND DISCUSSION

To see the differences between the coffee samples and the chicory, soy and wheat samples, first the UV-Vis spectra of the extracts were recorded. These spectra are shown in Figure 1.

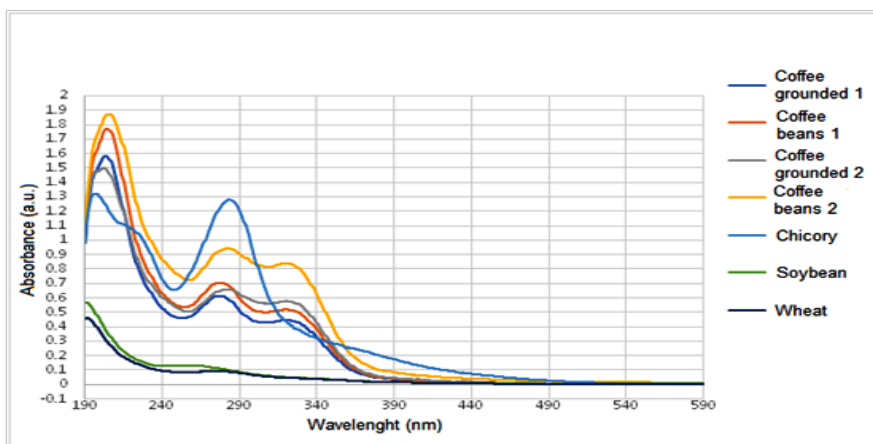


Figure 1. UV-Vis spectra of extracts.

As can be seen from figure 1, in the spectra of coffee extracts there are two absorption maxima at 275 nm and 320 nm, of which the one corresponding to the wavelength of 275 nm is that of caffeine [7]. It is found both in the case of producer 1 and producer 2 that the grounded coffee extracts contain less caffeine than those obtained from coffee beans. Also, the extracts of coffee from producer 2 contain more caffeine than those from producer 1. In the chicory extract there is a single absorption maximum at 280 nm, which is not caffeine because it is known that chicory does not contain this compound. Soy and wheat extracts show a weak absorption in UV-Vis. Taking into account the mentioned, it can be concluded that only on the basis of UV-Vis spectra it is not possible to estimate if coffee samples is or not counterfeit.

In the second step, the high-performance thin-layer chromatography (HPTLC) separation of the compounds from the extracts was attempted and also the possibility of finding specific markers. In order to optimize the separation of compounds several mobile phase systems presented in Table 1 were tested.

Table 1. The tested mobile phase systems

No.	Mobile phase solvents	Composition (v/v/v)	Reference
1	chloroform – diclormethane – <i>i</i> -propanol	4 : 2 : 1	
2	<i>i</i> -propanol – methyl-ethyl-cetone – chloroform	1 : 3 : 1	
3	<i>n</i> -hexane – acetone	37 : 13	
4	<i>n</i> -buthyl-acetate – ethyl-acetate – methanol – water	5 : 4 : 1 : 0.1	
5	toluene – ethyl-acetate	9 : 2	[8]
6	chloroform – methanol	8.5 : 1.5	[9]
7	<i>n</i> -hexan – ethyl-acetate	7 : 3	[10]
8	dichlormetane – ethyl-acetate	4 : 1	[11]
9	chloroform – ethylic ether	2 : 1	[12]
10	chloroform – methanol	4 : 1	[13]
11	ethyl-acetate – methanol	9 : 1	[14]
12	petroleum ether – acetone	9 : 1	[14]
13	<i>n</i> -hexan – ethylic ether – ethyl-acetate	1 : 1 : 1	[15]
14	toluen – ethyl-acetate – methanol	40 : 9 : 1	[16]
15	chloroform – acetonitrile	3 : 2	[17]
16	ethylic ether – petroleum ether	1 : 9	[18]
17	chloroform – methanol – acetonitrile	6 : 1.5 : 2.5	

With the exception of mobile phases 6 and 15, all systems proved unsuitable for the separation of the target compounds in order to obtain relevant information about the presence of the alleged adulterants.

Mobile phases 6 and 15 provided satisfactory separation, so a new solvent system was tested as a combination of these two mobile phases, namely system 17.

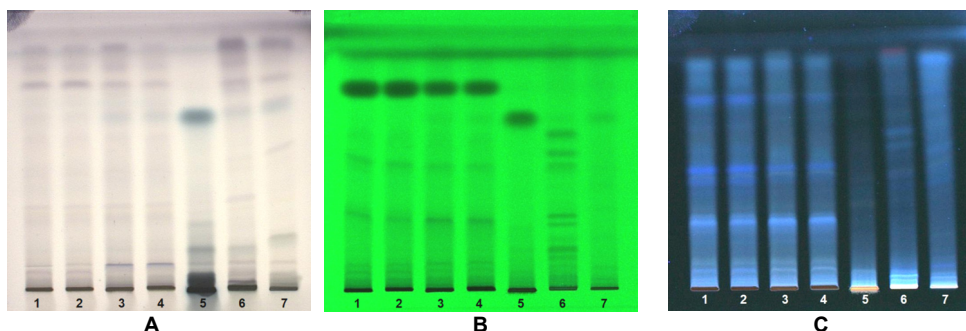


Figure 2. The image of the plate in: A - visible light after spraying with vanillin- H_2SO_4 solution; B – UV light at 254 nm and 366 nm: 1- Coffee grounded 1; 2 - Coffee beans 1; 3 - Coffee grounded 2; 4 - Coffee beans 2; 5 – Chicory; 6 – Soybean; 7 – Wheat

The only image in the visible light that provides adequate information is that of the plate sprayed with vanillin- H_2SO_4 solution (Figure 2A).

The last three purple bands from the upper part of the plate visible in the coffee samples are also observed in soy and wheat samples, indicating the presence of the same or similar compounds. Also, an intense blue-green coloured compound can be observed in the chicory sample, which is less visible in the soybean and wheat samples, but also in both coffee samples from producer 2. At $R_f = 0.31$ a violet-coloured compound is observed in both coffee and soy samples, at $R_f = 0.15$ there is a green band in chicory and soy samples, and at $R_f = 0.1$ a characteristic violet band is observed chicory, soy and wheat samples. However, this information is not enough for the detection of a possible counterfeit, thus the images of the plates obtained in UV light must also be analyzed in order to obtain more information.

By examining the image of the plate without derivatization under UV light at 254 nm (Figure 2B), the appearance of additional bands for soy is observed. At $R_f=0.47$, one compound is observed in all four coffee samples and in soy, and the compounds that appear in coffee at the bottom of the plate are also present in chicory and wheat. On the other hand, the cereal compounds supposed to belong to the coffee samples are not visible here

and therefore it can be stated that they are different from those present in coffee. The image of the plate in UV light at 366 nm confirms the information obtained from the other images.

In order to better highlight the differences between the fingerprints of the coffee, chicory, soybean and wheat samples and to reveal their significant contribution in samples characterization, the statistical analysis of the digitized images was carried out using Principal Component Analysis (PCA) with Varimax orthogonal rotation of factor axes. Thus, following this analysis, it was found that the R_f domains that explain a maximum amount of variance for the analyzed samples are: 0.01-0.07; 0.22-0.29; 0.47-0.49 for coffee; 0.07-0.67; 0.71-1.00 for chicory; 0.14-0.17; 0.67-1.00 for soybean and 0.00-0.05; 0.07-0.08; 0.80-0.82; 0.88-0.94 for wheat. It is observed that there are zones of retention factor that are specific to each sample and that can make the difference between coffee samples and possible adulterants.

CONCLUSIONS

This work led to the development a new cost-effective and fast method for the evaluation of the adulteration of coffee proving that the HPTLC with statistics analysis could be used to detect the adulterants in coffee.

The developed method can be used for quality control both in the food industry and the product sales market.

The development of the method taking into account other common like husks, barley and sticks adulterants is advised in order to enlarge the method for all adulterants. Also, future research may concentrate on detection more than one adulterant as the coffee may be generally counterfeit with.

EXPERIMENTAL SECTION

Materials and chemicals

All reagents and solvents were purchased from Merck (Darmstadt, Germany) and were of analytical purity. The coffee, soybeans, whole wheat and chicory were purchased from a local store.

Samples preparation

First, the soybeans and wheat were roasted to a very dark coffee-like color. Then, all materials were grounded and 1g of each was mixed with 10ml of ethanol 80%. The samples were macerated for 14 days, filtered and kept in the refrigerator until they were analyzed.

Spectrophotometric analysis

The absorption spectra of each sample were recorded in the wavelength range between 190 and 900 nm using a T80+ double beam spectrophotometer (PG Instruments Limited). The samples were diluted 400 times before the UV-Vis spectrophotometric analysis.

Thin-Layer Chromatographic analysis

The chromatographic analysis was carried out on HPTLC glass plates, with silica gel 60F₂₅₄, 10x10 cm, using different solvent mixtures as mobile phases. The elution of the plates was carried out at room temperature in a chromatographic chamber (Camag) presaturated with the mobile phase for 30 minutes. Aliquotes of 10 µL of each coffee sample, 5 µL of the chicory sample and 20 µL each of the soy and wheat samples were applied to the chromatographic plate using a semi-automatic applicator (Linomat 5, Camag) as bands of 8 mm, at a distance of 15 mm from the base of the plate and 13 mm from the left edge, with a flow rate of 40 nL/s. After elution the plate was heated to 110 °C for 20 minutes and then was immersed for 2 seconds in the solution of ethanolic solution of vanillin and sulfuric acid (10%). Visualization of the compounds was performed in visible light and in UV light at 254 nm and at 366 nm using the Reprostar 3 (Camag) visualization device.

Statistical analysis

In order to reveal characteristic zones of retention that differentiate coffee samples from adulterants, the Factor Analysis method with Varimax rotation algorithm was applied on data matrix from digitized images of the chromatographic plate using the Statistics 11.0 software package (StatSoftinc., USA).

REFERENCES

1. D.S. Dominguez; E.D. Pauli; J.E. M. Abreu; F.W. Massura; V. Cristiano; M.J. Santos; S.L. Nixdorf; *Food Chem.*, **2014**, *146*, 353-362.
2. A.I. Ruiz-Matute; A. Montilla; M.L. Sanz; I. Martinez-Castro, M.D. Castillo; *J. Sep. Sci.*, **2007**, *30*, 557-562.
3. H. Ebrahimi-Najafabadi; R. Leardi; P. Olivieri; M.C. Casolino; M. Jalali-Heravi; S. Lanteri; *Talanta*, **2012**, *99*, 175-179.
4. M. Flores-Valdez; O.G. Meza-Márquez; G. Osorio-Revilla; T. Gallardo-Velázquez; *Foods*, **2020**, *9*, 851-861.

5. D.S. Domingues; E.D. Pauli; J.E.M. de Abreu; F.W. Massura; V. Cristiano; M.J. Santos; S.L. Nixdorf; *Food. Chem.*, **2014**, *146*, 353-362.
6. A. Th. Toci; A. Farah; H. Redigolo Pezza; L. Pezza; *Crit. Rev. Anal. Chem.*, **2016**, *46*, 83–92.
7. U.T.C.P. Souto; M.J.C. Pontes; E.C. Silva; R.K.H. Galvão; M.C.U. Araújo; F.A. C. Sanches; F.A.S. Cunha; M.S.R. Oliveira; *Food Chem.*, **2010**, *119*, 368-371.
8. B. Chengaiah; B. Pratap; M. Alagusundaram; M. Ruthu; V. Sarovar Reddy; *60th Indian Pharmaceutical Congress*, **2008**, PA-221.
9. R. Aeschbach; A. Kusy; H. Maier; *Z. Lebensm. Unters. Forsch.*, **1982**, *175*, 337-341.
10. Y. Roisin, J.M. Pasteels; J.C. Braekman; *Biochem. Syst. Ecol.*, **1987**, *15*, 253-261.
11. J.E. Thompson; P.T. Murphy; P.P. Bergquist; E.A. Evans; *Biochem. Syst. Ecol.*, **1987**, *15*, 595-606.
12. K. Nie; W. An Wijian; L. Xia; *Chinese J. Herb Med.*, **1994**, *25*, 539-541.
13. P.J. Houghton, I.M. Said; *Phytochemistry*, **1986**, *25*, 2910-2912.
14. H. Achenbach; H. Hemrich; *Phytochemistry*, **1991**, *30*, 1957-1962.
15. L.A.C. Pieters; A.J. Vlietinck; *J. Nat. Prod.*, **1989**, *52*, 186-190.
16. F. El Babili; C. Moulis; M. Bon; M.J. Respaud; I. Fouraste; *Phytochemistry*, **1998**, *48*, 165-169.
17. E.A. Sattar; J.S. Mossa; I. Muhammad; F.S. El-Faraly; *Phytochemistry*, **1995**, *40*, 1737-1741.
18. U. Warning; F. Bohlmann; R.M. King; L. Haegi; *J. Nat. Prod.*, **1988**, *51*, 513-516.

DERIVATIZATION OF ROSUVASTATIN AS METHYL ESTER FOR ITS ANALYSIS BY GAS CHROMATOGRAPHY-MASS SPECTROMETRY IN PLASMA

Cristian Ionuț CIUCANU^{a,*}, Ionel CIUCANU^{b,*}, Sorin OLARIU^a

ABSTRACT. A new analytical procedure for rapid and selective derivatization of rosuvastatin directly in plasma into their corresponding methyl esters was developed for gas chromatography-mass spectrometry analysis. This work is the first method of selective derivatization of the carboxyl group from rosuvastatin to methyl ester. The lipids from plasma were extracted with heptane before derivatization. The methyl esters were obtained by reaction with methyl iodide in solution of dimethyl sulfoxide and in the presence of anhydrous potassium carbonate. The optimal conditions for selective methylation have been established. The derivatization was carried out in 2 min. The method was validated for the analysis of rosuvastatin in plasma. The methyl ester of rosuvastatin was identified by electron ionization mass spectrometry. The electron ionization mass spectrometer detector response was linear up to 300 ng/mL. The limit of detection and limit of quantification values in total ion chromatogram method were 0.4 ng/mL and 1.2 ng/mL, respectively.

Keywords: *Rosuvastatin, Plasma, Methyl esterification, Gas chromatography-mass spectrometry analysis.*

INTRODUCTION

Rosuvastatin is among the most effective anti-atherosclerotic drugs with a strong impact on cardiovascular diseases [1].

^a *University of Medicine and Pharmacy “Victor Babes” of Timișoara, Faculty of Medicine, Piața Eftimie Murgu 2, RO-300041, Timișoara, Romania*

^b *West University of Timisoara, Faculty of Chemistry, Biology, Geography, 16th Pestalozzi Street, 300115, Timișoara, Romania*

* *Corresponding authors: ciucanu.cristian@gmail.com; ionel.ciucanu@gmail.com*



Usually, the analysis of rosuvastatin in biological fluids was performed by liquid chromatography with a detector in the ultraviolet range [2], or in fluorescence [3] or by mass spectrometry (MS) [4]. Some liquid chromatographic (LC) analysis has many drawbacks such as low sensitivity, narrow linearity ranges, high sample volume, and expensive automated extraction procedure. Gas chromatography (GC) has been less used in the separation of statins, due to their high boiling points, which leads to a derivatization reaction to increase their volatility. However, the advantages of GC–MS analysis are a high sensitivity and selectivity to determine rosuvastatin in plasma. GC analysis of statins was performed without derivatization [5] or as silylated derivatives [6,7]. Rosuvastatin has not yet been derivatized as methyl ester for GC analysis.

Quantitative analysis of rosuvastatin from plasma is strongly influenced by the presence of proteins and plasma lipids. Proteins can retain uncontrolled amount of drug and a high content of plasma lipids give unwanted peaks and a high background noise. The matrix effects are very evident in plasma samples from patients with high lipid levels [8]. Consequently, in both LC and GC analysis, sample preparation prior to analysis for protein solubilization and lipid elimination are important steps to avoid these disadvantages. Liquid-liquid extraction with different organic solvents could be a solution, because organic solvents generate precipitation and they extracted also plasma lipids. Chloroform, ethyl acetate, n-hexane, dichloromethane, n-hexane-dichloromethane-isopropanol (20:10:1, v/v/v) was investigated and ethyl acetate was found with no-concentration-dependent extraction recovery and acceptable matrix effect [9]. A mixture of chloroform–methanol has been widely used to extract lipids from different tissues and biological fluids, dichloromethane–methanol and methyl-tert-butyl ether–methanol solvent mixtures have also been reported as good solvents for lipid extraction that provide equivalent lipid recoveries [10]. However, rosuvastatin is slightly soluble in these solvents.

Solid phase extraction may have a higher selectivity for plasma lipids. Both cation and anion exchange resins have been used to retain lipids [8], but they will also retain rosuvastatin because it has a carboxylic group. Solid phase extraction on hydrophobic-lipophilic balanced copolymer sorbent [11] retains non-polar lipids.

The aim of this work is a selective derivatization of rosuvastatin as methyl ester in plasma for GC analysis. The work has a novelty value because it is the first method of derivatization of rosuvastatin in its methyl ester for GC-MS analysis. The method has the advantage that it requires less expensive equipment compared to liquid chromatography coupled with mass spectrometry.

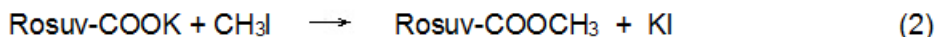
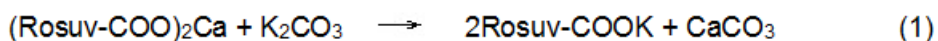
RESULTS AND DISCUSSION

Rosuvastatin is a synthetic drug administered as calcium salt. Rosuvastatin molecules are taken up by albumin, up to the saturation of the sites available for this purpose. Rosuvastatin molecules are released more easily from albumin when the albumin is solubilized in the reaction solvent. Among the dipolar aprotic solvents, dimethyl sulfoxide has the highest solubilizing power of albumin [12].

The esterification of rosuvastatin with methyl iodide is a nucleophilic substitution [13]. The main reactions that occur during the esterification of rosuvastatin with methyl iodide (CH_3I) and solid K_2CO_3 are shown in the Scheme 1.

The direct reaction between the calcium salt of rosuvastatin and methyl iodide does not lead to methyl esters. For this reason, calcium salt is transformed into potassium salt by adding solid potassium carbonate.

The first step is the dissolution of the solid K_2CO_3 in dimethyl sulfoxide. The solubility of K_2CO_3 in dimethyl sulfoxide is very low (47 g/L). However, the dissolved K_2CO_3 is consumed in this reactions with rosuvastatin (Eq. 1), but is continuously replaced by the dissolution of the solid base. Finally, the rosuvastatin anion will react with methyl iodide and will generate methyl esters (Eq. 2). Anhydrous powder of K_2CO_3 is hygroscopic was also used in this method for the purpose of retaining water from the system. For this reason, potassium carbonate was used in molar excess up 40 compared to rosuvastatin. The volumetric excess of methyl iodate was up to 10.



Scheme 1: The main reactions of the esterification process

Studies under certain stress conditions have shown that rosuvastatin is stable in the presence of bases and degrades in an acidic environment as well as in heat [14]. Therefore, performing the reaction in a weak basic medium of K_2CO_3 and at room temperature avoids possible degradation reactions.

The injection of methylated products may introduce small amounts of plasma lipids into the injector port. Proteins and other polar compounds were partially retained on solid K_2CO_3 . In order to avoid this contamination, the capillary column must be protected with a guard capillary column.

Figure 1 shows the GC–MS total ion chromatogram. The chromatographic peaks have a symmetrical shape.

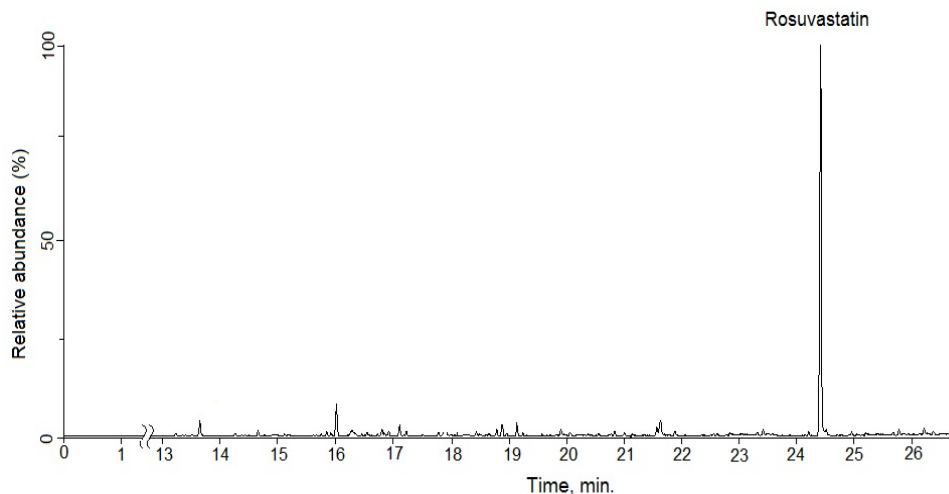


Figure 1. GC–MS total ion chromatogram of rosuvastatin as methyl ester into a plasma sample. Chromatographic and mass spectrometric conditions are given in the Experimental section.

Figure 2 shows the electron ionization (EI) mass spectrum of rosuvastatin methyl ester. The methyl ester of rosuvastatin was identified based on the molecular ion (M^+) at m/z 495 and the characteristic fragment ions. The fragment ions at m/z 463 and m/z 459 are generated by the loss of one methanol molecule and two water molecules respectively from the molecular ion. The fragment ion at m/z 445 may result from the m/z 463 ion due to the loss of a water molecule. The ion at m/z 421 may be the McLafferty rearrangement ion at the methyl ester group in the hydrocarbon chain. The fragment ion at m/z 403 may represent the expulsion of a water molecule from m/z 421. The fragment ions at m/z 392, m/z 378, m/z 348, and m/z 322 may result from the cleavage of the C–C bonds from the hydrocarbon chain with the carboxylic methyl ester group. Thus, for example, the ion at m/z 392 results from the cleavage between C3 and C4. One pathway for the formation of the base ion at m/z 258 may be the elimination of a sulphur dioxide molecule from the ion at m/z 322.

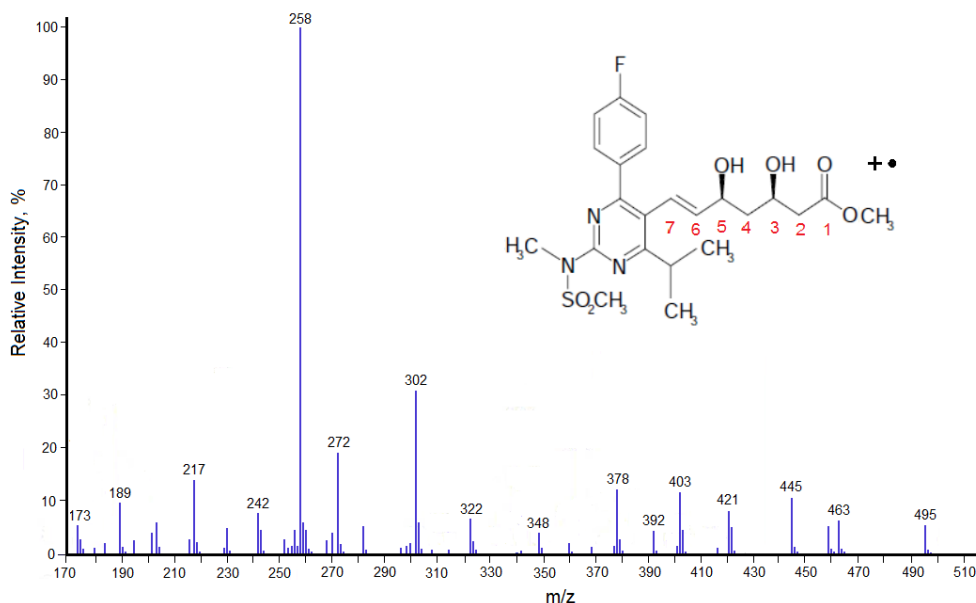


Figure 2. Electron ionization spectrum and chemical structure of rosvastatin methyl ester.

Quantitative evaluation in this method was performed by the internal standard method [15], using anthracene a standard, which is not affected in the derivatization process. The MS detector response was linear up to 300 ng/mL. The limit of detection (LOD) and limit of quantification (LOQ) values in TIC method were 0.4 ng/mL and 1.2 ng/mL, respectively. The accuracy was tested by adding 6 ng/ μ L, 30 ng/mL and 60 ng/mL of rosvastatin into the sample. The average recovery values ($n = 5$), expressed as mean \pm standard deviation (SD), were 98.2 ± 1.2 ; 98.8 ± 0.9 ; and 99.3 ± 0.5 , respectively.

CONCLUSIONS

This paper provides a sensitive and selective method for the derivatization of rosvastatin as a methyl ester for GC analysis. The methyl ester of rosvastatin was identified by mass spectrometry based on molecular ion and characteristic fragment ions. The proposed method was optimized and validated. This work is the first derivatization method of the carboxylic group from rosvastatin to methyl ester. The derivatization was

performed in 2 min. The lipids from plasma were extracted three times with heptane before derivatization. Dimethyl sulfoxide was used because it proved to be the best reaction medium, but also because it is very good for releasing rosuvastatin from plasma albumin. The method is simple and fast and can have applications in monitoring the concentration of rosuvastatin in plasma in patients with atherosclerosis [16] that can affect different organs.

EXPERIMENTAL SECTION

Standards and reagents

Rosuvastatin calcium salt ($\geq 98\%$) and anthracene (internal standard) were from Sigma-Aldrich (MO, USA). Methyl iodide, dimethyl sulfoxide (DMSO), chloroform, dichloromethane, potassium carbonate, heptane, and molecular sieves were purchased from Merck (Darmstadt, Germany). All reagents were analytical grade. The potassium carbonate powder was dehydrated by heating at 200°C and then stored in an airtight system to prevent the contact of the powder with moisture.

Collection and storage of blood sample

This study compiled the Declaration of Helsinki regarding the ethical principles for medical research and was approved by the Ethics Committee of the Scientific Research of the University of Medicine and Pharmacy Timisoara. All participants gave written informed consent. The blood sample was taken into commercially available anticoagulant-treated tubes by antecubital venipuncture after at least 12 h of fasting and was immediately centrifuged at $1500\times g$ at room temperature for 10 min. The plasma was apportioned into single use aliquots, which were then stored at -70°C until analysis.

Statistical analysis

Microsoft Excel 2016 (Microsoft Corp. USA) and Statistical Test Calculator online version 2018 from Social Science Statistics (<https://www.socscistatistics.com/tests/>) were used for statistical analyses.

Derivatization method of rosuvastatin as methyl ester

The methylation reactions were carried out in 2 mL glass vials with silicone septa lined screw caps. An aliquot of plasma sample (200 μL) was introduced with a chromatographic syringe into the glass vial with 0.5-1.0 mL of dimethyl sulfoxide. Rosuvastatin was dissolved in dimethyl sulfoxide and

was added to the sample. Anhydrous powder of potassium carbonate salt (40 mg) was added to the sample solution and was vortexed for 2 min at room temperature. After the addition of a volume of 0.5 mL of heptane, the mixture was vortexed a few seconds and the heptane layer was removed with a syringe. This lipid extraction step was repeated three times.

Then methyl iodide (10 μ L) was added and the glass vial was vortexed at room temperature (20°C) for 2 min. Methylation was performed without inert gas atmosphere or special drying conditions. Rosuvastatin methyl ester was extracted with chloroform (3x0.5 mL). The extraction solvent can be evaporated under nitrogen flow and the dried residue containing rosuvastatin methyl ester was re-dissolved in dichloromethane for GC injection.

Instrumentation

All GC–MS analyses were carried out on a gas chromatograph that had installed both a FID detector and a mass spectrometer model Varian 450 GC 240 MS Ion Trap (Agilent, CA, USA). A Varian Workstation software was used for data acquisition and processing. The GC was equipped with HP-1 fused silica capillary column from Hewlett-Packard (SUA) with 30m length, 0.25mm internal diameter, and 0.25 μ m polydimethylsiloxane cross-bonded film. The capillary column was protected by contaminants with a guard capillary column (5 m length and 0.25 mm inner diameter). A split/splitless injector was used in split mode with a split ratio of 50:1. Sample injection was splitless for 1.0 min. The GC inlet linear had a plug of silylated glass wool for improving the vaporization and for the protection of the capillary column. The carrier gas was high-purity helium at a flow rate of 1 ml/min. The GC oven temperature was started from 120°C and then increased to 270°C with 30°C/min and kept for 20 min. After that, the temperature was increased at 50°C rate to 310°C and kept at the final temperature for 5 min. The temperature of the injector was set to 300°C. The transfer line temperature was 280°C. The temperature of the ion source was set to 220°C. The mass spectra were recorded in the positive-ion electron impact ionization mode in the scan range m/z 50–600. The energy of the emitted electrons was 70 eV and was turned off for the first 3 min of the chromatographic run to avoid filament damage during sample analysis. Chromatograms were assessed in total ion current mode for both qualitative and quantitative analyses.

REFERENCES

1. C.I. Ciucanu; S. Olariu; D.C. Vlad; V. Dumitrașcu; *Medicine*, **2020**, *99*, e23356.
2. Y. Shah; Z. Iqbal; L. Ahma; A. Khan; M.I. Khan; S. Nazir; F. Nasir; *J. Chromatogr. B*, **2011**, *879*, 557–563.
3. S. Caglar; S. Toker; *J. Chromatogr. Sci.*, **2013**, *51*, 53–58.
4. M.S. Elgawish; M.K. Soltan; M.M. Sebaiy; *J. Pharm. Biomed. Anal.*, **2019**, *174*, 226–234.
5. E. Kublin; E. Malanowicz; B. Kaczmarek-Graczyk; K. Kzerwiska; E. Wyszomirska; A.P. Mazurek; *Acta Poloniae Pharm. - Drug Res.*, **2015**, *72*, 429-437.
6. M.J. Morris; J.D. Gilbert; J.Y. Hsieh; B.K. Matuszewski; H.G. Ramjit; W.F. Bayne; *Biol. Mass Spectrom.*, **1993**, *22*, 1-8.
7. H. Sirén; L. Kajjanen; S. Kaartinen, M. Väre; P. Riikonen; E. Jernström; *J. Pharm. Biom. Anal.*, **2014**, *94*, 196–202.
8. O.A. Ismaiel; T. Zhang; R.G. Jenkins; H.T. Karnes; *J. Chromatogr. B*, **2010**, *878*, 3303–3316.
9. D. Zhang; J. Zhang; X. Liu; C. Wei R.; Zhang; H. Song; H. Yao; G. Yuan; B. Wang; R. Guo; *Pharmacol. Pharm.*, **2011**, *2*, 341–346.
10. V. Matyash; G. Liebisch; T.V. Kurzchalia; A. Shevchenko; D. Schwudke; *J. Lip. Res.*, **2008**, *49*, 1137-1146.
11. C.K. Hull; P.D. Martin; M.J. Warwick; E. Thomas; *J. Pharm. Biomed. Anal.*, **2004**, *35*, 609–614.
12. G. Houen; *Acta Chim. Scand.*, **1996**, *50*, 68-70.
13. C.I. Ciucanu; D.C. Vlad; I. Ciucanu; V. Dumitrașcu; *J. Chromatogr. A*, **2020**, *1624*, 461259.
14. A. Khedr; F. Belal; F. Ibrahim; T. Elawady; *Anal. Methods*, **2013**, *5*, 6494-6502.
15. I. Ciucanu; L. Pilat; C.I. Ciucanu; E. Șișu; V. Dumitrașcu; *Bioanalysis*, **2016**, *8*, 2147–2156.
16. C.I. Ciucanu; S. Olariu; D.C. Vlad; V. Dumitrașcu; *Biochem. Biophys. Rep.*, **2020**, *24*, 100822.

PRODUCTION OF RECOMBINANT, NON-TAGGED PHENYLALANINE AMMONIA-LYASES EMPLOYING TEV PROTEASE-REMOVABLE AFFINITY TAGS

Alina FILIP^{a,*}, Zsófia BATA^{b,c}, Anca Elena ANGHEL^a,
László POPPE^{a,b}, László Csaba BENCZE^{a,*}

ABSTRACT. Nowadays, protein purification by the aid of affinity tags can be carried out with high speed and efficiency. However, in several cases, affinity tags can significantly alter the key properties of enzymes, especially activity and/or thermostability.

This study focused on the purification of the non-tagged phenylalanine ammonia-lyase from *Petroselinum crispum* (PcPAL), as well as on the purification of the TEV (Tobacco Etch Virus) protease, the molecular scissors used to remove the affinity tag from the recombinantly expressed PcPAL. Removal of the 6xHis-tag led to a 1.5-fold increase in the specific activity of PcPAL, while the absence of the affinity tag did not significantly alter the thermostability of the protein. The purity and oligomerization state of the proteins of interest were also analyzed by size exclusion chromatography, both before and after the removal of the affinity tag, confirming the stability of the tetrameric fold of PcPAL.

Keywords: *affinity tags, phenylalanine ammonia-lyase, TEV (Tobacco Etch Virus) protease, thermostability, specific enzyme activity, oligomerization state.*

^a *Enzymology and Applied Biocatalysis Research Center, Faculty of Chemistry and Chemical Engineering, Babeş-Bolyai University of Cluj-Napoca, Arany János str. 11, 400028, Cluj-Napoca, Romania*

^b *Department of Organic Chemistry and Technology, Budapest University of Technology and Economics, Műegyetem rkp. 3, 1111, Budapest, Hungary*

^c *Institute of Enzymology, ELKH Research Center of Natural Sciences, Magyar tudósok krt. 2, 1117, Budapest, Hungary*

* *Corresponding authors: alina.filip@ubbcluj.ro, laszlo.bencze@ubbcluj.ro*



INTRODUCTION

The isolation and purification of recombinant proteins has never been easier than after the discovery of the various affinity labels, developed by the collaboration of genetic and protein engineering. Tagging the protein of interest mainly consists of insertion—at one of the two ends of the corresponding open reading frame—of the specific codons encoding the future amino acid label. A wide variety of affinity tags has been developed, with different functions/roles and of variable lengths, such as MBP, GST, FLAG or His-tag, with either *N*- or *C*-terminal positioning [1-5], demonstrating their importance in the field of recombinant protein technologies.

Beyond their high importance in the purification procedures of recombinant proteins, tags might serve further goals. For example, artificial polypeptide tags have been shown to convey specific influence on solubility [2,6,7], stability and thermostability [8-10], expression yields, folding of the proteins, enzyme activity [10-12], as well as on protein-protein interactions, and protein crystallization processes [11,13,14].

Among the multitude of available affinity tags, the most widely known and employed one is the polyhistidine affinity tag, consisting of a sequence of 5-10 histidines (most often hexa- or deca-histidine (6xHis- or 10xHis-tag, respectively)) [10,13,15]. In the purification process, after the cell lysis step, the tagged protein is purified by the metal affinity chromatography method (IMAC), using a column filled with agarose support, modified with nitrilotriacetic acid function at the surface, which allows the formation of coordinative bonds with metal ions (Fe^{2+} , Co^{2+} , Ni^{2+} , Cu^{2+} , Zn^{2+}). The imidazole moieties of the histidines in the His-tag further coordinate the immobilized metal ions [15-18]. While the binding efficiency is high, especially at neutral pH, the fused proteins can be smoothly eluted by imidazole solutions of elevated concentrations [18,19]. Besides ensuring a high purification yield, the 6(10)xHis-label also excels in its small size (~2.5 kDa), low toxicity, and the ability to function both as acid and as base through its nucleophilic imidazole moieties. Furthermore, specific anti-His antibodies are available, allowing immunodetection techniques [20], flow cytometry (FCM) [21], and tracking the expression and even the cellular localization of the His-tagged proteins [22].

However, several studies revealed disadvantages associated with the use of affinity labels. Considering strictly the 6xHis-tag, some key properties (activity and thermostability) of the enzyme of interest have been altered or even enzyme inactivation occurred [6,10]. As an example, in the case of β -lactamase and MtDapB enzymes, the His-tagged proteins have T_m values with 2-3 °C higher than those of the corresponding non-tagged variants [8]. Furthermore, it was found that besides the presence/absence of

the His-tag, the composition of the buffer solution can also influence experiment reproducibility and enzyme specific activity, due to conformational changes, having importance because in several cases the activity measurements of the tagged/non-tagged enzymes have been performed in different buffer systems [23-25]. For some corn-derived proteins, the release/detachment of the His-tag led to protein aggregation and reduced solubility. In this case, attaching the His-tag to a solubilization label (TDX) greatly improved the solubility and expression level of the protein in question [26].

In the case of proteins of thermophilic origin, the effect of the label is even more interesting: while at first sight the difference in T_m (only 1-2 °C) between the tagged and non-tagged protein was not noticeable, within the enzyme refolding process the label seemed to destabilize protein refolding, with practically no observable refolding transition. Not only the reversibility of thermal unfolding was drastically affected, but also the specific activity of the enzyme, which decreased significantly, by 17-fold [9].

His-tags may influence the crystallization of proteins. Although successful crystallizations of His-tagged proteins were widely reported [27,28], the inducibility of octopine dehydrogenase crystallization changed as a function of the length of the His-tag [28]. In other studies, protein crystallization failed in the presence of affinity tags [13,14]. In the case of phenylalanine ammonia-lyases, direct comparison of the enzyme, with and without its His-tag, has not been performed until now, although in the last decade most of the different PALs have been recombinantly expressed with an affinity tag. Recently, the non-tagged *PcPAL* variants showed increased crystallization ability [29].

To obtain non-tagged recombinant proteins—best approaching the native protein sequence—the removal of affinity tags through enzymatic cleavage involving a TEV (Tobacco Etch Virus) protease is mostly employed [2,30].

The TEV protease (EC 3.4.22.44) is an extensively studied enzyme, used in the purification process of affinity-tagged proteins [30,31], due to its ubiquity, leading to the expansion of its application in the field of biotechnology (protease therapeutics, *in vitro* enzymology tests, spectrometry-based proteomics, *in vivo* targeting etc.) [32-35]. To avoid the drawback of its limited solubility, the TEV protease can be co-expressed with an MBP (maltose-binding protein) affinity tag [2,36]. This ~ 29 kDa protease (Nla – nuclear-inclusion-a endopeptidase) utilizing the His⁴⁶-Asp⁸¹-Cys¹⁵¹ catalytic triad [7,37] has a particular selectivity for cleaving at the sequence [ENLYFQ(G/S)], to perform the endoproteolytic cleavage between the Q-G or Q-S amino acid residues [7,38]. Unfortunately, TEV protease is also difficult to isolate, therefore numerous mutations aimed to increase the solubility of the protein and, importantly, to stop the autolysis during purification. The best performing variant, in terms of autolysis prevention, is mutant S219V [7,37bc, 39].

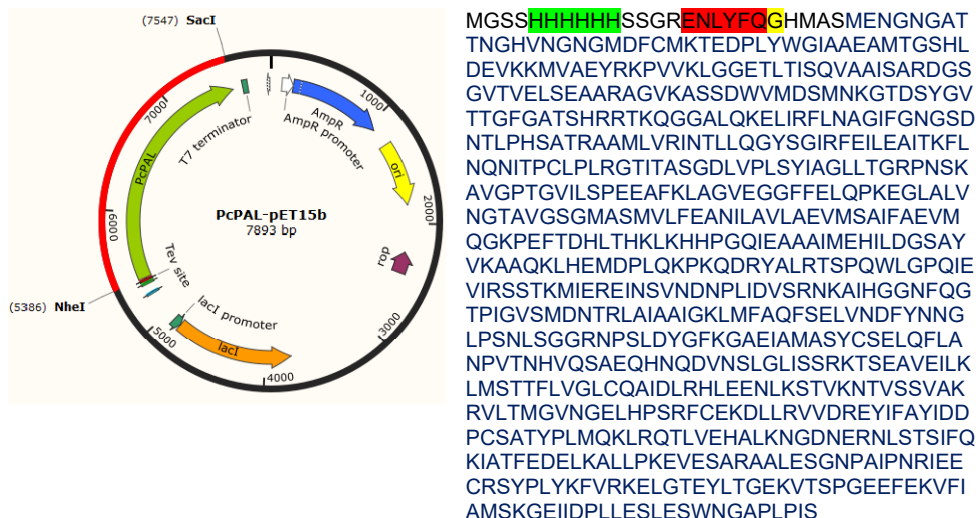
Within this study, we focused on the use of the TEV protease for removing the affinity tag of phenylalanine ammonia-lyase from *Petroselinum crispum* (*PcPAL*), to obtain the non-tagged, recombinant *PcPAL* for comparison to its His-tagged variants. A further goal was to employ the optimized purification protocol of the non-tagged *PcPAL* for the purification/characterization of several mutant *PcPAL* variants with high biocatalytic usefulness. *PcPAL* belongs to the MIO-dependent aromatic ammonia-lyase enzyme family, which catalyze the non-oxidative ammonia elimination from aromatic amino acids to the corresponding α,β -unsaturated acids and/or the reverse ammonia addition to *trans*-cinnamic acid derivatives, to form L-phenylalanine analogues [40]. Among the most studied PALs, *PcPAL* is known to accept a wide range of substrates, while rational/semi-rational protein engineering further extended its substrate scope [27,41]. The engineered PALs provide biotechnologies leading to important building blocks for the pharmaceutical industry [42,43,44]. Furthermore, the optimized His-tag removal procedure can be further applied to the purification of other MIO enzymes, from different organisms (*AtPAL*, *RtPAL*, *AvPAL*, *KkPAL*, *RxPAL*, *TcPAM*, *PaPAM*, *PfPAM*) [19,41], as well as to other enzymes, such as lipases or decarboxylases (*ScFDC1*) [45], subjects of interest within our current research topics.

RESULTS AND DISCUSSION

1. Expression and purification of the hexahistidine-tagged, wild-type and mutant *PcPAL* variants, followed by His-tag removal

While the purification of recombinant enzymes is highly facilitated by the presence of His-tags—generally derived from the expression vector—, their attachment often requires an additional linker sequence of 6-12 amino acids. Thus, the presence of the His-tag and linker might alter enzyme activity/stability or crystallization ability [2,6-12].

The genetic construct used for the purification of the recombinant *PcPAL* is represented by the pET15b-*PcPAL* expression plasmid (Figure 1), which, after IPTG-induced expression in corresponding *Escherichia coli* (*E. coli*) pET15b-*PcPAL* hosts, provided a 741 amino acid, recombinant *PcPAL*, an *N*-terminal 6xHis affinity tag (highlighted in green), and the [ENLYFQG] TEV-protease recognition site. The *N*-terminal sequence additional to the original ORF (open reading frame) of *PcPAL* totals 25 amino acid residues.



Following our optimized expression and isolation procedure of the His-tagged PALs [19,29], the *PcPAL* containing the removable His-tag was successfully obtained (Figure 2), with the highest protein amount eluting from the Ni-NTA affinity column with the 200 mM imidazole solution (Figure 2b, lane 2). At this imidazole concentration, besides the main target protein, two additional proteins of ~15 and 10 kDa were also eluted. Therefore, after a 4-fold concentration step, an additional purification step has been performed by size-exclusion chromatography (SEC), using a Superdex 200 10/300 GL column.

Finally, the solutions containing the affinity tagged *PcPAL* in high purity—the SEC purified fraction, and the fractions eluted with 300 mM and 400 mM imidazole solutions (Figure 2b, lanes 3, 4)—were dialyzed and further subjected to the 6xHis label removal process.

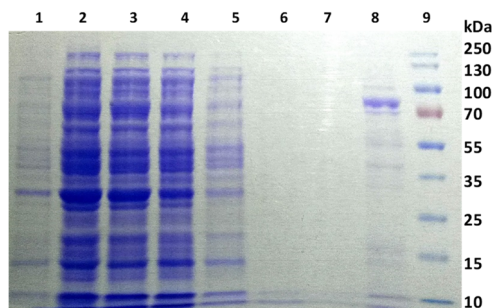


Figure 2a. SDS-PAGE analysis of samples from the purification steps of the affinity-tagged *PcPAL*. **1** – cells before induction, **2** – cells after induction, **3** – supernatant from the cellular lysis step, **4** – flow through – Ni-NTA purification step, **5** – first washing step with low salt solution, **6** – washing step with high salt solution, **7** – second washing step with low salt solution, **8** – fr. 20 mM imidazole, **9** – molecular weight marker.

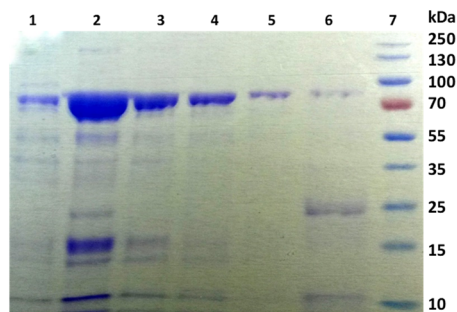


Figure 2b. SDS-PAGE analysis of samples from the optimization of the purification steps of affinity-tagged *PcPAL*. **1** – fr. 50 mM imidazole, **2** – 80 kDa fr. 200 mM imidazole, **3** – fr. 300 mM imidazole, **4** – fr. 400 mM imidazole, **5** – fr. 500 mM imidazole, **6** – fr. 1 M imidazole, **7** – molecular weight marker.

fr. = fraction eluted with

2. Expression and purification of the S219V TEV protease

For the expression of the stable S219V TEV protease variant, the recombinant pRK793 MBP–TEV S219V plasmid construct has been employed (Figure 3) [37c]. The construct encodes for the maltose-binding protein (MBP) as fusion protein (shown in black), located at the *N*-terminal part, followed by the TEV-protease cleavage sequence, ENLYFQG, which allows the removal of the MBP fusion-tag by self-cleavage, thus providing the TEV protease (shown in red) with an *N*-terminal 6xHis-tag [1,7,38], that enables its facile purification by immobilized metal ion affinity chromatography (Ni-NTA).

It is important to point out that the mutant S219V TEV protease variant is optimized for a much higher self-cleavage stability. While the GHKVFMS sequence is considered as a “secondary” recognition site for cleavage, replacing the serine (S) residue from position 219 with valine (V) reduces the cleavage efficiency at this site [7,9,37bc,39].

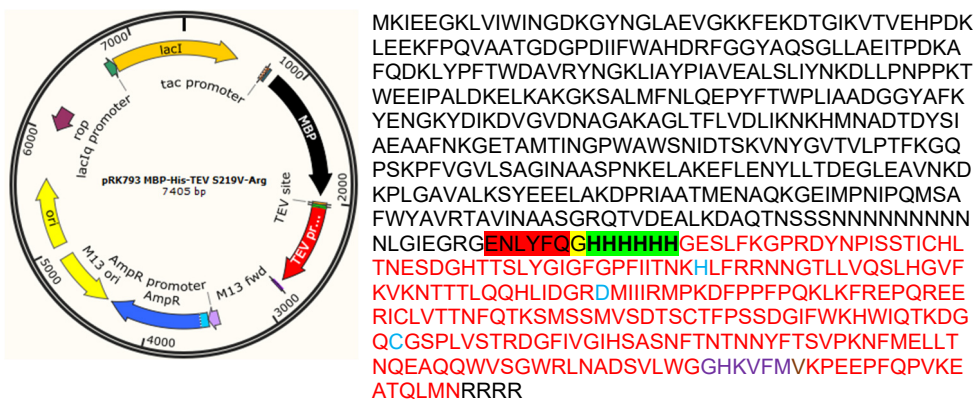


Figure 3. a) Plasmid map of the pRK793 MBP–TEV S219V construct. (Addgene plasmid # 8827) [37c]. **b)** The translated sequence encoding the MBP (black)-fused, 6xHis-tagged (green) TEV protease, which, upon self-cleavage at the ENLYFQ (red) site provides the non-fused, 6xHis-tagged S219V TEV protease. The amino acids of the His-Asp-Cys catalytic triad (blue) and V219 (brown) are also highlighted.

According to previous reports, the autocleavage occurs between M218 and S219 of the GHKVFMS secondary recognition sequence, resulting, besides the ~ 29 kDa full-length and active TEV protease, an additional, 25 kDa inactive, truncated variant [7,37,38]. Furthermore, several studies pointed out the difficulty to isolate the TEV-protease in intact and unprecipitated/non-aggregated form. Finding the optimal salt concentration, pH, and purification temperature to prevent aggregation, are crucial and govern the solubility of the recombinantly expressed/purified S219V TEV variant.

Within our expression and isolation protocol, the removal of MBP (~42 kDa) was achieved using washing solutions of different imidazole content (0-400 mM) (Figure 4), while the targeted TEV protease (molecular weight of ~29 kDa) has been successfully eluted under higher imidazole concentrations (500-1000 mM), with >90% purity (Figure 4b, lanes 5, 6). Fractions 4, 5, and 6 were combined and dialyzed, obtaining the purified, 6xHis-tagged TEV-protease (Figure 4b, lane 9). The reported conditions, related to the optimal protein concentration (< 1.7 mg/ml) and storage at - 80 °C, with 50% glycerol [37c], were precisely respected to avoid enzyme precipitation and, implicitly, self-digestion.

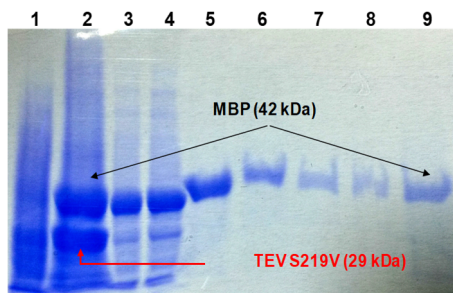


Figure 4a. Polyacrylamide gel (10%) containing samples from the purification steps of **TEV S219V**. **1** – cells before induction, **2** – cells after induction, **3** – supernatant from the cellular lysis step. Ni-NTA purification procedure: **4** – flow through, **5** – washing step with low salt solution, **6** – washing step with high salt solution, **7** – washing step with low salt solution, **8** – fr. 20 mM imidazole, **9** – fr. 400 mM imidazole.

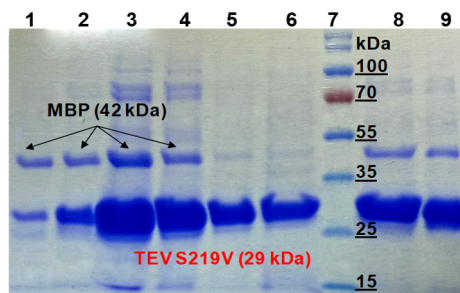


Figure 4b. Polyacrylamide gel (12%) containing samples from the purification steps of **TEV S219V**. **1** – fr. 100 mM imidazole, **2** – fr. 200 mM imidazole, **3** – fr. 300 mM imidazole, **4** – fr. 400 mM imidazole, **5** – fr. 500 mM imidazole, **6** – fr. 1 M imidazole, **7** – molecular weight marker, **8** – the mixture of samples **4**, **5** and **6** before dialysis, **9** – sample **8** after dialysis.

fr. = fraction eluted with

3. Removal of the 6xHis affinity tag of *PcPALs* through digestion with S219V-TEV protease

Obtaining a relatively large amount of the desired protein without His-tag, with high purity and maintained level of activity is challenging. Initially, the digestion reaction of the affinity-tagged *wild-type PcPAL* was optimized regarding the cleavage temperature, by comparing the efficiency of the TEV-protease mediated digestions performed at 4 °C or 25 °C, at pH 8.0. It was observed that removal of the 6xHis-tag was achieved almost quantitatively at 4 °C, where the majority of the *wt-PcPAL* (>80%) eluted from the column within the *flow-through* fraction (Figure 5a, lane 5), supporting the loss of the affinity tag, while the 6xHis-tagged TEV enzyme and a smaller fraction of the non-cleaved, affinity tagged *PcPAL* remained bound to the Ni-NTA resin, being eluted with 200 mM imidazole solution (Figure 5a, lane 6). Performing the cleavage at 25 °C was less efficient, the ratio of non-tagged (Figure 5a, lane 1) and 6xHis-tagged (Figure 5a, lane 2) *PcPAL* being of ~1, suggesting a ~50% cleavage efficiency. Unfortunately, autolysis of TEV protease, resulting in the 25 kDa fragment from the 29 kDa fragment was still observed (Figure 5a, lane 3 and 7) after 20 h of reaction time. Therefore, in further optimized steps, a shorter digestion (reaction) time of 12 h was employed.

During the optimization process, the effect of salt concentration, glycerol content of the reaction buffer, the effect of stirring (with or without) and of the decreased reaction time (12 h) on the cleavage efficiency were also addressed (Table 1).

The optimization process revealed that the highest TEV cleavage efficiency could be obtained by using 50 mM Tris, 300 mM NaCl, supplemented with 20% glycerol as reaction buffer and by performing the reaction without stirring, at pH 8.0, 4 °C, for 12 h reaction time. In this case, the percentage of non-tagged *PcPAL* eluting within the *flow-through* fraction was ~65%.

The optimized protein cleavage protocol was also successfully employed to produce several engineered *PcPAL* variants in their non-tagged forms, such as F137A, I460V (Figure 5b) and F137A/I460V, suitable for further protein crystallization experiments.

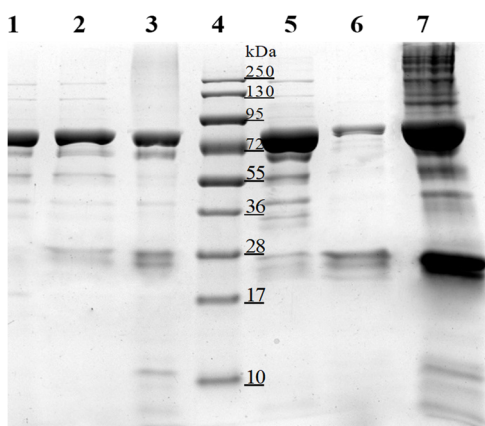


Figure 5a. Polyacrylamide gel (10%) containing samples from the Ni-NTA purification steps of the *PcPAL* cleaved with TEV-protease. *Cleavage at 25 °C*: 1 – flow through, 2 – fr. 200 mM imidazole, 3 – supernatant before Ni-NTA purification step, 4 – molecular weight marker; *cleavage at 4 °C*: 5 – flow through, 6 – fr. 200 mM imidazole, 7 – supernatant from the cellular lysis step loaded on the Ni-NTA column.

fr.=fraction eluted with

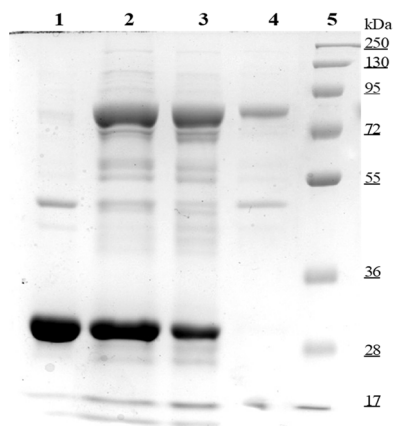


Figure 5b. Polyacrylamide gel (12%) representing the digestion steps of the I460V-*PcPAL* enzyme under the conditions specified in Table 1. 1 – TEV protease; 2 – cleavage reaction mixture/supernatant (the TEV enzyme and the I460V-*PcPAL* enzyme with or without His-tag); 3 – fr. 200 mM imidazole (non-digested enzyme). 4 – flow-through (I460V-*PcPAL* without His-tag); 5 – molecular weight marker.

Table 1. The different reaction conditions tested during the optimization process of the digestion reaction performed by the S219V TEV-protease.

Solutions	1	2	3	4	5	6	7	8	9
Tris	50 mM	50 mM	50 mM	50 mM	50 mM	50 mM	20 mM	50 mM	50 mM
NaCl	-	-	-	300 mM	300 mM	300 mM	100 mM	150 mM	150 mM
Glycerol	-	20%	-	-	20%	20%	20%	10%	10%
Stirring	-	-	+	-	-	+	-	+	-
Cleavage yield	30%	30%	5%	50-55%	65%	2-5%	45%	5-10%	5-10%

4. Analysis of the oligomerization state and homogeneity of the 6xHis-tagged and non-tagged recombinant *PcPALS*

The homogeneity and oligomerization state of all purified enzymes obtained in this study were determined by size exclusion chromatography. In the case of *PcPAL*, the signal with the retention volume of 1.49 mL, according to the calibration curve (for details see the Experimental section) corresponds to the native, tetrameric oligomerization state of *PcPAL*, of ~310 kDa. At retention volume 1.3 mL, generally in the form of a peak of low intensity, most probably the aggregation forms of the protein are eluted, which might appear during the concentration steps. Another weak intensity signal elutes at 2.0 mL, corresponding to a 35-40 kDa-sized protein fraction, according to the calibration curve. Based on the areas of the signals, the purity of the protein of interest could be estimated as ~ 90%.

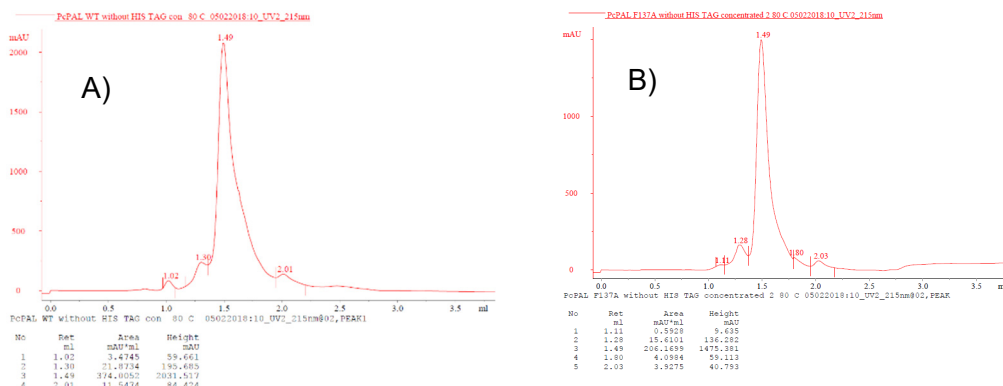


Figure 6. Representative SEC-derived chromatograms of the non-tagged *PcPALS* obtained using the Superdex 200 5/150 GL column: **A)** *wt-PcPAL*, **B)** *F137A-PcPAL*. Similar chromatograms have been obtained also for variants *I460V-PcPAL* and *I460V/F137A-PcPAL*.

5. Thermal unfolding of the non-tagged *PcPAL* variants

The thermal unfolding profiles of *wild-type PcPAL* and *PcPAL* mutants (F137A, I460V and F137A/I460V), before and after affinity tag removal, are shown in Figure 7, and the T_m values are listed in Table 2.

Generally, after removing the sequence of 25 amino acids from the *N*-terminal end of *PcPAL*, a slight decrease of the T_m value ($\sim 2^\circ\text{C}$) was recorded in comparison with the T_m of the 6xHis-tagged homologues, with the exception of the I460V-*PcPAL* mutant, where identical temperature unfolding profiles (Figure 7) have been obtained for the tagged and non-tagged variants.

The T_m value reported in the literature [37c,d] for the S219V-TEV protease (45°C) was also confirmed by our results, further supporting the high quality of the isolated recombinant S219V TEV-protease variant.

Table 2. Melting temperatures (T_m) of *wt-PcPAL* and mutant *PcPAL*s, before and after removing the 6xHis-tag

Entry	<i>PcPAL</i>		T_m ($^\circ\text{C}$)		T_m ($^\circ\text{C}$)
1	<i>wild-type</i>	Without His-tag	73.0 ± 0.2	With His-tag	75.0 ± 0.2
2	F137A		74.6 ± 0.5		76.5 ± 0.3
3	I460V		74.2 ± 0.5		74.1 ± 0.3
4	F137A/I460V		73.2 ± 0.2		74.7 ± 0.2
5	TEV		(S219V) 45°C		(<i>wt</i>) 52.1

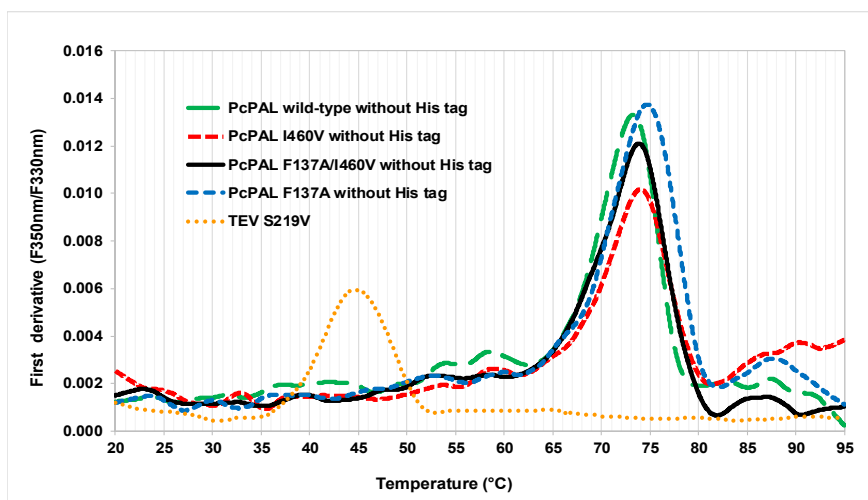


Figure 7. Thermal unfolding profile of the TEV S219V protease and of the *wild-type* and mutant (F137A, I460V, F137A/I460V) *PcPAL* variants. The melting temperatures of the *PcPAL* variants without 6xHis-tag ranged between $73\text{--}74.6^\circ\text{C}$. For S219V-TEV protease the T_m value was 45°C .

6. Specific enzyme activities of tagged and non-tagged PcPAL

The enzymatic activity of the *wild-type* PcPAL, with and without the 6xHis-affinity tag, was determined. The activity tests were performed at 1 mM L-phenylalanine concentrations in the presence of 4 μg of PAL, at 30 °C, monitoring by UV the production of *trans*-cinnamic acid at 290 nm (Figure 8). The specific activity obtained was $0.340 \mu\text{mol min}^{-1} \text{mg}^{-1}$ for the PcPAL with the *N*-terminal 6xHis-tag and $0.523 \mu\text{mol min}^{-1} \text{mg}^{-1}$ for the non-tagged PcPAL. The specific activity of the non-tagged PcPAL was ~ 1.5 -fold higher than that of its *N*-terminally His-tagged variant.

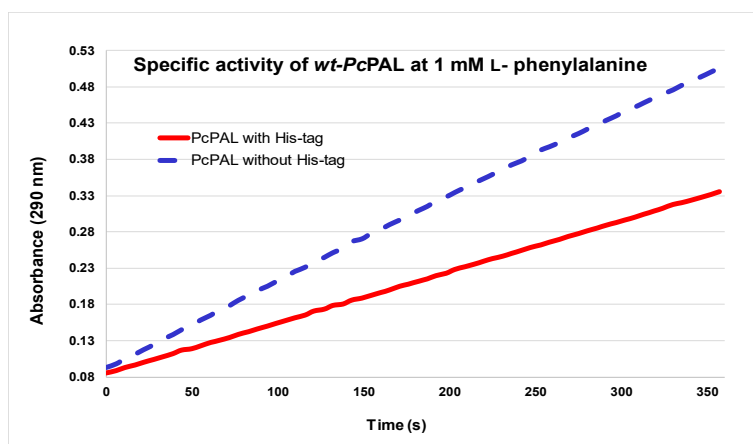


Figure 8. Specific activity of *wt-PcPAL* variants with and without His-tag in the ammonia elimination reaction of 1 mM L-phenylalanine, monitoring by UV absorption the production of *trans*-cinnamic acid at 290 nm.

CONCLUSIONS

Several PcPAL variants with removable His-tag and S219V-TEV protease were successfully obtained—by expression in *E. coli*, followed by affinity purification—in high concentrations and with high enzymatic activities. The melting temperature ($T_m = 45$ °C) and the digestion efficiency of the S219V-TEV protease is in accordance with reported data, supporting its successful purification.

Optimization of the TEV-protease digestion reactions allowed efficient removal of the *N*-terminal His-tags from the isolated PcPALs, providing $\sim 65\%$ recovery of the non-tagged form. The oligomerization state and purity of the enzymes were not affected by the 6xHis-tag removal, as revealed by the

size exclusion chromatography and SDS-PAGE analyses, respectively. Furthermore, the change in the T_m value was not significant for the non-6xHis-tagged enzymes, compared to their 6xHis-tagged form. On the other hand, the enzymatic activity of the non-tagged *wt-PcPAL* was ~1.5-fold higher than of its *N*-terminally tagged variant, indicating significant negative influence of *N*-terminal tags on the activity of *wt-PcPAL*.

EXPERIMENTAL SECTION

All the materials, supplies and equipment were provided by the Enzymology and Applied Biocatalysis Research Center of Babeş-Bolyai University, the Bioorganic Chemistry Group of Budapest University of Technology and Economics, or the Institute of Enzymology, ELKH. We thank Prof. Beáta G. Vértessy (Budapest University of Technology and Economics) for the scientific and infrastructural support in the design and molecular assembly of the employed plasmid constructs.

Plasmid pRK793 was a gift from David Waugh (Addgene plasmid # 8827; <http://n2t.net/addgene:8827>; RRID: Addgene_8827).

Expression and purification of the *wild-type* and mutant *PcPAL* variants with His-tag

Sterile LB (Luria Bertani) medium (50 mL), supplemented with 50 µg/mL of carbenicillin and 30 µg/mL of chloramphenicol, was inoculated with 20 µL of Rosetta (DE3) pLysS *E. coli* cells, previously transformed with the pET15b_*PcPAL* plasmid (encoding the *wt*- or mutant *PcPAL*s with the removable 6xHis-tag). A portion (10 mL) of the preculture grown overnight (37 °C, 200 rpm) was used to inoculate 2 L of LB medium. The cell culture was further incubated at 37 °C, 200 rpm until the OD₆₀₀ reached ~0.6. At this point, the expression was induced by adding 0.5 mM IPTG (isopropyl β-D-1-thiogalactopyranoside). After induction, the cell growth was maintained at 25 °C for another 15 h, followed by harvesting the cells by centrifugation (5.000 g for 20 min), resulting in 25 g of wet cell mass.

The isolated cells were resuspended in 60 mL of lysis buffer [50 mM Tris, 300 mM NaCl, 0.5 mM EDTA, pH 8.0; supplemented with RNase (0.2 mg), lysozyme (1 mg), a solution of PMSF (10 mg) in EtOH (0.5 mL), benzamidine (2.5 mg/1 mL of dH₂O), 1 tablet of protease inhibitor cocktail from Roche and 0.05 mM TCEP], and the ice-cold cell suspension was lysed by sonication, using a Sonics Vibra-Cell instrument for 30 min (1.4 MJ, intensity 40%, pulse on for 6 seconds, pulse off for 2 seconds, T < 16 °C).

The cellular debris was removed by centrifugation (12.000 g, 20 min, 4 °C) and the supernatant was loaded on a Ni-NTA-agarose column (2 mL of Superflow resin from Qiagen) using a peristaltic pump. A series of washing solutions of different ionic strengths were used to remove the non-specifically bound proteins (Table 3). The enzyme of interest was isolated with a 250 mM imidazole solution and dialyzed overnight in 5 L of Tris buffer (Dialysis buffer). A 10 kDa cut-off centrifugal filter was used to concentrate the protein solution, followed by homogeneity analysis via size exclusion chromatography, using a Superdex 200 5/150 GL column.

The concentration of the protein solution was determined by the BCA method, and the enzyme was aliquoted and stored at -20 °C with 20% glycerol. Samples from all steps of the expression and purification processes were analyzed by SDS-PAGE, using 10-12% polyacrylamide gels.

Expression and purification of the S219V TEV protease

In the TEV protease expression protocol, several steps differed from those applied within the purification protocol of PALs. Inoculation of the 3 L LB liquid culture was performed with 4% (v/v) of the overnight preculture (grown for 16 h, at 37 °C, 200 rpm). When the culture medium reached an OD₆₀₀ of 0.9 (after growth at 37 °C, 200 rpm), IPTG was added to a final concentration of 0.4 mM to induce TEV protein expression. The growth of the cellular mass was continued at 200 rpm, 18 °C for another 8 h, followed by cell harvesting by centrifugation (5.000 g, 25 min, 4 °C) and storage at -20 °C.

For cellular lysis, the cells were resuspended in 60 mL of lysis buffer supplemented with 10 mg of lysozyme, 3 mg of RNase and a solution of PMSF (10 mg) in EtOH (0.5 mL), followed by sonication for 50 min (with an energy of 1.4 MJ, and pulse on for 4 seconds, pulse off for 8 seconds, at 40% amplitude, T < 16 °C). The cell lysate was centrifuged (12.000 g, 15 min, 4 °C) and the supernatant was loaded on a Ni-NTA-agarose column, containing 2 mL of Ni-NTA Superflow resin, pre-equilibrated with binding buffer (50 mM Tris-HCl, 300 mM NaCl, 20 mM imidazole, pH 8.0).

After loading the protein solution, the Ni-NTA column was washed thoroughly with a series of buffers to remove non-specifically bound proteins, and to remove as much as possible the MBP, as follows: LS solution – 20 mL, HS solution – 10 mL, LS solution – 20 mL, followed by washing with different concentrations of imidazole (20 mM - 1000 mM). The presence of high protein content in the imidazole fractions was detected with the Bradford reagent. The imidazole from the eluted protein samples was removed by dialysis at 4 °C overnight, followed—after the addition of 20% glycerol—by protein concentration determination using the BCA method. The TEV protease can be used directly in experiments or stored at -80 °C in a 20% glycerol containing buffer.

All the protein isolation/purification steps were performed at 4 °C.

Table 3. The list of solutions used in the purification stages of the two types of enzymes and their composition.

Solution name	Components of the solution	
Buffer solution for cell lysis, pH 8.0	<ul style="list-style-type: none"> • 50 mM Tris • 0.5 mM EDTA • 300 mM NaCl 	<ul style="list-style-type: none"> • 1.14 mM PMSF • 0.015 mM lysozyme • 0.003 mM RNase
Low salt solution (LS), pH 8.0	<ul style="list-style-type: none"> • 30 mM KCl • 50 mM HEPES 	
High salt solution (HS), pH 8.0	<ul style="list-style-type: none"> • 300 mM KCl • 50 mM HEPES 	
Imidazole solutions, pH 7.5 (dissolved in LS)	<ul style="list-style-type: none"> • 0.025 M imidazole • 0.050 M imidazole • 0.075 M imidazole 	<ul style="list-style-type: none"> • 0.250 M imidazole • 0.500 M imidazole • 1 M imidazole
Dialysis buffer, pH 7.5	<ul style="list-style-type: none"> • 20 mM Tris • 100 mM NaCl • 1 mM PMSF 	

His-tag removal from *PcPAL* by digestion with TEV S219V

The S219V TEV-protease and the affinity-tagged *PcPAL* (*wild-type* or mutant variants) were mixed in a ratio of 2:10. Accordingly, 0.2 mg of TEV-protease and 2 mg of *PcPAL* were mixed in a final volume of 2 mL in Tris buffer (50 mM Tris and 300 mM NaCl, 20% glycerol, pH 8) and the reaction mixture was kept at 4 °C for 12 h under the different conditions indicated in Table 1. Further, the mixture was loaded onto a Ni-NTA affinity column (2 mL of Ni-NTA Superflow resin) and, after 10 minutes of incubation, the non-tagged *PcPAL* enzyme was recovered within the flow-through fractions and washing saline solutions. The TEV-protease and the non-cleaved 6xHis-tagged *PcPAL*–remained bound to the resin–have been eluted with 200 mM imidazole solution. The obtained solutions of *PcPAL* were dialyzed in 20 mM Tris and 100 mM NaCl, pH 8.0, followed by SDS-PAGE analysis for purity assessment. Further, size exclusion chromatography (Superdex 200 10/300 GL) was used for the assessment of the homogeneity and oligomerization state of the isolated non-tagged *PcPAL*s.

Thermal unfolding profiles by NanoDSF measurements

Thermal unfolding analysis of S219 TEV protease, *wt*- and mutant *PcPAL* variants was performed using Nanoscale differential scanning fluorimetry (NanoDSF), using the Prometheus NT.48 instrument (Figure 9).

The determination of thermal stability (T_m) of enzymes is based on the intrinsic fluorescence of tyrosine and tryptophan, where T_m is determined as the inflection point of the curve representing the ratio of the tryptophan fluorescence at 330 and 350 nm in function of the employed temperature ramp. The UV Monolith capillaries (NanoTemper Technologies) were loaded with 10 μL of the protein solution (1 mg mL^{-1} in 100 mM Tris, 120 mM NaCl buffer, pH 8.8), followed by their placement in the capillary array (rails) of the device. The protein unfolding was monitored in a temperature range of 30 $^{\circ}\text{C}$ to 95 $^{\circ}\text{C}$, with an increment of 1 $^{\circ}\text{C min}^{-1}$.

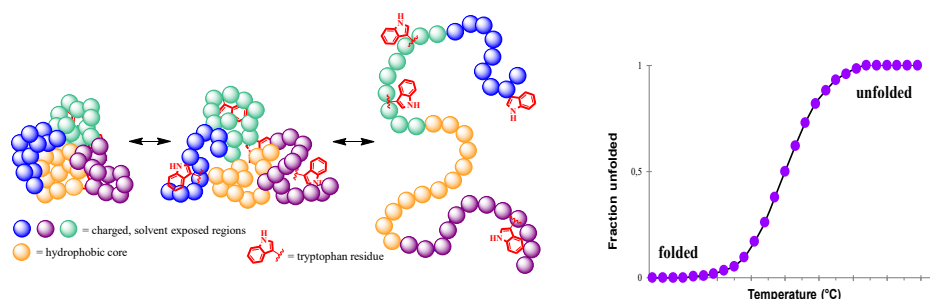


Figure 9a. Schematic representation of the protein unfolding, representing the general fold of soluble, globular proteins, with their polar surface (green, blue, violet) exposed to the solvent and the hydrophobic core region (orange), which upon denaturation exposes its hydrophobic residues (among them Trp, Tyr and Phe) to the surface. **b.** The transition state curve of the thermal protein unfolding process, with the melting temperature (T_m) positioning at the inflection point of the curve, representing the ratio of tryptophan fluorescence measured at 330 and 350 nm, in function of the employed temperature ramp.

Size-exclusion chromatography

Size exclusion chromatography was performed using Superdex 5/150 GL 200 and Superdex 10/300 GL 200 columns attached to an Äkta FPLC system (GE Healthcare). The calibration curve for SEC was obtained using 8 proteins of known molecular weight: Ribonuclease A (13.7 kDa), Carbonic anhydrase (29 kDa), Ovalbumin (43 kDa), BSA (66 kDa), Alcohol dehydrogenase (150 kDa), β -amylase (200 kDa), Apoferritin (443 kDa) and Thyroglobulin (669 kDa), for which retention volumes on the Superdex 5/150 GL 200 column have been assessed (Figure 10 and table 4), serving for the calibration curve correlating K_{av} elution parameter as a function of the Log_{MW} . Based on the first-order equation obtained below ($y = -0.3276x + 1.9719$) - Figure 11, the molecular weight of the analyzed protein sample was estimated. Within the analytical scale SEC, the sample injection volume was 50 μL , the elution was performed at a flow-rate of 0.3 mL min^{-1} and at 25 $^{\circ}\text{C}$.

PRODUCTION OF RECOMBINANT, NON-TAGGED PHENYLALANINE AMMONIA-LYASES ...

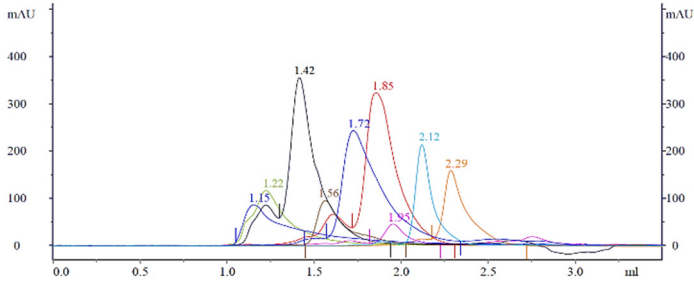


Figure 10. Chromatograms obtained from the individual injections of the different proteins of known molecular weight on the Superdex 200 5/150 GL column, used for the calibration curve of the enzymes used for determination.

Table 4. Calibration curve set-up for Superdex 200 5/150 GL using an extended Gel Filtration Calibration Kit with proteins of molecular mass in the range 13700 to 669000 Da.

Standard protein	Molecular Weight (Da)	Volume of elution (V _e) mL	K _{av}	Log ₁₀ MW
Thyroglobulin	669000	1.22	0.03784	5.8254
Apoferritin	443000	1.42	0.14595	5.6464
β-amylase	200000	1.56	0.22162	5.3010
Alcohol dehydrogenase	150000	1.73	0.31351	5.1761
Bovine Serum Albumin	66000	1.85	0.37838	4.8195
Ovalbumin	43000	1.95	0.43243	4.6335
Carbonic anhydrase	29000	2.12	0.52432	4.4624
Ribonuclease A	13700	2.29	0.61622	4.1367

*K_{av}=(V_e-V_o)/(V_c-V_o); V_c=3 mL (column volume, Superdex 200 5/150 GL); V_o=1.15 mL (column void volume) - determined by injecting Dextran Blue 2000 (2000 kDa); V_e=elution volume of the analyzed sample/peak.

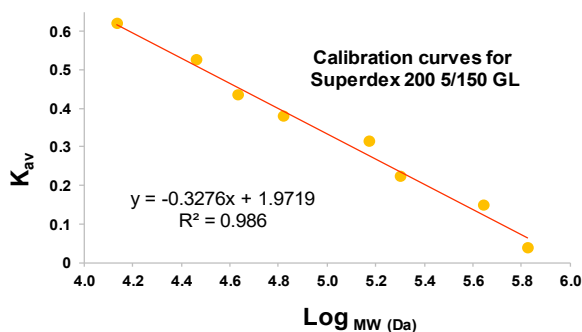


Figure 11. Plot of the elution volume parameter (K_{av}) against the logarithm of molecular weight of the eight different protein samples used for the calibration.

Enzyme activity measurements

The specific activity of the non-tagged and 6xHis-tagged *wild-type* PcPAL was determined spectrophotometrically, using Tecan Microplate Reader Spark® and a Corning 96-well UV-Transparent plate, monitoring the production of *trans*-cinnamic acid at 290 nm, where the corresponding L-Phe shows negligible absorption. The enzyme activity measurements were performed in triplicate, in a final volume of 200 µL, using 50 mM Tris-HCl, 100 mM NaCl (pH 8.8) as reaction buffer, at 30 °C for 6 min, each sample containing 4 µg (2.48 µM) from the corresponding PcPAL.

ACKNOWLEDGEMENTS

F.A. thanks for the financial support from the Ministry of Research, Innovation and Digitization, CNCS/CCCDI—UEFISCDI, project number PN-III-P1-1.1-PD-2019-1222/PD98 and from the project: Entrepreneurship for innovation through doctoral and postdoctoral research, POCU/380/6/13/123886, co-financed by the European Social Fund, through the Operational Program for Human Capital 2014–2020. Authors thank Prof. Beáta G. Vértessy for the infrastructure at the Institute of Enzymology (Budapest, Hungary) and the valuable discussions.

REFERENCES

1. D. Walls; S.T. Loughran, *Protein Chromatography: Methods and Protocols, Methods Mol. Biol.*, **2011**, *681*, 151–175.
2. S. Van den Berg; P.A. Lofdahl; T. Hard; H. Berglund, *J. Biotechnol.* **2006**, *121*, 291–298.
3. S. Harper; D.W. Speicher, *Methods Mol. Biol.*, **2011**, *681*, 259–280.
4. A. Einhauer; A. Jungbauer, *J. Biochem. Biophys. Meth.*, **2001**, *49*, 1–3, 455–465.
5. J.J. Lichty; J.L. Malecki; H.D. Agnew; D.J. Michelson-Horowitz; S. Tan, *Protein Expr. Purif.*, **2005**, *41*, 1, 98–105.
6. J. Arnau; C. Lauritzen; G.E. Petersen; J. Pedersen, *Protein Expr. Purif.*, **2006**, *48* (1), 1–13.
7. H. Nam; B-J. Hwang; D-Y. Choi; S. Shin; M. Choi, *FEBS Open Bio.*, **2020**, *10*, 619–626.
8. W.T. Booth; C.R. Schlachter; S. Pote; N. Ussin; N.J. Mank; V. Klapper *et al.*, *ACS Omega*, **2018**, *3*, 760–768.
9. D.M. Charbonneau; F. Meddeb-Mouelhi; M. Beauregard, *Protein Pept. Lett.*, **2012**, *19*, 264–269.
10. V.P. Kutysenko; G.V. Mikoulinskaia; S.V. Chernyshov; A.Y. Yegorov; D.A. Prokhorov; V.N. Uversky, *Int. J. Biol. Macromol.*, **2019**, *124*, 810–818.

11. E. Niedzialkowska; O. Gasiorowska; B.K. Handing; A.K. Majorek; J.P. Porebski; G.I. Shabalin; E. Zasadzinska; M. Cymborowski; W. Minor; *Protein Sci.*, **2016**, *25*, 720–733.
12. C. Han; Q. Wang; Y. Sun; R. Yang; M. Liu; S. Wang *et al.*, *Biotechnol. Biofuels*, **2020**, *13*:30, 2223.
13. M. Carson; H.D. Johnson; H. McDonald; C. Brouillette; J.L. Delucas, *Acta Crystallogr., Sect. D: Biol. Crystallogr.*, **2007**, *63*, 295–301.
14. M.C. Deller; L. Kong; B. Rupp, *Acta Crystallogr., Sect. F: Struct. Biol. Commun.*, **2016**, *72*, 72–95.
15. M.E. Kimple; J. Sondek, *Curr. Protoc. Prot. Sci.*, **2018**, *73*, 1, 9.9.1–9.9.19.
16. G. Lilius; M. Persson; L. Bulow; K. Mosbach, *Eur. J. Biochem.* **1991**, *198*, 499–504.
17. M.C. Smith; T.C. Furman; T.D. Ingolia; C. Pidgeon, *J. Biol. Chem.*, **1988**, *263*, 7211–7215.
18. H. Block; B. Maertens; A. Spriestersbach; N. Brinker; J. Kubicek; R. Fabis, *et al.*, *Methods Enzymol.* **2009**, *463*, 439–473.
19. **a)** N.A. Dima; A. Filip; L.C. Bencze; M. Oláh; P. Sátorhelyi; B.G. Vértessy *et al.*, *Stud. Univ. Babeş-Bolyai Chem.*, **2016**, *61*, 21–34. **b)** A. Filip; L.C. Bencze; C. Paizs; L. Poppe; F.D. Irimie, *Stud. Univ. Babeş-Bolyai Biol.* **2015**, *60*(Sp. Iss), 39–43. **c)** P. Csuka; V. Juhász; S. Kohári; A. Filip; A. Varga; P. Sátorhelyi; *et al.*, *ChemBioChem*, **2018**, *19*, 1–9. **d)** A. Varga; Z. Bata; P. Csuka; M.D. Bordea; B.G. Vértessy; A. Marcovici; F.D. Irimie, L. Poppe, L.C. Bencze; *Stud. Univ. Babeş-Bolyai Chem.*, **2017**, *3*, 293–308. **e)** A. Varga; P. Csuka; O. Sonesouphap; G. Bánóczy, M.I. Toşa; G. Katona, *et al.*, *Catal. Today*, **2021**, *366*, 185–194. **f)** K. Kovács; G. Bánóczy; A. Varga, I. Szabó; A. Holczinger; G. Hornyánszky; I. Zagyva; C. Paizs; B.G. Vértessy, L. Poppe; *PLoS ONE* **2014**, *9*, e85943.
20. N. Debeljak; L. Feldman; K.L. Davis; R. Komel, A.J. Sytkowski, *Anal. Biochem.* **2006**, *359*(2), 216–223.
21. H.C. Wilken; S. Rogge; O. Götze; T. Werfel; J. Zwirner, *J. Immunol. Meth.*, **1999**, *226*(1-2), 139–145.
22. Y-T. Lai; Y-Y. Chang; L. Hu; Y. Yang; A. Chao; Z-Y. Du, *et al.*, *PNAS*, **2015**, *112*(10), 2948–2953.
23. K.A. Majorek; M.L. Kuhn; M. Chruszcz; F.W. Anderson; W. Minor; *Protein Sci.*, **2014**, *23*, 1359–1368.
24. A. Panek; O. Pietrow; P. Filipkowski; J. Synowiecki; J., *Acta Biochim. Pol.*, **2013**, *60*, 163–166.
25. A.P.U. Araújo; G. Oliva; F. Henrique-Silva; C.R. Garratt; O. Caceres; M.L. Beltramini, *Biochem. Biophys. Res. Commun.* **2000**, *272*, 480–484.
26. W. Xiao; L. Jiang; W. Wang; R. Wang; J. Fan, *J. Biosci. Bioeng.*, **2018**, *125*(2), 160–167.
27. E.Z.A. Nagy, S.D. Tork; L.A. Pauline; A. Filip; F.D. Irimie; L. Poppe *et al.* *ACS Catal.* **2019**, *9*, 8825–8834.
28. S.H.J. Smits; A. Mueller; M.K. Grieshaber; L. Schmitt, *Acta Cryst. F: Struct. Biol. Commun.*, **2008**, *64*, 836–839.
29. **a)** A. Filip, *Wild-type* and tailored phenylalanine ammonia-lyases for the synthesis of unnatural L- and D-arylalanines (Doctoral Thesis), Babeş-Bolyai University of Cluj-Napoca, **2019**, 50-68. **b)** Z. Bata; Z. Molnár; E. Madaras; B. Molnár; E. Sánta-Bell; A. Varga *et al.*, *ACS Catal.*, **2021**, *11*, 4538–4549.

30. A.J. Barrett; J.K. McDonald, *Biochem. J.*, **1986**, 237, 935.
31. J.A. Mótyán; F. Tóth; J. Tözsér; *Biomolecules*, **2013**, 3, 923–942.
32. C.S. Craik; J.M. Page; L.E. Madison, *Biochem. J.*, **2011**, 435, 1–16.
33. B. Miladi; H. Bouallagui; C. Dridi; A. El Marjou; G. Boeuf; P. Di Martino, *et al. Protein Expr. Purif.*, **2011**; 75(1), 75–82.
34. P. Giansanti; L. Tsiatsianiv Y.T. Low; J.A. Heck, *Nat. Protoc.* **2016**, 11, 993–1006.
35. F. Xiao; Widlak, W.T. Garrard; *Nucleic Acids Res.* **2007**, 35(13), 1–7.
36. K. Melcher, *Anal. Biochem.*, **2000**, 277, 109–120.
37. **a)** J.L. Riechmann; S. Lain, J.A. Garcia; *J. Gen. Virol.*, **1992**, 73, 1–16. **b)** W.G. Dougherty; B.L. Semler; *Microbiol. Rev.* **1993**, 57, 781–822. **c)** R.B. Kapust; J. Tozser; J.D. Fox; D.E. Anderson; S. Cherry; T.D. Copeland; D.S. Waugh; *Protein Eng.*, **2001**, 12, 993–1000. **d)** L.D. Cabrita; G. Dimitri; A.L. Robertson; Y. Dehouck; M. Rooman; S.P. Bottomley, *Protein Sci.*, **2007**, 16, 2360–2367.
38. A. Zlobin and A. Golovin, *ACS Omega* **2022**, 7, 44, 40279–40292.
39. **a)** D.S. Waugh; *Protein Expr. Purif.* **2011**, 80, 283–293; **b)** A.C. Denard; C. Paresi; R. Yaghi; N. McGinnis; Z. Bennett; L. Yi, G. Georgiou; B.L. Iverson, *ACS Synth. Biol.* **2021**, 10, 63–71; **c)** H. Mohammadian; K. Mahnam; H. Mirmohammad Sadeghi; M.R. Ganjalikhany V. Akbari, *RPS* **2020**, 15(2), 164–173.
40. T.S. Ahmed; F. Parmeggiani; N.J. Weise; S.L. Flitsch; N.J. Turner, *ACS Catal.*, **2018**, 8, 3129–3132.
41. **a)** A. Filip, E.Z.A. Nagy; S.D. Tork; G. Bánóczy. M.I. Toşa; *F.D. Irimie et al. ChemCatChem.*, **2018**, 10, 2627–2633; **b)** S.D. Tork; E.Z.A. Nagy; L. Cserepes; D.M. Bordea; B. Nagy; M.I. Toşa; *et al. Sci. Rep.*, **2019**, 9, 1; **c)** S.D. Tork; M.E. Moisa; L. Cserepes; A. Filip; L.C. Nagy; F.D. Irimie; L.C. Bencze, *Sci. Rep.*, **2022**, 12(1), 10606; **d)** L.C. Bencze, A. Filip; G. Bánóczy; M.I. Toşa F.D. Irimie; A. Gellért *et al.*, *Org. Biomol. Chem.*, **2017**, 15, 3717–3727.
42. LA. Hardegger; P. Beney; D. Bixel; C. Fleury; F. Gao; AGG. Perrenoud *et al.*, *Org. Proc. Res. Dev.*, **2020**, 24(9), 1763–1771.
43. F. Parmeggiani; N.J. Weise; S.T. Ahmed; N.J. Turner, *Chem. Rev.* **2018**, 118, 73–118.
44. E.Z.A. Nagy; S.D. Tork; A. Filip; L. Poppe; M.I. Tosa; C. Paizs; L.C. Bencze; Other Carbon–Nitrogen Bond-Forming Biotransformations, Production of L- and D-phenylalanine analogues using tailored phenylalanine ammonia-lyases in *Applied Biocatalysis, The Chemist's Enzyme Toolbox*, J. Whittall and Peter W. Sutton; Wiley, Hoboken, USA, **2021**, Chapter 5; 5.5; 42 (4), 215–221. ISBN: 978-1-119-48701-2.
45. **a)** D. Duță; A. Filip; L.C. Nagy; E.Z.A. Nagy; R. Tőtós; L.C. Bencze, *Sci. Rep.*, **2022**, 12, 3347. **b)** E.Z.A. Nagy; L.C. Nagy; A. Filip; K. Nagy; E. Gál; R. Tőtós; L. Poppe; C. Paizs; L.C. Bencze; *Sci. Rep.*, **2019**, 9, 1–10.

POLYLACTIC ACID INTER-CHAIN INTERACTIONS

Izabella IRSAI^a, Szilárd Zoltán PESEK^a,
Radu SILAGHI-DUMITRESCU^{a,*}

ABSTRACT. Geometry optimization of perpendicular, antiparallel and parallel dimers were employed in order to analyze the relative energy values. The weakest interactions are seen for the perpendicular structures; among those, the strongest are for π , 3_{10} , while the DeSantis structure affords no local minimum at all. The strongest interactions are seen with parallel structures – of which the largest interaction energies are with the DeSantis and the π monomers (up to 2.8 and 4.2 kcal/mol per unit of lactic acid, respectively).

Keywords: *polylactic acid (PLA), supramolecular, computational*

Poly(lactic acid) (PLA) is a biodegradable, biocompatible and compostable aliphatic polyester. It is composed of lactide (LA) repeat units, typically either in the form of poly(L-lactic acid) (PLLA) or poly(D-lactic acid) (PDLA). Both homopolymers are semicrystalline; the naturally occurring form PLLA is about 37% crystalline. When L-isomers and D-isomers are copolymerized in equal proportions, a racemic poly(lactide) is formed. Its molecular chains cannot easily pack together to crystallize, because the side groups are located on both sides of the polymer backbone; consequently, racemic poly(lactide) (PLDLA) is entirely amorphous. Non-racemic copolymers are usually mixed from L-lactide and a racemic (50:50) mixture of L-lactide and D-lactide (PLDLLA).[1,2]

Experimental characterization of PLA often involves measurements of crystallinity, average molecular weight, molecular weight distribution (polydispersity), impurities (such as residual monomers, water, and free radicals), and glass transition temperature. The thermal, mechanical and

^a Babeş-Bolyai University, Faculty of Chemistry and Chemical Engineering, 11 Arany Janos str., RO-400028, Cluj-Napoca, Romania

* Corresponding author: radu.silaghi@ubbcluj.ro



biodegradation properties of PLA are largely dependent on the ratio and distribution of the two stereoisomers of LA within the polymer chains. Water can act as a plasticizer of PLA, which might result in a decrease of T_g even below body temperature (37°C).[3–5]

The thermal properties of PLA can be changed by copolymerization of PLA with monomers such as glycolide, some lactone derivatives, trimethylene carbonate and also by the addition of cross-linkers and plasticizers. Amorphous PLA and low-crystalline PLA are clear materials with high gloss, while highly crystalline PLA is an opaque white material. It is brittle at room temperature. The amorphous PLA is soluble in most organic solvents such as tetrahydrofuran, chlorinated solvents, benzene, acetonitrile, and dioxane. Crystalline PLA is soluble in chlorinated solvents and benzene at elevated temperatures. Semicrystalline PLA is preferred to amorphous polymer when better mechanical properties are desired. The molar mass of the polymer as well as the degree of crystallinity has a significant influence on the mechanical properties.[6,7,16,8–15]

The molecular-level organization of PLA in materials such as described above is mostly unclear. We have previously considered the possibility that the PLA monomer, in light of its structural reminiscence to the amino acid alanine (technically, the amino group of alanine would be replaced by a hydroxy group in PLA), would form peptide-type elements of secondary structure. Peptide/protein secondary structure elements include repetitive structural motifs based mostly on hydrogen bonds within the chain (for helical structures) or between chains (for pleated sheet structures). We have previously explored in some detail the performance of computational methods in describing peptide secondary structural elements for short peptides (e.g., decamers).[17–20] To this end, we reported geometry optimization results on 4 different types of secondary structures in decaameric units of PLA – helical (α , π , 3_{10}) and β -sheet. Based on *ab initio* calculations, the α , π and 3_{10} structures were found to have very similar energies, with π slightly favored by values within the error limits of the method; in contrast, semiempirical and empirical methods predicted other structures as favorites – and with distinctly larger energy differences. Three types of weak interactions appear to dictate the relative stabilities of secondary structure elements in PLA structures: carbonyl-CH, carbonyl-CH₃, and carbonyl-ester.[21,22]

Spectroscopic parameters were also predicted for the putative PLA secondary structure elements, in an attempt to aid our on-going efforts in synthesis and characterization of polylactic acid variants.[23] The calculated chemical shifts of both ^{13}C NMR and ^1H NMR are slightly larger than the experimental ones. The conclusion was that the secondary structure (if any)

of poly(lactic acid) cannot be conclusively clarified from the calculated IR and NMR spectra, suggesting either a need for using more appropriate computational methods or the occurrence of previously unconsidered elements of secondary structure, or the total lack thereof.[23]

All of the previous computational studies have focused on isolated single chains of PLA. Such studies would be relevant for gas-phase experiments such as in mass spectrometry, but less so for condensed-phase situations. The route towards predicting solid-state PLA structures via quantum mechanical calculations is difficult, if at all possible, with current methodology; lower-level theory models would be even more problematic as we have previously shown.[21] A first step towards such predictions would nevertheless be an attempt to model the interaction of at least two chains of PLA. The nature of the secondary structure elements in PLA implies distinctly difficult capabilities of interchain interactions ranging from two extremes: the α -helix, where the exterior of the chain features mostly methyl groups which may significantly limit the strength of potential intermolecular interactions, and the β -chains that are optimally designed for intermolecular interactions. To this end, reported here is a molecular-level investigation of the inter-chain weak interactions involving decameric PLA units, as part of an effort ultimately aiming to provide useful data for predicting and controlling macroscopic properties of PLA-based materials.

RESULTS AND DISCUSSION

The helical and sheet structures of the decameric units of PLA were built only for poly(L-lactic acid) (PLLA). We have previously reported that the energies of the PLLA are generally smaller than in the case of poly(DL-lactic acid) (PDLLA) copolymers.[21]

Overall, two types of weak interactions appear to dictate the relative stabilities of the dimers. One of the non-covalent interactions involves the oxygen atoms of the carbonyl group of one monomeric unit and the hydrogen atoms from the main chain of the other monomeric unit. The other type of non-covalent interaction implies the oxygen atoms of the carbonyl group of one molecule and the hydrogen atom from the methyl group of the second molecule. These C=O \cdots H distances are thus found, in certain instances, to be shorter than the corresponding sum of van der Waals radii (2.72 Å). Figure 1 illustrates a typical dimer structure, with atom numbering further used in the Tables.

The stability of the generated geometries was determined as the difference between the energy obtained during the dimer optimization and 2x the value of the energy received from the monomer optimization.

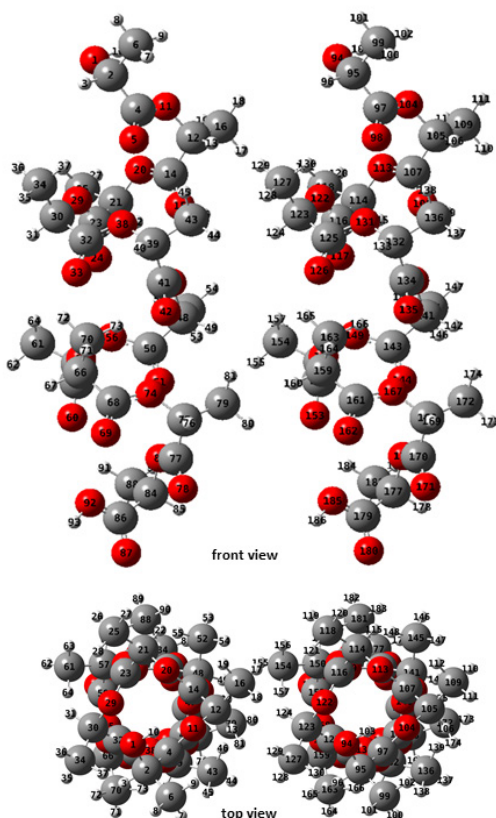


Figure 1. Graphical representation of α PLA dimers; red represents oxygen, gray the carbon and white the hydrogen atoms.

Perpendicular dimers

In the case of the perpendicular dimers, the two decameric chains were placed at 90° with respect to each other, intersecting at the middle of the chains. Two types of input geometries were built; one is based on monomers built in the canonical form and the other is based on the HF 3-21G* pre-optimized monomers (Tables 1 and 2).

POLYLACTIC ACID INTER-CHAIN INTERACTIONS

Table 1. Initial distances (“Initial”, Å) between monomers, relative energies (ΔE , kcal/mol), weak interactions (Å) and graphical representations of the perpendicular α -dimers, cf. unrestricted geometry optimizations.

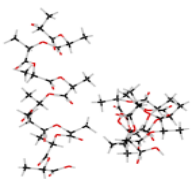
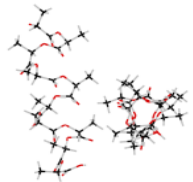
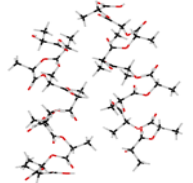
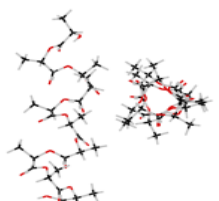
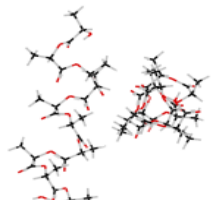
Initial	ΔE	C=O...H(CH)	C=O...H(CH ₃)	Other	Distance	Representation
2	8.41		O42-H119		2.38	
			H44-O117		2.48	
			H73-O117		2.58	
			O69-H129		2.37	
3	8.47		O42-H119		2.36	
			H44-O117		2.44	
			H73-O117		2.59	
			O69-H129		2.36	
4	17.58	O5-H151			2.23	
		H13-O144			2.36	
			H18-O171		2.44	
			O33-H156		2.59	
		H40-O117			2.24	
			O42-H119		2.48	
				H71-O94(hyd)	2.53	

Table 2. Initial distances (“Initial”, Å) between monomers, relative energies (ΔE , kcal/mol), weak interactions (Å) and graphical representations of the perpendicular α -dimers (monomers not pre-optimized separately).

Initial	ΔE	C=O...H(CH)	C=O...H(CH ₃)	Distance	Representation
2	7.53	O24-H169		2.48	
			O24-H174	2.62	
			H26-O162	2.33	
		H31-O135		2.33	
3	9.58		O33-H147	2.61	
			O24-H169	2.45	
			O24-H174	2.52	
			H26-O162	2.41	
		H31-O135		2.20	
		O33-H142		2.44	
			O51-H173	2.65	
	H63-O144	2.45			

The α dimers were constructed by translating the monomer unit by values between 2-6 Å. If the two monomers are situated at an initial 2-3 Å, the perpendicular direction is preserved and four weak interactions between the monomers are established in each of these cases. If the initial structure is based on the optimized monomers, only $\text{C}=\text{O}\cdots\text{H}(\text{CH}_3)$ interactions are established. However, if the optimization is started from initial 4-5 Å distances between the two optimized monomers, the two units reorient to almost parallel and the number of interactions subsequently increases (Table 1). The weaker the interactions, the more stabilized are the structures, so that the parallel structures are more stable by around 8 kcal/mol as compared to those that remained perpendicular. Overall, each intermolecular interaction adds around 2 kcal/mol to the stabilization energy.

For the 6 Å dimers (not shown), the monomers shifted upon geometry optimization so that they would interact only via the terminal groups, without involving the carboxylic oxygen and hydrogen. The structures resulting from the optimization started at 2 or 3 Å were very similar to each other, with only $\text{C}=\text{O}\cdots\text{H}(\text{CH})$ and $\text{C}=\text{O}\cdots\text{H}(\text{CH}_3)$ interactions holding the molecules together, with an average of 1.5 kcal/mol per such interaction.

When the two optimized π monomers were placed at initial distances of 2.5-4.5 Å (Tables 3 and 4), the two units remained perpendicular after geometry optimizations, with six $\text{O}\cdots\text{H}$ interactions per dimer, at ~ 2 kcal/mol per interaction (Table 3). If the initial distance between the two monomers was set below 2.5 Å, they migrated to a parallel structure (see dedicated section below). Only $\text{C}=\text{O}\cdots\text{H}(\text{CH})$ and $\text{C}=\text{O}\cdots\text{H}(\text{CH}_3)$ intermolecular interactions were formed; the carboxylic and hydroxyl oxygen atoms did not participate in dimer stabilizations.

The dimers from the starting structures based on the canonical form placed with starting inter-chain distances of 1.5-2.5 Å led to perpendicular orientations after geometry optimizations (Table 4). It is again the $\text{C}=\text{O}\cdots\text{H}(\text{CH})$ and $\text{C}=\text{O}\cdots\text{H}(\text{CH}_3)$ interactions that hold together the final forms in both optimizations. The intermolecular interaction energy is 3 kcal/mol. Increasing the starting distance to 3.5 Å increases the energy to 4.6 kcal/mol, as the hydroxyl and carboxyl groups also participate in the stabilization; however, in this case the dimers are no longer perpendicular to each other. Placing the monomers at a longer distance (5.5 Å) the relative energy value reaches 3.6 kcal/mol, but only one interaction occurs - between the first molecule's hydroxylic hydrogen atom and the second molecule's oxygen atom (structure not shown).

POLYLACTIC ACID INTER-CHAIN INTERACTIONS

Table 3. Initial distances (“Initial”, Å) between monomers, relative energies (ΔE , kcal/mol), weak interactions (Å) and graphical representations of the perpendicular π -dimers.

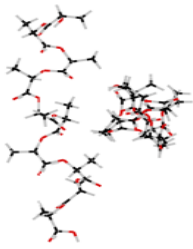
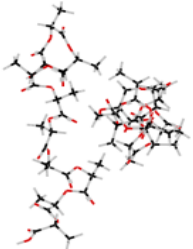
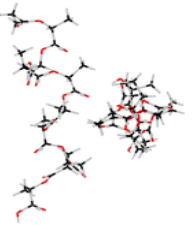
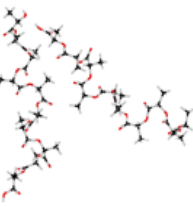
Initial	ΔE	C=O...H(CH)	C=O...H(CH ₃)	Distance	Representation
2.5	13.61		O25-H149	2.69	
			H27-O145	2.27	
			O43-H157	2.43	
		H50-O127	2.29		
			O52-H129	2.37	
			H74-O127	2.42	
4.5	14.14		O25-H147	2.45	
			H27-O145	2.38	
		O43-H152	2.38		
			O43-H157	2.52	
			H47-O145	2.60	
			H72-O127	2.42	

Table 4. Initial distances (“Initial”, Å) between monomers, relative energies (ΔE , kcal/mol), weak interactions (Å) and graphical representations of the perpendicular π -dimers (monomers not pre-optimized separately).

Initial	ΔE	C=O...H(CH)	C=O...H(CH ₃)	Other	Distance	Representation
2.5	15.12		O43-H149		2.63	
			O43-H157		2.56	
			H45-O145		2.44	
		H50-O127	2.40			
		H82-O127	2.48			
3.5	27.74			O2(hyd)-H94(carb)	1.70	
			O16-H179	2.37		
		H23-O172	2.14			
			O43-H156	2.34		
			H45-O154	2.42		
			H47-O172	2.51		

The optimized 3_{10} monomers placed at 1.5-3.5 Å after the dimer optimizations remain perpendicular (Table 5). In all two cases seen in Table 5, the interactions are established between the same atoms, with similar relative energies.

Table 5. Initial distances (“Initial”, Å) between monomers, relative energies (ΔE , kcal/mol), weak interactions (Å) and graphical representations of the perpendicular 3_{10} -dimers.

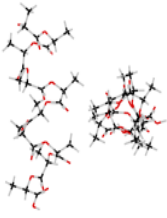
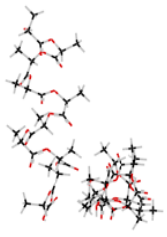
Initial	ΔE	C=O...H(CH)	C=O...H(CH ₃)	Other	Distance	Representation
3.5	6.69	O24-H133			2.29	
			O24-H166		2.71	
			H53-O162		2.55	
4.5	9.33	O24-H133			2.18	
			H26-O126		2.45	
			O51-H137		2.50	
			H53-O135		2.70	

The 3_{10} structure with an initial distance of 4.5 Å differs very little from the real perpendicular structures, showing one more weak interaction between the carbonyl oxygen atom and hydrogen of a methyl group than in the other cases - therefore the relative energy is seen to increase to ~10 kcal/mol.

Starting from structures based on canonical forms, the two units maintain the perpendicular directions at 1.5-2.5 Å distances. The geometries, relative energies, number and type of interactions are the same. If the distance between the initial molecules is longer than 4.5 Å then the monomers are shifted during the geometry optimization. The carboxylic oxygen also participates in the dimer formation. The interactions are created between the same atoms - only the lengths of these are changed by 0.1 Å, and hence the relative energy varies as well (Table 6).

POLYLACTIC ACID INTER-CHAIN INTERACTIONS

Table 6. Initial distances (“Initial”, Å) between monomers, relative energies (ΔE , kcal/mol), weak interactions (Å) and graphical representations of the perpendicular 3_{10} -dimers (monomers not pre-optimized separately).

Initial	ΔE	C=O...H(CH)	C=O...H(CH ₃)	Other	Distance	Representation
2.5	8.13		O42-H115		2.22	
			H44-O108		2.35	
			O69-H119		2.42	
		H71-O117	2.62			
4.5	16.25		O69-H121		2.44	
			O69-H129		2.51	
			H71-O117		2.51	
			O92(carb)-H156		2.49	

Optimization of the β dimers did not retain the initial perpendicular arrangement, whether starting from structures based on canonical form or previously optimized monomers - with one exception. The optimization of pre-optimized monomers laid at 1-2 Å led to structures in which the intermolecular interaction energy is around 2.8 kcal/mol (Table 7). The closer placement results in a geometry with one more interaction than that placed at 2 Å. The 2-Å and 3-Å structures have the same C=O...H(CH) interactions, and both have two C=O...H(CH₃) interactions; the 3-Å structure seems to be more stable, although it differs more from the ideal perpendicular form.

As shown in Table 8, the resulting structures based on the canonical forms of the β structures have more stable geometries than those based on the optimized monomers of Table 7.

Table 7. Initial distances (“Initial”, Å) between monomers, relative energies (ΔE , kcal/mol), weak interactions (Å) and graphical representations of the perpendicular β -dimers.

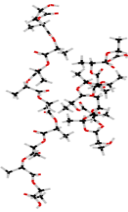
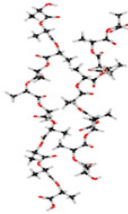
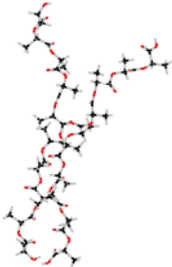
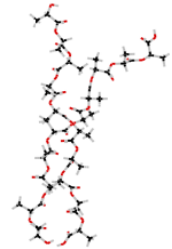
Initial	ΔE	C=O...H(CH)	C=O...H(CH ₃)	Distance	Representation
2	11.35	O42-H133		2.10	
		H49-O126		2.25	
			O51-H138	2.65	
			H63-O117	2.43	
3	22.63	O42-H133		2.25	
		H49-O126		2.12	
			H64-O117	2.44	
			O69-H112	2.70	

Table 8. Initial distances (“Initial”, Å) between monomers, relative energies (ΔE , kcal/mol), weak interactions (Å) and graphical representations of the perpendicular β -dimers (monomers not pre-optimized separately).

Initial	ΔE	C=O...H(CH)	C=O...H(CH ₃)	Other	Distance	Representation
2	29.08		H40(3)-O144		2.35	
		O42-H151(1)			2.25	
			H55(3)-O135		2.32	
			O60-H130(3)		2.45	
			H82(3)-O108		2.69	
				O87(carb)-H95(hyd)	2.09	
3	34.35			O94(hyd)-H93(carb)	1.71	
		O33-H151(1)			2.26	
		H40(1)-O144			2.10	
			H55(3)-O135		2.46	
			O60-H130(3)		2.48	
			H82(3)-O108		2.69	
			O87(carb)-H95(hyd)	2.08		

POLYLACTIC ACID INTER-CHAIN INTERACTIONS

Initial	ΔE	C=O...H(CH)	C=O...H(CH ₃)	Other	Distance	Representation
4	12.12	O33-H160(1)			2.17	
		H40(1)-O144			2.18	
			O42-H165(3)		2.46	

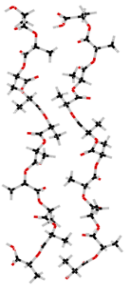
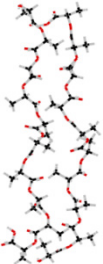
Table 9. Initial distances (“Initial”, Å) between monomers, relative energies (ΔE , kcal/mol), weak interactions (Å) and graphical representations of the perpendicular DeSantis-dimers.

Initial	ΔE	C=O...H(CH)	C=O...H(CH ₃)	Other	Distance	Representation
2	30.88			H4-O181(carb)	2.39	
			O25-H167		2.54	
			H45-O136		2.66	
			H46-O145		2.38	
			H72-O109		2.29	
			O97-H103		2.65	
3	24.72			H23-O181(carb)	2.72	
				H28-O163	2.70	
				H28-O186(carb)	2.64	
		O34-H152			2.26	
		H41-O145			2.18	
			H56-O136		2.43	
			O61-H120		2.54	
			H83-O109		2.69	

Similarly to the β -dimers, the optimization of the DeSantis dimers did not result in any perpendicular geometries (Tables 9 and 10). If in the initial structure based on the pre- monomers the two units are at 2 Å, the dimers become parallel, and the intermolecular energy is 5.5 kcal/mol. The initial monomers located at more than 4 Å led to geometries which are neither parallel nor

perpendicular. The minimum value of the intermolecular energy (3.09 kcal/mol) is at the 4-Å laid monomers, with 8 individual interchain short contacts. If the initial monomers are at 7 Å the two molecules are moving away from each other, and only at one end a weak interaction is formed. With the monomers based on the canonical form placed at 2-3 Å, optimization leads to parallel structures. Six common interactions are seen in the two optimized forms, but the carboxyl-hydrogen interactions occur at the different end of the chains. The highest relative energy value appears at the 3-Å dimer in Table 10. Like in the structures based on optimized monomers, the larger distances conduct to dimers in which the molecules are neither parallel nor perpendicular (Table 10).

Table 10. Initial distances (“Initial”, Å) between monomers, relative energies (ΔE , kcal/mol), weak interactions (Å) and graphical representations of the perpendicular DeSantis-dimers (monomers not pre-optimized separately).

Initial	ΔE	C=O...H(CH)	C=O...H(CH ₃)	Other	Distance	Representation
2	32.06			H14-O181(carb)	2.47	
				O25-H167	2.34	
				O34-H152	2.23	
				H41-O145	2.25	
				H56-O136	2.43	
				O61-H131	2.50	
				H72-O109	2.28	
				O79-H103	2.64	
H83-O99	2.43					
3	34.97			O6(carb)-H94	1.70	
				H14-O172	2.45	
				O34-H152	2.21	
				H41-O145	2.14	
				H56-O136	2.45	
				O61-H131	2.49	
				H72-O109	2.46	
				H83-O99	2.37	

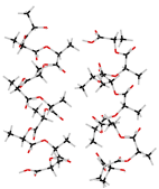
Antiparallel dimers

For these structures, in most of the cases starting from the canonical form the convergence could not be achieved, and therefore only the results of the dimers of dimers based on optimized monomers are discussed here.

POLYLACTIC ACID INTER-CHAIN INTERACTIONS

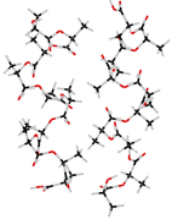
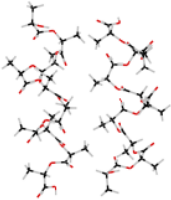
Upon geometry optimization of the α dimers, regardless of how far the dimers are placed (3-5 Å), the same final geometry was obtained – detailed in Table 11. The two units are stabilized by six weak interactions; five of them are C=O...H(CH₃) and one C=O...H(CH). Each intermolecular interaction brings around 3 kcal/mol in terms of energy stabilization.

Table 11. Initial distances (“Initial”, Å) between monomers, relative energies (ΔE , kcal/mol), weak interactions (Å) and graphical representations of the antiparallel α -dimers.

Initial	ΔE	C=O...H(CH)	C=O...H(CH ₃)	Distance	Representation
3	18.14		O24-H165	2.43	
			H26-O153	2.35	
		O51-H133		2.28	
			H53-O126	2.30	
			O78-H111	2.58	
			H80-O98	2.34	

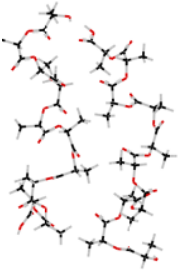
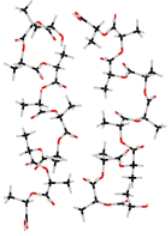
For the 3₁₀ antiparallel dimers (Table 12), the intermolecular interaction energies are about 0.6-0.7 kcal/mol per O---H contact. If the two units are placed further than 6 Å, an interaction between a carboxyl and a hydroxyl group appears and the intermolecular interaction energy increases to 2.8 kcal/mol.

Table 12. Initial distances (“Initial”, Å) between monomers, relative energies (ΔE , kcal/mol), weak interactions (Å) and graphical representations of the antiparallel 3₁₀-dimers.

Initial	ΔE	C=O...H(CH)	C=O...H(CH ₃)	Other	Distance	Representations
2.5	4.96		O15-H160		2.28	
			H13-O153		2.26	
			H17-O162		2.41	
		O42-H124			2.33	
		H49-O126			2.23	
			O51-H128		2.42	
		O78-H96			2.15	
3.5	3.88		H90-O98		2.69	
			O15-H155		2.39	
			H17-O153		2.43	
			O42-H156		2.47	
		O51-H129	2.72			
O78-H96		2.28				

The optimizations of the π dimers led to two types of results, cf. Table 13. If the initial π monomers are placed at 1 Å, the obtained orientation of the dimers is perpendicular; C=O...H(CH) and C=O...H(CH₃) weak interactions are key in this structure. Carboxyl and hydroxyl groups additionally participate when the two monomers are at 2-3 Å initial distances. The preferred relative orientation is antiparallel. The intermolecular interaction energy decreases from 3.5 kcal/mol to 2.2 kcal/mol, although the number of interactions is the same.

Table 13. Initial distances (“Initial”, Å) between monomers, relative energies (ΔE , kcal/mol), weak interactions (Å) and graphical representations of the antiparallel π -dimers.

Initial	ΔE	C=O...H(CH)	C=O...H(CH ₃)	Other	Distance	Representations
2	34.74			O2(hyd)-H94(carb)	1.66	
				O25-H185	2.46	
				H29-O181(carb)	2.28	
				H32-O163	2.23	
				O34-H165	2.31	
				O52-H140	2.49	
				H64-O136	2.61	
				O79-H111	2.25	
				H63-O109	2.55	
				H83-O109	2.51	
3	21.57			O2(hyd)-H183	2.31	
				H4-O181(carb)	2.68	
				O6-H185	2.60	
				O34-H165	2.45	
				H36-O163	2.32	
				O52-H116	2.41	
				O52-H140	2.49	
				H59-O109	2.24	
				O79-H111	2.33	
				H83-O109	2.41	

After the optimization the β dimers remain antiparallel (Table 14). Weak interactions are noted between carboxyl and hydroxyl groups of the two molecules, varying between 4 and 9, and the interaction energy decreases from 4.5 kcal/mol (2 Å) to 3.5 kcal/mol (3 Å) and 3 kcal/mol (4 Å), respectively.

Two types of geometries are obtained upon optimizing the structure described by DeSantis. When the two units are positioned at 2-4 Å, they remain antiparallel with interaction energy of ~ 3.4 kcal/mol per interaction. If the two units are placed further than 5 Å, they will be perpendicular, and the interactions are formed at the termini of the chains (Table 15).

POLYLACTIC ACID INTER-CHAIN INTERACTIONS

Table 14. Initial distances (“Initial”, Å) between monomers, relative energies (ΔE , kcal/mol), weak interactions (Å) and graphical representations of the antiparallel β -dimers.

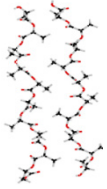
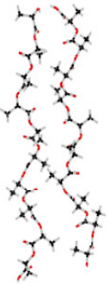
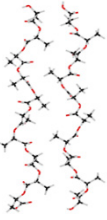
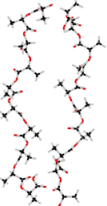
Initial	ΔE	C=O...H(CH)	C=O...H(CH ₃)	Other	Distance	Representations
2	17.98			O4(hyd)-O185	2.39	
			H18-O108		2.24	
			O60-H129		2.22	
			H81-O108		2.35	
3	32.31			O1(hyd)-H186(carb)	1.66	
		H13-O171			2.27	
			O24-H155		2.51	
		O33-H151			2.30	
		H40-O144			2.23	
			H44-O135		2.42	
			O51-H128		2.71	
		O60-H124			2.37	
			H81-O108		2.33	
			H18-O171		2.31	
			O33-H156		2.31	
			H44-O135		2.49	
			O60-H129		2.45	
			H81-O108		2.31	

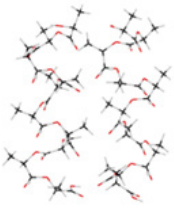
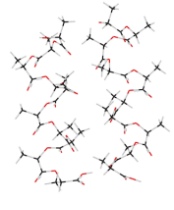
Table 15. Initial distances (“Initial”, Å) between monomers, relative energies (ΔE , kcal/mol), weak interactions (Å) and graphical representations of the antiparallel DeSantis-dimers.

Distance	ΔE	C=O...H(CH)	C=O...H(CH ₃)	Other	Distance	Representations
2	19.01			O2(hyd)-H174	2.31	
			O43-H148		2.39	
		H59-O127			2.36	
		O79-H107			2.25	
				O88(carb)-H97	2.30	
		H92-O99		2.55		
4	14.84			O2(hyd)-H174	2.31	
		O79-H107			2.40	
				O88(carb)-H97	2.47	
		H92-O99			2.40	

Parallel dimers

The parallel structures were obtained by translating a decameric unit with 1-6 Å. Starting from the previously optimized α monomers the two helices hold their directions at any distance apart (Table 16). If they are positioned at 1 - 2 Å, the interaction energy is 3.2 kcal/mol per interaction- and slightly larger if the initial distance is 3-5 Å.

Table 16. Initial distances (“Initial”, Å) between monomers, relative energies (ΔE , kcal/mol), weak interactions (Å) and graphical representations of the parallel α -dimers.

Initial	ΔE	C=O...H(CH)	C=O...H(CH ₃)	Other	Distance	Representations	
2	25.93		O5-H121			2.52	
				H7-O94(hyd)		2.38	
			O33-H129			2.40	
			H40-O117			2.61	
			O60-H183			2.47	
			H72-O144			2.46	
				O87(carb)-H178		2.12	
				H97(carb)-O171		1.67	
3	26.78		O5-H129			2.41	
				H7-O94(hyd)		2.38	
			O33-H156			2.54	
			H45-O117			2.49	
			O60-H183			2.50	
			H72-O144			2.32	
				O87(carb)-H178		2.11	
				H93(carb)-O171		1.69	

The α structures based on the canonical form laid at 1-3 Å maintain the parallel orientation upon geometry optimization (Table 17). Increasing the distance, the dimers lose their parallel orientations and at 6 Å the two units become perpendicular (not shown). Only two interactions keep the molecules together, and the interaction energy per interaction is 3.1 kcal/mol.

For the dimers based on optimized π monomers, longer initial inter-chain distances led to smaller numbers of interactions, but the intermolecular binding energy per individual non-covalent contact increases from 3.8 kcal/mol to 5.6 kcal/mol. In no case do the optimized dimers actually feature parallel structures (Table 18). Four interactions occur in the optimized monomers placed at 3 Å; the relative energy is the same as at 2 Å dimers, but the number of interactions is only half compared to the 2-Å structure.

POLYLACTIC ACID INTER-CHAIN INTERACTIONS

Table 17. Initial distances (“Initial”, Å) between monomers, relative energies (ΔE , kcal/mol), weak interactions (Å) and graphical representations of the parallel α -dimers (monomers not pre-optimized separately).

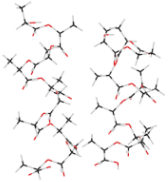
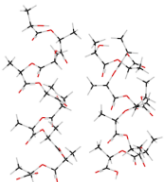
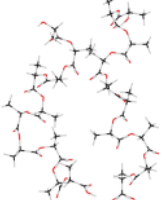
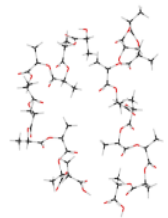
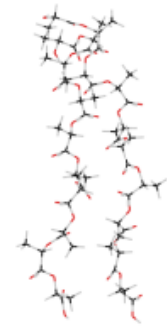
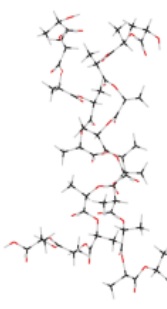
Initial	ΔE	C=O...H(CH)	C=O...H(CH ₃)	Other	Distance	Representations
2 Å	4.12		O15-H129		2.41	
			O42-H128		2.33	
				H80-O180(carb)	2.40	
			H81-O153	2.68		
3 Å	4.12		O15-H129		2.42	
			O42-H128		2.33	
				H80-O180(carb)	2.40	
			H81-O153	2.68		

Table 18. Initial distances (“Initial”, Å) between monomers, relative energies (ΔE , kcal/mol), weak interactions (Å) and graphical representations of parallel π -dimers.

Initial	ΔE	C=O...H(CH)	C=O...H(CH ₃)	Other	Distance	Representations
2	27.25			H1(carb)-O181(carb)	1.68	
			O16-H139	2.44		
			H19-O109	2.58		
			H28-O127	2.44		
			O70-H156	2.51		
	O88(carb)-183	2.32				
3	27.9			H1(hyd)-O181	1.67	
		H4-O99		2.47		
			H28-O127	2.34		
			O88-H183	2.38		

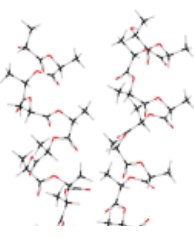
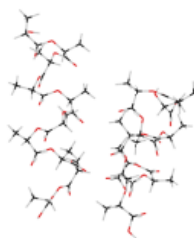
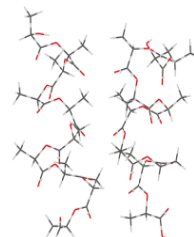
The parallel-placed π monomers based on the canonical form do not maintain their orientation upon geometry optimization, as they become intertwined with each other. Most interactions are of the $\text{C}=\text{O}\cdots\text{H}(\text{CH})$ and $\text{C}=\text{O}\cdots\text{H}(\text{CH}_3)$ types, with no involvement of the carboxyl and hydroxyl groups. A 1.8 kcal/mol stabilization energy per interaction is seen in the 2-Å dimer (Table 19).

Table 19. Initial distances (“Initial”, Å) between monomers, relative energies (ΔE , kcal/mol), weak interactions (Å) and graphical representations of the parallel π -dimers (monomers not pre-optimized separately).

Initial	ΔE	$\text{C}=\text{O}\cdots\text{H}(\text{CH})$	$\text{C}=\text{O}\cdots\text{H}(\text{CH}_3)$	Distance	Representation
2	25.89	O16-H107		2.32	
			O16-H130	2.28	
			H20-O99	2.56	
		O34-H125		2.33	
		O34-H143		2.51	
			O34-H148	2.53	
			H41-O136	2.36	
			H46-O118	2.49	
		O52-H161		2.37	
			H56-O145	2.27	
		H59-O154		2.06	
			H64-O136	2.35	
	O70-H176	2.42			
	H92-O172	2.35			
4	28.25	O16-H107		2.32	
			H20-O99	2.56	
		O34-H125		2.33	
			O34-H148	2.40	
		H41-O136		2.43	
			H46-O118	2.48	
			O52-H166	2.55	
			H56-O145	2.61	
		H59-O154		2.19	
			H64-O136	2.31	
			O70-H176	2.33	
			H82-O163	2.56	

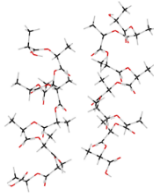
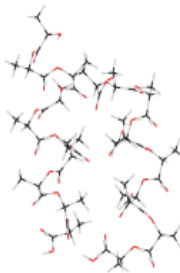
The dimer based on optimized 3_{10} monomers remains parallel if the two units are placed at 1-3 Å, but the monomers are slightly shifted relative to each another (Table 20). The dimer is held together by $\text{C}=\text{O}\cdots\text{H}(\text{CH})$ and $\text{C}=\text{O}\cdots\text{H}(\text{CH}_3)$ weak interactions, at ~ 2 kcal/mol each. On the other hand, upon increasing the initial distance to 4 Å there are more inter-chain interactions.

Table 20. Initial distances (“Initial”, Å) between monomers, relative energies (ΔE , kcal/mol), weak interactions (Å) and graphical representations of the parallel 3_{10} -dimers.

Initial	ΔE	C=O...H(CH)	C=O...H(CH ₃)	Distance	Representation
2	12.47	O42-H151		2.55	
			H44-O144	2.40	
			H45-O117	2.62	
			O69-H175	2.43	
			O69-H183	2.55	
			H71-O153	2.57	
3	11.95		H44-O117	2.37	
		O69-H151		2.16	
		H76-O144		2.33	
			O78-H183	2.45	
			H80-O171	2.62	
4	14.9		H17-O117	2.41	
		O42-H151		2.47	
			H46-O117	2.70	
		H49-O144		2.65	
			H54-O144	2.55	
		O69-H151		2.70	
		H76-O153		2.29	

The 3_{10} monomers based on the canonical form placed at 2-4 Å maintain the parallel orientation upon geometry optimization (Table 21), but the two monomers are shifted with respect to each other. The relative orientation of the monomers obtained starting with the monomers at 5 Å is not parallel anymore; the connection is formed only at one end of the monomers (not shown).

Table 21. Initial distances (“Initial”, Å) between monomers, relative energies (ΔE , kcal/mol), weak interactions (Å) and graphical representations of the parallel 3_{10} -dimers (monomers not pre-optimized separately).

Initial	ΔE	C=O...H(CH)	C=O...H(CH ₃)	Other	Distance	Representations
2	5.86		O15-H119		2.51	
			H45-O117		2.45	
			H71-O144		2.51	
3	24.11		O24-H138		2.45	
		O51-H133			2.49	
			O51-H165		2.49	
		H58-O126			2.24	
			H63-O98		2.40	
				O78-H186(carb)	1.71	
				H80-O185(carb)	2.56	
			H90-O153		2.33	
			O51-H133		2.49	
			O51-H165		2.49	
			H58-O126		2.24	
				H63-O98	2.40	
		O78-H186(carb)	1.71			
		H80-O185(carb)	2.56			
		H90-O153	2.33			

Only the optimizations of the β monomers placed at 1 Å did converge. If the two monomers are moved away from each other no connections are made. In the 1-Å case the structure remains parallel, and seven interactions, of 2.9 kcal/mol each, keep the molecules together (Table 22).

If the initial geometry is based on the canonical form, the two β sheets are coiling around each other (Table 23). This entails fifteen intermolecular contacts/interactions, at ~ 1 kcal/mol each. If the two monomers are further than 1 Å, no connections are formed (as in the case of β dimers based on optimized monomers).

POLYLACTIC ACID INTER-CHAIN INTERACTIONS

Table 22. Initial distances (“Initial”, Å) between monomers, relative energies (ΔE , kcal/mol), weak interactions (Å) and graphical representations of the parallel β -dimers.

Initial	ΔE	C=O...H(CH)	C=O...H(CH ₃)	Other	Distance	Representation
1	20.59			O1(hyd)-H97	2.34	
			O15-H111		2.19	
			H36-O117		2.40	
		O42-H133		2.45		
			O51-H137		2.44	
		H58-O153		2.19		
			O78-H174		2.31	


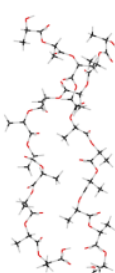
Table 23. Initial distances (“Initial”, Å) between monomers, relative energies (ΔE , kcal/mol), weak interactions (Å) and graphical representations of the parallel β -dimers (monomers not pre-optimized separately).

Initial	ΔE	C=O...H(CH)	C=O...H(CH ₃)	Other	Distance	Representation
1 Å	11.42	O6-H97			2.58	
			O6-H112		2.57	
		H13-O108			2.43	
			O24-H115		2.25	
		H31-O126			2.55	
		O42-H133			2.20	
			H46-O126		2.58	
		H49-O144			2.72	
		O60-H151			2.30	
		H67-O162			2.43	
			H82-O162		2.41	
			H71-O171		2.70	
			O78-H184		2.71	
				O87(carb) – H173	2.63	
		H93(carb) – O180	1.82			

The parallel structure is maintained in the DeSantis dimers based on optimized monomers at 2 Å. Increasing the distance to 3 Å, this orientation is lost (Table 24) and the intermolecular interaction energy decreases from

5.2 kcal/mol to 3.3 kcal/mol. However, the number of interactions increases, and the carboxyl groups evolve more interactions than in the case of dimers laid at 2 Å. If the initial monomers are further than 3 Å, no weak interactions are noted between them (not shown).

Table 24. Initial distances (“Initial”, Å) between monomers, relative energies (ΔE , kcal/mol), weak interactions (Å) and graphical representations of the parallel DeSantis-dimers.

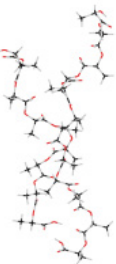
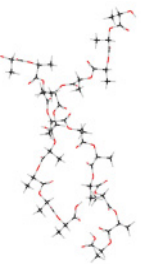
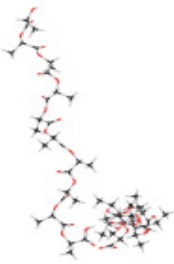
Initial	ΔE	C=O...H(CH)	C=O...H(CH ₃)	Other	Distance	Representations
2	41.82			H1(carb)-O181(carb)	1.70	
				O2(hyd)-H104(hyd)	1.82	
				H4-O99	2.35	
				O25-H131	2.45	
				H46-O136	2.42	
				O52-H157	2.45	
				H73-O163	2.55	
				O79-H94(carb)	1.66	
3	35.98			H1(carb)-O181(carb)	1.71	
				O25-H130	2.37	
				H28-O95(hyd)	2.50	
				H29-O109	2.36	
				O34-H116	2.28	
				H46-O136	2.24	
				O52-H157	2.41	
				H73-O163	2.72	
				O79-H94(carb)	1.64	
				H56-O181(carb)	2.63	
O61-H94(carb)	1.68					

METHODS

Five types of decameric units of polylactic acid were built and optimized using the Hyperchem package as previously described.[21,23] These are analogous to those seen in protein structure - helical structures (α , π , 3_{10}), a β -sheet, and the structure proposed by DeSantis.[21] The dimers were constructed by translating a decameric unit by various values (generally in the range of 2-10 Å), as illustrated in the Tables and text.

Parallel, antiparallel as well as perpendicular structures were considered. Geometry optimizations were performed with the HF method and 3-21G* basis set as implemented in Gaussian, without any constraints on the geometry – including the inter-dimer distance or orientation.[24] Larger basis sets and either a post-HF or a specialized density functional theory variant would afford more accurate results, but they were deemed computationally prohibitive for the set of models examined here.

Table 25. Initial distances (“Initial”, Å) between monomers, relative energies (ΔE , kcal/mol), weak interactions (Å) and graphical representations of the parallel DeSantis-dimers (monomers not pre-optimized separately).

Initial	ΔE	C=O...H(CH)	C=O...H(CH ₃)	Other	Distance	Representations
2	34.80			H1(carb)-O181	1.71	
				O25-H140	2.33	
				H32-O145	2.27	
				H46-O136	2.57	
				O52-H152	2.28	
				H63-O172	2.54	
				H73-O163	2.49	
				O79-H94(carb)	1.70	
3	35.63			H1(carb)-O181	1.71	
				O25-H129	2.42	
				O25-H140	2.36	
				H32-O145	2.21	
				O43-H157	2.45	
				H46-O136	2.37	
				O52-H158	2.72	
				H63-O172	2.47	
4	26.27			H73-O162	2.56	
				O79-H94(carb)	1.71	

CONCLUSIONS

Optimizations of α , π , 3_{10} deca-lactic acid helices placed perpendicularly to each other does in several cases retain this geometry. The geometries obtained from the optimizations of nearly all 3_{10} helices are perpendicular. Optimization of perpendicular β dimers led only once to perpendicular direction. In turn, the structure described by DeSantis does not yield perpendicular dimers after the optimizations. In the case of α and DeSantis dimers, parallel instead of perpendicular structures are obtained upon geometry optimization. This is not valid for π , 3_{10} and β dimers: their most stable geometries are neither parallel nor perpendicular.

Minima for antiparallel and parallel dimer structures were obtained for all the five types of secondary structure – though in several cases severe distortions were noted (e.g., coiling or disordered structures of the monomers).

Table 26 shows a summary of the data collected in the present study – i.e., inter-chain interaction energies calculated per unit of lactic acid. These values are expected to be useful in predicting interaction energies between chains of lengths different from the decameric structures examined in the present study. The weakest interactions are seen for the perpendicular structures; among those, the strongest are for π , 3_{10} , while the DeSantis structure affords no local minimum at all. The strongest interactions are seen with parallel structures – of which the largest interaction energies are with the DeSantis and the π monomers (up to 2.8 and 4.2 kcal/mol per unit of lactic acid, respectively), and the weakest interactions are seen for the α and 3_{10} helices. These results are in line with expectations, insofar as these two canonical helical forms are more compact and predominantly offer methyl groups towards the outside of the helix[21], whereas the DeSantis structure mimics partial structural data obtained from crystalline PLA.[23]

Table 26. Relative energies (kcal/mol) of inter-chain interactions per unit of lactic acid.

ΔE	α	π	3_{10}	β	DeSantis
Perpendicular	1.0	1.5	0.9-1.6	1.2	-
Antiparallel	1.8	2.2-3.5	0.4-0.5	1.8-3.2	1.5-1.9
Parallel	0.4-2.7	2.6-2.8	0.6-2.4	1.1-2.1	2.6-4.2

ACKNOWLEDGMENTS

Funding from the Romanian Ministry of Education and Research (PN-III-P2-2.1-PED2019-2293) is gratefully acknowledged.

REFERENCES

1. A. Södergård; M. Stolt; *Prog. Polym. Sci.* **2002**, *27*, 1123–1163.
2. K. Sreekumar; B. Bindhu; K. Veluraja; *Polym. from Renew. Resour.* **2021**, *12*, 60–74.
3. W. Gao; Z. Wang; F. Song; Y. Fu; Q. Wu; S. Liu; *Polymers (Basel)*. **2021**, *13*, 3492.
4. J. Orellana Barrasa; A. Ferrández-Montero; B. Ferrari; J.Y. Pastor; *Polymers (Basel)*. **2021**, *13*, 2899.
5. J.-W. Park; J.-H. Shin; G.-S. Shim; K.-B. Sim; S.-W. Jang; H.-J. Kim; *Polymers (Basel)*. **2019**, *11*, 349.
6. G. Zhao; F.P.C. Gomes; H. Marway; M.R. Thompson; Z. Zhu; *Macromol. Chem. Phys.* **2020**, *221*,
7. S. Behtaj; F. Karamali; E. Masaeli; Y.G. Anissimov; M. Rybachuk; *Biochem. Eng. J.* **2021**, *166*, 107846.
8. E. Sharifisamani; F. Mousazadegan; R. Bagherzadeh; M. Latifi; *Polym. Eng. Sci.* **2020**, *60*, 1520–1529.
9. T. Batakliiev; V. Georgiev; C. Kalupgian; P.A.R. Muñoz; H. Ribeiro; G.J.M. Fechine; R.J.E. Andrade; E. Ivanov; R. Kotsilkova; *Appl. Compos. Mater.* **2021**, *28*, 1175–1192.
10. M. Jafari; N. Jalalifar; B. Kaffashi; *J. Appl. Polym. Sci.* **2021**, *138*, 49924.
11. S. Wang; B. Liu; Y. Qin; H. Guo; *Membranes (Basel)*. **2021**, *11*, 640.
12. A. Buzmakov; A. Dunaev; Y. Krivososov; D. Zolotov; I. Dyachkova; L. Krotova; V. Volkov; A. Bodey; V. Asadchikov; V. Popov; *Polymers (Basel)*. **2021**, *13*, 1021.
13. A. Kumar; L. Collini; A. Daurel; J.-Y. Jeng; *Addit. Manuf.* **2020**, *33*, 101168.
14. Q. Wang; C. Ji; J. Sun; Q. Zhu; J. Liu; *Molecules* **2020**, *25*, 3306.
15. M. Özcan; D. Hotza; M.C. Fredel; A. Cruz; C.A.M. Volpato; *J. Compos. Sci.* **2021**, *5*, 78.
16. Á. Kmetty; K. Litauszki; *Polymers (Basel)*. **2020**, *12*, 463.
17. A. Lupan; A.-Z.Z. Kun; F. Carrascoza; R. Silaghi-Dumitrescu; *J. Mol. Model.* **2013**, *19*, 193–203.
18. Y.M. Xie; H.F. Schaefer; R. Silaghi-Dumitrescu; B. Peng; Q.S. Li; J.A. Stearns; T.R. Rizzo; *Chem. Eur. J.* **2012**, *18*, 12941–12944.
19. F. Carrascoza; S. Zaric; R. Silaghi-Dumitrescu; *J. Mol. Graph. Model.* **2014**, *50*, 125–133.
20. R. Silaghi-Dumitrescu; *Stud. Univ. Babeş-Bolyai Chem.* **2010**, 31–36.
21. I. Irsai; C. Majdik; A. Lupan; R. Silaghi-Dumitrescu; *J. Math. Chem.* **2012**, *50*, 703–733.

22. I. Irsai; A.M.V. Brânzanic; R. Silaghi-Dumitrescu; *Stud. Univ. Babeş-Bolyai Chem.* **2021**, *66*, 107–121.
23. I. Irsai; A. Lupan; C. Majdik; R. Silaghi-Dumitrescu; *Stud. Univ. Babeş-Bolyai Chem.* **2017**, *62*, 495–513.
24. M.J. Frisch; G.W. Trucks; H.B. Schlegel; G.E. Scuseria; M.A. Robb; J.R. Cheeseman; J. Montgomery J.A.; T. Vreven; K.N. Kudin; J.C. Burant; J.M. Millam; S.S. Iyengar; J. Tomasi; V. Barone; B. Mennucci; M. Cossi; G. Scalmani; N. Rega; G.A. Petersson; *et al.*; in (Gaussian, Inc., **2009**).

MODELLING OF ACIDS AND BASES REVISITED

Lorentz JÄNTSCHI^{a,b}

ABSTRACT. Models for dissociation and mixing of acids and bases are the main subject of many analytical chemistry textbooks. Preparing the solutions for any titration generally involves diluting acids and bases. The mathematics behind precise calculation of pH and pOH is treacherous even for monoprotic acids and bases, becoming mathematically complex when processes of chemical complexation are considered and one should consider any simplifying approximation when available.

Keywords: *dilution, acids, bases, 3D visualization, simulation software*

INTRODUCTION

Titration is a common laboratory method of quantitative chemical analysis to determine the concentration of an identified analyte.

Titrant (reagent) is generally prepared as a standard solution of known concentration. Then the titrant is mixed to react with a solution of analyte (titrand) to determine the analyte's concentration. The volume of titrant that reacted (until equivalence point) with the analyte is termed the titration volume.

There are several textbooks dedicated to the study of the titration process, and Hodisan's is one of them [1].

A titration curve is a curve in graph, the x-coordinate representing the volume of titrant added since the beginning of the titration, and the y-coordinate representing the concentration of the analyte at the corresponding stage of the titration.

^a *Department of Physics and Chemistry, Faculty of Engineering of Materials and Environment, Technical University of Cluj-Napoca, RO-400641, Cluj-Napoca, Romania, lorentz.jantschi@chem.utcluj.ro*

^b *Doctoral School of Chemistry, Faculty of Chemistry and Chemical Engineering, Babeş-Bolyai University, 11 Arany Janos str., RO-400028, Cluj-Napoca, Romania, lorentz.jantschi@ubbcluj.ro*



There are different types of titrations with different procedures and goals. However, the most common types of qualitative titration are acid–base and redox.

In an acid–base titration, the y-coordinate usually represents the pH of the solution, but electrical potential can also be used (p. 92 in [1]). There are two reference moments (points) in titration: the initial (before titration starts) and the equivalence (the moment when the consumption of the analyte by the reagent is identified). However, when an instrumental method of determination is involved, the process usually continues after the equivalence point and the exact position of it on the x-coordinate is determined later [2].

If one reagent is weak (acid or base) and the other is strong (base or acid), the titration curve is irregular and the measured (pH for instance) shifts less with small additions of titrant near the equivalence point. Titration curves for the titration between a weak acid and a strong base are depicted in [3], [4], and [5], between a weak base and a strong acid in [6], [7], and [8], between a weak acid and a weak base in [9], [2], [10], while some connections with buffer solutions are discussed in [11].

Measuring the pH of the solution during titration may have as alternative or accompanying a visual change in colour of the solution if an indicator is used. The next table (Table 1) lists some of those indicators.

It should be noted that each of those indicators are in fact weak acids or bases themselves, so adding them into the reaction flask changes a little the equilibrium point. This is the reason for which, when used, they are used in very small amounts, and one of their important qualities is that they produce the change in colour even if are much diluted.

Equivalence point in titration between a weak acid and a strong base is slightly shifted to the right relative to the pH of neutral water. Thus, for instance, when oxalic acid is titrated with sodium hydroxide, the expectation is to have the equivalence occurring at a pH between 8 and 10. One should notice that Phenolphthalein (entry 19 in Table 1) would be an appropriate visual indicator of the equivalence point. Following the same reasoning, a weak base and a strong acid equivalence point is slightly shifted to the left relative to the pH of neutral water; when ammonia solution is titrated with hydrochloric acid, the expectancy is to have the equivalence occurring at a pH between 4 and 6. One should notice that Methyl red (entry 11 in Table 1) would be an appropriate visual indicator of the equivalence point. Titrations between a weak acid and a weak base have titration curves which are irregular; because of this, no definite indicator may be appropriate and a pH meter is better suited to monitor the reaction. In an acid–base titration, one can see the titration curve representing the strength of the corresponding acid and base. For a strong acid and a strong base, the curve will be relatively

smooth and very steep near the equivalence point. Near the equivalence point, a small change in titrant volume produces a large pH change, thus in this instance many indicators would be appropriate.

Table 1. Colour change based indicators (adapted and corrected from [12], p. 46)

No.	Name	pH range	λ_{\max} [nm]	Colour change
1	Dihydroxyphthalophenone, Phenolphthalein	(-2.0, -1.0)	374,552	o/-
2	o-Cresolsulfonphthalein, Cresol red	(0.5, 2.5)	519	p/y
3	Trinitrophenol, Picric acid	(0.6, 1.3)	465	-/y
4	Thymolsulfonphthalein, Thymol blue	(1.2, 2.8)	594	r/y
5	m-Cresolsulfonphthalein, Metacresol purple	(1.2, 2.8)	434, 578	r/y
6	Dinitrophenol, α -Dinitrophenol	(2.4, 4.0)	360	-/y
7	Tetrabromofenolsulfonphthalein, Bromophenol blue	(3.0, 4.6)	437, 592	y/b
8	Sodium diphenyldiazo-naphthylaminesulfonate, Congo red	(3.0, 5.0)	343, 496	b/r
9	Benzenesulfonic acid, Methyl orange	(3.1, 4.4)	464	r/o
10	Tetrabromo-m-cresolphthalein sulfone, Bromocresol green	(3.8, 5.4)	423	y/b
11	Dimethylaminoazobenzene-2-carboxylic acid, Methyl red	(4.4, 6.2)	435, 520	r/y
12	5,5'-Dibromo-o-cresolsulfonphthalein, Bromocresol purple	(5.2, 6.8)	419	y/p
13	Dibromothymolsulfonphthalein, Bromothymol blue	(6.0, 7.6)	431	y/b
14	o-Cresolsulfonphthalein, Cresol red	(6.5, 8.5)	573	y/p
15	Hydroxyphenylazo-vinylenebenzenesulphonate, Brilliant yellow	(6.6, 7.8)	400	y/o
16	Phenolsulfonphthalein, Phenol red	(6.8, 8.2)	415, 560	y/p
17	m-Cresolsulfonphthalein, Metacresol purple	(7.4, 9.0)	434, 578	y/p
18	Thymolsulfonphthalein, Thymol blue	(8.0, 9.6)	376	y/b
19	Dihydroxyphthalophenone, Phenolphthalein	(8.3,10)	374,552	-/p/-
20	Thymol phenolphthalein, Thymolphthalein	(9.3, 10.5)	595	-/b
21	5-(3-Nitrophenylazo)salicylic acid sodium salt, Alizarin yellow	(10.1, 12.0)	375	y/r
22	C ₂₈ H ₁₉ N ₅ Na ₂ O ₆ S ₄ , Clayton yellow	(12.2, 13.2)	403	y/r

λ_{\max} : UV-Vis maximum absorption wavelength(s); Colours: orange, purple, yellow, red, blue

The process of titration is a recurrent process - small amounts of reagent are consecutively added, and in general can be watched by permanent measurement of either a simple property such as pH [13], mass [14], current intensity [15], potential [16], volume [17], or a complex property such as adsorption [18], heat of reaction [19], which needs a complex evaluation.

Since the numerical solutions of nonlinear equations associated with chemical equilibriums are often stressing the computation capability of the numerical processor, as both pH and pOH often are around the value of 7, near the machine epsilon of single precision computations, this manuscript aims to investigate the numerical stability of some models for dilution of acids and bases.

MATHEMATICAL MODELLING

Let us use a, b, c, w, g, h, u and v as variables (Eq. (1), where N_0 stands for “number of” moles) expressing corresponding quantities.

$$\begin{aligned} a &= N_0(A^-), b = N_0(B^+), c = N_0(AB), w = N_0(H_2O), \\ g &= N_0(HO^-), h = N_0(H^+), u = N_0(HA), v = N_0(BOH) \end{aligned} \quad (1)$$

It should be noted that Eq. (1) are more than simple notations; it is also assumed that the variables are common for all equations, which, in terms of chemistry is translated that all species may exist, in (a general) equilibrium, as a chemical system.

Let d be the (molar) fraction (mol/mol) of a HA solution (HA + H₂O); then x moles of HA + H₂O contain xd HA and $x(1-d)$ H₂O.

Let e be the (molar) fraction (mol/mol) of BOH solution (BOH + H₂O); then y moles of BOH + H₂O contain ye BOH and $y(1-e)$ H₂O.

Upon mixing these two solutions, Table 2 gives the balance for the mixture.

Table 2. HA + BOH + H₂O balance without complexation (see Eq. (1) and Eq. (13))

Mixture	$x \cdot dHA + x \cdot (1-d)H_2O + y \cdot eBOH + y \cdot (1-e)H_2O$	
Equilibrium	$aA^- + bB^+ + cAB + wH_2O + gHO^- + hH^+ + uHA + vBOH$	
Species total	z	$a + b + c + w + g + h + u + v$
Charges balance	$a + g$	$h + b$
A total	xd	$a + c + u$
B total	ye	$b + c + v$
HO total	$x(1-d) + ye + y(1-e)$	$w + g + v$
H total	$xd + x(1-d) + ye + y(1-e)$	$w + h + u$
acidity constant	$k_a u z$	ah
basicity constant	$k_b v z$	bg
salt dissociation constant	$k_c c z$	ab
water dissociation constant	$k_w w z$	gh

If $d = 0$ (instead of HA, the solution is only water), then the system defined in Table 2 simplifies to the one given in Table 3.

Table 3. BOH + H₂O balance without complexation (see Eq. (1) and Eq. (13))

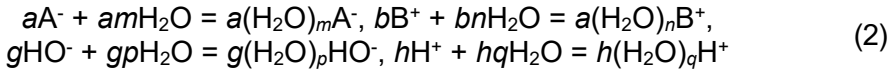
Mixture ($d = 0$)	$xH_2O + y \cdot eBOH + y \cdot (1-e)H_2O$	
Equilibrium ($a = c = u = 0$)	$bB^+ + wH_2O + gHO^- + hH^+ + vBOH$	
Species total	z	$b + w + g + h + v$
Charges balance	g	$h + b$
B total	ye	$b + v$
HO total	$x + y$	$w + g + v$
H total	$x + y(1-e)$	$w + h$
basicity constant	$k_b v z$	bg
water dissociation constant	$k_w w z$	gh

Similarly, if $e = 0$ (instead of BOH, the solution is only water), then the system defined in Table 2 simplifies to the one given in Table 4.

Table 4. HA + H₂O balance without complexation (see Eq. (1) and Eq. (13))

Mixture ($e = 0$)	$x \cdot d\text{HA} + x \cdot (1-d)\text{H}_2\text{O} + y\text{H}_2\text{O}$	
Equilibrium ($b = c = v = 0$)	$a\text{A}^- + w\text{H}_2\text{O} + g\text{HO}^- + h\text{H}^+ + u\text{HA}$	
Species total	z	$a + w + g + h + u$
Charges balance	$a + g$	h
A total	xd	$a + u$
HO total	$x(1-d) + y$	$w + g$
H total	$x + y$	$w + h + u$
acidity constant	$k_a u z$	ah
water dissociation constant	$k_w w z$	gh

When complexation is considered (Eq. (14)), by applying the conservation of atoms numbers, the following equations are established (Eq. (2)).



When complexation is considered (Eq. (14)), part of the water molecules (exactly $a \cdot m + b \cdot n + g \cdot p + h \cdot q$ moles) is fixed into the clusters and the equilibrium is slightly changed. Thus, for the same x moles of HA + H₂O solution of d (molar) fraction (mol/mol) mixed with y moles of BOH + H₂O solution of e (molar) fraction (mol/mol), the new balance for the mixture is given in Table 5.

Table 5. HA + BOH + H₂O balance with complexation (see Eq. (1) and Eq. (14))

Mixture	$x \cdot d\text{HA} + x \cdot (1-d)\text{H}_2\text{O} + y \cdot e\text{BOH} + y \cdot (1-e)\text{H}_2\text{O}$	
Equilibrium	$a(\text{H}_2\text{O})_m\text{A}^- + b(\text{H}_2\text{O})_n\text{B}^+ + c\text{AB} + w\text{H}_2\text{O} + g(\text{H}_2\text{O})_p\text{HO}^- + h(\text{H}_2\text{O})_q\text{H}^+ + u\text{HA} + v\text{BOH}$	
Species total	z	$a + b + c + w + g + h + u + v$
Charges balance	$a + g$	$h + b$
A total	xd	$a + c + u$
B total	ye	$b + c + v$
HO total	$x(1-d) + y$	$w + g + v + am + bn + gp + hq$
H total	$x + y(1-e)$	$w + h + u + am + bn + gp + hq$
acidity constant	$k_a u z w^{m+q}$	ahz^{m+q}
basicity constant	$k_b v z w^{n+p}$	bgz^{n+p}
salt dissociation constant	$k_d c z w^{n+q}$	abz^{n+q}
water dissociation constant	$k_w w z w^{p+q}$	ghz^{p+q}

If $d = 0$ (instead of HA, the solution is only water), then the system defined in Table 5 simplifies to the one given in Table 6.

Table 6. BOH + H₂O balance with complexation (see Eq. (1) and Eq. (14))

Mixture ($d = 0$)	$x\text{H}_2\text{O} + y \cdot e\text{BOH} + y \cdot (1-e)\text{H}_2\text{O}$	
Equilibrium ($a = c = u = 0$)	$b(\text{H}_2\text{O})_n\text{B}^+ + w\text{H}_2\text{O} + g(\text{H}_2\text{O})_p\text{HO}^- + h(\text{H}_2\text{O})_q\text{H}^+ + v\text{BOH}$	
Species total	z	$b + w + g + h + v$
Charges balance	g	$h + b$
B total	ye	$b + v$
HO total	$x + y$	$w + g + v + bn + gp + hq$
H total	$x + y(1-e)$	$w + h + bn + gp + hq$
basicity constant	$k_b v z w^{n+p}$	bgz^{n+p}
water dissociation constant	$k_w w z w^{p+q}$	ghz^{p+q}

If $e = 0$ (instead of BOH, the solution is only water), then the system defined in Table 5 simplifies to the one given in Table 7.

Table 7. HA + H₂O balance with complexation (see Eq. (1) and Eq. (14))

Mixture ($e = 0$)	$x \cdot d\text{HA} + x \cdot (1-d)\text{H}_2\text{O} + y\text{H}_2\text{O}$	
Equilibrium ($b = c = v = 0$)	$a(\text{H}_2\text{O})_m\text{A}^- + w\text{H}_2\text{O} + g(\text{H}_2\text{O})_p\text{HO}^- + h(\text{H}_2\text{O})_q\text{H}^+ + u\text{HA}$	
Species total	z	$a + w + g + h + u$
Charges balance	$a + g$	h
A total	xd	$a + u$
HO total	$x(1-d) + y$	$w + g + am + gp + hq$
H total	$x + y$	$w + h + u + am + gp + hq$
acidity constant	$k_a u z w^{m+q}$	ahz^{m+q}
water dissociation constant	$k_w w z w^{p+q}$	ghz^{p+q}

RESULTS AND DISCUSSION

General considerations about the numerical simulation

Table 2 gives the general system of equations, characterizing the dissociation in water for the HA + BOH + H₂O (neutralization) system, without considering the ions complexation processes, while Table 5 gives the general system of equations, characterizing the dissociation in water for the HA + BOH + H₂O (neutralization) system and considering the ions complexation processes. However, to solve these equations analytically, no symbolic calculation software (including ptc MathCad and Wolfram Mathematica) is able to provide calculation formulas (not even for the simpler case, without complexation).

The formulation of the general problem is of non-negative least squares type (for typical uses see for instance [20]). One should notice that the simplex method (or algorithm) is not applicable, since the system also contains non-linear equations (last four equations in Tables 2 and 5). The

solution for the general cases (Table 2 and Table 5) is not simple at all and requires a few mathematical tricks (cite [21-25]) which are out of scope in the discussion here.

Two limit cases were considered here: BOH dilution (Table 3 without complexation and Table 6 with complexation) and HA dilution (Table 4 without complexation and Table 7 with complexation). When referring to the experimental data regarding the acidity, basicity and dissociation constants, it cannot be said for sure that their values were patched to correct for the complexation effects so that the definitions of those constants were in perfectly valid agreement with their values. Since the complexation processes always exist (Eq. (14)), it is possible that their corresponding twins (Eq. (15)) are in fact usually determined. Here both scenarios are considered, and corresponding plots are given.

BOH + H₂O and HA + H₂O systems without complexation

The system of equations defined in Tables 3 and 4 may be conveniently processed to express the variables of interest. In Tables 3 and 4, one more equation than the number of unknown variables is given, but not all equations are independent. No matter how one may approach the system, exactly four out of the first five equations are independent. One may say that the system defined in Tables 3 and 4 admits only one unique solution (and this makes physical sense) but a mathematical solving of the system reveals the need to deal with more than one solution (in fact, the polynomial has three real roots but only one is positive) from which we need to select the solution which have physical sense. Specifically, any solution with non-positive (" ≤ 0 ") values for any of the variables makes no physical sense.

The equation giving the quantity of H⁺ (h) from the BOH + H₂O system (Table 3) is given as Eq. (3), in which the true value of h is the positive ($h > 0$) root of the equation.

$$\begin{aligned} f_3 h^3 + f_2 h^2 - f_1 h - f_0 &= 0, \\ f_3 &= (1+k_b)(1+k_w), f_2 = k_b(1-e+k_w)y + e k_w y + k_b(1+k_w)x, \\ f_1 &= (x+y)(e(k_b-k_w)y + (1+k_b)k_w(x+y)), f_0 = k_b k_w (x+y)^3 \end{aligned} \quad (3)$$

The equation giving the quantity of HO⁻ (g) from the BOH + H₂O system (Table 3) is given as Eq. (4), in which the true value of g is the positive ($g > 0$) root of the equation.

$$\begin{aligned} f_3 g^3 + f_2 g^2 - f_1 g - f_0 &= 0, \\ f_3 &= (k_b-k_w)(1+k_w), f_2 = e(k_b-k_w)(1+2k_w)y + k_w(1+k_w)(x+y), \\ f_1 &= (k_b-k_w)k_w((x+y)^2 - (ey)^2), f_0 = (x+y)(k_w(x+y-ey))^2 \end{aligned} \quad (4)$$

The equation giving the quantity of H^+ (h) from the $HA + H_2O$ system (Table 4) is given as Eq. (5), in which the true value of h is the positive ($h > 0$) root of the equation.

$$\begin{aligned} f_3 h^3 + f_2 h^2 - f_1 h - f_0 &= 0, \\ f_3 &= (k_a - k_w)(1 + k_w), \quad f_2 = d(k_a - k_w)(1 + 2k_w)x + k_w(1 + k_w)(x + y), \\ f_1 &= (k_a - k_w)k_w((x + y)^2 - (dx)^2), \quad f_0 = (x + y)(k_w(x + y - dx))^2 \end{aligned} \quad (5)$$

The equation giving the quantity of HO^- (g) from the $HA + H_2O$ system (Table 4) is given as Eq. (6), in which the true value of g is the positive ($g > 0$) root of the equation.

$$\begin{aligned} f_3 g^3 + f_2 g^2 - f_1 g - f_0 &= 0, \\ f_3 &= (1 + k_a)(1 + k_w), \quad f_2 = k_a(1 - d + k_w)x + dk_w x + k_a(1 + k_w)y, \\ f_1 &= (x + y)(d(k_a - k_w)x + (1 + k_a)k_w(x + y)), \quad f_0 = k_a k_w (x + y)^3 \end{aligned} \quad (6)$$

One should notice the symmetry in the equations (by symmetry Eq. (3) and (6) are paired; Eq. (4) and (5) are also paired). The presence of the symmetry stands as proof that the formulas have no typo errors.

BOH + H₂O and HA + H₂O systems with complexation

Moving to seek for solutions to the complexation problem (Tables 6 and 7), the problem is not simple anymore and also no analytical formula can be derived with the current symbolic calculation software. Thus, this case falls (again and) already in the numerical optimization. However, since it appears in an important theoretical and practical case - dilution of acids and bases with important impact into protonated systems [26] - it is further discussed and exemplified here.

In the case of BOH complexation in water (Table 6) one approach leading to a solution is expressing all others as functions of b (quantity of $(H_2O)_n B^+$) and g (quantity of $(H_2O)_p HO^-$), and Eq. (7) gives the result of this approach.

$$\begin{aligned} d = a = c = u = 0; \quad v = ye - b - c; \quad h = g + a - b; \\ w = x(1-d) + y - g - v - am - bn - gp - hq \text{ or } x + y(1-e) - h - u - am - bn - gp - hq; \\ z = a + b + c + g + h + u + v + w \\ 0 = k_b v z w^{\rho+n} - b g z^{\rho+n} \\ 0 = k_w w z w^{\rho+q} - g h z^{\rho+q} \end{aligned} \quad (7)$$

The last two equations in Eq. (7) can be solved by constrained optimization ($b, g, h, v, w, z > 0$; $b < ye, g < (x+y)/(p+1)$).

Similarly, in the case of HA complexation in water (Table 7) one approach leading to a solution is to express all others as functions of a (quantity of $(\text{H}_2\text{O})_m\text{A}^-$) and h (quantity of $(\text{H}_2\text{O})_q\text{H}^+$), and Eq. (8) gives the result of this approach.

$$\begin{aligned}
 e &= b = c = v = 0; u = xd - a - c; g = h + b - a; \\
 w &= x(1-d)+y-g-v-am-bn-gp-hq \text{ or } x+y(1-e)-h-u-am-bn-gp-hq; \\
 z &= a+b+c+g+h+u+v+w \\
 0 &= k_a u z w^{m+q} - a h z^{m+q} \\
 0 &= k_w w z w^{p+q} - g h z^{p+q}
 \end{aligned} \tag{8}$$

Once the values of b and g are obtained by solving the last two equations of Eq. (7), the value of the rest of the variables are to be found from the other equations part of the Eq. (7), and Eq. (8) is addressed in a similar manner. The value of the pH and of the pOH are simply expressed by Eq. (9).

$$\text{pH} = \log_{10} h - \log_{10} z, \text{ pOH} = \log_{10} g - \log_{10} z \tag{9}$$

Numerical results and discussion

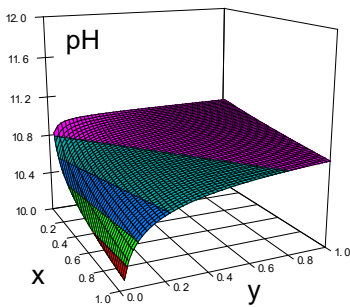
The numerical implementation of the models has shown that it is difficult to draw definite conclusions about the path followed by the process in the case of complexation, and this is a negative result. It seems that there exists at least another saddle point which prevents the global optimization to reach the global optimum. In the Table 8 such an example is given for the case of $\text{BOH} + \text{H}_2\text{O}$. As inspecting the values in Table 8 reveals, Case 1 is a typical case of near-total dissociation (the quantity of undissociated BOH is about 30000 times smaller than the quantity of B^+) while Case 2 is a case of partial dissociation (the quantity of undissociated BOH is about 2 times smaller than the quantity of B^+). Even so, the big difference is actually from the dissociation of water. As such, in Case 1 a significant amount of water molecules are dissociated when compared to Case 2, and this fact is visible through the quantity of hydrogen ions (h in Table R1; about $9 \cdot 10^{-4}$ moles in Case 1 vs. $2 \cdot 10^{-13}$ moles in Case 2) and from amount of free and undissociated water molecules (w in Table 8; about $1.4 \cdot 10^{-2}$ moles in Case 1 vs. $2.7 \cdot 10^{-2}$ moles in Case 2).

Table 8. $b(\text{H}_2\text{O})_n\text{B}^+ + w\text{H}_2\text{O} + g(\text{H}_2\text{O})_p\text{HO}^- + h(\text{H}_2\text{O})_q\text{H}^+ + v\text{BOH}$ equilibrium: two numerical solutions to Eq. (7)

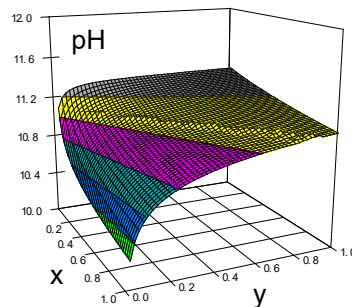
Parameters and Equations	Case 1	Case 2
$n = p = q = 4; d = a = c = u = 0; k_w = 10^{-14}, k_b = 10^{4.747}$ (dissociation constant of a very strong base; hypothetical value); $e = 0.1, x = y = 0.02$ moles		
b	$1.9999 \cdot 10^{-3}$	$1.3358 \cdot 10^{-3}$
g	$2.8920 \cdot 10^{-3}$	$1.3358 \cdot 10^{-3}$
h	$8.9205 \cdot 10^{-4}$	$2.1176 \cdot 10^{-13}$
v	$6.7571 \cdot 10^{-8}$	$6.6415 \cdot 10^{-4}$
w	$1.3972 \cdot 10^{-2}$	$2.7313 \cdot 10^{-2}$
z	$1.9756 \cdot 10^{-2}$	$3.0650 \cdot 10^{-2}$
$a+b+c+g+h+u+v+w-z$	$1.76 \cdot 10^{-8}$	$-1.25 \cdot 10^{-6}$
$a+g-h-b$	$5.00 \cdot 10^{-8}$	$-2.12 \cdot 10^{-13}$
$b+c+v-ye$	$-3.24 \cdot 10^{-8}$	$-5.00 \cdot 10^{-8}$
$w+g+v+am+bn+gp+hq-x(1-d)-y$	$-1.32 \cdot 10^{-7}$	$-6.50 \cdot 10^{-7}$
$w+h+u+am+bn+gp+hq-x-y(1-e)$	$-1.50 \cdot 10^{-7}$	$-6.00 \cdot 10^{-7}$
$k_b v z w^{\rho+n} - b g z^{\rho+n}$	$-2.59 \cdot 10^{-20}$	$3.52 \cdot 10^{-13}$
$k_w w z w^{\rho+q} - g h z^{\rho+q}$	$-5.99 \cdot 10^{-20}$	$-2.18 \cdot 10^{-28}$
total residual (unexplained) error*	$3.8 \cdot 10^{-7}$	$2.6 \cdot 10^{-6}$

Note: *as sum of absolute values (with the number of digits given in Table 8); with Float 64-bit precision the total residuals are $2.6 \cdot 10^{-18}$ (Case 1) and $3.5 \cdot 10^{-13}$ (Case 2) respectively.

The following figures depict the change in pH and in pOH due to dilution for one base (NH_4OH , with $n = 4, p = 4$ and $q = 4$ [27] and $k_b = 10^{4.747}$).

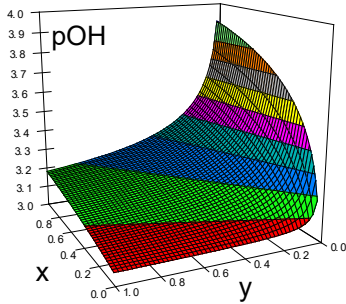


(a) Values obtained with Eq. (3)

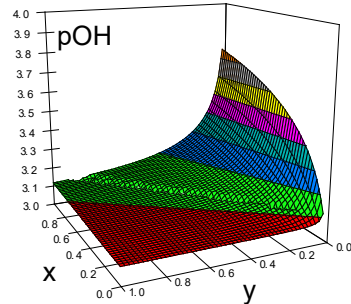


(b) Values obtained with Eq. (7)

Figure 1. pH of y moles of $0.1 \text{ mol/mol NH}_3 + \text{H}_2\text{O}$ solution diluted with x moles H_2O - with (a) and without (b) assumption of complexation



(a) Values obtained with Eq. (4)

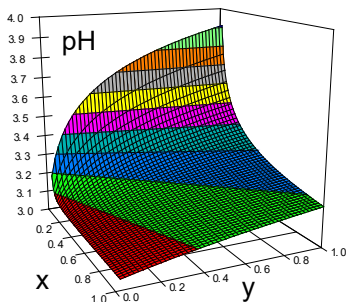


(b) Values obtained with Eq. (7)

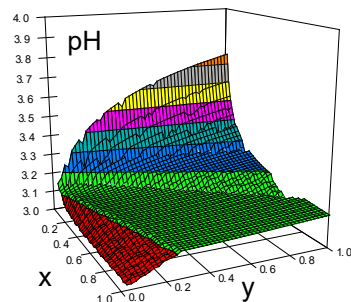
Figure 2. pOH of y moles of 0.1 mol/mol $\text{NH}_3 + \text{H}_2\text{O}$ solution diluted with x moles H_2O - with (a) and without (b) assumption of complexation

For small amounts of added water (x) under the assumption of complexation, there is a considerable amount of water required for complexation. For each NH_4OH dissociated molecule, 8 water molecules are required to construct $(\text{H}_2\text{O})_4\text{NH}_4^+$ and $(\text{H}_2\text{O})_4\text{HO}^-$ complexes ($p = 4$ and $n = 4$ in Eq. (5)). Similarly, for each H_2O dissociated molecule, another 8 water molecules are required to construct $(\text{H}_2\text{O})_4\text{H}^+$ and $(\text{H}_2\text{O})_4\text{HO}^-$ complexes ($p = 4$ and $q = 4$ in Eq. (5)). This is the most likely explanation for which the solution of Eq. (15) model jumps between two local minima like in Table R1 and visible in Fig. 1(b) and Fig. 2(b) as vertical surfaces. The relative change in pH and pOH is still small (no more than 0.1 log units) and is larger for small amounts of water and large amounts of ammonium hydroxide.

The following figures depict the change in pH and in pOH due to dilution for one acid (CH_3COOH , with $p = 4$, $q = 4$ and $m = 6$ [28] and $k_a = 10^{-4.754}$).



(a) Values obtained with Eq. (5)



(b) Values obtained with Eq. (8)

Figure 3. pH of x moles of 0.1 mol/mol $\text{CH}_3\text{COOH} + \text{H}_2\text{O}$ solution diluted with y moles H_2O - with (a) and without (b) assumption of complexation

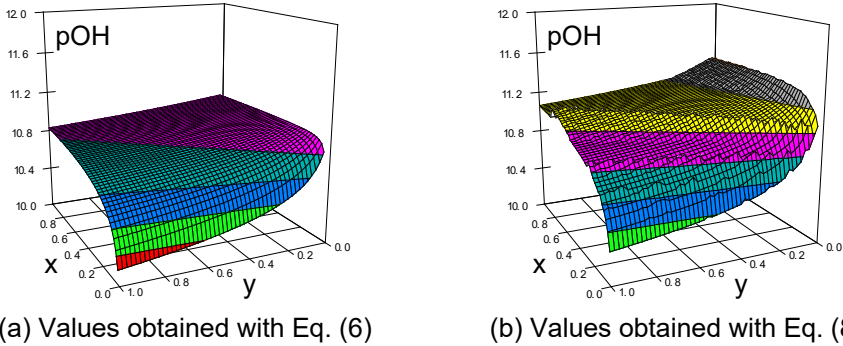
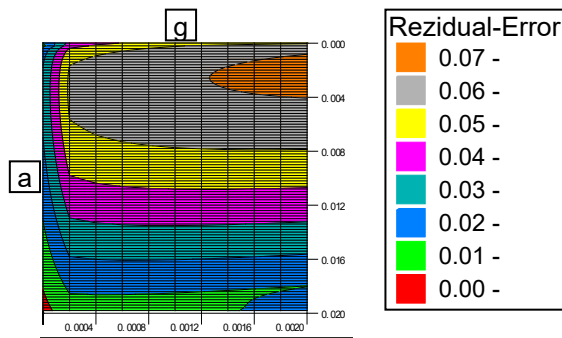


Figure 4. pH of x moles of 0.1 mol/mol CH₃COOH + H₂O solution diluted with y moles H₂O - with (a) and without (b) assumption of complexation

Equations as given in Tables 2 and 5 support further generalization. Let's assume that we have the equilibrium constants as function of temperature (for instance as in [29] p. 137). In that case, at any arbitrary temperature in the applicability domain of the defined functions of temperature, the standard values of the constants are simply replaced by the new values, at the new temperature.

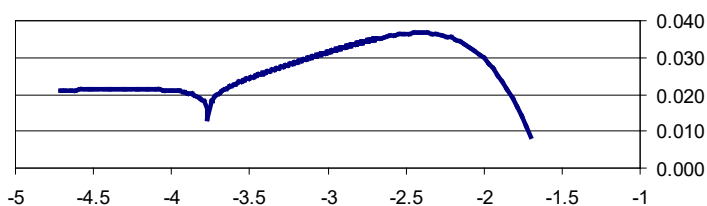
The main difficulty encountered in obtaining the global minima defining the equilibrium in the solution for which the complexation phenomena are considered into the model were due to the shape of the residual error. Considering the case of the acetic acid diluted with water for which pH and pOH are represented in Figures 3 and 4 for x and y ranging from 0.02 mol to 1 mol while Figure 5 represents the residual error (Rezidual-Error(a, g) from Figure 5) for initial guess values of a and g ranging from 0.00 to 0.02 mol.



$$\text{Rezidual-Error}(a, g) = (k_a u z w^{m+q} - a h z^{m+q})^{1/8} + (k_w w z w^{p+q} - g h z^{p+q})^{1/8}$$

Figure 5. Residual error in finding of the quantities of chemical species for x = 0.2 mol of CH₃COOH + H₂O 0.1 mol/mol diluted with 0.02 mol of H₂O: a region containing the global minima (near a = 0 and g = 0) and another valley region (near a = 0.02 and g = 0)

Figure 5 reveals that the choice of initial values is determinant in finding of the global minima. A good initial guess for the case depicted in Figure 5 lies in the upper part of the representation (for instance $a = 0.002$ mol, $g = 0.0002$ mol) - and this choice leads to the global minima being in the right side of the ridge (orange spot in Figure 5) while a poor initial guess lies in the lower part of the representation (for instance $a = 0.016$ mol, $a = 0.0002$ mol) - and this choice leads to a local minima being in the wrong side of the ridge (see Figure 6).



$$\text{Residual-Error}(a, g) = (k_a u z w^{m+q} - a h z^{m+q})^{1/8} + (k_w w z w^{p+q} - g h z^{p+q})^{1/8}$$

Figure 6. Residual error for $x = 0.2$ mol of $\text{CH}_3\text{COOH} + \text{H}_2\text{O}$ 0.1 mol/mol diluted with 0.02 mol of H_2O when $g = 5 \cdot 10^{-10}$ as function of a (in logarithmic scale)

The main trouble in the optimization actually resides in the fact that the global minima is located in a steep ravine (see Figure 6) which is not visible in a regular grid search (like the one used in Figure 5). For this reason a successful optimization must either start from a very good starting point or use heuristics capable of identifying the global minima.

CONCLUSIONS

The study aimed to investigate the differences which may appear in dissociation by using pH and pOH as indicators of dissociation when complexation of the dissociated ions is accounted. The models for acids and bases mixing and dilution were derived. Analytic solutions were derived for solving without complexation and a numeric approach was used for solving with complexation. Stability of the numeric approach was found questionable and some local minima may be responsible for the failure of the global minimum search. When the models with and without complexation were compared, small differences in the values of pH were obtained for solutions of CH_3COOH and NH_4OH . The proposed approach can be applied for dilution and mixing of any acid and base as long as the acidity, basicity and dissociation constants are known.

Starting from general equilibrium equations (Tables 2 and 5) numerical solutions for acid-base titrations can be derived as well.

EXPERIMENTAL SECTION

Chemical activity (a in Eq. (10)) measures effective concentration of a species (Sp in Eq. (10)) in a mixture, in the sense that the species' chemical potential (μ in Eq. (10)) depends on the activity of a real solution in the same way that it would depend on concentration for an ideal solution [30,31] (Eq. (1)).

$$a(Sp) = \exp\left(\frac{\mu(Sp) - \mu^\circ(Sp)}{RT}\right) \quad (10)$$

where R is the constant of gases ($R = 8.31446261815324 \text{ J/mol}\cdot\text{K}$), T the temperature and $\mu(Sp)$ and $\mu^\circ(Sp)$ are the chemical potential and its standard value which depends on the choice of the standard state. Activity depends on temperature, pressure and composition of the mixture.

For a solvent in the liquid state (such as for H_2O) the standard state is that of the pure substance in the liquid or solid phase at the standard pressure p° (of $10^5 \text{ Pa} = 1 \text{ bar}$). For a solute (such as a salt AB) in liquid solution it is the (hypothetical) state of solute at the standard molality m° (of 1 mol/kg) or standard concentration c° (of 1 mol/dm^3) and exhibiting infinitely dilute solution behaviour.

Equilibrium constants (K) are strictly thermodynamically defined [32] in terms of (relative) activities. For a general chemical reaction involving R_1, R_2, \dots, R_r as reactants, S_1, S_2, \dots, S_s as products, and $\alpha_1, \alpha_2, \dots, \alpha_r, \beta_1, \beta_2, \dots, \beta_s$ as stoichiometric coefficients, the equilibrium constant is defined as in (Eq. (11)).

$$K(\alpha_1 R_1 + \dots + \alpha_r R_r \rightleftharpoons \beta_1 S_1 + \dots + \beta_s S_s) \\ = \prod_{i=1}^s (a(S_i))^{\beta_i} / \prod_{j=1}^r (a(R_j))^{\alpha_j} \quad (11)$$

The activity for each species is defined in terms of some measurable quantity, e.g., a concentration, a partial pressure, a mole fraction, so that the activity approaches this quantity as the system approaches a certain limiting state.

Standard free energy change (ΔG°) is related to the equilibrium constant (K) via Eq. (12).

$$-RT\ln K(\sum_i \alpha_i R_i \rightleftharpoons \sum_j \beta_j S_j) = \Delta G^\circ(\sum_i \alpha_i R_i \rightleftharpoons \sum_j \beta_j S_j) \quad (12)$$

When relating the dissociation in water with known quantities, the definition formulas for acidity constant (K_a), basicity constant (K_b), dissociation constant (K_D) and ionic product of water (K_w) should be used. In Eq. (13), the volume of the solution was noted with z for convenience, and ΔG° is the standard free enthalpy of the reaction.

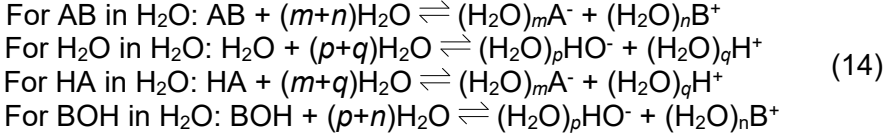
$$\begin{aligned} K(AB \rightleftharpoons A^- + B^+) &= K_D = a(A^-)a(B^+)/a(AB) \\ K(H_2O \rightleftharpoons HO^- + H^+) &= K_w = a(HO^-)a(H^+)/a(H_2O) \\ K(HA \rightleftharpoons A^- + H^+) &= K_a = a(A^-)a(H^+)/a(HA) \\ K(BOH \rightleftharpoons HO^- + B^+) &= K_b = a(HO^-)a(B^+)/a(BOH) \end{aligned} \quad (13)$$

When one express ionic product of water $K_w = a(H^+)a(HO^-)$ it actually omits the activity of water, $a(H_2O)$, which means that the value of K_w differs from the value of K_w from Eq. (4). Table 2 gives some values for comparison ($K_w = K_w \cdot M(H_2O)/\rho(H_2O)$, where M the molar mass [g/mol] and ρ the density [g/l]).

Table 9. Constant of dissociation and ionic product of water at some temperatures

t (°C)	K_w [l/mol]	K_w	pK_w [33]
0	$2.02 \cdot 10^{-17}$	$1.12 \cdot 10^{-15}$	14.95
25	$1.84 \cdot 10^{-16}$	$1.02 \cdot 10^{-14}$	13.99
50	$9.89 \cdot 10^{-16}$	$5.49 \cdot 10^{-14}$	13.26
75	$3.59 \cdot 10^{-15}$	$2.00 \cdot 10^{-13}$	12.70
100	$1.01 \cdot 10^{-14}$	$5.62 \cdot 10^{-13}$	12.25

One usually writes a dissociation (in water) process as $HA \rightleftharpoons H^+ + A^-$ (for acids), $BOH \rightleftharpoons B^+ + HO^-$ (for bases), $H_2O \rightleftharpoons H^+ + HO^-$ (for water) and $AB \rightleftharpoons B^+ + A^-$ (for salts), but those scholastic equations do not quite describe the process accurately, and definitely may lead to errors when involved as they are into calculations. When discussing about water alone, H^+ is actually trapped by a variable number (q) of water molecules ($H^+ + qH_2O \rightleftharpoons (H_2O)_qH^+$), and different protonated species actually exist ($(H_2O)_qH^+$) containing 3 to 12 ($q = 3, 4, \dots, 12$) water molecules, the most likely being: $(H_2O)_4H^+$ (Eigen cation, [29] p. 103). Moving forward to ions dissolved in water (anions, A^- and cations B^+), the number (m, n) of surrounding water molecules (forming $(H_2O)_mA^-$ and $(H_2O)_nB^+$ clusters) varies from 4 to 6 for certain strong anions and cations (see [27]). The corresponding equations of the chemical equilibriums are then formally expressed by Eq. (14).



If K_{DW} , K_{WW} , K_{aW} and K_{bW} are the equilibrium constants for the processes from Eq. (14), then their relations with the Eq. (13) constants are the ones from Eq. (15), in which the activities of clustered species were (formally) considered to be equal with the corresponding free species: $a(\text{A}^-) = a((\text{H}_2\text{O})_m\text{A}^-)$, $a(\text{B}^+) = a((\text{H}_2\text{O})_n\text{B}^+)$, $a(\text{HO}^-) = a((\text{H}_2\text{O})_p\text{HO}^-)$, and $a(\text{H}^+) = a((\text{H}_2\text{O})_q\text{H}^+)$.

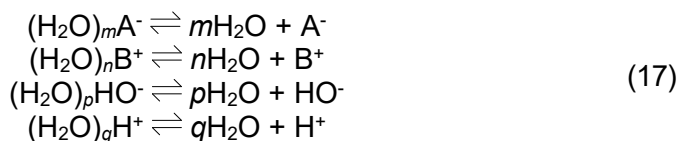
$$\begin{aligned}
 K_{\text{DW}} &= K_{\text{D}}/(a(\text{H}_2\text{O}))^{m+n} \\
 K_{\text{WW}} &= K_{\text{W}}/(a(\text{H}_2\text{O}))^{p+q} \\
 K_{\text{aW}} &= K_{\text{a}}/(a(\text{H}_2\text{O}))^{m+q} \\
 K_{\text{bW}} &= K_{\text{b}}/(a(\text{H}_2\text{O}))^{p+n}
 \end{aligned} \tag{15}$$

At infinite dilution $a(\text{H}_2\text{O}) \rightarrow 1$, and then $K_{\text{DW}} \rightarrow K_{\text{D}}/[\text{H}_2\text{O}]^{m+n}$, $K_{\text{WW}} \rightarrow K_{\text{W}}/[\text{H}_2\text{O}]^{p+q}$, $K_{\text{aW}} \rightarrow K_{\text{a}}/[\text{H}_2\text{O}]^{m+q}$, $K_{\text{bW}} \rightarrow K_{\text{b}}/[\text{H}_2\text{O}]^{p+n}$ (where $[\cdot]$ stands for molar concentration). One should notice in Eq. (15) that the constants of Eq. (14) do not have the same units as their corresponding standard versions from Eq. (13). At 273.15 K, $\rho(\text{H}_2\text{O}) \approx 999.84$ g/l and $a(\text{H}_2\text{O}) \rightarrow 55.5$ mol/l while at 298.15 K, $\rho(\text{H}_2\text{O}) \approx 997.05$ g/l and $a(\text{H}_2\text{O}) \rightarrow 55.34$ mol/l. In any instance, the units of the Eq. (13) and Eq. (14) equilibrium constants are scaled by the units of the corresponding water molecules (see the dimensional analysis from Eq. (16), and for further details see Table 7 at p. 12 in [34]).

$$\begin{aligned}
 \dim K_{\text{DW}} &= \dim K_{\text{D}} \cdot (\text{L}^3/\text{N})^{m+n} = (\text{L}^3/\text{N})^{m+n-1} \\
 \dim K_{\text{WW}} &= \dim K_{\text{W}} \cdot (\text{L}^3/\text{N})^{p+q} = (\text{L}^3/\text{N})^{p+q-1} \\
 \dim K_{\text{aW}} &= \dim K_{\text{a}} \cdot (\text{L}^3/\text{N})^{m+q} = (\text{L}^3/\text{N})^{m+q-1} \\
 \dim K_{\text{bW}} &= \dim K_{\text{b}} \cdot (\text{L}^3/\text{N})^{p+n} = (\text{L}^3/\text{N})^{p+n-1}
 \end{aligned} \tag{16}$$

All activities are, by convention, dimensionless quantities; thus, for numeric simulation purposes their quantities will be safely substituted with molar fractions and when ionic strength deviates significantly from 1, these formulas can be subject to revision.

In the vapour or gaseous state, water molecules are largely independent of one another and occur mostly as monomers $(\text{H}_2\text{O})_k$ with $k = 1$. Dissociation is expected to appear in gaseous state for the charged species as well (Eq. (17)).



Eq. (17) processes can be considered part of the equilibrium in the gaseous state and are strongly dependent on the pressure (decreasing of the pressure such as in the mass spectrometer favours dissociation, [35]). As Eq. (17) reveals, each ionic species from Eq. (13) has a corresponding complex ion in Eq. (14).

Some acidity constants

A list of acidity constants for common inorganic acids has been collected from multiple sources and it is given as Table 10, and can be used to model the dilution.

Table 10. pKa values at standard ambient conditions (25°C, 1 bar, and zero ionic strength)

Acid	pKa	Ref
HF	3.19	[36]
H ₂ O ₂	11.62	[37]
H ₂ S; HS ⁻	7.05; 19	[37]
HIO ₃	0.78	[37]
HClO ₄	-11.55±0.75	[38]
HNO ₂	3.25	[37]
H ₃ PO ₄ ; H ₂ PO ₄ ⁻ ; HPO ₄ ²⁻	2.16±0.02; 7.21; 12.32	[37, 39]
H ₂ SO ₄ ; HSO ₄ ⁻	-6.55±2.05; 1.99	[37, 38]
H ₂ SO ₃ ; HSO ₃ ⁻	1.81±0.04; 7.2	[37, 40]
H ₂ O	13.995	[37]
HSCN	-1.28±0.03	[41]
HCl	-7.3±0.04	[42]
HBr	-9.84±0.06	[42]
HI	-10.29±0.08	[42]
HNO ₃	-1.37 _{0.03}	[43]
H ₃ O ⁺	0.0	[43]
NH ₃	35	[43]
NH ₄ ⁺	9.25	[43]

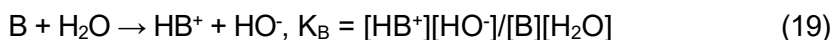
Although K_A for HI is about $10^{7.5}$ times greater than K_A for HNO₃ ($\text{p}K_A(\text{HI}) - \text{p}K_A(\text{HNO}_3) \approx 7.51$ in Table 2), the reaction of either HI or HNO₃ with water gives an essentially stoichiometric solution of H₃O⁺ and I⁻ or NO₃⁻. A 0.1 M aqueous solution of any strong acid actually contains 0.1 M H₃O⁺, regardless of the identity of the strong acid. This phenomenon is called the

leveling effect [44]: any species that is a stronger acid than the conjugate acid of water (H_3O^+) is leveled to the strength of H_3O^+ in aqueous solution because H_3O^+ is the strongest acid that can exist in equilibrium with water (it is the manifestation of any species dissolved in water). Consequently, it is impossible to distinguish between the strengths of very strong acids such as HI and HNO_3 in aqueous solution, and usually alternative approaches are employed to determine their relative acid strengths.

Three definitions share the word base: Arrhenius bases, Brønsted bases, and Lewis bases. Even though all three definitions agree that bases are substances which react with acids to form salts, as originally proposed in 1754 by Rouelle [45], there are some differences which may cause difficulties in blunt application of Eq. (13.4), especially in the vicinity of the equilibrium. Thus, in 1886, Arrhenius proposed that a base is a substance which dissociates in aqueous solution to form HO^- [46]. According to the Brønsted–Lowry acid–base theory [47, 48], a base is a substance that can accept hydrogen cations (H^+)—otherwise known as protons. This does include aqueous hydroxides since OH^- does react with H^+ to form water, so that Arrhenius bases are a subset of Brønsted bases, but there are also other Brønsted bases which accept protons, such as NH_3 , while the Lewis theory generalizes the Brønsted–Lowry model [49]. It should be noted that according to the Brønsted–Lowry acid–base theory, the constant of basicity defined by Eq. (13.4) should be rewritten as in Eq. (18):



Some authors state that basicity constant does not require a separate definition, and can be defined through acidity (Eq. (19)).



However, notable is the difference between Eq. (19) and Eq. (13.4) by the presence in the expression (of the chemical equation and of the associated mathematical equation) of the water. One should point out that the definitions are equivalent at infinite dilution but are significantly different in concentrate solutions and near the equilibrium.

ACKNOWLEDGMENTS

This manuscript was prepared in the memory of Prof. Teodor Hodişan, a valuable mentor and hearty friend.

REFERENCES

1. T. Hodişan; Analiza titrimetrică. In *Curs de Chimie Analitică: Analiza cantitativă*. Universitatea Babeş-Bolyai: Cluj-Napoca, Romania, **1989**; Chapter 3, pp. 92-226.
2. L. Jäntschi; H.I. Naşcu; *Leonardo J. Sci.*, **2002**, *1*, 53–68.
3. D. Midgley; C. McCallum; *Talanta*, **1974**, *21*, 723–733.
4. M. Celeste; C. Azevedo; Ana M. V. Cavaleiro; *J. Chem. Educ.*, **2012**, *89*, 767–770.
5. R.M. Caraballo; L.M. Saleh Medina; S.G.J. Gomez; P. Vensaus; M. Hamer; *J. Chem. Educ.*, **2021**, *98*, 958–965.
6. F.E. Critchfield; J.B. Johnson; *Anal. Chem.*, **1958**, *30*, 1247–1249.
7. B. García; S. Ibeas; F.J. Hoyuelos; J.M. Leal; F. Secco; M. Venturini; *J. Org. Chem.*, **2001**, *66*, 7986–7993.
8. J.G. Mayeka; F.P. Mabiki; *J. Chem. Pharm. Res.*, **2019**, *11*, 117-126.
9. R.A. Stairs; *J. Chem. Educ.*, **1978**, *55*, 99.
10. N. Kapilraj; S. Keerthanan; M. Sithambaresan; *J. Chem.*, **2019**, *2019*, 2031342.
11. M. Arocena; *Chem. Teach. Int.*, **2021**, *4*, 47-54.
12. H.I. Naşcu; L. Jäntschi; Metode chimice de analiză - interferenţe cu analizele instrumentale. In *Chimie Analitică și Instrumentală*. AcademicPres & AcademicDirect: Cluj-Napoca & Internet, Romania, **2006**; Chapter 3, pp. 43-58.
13. M. Sarfraz; N. Sultana; M.I. Tariq; *Studia UBB Chemia*, **2018**, *63*, 125-136.
14. I. Helm; L. Jalukse; M. Vilbaste; I. Leito; *Anal. Chim. Acta*, **2009**, *648*, 167-173.
15. A. Manzoli; I.N. Tomita; F.L. Fertonani; G. de Oliveira - Neto; M. Mascini; H. Yamanaka; *Anal. Lett.*, **2004**, *37*, 1823-1832.
16. A. Johansson; L. Pehrsson; *Analyst*, **1970**, *95*, 652-656.
17. D.M. King; A.J. Bard; *Anal. Chem.*, **1964**, *36*, 2351-2352.
18. J.T. Wang; Z.H. Li; C.Y. Chen; L. Tong; Z.Y. Liu; X.S. Bao; X.H. Zhao; *Sens. Lett.*, **2015**, *13*, 888-894.
19. F.A. Chowdhury; H. Yamada; T. Higashii; K. Goto; M. Onoda; *Ind. Eng. Chem. Res.*, **2013**, *52*, 8323-8331.
20. B. Rasmus; D.J. Sijmen; *J. Chemom.* **1997**, *11*, 393–401.
21. J.R. Sharma; D. Kumar; L. Jäntschi; *Symmetry*, **2019**, *11*, 891.
22. D.Kumar; J.R. Sharma; L. Jäntschi; *Mathematics*, **2019**, *7*, 919.
23. J.R. Sharma; S. Kumar; L. Jäntschi; *Symmetry*, **2019**, *11*, 1452.
24. J.R. Sharma; S. Kumar; L. Jäntschi; *Mathematics*, **2020**, *8*, 1091.
25. S. Kumar; J. Bhagwan; L. Jäntschi; *Symmetry*, **2022**, *14*, 1881.
26. K.R. Asmis; N.L. Pivonka; G. Santambrogio; M. Brümmer; C. Kaposta; D.M. Neumark; L. Wöste; *Science*, **2003**, *299*, 1375–1377.
27. L.L. Pruteanu; L. Jäntschi; M.L. Ungureşan; S.D. Bolboacă; *Studia UBB Chemia*, **2016**, *61*, 151–162.
28. M.V. Fedotova; S.E. Kruchinin; *J. Mol. Liq.*, **2011**, *164*, 201–206.
29. L. Jäntschi. In *General Chemistry Course*. AcademicDirect: Cluj-Napoca, Romania, **2013**. http://ph.academicdirect.org/GCC_v10.pdf

30. G.N. Lewis; *Proc. Am. Acad. Arts Sci.*, **1907**, 43, 259–293.
<http://doi.org/10.2307/20022322>
31. IUPAC, Activity (relative activity), a. In: Compendium of chemical terminology: IUPAC recommendations, 2nd ed. Blackwell Science: Oxford, UK **1997**, p. 49.
<http://doi.org/10.1351/goldbook.A00115>
32. J. Inczédy, T. Lengyel, A.M. Ure. In: IUPAC Compendium of analytical nomenclature: definitive rules 1997, **1998**, § 3.1.
http://media.iupac.org/publications/analytical_compendium/
33. A.V. Bandura; S.N. Lvov; *J. Phys. Chem. Ref. Data*, **2006**, 35, 15–30.
<http://doi.org/10.1063/1.1928231>
34. L. Jäntschi. In *Prezentarea și prelucrarea datelor experimentale*. U.U.Pres: Cluj-Napoca, Romania, **2013**.
35. Y.K. Lau; S. Ikuta; P. Kebarle; *J. Am. Chem. Soc.*, **1982**, 104, 1462-1469.
36. PubChem. Hydrofluoric acid (CID 14917, CAS 7664-39-3). URL:
<https://pubchem.ncbi.nlm.nih.gov/compound/14917>
37. D.R. Lide (Ed.) Dissociation Constants of Inorganic Acids and Bases. In *CRC Handbook of Chemistry and Physics*. Taylor & Francis Group: Boca Raton & Internet, FL, USA, **2009**; Chapter 8, pp. 1194-1195.
38. A.V. Levanov; O.Y. Isaikina; U.D. Gurbanova; V.V. Lunin; *J. Phys. Chem. B*, **2018**, 122, 6277-6286.
39. E.A. Guggenheim; *Trans. Faraday Soc.*, **1966**, 62, 2750-2753.
40. T.M. Townsend; A. Allanic; C. Noonan; J.R. Sodeau; *J. Phys. Chem. A*, **2012**, 116, 4035–4046.
41. Y. Chiang; AJ Kresge; *Can. J. Chem.*, **2000**, 78, 1627–1628.
42. A.V. Levanov; U.D. Gurbanova; O.Y. Isaikina; V.V. Lunin; *Russ. J. Phys. Chem. A*, **2019**, 93, 93-101.
43. N.J. Tro; *A General Chemistry Textmap*. Supplant to *Chemistry: A Molecular Approach (5th Ed)*. Pearson Education, Inc.: Hoboken, NJ, USA, **2020**; Chapter 16, Section 4.
44. R.S. Macomber; *J. Chem. Educ.*, **1984**, 61, 128.
45. W.B. Jensen; *J. Chem. Educ.*, **2006**, 83, 1130.
46. S. Arrhenius; *Ann. Phys.*, **1886**, 266, 51-76.
47. J.N. Brönsted; *Recl. Trav. Chim. Pays-Bas*, **1923**, 42, 718–728.
48. T.M. Lowry; *J. Soc. Chem. Ind. London*, **1923**, 42, 43–47.
49. G.N. Lewis. In: *Valence and the Structure of Atoms and Molecules*. Chemical Catalog Company: NY, NY, U.S.A. **1923**, p. 142.

THE EFFECT OF SOLVENT AND TEMPERATURE ON PROTONATION CONSTANTS OF DL-PHENYLALANINE IN DIFFERENT AQUEOUS SOLUTIONS OF METHANOL AT DIFFERENT TEMPERATURES

Niloofer Soltani AHMADI^a, Farhoush KIANI^{b,*}, Seyed-Ahmad SHAHIDI^A, Azade GHORBANI-HASANSARAEI^a, Fatemeh ZABIHI^c, Fardad KOOHYAR^{d,*}

ABSTRACT. This research work has two sections. In first section, the equilibrium constant for protonation processes of DL-phenylalanine (K_1 , and K_2) were determined in binary mixed solvents of water–methanol, containing 0, 10, 20, 30, 40, 50, 60, 70, and 80 % (v/v) methanol, at $T = 298.15$ K and constant ionic strength ($0.1 \text{ mol}\cdot\text{dm}^{-3}\text{NaCl}$). The obtained data (K_1 , and K_2) were analyzed using Kamlet, Abboud, and Taft parameters. In second section, for DL-phenylalanine in aqueous solution, the values K_1 , and K_2 were determined at $T = (298.15, 303.15, 308.15, 313.15, \text{ and } 318.15)$ K and constant ionic strength ($0.1 \text{ mol}\cdot\text{dm}^{-3}\text{NaCl}$). Using these K_1 , and K_2 , the thermodynamic properties (changes of enthalpy, ΔH , changes of entropy, ΔS , and changes of Gibbs free energy, ΔG) were calculated for DL-phenylalanine in aqueous solution. In both sections, the values of K_1 , and K_2 were determined using the spectrophotometric and potentiometric methods.

Keywords: *protonation constants, DL-Phenylalanine, potentiometric, spectrophotometric, changes of enthalpy, changes of entropy, and changes of Gibbs free energy.*

^a Department of Food Science and Technology, Ayatollah Amoli Branch, Islamic Azad University, Amol, Iran

^b Department of Chemistry, Faculty of Science, Ayatollah Amoli Branch, Islamic Azad University, Amol, Iran

^c Department of Physic, Center of Fooladin Zobe Amol, University of Applied Science and Technology, Iran

^d Department of Chemistry, Rhodes University, Makhanda/Grahamstown, 6140 South Africa

* Corresponding authors: farhoush_kiani@yahoo.com; fkoohyar.uni@gmail.com



INTRODUCTION

Amino acids are classified as biologically significant organic compounds, which are made from amine (-NH₂) and carboxylic acid (-COOH) functional groups, along with a side chain specific to each amino acid [1-2].

The attachment of the amine and the carboxylic acid group together to the first (alpha-) carbon atom is very important in biochemistry of amino acids [3].

Amino acids exist as zwitterions at the isoelectric point, in which both the amino and carboxylic acid groups are almost totally ionized; the physical properties of the amino acids are largely governed by the degree of ionization at different pHs. The side chain of an amino acid can alter its physical properties by modifying: the net charge at a given pH, the relative affinity for water, and the pH at which there is no net charge (the isoelectric point). Of course, peptides are themselves composed of covalently bonded amino acids; their properties will therefore be dominated by the nature of the side chains on the constituent amino acids [4].

Phenylalanine is an essential α -amino acid with the formula C₉H₁₁NO₂. It can be viewed as a benzyl group substituted for the methyl group of alanine, or a phenyl group in place of terminal hydrogen of alanine [5].

Phenylalanine exists in two forms: L-phenylalanine and D-phenylalanine. They are nearly identical but have slightly different molecular structure. The L-form is found in foods and used to produce proteins in human body while, D-form can be synthesized to use in certain medical applications [6].

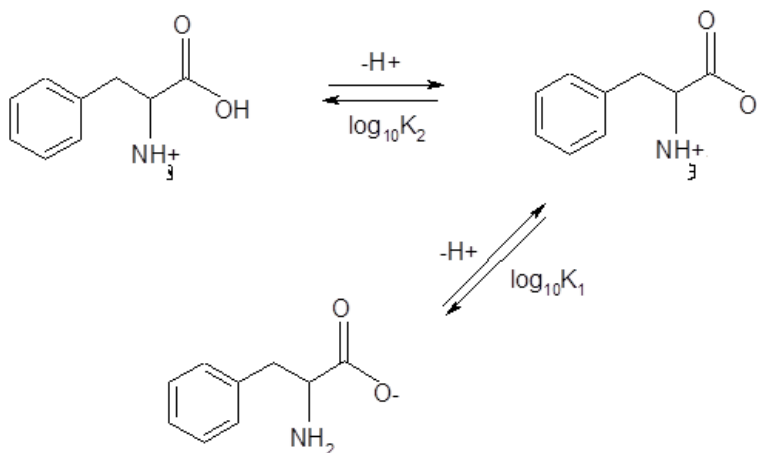
Protonation constant of different species of amino acids and dipeptides were studied in different research works [7-8]. The protonation constant is used for determining solubility and permeability of solutions in the environmental and pharmaceutical fields [9-10]. There are various experimental methods to measure acid dissociation constant, such as HPLC, potentiometer, and spectrophotometry [11-12]. Solving is the first step to determine the physicochemical properties of a substance. Therefore, it is essential to measure the solubility of a substance in special solvent at different temperatures and various ionic strengths which can describe the thermodynamic system of solution, such as enthalpy and entropy changes of dissolving processes.

In modern food industry, amino acids are important to improve quality of food products. Among them D-L Phenylalanine is used as a food additive and it is essential to determine their thermodynamic properties and protonation constants.

In the present study, the protonation constants (K₁ and K₂) were determined for DL- phenylalanine in mixed solvent of water and methanol at constant temperature. These data were analyzed using Kamlet, Abboud, and

THE EFFECT OF SOLVENT AND TEMPERATURE ON PROTONATION CONSTANTS
OF DL-PHENYLALANINE IN DIFFERENT AQUEOUS SOLUTIONS ...

Taft parameters. Also, K_1 and K_2 were determined in aqueous solution at temperatures $T = (298.15, 303.15, 308.15, 313.15, \text{ and } 318.15)$ K. using these data, values of ΔH , ΔS , and, ΔG were calculated for DL-phenylalanine in aqueous solution.



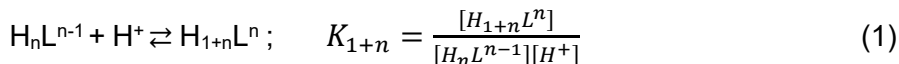
Scheme 1. Chemical structure of DL-Phenylalanine

RESULTS AND DISCUSSION

Determination of protonation constant for D-L- phenylalanine

The protonation constants of DL-Phenylalanine were determined spectrophotometrically based on the relation $A = f(\text{pH})$ [13].

The computer program Squad was used to calculate the measured absorbance, A [(200–400) nm in the interval of 0.5 nm], and p_cH from the spectrophotometric titration [14, 15]. To fit the data in the computer program, the error square sum of the difference in the experimental absorbance and the calculated ones were minimized. The protonation constants with different stoichiometries can be determined by the program. Each titration had an experimental point (absorbance against p_cH) above 35 (maximum 50). The solutions were used without change during the experiments, and the absorbance values remained unchanged. Table 1 shows the results of spectrophotometric and potentiometric pH titrations for the acidity constants of the proton donors of the DL-Phenylalanine, Eq. 5, in various aqueous solutions of methanol and under various temperatures at aqueous solution accompanied by the values presented in the literature for comparison [16].



Where L shows DL-Phenylalanine molecule and n (charge of the ion) can be 0, 1, or 2 for the different protonation equilibria of the base.

Amino acids exist as zwitterions at the isoelectric point, in which both the amino and carboxylic acid groups are almost totally ionized; the physical properties of the amino acids are largely governed by the degree of ionization at different pHs. It is obvious that for a dibasic acid the first ionization constant K_1 is the sum $k_1 + k_2$ and the second ionization constant K_2 is $(k_{12} \cdot k_{21}) / (k_{12} + k_{21})$, where the subscript 12 denotes loss of proton 2 following loss of proton 1 and subscript 21 denotes loss of proton 1 following loss of proton 2. The chemical interpretation of the changes is not straightforward, even though from model compounds the carboxyl proton is predicted to be the most acidic. The calculations involving the microscopic constants indicate that the first and second K correspond to removal of the carbonyl proton and the ammonium proton respectively. It can be determined by NMR spectroscopy exactly [17- 20].

Depending on the acidity of the medium (solution), hydrogen ions can add to DL-Phenylalanine molecule (Scheme 1) in two steps. In first and second step of protonation of DL-Phenylalanine, proton is added to carboxyl group and amine group, respectively. The second (Eq. 2), and first (Eq. 3) steps of protonation of DL-Phenylalanine occur according Eqs. 6 and 7:



The protonation constants achieved in this examination are in fine agreement with those reported previously [21]. There are a few differences due to the various experimental methods that have been employed to determine the values. In Figure 1, the equilibrium distribution of various species of DL-Phenylalanine in water is indicated as a function of p_cH .

Figure 1 helps us find out the values of K_s for DL-Phenylalanine in water at various aqueous solutions of methanol and various temperatures. In Figure 1, the points a and b are the isoelectric points. In these points, the concentrations of the acid and the base are equal to each other. For an acid (HA), the below equation shows the relationship between $\log_{10}K$ and pH:

$$\log_{10}K = pH + \log [A^-]/[HA] \quad (4)$$

THE EFFECT OF SOLVENT AND TEMPERATURE ON PROTONATION CONSTANTS
OF DL-PHENYLALANINE IN DIFFERENT AQUEOUS SOLUTIONS ...

In Eq. 4, $[A^-]$ and $[HA]$ are the concentrations of acid HA and base A^- , respectively. At isoelectric points (a and b), $[A^-] = [HA]$ and $pH = \log_{10}K_a$. The calculations are based on the protonation constant values in various aqueous solutions of methanol and various temperatures given in Table 1 and Table 3, respectively.

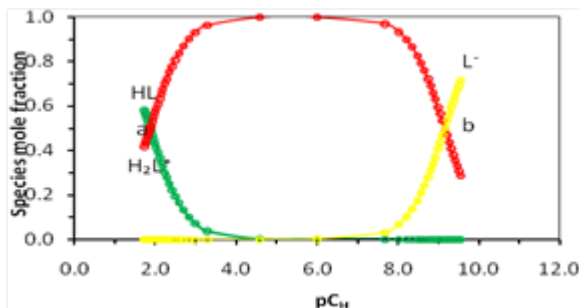


Figure 1. Distribution diagram of the different species of DL-Phenylalanine in water at 298.15 K and an ionic strength of $0.1 \text{ mol}\cdot\text{dm}^{-3}$ (NaCl).

Investigation of solvent effect

This research work shows that the different steps of protonation of DL-Phenylalanine, in water-alcohol mixed solvents, have different behaviors. The value of first protonation constant, K_1 , increase and also the values of second protonation constant, K_2 , decrease with increasing mole fraction of alcohol in water-alcohol mixed solvents (Table 1). It is very difficult to interpret the variation of the protonation constant values of DL-Phenylalanine regarding to the volume percentage of the methanol, in water-methanol solvent, using the dielectric constant of the solutions as the only parameter.

Table 1. Protonation constant of DL-Phenylalanine in aqueous solutions of methanol at 298.15 K and in NaCl 0.1 M

Alcohol V %	H ₂ O+Methanol		
	Log ₁₀ K ₂	Log ₁₀ K ₁	Ref.
0	1.86±0.03	9.15±0.02	21
10	2.02±0.03	8.96±0.01	This work
20	2.08±0.02	8.86±0.04	This work
30	2.12±0.04	8.75±0.03	This work
40	2.16±0.04	8.61±0.02	This work
50	2.22±0.03	8.47±0.03	This work
60	2.29±0.02	8.34±0.01	This work
70	2.36±0.04	8.226±0.03	This work
80	2.42±0.01	8.13±0.02	This work

In general, the standard Gibbs energy of protonation equilibria includes two terms: an electrostatic term, which can be estimated by the Born equation [22, 23], and a nonelectrostatic term, which includes specific solute-solvent interaction. When the electrostatic effects predominate on nonelectrostatic effects, according to the Born equation (Eq. 5), the plot of $\log_{10}K$ versus the reciprocal of dielectric constant of the media, ϵ , should be linear diagram as the below:

$$\Delta\log K = (121.6n/r)(1/\epsilon - 0.0128) \quad (5)$$

where r is the common radius of the ions and n is the square summation of the charges involved in the protonation equilibria.

For example, $n = 0$, or 2 for the charge types $HL + H^+ \rightleftharpoons H_2L^+$, $L^- + H^+ \rightleftharpoons HL$, respectively. As it can be seen in Fig. 2, the correlation between $\log_{10}K_1$, and $\log_{10}K_2$ with reciprocal of the dielectric constant of the water-methanol mixtures are almost linear (with correlation coefficient between 0.91-0.93). It indicates that the protonation constants depend not only on the electrostatic forces but also strongly depend on the solute-solvent interactions of the different species in the mixtures [23]. Therefore, it is necessary to clarify the nature of solute-solvent interactions for a better understanding of the solvent effects.

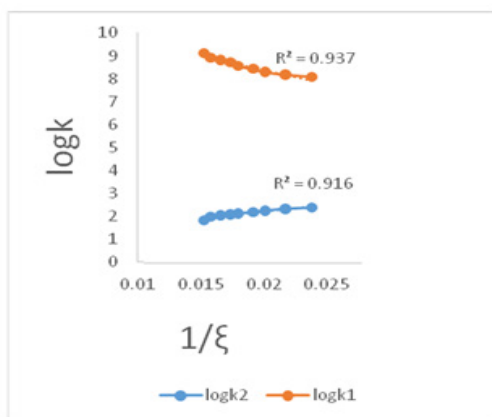


Figure 2. Plots of the experimental values of $\log_{10}K_1$, $\log_{10}K_2$ versus the reciprocal of the dielectric constant of different mixed solvents (water-methanol) at 298.15 K and an ionic strength of 0.1 mol.dm⁻³ (NaCl).

To study on the effect of solute-solvent interaction in the protonation or other equilibrium constants, a multi-parametric equation was used. This equation is based on the linear solvation energy relationship (LSER) theory and was developed by Kamlet, Abboud, and Taft (KAT) [24, 25]. The KAT equation contains non-specific as well as specific solute-solvent interactions, separately. These interactions can be subdivided into solvent Lewis-acidity interactions (hydrogen-bond acceptor, HBA solute, and hydrogen-bond donor, HBD solvent) and solvent Lewis-basicity interactions (HBD solute-HBA solvent). In general, all of these parameters constitute more comprehensive measures of solvent polarity than the dielectric constant or any other single physical characteristic, because they reflect more reliably the complete picture of all intermolecular forces acting between solute and solvent molecules. This approach has been widely and successfully applied in the correlation analysis of all kinds of solvent-dependent processes [26]. Using the solvatochromic solvent parameters (α , β , and π^*), a multiparametric equation, Eq. 6, has been proposed. This equation has been previously introduced [27,28].

$$\log K = A_0 + a\alpha + b\beta + p\pi^* \quad (6)$$

In Eq. 6, A_0 represents the regression value and π^* is the index of the solvent dipolarity/polarizability which is a measure of the ability of a solvent to stabilize a charge or a dipole by its own dielectric effects. The coefficient a represents the solvent hydrogen-bond donor (HBD) acidity. In a solvent, this coefficient (α) describes the ability of a solvent to donate a proton to a solute and generate hydrogen bond. The coefficient β is the solvent hydrogen-bond acceptor (HBA) basicity. This coefficient (β) describes the ability of a solvent to accept a proton, from a solute, and generate hydrogen bond. The regression coefficients (a , b , and p) can show the relative susceptibilities of the solvent dependence of $\log_{10}K_s$ to the solvent parameters. In order to explain the $\log_{10}K$ values through the KAT solvent parameters, the protonation constants were correlated with the solvent properties by means of single, dual, and multiple regression analysis by a suitable computer program (Microsoft Excel Solver and Linest) [29,30]. We used the Gauss–Newton non-linear least-squares method, in the computer program, to refine the $\log_{10}K$ by minimizing the error squares sum from Eq. 7.

$$U = \sum (\log_{10}K_{\text{exp}} - \log_{10}K_{\text{calc}})^2 \quad (7)$$

The procedure that is used in the regression analysis involves a rigorous statistical treatment to find out which parameter, in Eq. 6, is the best suited for water-methanol mixed solvents. So, a stepwise procedure and least-squares analysis were applied to select the significant solvent properties to be

influenced in the model and to obtain the final expression for the protonation constants. Therefore, the KAT equation, Eq. 6, was reduced to single, dual, and multiparameters for correlation analysis of $\log_{10}K$ in various solvent mixtures. The used computer program can calculate the values of A_0 , a , b , p , and some statistical parameters including the r^2 regression coefficient, f-test (f), the residual sum of squares (rss), standard deviation of any parameter and the overall standard error (ose) for $\log_{10}K$. For all water-methanol mixtures that were used in this work, the KAT parameters and the dielectric constants values were obtained from the plot of each property versus the mole fraction of methanol (in various methanol- water solutions). Some other percentages of aqueous solutions of methanol are listed in Table 3 [31, 32].

Table 2. KAT solvatochromic and the dielectric constants of different aqueous methanol.

Methanol % (v/v)	α^a	β^a	π^{*a}	ϵ^b
0	1.17	0.47	1.09	78.60
10	1.15	0.49	1.04	74.83
20	1.13	0.51	0.99	70.86
30	1.11	0.53	0.94	66.67
40	1.09	0.55	0.89	62.26
50	1.08	0.57	0.85	57.60
60	1.06	0.58	0.80	52.70
70	1.04	0.60	0.75	47.54
80	1.02	0.62	0.70	42.15

a: Ref. [31], b: Ref. [32]

Although the solvent polarity is known as the main reason of the variation of $\log_{10}K$ values in water-methanol mixtures, the single-parameter and multiparameter correlations of $\log_{10}K_1$, and $\log_{10}K_2$ with π^* , α , and β didn't give us good results in all cases. However, the correlation analysis of $\log_{10}K_1$, and $\log_{10}K_2$ values with dual parameter equations show the more significant results compared to the single and/or multiparameter models. The obtained expressions of the KAT equation for each property, as dual-parameters, are shown below:

$$\log_{10}K_2 = 1.21(0.82) + 2.04(0.65)\beta - 0.22(0.44)\pi^*$$

$$r^2 = 0.997 \quad OSE = 1.21 \cdot 10^{-2} \quad rss = 8.9 \cdot 10^{-4} \quad F = 1373.54 \quad (8)$$

$$\log_{10}K_1 = 10.89(0.71) - 4.39(0.56)\beta + 0.32(0.38)\pi^*$$

$$r^2 = 0.998 \quad OSE = 1.17 \cdot 10^{-2} \quad rss = 8.2 \cdot 10^{-4} \quad F = 1735.35 \quad (9)$$

We obtained the KAT equations (eqs. 8 and 9) for DL-Phenylalanine, in both equations the correlation analysis of the dual parameter of the KAT equation, the value of coefficient β is greater than value of coefficient π^* ($\beta > \pi^*$). It can be seen in Eq. 8, for the first ionization process the value of coefficient β parameter has positive value in this system, the hydrogen-bond acceptor basicity parameter plays a major role and the polarity parameter of the solvent has less significance. Therefore, $\log_{10}K_2$ values increase with increasing of the hydrogen bond basicity parameter. In Eq. 9 the second ionization process the value of coefficient β parameter is negative. This indicates the hydrogen-bond acceptor basicity parameter plays a major role. So, $\log_{10}K_1$ values decrease with an increase in the hydrogen bond basicity parameter [38, 39].

Investigation of temperature effect: thermodynamic analysis

The changes in Gibbs energy (ΔG), enthalpy (ΔH), and entropy (ΔS) are important thermodynamic parameters. The ΔG is the key parameter, because its value under a particular set of reactant concentrations dictates the direction of biomolecules equilibria in solutions. If its sign is negative, the binding reaction or conformational transition will proceed spontaneously to an extent governed by the magnitude of ΔG . If its sign is positive, the magnitude of ΔG specifies the energy needed to drive the reaction to form a product. The free energy is a balance between enthalpy and entropy [38, 39].

Table 3. protonation constant of DL-Phenylalanine in aqueous solution at temperatures 298.15 K to 318.15 K and in NaCl 0.1 M

Specie	T (K)	$\log K_2$	$\log K_1$	Ref
	298.15	1.86±0.02	9.15±0.02	21-25
	303.15	1.91±0.03	9.06±0.01	This work
DL-Phenylalanine	308.15	2.03±0.01	8.95±0.02	This work
	313.15	2.08±0.03	8.83±0.03	This work
	318.15	2.13±0.02	8.69±0.04	This work

The change in Gibbs energy in gas or solution phases can be calculated from Eq. 10:

$$\Delta G^\circ = -RT \ln K_a \approx 2.303 RT \text{ p}K_a \quad (10)$$

In Eq. 10, R is the universal gas constant (8.314 J. K⁻¹.mol⁻¹), T is the temperature (K), and K_a is the equilibrium constant. The values of ΔH and ΔS can be determined using the van't Hoff equation and by plotting $\ln K_a$ vs. 1/T [35]:

$$pK_a = \Delta H/2.303RT - \Delta S/2.303 R \quad (11)$$

The signs ΔG , ΔH , and ΔS can show the state of chemical reactions. The Chemical reactions can be spontaneous at each temperature when ΔH is negative and ΔS have positive values. Other states are observable in the references 35 to 39 [35- 39]. The values of temperature can affect the state of the chemical reactions when ΔH and ΔS have the same sign. As a result, the first and second ionization reactions of DL-Phenylalanine are spontaneous at low temperature.

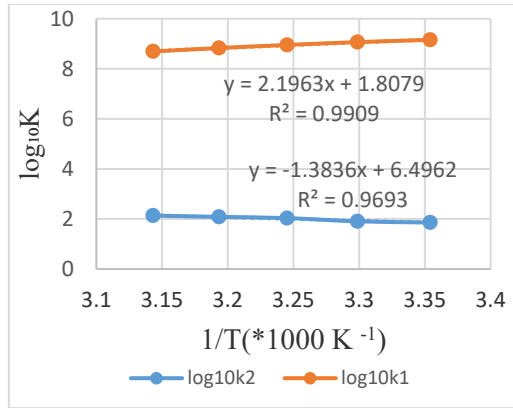


Figure 3. Curve - $\log_{10} K_a$ values vs. $1/T$ for DL-Phenylalanine.

It can be seen in Table 3 that in the protonation process of DL-Phenylalanine, $\log_{10}K_2$ increases with increasing temperature and also, $\log_{10}K_1$ decreases with increasing temperature.

Finally, we plotted $\log_{10}K$ versus $1/T$ for DL-Phenylalanine (Fig. 3). Using the slope and intercept of Eq. 11, the values of ΔH and ΔS were obtained.

Table 4. Thermodynamic properties for DL-Phenylalanine solved in water in constant ionic strength.

Specie DL-Phenylalanine	ΔH (kJ.mol ⁻¹)	ΔS (J.mol ⁻¹ .K ¹)	ΔG (kJ.mol ⁻¹)				
			298.15 K	303.15 K	308.15 K	313.15 K	318.15 K
First ionization process	-26.5	-124.6	10.6	11.2	11.9	12.5	13.1
Second ionization process	42.1	-34.6	52.4	52.6	52.7	52.9	53.1

In addition, the values of ΔG for the deprotonation processes of DL-Phenylalanine were calculated using the pK_a values (Eq. 10) at each temperature. As shown in Table 4, the values of ΔG increase with increasing temperature; ΔS and ΔH are negative for the first ionization process and ΔS is negative for the second ionization process and ΔH is positive for the second ionization process. It is well known that $\Delta G = \Delta H - T\Delta S$. In this research work, the absolute value of $T\Delta S$ is more than the absolute value of ΔH . Therefore, the value of ΔG will be positive (see Table 4).

CONCLUSIONS

In this research work, the equilibrium constants of protonation process for DL-Phenylalanine were experimentally determined at the various temperatures and the different aqueous solutions of methanol. The results show that the value of $\log_{10}K_2$ increases and the value of $\log_{10}K_1$ decreases with increasing alcohol content of mixtures. In addition, the same results were observed when the temperatures increased in water solvent. The correlations of the constants with either a macroscopic parameter, such as dielectric constant, or a microscopic parameter, such as the Kamlet, Abboud, and Taft (KAT) solvatochromic parameters, were determined. The results showed the correlation between $\log_{10}K_2$ and $\log_{10}K_1$ with reciprocal of the dielectric constant of the water–methanol mixtures are almost linear and the KAT dual-parameter correlations show important improvements with respect to single- or multi-parameter models. The obtained results by examination of thermodynamic properties show that ΔG increases when the temperatures increase, ΔS , and ΔH are negative during the first ionization and ΔH is positive during the second ionization whereas ΔS is negative during the second ionization.

EXPERIMENTAL SECTION

Chemicals

DL-Phenylalanine, Scheme 1, was purchased from Sigma-Aldrich Company as reagent grade materials. Sodium hydroxide (NaOH) and hydrochloric acid (HCl) solutions were prepared from a titrisol solution (Merck Company). Sodium chloride (Merck Company) was dried using the vacuum at room temperature for at least 72 h before using. All dilute solutions were prepared using double-distilled water with a conductance equal to $1.2 \pm 0.1 \mu\text{S}$.

Apparatus

A Metrohm model 781 pH ion-meter was applied to determine the electromotive force (E). A 80-cm³ thermostated double-walled glass vessel was used for all titrations. A UV-Vis Shimadzu 2100 spectrophotometer, with a Pentium 4 computer, as well as thermostat, matched at 10 mm quartz cells, were used for spectrophotometric and potentiometric measurements at the same time. To have data and put them in an excel program to calculate protonation constants. In addition, a flow type measurement cell was used. A circular thermostat was used to keep the temperature constant at the range ± 0.1 K. To measure the absorbance and the emf (electromotive force) of the solution at the same time, a peristaltic pump was used. This apparatus facilitates the circulation of the solution from the potentiometric cell to the spectrophotometric cell. To prevent carbon dioxide from staying in the system, a flow of purified nitrogen was allowed to pass through a sodium hydroxide solution and then it bubbled slowly through the reaction solution.

Procedure

In this study, the measurements were achieved at 298.15 K and a constant ionic strength of 0.1 mol.dm⁻³ sodium chloride (NaCl) and with 0.1 mol.dm⁻³ sodium hydroxide solution both with the same ionic strength and mole fraction of organic solvent [(0–80) % methanol v/v]. Also in this work under various temperatures (298.15 K to 318.15 K), the procedure was repeated at an ionic strength of 0.1 mol/dm³. The protonation constants were evaluated from the measurements of absorbance against emf by titration of 25 mL of DL-Phenylalanine [(1.0 $\times 10^{-5}$ to 5.0 $\times 10^{-5}$ mol.dm⁻³)].

In the first phase, the electrode system calibration was performed by Gran's method [40]. To this aim, a specified amount of an acidic solution (0.01 mol.dm⁻³HCl), at the same temperature, solvent composition and constant ionic strength that were going to be used in subsequent experiments, was placed in the double-wall thermostated vessel. Next phase was the electrode immersion in the solution in the vessel and titration of the acidic solution with a strong base (0.1 mol.dm⁻³NaOH, each addition 50 μ L). Following each addition of the titrant, the potential effect was allowed to become stable. Next, to calculate the cell parameter (E°), and electrode calibration slope, Nernstian parameter (k), the reported emf values were used. This method was continued to pH $\cong 1.5$.

Secondly, a sodium hydroxide solution (0.1 mol.dm⁻³) was used to titrate 25 mL of an acidic solution (0.01 mol.dm⁻³HCl) of DL-Phenylalanine (1.0 $\times 10^{-5}$ to 5.0 $\times 10^{-5}$ mol.dm⁻³) at the same temperature, ionic strength, and solvent composition. Then, the emf and the absorbance values (in the

range of 200 to 400 nm and interval of 0.5 nm) were determined. The procedure was repeated in various compositions of the mixed solvent in ionic strength 0.1 mol/l and various temperatures. Following the method explained in the literature [41, 42], the reported emf values were then converted to p_cH ($-\log [H^+]$).

In a solution, the measured potential of the cell could be expressed as Eq. 12:

$$E_{\text{cell}} = E^{\circ}_{\text{cell}} + k \log_{10}[H^+] + k \log_{10}\gamma H^+ + E_{LJ} \quad (12)$$

Where E°_{cell} represents the standard potential of the cell, E_{LJ} denotes the liquid junction potential, $k = 2.303RT/F$ in which R , T and F have the usual meaning, and γH^+ shows the activity coefficient of hydrogen ion. Measurement of emf (electromotive force) versus H^+ concentration, in solution, is very useful because the computing of activity coefficients of hydrogen ion, in various aqueous mixtures of organic solvents, is very difficult. In this research work, the ionic strength of the solution is kept constant therefore the activity coefficient of hydrogen ion is also constant. The non-ideality of solutions is then included in E'_a (the specific constant of the potentiometric cell in the acidic region), therefore:

$$E_{\text{cell}} = E'_a + k \log_{10}[H^+] \quad (13)$$

Where E'_a is $E^{\circ}_{\text{cell}} + k \log_{10}\gamma[H^+] + E_{LJ}$. In calibration step, the values of E'_a and k were readily calculated from linear regression between E and $\log_{10}[H^+]$ [43, 44].

In the acidic region, the concentration of hydrogen ion can be expressed as:

$$[H^+] = (M_{\text{HCl}}V_o - M_{\text{NaOH}}V_1)/(V_o + V_1) \quad (14)$$

Where, M_{HCl} and M_{NaOH} are the molarities of hydrochloric acid and sodium hydroxide, respectively. V_o and V_1 are the volumes of hydrochloric acid and sodium hydroxide, respectively, which were added to solution. Finally:

$$p_cH = (E'_a - E_{\text{cell}})/k \quad (15)$$

In equation 4, P_cH (or pH) is $-\log[H^+]$.

REFERENCES

1. J. Wang; Analytical electrochemistry (3rd ed), **2006**, New York, USA.
2. A. Catsch; A.E. Harmuth-Hoene; *J. Pharmacol. Ther.* Part A: Chemotherapy, Toxicology and Metabolic Inhibitors, **1976**, *1*, 30-35.
3. J.U. Lurie; *Handbook of Analytical Chemistry*, Mir: Moscow, **1975**.
4. P.D. Bailey; *An Introduction to Peptide Chemistry*; New York, **1992**.
5. Nomenclature and Symbolism for Amino Acids and Peptides. IUPAC-IUB Joint Commission on Biochemical Nomenclature. **1983**.
6. H. Wan; J. Ulander; *J. Expert Opin. Drug Metab. Toxicol*, **2006**, *2*, 139-55.
7. M. Monajemi; F. Gharib; H. Aghaei; G. Shafiee; A. Thghvamanesh; A. Shamel; *J. Main Group Met. Chem*, **2003**, *26*, 39-47.
8. K.K. Tam; T.N. Krisztina; *J. Anal Chim Acta*, **2001**, *434*, 157-176.
9. T. Komoda; T. Matsunaga; Biochemistry for Medical Professionals, **2015**.
10. I. Wagner; H. Musso; *J. Angew. Chem. Int. Ed. Engl.*, **1983**, *22*, 816-820.
11. A. Albert; The determination of ionization constants: a laboratory manual. **2012**, Springer, New York City, USA.
12. G. Thomas; Medicinal Chemistry: An Introduction; **2008**, John Wiley and Sons: West Sussex.
13. M.T. Beck; I. Nagypal; Chemistry of Complex Equilibria, **1990**, Ellis Harwood, New York, USA.
14. D.J. Leggett; The Determination of formation constants. **1985**, Modern Inorganic Chemistry. Springer, Boston, USA.
15. M. Meloun; M. Javurek; J. Havel; *Talanta*, **1986**, *33*, 513.
16. F. Kiani; A.A. Rostami; S. Sharifi; A. Bahadori; *J. Molecular Structur (Theochem)*, **2010**, *956*, 20-25.
17. F. Kiani; A.A. Rostami; S. Sharifi; A. Bahadori; M.J. Chaichi; *J. Chem. Eng. Data*. **2010**, *55*, 2732-2740.
18. M. Borkovec; M. Brxnda; G.J.M. Koper; B. Spiess; *Anal. Appl. Chem.* **2002**, *56*, 695-701.
19. H. Nagai; K. Kuwabara; G. Carta; *J. Chem. Eng. Data*. **2008**, *53*, 3, 619-627.
20. T.D. Tanalp; A. Doğan; *J. Sol. Chem.* **2021**, *50*, 2, 1-12.
21. T. Nilsson; *J. Lantbrukshoegskolans Annaler*, **1970**, *36*, 179-219.
22. J. Barbosa; D. Barron; J.L. Beltran; S. Buti; *J. Talanta*, **1998**, *45*, 817-819.
23. J. Barbosa; I. Toro; V. Sanz-Nebot; *J. Anal. Chim. Acta, B*, **1997**, *347*, 295-301.
24. R.W. Taft; K.L.M. Abboud; M.J. Kamlet; *J. Org. Chem*, **1984**, *49*, 2001-2015.
25. M.J. Kamlet; J.L.M. Abboud; M.H. Abraham; R.W. Taft; *J. Org. Chem*, **1983**, *48*, 2877-2886.
26. C. Reichardt; Solvents and Solvent Effects in Organic Chemistry, 3rd ed. **2004**, VCH, New York, USA.
27. A. Shamel; A. Saghiri; F. Jaberi; A. Farajtabar; F. Mofidi; S. A. Khorrami; F. Gharib; *J. Solution Chem*, **2012**, *41*, 1020-1043.
28. A. Farajtabar; F. Jaberi; F. Gharib; *J. Spectrochim. Acta*, **2011**, *83*, 213-217.

THE EFFECT OF SOLVENT AND TEMPERATURE ON PROTONATION CONSTANTS
OF DL-PHENYLALANINE IN DIFFERENT AQUEOUS SOLUTIONS ...

29. E.J. Billo; *Excel for Chemists: A Comprehensive Guide*, 2001, 2nd edition, Wiley-VCH.
30. N. Maleki; B. Haghighi; A. Safavi; *J. Microchem*, **1999**, 62, 229 -238.
31. G. Akerlof; *J. Am Chem. Soc.*, **1932**, 54, 4125-4133.
32. M. Smiechowski; *Chem. Phys. Lett*, **2001**, 501, 123-129.
33. J.B. Chaires; *J. Annu Rev Biophys*, **2008**, 37, 135-158.
34. B.K. Shukla; U. Yadava; M. Roychoudhury; *J. Mol. Liq*, **2015**, 212, 325-330.
35. M. Ogurlu; *J. Microporous. Mesoporous. Mater*, **2009**, 119, 276-287.
36. A.Y. Dursun; *Biochem. Eng. J*, **2006**, 28, 187-200.
37. P.M. Pimentel; M.A.F. Melo; D.M.A. Melo; A.L.C. Assuncao; D.M. Henrique; C.N. Silva; G. González; *J. Fuel Process. Technol*, **2008**, 89, 62-77.
38. G.B. Savadkoohi; F. Kiani; A. Morsali; *Russian J. Phys. Chem. A*, **2021**, 95, 1, 71-76.
39. T. Valizadeh; F. Kiani; F. Gharib; F. Zabihi; F. Koohyar; *Russian J. Phys. Chem. A*, **2020**, 94, 1, 88-94.
40. L. Pehrsson; F. Ingman; a A. Johansson; *J. Talanta.*, **1976**, 23, 769-771.
41. P. Gameiro; S. Reis; J.L.F.C. Lima; B. de Castro; *J. Anal. Chim. Acta*, **2001**, 405, 167-173.
42. D.A. Skoog; D.M. West; F.J. Holler; S.R. Crouch, *Fundamentals of analytical chemistry*, 9th Edition, **2013**, Cengage Learning.
43. J.S. Ferrer; E. Couallier; M. Rakib; G. Durand; *J. Electrochim. Acta*, **2007**, 52, 5773-5775.
44. F. Gharib; F. Farajtabar; A.M. Farahani; F. Bahmani; *J. Chem. Eng. Data*, **2010**, 55 1, 327-332.

INVESTIGATION ON THE POTENTIAL USAGE OF LIGNOCELLULOSIC WASTES FOR Cd(II) REMOVAL

Andrada MAICANEANU^{a,b}, Cerasella INDOLEAN^{b*}

ABSTRACT. Various lignocellulosic waste materials were assessed for their potential usage as biosorbents for Cd(II) removal from wastewaters. Sunflower seed shells, carrot peel, bean pods, eggplant peel, and orange peel in dry form and different grain sizes were evaluated. Contact time, initial Cd(II) concentration, and biosorbent amount were also tested. Eggplant peel was the most efficient biosorbent with an experimental biosorption capacity of 9.33 mg/g, a monolayer capacity (Langmuir) of 18.05 mg/g, and maximum % yield removal of 97.33%. Experimental data best fitted the Langmuir isotherm model (exception, orange peel) and the pseudo-second-order kinetic model (all materials).

Keywords: *cadmium(II), biosorption, waste valorisation, circular economy, sunflower seed shell, carrot peel, bean pod, eggplant peel, orange peel*

INTRODUCTION

Pollutants, such as heavy metals, are serious threats to the environment. Most of the metals are non-biodegradable, highly toxic and carcinogenic in nature [1].

Cadmium metal ions are very dangerous pollutants due to their high solubility in water, which makes them mobile in soil with a serious tendency to bioaccumulate [2]. They occur naturally in soil of volcanic areas but are becoming abundant in many territories as a result of uncontrolled industrialization, unsustainable urbanization, and intensive agricultural practices [2-4].

^a *Madia Department of Chemistry, Biochemistry, Physics and Engineering, Indiana University of Pennsylvania, Indiana, PA 15705, USA*

^b *Department of Chemical Engineering, Faculty of Chemistry and Chemical Engineering, Babeş-Bolyai University, 11 Arany Janos St., RO-400028 Cluj-Napoca, Romania*

* *Corresponding author: liliana.indolean@ubbcluj.ro*



Excessive accumulation of cadmium, Cd(II), in vegetables poses a serious threat to human health; therefore, it is urgent to screen and cultivate vegetables with low, or, if it is possible, non-existent cadmium accumulation in the edible parts [4].

Cultivation of agricultural crops and harvesting, generate an abundant amount of waste (e.g., peels, shells, straw, etc.) that can be used for wastewater treatment. It is estimated that approximately 998 million tons of agricultural waste is produced annually [5].

Nowadays, the potential of food and agricultural waste to remove heavy metals from contaminated water and soil has been intensively studied [6-8].

Vegetable wastes are easily available and have no economic use. The applicability of vegetable waste as low-cost adsorbent leads to significant decrease of waste discharge in the environment [9].

Biosorbents are composed of mainly cellulose, hemicelluloses, lignin, extractives, and many other compounds such as lipid, starch, hydrocarbons, simple proteins, and ash [10]. The biosorption mechanism onto biomass can consist of several steps including chemisorption, complexation, physisorption, diffusion through pores, and ion exchange [8].

In the removal of metals from aqueous solution, different types of plant parts are used such as stems, stalks, leaves, husk, shells, roots, barks, and many others [4].

Adsorption/biosorption process is considered to be attractive in terms of its performance for heavy metals removal from dilute waste solutions. Heavy metals are removed on different rates depending on the adsorbent / biosorbent and the metal itself [7].

In this study, the biosorption potential for cadmium (II) of some lignocellulosic wastes materials resulted from domestic use of carrots (*Daucus carota*), sunflower (*Helianthus annuus*), beans (*Phaseolus vulgaris*), eggplants (*Solanum Melongena L*), and orange (*Citrus sinensis*) was explored.

Sunflower seed shells (SFss), carrot peel (Cp), bean pods (Bp), eggplant peel (EPp), and orange peel (Op) were investigated under various working parameters.

RESULTS AND DISCUSSION

The results obtained for the investigation of Cd(II) removal on lignocellulosic waste materials are presented as follows, in terms of biosorption capacity and % yield for all the parameters examined.

Grain size influence was studied for all materials using the following reaction conditions: $C_i = 25 \text{ mg Cd(II)/L}$, 1 g biosorbent, $22 \pm 2^\circ\text{C}$, 5.48 pH, and 500 rpm for 180 min with <0.4, 0.4-0.6, and 0.6-1.25 mm fractions. Two main trends were observed: (a) for SFs and Op a decrease in % yield removal (Table 1) and biosorption capacity was observed, suggesting that internal diffusion might become rate-determining step; (b) for Cp, Bp (Figure 1), and EPp, % yield removal and biosorption capacity, (Table 1), increased indicating that the biosorption process takes place mainly on the outer surface of the grain (lower porosity or inaccessible pores).

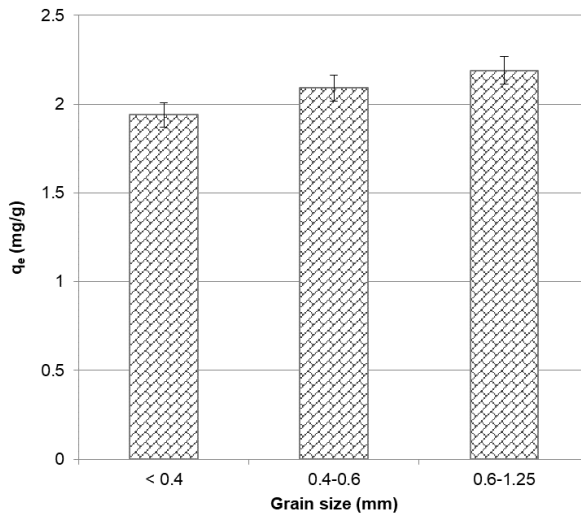


Figure 1. Grain size influence over biosorption capacity for Cd(II) removal on bean pods; $C_i = 25 \text{ mg/L}$, 1 g, $22 \pm 2^\circ\text{C}$, 5.48 pH, 500 rpm.

Biosorbent quantity influence was studied for all materials using the following reaction conditions: $C_i = 25 \text{ mg Cd(II)/L}$, 0.4-0.6 mm, $22 \pm 2^\circ\text{C}$, 5.48 pH, and 500 rpm for 180 min with 0.5, 1, and 2 g of lignocellulosic material. As the biosorbent quantity increases, the % yield removal increases, while biosorption capacity (mg per mass unit) decreases, Table 1, since for the same initial concentration, a higher surface/quantity is available, which leads to a smaller Cd(II) amount being removed per mass unit. Figure 2 shows as an example, the extent of biosorbed Cd(II) amount decrease for SFs.

Cd(II) concentration influence was studied for all materials using the following reaction conditions: 1 g, 0.4-0.6 mm, $22 \pm 2^\circ\text{C}$, 5.48 pH, and 500 rpm for 180 min with concentrations in 25-115 mg/L range. Time evolution was also followed for all the concentrations used. An increase in Cd(II) concentration

led to a decrease in removal % yield and an increase in the biosorption capacity (Table 1). This results suggest that the optimum initial concentration must be correlated with desired % yield removal based on the specific conditions (industrial, municipal, leachate). Figure 3 shows the evolution of biosorption capacity for EPp as was one of the two (along with Bp) for which an increase was observed over the whole range of concentrations. For SFss and Cp the biosorption capacity decreased for the maximum concentration studied (115 mg/L), Table 1.

Table 1. Cd(II) removal % yields (top) and biosorption capacities, in mg/g, (bottom) for the considered lignocellulosic wastes under various working conditions.

	Grain size (mm)			Amount (g)			Cd(II) concentration (mg/L)				
	<0.4	0.4-0.6	0.6-1.25	0.5	1	2	25	50	75	95	115
SFss	95.71	92.58	90.61	84.12	92.58	96.41	92.58	87.95	88.76	65.13	40.70
	2.48	2.40	2.35	4.36	2.40	1.25	2.40	4.58	6.79	6.20	4.77
Cp	88.64	89.90	90.32	88.53	89.80	90.85	89.80	87.46	86.48	77.10	55.80
	2.30	2.33	2.34	4.58	2.33	1.18	2.33	4.55	6.72	7.34	6.54
Bp	74.97	80.53	84.47	93.40	80.53	83.31	80.53	82.59	81.08	83.73	69.54
	1.94	2.09	1.08	4.84	2.09	1.08	2.09	4.30	6.30	7.97	8.15
EPp	96.87	95.71	97.10	94.09	95.71	97.33	95.71	95.39	93.18	96.85	76.71
	2.51	2.48	2.52	4.87	2.48	1.26	2.48	4.96	7.35	9.22	9.33
Op	94.70	92.61	89.11	88.99	92.61	90.88	92.61	-	81.85	-	-
	2.38	2.37	2.26	4.51	2.37	1.12	2.37	-	4.06	-	-

Table 2. Langmuir and Freundlich coefficients for Cd(II) biosorption onto lignocellulosic wastes; $C_i = 25-115$ mg/L, 1 g, 0.4-0.6 mm, $22 \pm 2^\circ\text{C}$, 5.48 pH, 500 rpm.

	Langmuir coefficients			Freundlich coefficients		
	K_L (L/mg)	q_{max} (mg/g)	R^2	n	K_f ($\text{mg}^{(1-1/n)} \text{L}^{1/n}/\text{g}$)	R^2
SFss	2.05×10^{-2}	5.75	0.9052	6.58	1.69	0.5438
Cp	4.97×10^{-2}	7.46	0.9690	3.39	1.51	0.8018
Bp	3.17×10^{-2}	7.04	0.9494	1.41	1.11	0.8169
EPp	2.00×10^{-2}	18.05	0.8941	2.69	0.25	0.5850
Op	5.38×10^{-2}	6.21	0.6403	3.56	1.45	0.9178

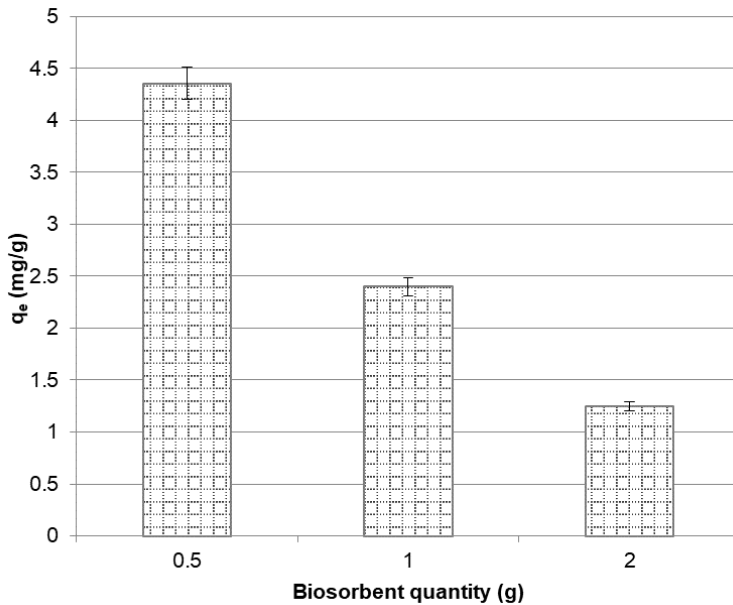


Figure 2. Biosorbent quantity influence over biosorption capacity for Cd(II) removal on sunflower seed shell; $C_i = 25$ mg/L, 0.4-0.6 mm, $22 \pm 2^\circ\text{C}$, 5.48 pH, 500 rpm.

The evolution of concentration in time shows, for all lignocellulosic materials, (C_p presented as an example in Figure 4), a significant drop in concentration in the first 10 minutes, with equilibrium reached after about 120 min for lower range of concentrations (25-75 mg/L) and 180 minutes for 95 and 115 mg/L.

Figure 5 presents the biosorption capacity for all lignocellulosic materials considered in this study for the same working conditions at 25 mg Cd(II)/L. The following sequence was identified, $EPp > SFss > Op > Cp > Bp$, with eggplant peel as the most efficient biosorbent among those analysed by us.

In literature, there are comparable data for Cd(II) biosorption onto lignocellulosic residues, for example 8.58 mg Cd/g for rice husk [8], 3.24 mg Cd/g for *Canola* biomass [11], 0.96 mg Cd/g and 0.98 mg Cd/g for sugarcane bagasse [12] and maize corncob [12], respectively.

Equilibrium experiments were performed in the concentration range of 25-115 mg Cd(II)/L, using 1 g biosorbent of 0.4-0.6 mm particle size, at $22 \pm 2^\circ\text{C}$, 5.48 pH, and 500 rpm. Langmuir and Freundlich isotherm models were used to establish how the biosorption process occurs. Results are presented in Table 2.

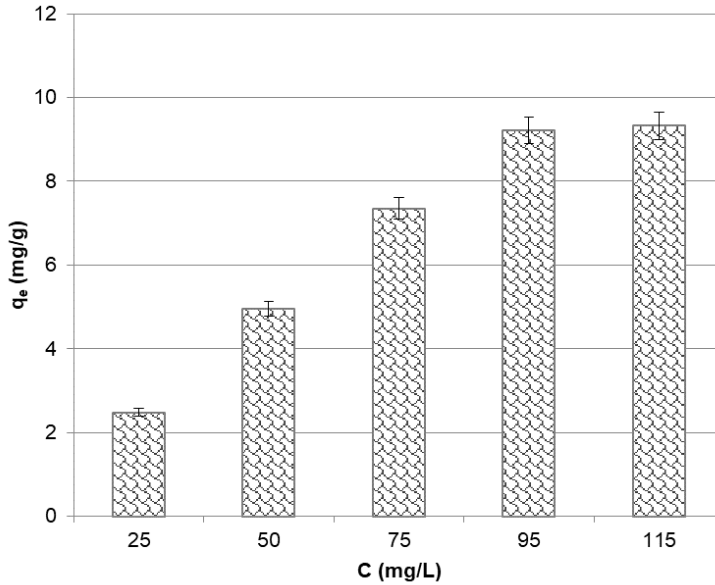


Figure 3. Initial concentration influence over biosorption capacity for Cd(II) removal on eggplant peel; 1 g, 0.4-0.6 mm, 22±2°C, 5.48 pH, 500 rpm.

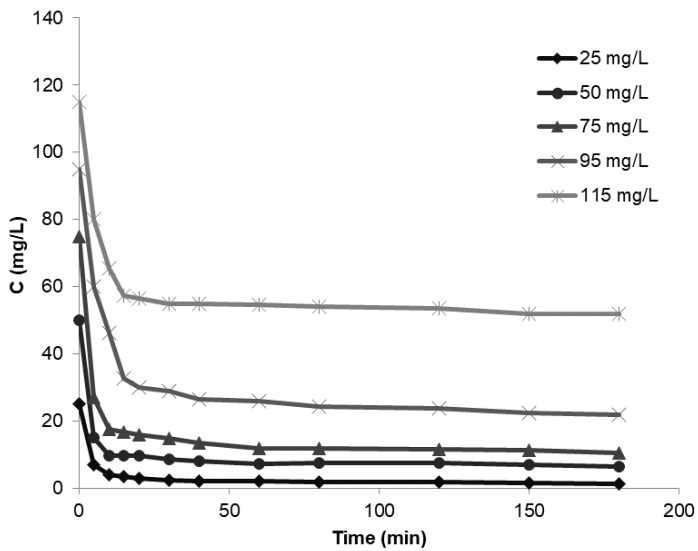


Figure 4. Cd(II) concentration time evolution for biosorption on carrot peel; 1 g, 0.4-0.6 mm, 22±2°C, 5.48 pH, 500 rpm.

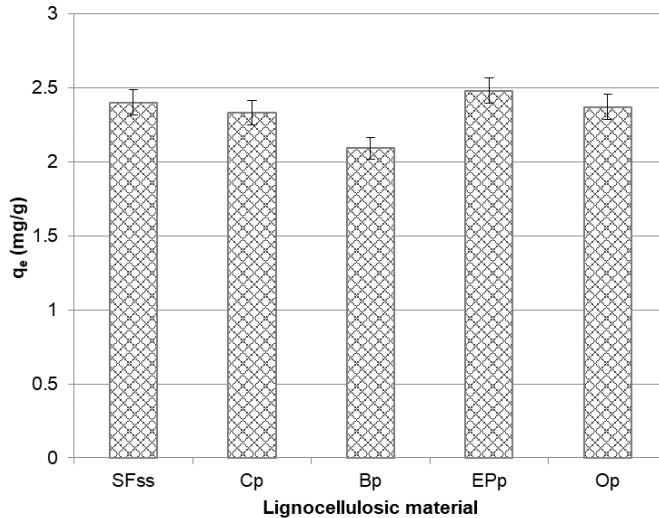


Figure 5. Comparative biosorption capacities for Cd(II) removal on lignocellulosic wastes; $C_i = 25 \text{ mg/L}$, 1 g , $0.4\text{-}0.6 \text{ mm}$, $22\pm 2^\circ\text{C}$, 5.48 pH , 500 rpm .

A closer look at the correlation coefficients indicates that with exception of orange peel (most likely due to its distinct cells, which will lead to specific surface properties upon drying), all the other lignocellulosic materials experimental data best fit on the Langmuir model, suggesting a monolayer adsorption, similar with other literature data [13,14]. The highest calculated value for the maximum adsorption capacity belongs to the eggplant peel in good correlation with the experimental data. Studies on similar systems in literature, show that the maximum adsorption capacity was $88.33 \text{ mg Pb(II)/g}$ for treated eggplant peel [14,15], 140 mg Pb(II)/g for eggplant peels activated charcoal [16], and a small Cd(II) removal efficiency for eggplant powder, in particular conditions ($Y, \% = 14\pm 4\%$) [17].

The rate constants, calculated biosorption capacities, and correlation coefficients for pseudo-first- and pseudo-second-order kinetic models are presented in Table 3 for one of the concentrations used in the kinetic study (50 mg Cd(II)/L). Based on these values it can be concluded that the biosorption onto the lignocellulosic materials tested best fit on the pseudo-second-order kinetic model, suggesting that the biosorption step is rate-determining. Highest rate constant was calculated for EPP in good correlation with the experimental results. Figure 6 presents the pseudo-second-order plots for SFss and clearly indicates that the increase in concentration does not change system's behavior.

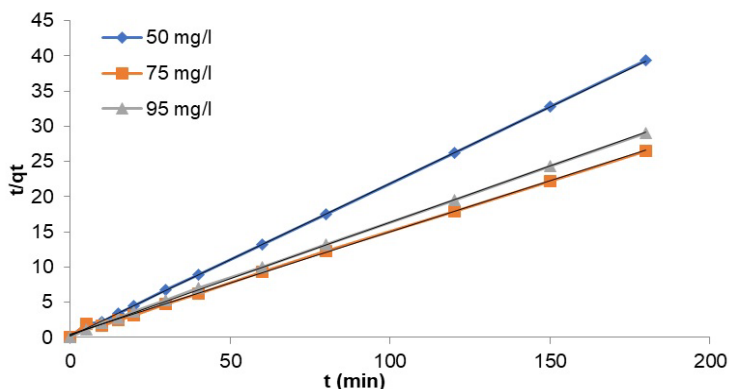


Figure 6. Pseudo-second-order plots for Cd(II) removal on sunflower seed shell; $C_i = 50\text{-}95\text{ mg/L}$, 1 g, 0.4-0.6 mm, $22\pm 2^\circ\text{C}$, 5.48 pH, 500 rpm.

Table 3. Pseudo-first-order and pseudo-second-order rate constants, calculated and experimental q_e values for Cd(II) biosorption onto lignocellulosic wastes; $C_i = 50\text{ mg/L}$, 1 g, 0.4-0.6 mm, $22\pm 2^\circ\text{C}$, 5.48 pH, 500 rpm.

	q_e (exp) (mg/g)	Pseudo-first-order			Pseudo-second-order		
		k_1 (1/min)	q_e (calc) (mg/g)	R^2	k_2 (g/mg·min)	q_e (calc) (mg/g)	R^2
SFss	4.58	6.58×10^{-2}	0.97	0.6057	2.03×10^{-1}	4.63	0.9997
Cp	4.55	1.91×10^{-2}	0.53	0.5776	2.30×10^{-1}	4.54	0.9999
Bp	4.30	1.67×10^{-2}	0.95	0.6172	2.33×10^{-2}	4.29	0.9997
EPp	4.96	3.31×10^{-2}	1.36	0.8957	7.93×10^{-2}	5.03	0.9999
Op	3.22	3.00×10^{-2}	2.47	0.8682	3.11×10^{-2}	4.20	0.9920

CONCLUSIONS

The proposed study on the investigation of the possible usage of lignocellulosic wastes for Cd(II) removal from wastewater showed that all the considered materials have great biosorption properties even at high concentrations (75-95 mg/L). The highest biosorption capacity and the concentration they were obtained at are as follows: EPp (9.33 mg/g – 115 mg/L); SFss (6.79 – 75 mg/L); Op (4.06 – 75 mg/L); Cp (7.34 mg/g – 95 mg/L); Bp (7.97 mg/g – 95 mg/L). Therefore it can be concluded that this type of materials could be successfully used for heavy metal ions removal from wastewater and also indicates that the presence of lignocellulosic materials (food waste) in solid waste landfills could potentially treat in-situ the generated leachate.

EXPERIMENTAL SECTION

Materials

The lignocellulosic wastes used in this work – sunflower seed shells (SFss), carrot peel (Cp), bean pods (Bp), eggplant peel (EPp), and orange peel (Op) – were subjected to various treatment steps before usage, as follows: washing in distilled water to remove impurities, drying at 105°C, grinding (mortar and pestle), and size separation using a set of sieves (0.4, 0.6, and 1.25 mm). The biosorbents prepared as described above were transferred to closed jars and kept for further usage. Figure 7 shows images of some of the biosorbents used in this study.

Cd(NO₃)₂·4H₂O of analytical purity was used to prepare the stock solution and chromatographic purity Cd(II) solution in nitric acid was used to calibrate the atomic absorption spectrometer. Distilled water was used throughout this work.

Experiments

Cd(II) biosorption process was conducted in batch conditions, in a thermostated batch reactor using a magnetic stirrer (500 rpm), for 180 min (preliminary tests showed that adsorption equilibrium will be reached during this time). Various parameters that could influence the biosorption process were considered. Thus, the experiments were carried out using 100 mL of Cd(II) solution of different initial concentrations (25-250 mg/L) prepared from the stock solution of 1 g/L, with various amounts of biosorbent (0.5-2 g), and several grain sizes (<0.4, 0.4-0.6, and 0.6-1.25 mm). Experiments were performed at the initial solution pH of 5.5-6.0.

Cd(II) concentration in solution was determined using a GBC SensAA Series atomic absorption spectrometer (175-900 nm), which was calibrated using Cd(II) high purity solution. All the experiments were realized in triplicate, the presented values are averaged values

Biosorption capacity, q_e (mg/g), and % yield for Cd(II) removal were calculated in order to establish the effectiveness of the tested samples.

$$q_e = \frac{(C_0 - C_e) \times V}{m} \quad (1)$$

$$\%Y = \frac{(C_0 - C_e)}{C_e} \times 100 \quad (2)$$

where: C_0 , C_e are the initial and equilibrium Cd(II) concentration in solution, in mg/L, V is the sample volume, in L, and m is the adsorbent quantity, in g.

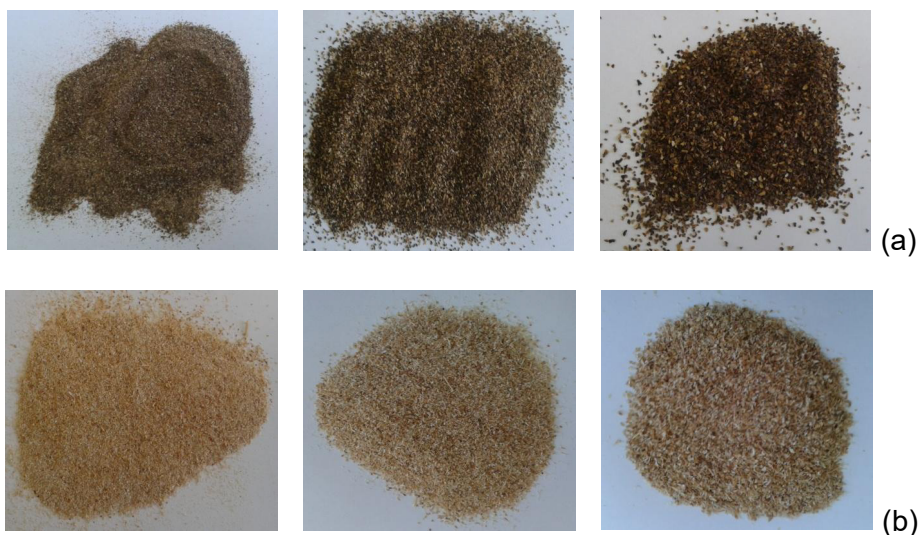


Figure 7. Eggplant peel (a) and bean pods (b) of the three grains size used.

Adsorption isotherms and kinetics

Langmuir and Freundlich isotherm models were used to perform the equilibrium analysis of the biosorption process of Cd(II) on the selected vegetables and citrus species samples.

Model's equations, in the linear form, are as follows:

- Langmuir model equation [18,19]:

$$\frac{1}{q_e} = \frac{1}{q_m K_L} \cdot \frac{1}{C_e} + \frac{1}{q_m} \quad (3)$$

- Freundlich model equation [19, 20]:

$$\log q_e = \log K_F + \frac{1}{n} \cdot \log C_e \quad (4)$$

where: q_m is the monolayer capacity of the adsorbent in mg/g, K_L is the Langmuir adsorption constant in L/mg, K_F is the Freundlich isotherm constant in $\text{mg}^{(1-1/n)}\text{L}^{1/n}/\text{g}$, and n is a constant related to intensity of adsorption (Freundlich).

Pseudo-first- and pseudo-second-order kinetic models were used to explain the adsorption mechanism:

- pseudo-first-order equation (linear) [21, 22]:

$$\ln(q_e - q_t) = \ln q_e - k_1 t \quad (5)$$

- pseudo-second-order equation (linear) [23, 24]:

$$\frac{t}{q_t} = \frac{1}{k_2 q_e^2} + \frac{t}{q_e} \quad (6)$$

where: k_1 is the pseudo-first-order rate constant in 1/min, k_2 is the pseudo-second-order rate constant in g/mg·min, q_t is the amount of Cd(II) adsorbed at time t in mg/g, and t is time in min.

REFERENCES

1. H.A. Alalwan, M.A. Kadhom, A.H. Alminshid, *J. Water Suppl.: Res. Technol.—AQUA*, **2020**, 69(2), 99-112.
2. M.J. McLaughlin, E. Smolders, F.J. Zhao, C. Grant, D. Montalvo, *Adv. Agron.*, **2021**, 166, 1–129.
3. M. Edelstein, Ben-Hur, M., *Sci. Hortic.*, **2018**, 234, 431-444.
4. E. Filippone, V. Tranchida-Lombardo, A. Vitiello, F. Ruiu, M. Di Salvatore, T.R. Galise, L. Laccetti, A. Amoresano, G. D'Ambrosio, L. Frusciante, G. Scopece, P. Chiaiese, *Agric.*, **2022**, 12, 1059-1079.
5. N. Karić, A.S. Maia, A. Teodorović, N. Atanasova, G. Langergraberf, G. Crini, A.R.L. Ribeiro, M. Đolić, *Chem. Eng. J. Adv.*, **2022**, 9, 100239-100256.
6. A. Fatahi, P. Ziarati, A. Jafarpour, L. Cruz-Rodriguez, *J. Sci. Discov.*, **2020**, 4(2), 1-13.
7. R.J. Nathan, C.E. Martin, D. Barr, R.J. Rosengren, *Appl. Water Sci.*, **2021**, 11,116-131.
8. D.S. Malik, C.K. Jain, A.K. Yadav, *Appl. Water Sci.*, **2017**, 7, 2113–2136.
9. E. Matei, M. Râpă, A.M. Predescu, A.A. Țurcanu, R. Vidu, C. Predescu, C. Bobirica, L. Bobirica, C. Orbeci, *Materials*, **2021**, 14, 4581-4608.
10. D. Sud, G. Mahajan, M.P. Kaur, *Bioresour. Technol.*, **2008**, 99, 6017–6027.
11. H. Azarpira, D. Balarak, Y. Mahdavi, *Der Pharma Chem.*, **2016**,
12. U.K. Garg, D. Sud, G. Jawa, V.K. Garg, *J. Hazard. Mater.*, **2008**, 154, 1149–1157.
13. A.S. Gulistan, T.H. Ibrahim, M.I. Khamis, Y. ElSaied, *Desalin. Water Treat.*, **2016**, 57(33), 15724-15732.
14. M.H.K. Darvanjooghi, S.M. Davoodi, A.Y. Dursun, M.R. Ehsani, I. Karimpour, E. Ameri, *Adsorp. Sci. Technol.*, **2018**, 36(3–4), 1112–1143.
15. T.M. Al. Shaikh, *Biointerface Res. Appl. Chem.*, **2020**, 10(5), 6522-6539.

16. T.H. Ibrahim, Z.B. Babar, M.I. Khamis, *Sep. Sci. Technol.*, **2015**, *50*, 91–98.
17. L. Massimi, A. Giuliano, M.L. Astolfi, R. Congedo, A. Masotti, S. Canepari, *Mater.*, **2018**, *11*, 334–349.
18. A.M. Khurram, U. Farooq, M.M. Athar, M. Salman, *Green Chem. Lett. Rev.*, **2019**, *12*(3), 217–224.
19. I. Langmuir, *J. Am. Chem. Soc.*, **1916**, *38*, 2221–2295.
20. H.M.F. Freundlich, *Z. Phys. Chem.*, **1906**, *57*, 385–470.
21. S. Lagergren, *K. Sven. vetensk. akad. handl.*, **1898**, *24*, 1–39.
22. A. Hikmatullah, H. Sayed Sadat, H. Sharifi, R. Ngambua Ngambua, H. Sayed Sanaullah, H. Shakeel, *Chem. Environ. Chem.*, **2022**, *6*, 200242–200249.
23. Y.S. Ho, *J. Hazard. Mat.*, **2006**, *136*, 681–689.
24. P. Bian, Y. Liu, X. Zheng, W. Shen, *Polymers*, **2022**, *14*, 2889–2903.

OPTIMIZATION OF METHYLENE BLUE DYE REMOVAL BY PEANUT HUSK USING PLACKETT-BURMAN DESIGN AND RESPONSE SURFACE METHODOLOGY

Kah-Tong CHAN^a and Siew-Teng ONG^{a,b,*}

ABSTRACT. The ability of peanut husk in removing Methylene Blue (MB) dye solution was studied in this project. The influence of various factors such as contact time, initial dye concentrations, pH and adsorbent dosage were examined in this project in order to study their effects towards the adsorption process. The percentage uptake of MB increases with contact time, pH and adsorbent dosage while it decreases with increasing initial dye concentrations. The functional group on peanut husk was determined using Fourier Transform Infrared Spectrophotometer (FTIR) and its surface morphology was characterized using Scanning Electron Microscope (SEM) and Atomic Force Microscope (AFM) analysis. The experimental data fitted well into the pseudo-second-order kinetic model with R^2 values close to unity. The experimental data is best fitted with Freundlich isotherm model by having R^2 of 0.9927. By using Plackett-Burman design, the factors that can bring significant impact towards the adsorption of MB by peanut husks were determined to be contact time, pH and adsorbent dosage. The optimum condition for the adsorption process was determined by Response Surface Methodology. It was found that the optimum condition was reached at 120 minutes of contact time, pH 10 and 0.035 g of adsorbent.

Keywords: Adsorption, Methylene Blue, Peanut husk, Plackett-Burman Design, Response Surface Methodology

^a Department of Chemical Science, Faculty of Science, Universiti Tunku Abdul Rahman, Jalan Universiti, Bandar Barat, 31900 Kampar, Perak, Malaysia

^b Centre for Agriculture and Food Research, Universiti Tunku Abdul Rahman, Jalan Universiti, Bandar Barat, 31900 Kampar, Perak, Malaysia

* Corresponding author: ongst@utar.edu.my; ongst_utar@yahoo.com



INTRODUCTION

Water pollution can bring critical impacts to the environment. Major source of this pollution comes from the textile industry due to the presence of dyes in the effluents that cannot be completely eliminated before discharge into the river or ocean. Other than dyes, large quantity of heavy metals, surfactants and dissolved solids were also found in the wastewater from the dyeing and finishing processes. The elimination of colours in effluents have become a major concern for both the industry as well as the society [1]. There is about 10 to 15 % of used dyes that released into the environment from the effluent from textile, paper and plastic industries as massive amount of dyes are utilized in these industries [2].

Quite often, appreciable amount of dyes remained in the effluent due to the inefficiencies of the conventional wastewater treatment. The treatment of wastewater cannot depend solely on biodegradation process because the dye itself and its degradation product may be toxic and carcinogenic [3]. The photosynthesis process is also affected by the coloured effluents which can decrease the penetration of light [4].

There are a lot of methods that can be used to eliminate the pollutants such as membrane separation process, chemical oxidation, coagulation, photocatalysis and electrochemical processes. Nevertheless, these methods are not preferred since there are many limitations and disadvantages [5]. Various studies have concluded that the most efficient technique to eliminate a variety of dyes is by the adsorption of dyes onto activated carbons. But due to the high generation cost, alternative adsorbents had been investigated to replace it [6,7].

The more realistic and low-cost method to remove various contaminants is by adsorption using agricultural by-products such as rice husk, peanut husk, palm kernel fibre and palm shell [5]. The conversion of agricultural waste to adsorbent is a great way to increase the value of these waste instead of disposal to landfill which bring ecological and economical concern [8]. Hydroxyl, amino and carboxyl groups present on the surface of agricultural wastes provide them great biosorption potential and can be further improved through various treatments [9].

The world total production of peanut is around 50 million metric tons in 2021. The largest manufacturer of peanut was China which contributes about 36 % (18 million metric tons) of the total production and followed by India [10]. Peanut kernels take up 70 % of the total weight while the rest 30 % are from the peanut husks. The major components in peanut husks are cellulose, hemicelluloses and lignin [11].

There are two major groups of dye which are anionic dye and cationic dye. MB is a cationic dye commonly used to colour textile, paper and wood. It is known as a cationic dye because it is able to dissociates into positively charged compound [2]. They are bright and high colour intensity dyes, therefore even when the concentrations are low, basic dyes are highly visible [12]. The elimination of MB has been attracting the interest of researchers because among all classes of dyes, cationic dyes are generally more toxic compared to others. Furthermore, the removal of dye can be challenging due to their unique properties such as stable and resistant to light and aerobic digestion and can act as an oxidizing agent [2].

RESULTS AND DISCUSSION

Characterization of Adsorbent

Fourier Transform Infrared Spectroscopy (FTIR) Analysis. The presence of functional groups on peanut husks before and after adsorption of MB was analysed using FTIR spectrophotometer at the wavenumber range of 4000 – 400 cm^{-1} . From the spectrum before adsorption (spectrum not shown), a strong and broad peak observed at 3411 cm^{-1} was due to the vibrations of hydroxyl groups of alcohols, carboxylic acids and phenols. The medium peak at 2929 cm^{-1} represented the sp^3 C-H stretch while the peak at 1735 cm^{-1} was the C=O stretching vibrations of esters. The presence of hemicelluloses was signified by a medium peak at 1639 cm^{-1} because it is the characteristic band of stretching carbonyl groups of hemicelluloses [13]. The CH_2 bending was represented by the medium peak at 1429 cm^{-1} . There were two medium peaks observed at 1377 and 1319 cm^{-1} which are the O-H bending of phenols. The broad and strong overlapping bands from 1157 - 1035 cm^{-1} indicated the C-O stretching vibrations and these absorptions may have occurred due to the phenolic structure [14].

By comparing the spectrum before and after adsorption, there was no big difference in the shape and intensity of the peaks. The O-H stretching vibrations at 3411 cm^{-1} shifted to 3421 cm^{-1} . The sp^3 C-H stretching band was shifted from 2929 to 2933 cm^{-1} . The CH_2 bending shifted from wavenumber 1429 to 1431 cm^{-1} . This could be related to the limitations in the sensitivity the instrument. In some of the previously reported works involving the adsorption studies by using other agro-based materials, the FTIR spectra before and after the adsorption process were also were similar to each other [15-17].

Scanning Electron Microscopy (SEM) Analysis. Figures 1(a) and 1(b) showed the SEM micrographs of peanut husks before and after adsorption of MB, respectively. A smoother and more even surface was observed in the micrograph of peanut husks before adsorption of dye. The surface of peanut

husks after adsorption was uneven and rougher compared to the raw peanut husks. This is most probably due to the adhesion and agglomeration of MB dye molecules onto the peanut husks, which also shown that peanut husks have the ability to remove MB from solution by adsorption.

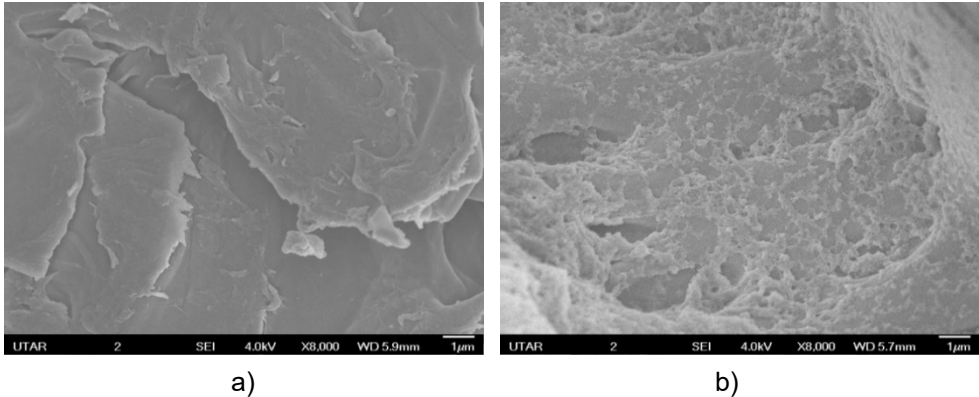


Figure 1 SEM micrograph of peanut husks with 8000× magnification: a) before adsorption b) after adsorption

Atomic Force Microscopy (AFM) Analysis. The AFM micrographs in Figures 2(a) and 2(b) presented the surface topology of peanut husks before and after adsorption of MB, respectively. The dark areas were more evident on the surface of peanut husks before the adsorption. The distribution of dark and light areas was quite average. The surface of peanut husks after adsorption was smoother because the pores were saturated with MB dye molecules. Besides, it can be observed that a lighter colour surface was in dominant indicating that they were almost at the same level. These results further confirm the ability of peanut husks to adsorb MB.

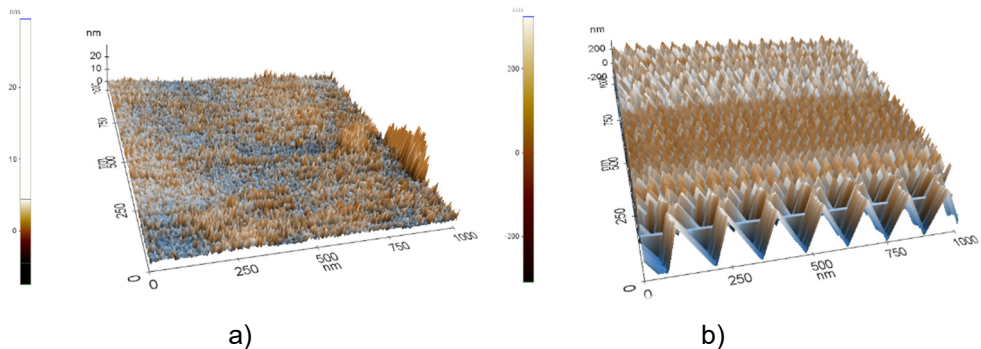


Figure 2. AFM micrograph of peanut husks a) before adsorption of MB; b) after adsorption of MB

Batch Adsorption Studies

Effect of contact time and initial dye concentration. Figure 3 showed the percentage uptake of three different concentrations of MB: 25, 50 and 100 mg/L by peanut husks from 0 to 240 minutes. The trend of adsorption was similar for all three concentrations of MB. The percentage uptake increases as contact time increases and the adsorption rate was high in the first 30 minutes. Then, percentage uptake of dye increases gradually until the equilibrium was achieved after 180 minutes.

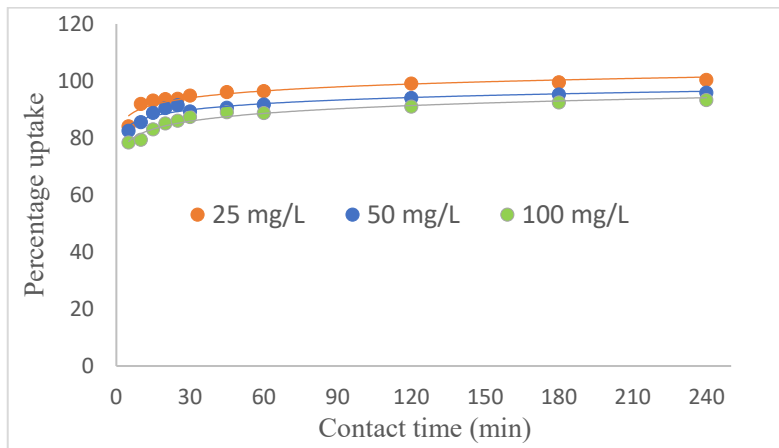


Figure 3. Effect of contact time and initial dye concentration on percentage uptake of MB

The adsorption was rapid in the beginning of the experiment because of large number of unoccupied adsorption sites available on adsorbent surface and the electrostatic attraction between surface of adsorbent, which is peanut husks and adsorbates, MB dye solution. After the first 30 minutes, the rate of adsorption decelerates and the percentage uptake reached its maximum after 180 minutes because all the adsorption sites were fully occupied by dye molecules [18]. As seen from Figure 3, the percentage uptake of MB decreases as the concentration of MB increases. When MB concentration is high, number of dye molecules available for binding also increases. However, the number of vacant binding sites remain the same and binding sites are easily saturated with dye molecules. The amount of dye molecules to binding sites ratio is large causing dye molecules to have lower chances to interact with binding sites. Hence, resulting in the decrease in percentage uptake of dye [19,20].

Effect of pH. Figure 4 illustrated the percentage uptake of MB at various pH values. The adsorption of dye can be greatly influenced by the surface charges of adsorbent and also the dye molecules. MB is a cationic dye which will be attracted to the negatively charged surface. So, the percentage uptake of MB will be enhanced when the surface of peanut husks is more negatively charged.

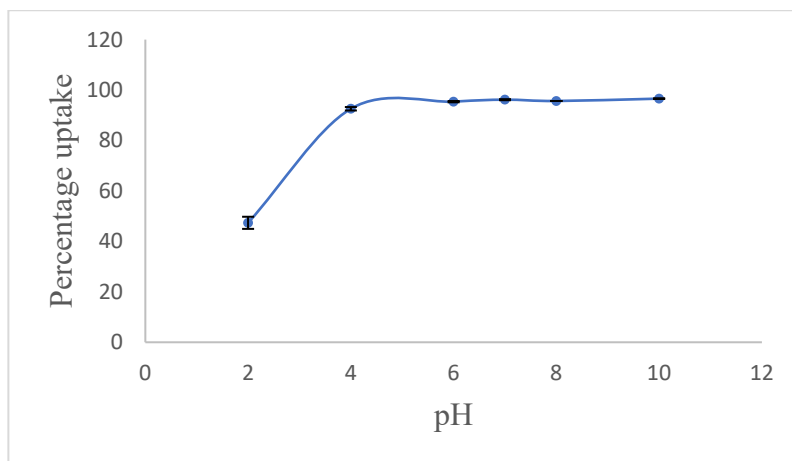


Figure 4. Effect of pH on percentage uptake of MB

The range of pH 4 to 10 was the optimum pH for maximum MB uptake. At pH 2 which is a highly acidic condition, only 47.36 % of MB has been removed. The percentage uptake has increased drastically from 47.36 % to 92.58 % at pH 4. The pH_{pzc} of peanut husks was determined to be 4.7. At pH 6, where $pH > pH_{pzc}$, the percentage uptake increased to 95.40 % and remained almost constant until pH 10 which is 96.60 %, the highest percentage uptake. At $pH < pH_{pzc}$, the functional groups on the adsorbent surface will undergo protonation and become positively charged with the addition of protons. Therefore, the electrostatic repulsion between positively charged peanut husks surface and cationic MB molecules resulted in the decrease in adsorption of dye molecules. At $pH > pH_{pzc}$, the situation reversed where the percentage uptake of cationic MB dye increased. The peanut husk will have a negatively charged surface when $pH > pH_{pzc}$ because positively charged groups on the adsorbent start to deprotonate. This condition favours the adsorption of cationic MB dye because of the electrostatic attraction between peanut husks surface that is having negative charge and positively charged MB dye molecules [5,21].

Effect of adsorbent dosage. The percentage uptake of MB by using different amount of peanut husks was presented in Figure 5. The lowest percentage uptake was observed for 0.01 g of peanut husks which was 86.51 % and the highest percentage uptake of MB dye, 94.82 % was observed for 0.06 g of peanut husks. According to Salleh et al. [5], this is due to increase in number of adsorption sites available for the attachment of dye molecules as adsorbent dosage rises. The amount of dye molecules to binding sites ratio is small causing dye molecules to have higher chances to interact with the binding sites.

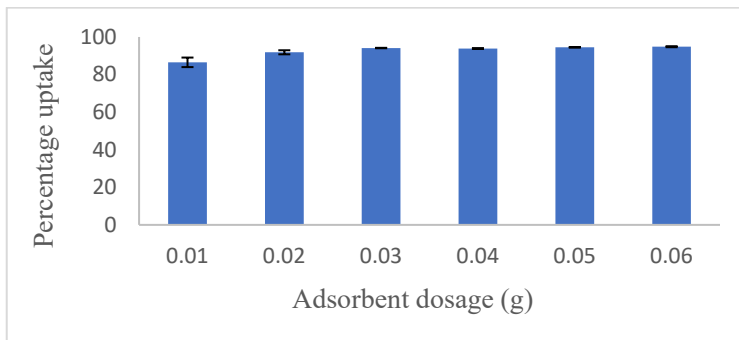


Figure 5. Effect of adsorbent dosage on percentage uptake of MB

Nonetheless, a slight decrease of percentage uptake at 0.04 g was noticed. Sometimes, an increase in dosage may lead the formation of aggregates between adsorbents that blocked the adsorption sites. Aggregation of adsorbents may cause the reduction in effective surface area and an increase in diffusional path length, which subsequently cause a reduction in the percentage uptake [22,23].

Adsorption Kinetic Studies

Pseudo-First-Order Kinetic Model. Pseudo-first-order kinetic model assumes that the number of vacant binding sites remained and rate change of concentration of surface adsorption sites are directly proportional to each other [24]. The linear pseudo-first-order model equation is presented as:

$$\log(q_e - q_t) = \log q_e - \frac{k_1}{2.303} t \quad (1)$$

where

q_e = Amount of adsorbate adsorbed at equilibrium (mg/g)

q_t = Amount of adsorbate adsorbed at time t (mg/g)

k_1 = Pseudo-first-order kinetics rate constant (min^{-1})
 t = Time in minutes

In many cases, the kinetics of adsorption by biological materials are described by pseudo-first order kinetics and therefore the adsorption data was analysed using this model. However, in this study, it was found that pseudo-first-order equation did not fit well for the whole range of concentrations studied. Besides, the equilibrium adsorption capacities calculated from this model gave higher deviations as compared to those determined based on pseudo-second-order kinetics model (Table 1). The low R^2 values obtained based on this pseudo-first-order equation also suggested that this kinetic model was not suitable to depict the adsorption of MB by peanut husks.

Table 1. Pseudo-first and pseudo-second-order kinetics model parameters

Initial concentration of MB (mg/L)	Pseudo-first-order			Pseudo-second-order				Experimental q_e (mg/g)
	q_e (mg/g)	k_1 (min^{-1})	R^2	q_e (mg/g)	h (mg/g·min)	k_2 (g/mg·min)	R^2	
25	14.0540	0.09719	0.7805	16.5622	10.8578	0.03870	0.9999	16.5725
50	30.2691	0.10179	0.7289	32.0889	21.2766	0.02071	0.9999	31.7514
100	67.7018	0.09880	0.7362	60.4014	32.0513	0.00831	0.9998	61.3936

Pseudo-Second-Order Kinetic Model. Pseudo-second-order kinetic model assumes that the square of number of unoccupied binding sites remained and the rate change of concentration of surface adsorption sites are directly proportional to each other. In this kinetic model, the rate-determining step is a chemisorption because the electrons exchanging or sharing between adsorbate and adsorbent involving valency forces [25]. The linear pseudo-second-order model equation is presented as:

$$\frac{t}{q_t} = \frac{1}{h} + \frac{t}{q_e} \quad (2)$$

$$h = k_2 q_e^2 \quad (3)$$

where

q_e = Amount of adsorbate adsorbed at equilibrium (mg/g)
 q_t = Amount of adsorbate adsorbed at time t (mg/g)
 k_2 = Pseudo-second-order kinetics rate constant (g/mg min)
 t = Time in minutes
 h = Initial adsorption rate (mg/g min)

Graph of t/q_t against t of 25, 50 and 100 mg/L of MB solution was plotted and the y-intercept the graph can be used to determine h value whereas gradient can be used to calculate q_e (Figure not shown). Then, by using equation 3, the value of k_2 can be calculated. The R^2 values for 25, 50 and 100 mg/L of MB were 0.9999, 0.9999 and 0.9998, respectively (Table 1). All R^2 values are very close to unity, also, the experimental q_e and the calculated q_e are having similar values. The experimental data fitted well into the pseudo-second-order kinetic model and this model was said to correlate well with the experimental data. This model was appropriate to be used to describe the adsorption of MB by peanut husks. Therefore, it is suggested that the adsorption process may be involving a chemisorption process. Figure 6 showed that the experimental data represented by the symbol agreed well with the theoretically generated curves.

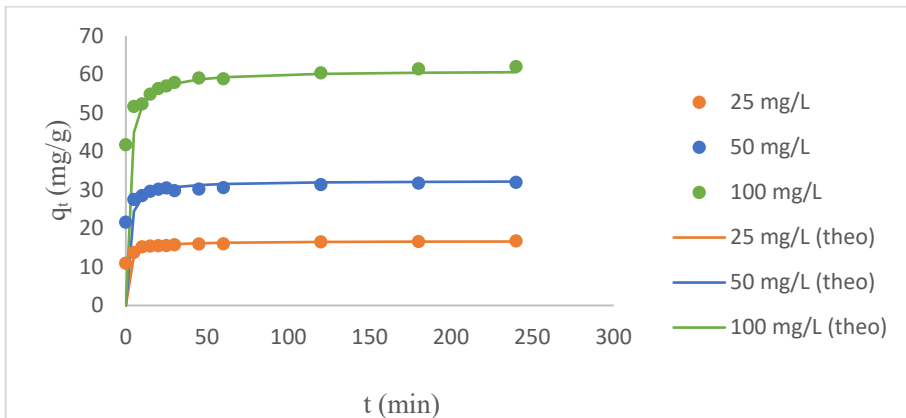


Figure 6. Comparison between theoretical (line) and experimental (symbol) data

Adsorption Isotherm Studies

Langmuir Isotherm Model. Langmuir isotherm model assumes that each adsorption site can be occupied by only one adsorbate molecule and the number of adsorption sites are fixed. There are no interactions between the adsorbate molecules, the adsorbate molecules are adsorbed onto the binding sites chemically. It is a monolayer adsorption that takes place on homogeneous surfaces [26]. The Langmuir model equation is written as:

$$q_e = \frac{q_m K_L C_e}{1 + K_L C_e} \quad (4)$$

By rearranging equation 4, the Langmuir model equation in linear form is written as:

$$\frac{C_e}{q_e} = \frac{C_e}{q_m} + \frac{1}{K_L q_m} \quad (5)$$

where

- q_e = Amount of adsorbate adsorbed at equilibrium (mg/g)
 q_m = Maximum adsorption capacity (mg/g)
 K_L = Langmuir constant related to energy of adsorbent (L/mg)
 C_e = Concentration of adsorbate at equilibrium (mg/L)

The gradient and y-intercept obtained from the linear plot can be used to calculate q_m and K_L values, respectively and they were found to be 117.6471 mg/g and 0.1540 L/mg, respectively (Table 2). Based on the q_m value, it is suggested that peanut husk is an attractive adsorbent with considerable high adsorption capacity towards MB as compared to some previously reported works [27-29].

Freundlich Isotherm Model. Freundlich isotherm model made a few assumptions that physicochemical sorption takes place on heterogeneous surfaces and it is a multilayer adsorption process. The interactions between the adsorbate molecules are present [30]. The Freundlich model equation is written as:

$$q_e = K_F C_e^{\frac{1}{n}} \quad (6)$$

By rearranging equation 6, the Freundlich model equation in linear form is written as:

$$\log q_e = \frac{\log C_e}{n} + \log K_F \quad (7)$$

where

- q_e = Amount of adsorbate adsorbed at equilibrium (mg/g)
 C_e = Concentration of adsorbate at equilibrium (mg/L)
 n = Freundlich constant for intensity
 K_F = Freundlich constant for adsorption capacity

Figure 7 presented the graph of $\log q_e$ against $\log C_e$ for adsorption of MB. By using the gradient obtained from the plot, the n value can be calculated. Besides, K_F value was determined from y-intercept of the plot. Values of n and K_F were determined to be 1.7343 and 18.3147, respectively. The R^2 value was 0.9927 which was very close to unity (Table 2). This shows that the equilibrium adsorption data is best fitted with Freundlich isotherm model and implies that the nature of MB adsorption on peanut husks is a multilayer, physicochemical sorption that takes place on heterogeneous surfaces.

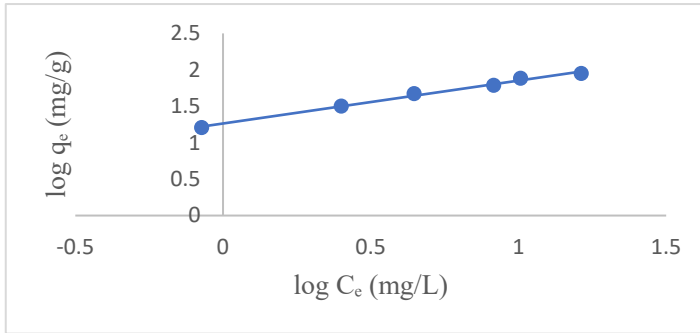


Figure 7. Freundlich isotherms for adsorption of MB

Brunauer-Emmett-Teller (BET) Isotherm Model. The assumptions made in BET isotherm model are the heat of adsorption is the same for all adsorbed layers except the first layer and first layer adsorbates will have the strongest interaction with the adsorbent compared to subsequent layers. It is a multilayer sorption takes place on homogeneous surface and number of adsorption sites are fixed [31]. The equation of BET model is written as:

$$q_e = \frac{K_B C_e q_m}{(C_s - C_e) \left[1 + (K_B - 1) \left(\frac{C_e}{C_s} \right) \right]} \quad (8)$$

By rearranging equation 8, the BET model equation in linear form is illustrated as:

$$\frac{C_e}{(C_s - C_e) q_e} = \left(\frac{K_B - 1}{K_B q_m} \right) \left(\frac{C_e}{C_s} \right) + \frac{1}{K_B q_m} \quad (9)$$

where

- C_e = Concentration of adsorbate at equilibrium (mg/L)
- C_s = Saturation concentration of solute (mg/L)
- q_e = Amount of adsorbate adsorbed at equilibrium (mg/g)
- q_m = Amount of adsorbate in forming a complete monolayer (mg/g)
- K_B = BET constant describing the energy of adsorbate-adsorbent interaction

The gradient and y-intercept from the linear plot of C_e/(C_s-C_e)q_e against C_e/C_s were utilized to determine K_B and q_m values (Figure not shown). The value of K_B was 431 while q_m value was 116.0093 mg/g. The C_s value was determined by calculating the maximum amount of adsorbate which is MB that can be dissolved in minimum volume of solvent. The C_s value of MB was 2250 mg/L. Table 2 indicated all the R² values and parameters obtained from Langmuir, Freundlich and BET isotherm models. The R² value for all

three isotherm models were very high, however, the Freundlich isotherm model showed a slightly better fit to the experimental data compared to Langmuir and BET models. This suggests that the binding sites on peanut husks are mostly heterogeneous and since peanut husks are biosorbents there may have various kind of surface adsorption sites [32].

Table 2. Values obtained from Langmuir, Freundlich and BET isotherm models

Langmuir isotherm		Freundlich isotherm		BET isotherm	
q_m (mg/g)	117.6471	n	1.7343	q_m (mg/g)	116.0093
K_L (L/mg)	0.1540	K_F	18.3147	K_B	431
R^2	0.9709	R^2	0.9927	R^2	0.9717

Optimization studies

Plackett-Burman (PB) Design. The most important factors that can give a significant impact to percentage uptake of dyes can be determined using PB [33]. Contact time, adsorbent dosage, pH and initial dye concentration were examined using PB design to select the significant factors that bring strong impact to the adsorption process. Twelve runs with different experimental conditions were performed and an ANOVA table was generated based on the experimental results. Table 3 presented the ANOVA results of PB. This model has p-value of 0.0010 which indicated that it is significant because p-value < 0.05. Out of the four factors, adsorbent dosage, pH and contact time were identified as the significant factors except initial dye concentration with p-value of 0.6416 which is larger than 0.05.

Table 3. ANOVA of PB for adsorption of Methylene Blue by peanut husks

Source	Sum of Squares	df	Mean Square	F Value	p-value
Model	11560.91	4	2890.23	17.01	0.0010
A-Contact time	1441.90	1	1441.90	8.48	0.0226
B-pH	6782.06	1	6782.06	39.91	0.0004
C-Initial dye concentration	40.19	1	40.19	0.24	0.6416
D-Dosage	3296.77	1	3296.77	19.40	0.0031
Residual	1189.55	7	169.94		
Lack of Fit	1189.55	6	198.26		

R-Squared 0.9067

Predicted R-Squared 0.7258

Adjusted R-Squared 0.8534

Adequate Precision 12.6303

Verification of Plackett-Burman Design Models. Validation of this model was done by employing function of desirability. The experimental condition with highest desirability generated by the software were performed.

Response Surface Methodology (RSM). The effect of different variables on MB uptake were studied using RSM and the variables involved were adsorbent dosage, pH and contact time. RSM generated 20 different sets of experiment and an ANOVA table was generated based on the experimental results. The ANOVA of RSM were presented in Table 4. The relationship between the three significant factors and the percentage uptake of MB were illustrated in the modified cubic model shown below:

Percentage Uptake

$$= 95.65 + 5.13 * A + 24.89 * B + 11.01 * C - 0.63 * AB - 0.43 * AC - 8.46 * BC - 4.92 * A^2 - 23.21 * B^2 - 3.95 * C^2$$

where

A = Contact time

B = pH

C = Adsorbent dosage

The p-value of model of experiment is smaller than 0.0001 as seen in Table 4 indicated that it was significant. Similarly, the p-value for the three significant factors were also less than 0.05. The high R² value which was 0.9890 showed that the experimental results agreed well with the expected results. The adjusted R² was 0.9791 while the predicted R² was 0.8378.

Table 4. ANOVA of RSM for adsorption of Methylene Blue by peanut husks

Source	Sum of Squares	df	Mean Square	F Value	p-value
Model	12491.99	9	1388.00	99.94	< 0.0001
A-Contact time	263.38	1	263.38	18.96	0.0014
B-pH	6194.90	1	6194.90	446.05	< 0.0001
C-Dosage	1212.26	1	1212.26	87.29	< 0.0001
AB	3.16	1	3.16	0.23	0.6439
AC	1.45	1	1.45	0.10	0.7536
BC	572.85	1	572.85	41.25	< 0.0001
A ²	66.60	1	66.60	4.80	0.0534
B ²	1481.26	1	1481.26	106.65	< 0.0001
C ²	42.88	1	42.88	3.09	0.1094
Residual	138.88	10	13.89		
Lack of Fit	138.88	5	27.78		

R-Squared 0.9890

Predicted R-Squared 0.8378

Adjusted R-Squared 0.9791

Adequate Precision 34.0345

They agreed with each other reasonably. Coefficient of variance (CV) was determined to be 4.68 % which showed that the reliability and precision of this model is high. The adequate precision obtained was 34.0345 which indicated an adequate signal because it is greater than 4. Ratio of signal to noise can be measured by adequate precision.

Figure 8 presented the 3D surface plot for the correlation between percentage uptake of MB, contact time and pH. Maximum dye uptake was observed at long contact time and high pH. As contact time increases, only a slight change in the percentage removal was observed because the equilibrium time has been reached. The maximum adsorption capacity of adsorbent can be determined at equilibrium time [33]. The percentage uptake increases as pH increases and remained almost constant after pH 6. High pH condition favours the adsorption of cationic MB dye because the positively charged groups on the adsorbent start to deprotonate and leads to high electrostatic attraction between peanut husks surface and cationic MB molecules.

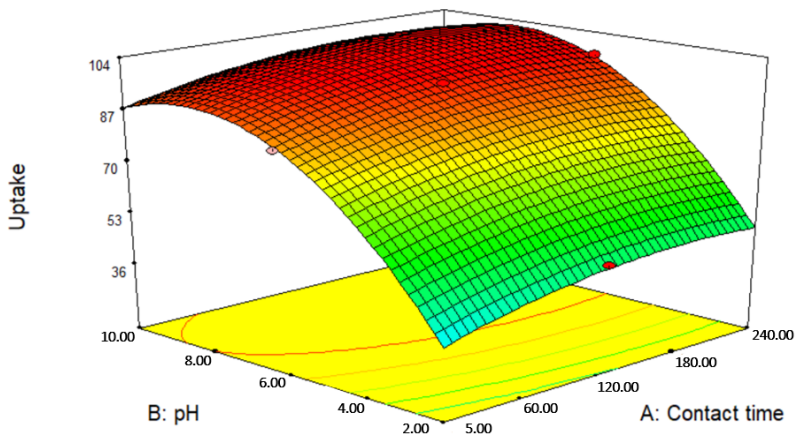


Figure 8. 3D surface plot for the percentage uptake of MB by peanut husks as a function of pH and contact time at 50 mg/L of initial MB concentration

Figure 9 illustrated the 3D surface plot for the relationship between percentage uptake of MB, adsorbent dosage and contact time. The trend of percentage uptake versus contact time is very similar to the one observed in Figure 8. As adsorbent dosage increases, the uptake of MB also increases. This is because there are more surface area and increasing number of vacant binding sites for attachment of dye molecules.

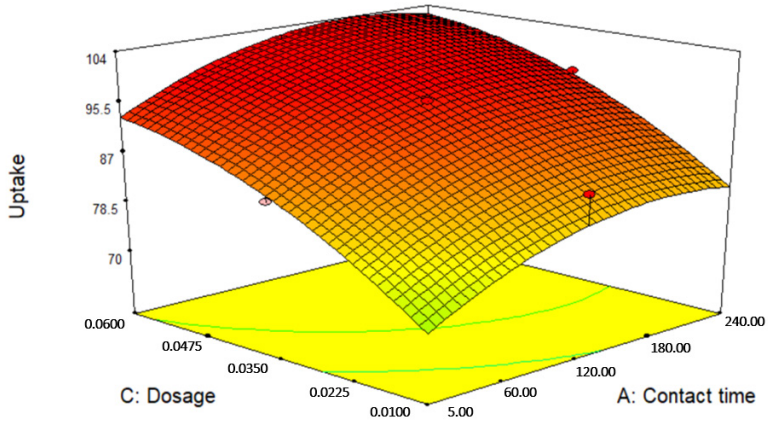


Figure 9. 3D surface plot for the percentage uptake of MB by peanut husks as a function of adsorbent dosage and contact time at 50 mg/L of initial MB concentration

Figure 10 illustrated the 3D surface plot for the relationship between percentage uptake of MB, adsorbent dosage and pH. The percentage uptake increases as adsorbent dosage increases and has the same pattern as observed in Figure 9. The trend of percentage uptake versus pH is also very similar to the one observed in Figure 8 where the percentage uptake remained almost constant after pH 6.

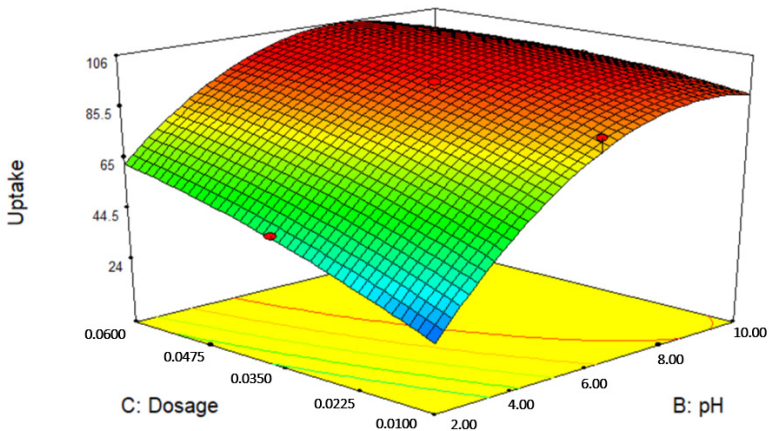


Figure 10. 3D surface plot for the percentage uptake of MB by peanut husks as a function of adsorbent dosage and pH at 50 mg/L of initial MB concentration

Verification of Response Surface Methodology Models. The equation generated was validated by performing the experiment under conditions with highest desirability. Percentage of differences calculated between expected and experimental results for each set of experiment was within 0.05 - 5.16 %. The percentage differences are considered low and this indicates that the generated model equation is valid.

CONCLUSIONS

Peanut husks were found to be a potential adsorbent to remove MB dye solution in this study. In FTIR analysis, there was no significant shift before and after adsorption of dye showing that the functional groups on peanut husks remained the same. SEM and AFM analysis further confirmed that there is adsorption of MB dye occurred on peanut husks by observing the surface morphology after adsorption and compared with peanut husks before adsorption. A good fit of experimental data into pseudo-second-order kinetic model suggested that chemisorption process was involved in this study with R^2 close to unity. In the isotherm study, compared to Langmuir and BET models, Freundlich model with R^2 of 0.9927 showed a slightly better fit to the experimental data. PB was performed to determine the significant factor in the removal of MB by peanut husks. Adsorbent dosage, pH and contact time were determined as the significant factors in this experiment. The optimum level of each significant variable to reach the maximum percentage uptake of dye was determined using RSM and a modified cubic model equation was generated. The percentage of differences calculated for each set of experiment was below 6 %. Optimum condition was reached at 120 minutes of contact time, pH 10 and 0.035 g of adsorbent.

EXPERIMENTAL SECTION

Preparation of adsorbent

Peanut husks were chosen as the adsorbent to be studied in this project. The peanut husks and kernels were first separated. The husks were washed thoroughly with water. Then, the husks were sun-dried for a few days and followed by drying in an oven for 24 hours at 65 °C to ensure the moisture was completely removed. The dry peanut husks were grounded with a blender into powder form and screened through a 1 mm sieve. The samples were then stored in a glass media bottle with silica gel.

Preparation of Methylene Blue solution

MB solution was chosen as the adsorbate in this study. The molecular weight of MB is 319.85 g/mol and its molecular formula is $C_{16}H_{18}ClN_3S$. The stock solution of 1000 mg/L was prepared by using a 1 L volumetric flask. Then, it was stored in a dark place to prevent degradation from direct sunlight. Dilution technique was then applied for the preparation of working solution.

Characterization of adsorbent

Fourier Transform Infrared Spectroscopy. The functional groups present on peanut husks can be studied using FTIR spectrometer model Spectrum RX1. The dried peanut husks were ground with KBr powder to a homogenous mixture and vacuum pressed into pellets for analysis. Both peanut husks before and after adsorption of dye were analysed at the wavenumber ranging from 4000 – 400 cm^{-1} .

Scanning Electron Microscopy. The surface morphology of peanut husks before and after adsorption of dye were studied at emissions current of 4.0 kV using SEM model JEOL-JSM-6701F.

Atomic Force Microscopy. The surface topology of peanut husks before and after adsorption of dye were studied using AFM model Park XE-70 AFM.

Batch experiments

A 0.03 g of peanut husks was added into a centrifuge tube containing 20 mL of MB solution. The mixture was agitated for 3 hours with 150 rpm on an orbital shaker. A control set without peanut husks was performed simultaneously to prove that the dye adsorption is because of the presence of peanut husks instead of the centrifuge tube wall. The mixtures were then centrifuged at 7000 rpm for phase separation. Dye concentration of supernatant was analysed at 664 nm which is the maximum wavelength of MB by using a UV-Vis spectrophotometer. All batch experiments were done in duplicate and mean results were obtained. Equation below was used to calculate the percentage uptake of dye:

$$\text{Percentage uptake} = \frac{C_o - C_t}{C_o} \times 100 \%$$

where

C_o = Initial MB concentration (mg/L)

C_t = MB concentration at time, t (mg/L)

The effect of initial dye concentration was examined by using 20 mL of 25 mg/L of MB solution with 0.03 g of peanut husks. The experiment was repeated with 50 and 100 mg/L of MB solution. For each solution, at predetermined time intervals which are 5, 10, 15, 20, 25, 30, 45, 60, 120, 180 and 240 minutes, the absorbance of dye was measured and the dye concentration was calculated.

HCl or NaOH solution of 0.01, 0.1 and 1 M were added dropwise into the solution to adjust it to desired pH. A 50 mg/L of MB solution with pH ranging from 2 to 10 was prepared for this study. The solution was then placed on the orbital shaker at 150 rpm for 3 hours to reach the equilibrium.

Different amount of adsorbent ranging from 0.01 g - 0.06 g was added into 50 mg/L MB dye solution, respectively. The mixture was then subjected to 3 hours of contact time for the adsorption process to reach equilibrium to determine the effect of adsorbent dosage on adsorption process.

Optimization studies

Plackett-Burman design was performed to eliminate the insignificant factors in the adsorption of dye. Contact time, adsorbent dosage, pH and initial dye concentration were studied in this analysis. The interaction between each significant factor and their optimum levels can be identified by using Response Surface Methodology. The factors involved were pH, contact time and adsorbent dosage. All experiments were done in duplicates and the mean absorbance were obtained. The Design Expert Version 7.1.3 was used in the statistical and experimental design of the adsorption process.

ACKNOWLEDGEMENTS

The financial support and research facilities by Universiti Tunku Abdul Rahman are acknowledged.

REFERENCES

1. N. Kannan; M.M. Sundaram; *Dyes Pigm.*, **2001**, *51*, 25-40
2. S.L. Lee; S.W. Liew; S.T. Ong; *Acta Chim. Slov.*, **2016**, *63*, 144-153
3. S.L. Chan; Y.P. Tan; A. H. Abdullah; S.T. Ong; *J. Taiwan Inst. Chem. Eng.*, **2016**, *61*, 306-315
4. S.T. Ong; C.K. Seou; *Desalination Water Treat.*, **2013**, *52*, 7673-7684
5. M.A.M. Salleh; D.K. Mahmoud; W.A.W.A. Karim; A. Idris; *Desalination*, **2011**, *280*, 1-13

6. S.T. Ong; E.H. Tay; S.T. Ha; W.N. Lee; P.S. Keng; *Int. J. Phys. Sci.*, **2009**, *4*, 683-690
7. S.T. Ong; W.N. Lee; P.S. Keng; Y.T. Hung; S.T. Ha; *Int. J. Phys. Sci.*, **2010**, *5*, 582-595
8. R. Malik; D.S. Ramteke; S.R. Wate; *Indian J. Chem. Technol.*, **2006**, *13*, 319-328
9. S. Sadaf; H.N. Bhatti; *J. Taiwan Inst. Chem. Eng.*, **2013**, *45*, 541-553
10. *World Agricultural Production*, United States Department of Agricultural, USA, **2022**, pp. 1-43
11. Inamuddin; A. Mohammad; A.M. Asiri; *Inorganic Pollutants in Wastewater: Methods of Analysis, Removal and Treatment*, Materials Research Forum LLC, Millersville, USA, **2017**, p. 195
12. L. Zafar; A. Khan; U. Kamran; S. Park; H.N. Bhatti; *Surf. Interfaces*, **2022**, *31*, 101897
13. B. Kumar; U. Kumar; *Korean J. Chem. Eng.*, **2015**, *32*, 1655-1666
14. S. Ricordel; S. Taha; I. Cisse; G. Dorange; *Sep. Purif. Technol.*, **2001**, *24*, 389-401
15. L. Das; P. Das; A. Bhowal, C. Bhattacharjee; *J. Environ. Manage.*, **2020**, *276*, 111272.
16. C.I. Tay; S.T. Ong; *J. Phys. Sci.*, **2019**, *30*, 137-156.
17. H.Y. Gan, L.E. Leow, S.T. Ong; *Acta Chim. Slov.*, **2017**, *64*, 144-158.
18. M.U. Farooq; M.I. Jalees; A. Iqbal; N. Zahra; A. Kiran; *Desalination Water Treat.*, **2019**, *160*, 333-342
19. D. Özer; G. Dursun; A. Özer; *J. Hazard. Mater.*, **2007**, *144*, 171-179
20. N.A. Taha; A. El-Maghraby; *Glob. Nest J.*, **2015**, *18*, 25-37
21. W. Zou; H. Bai; S. Gao; K. Li; X. Zhao; R. Han; *Desalination Water Treat.*, **2012**, *49*, 41-56
22. N. Besharati; N. Alizadeh; S. Shariati; *J. Mex. Chem. Soc.*, **2018**, *62*, 110-124
23. N. Tahir; H.N. Bhatti; M. Iqbal; S. Noreen; *Int. J. Biol. Macromol.*, **2017**, *94*, 210-220
24. S. Lagergren; *Kungl. Svenska Vetenskapsakad. Handl.*, **1898**, *24*, 1-39
25. Y.S. Ho; G. McKay; *Process Biochem.*, **1999**, *34*, 451-465
26. I. Langmuir; *J. Am. Chem. Soc.*, **1918**, *40*, 1361-1403
27. L. Lonappan; T. Rouissi; R.K. Das; S.K. Brar; A.A. Ramirez; M. Verma; R.Y. Surampalli; J.R. Valero; *Waste Manag.*, **2016**, *49*, 537-544
28. L. Meili; P.V.S. Lins; M.T. Costa; R.L. Almeida; A.K.S. Abud; J.I. Soletti; G.L. Dotto; E.H. Tanabe; L. Sellaoui; S.H.V. Carvalho; A. Erto; *Prog. Biophys. Mol. Biol.*, **2019**, *141*, 60-71
29. T.C. Egbosiuba; A.S. Abdulkareem; A.S. Kovo; E. A. Afolabi; J.O. Tijani; M. Auta; W.D. Roos; *Chem Eng Res Des.*, **2020**, *153*, 315-336
30. H.M.F. Freundlich; *J. Phys. Chem.*, **1906**, *57*, 385-471
31. S. Brunauer, P.H. Emmett, E. Teller; *J. Am. Chem. Soc.*, **1938**, *60*, 309-319
32. S.T. Ong; C.K. Lee; Z. Zainal; *Bioresour. Technol.*, **2007**, *98*, 2792-2799
33. S.T. Ong; E.C. Khoo; P.S. Keng; S.L. Hii; S.L. Lee; Y.T. Hung; S.T. Ha; *Desalination Water Treat.*, **2011**, *25*, 310-318

TESTING MWCNT-COOH/Fe₃O₄ NANOCOMPOSITE FOR THE REMOVAL OF AMPICILLIN FROM SYNTHETIC AQUEOUS SOLUTIONS

Ildiko LUNG^a, Adina STEGARESCU^a, Ocsana OPRIȘ^a,
Maria-Loredana SORAN^{a,*}

ABSTRACT. The aim of this paper consisted of the carbon nanotube nanocomposite testing for the removal of ampicillin from aqueous solutions. To determine the optimum experimental conditions for ampicillin adsorption on nanocomposite, several parameters were selected: the pH, initial concentration of pollutant, adsorbent dose and contact time. The high-performance liquid chromatography was used to determine the residual ampicillin concentration from aqueous solutions. The best removal of the antibiotic on the tested nanocomposite was obtained with an initial concentration of 40 mg L⁻¹ with 1 g L⁻¹, pH 2 in 20 min.

Keywords: ampicillin, adsorption, nanocomposite, carbon nanotubes, water decontamination

INTRODUCTION

The innovation and modern development of the antibiotic industry have seen a giant leap since the discovery of penicillin by Sir Alexander Fleming in 1928 [1]. Contamination of water with polluting agents with an increasingly high degree of toxicity, such as heavy metals, organic substances, pesticides or antibiotics, has become a major current issue that requires finding effective depollution solutions [2]. An intensively addressed field for this purpose is nanotechnology because materials with nanometric dimensions have large specific surfaces with good adsorption properties [3]. Thus, finding new water treatment technologies is essential for a sustainable

^a National Institute for Research and Development of Isotopic and Molecular Technologies, 67-103 Donat, 400293 Cluj-Napoca, Romania,

* Corresponding author: loredana.soran@itim-cj.ro



environment and for preventing the transfer of dangerous substances in the food chain, because aquatic environments serve as “repositories” for antibiotics from the pharmaceutical industry, hospitals, animal farms, wastewater from treatment plants, municipal waste [4].

Several methods have been developed to treat antibiotic-contaminated waters, such as oxidation, degradation, electro degradation, reverse osmosis, nanofilter membranes, catalytic degradation, and adsorption [5]. Different adsorbents were used for this process, including adsorbents based on agricultural waste, nanomaterials and layered double hydroxides. The main adsorption mechanisms for antibiotic removal are the electrostatic attraction, $\pi - \pi$ interaction and hydrogen bonding. Adsorption is a widely available technique due to its high efficiency, operational simplicity and feasibility. However, the efficiency of the adsorption method is greatly affected by the properties of the adsorbents used [6, 7].

The development of carbon-based nanomaterials such as carbon nanotubes (CNTs) is of great interest for use in pollutant removal processes, due to meeting the criteria required for good adsorption: high specific surface area, large pore volume, physical interactions and strong chemicals with pollutants, etc. [8].

Ampicillin, one of the most widely used antibiotics degrades most in an acidic and basic environment, while UV light and heat have a negligible degradation effect. Time has only a slight degradation effect [9]. For this reason, it is imperative to develop effective materials for their removal from the waters. Previous studies reveal that activated carbon has excellent properties as an adsorbent for organic contaminants in water. On the other hand, CNTs having a much more porous surface than activated carbon makes them ideal candidates for the adsorption of bulky organic compounds such as bisphenol A, diclofenac, oseltamivir, sulfamethoxazole and ampicillin. The use of CNTs in adsorption, filtration or photocatalytic degradation technologies, in the case of contaminated waters, is currently limited to small-scale experiments (laboratory) and the development of a pilot system for large-scale (industry) is necessary [9, 10].

In this article, the efficiency of the MWCNT-COOH/Fe₃O₄ nanocomposite in removing ampicillin from synthetic water samples was investigated. The preparation and characterization method of the nanocomposite used for this study was published in a previous article [11].

RESULTS AND DISCUSSION

Ampicillin (Figure 1) was the antibiotic selected in this study, because it is an drug from the category of broad-spectrum penicillin, with indications in various bacterial infections located at the respiratory level and otorhinolaryngological

infections (bronchitis, pharyngitis, sinusitis) or infections in the digestive system and urogenital.

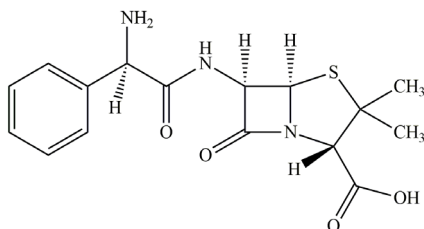


Figure 1. The chemical structure of ampicillin.

To establish the optimal conditions for the ampicillin adsorption process on the selected adsorbent, the influence of some physico-chemical parameters was followed.

Influence of pH

An important parameter is pH because it can affect the structure of ampicillin. Thus, at pHs between 2.9 and 7.2, ampicillin was positively charged, while at pHs above 7.2, ampicillin was negatively charged [12, 13].

The experiments were carried out by varying the pH between values 2 and 10 of an initial ampicillin concentration of 40 mg L⁻¹. The mixtures obtained from 5 mg of adsorbent and 5 mL of ampicillin solution were stirred at 400 rpm for 20 min at a temperature of 25°C. The results obtained are presented in Figure 2.

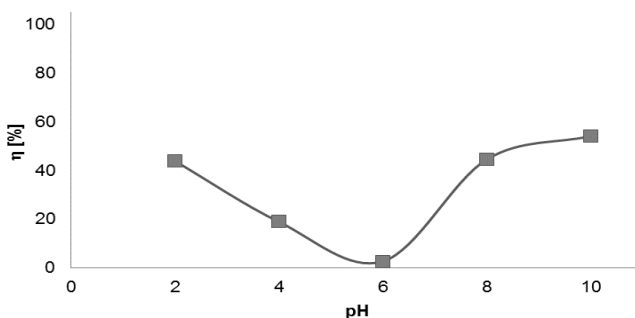


Figure 2. Influence of pH on the extent of ampicillin removal on CNT-COOH/Fe₃O₄.

The degree of ampicillin adsorption on the tested adsorbent increases in both acidic and basic media. For the following experiments, the pH value 2 was selected.

Influence of adsorbent dose

This study was carried out by mixing 5 mL of ampicillin solution (40 mg L^{-1} , at pH 2), with different amounts of adsorbent (between $0.25 - 2 \text{ mg L}^{-1}$). The mixtures were stirred at 400 rpm at 25°C for 20 min, and the resulting solution was filtered and analyzed.

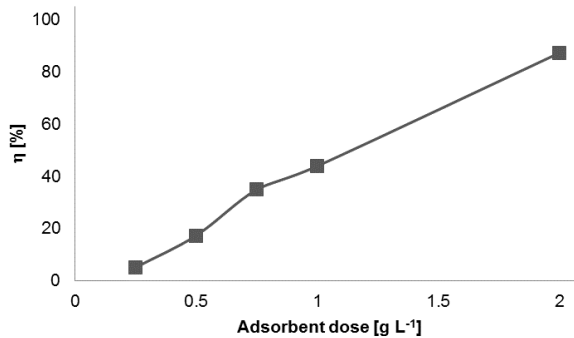


Figure 3. The influence of the adsorbent dose on the degree of ampicillin removal on MWCNT-COOH/ Fe_3O_4 .

The efficiency of the adsorption process increased with the increase of the adsorbent dose (Figure 3). A high degree of removal was obtained (87.2%) using an adsorbent dose of 2 g L^{-1} . For economic reasons, the subsequent studies were carried out using 1 g L^{-1} of MWCNT-COOH/ Fe_3O_4 .

Influence of ampicillin initial concentration

5 mL ampicillin solution of different concentrations ($40-100 \text{ mg L}^{-1}$) at pH 2 were stirred with the amount of adsorbent established in the previous study (5 mg). The mixtures were stirred at 400 rpm for 20 min at 25°C .

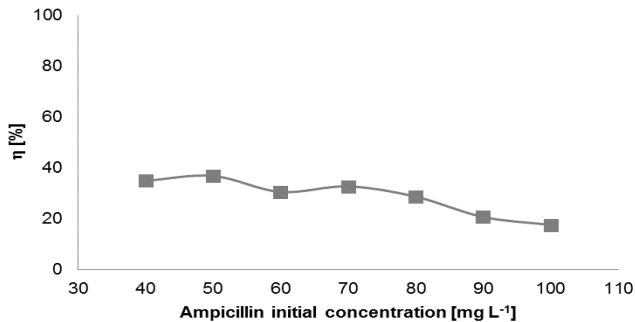


Figure 4. Influence of the initial concentration on the degree of ampicillin removal on MWCNT-COOH/ Fe_3O_4 .

As can be seen from Figure 4, the extent of ampicillin removal decreased with increasing initial concentration. Using MWCNT-COOH/Fe₃O₄ as adsorbent, the ampicillin removal degree was below 50%. For the following studies, the concentration of 40 mg L⁻¹ was chosen.

Since the adsorption process takes place at a very acidic pH, in this study, the degradation of ampicillin was followed over time both in the initial solution and in the solutions in which the adsorption of ampicillin was carried out with the selected adsorbent. To follow the degradation process, the solutions were chromatographically analyzed for 72 h. The results obtained are shown in Figure 5.

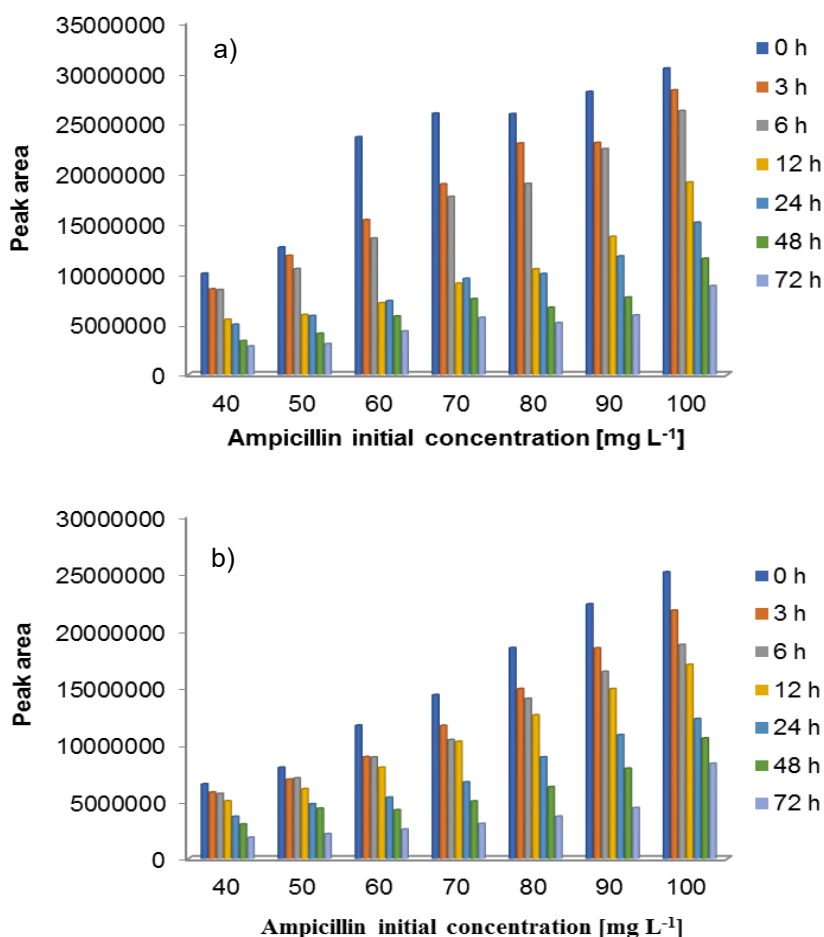


Figure 5. Ampicillin degradation over time: a) without adsorbent and b) with MWCNT-COOH/Fe₃O₄.

As can be seen (Figure 5), ampicillin degrades over time in a strongly acidic environment, but to obtain the best and fastest results, it is preferable to use especially the nanocomposite MWCNT-COOH/Fe₃O₄.

Influence of contact time

Samples of 5 mg of MWCNT-COOH/Fe₃O₄ were stirred at 400 rpm with 5 mL of ampicillin solution of concentration 40 mg L⁻¹ at 25°C, in a time interval of 5-20 min. The solute separated a strong magnet was analyzed, and the results obtained are presented in Figure 6.

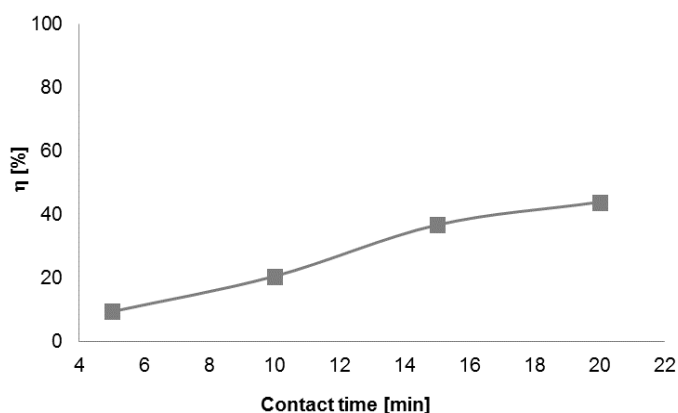


Figure 6. Influence of contact time on the removal degree of ampicillin on CNT-COOH/Fe₃O₄.

As the contact time increases, the degree of ampicillin removal on the adsorbent increases, reaching to 43.9%.

The proposed mechanism

The analysis of the results obtained made possible to propose an adsorption mechanism for ampicillin on MWCNT-COOH/Fe₃O₄ nanocomposite. This mechanism is presented in Fig. 7. As can be seen from Fig. 7, the interaction between ampicillin and MWCNT-COOH/Fe₃O₄ nanocomposite can be governed by hydrogen bonds, van der Waals interactions or polar interactions. It is possible to occur hydrogen bonding or electrostatic interactions between the functionalized carbon nanotubes and the antibiotic because the adsorbent capacity is maximum in acidic conditions (pH 2) [14, 15].

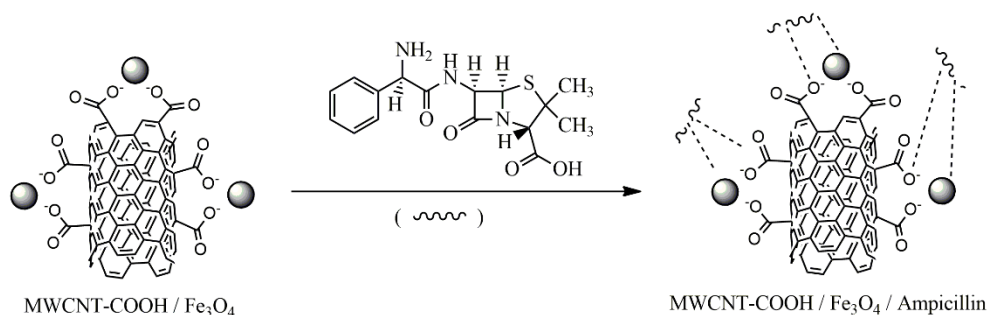


Figure 7. Mechanism of ampicillin adsorption on MWCNT-COOH/Fe₃O₄ nanocomposite

CONCLUSIONS

In this paper, the adsorption performance of MWCNT-COOH/Fe₃O₄ nanocomposite for ampicillin removal from aqueous solutions has been assessed. To establish the optimal conditions for ampicillin removal several parameters were studied. Among the studied parameters were the pH, adsorbent dose, contact time and the initial ampicillin concentration. A degree of approx. 44% of ampicillin elimination was obtained in the following experimental conditions: 40 mg L⁻¹ ampicillin concentration in the aqueous solution, pH 2, 20 min of contact time with 1 g L⁻¹ adsorbent dose.

Considering that the concentration of ampicillin in water is much lower than that used in this experiment, as well as the magnetic properties of the nanocomposite, this can be suitable for ampicillin removal from real effluents.

EXPERIMENTAL SECTION

Materials

Injectable ampicillin was purchased from a local pharmacy. HCl and NaOH used for the pH adjustment of the aqueous solutions were purchased from Sigma-Aldrich (Germany) and VWR Chemicals, respectively. The ultrapure water obtained by a Direct-Q® 3 UV Water Purification System Merck (Germany) was used for synthetic solutions preparation used in adsorption experiments. The MWCNT functionalized with COOH groups and MWCNT-COOH/Fe₃O₄ nanocomposites were synthesized in our laboratory according with the methods published in our previous paper [11].

Adsorption studies

The adsorption process was carried out under static conditions (“batch technique”) consisting of contacting a synthetic aqueous solution of the studied pollutant species with the adsorbent in a Berzelius glass. The mixture was stirred (400 rpm/min) for a certain time, after which the two phases were separated with the help of a magnet, and the solute was analyzed.

The efficiency of the adsorption process is given by the degree of removal of the pollutant, which is calculated with the relation:

$$\eta (\%) = \frac{(C_0 - C_t)}{C_0} 100$$

where: η (%) represents the degree of removal/retention of the pollutant, C_0 and C_t (mg L^{-1}) represent the concentration of the pollutant in the solution at the initial moment and at time t (min).

Ampicillin determination

Analysis of ampicillin was performed using a Shimadzu LC2010 high-performance liquid chromatograph. The analysis of ampicillin from synthetic water samples was carried out on a Nucleodur column (100×3 mm, $3 \mu\text{m}$) thermostated at 30°C . The mobile phase used was ultrapure water with 0.1% formic acid (A) and acetonitrile (B). Ampicillin was eluted with the elution gradient shown in Table 1 at a flow rate of 0.5 mL min^{-1} . The equilibration time of the column was 5 min and the injection volume used was $20 \mu\text{L}$. Three chromatograms were recorded for each sample.

Table 1. Gradient program used for chromatographic separation of ampicillin. Mobile phase: ultrapure water with 0.1% formic acid (A) and acetonitrile (B).

Time (min)	A (%)	B (%)
0:00	95	5
1:00	95	5
9:00	80	20
10:00	95	5
15:00	Stop	Stop

ACKNOWLEDGMENTS

Financial support from the Romanian Ministry of Research and Innovation, Core Programme, Project PN 19 35 02 03 (36N/13.02.2019) is gratefully acknowledged.

REFERENCES

1. A. Fleming; *Brit. J. Exp. Pathol.*, **1929**, *10*, 226–236.
2. P. Meiling; K. Naoki; I. Hiroshi; *J. Chem. Chem. Eng.*, **2015**, *9*, 433–441.
3. X. Ren; C. Chena; M. Nagatsu; X. Wang; *J. Chem. Eng.*, **2011**, *170*, 395–410.
4. J.O. Eniola; R. Kumar; M.A. Barakat; *Environ. Sci. Poll. Res.*, **2019**, *26*, 34775–34788.
5. N. Rahman; P. Varshney; *RSC Adv.*, **2020**, *10*, 20322–20337.
6. L. Chu; S. Zhuang; J. Wang; *Radiat. Phys. Chem.*, **2018**, *145*, 34–38.
7. E.A. Serna-Galvis; J. Silva-Agrede; A.L. Giraldo-Aguirre; O.A. Florez-Acosta; R.A. Torres-Palma; *Ultrason. Sonochem.*, **2016**, *31*, 276–283.
8. M.K. Liu; Y.Y. Liu; D.D. Bao; G. Zhu; G.H. Yang; J.F. Geng; H.T. Li; *Sci. Rep.*, **2017**, *7*, 43717(1-8).
9. S. Naveed; N. Mateen; S. Nazeer; *J. App. Pharm.*, **2014**, *6*, 314–321.
10. S. Kurwadkar; T.V. Hoang; K. Malwade; S.R. Kanel; W.F. Harper Jr; G. Struckhoff; *Nanotech for Environ. Eng.*, **2019**, *4*, 12.
11. A. Stegarescu; H. Cabrera; H. Budasheva; M.L. Soran; I. Lung, F. Limosani; D. Korte; M. Amati; G. Borodi; I. Kacso; O. Opris; M. Dan; S. Bellucci; *Nanomaterials*, **2022**, *12*, 3008.
12. X. Li; N. Zhang; L. Yang; *IOP Conf. Series: Earth Environ. Sci.*, **2020**, *467*, 012184.
13. N. Rahman; P. Varshney; *RSC Adv.*, **2020**, *10*, 20322.
14. M.E. Bidhendi, Z. Poursorkh, H. Sereshti, H.R. Nodeh, S. Rezanian, M.A. Kamboh; *Int. J. Environ. Res. Public Health*, **2017**, *20*, 4223.
15. C. Saucier, P. Karthickeyan, V. Ranjithkumar, E.C. Lima, G.S. dos Reis, I.A.S. de Brum; *Environ. Sci. Pollut. Res.*, **2017**, *24*, 5918.

INVESTIGATION OF THE FUNCTIONAL LAYER FORMATION ON THE SURFACE OF CARBON MATERIAL

Saken ABDIMOMYN^a, Azhar ATCHABAROVA^{a,*},
Dinara ABDUAKHYTOVA^a, Rustam TOKPAYEV^a,
Kanagat KISHIBAYEV^a, Tamina KHAVAZA^a, Andrey KURBATOV^a,
Graziella Liana TURDEAN^b, Mikhail NAURYZBAYEV^a

ABSTRACT. In this study, a comparison of walnut-based carbon materials (CM) obtained by hydrothermal carbonization (HTC) and HTC in combination with steam gas activation (SGA) was carried out. In order to study the effect of steam activation on the functional layer formation, the obtained materials were studied by SEM, nitrogen adsorption/desorption by Brunauer-Emmett-Teller (BET) method, Raman spectroscopy, X-ray diffraction spectroscopy (XRD), X-ray fluorescence elemental analysis (XRF). Functional groups (FG) were evaluated qualitatively and quantitatively by Fourier transform infrared spectroscopy (FTIR), acetone extract analysis of CM by gas chromatography-mass spectrometry (GC-MS), and potentiometrically Boehm titration. The described mechanism of the influence of the base nature on the surface functionality correlates well with the results of the powder addition method. The HTC or HTC+SGA treatment provides a wide range of possibilities for further controlled modification of the carbon sorbent surface for specific adsorption purposes.

Keywords: hydrothermal carbonization, carbon material, thermal carbonization, walnut shell, activated carbon, functional layer.

INTRODUCTION

Our days, the pollution of water resources with heavy metals (HM) and organic compounds (OC) is a great challenge that must be solved to assuring a high-quality lifestyle [1,2]. In this context, carbon materials are

^a Center of Physical Chemical Methods of Research and Analysis, al-Farabi Kazakh National University, Almaty, Kazakhstan

^b Babeş-Bolyai University, Faculty of Chemistry and Chemical Engineering, 11 Arany Janos str., RO-400028, Cluj-Napoca, Romania

* Corresponding author: atchabarova.azhar@kaznu.kz



promising compounds as adsorbents because of their low cost, high specific surface area, chemical inertness, and a great variety of surface functional groups [3-5]. Also, a chemical modification of CM has beneficial effects and is a widely used method to improve the adsorption properties and electrochemical characteristics of CM by increasing the specific surface area of the sample and forming a functional layer on the activated carbon surface.

Usually, chemical modification occurs by CO₂, H₂O_{vapor}, NaOH, KOH, ZnCl₂, FeCl₃, K₂CO₃, H₂SO₄, H₃PO₄, and HNO₃ treatment [9, 10]), but an electrochemical modification [6] could be also performed.

In function of the applied chemical modification procedure the following properties can be modified (i) specific surface area (S_{specific}) (e.g., see the study of macadamia nutshells, corn cobs, and rice husks activated with either CO₂ or H₂O_{vapor} [8]), (ii) a decrease of the volume of mesopores, the degradation of the carbon skeleton, the narrowing of pores if the activation treatment with KOH and NaOH occurs at prolonged high temperatures [7], (iii) partial destruction of the carbon structure, breaking of carbon-carbon bonds, and addition of oxygen leading to the formation of carboxylic, anhydride, carbonyl, lactone, phenolic, ketone, and ether groups on the activated carbon surface after treatment with HNO₃ of the porous carbon material [11]. It should be noticed, that in these cases, the pore size distribution and surface area are determined by the ratio between the chemical activator and the carbon raw material [12].

Either chemical modification or electrochemical modification of CM leads to an increase in selectivity and adsorption capacity of heavy metals ions and organic compounds and consequently to their use as sensing interfaces for catecholamines [13], glucose [14], dopamine, adrenaline, uric acid [15, 16], Cu²⁺, Ni²⁺, and Pb²⁺ [17-19] determination.

It is worth mentioning that last years, much attention is paid to the development of sorbents and enterosorbents based on components of plant origin and living organisms. Adsorbents of this type are the following: alginates [20], pectins [21], and chitin [22]. However, the technologies for obtaining such polysaccharides are relatively high energy- and time-consuming. In addition, enterosorbents have rather low mechanical strength and relatively high cost, which limits their widespread use. Consequently, agricultural wastes (walnut shells, grape and apricot seeds, spruce and pinecones, etc.) are the most promising raw materials for activated carbon materials (ACM) preparation [23].

This work aims to study the carbon materials (CM) based on walnut shells and the effect of vapor-gas activation on the formation of a functional layer on the surface of the activated carbon (AC). The morpho-structural features of the AC were obtained by BET, SEM, XRD, XRF, Raman spectroscopy investigations.

Also, FTIR, Boehm's titration, GC-MS methods were used to explain the mechanism of interaction of aqueous solution components with the surface of the AC.

RESULTS AND DISCUSSION

Study of the basic physico-chemical characteristics of the AC samples

The use of porous structures with high specific surface area and different pore size distribution is of key importance for the high capacity of the materials in adsorption and electrochemical processes.

The results of N₂ adsorption-desorption analysis by the BET method and the pore distribution are presented in Table 1 and Figures 1. The treatment of CM with acute water vapor opens the micropores, which leads to an increase of S_{specific}, evidenced by the increase in the average size of micropores from 1.24 nm to 1.74 nm, and the corresponding decrease of the percentage of microporosity from 87.5 and 84.09 %, respectively.

Table 1. Results on the specific surface area and porosity of activated carbons based on plant waste

Activated carbon	S _{specific} / m ² ·g ⁻¹	V _{total} / cm ³ ·g ⁻¹	V _{mN₂} / cm ³ ·g ⁻¹	% of micropores	Micropore volume till 2 nm from N ₂ / cm ³ ·g ⁻¹	Average pore width / nm	Adsorption enegy (Dubinin-Radushkyevich method) / kJ mol ⁻¹
HTC	464.9	0.24	0.21	87.50	0.20	1.24	20.86
HTC+SGA	738.0	0.22	0.19	84.09	0.16	1.74	14.92

The obtained BET results demonstrate that the ACM samples before and after activation retain a microporous structure up to 2 nm (Figures 1 inset).

It can be concluded that the presence of pores no larger than 4 nm in the ACM sample after HTC indicates an activated carbon mesoporous structure which allows the hydrated ions to penetrate freely into the structure of the material. However, as can be seen from Figure 1, the disappearance of the pores greater than 4 nm width and the increase of the intensity of pores with 2 nm width after activation is probably due to the release of non-carbon components, such as oxygen and nitrogen, during the activation process. This leads to the formation of a large distribution of micropores in the sample structure.

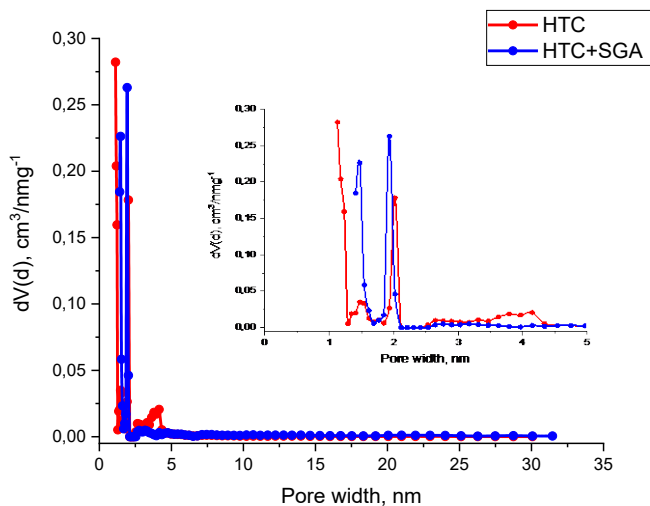


Figure 1. Pore size distributions of CM activated by HTC and HTC+SGA.

The adsorption isotherm for the ACM samples after hydrothermal carbonization (Figure 2, red line) is described by the Freundlich isotherm. According to this, there are adsorption sites with high and low affinity to the adsorbate on the heterogeneous surface. The high-affinity sites are engaged first, which explains the sharp increase at low pressure. Another reason is probably the lateral repulsion between the adsorbed molecules [24].

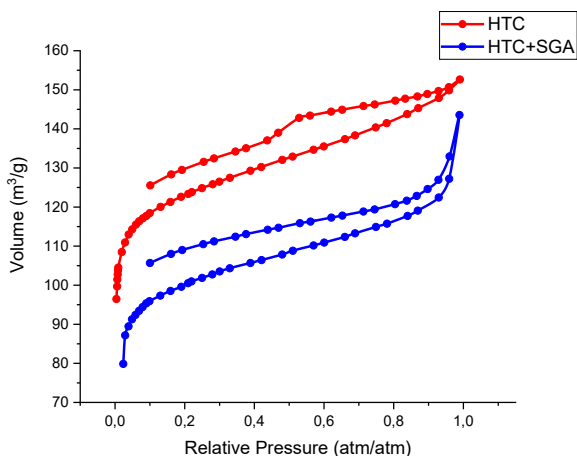


Figure 2. Nitrogen adsorption-desorption isotherms of CM activated by HTC (red line) and HTC+SGA (blue line).

INVESTIGATION OF THE FUNCTIONAL LAYER FORMATION
ON THE SURFACE OF CARBON MATERIAL

The results of nitrogen adsorption isotherms indicate that steam gas activation of carbon increases the number of adsorption sites, which leads to the hypothesis of additional layer formation, due to the destruction of non-carbon components of the matrix and the chemical conversion of water from the surface.

To confirm the hypothesis of an increase in S_{specific} due to matrix destruction, a micrograph of the sample surface was performed. The microphotographs of CM after HTC and HTC+SGA activation are presented in Figures 3. The surface of powders is shown as textural rough, with pores of different sizes distributed randomly. It can be concluded that steam gas activation of AC samples leads to an increase in surface area, due to the penetration of water vapor in pores. The formation of porous and defective carbon structure can be explained by the release of non-carbon elements such as H_2 , O_2 , and N_2 from the carbonizat's surface during the pyrolysis process, with the formation of a rigid carbon skeleton having a rudimentary porous structure. The structure of the samples after SGA is represented by flaky and round rod-like structures aggregated into larger particles.

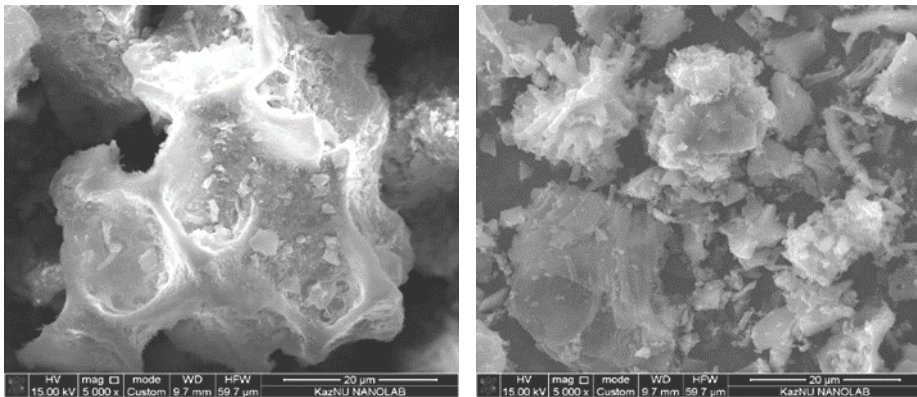


Figure 3. Surface morphology of CM samples based on walnut shells activated by HTC (A) and HTC+SGA (B)

According to the XRF analysis results (Table 2), ACM based on walnut shells contains significant amounts of K and Ca and trace amounts of other elements. The accumulation of K and Ca by plants and the subsequent formation of complexes and compounds based on covalent bonds leads to the finding of residual elements in the structure of the carbon matrix either after carbonization or after the activation treatment. It is assumed that after activation, the content of elements decreases due to the diffusion of ions into the aqueous component of the mixture.

Table 2. Results of elemental analysis by XRF of ACM based on plant waste

	Concentration of elements / %										
	Mg	Si	P	S	Cl	K	Mn	Fe	Cu	Zn	Ca
HTC	0.16	0.48	0.11	0.05	0.04	2.32	0.04	4.54	0.03	0.03	7.21
HTC+SGA	0.00	0.22	0.06	0.03	0.02	1.32	0.01	0.59	0.03	0.02	1.89

The effect of steam-gas activation on the crystal structure formation was evaluated by Raman spectroscopy (Figure 4, Table 3) and XRD methods (Figure 5).

The Raman spectrum of the CM sample activated by HTC+SGA (Figure 4) is characterized by two characteristic bands which are observed in the regions of 1580, and 1600 cm^{-1} and which correspond to the undisturbed graphite lattice where the ideal modes of the vibrations of graphite lattice have E_{2g} symmetry. At 1620 cm^{-1} is the characteristic graphite scattering peak and the first order D_2 band.

The spectrum of the sample HTC+SGA shows additional first-order bands (D bands or defect bands), which are characteristic of disordered graphite. Its intensity increases in comparison with the G band as the degree of disorder in the graphite structure increases. The most intense of them is the D_1 band, which appears at 1360 cm^{-1} and corresponds to the graphite lattice vibration mode with A_{1g} symmetry [7].

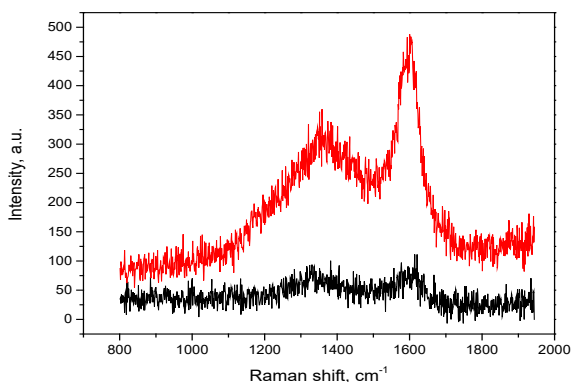


Figure 4. Raman spectra of CM based on walnut shells activated by HTC (black line), HTC+SGA (red line)

Table 3. I_G/I_D ratio value and L_a calculation for activated carbons

	I_G/I_D ratio	L_a / nm
HTC	0.85	4.98
HTC + SGA	0.67	6.67

INVESTIGATION OF THE FUNCTIONAL LAYER FORMATION ON THE SURFACE OF CARBON MATERIAL

It was found that the I_D/I_G ratio decreased after activation with water vapor, which indicates an increase in the crystallinity of the sample (Table 3). The phenomenon confirms the combustion of non-carbon components, while the carbon skeleton remains. A correlation between the I_D/I_G ratio and the crystallite size (L_a) is observed. This behavior is a consequence of burning out the amorphous structure of carbon. The crystallinity of the samples demonstrated by Raman investigation was estimated by peak integration. It was equal to 94.19 and 70.81% for HTC and HTC+SGA activation, respectively [26].

The diffractograms of CM activated by HTC and HTC+SGA (Figure 5) showed wide peaks at $2\Theta \sim 20 - 28^\circ$ and 44° , which are characteristic peaks of raw material based on the plant. The presence of peaks at $2\Theta \sim 20 - 28^\circ$ is confirmed by the amorphous structure of the obtained CM, which is due to the nature of the lattice plane structure (002) of the graphite carbon black.

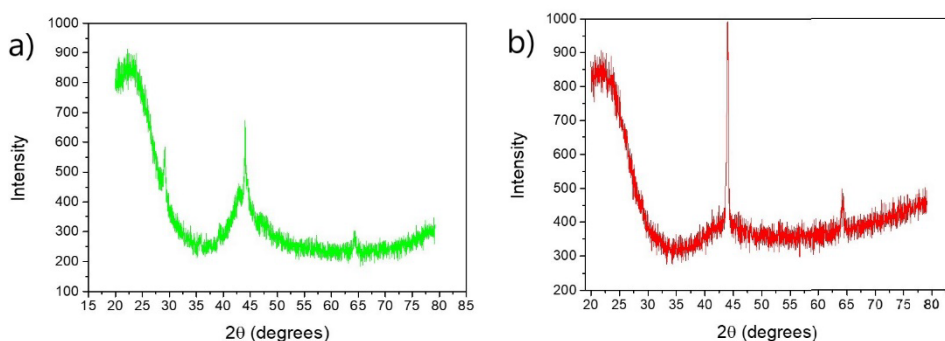


Figure 5. XRD spectra of CM activated by HTC (A) and HTC+SGA (B).

Determination of functional groups on the carbon samples surface

It is necessary to qualitatively and quantitatively determine the hydrophilicity and hydrophobicity of carbon materials which are due to the distribution and concentration of surface functional groups to further optimize the process of chemical and electrochemical modification by selecting modifiers, solution pH, electrolyte composition, electrolyte activity, and electrochemical modification methods.

Qualitative and quantitative determination of functional groups present on the carbon materials surface was carried out using infrared spectroscopy, GC-MS, and potentiometric Boehm titration methods.

By FTIR investigation (Figures 6), it was found that the samples based on the walnut shell are characterized by the presence of conjugated $-C=C-$, aromatic ring, and Ph- in the interval $\nu = 1599-1605 \text{ cm}^{-1}$; Ar-OH- at $\nu = 1359.98$; $-CH_2-CO-$, $-OH$, $-CN-$ at $\nu = 1398-1401 \text{ cm}^{-1}$; Alk-O- CH_3 , Ar-O- CH_3 at $\nu = 2831.85 \text{ cm}^{-1}$; $-NH-SO-$, $-CH_2-SOH$, $-CH_2-CO-CH_2$ at $\nu = 1701 \text{ cm}^{-1}$; and the presence of intermolecular hydrogen bonds between $\nu = 3404-3408 \text{ cm}^{-1}$. However, the intensities of the above bands increase for ACM by HTC + SGA. In addition, steam-gas activation of carbon promotes the formation of functional groups $-OH$ at $\nu = 3.745 \text{ cm}^{-1}$, $-NH-SO-$, $-CH_2-COH-$, $-CH_2-CO-CH_2$ at $\nu = 1701 \text{ cm}^{-1}$, which indicates the formation of the functional layer on its surface.

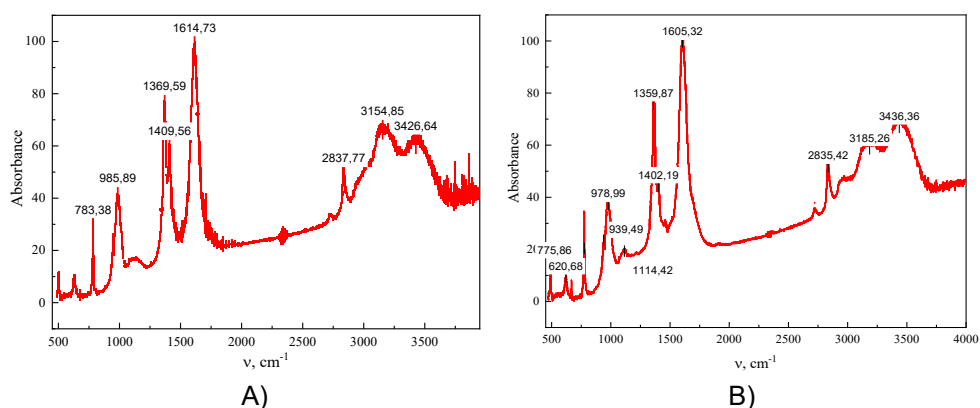


Figure 6. FTIR spectrum of the walnut shell sample activated by HTC (A) and HTC+SGA (B).

According to a literature review, the following functional groups could be formed on the surface of the carbon material activated by steam gas activation [27]. Thus, carboxyl surface groups ($R-COO-$, have characteristic acidic hydrolysis in aqueous solutions and can form anhydrides if they are close to the basal planes of carbon), single hydroxyl groups ($-OH$, at the edge of the "aromatic" layers will be phenolic in nature), carbonyl groups ($C=O$, obtained by the formation of lactones or simple ester groups from adjacent carboxyl and hydroxyl groups) are identified [28]. In our case, the GC-MS analysis of the samples extracted in acetone shows the presence of polar substances with the previously mentioned functional groups: $-C=O$, $-COOH$, $-OH$, $-C-O-C-$, aryl- and alkyl derivatives, $-C(O)-NH-R$, etc. The formation of polar functional groups on the functional layer of ACM is probably due (i) to the chemical interaction of CM with acute water vapor, or (ii) to the chemical adsorption of water molecules on the CM surface. The GC-MS results are in correlation with the information obtained from the IR spectra.

INVESTIGATION OF THE FUNCTIONAL LAYER FORMATION
ON THE SURFACE OF CARBON MATERIAL

The qualitative determination of surface FG on carbon material is insufficient for further prediction of material behavior under conditions of chemical and electrochemical modification. For this reason, the potentiometric Boehm titration method was performed. As seen in Table 4, the distribution of functional group concentrations of different natures, expressed by mols per 1 gram or 1 m² of the CM surface, was calculated.

Table 4. The concentration of functional groups on the CM surface (HTC + SGA)

	C _i * 10 ³ , mol/g			C _i * 10 ⁶ , mol/m ²		
	C-OH	C=O	-COOH	C-OH	C=O	-COOH
HTC+SGA	1.15	0.87	6.31	1.53	1.15	8.37

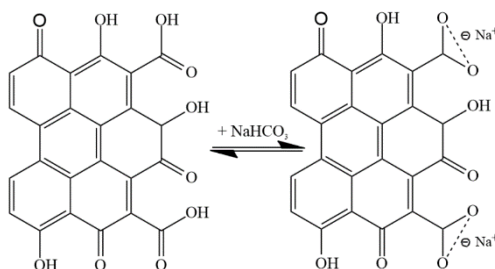
According to Boehm's method the phenolic, lactone, and carboxyl functional groups follow a neutralization reaction with 0.1 M solutions of bases of different strengths: NaOH, Na₂CO₃, and NaHCO₃, respectively. The mechanism of the neutralization reaction between the surface organic FG and 0.1 M of different base solutions is described below.

A differential potentiometric titration curve when adding NaHCO₃ is presented in Figure 7B. The presence of 2 peaks is due to the acid-base interaction of the following proposed mechanism (reaction 1):



Scheme 1

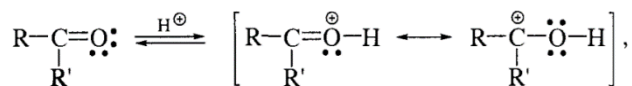
As known, the weak base NaHCO₃ has a good affinity to the carboxyl group, allowing the reaction (Scheme1) to occur at the carbon FG group - solution interface. It is possible to assume the equality of the concentrations of carboxyl groups to the average value of N(NaHCO₃) (reaction 2) [29].



Scheme 2

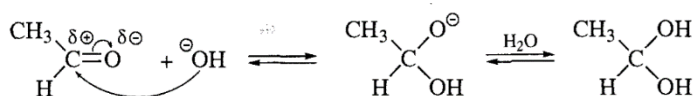
However, when 0.1 M NaOH is added to activated carbon (Figure 7A), an ionization of almost all FGs from the surface of the carbon matrix occurs, which is visible on the differential potentiometric titration curve by a single peak.

According to the literature review, the pK_a values of their conjugated acids varied from 6 - 8. They form oxonium ions with strong protonic acids, that subsequently are stabilized by resonance structures presented in scheme 3 [30]:



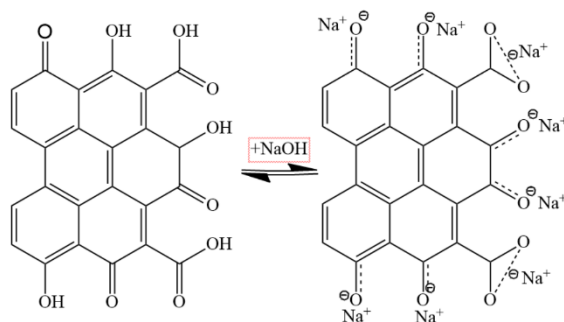
Scheme 3

Also, when the strong base NaOH is added, hydration of the surface aldehyde group occurs due to the high nucleophilicity of the hydroxide ion. For this reason, the hydroxide ion quickly attacks the positively charged carbon by the following mechanism (Scheme 4) [31]:



Scheme 4

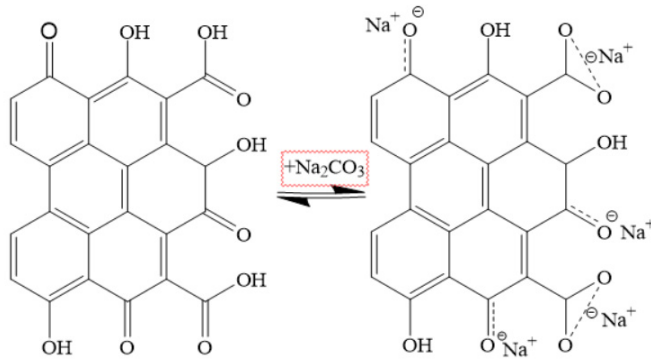
As a result, the addition of a strong protonic acid leads to the formation of hydroxyl groups, which are neutralized by NaOH (reaction 5).



Scheme 5

Functional groups (having pK_a in the range of 4 - 10) as carboxyl, lactone, and carbonyl groups are neutralized following the reaction (6), when Na_2CO_3 is added (Figure 7C). In this case, hydroxyl groups are not affected due to their high hydration energy.

INVESTIGATION OF THE FUNCTIONAL LAYER FORMATION
ON THE SURFACE OF CARBON MATERIAL



Scheme 6

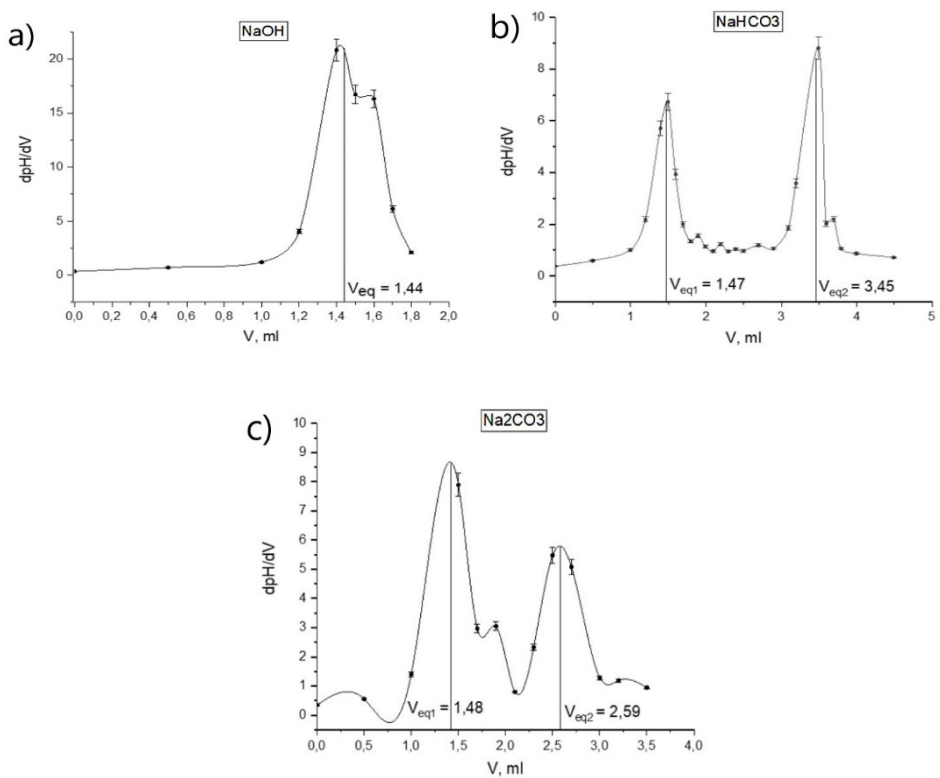


Figure 7. First derivative of the titration curves for direct titration of the functional groups of ACM with 0.1 M solutions of NaOH (A), NaHCO_3 (B), Na_2CO_3 (C).

Powder addition method

Using the powder addition method, the pH point of zero charge (pH_{pzc}) of CM activated by HTC+SGA in 0.01 M solutions of Na_2SO_4 and K_2SO_4 were determined. Thus, the pH of the solutions was measured after 24 hours that CM powders were mixed with Na_2SO_4 or K_2SO_4 (Figure 8). With both used solvents, the carbon material exhibits basic surface properties due to the presence of surface oxygen-containing groups. A plateau is observed on the graph at $\text{pH}_i = 4-5$, which indicates that the carboxyl and carbonyl surface groups are in molecular form. However, it should be noted that the hydroxyl groups are also in the molecular form due to the $\text{pK}_a = 9 - 10$. There is a correlation between $\text{pH}_f - \text{pH}_i$ versus pH_i in the $\text{pH} = 4-5$ range, which suggests that the pK_a values of the carboxyl and carbonyl groups are placed between 4-6 [32].

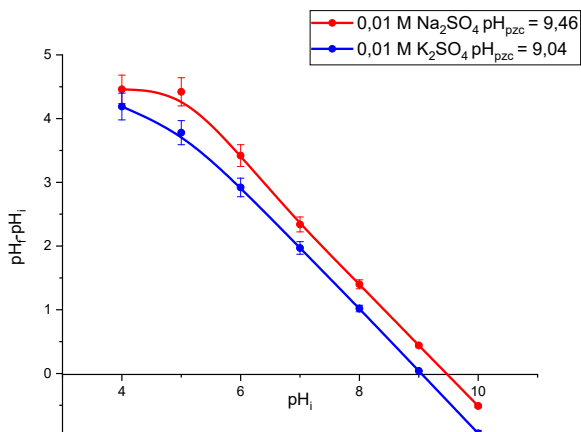
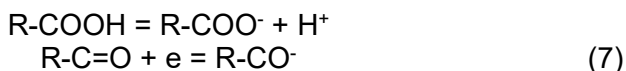


Figure 8. The pH_{zpc} determination for CM activated by HTC+SGA estimated in 0.01 M Na_2SO_4 (red line), 0.01 M K_2SO_4 (blue line).

The linear decrease of the values of $\text{pH}_f - \text{pH}_i$ difference is observed in the $\text{pH} = 5-9$ range and is a consequence of carboxyl groups ionization, and carbonyl groups dissociation on CM surface. Consequently, the assumed mechanism of groups dissociation and ionization follows the reactions 7:



The complete dissociation of the $-\text{OH}$ groups from the surface, following reaction 8, corresponding to $\text{pH}_i = 9 - 9.5$, is attributed to quinone and phenolic groups on the surface. [33].



It must be noticed that the difference in $\text{pH}_f - \text{pH}_i$ values depend on the nature of the cation, being with 0.5 pH units higher in the case of Na^+ than for K^+ , respectively. This is probably due to less hydration of the K^+ cation which promotes either its penetration into the pores of the carbon sorbent or the establishment of a rapid equilibrium at the carbon-solution phase boundary [34]. A consequence of this assumption is the consideration of the series $\text{H}^+ < \text{Li}^+ < \text{Na}^+ < \text{K}^+$, where the hydration energy decreases from right to left according to the electrostatic theory of solvation. Therefore, the Na^+ ion has the most pronounced acidic properties compared to the K^+ ion [35].

From the results of the powder addition method, it can be concluded that the formation of the oxygen-containing functional layer (OFL) on the surface is caused by the degree of oxidation of carbon material and the nature of the modifier, and can allow acid-base interactions on the surface of the carbon material. It can be assumed that the material surface is partially protonated and undissociated at $\text{pH} < 5$, and the carbon matrix removes anionic particles from the diffusion region of the electrical double layer. But at $\text{pH} > 5$, the surface partially acquires a negative charge due to the dissociation of carboxyl and carbonyl groups. It is noticeable that the dissociation of hydroxyl groups gives an additional negative charge to the surface, at $\text{pH} > 9$.

Thus, the formation of acid-base centers on the surface of the activated carbon material opens the possibility for different applications like the specific adsorption of heavy metals from aqueous solutions [17].

CONCLUSION

Activated carbon materials having sorbents properties, based on walnut shells were obtained by hydrothermal carbonization with steam gas activation method (*i.e.*, HTC and HTC+SGA), respectively. Steam gas activation was carried out to increase the porosity and to form a functional layer on the surface on the material. BET results and pore size distribution revealed that the activation of the carbon sorbent leads to a 2-fold increase in the surface area compared with the walnut shell carbonizate. It indicates the opening of micropores and their increase due to carbon oxidation ($S_{\text{specific}} = 464.9 \text{ m}^2/\text{g}$ for the CM activated by HTC, $S_{\text{specific}} = 738.0 \text{ m}^2/\text{g}$ for the CM activated by HTC+SGA). Oxygen-containing functional groups on the surface were qualitatively determined by both FTIR and GC-MS measurements. The functional groups -OH, -C=O, and -COOH were quantified by potentiometric Boehm titration method. The supposed mechanism of the neutralization of

the functional groups depending on the nature of the used base is described. The powder addition method for pH_{pzc} determination confirms the presence of oxygen-containing FG and the results are in good correlation with those obtained by titration, FTIR, and GC-MS.

Thus, the activated carbon sorbent is characterized by acid-base centers, which open the way to possible modifications of the surface for specific adsorption of heavy metals and organic substances from aqueous solutions with modern applications.

EXPERIMENTAL SECTION

Reagents and equipment

The following reagents were used in this work: KBr, K_2SO_4 , Na_2SO_4 , acetone, H_2SO_4 (from Sigma Aldrich), ethyl alcohol, (99%); ultra-high dispersion polyethylene powder (UHPP, from GUR®, USA), argon, (from Sigma Aldrich). All chemicals were of chem purity.

Methodology of carbon materials obtaining

Carbon materials (CM) based on walnut shells were obtained by hydrothermal carbonization at $T = 240\text{ }^\circ\text{C}$ for 24 hours (HTC) in a steel autoclave reactor. The ratio of the material to water was 1: 2. In order to increase the specific surface of CM and the formation of oxygen-containing functional groups on the surface, the material was activated by acute water vapor at $T = 800\text{-}850\text{ }^\circ\text{C}$ for 60-70 minutes (HTC+SGA). Further, the sorbent was crushed to a fraction of $56\text{ }\mu\text{m}$ on a planetary monomill (model PULVERISETTE 6, from Fritsch, Russia) [23, 25].

Methods of carbon sorbents studying

The nitrogen adsorption/desorption method was used to evaluate the carbon sorbents' morphological features. S_{specific} and adsorption isotherms were obtained according to the BET polymolecular adsorption model. The total pore volume (V_{tot}) and micropore volume (V_{micro}) were calculated using density functional theory (DFT).

The SEM was used to evaluate the surface morphology of the samples using a field emission scanning electron microscope (model FE-SEM, equipped with an ultra-high resolution field emission scanning electron microscope, type Hitachi SU8020, Japan). The content of carbon sorbents mineral impurities was determined by X-ray fluorescence spectroscopy (EDXRF, using energy dispersive X-ray fluorescence spectrophotometer, type Epsilon 3 PANalytical B, from Malvern Panalytical, United Kingdom), X-ray diffraction

(XRD, using a X-ray diffractometer, type PANalytical, Philips, from Malvern Panalytical, United Kingdom, with Cu, K α radiation, λ - 1.5418 Å), and Raman spectroscopy methods (using inVia™ confocal Raman microscope from Renishaw, United Kingdom) were used to characterize different allotropic modifications of carbon in the sample structure.

Methods the surface charge and surface functional groups determination of the carbon sorbents

The FTIR measurements using a spectrometer (model FSM-1201, from LightMachinery, Canada) were performed to qualitatively evaluate the functionality of carbon sorbents in the interval of wave number ν = 4000-500 cm⁻¹. The mass ratio of KBr:CM was 700:1.

The CM extract in acetone was prepared to qualitatively determination of the polar functional groups. A quantity of 0.5 g ACM was added to 5 ml of acetone and was ultrasounded for 60 minutes. Then, the obtained suspension was filtered using a 0.5 μ m pore size membrane filter. The acetone extract was analyzed on a GC-MS (model 7890B GC & 5977A MSD, Agilent, USA).

The potentiometric Boehm titration method determined the nature and the quantitative content of oxygen-containing functional groups (OFG). For a better wettability of the ACM with basic solutions, the sample was prepared as follows. A quantity of 1.000 \pm 0.001 gr of ACM mixed with 25.0 cm³ of bidistilled water was degassed under ultrasound for 10 minutes; then 0.1 mol/L of NaOH solution was added to flasks, pumped out with air, and left for 3 days. The solutions were filtered, and 5 cm³ of 0.1 mol/L HCl was added. The titration was done with a freshly prepared 0.1 mol/L NaOH solution and the equivalence point was estimated by potentiometry. Titration was carried out with a potentiometric automatic titrator (model ATP-02) equipped with a glass electrode.

The amount of NaOH used to neutralize the functional groups (N_i) was calculated according to the literature [36].

According to the stoichiometry, the neutralization reaction C(-COOH) is equal to the average value of $N(\text{NaHCO}_3)$; $\text{C}(-\text{C}=\text{O}) = N(\text{Na}_2\text{CO}_3) - N(\text{NaHCO}_3)$; $\text{C}(-\text{OH}) = N(\text{NaOH}) - N(\text{Na}_2\text{CO}_3)$.

The method of powder addition was used to determine the pH at which the surface charge of the activated carbon (ACM) is zero. A 0.01 M Na₂SO₄ and 0.01 M K₂SO₄ were used as electrolytes. They do not exhibit specific adsorption on the ACM. Adjustment of pH between 4 - 10 was performed using NaOH, KOH, and H₂SO₄ solutions without CO₂. The initial pH of the solution (pH_i) was recorded, and a certain amount of ACM (~5 g/L) was added to each test tube and filled with Ar. The final pH_f value was measured after 24 hours of stirring on a shaker. The pH_{pzc} was calculated as the extrapolation to pH_f - pH_i = 0 from the pH_f - pH_i = f(pH_i) plot.

ACKNOWLEDGEMENT

This research was funded by the Science Committee of the Ministry of Education and Science of the Republic of Kazakhstan (Grant No. AP09058570).

REFERENCES

- 1 A.G.B. Pereira, F.H.A. Rodrigues, A.T. Paulino, A.F. Martins, A.R. Fajardo; *J. Clean. Prod.*, **2021**, *284*, 124703.
- 2 Ch. Su, Y. Guo, L. Yu, J. Zou, Z. Zeng, L. Li; *Mat. Chem. and Phys.*, **2021**, *258*, 123930.
- 3 E. Frackowiak, B. Francois; *Carbon*, **2001**, *39*, 937-950. 4
- 4 M.A. Islam, S. Sabar, A. Benhouria, W.A. Khanday, M. Asif, B.H. Hameed; *J. Taiwan Inst. Chem. Engrs.*, **2017**, *74*, 96-104.
- 5 J.L. Figueiredo; *J. Mater. Chem.*, **2013**, *1*, 9351-9364.
- 6 P. González-García; *Renew. Sust. Energ. Rev.*, **2018**, *82*, 1393-1414.
- 7 S. Roldán, I. Villar, V. Ruíz, C. Blanco, M. Granda, R. Menéndez, R. Santamaría; *Energy Fuels*, **2010**, *24*, 3422-3428.
- 8 A. Aworn, P. Thiravetyan, W. Nakbanpote; *J. Anal. Appl. Pyrolysis*, **2008**, *82*, 279-285.
- 9 S.K. Theydan, M.J. Ahmed; *Powd. Tech.*, **2012**, *224*, 101-108.
- 10 Y.A. Rahim, S.N. Aqmar, D.R. Dewi; *Mater. Sci. Eng.*, **2012**, *4*, 22-26.
- 11 C. Yang, Q. Pan, Q. Jia, Y. Xin, W. Qi, H. Wei, S. Yang, B. Cao; *Appl. Surf. Sci.*, **2020**, *502*, 144-423.
- 12 Y. Nagakawa, M. Molina-Sabio, F. Rodríguez-Reinoso; *Micropor. Mesopor. Mater.*, **2007**, *103*, 29-34.
- 13 G. Cui, J.H. Yoo, J.S. Lee, J. Yoo, J.H. Uhm, G.S. Cha, H. Nam; *Analyst*, **2001**, *126*, 1399-1403.
- 14 K. Pliuta, A. Chebotarev, A. Koicheva, K. Bevziuk, D. Snigur; *Anal. Methods*, **2018**, *10*, 1472-1479.
- 15 M. Velmurugan, N. Karikalan, S.M. Chen, Y.H. Cheng, C. Karupiah; *J. Colloid Interface Sci.*, **2017**, *500*, 54-62.
- 16 H.L. Chiang, C.P. Huang, P.C. Chiang; *Chemosphere*, **2002**, *47*, 257-265.
- 17 J.R. Rangel-Mendez, M. Streat; *Water Res.*, **2002**, *36*, 1244-1252.
- 18 T. Van Tran, Q.T.P. Bui, T.D. Nguyen, N.T.H. Le, L.G. Bach; *Adsorpt. Sci. Technol.*, **2017**, *35*, 72-85.
- 19 G. Yang, H. Chen, H. Qin, Y. Feng; *Appl. Surf. Sci.*, **2014**, *293*, 299-305.
- 20 Z. Wang, Y. Huang, M. Wang, G. Wu, T. Geng, Y. Zhao, A. Wu; *J. Environ. Chem. Eng.*, **2016**, *4*, 3185-3192.
- 21 S. Schiewer, S.B. Patil; *Bioresour. Technol.*, **2008**, *99*, 1896-1903.
- 22 W. Boulaiche, B. Hamdi, M. Trari; *Appl. Water Sci.*, **2019**, *9*, 1-10.

INVESTIGATION OF THE FUNCTIONAL LAYER FORMATION
ON THE SURFACE OF CARBON MATERIAL

- 23 A.A. Atchabarova, R.R. Tokpayev, A.T. Kabulov, S.V. Nechipurenko, R.A. Nurmanova, S.A. Yefremov, M.K. Nauryzbayev; *Eurasian Chem.-Technol. J.*, **2016**, 18, 141-147.
- 24 Arthur W. Adamson; "Physical Chemistry of Surfaces", Arthur W. Adamson, Alice P. Gast; A Wiley-Interscience publication, **1997**, 808 p.
- 25 A. Atchabarova, R. Tokpayev, A. Kabulov, S. Nechipurenko, S. Yefremov, M. Nauryzbayev; *Bull. of Univ. of Karaganda-Chem.*, **2016**, 83, 66-71.
- 26 J. Serafin, M. Ouzzine, O.F. Cruz Junior, J. Sreńscek-Nazzal; *Biomass Bioenergy*, **2021**, 144, 105925.
- 27 H.P. Boehm; *Carbon*, **1994**, 32, 759-769.
- 28 X. Fan, Y. Lu, H. Xu, X. Kong, J. Wang; *J. Mater. Chem.*, **2011**, 21, 18753-18760.
- 29 D.S. Dmitriev, M.V. Ivakhiv, D.V. Agafonov; *Bull. of the St. Petersburg State Inst. of Techn.*, **2018**, 44, 21-25.
- 30 V.F. Traven; "Organic chemistry", *Academic Book*, Moscow, **2004**, 727 p.
- 31 I.D. Harry, B. Saha, I.W.; *J. Colloid Interface Sci.*, **2006**, 304, 9-20.
- 32 R.C. Bansal, J.-B. Donnet; "Surface Groups on Carbon Blacks", in *Carbon Black*, J.-B. Donnet, R.C. Bansal, M.-J. Wang Eds.; Routledge, New York, **1993**, 46 p.
- 33 M. Kosmulski; *J. Colloid Interface Sci.*, **2009**, 337, 439-448.
- 34 B.B. Damaskin; "Electrochemistry", B.B. Damaskin, O.A. Petrii, G.A. Tsirlina; Koloss-Chemistry, Moscow, **2006**, 672 p.
- 35 G. Kh. Shabekova; "The current state of the theory of solvation and dissolution", G. Kh. Shabekova, L.I. Syzdykov; Kazak Universities, Almaty, **2004**, 352 p.
- 36 J. Schönherr, J. R. Buchheim, P. Scholz, P. Adelhelm; *J. of Carb. Research*, **2018**, 4, 21.

ANALYSIS OF PRODUCTS FROM THE PYROLYSIS OF PLASTICS WASTE FROM A PRINTING PLANT: A PILOT SCALE STUDY

Arnella NECHITA ROTTA^{a,b}, Cristina BOTA^a, Balázs BRÉM^c,
Dan Ioan PORUMB^c, Emese GÁL^{c*}

ABSTRACT. As plastic production increases, new waste management methods are required. Chemical recycling, such as pyrolysis, has the potential to raise recycling rates taking into account that it can use more waste plastics than standard mechanical recycling. Four types of bits of plastic: polyethylene (PE), polypropylene (PP), polystyrene (PS), and biaxial-oriented polypropylene (BOPP) fractions from the printing plant were collected; the possibility of recycling them by batch pyrolysis was investigated. Characterization of the obtained pyrolysis oils was carried out by gas chromatography-mass spectrometry (GC-MS), the analysis showed a mixture of aliphatic (saturated and unsaturated) compounds, in the case of PE and PP, while in the case of PS, aromatics and low quantities of other hydrocarbons were detected. In the case of BOPP the distribution of the pyrolysis products is not as uniform as in the case of PE, PP, or PS plastic samples. The FT-IR results showed clear peaks of aliphatic compounds in two liquid oil samples of PE, and PP that further confirmed the GC-MS results. More than 60% monomer (styrene) can be recovered from the PS pyrolysis, besides other aromatic compounds in low concentration. The pyrolysis oils have a reasonable heating value (calorific value) in the range of 36–45 KJ/g, close to conventional diesel. Therefore, the pyrolysis oils has the potential to be used as an alternative source of energy as fuel, after blending with conventional fuel, or heating combustion products. The research results will contribute to the development of waste valorization via plastic upcycling from a printing press, without using an expensive catalyst or reactor system.

Keywords: thermochemical process, plastic upcycling, pyrolysis oil, GC/MS analysis, hydrocarbons.

^a Rottaprint, Str. Libertății 295, 407035, Apahida, jud. Cluj

^b Technical University of Cluj-Napoca, Faculty of Materials and Environmental Engineering, Bd. Muncii 103-105, RO-400641, Cluj-Napoca, Romania

^c Babeş-Bolyai University, Faculty of Chemistry and Chemical Engineering, 11 Arany Janos str., RO-400028, Cluj-Napoca, Romania

* Corresponding author: emese.gal@ubbcluj.ro



INTRODUCTION

Plastic waste are one of the most widespread in nature, their production and consumption are increasing at an alarming rate, due to, both population and economic growth, and lifestyle changes which have the greatest impact. The resulted global plastic waste doubled between 2000 and 2019, reaching 353 million tons. Only 15 % is collected for recycling, just 9 % is successfully recycled, another 19 % is incinerated, and 50 % is landfilled. At this rate the estimated plastic waste generation will be almost triple by 2060 [1, 2]. According to a new report of the Organization for Economic Cooperation and Development, in the European countries, the amount of plastic waste generated annually per person is around 114 kg [3]. During last years pyrolysis has received a lot of attention both in the industrial and scientific communities as a promising, versatile procedure in order to convert plastic waste into valuable resources [4]. Chemical recycling such as pyrolysis, can significantly increase the recycling rates due to the fact that this procedure can convert a wide range of waste plastics in contrast to the traditional mechanical recycling procedure [5]. Pyrolysis is a common technique used for thermal degradation of waste plastics at different temperatures, to convert them into energy, in the production of solid, liquid, or gaseous fuels. In comparison to incineration and gasification, pyrolysis occurs in the absence of oxygen, resulting lower CO₂ emissions and lower amount of toxic impurities [6, 7, 8]. A variety of catalysts [4, 11], reactor types [9], and temperature intervals [10] are described in the literature, but fine-tuning an efficient and selective pyrolysis process to narrow the product distribution for commercial production remains difficult. During pyrolysis, long-chain organic molecules are broken into smaller hydrocarbons, the produced pyrolysis oil can be used as fuel for turbines, boilers, furnaces, etc. Depending on the chemical structure, different plastics have different degradation temperatures. The thermal degradation temperature for common plastics starts at 350 °C, but in the case of PVC the degradation temperature starts at 220 °C; furthermore, obtaining the appropriate product (oil, gas or char) is heavily influenced by the operating temperature. In the case of PE and PP, without using any catalyst and applying a higher pyrolysis temperature, at 500 - 600 °C, the resulting products are mainly C₂₀+ hydrocarbons, as solid wax at room temperature. In the thermal cracking procedure of PE, the resulting product mixture is mainly C₁-C₄ (gases) and C₅-C₁₀ non-aromatic hydrocarbons and waxes respectively [13]. A few research works have been reported on the pyrolysis of BOPP, however, mixed plastic waste of different multilayer plastics with a variety of catalysts, such as ZSM-5 zeolite, Ni/Al₂O₃, ZnO, etc., can be found in the literature [20, 21].

A lower temperature range is recommended, 300-500 °C if the desired product is liquid/ pyrolysis oil, and this condition is applicable for all plastics waste types [12]. Pyrolysis involving a feedstock, without any catalyst, can be considered the baseline of the pyrolysis processes, popularly referred to as thermal pyrolysis [22]. In non-catalytic pyrolysis, long-chain polymers are broken into smaller fractions, carbon-carbon linkage can be broken randomly, no rearrangement of the fragments occurs, resulting a wide distribution of products.

J. Lee and coworkers studied the low-density polyethylene (LDPE) waste pyrolysis conditions, both using H-ZSM-11 catalyst and without catalyst. The temperature range applied in the pyrolysis test was between 500 - 900 °C. Using the H-ZSM-11 catalyst, was observed increased pyrolytic gas and propylene yield, which was attributed to propane dehydrogenation promoted by the catalyst via monomolecular and protolytic pathways. In the case of non-catalytic pyrolysis, it was found that the distribution of the fuel-range hydrocarbons in the pyrolytic liquid was dominated by motor oil-range hydrocarbons, over 50% of the obtained product quantities [15]. The use of acidic H-ZSM-11 catalyst dramatically increased the yield of pyrolytic gas [14]. The quantities of pyrolytic gas in non-catalytic experiments did not exceed 30% even at high temperatures (900 °C) [15].

Compared to other solid waste, plastics have some unfavorable pyrolytic properties, such as low thermal conductivity, stickiness, low softening and melting temperatures; to achieve the most favorable product composition and minimize secondary reaction possibilities it is very important to use the appropriate pyrolysis reactor. Several reactor configurations have been proposed and developed to minimize heat transfer limitations and avoid common processing issues in the waste plastics pyrolysis [16, 17, 18].

The batch reactor producing pyrolysis oil available on the market is produced by a Japanese company; in this equipment PS, PP, and PE can be pyrolyzed at a relatively low temperature, producing high yields of pyrolysis oil [19].

The most widely used equipment for pyrolysis oil characterization is GC-FID/MS, an analytical method that can provide precise chemical compositions, and quantitative content as well. Fourier Transform Infrared Spectroscopy (FT-IR) is also used to analyze the pyrolysis oils and the wax/char product. The C-H stretching vibrations of the -CH₃, -CH₂, and -CH groups appeared at 2800–3000 cm⁻¹; the presence of olefins can be identified due to the presence of C=C stretching vibration bands, which can be observed at approximately 1640–1650 cm⁻¹.

The factors that influence the oil conversion rate are: the type of plastic (PE, PP, PS, BOPP), the quality and quantity of additives and the proper temperature range of the pyrolysis process. The main objective of this

study was to evaluate the pyrolysis process and the obtained products, using a commercially available pyrolysis batch reactor in a non-catalytic process for the valorization of plastic waste to fuel-range chemicals.

Characterization of plastic waste and pyrolysis product

Product Analysis

The obtained pyrolysis oil was characterized using different techniques such as GC-MS and FT-IR; the physicochemical and thermal characteristics of pyrolysis oil were analyzed using ASTM methods. The caloric values of pyrolysis oil from different types of plastic waste were measured following the standard ASTM D240 [30] method with a Bomb Calorimeter (Parr 6200 Calorimeter) instrument. The flashpoint was determined using a Cole-Parmer Koehler K16000 Pensky-Martens automatic analyzer. The density was measured using a DMA 4500 densimeter. Three replicates measurements were performed. Aniline point or "aniline point temperature," is the lowest temperature (°F or °C) at which equal volumes of aniline (C₆H₅NH₂) and the resulting oil form a single phase. The relative aromatic content of the oil is indicated by its aniline point, determined with an aniline point apparatus.

The results of these measurements for each pyrolysis oil are summarized in Table 1. The density of obtained pyrolysis oil from PE and PP ranged from 0.72-0.76 g/cm³, which is lower than diesel density (0.7999g/cm³), but a higher density value was obtained in the case of PS, which was 0.92 g/cm³. The flash point of a liquid fuel is defined as the lowest temperature at which the vapors above the liquid ignite when an external flame is applied. It is considered an important parameter in fuel handling to prevent fire hazards during storage. The flash points of the liquid fractions start at 21 °C for PE and 37 °C for BOPP, respectively which are comparable with light petroleum distillate fuels. The flashpoint values for the obtained pyrolysis oils are much smaller than in the case of diesel, which corresponds to the data found in the literature [23].

The aniline point measurement is useful in order to determine the presence of aromatic compounds in fuel samples. The aniline point temperature in highly aromatic samples is low, 21.7 °C for the pyrolysis oil obtained from PS; however, in other liquid products this value is much higher, indicating low concentration in aromatic compound fractions.

The calorific value is one of the most important characteristics used to evaluate the quality of fuel for future applications. Calorific values of pyrolysis oil obtained from various plastic waste vary from 36.67 KJ/g-45.10 KJ/g, the lowest value was obtained in the case of BOPP; these values are found to be similar to those reported in the literature [20].

Table 1. Physicochemical and thermal properties of the obtained pyrolysis oil.

S. No	Param.	Unit	PE white	SD*	PE with ink	SD*	PS	SD*	PP transp.	SD*	BOPP with ink	SD*
1	Density (at 20°C)	g/cm ³	0.7596	0.031	0.7648	0.027	0.9252	0.045	0.7631	0.052	0.7251	0.058
2	Flash point	°C	22	0.520	21	0.630	30	0.487	22	0.358	37	0.421
3	Gross Caloric Value	KJ/g	44.78	1.342	42.48	1.536	41.81	0.943	45.10	1.502	36.67	1.605
4	Aniline point	°C	72.2	2.557	67.8	1.867	21.7	1.056	67.6	1.842	57.7	2.067
5	I.D. (diesel index)		86.83	-	80.65	-	47.57	-	81.09	-	84.65	-

*SD was calculated from triplicate analysis results

Chemical fingerprinting of pyrolysis oil

The chemical composition of pyrolysis oil was performed through GC-MS (Shimadzu equipped with an AOC-20i+s injector, and a ZB-Wax MS capillary column (30 m × 0.25 mm, 0.25 μm film thickness, Phenomenex). The temperature of the injector was set to 285 °C and the MS transfer line was set to 220 °C. The oven temperature was held at 40 °C, for 15 min, then programmed to rise from 40 °C to 320 °C, at 5 °C/min, and held at this temperature for 15 min. The carrier gas was helium (99.99990% from Linde), at a constant flow rate of 0.80 mL/min. The injection volume was 1 μL, made in split mode (50:1). The detector was set to electron impact mode (EI, 70 eV) with an acquisition range (m/z) from 35 to 800 in scan mode. NIST (NIST 27, 147 libraries) mass spectral database was used to compare the mass spectra of the unknown organic compounds and the peak percentages were assessed for their total ion chromatogram (TIC) peak area.

The functional groups in pyrolysis oil were confirmed by FT-IR measurements, Bruker Vector 22 instrument. The analysis was performed using 20 scans with an average of 4 cm⁻¹ IR signals, within the wavenumber range 500-4000 cm⁻¹.

The presence of aliphatic/ aromatic compounds in pyrolysis oil was also confirmed by NMR (¹H, ¹³C) measurements in deuterated chloroform used as the standard for the chemical shift δ= 7.27 ppm for ¹H and δ=77.0 ppm for ¹³C, on Bruker Avance 600 MHz spectrometer.

RESULTS AND DISCUSSION

Pyrolysis product yield (oil, wax, and gas) was estimated based on the weight obtained for the wax and oil at the end of the pyrolysis process, which is given in Figure 1.

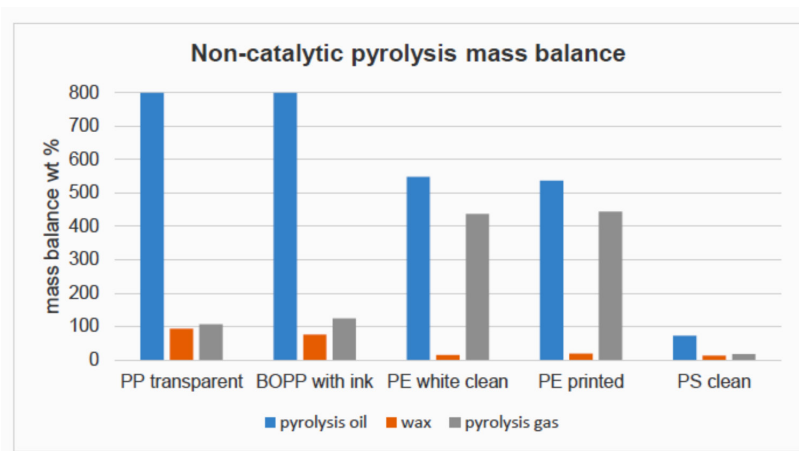


Figure 1. Pyrolysis product yield, using plastic waste in pyrolysis experiments.

In the case of thermal pyrolysis (without catalyst) the ratio of the obtained products is influenced by the initial plastic waste, and the used ink on plastic has little influence on the pyrolysis product amount. The input quality of waste plastics determines the quality and quantity of desirable products. The yield of the liquid fraction obtained from PP waste PP (~80%) is similar to the value described in the literature [24].

The obtained char from the waste plastics pyrolysis varied in the range of 5-45%, depending upon the type of plastic used. The percentage of char formation seems to be higher in the case of PE white and printed. The amount of char in the case of PP and BOPP is almost identical. The yield distribution of three product types (oil, char, and gas) in the case of PS pyrolysis is 72.2%, 14.8%, and 13%, respectively, which are comparable with data reported in the literature obtained using catalysts [26]; the liquid product is the main pyrolysis product in both cases.

The obtained wax from PE pyrolysis is brownish with high viscosity at room temperature, the char from PP pyrolysis is blackish with a non-compact structure, and are predominantly composed of alkanes and alkenes hydrocarbons, which is also confirmed by FT-IR analysis.

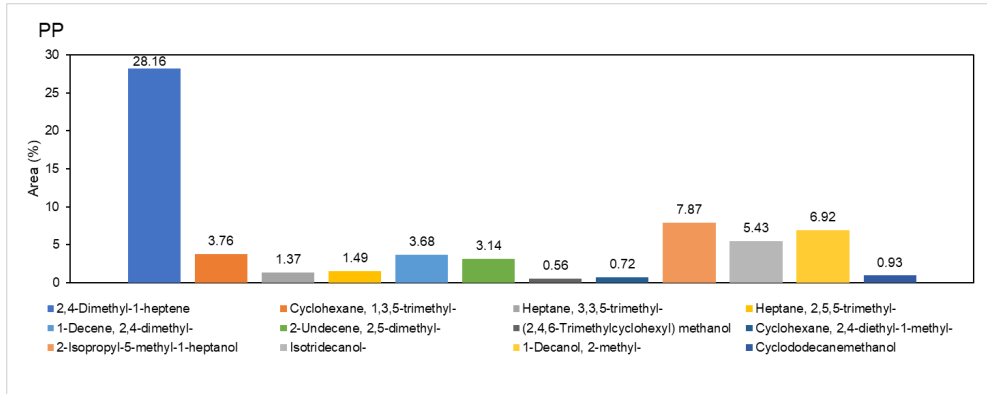
Analysis of pyrolysis oil through GC–MS showed significant production of a large fraction of unsaturated hydrocarbons including linear alkenes (dienes, trienes). Mid-chain β -scission reactions of midchain secondary alkyl radicals are generally responsible for the formation of linear alkenes.

From the pyrolysis of PP, a complex mixture of liquid oil containing saturated hydrocarbons and olefins can be obtained. Aromatic compounds are obtained when the pyrolysis took place in presence of a catalyst; in our case, without using a catalyst, in the GC/MS analysis no aromatic compounds were detected. Supriyanto et al. [26] proposed a mechanism in which they explained the PP pyrolysis products formation, including the formation of 2,4-dimethyl-1-heptene (~28%), the main compound found in PP oil (Fig. 2. A). The presence of 2,4-dimethylhept-1-ene in high yield can confirm that, during the thermal decomposition of polyolefines, the isomerization reaction is widely preferred. Taking account that the raw material for BOPP is polypropylene (PP), the resulting pyrolysis oil in the same condition, yielded the same product, but in higher yield of 2,4-dimethyl-1-heptene 37% (Fig. 2. B). The main components of pyrolysis oil from BOPP are largely the same as those of PP oil.

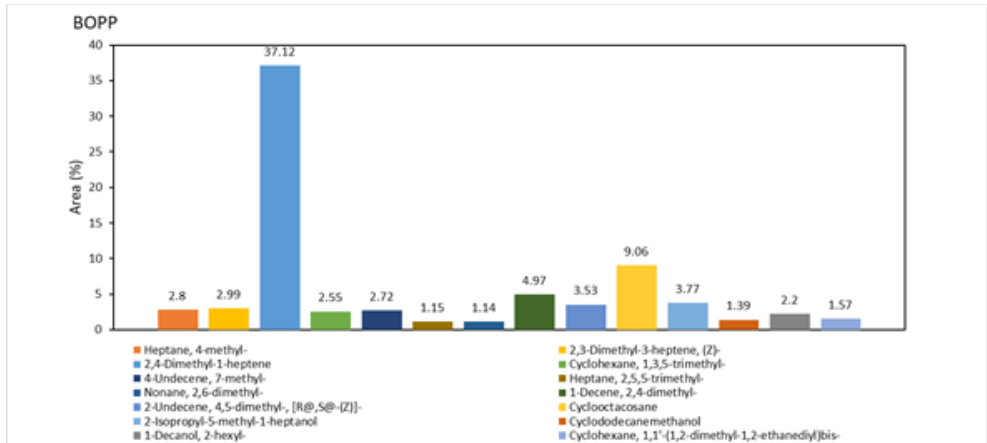
The liquid fuel can be classified into light ($C_7 - C_{11}$), middle ($C_{12} - C_{20}$), and heavy ($C_{21} - C_{36}$) fractions [27]. In the composition of pyrolysis oil obtained from PE (white, and with ink) no aromatic compounds could be identified. The components of the liquid fuel were mainly 1-alkenes and n-alkanes ranging from C_8 to C_{24} . In the sample obtained from PE white (Fig. 2. C), the most abundant alkanes are C_8 , C_{11} , C_{13} , and C_{17} ; these compounds are present in large quantities (<4%). However, the specific component proportions of the liquid fuels were different. The most abundant saturated hydrocarbon contained in the sample obtained from PE with ink (Fig. 2. D) is C_{15} (<5%), and the middle fraction is in a larger quantity (<50%). Based on GC/MS analysis no saturated branched hydrocarbons could be detected in any of the PE pyrolysis oil as described by E. Hajekova and coworkers, which explained the formation of linear hydrocarbons using the free-radical mechanism of thermal degradation [28].

The PS pyrolysis oil (Fig. 2. E) contains a major compound, in these conditions, more than 68% is the monomer, styrene, and the other resulting compounds are also aromatic compounds; toluene and ethyl benzene also appear in lower concentrations - between 5-10%.

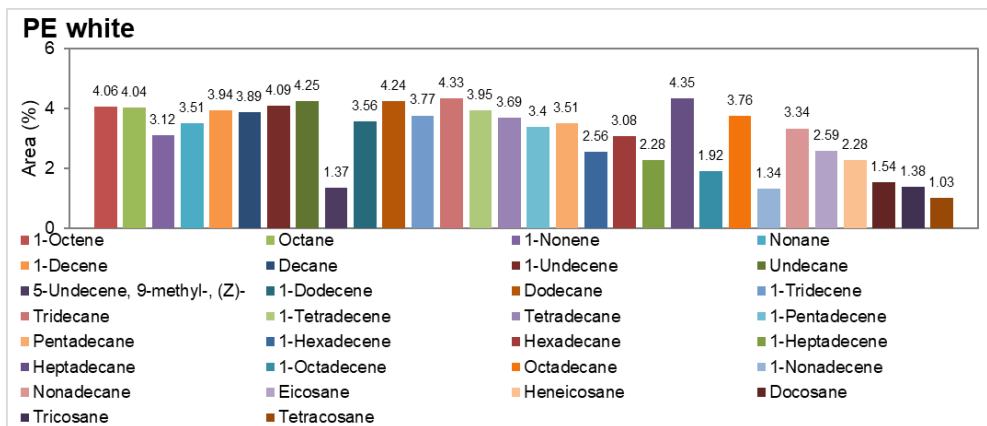
A.



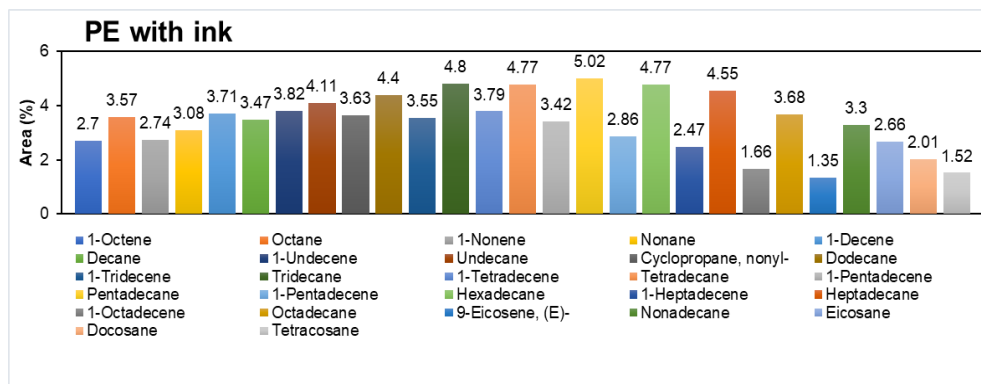
B.



C.



D.



E.

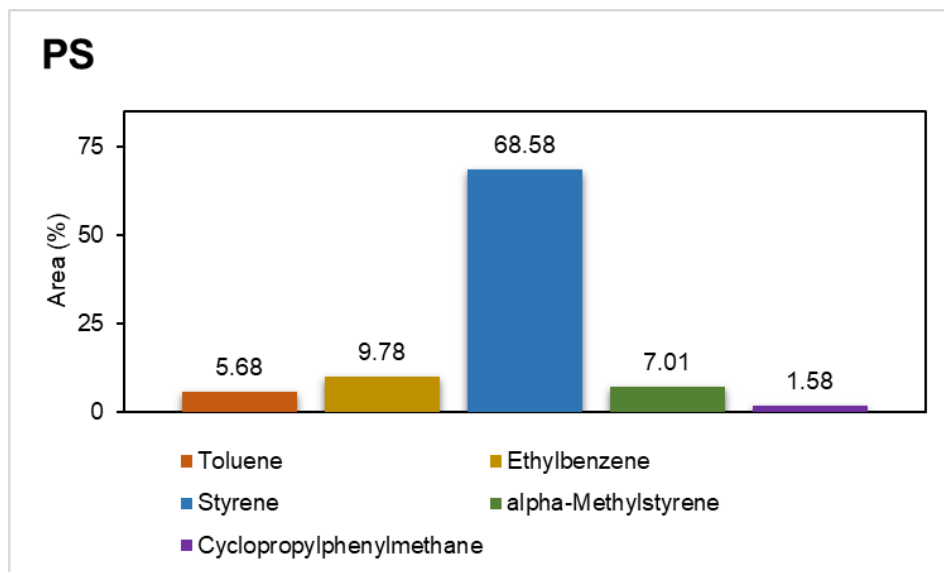


Figure 2 A-E. Distribution of compounds in pyrolysis oil based on GC/MS analysis

According to GC/MS analysis, pyrolysis of PE-type plastic waste led to more than 50% saturated hydrocarbons; the presence of printing inks has little effect on the quality of the compounds in the oil. In the case of PP and BOPP pyrolysis oil, the major components were unsaturated hydrocarbons, while most of the PS pyrolysis oil consists in aromatic compounds, with a high percent of styrene (Fig. 3).

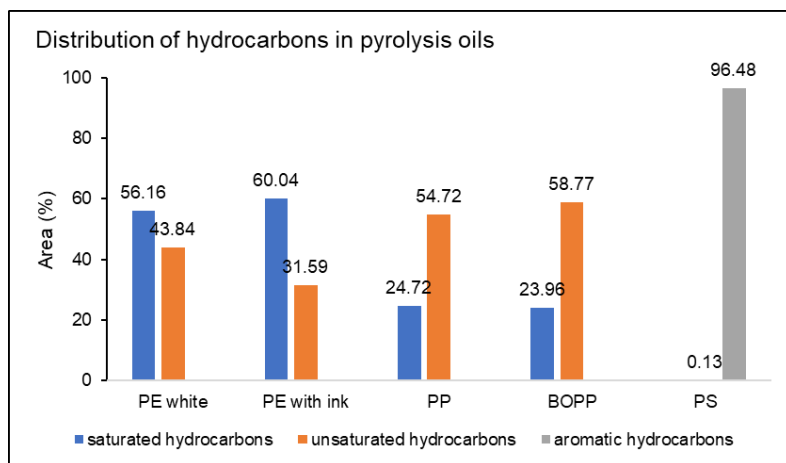


Figure 3. Distribution of hydrocarbon types in pyrolysis oil based on GC/MS analysis

The chemical composition of pyrolysis oil, by different functional groups, was studied using FT-IR. The obtained data corroborated with GC-MS measurements revealed the presence of aliphatic functional groups in the PE, PP and BOPP pyrolysis oil, and aromatics in PS oil respectively (Fig. 4).

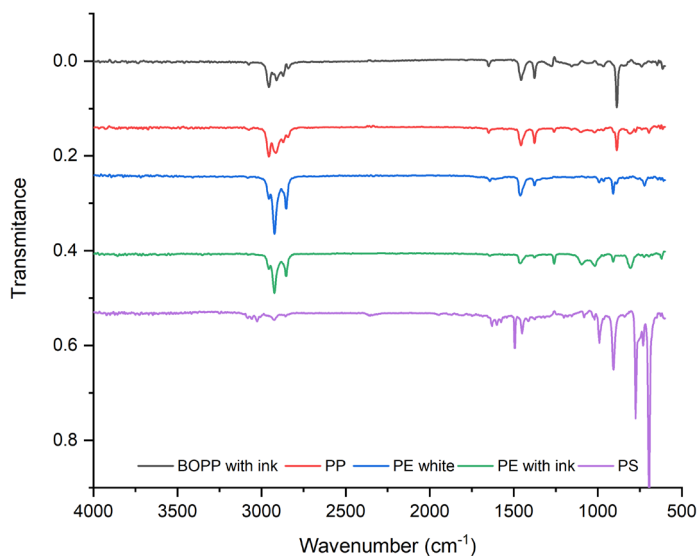


Figure 4. Comparison of FT-IR spectra of pyrolysis oil obtained from different raw materials

The observed peaks at 2853, 2923, and 2956 cm^{-1} confirmed the presence of the CH stretch of alkanes, and 1465 cm^{-1} CH scissoring from saturated hydrocarbons, which was identified in all of the pyrolysis oils from PE (Table 2). The aromatic hydrocarbon's presence was confirmed by the observed peak at 3026 cm^{-1} corresponding to the =C-H stretch, 1493 cm^{-1} C=C stretch, 1456 cm^{-1} C-C stretch from the aromatic ring, and 695 cm^{-1} for C-H also from aromatic compounds (Table 2).

Table 2. FT-IR data of liquid oil obtained from non-catalytic pyrolysis.

Peaks (cm^{-1})	PE white	PE with ink	PP	PS	BOPP with ink	Bond	Functional group
695	X	X	✓	✓	✓	C-H "oop"	Aromatics
965	✓	✓	✓	X	✓	C=C bending	Alkenes (disubstituted, trans)
1377	✓	✓	✓	✓	X	=C-H bend	Alkenes
1456	X	X	✓	✓	✓	C-C stretch	Aromatic (ring)
1465	✓	✓	X	X	X	C-H scissoring	Saturated CH
1493	X	X	X	✓	X	ring C=C stretch	Aromatics
1640	✓	✓	✓	✓	✓	C=C stretch	Alkenes
2853	✓	✓	✓	X	✓	C-H stretch	Alkanes
2923	✓	✓	✓	X	✓	C-H stretch	Alkanes
2956	✓	✓	✓	X	✓	C-H stretch	Alkanes
3026	X	X	X	✓	X	C-H stretch	Unsaturated

The obtained residues (wax) were also analyzed by FT-IR measurements, and the identified peaks from 2965, 2921, and 2854 cm^{-1} C-H stretch, 1470, and 1465 cm^{-1} C-H scissoring were attributed to alkanes. Peaks from 1381 cm^{-1} are associated with =C-H bend from unsaturated hydrocarbons (Fig. 5). The resulted degradation products were influenced by the structure of the original polyolefin. The PP-derived wax is more branched as compared with PE-derived wax [28].

The ^1H NMR spectra of PP and BOPP pyrolysis oil showed no difference, indicating that their chemical composition is quite similar (Fig. 6. b and d spectra). Pyrolysis oil from PP (Fig. 6. b) presents chemical shifts ranging from 0.82 to 4.70 ppm for all protons. In the aromatic region of the spectra no signals were observed, that could be associated with aromatic protons. The doublets from 4.70 ppm are known as the terminal double-bonded protons of the methyldene group.

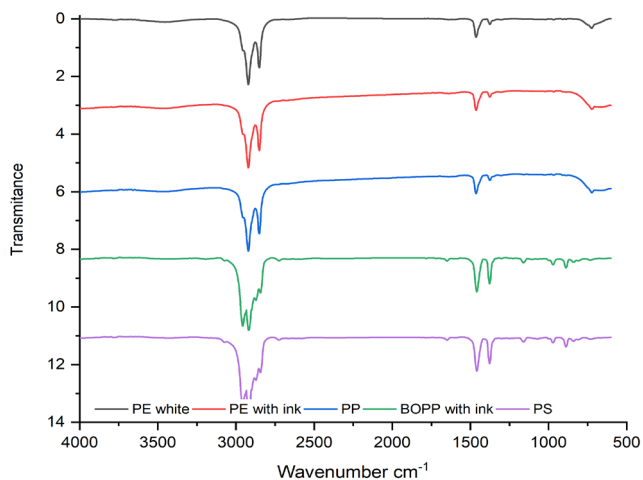


Figure 5. Comparison of FT-IR spectra of pyrolysis residue obtained from different raw materials

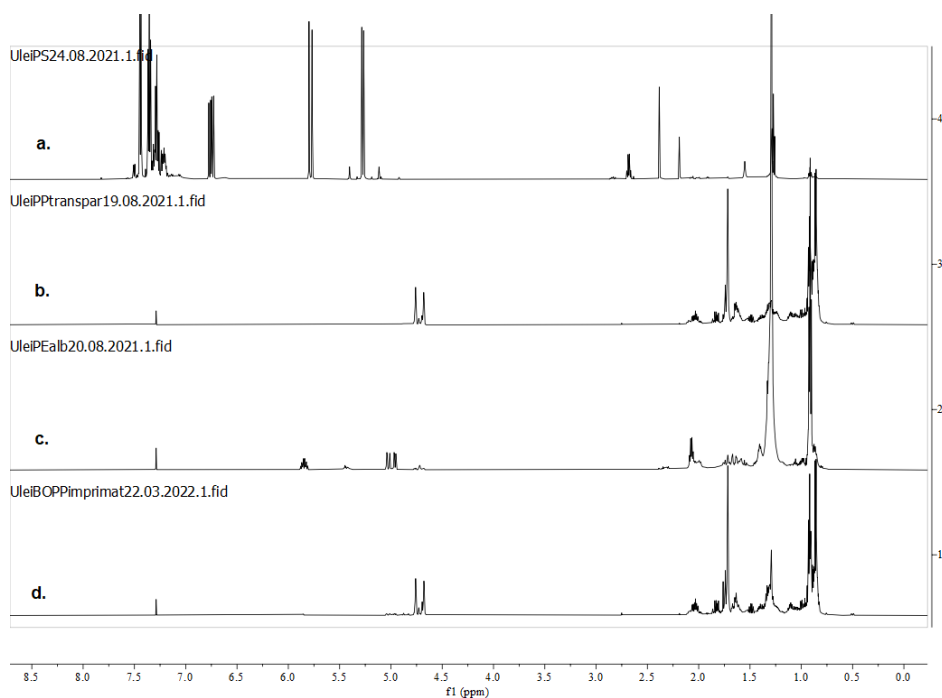


Figure 6. a-d Comparison of ^1H NMR (CDCl_3 , 600MHz) spectra of pyrolysis oil obtained from different raw materials: a - PS oil; b - transparent PP oil; c - white PE oil; d - BOPP with ink oil

The multiplet signals at 4.92–5.01 ppm and 5.78–5.85 ppm observable in oil samples from PE (Fig. 6. c.) were assigned to protons of the vinyl end group. In this region of spectra, other signals from vinylidene and vinylene, cannot be observed.

The ^1H NMR spectra shown in Fig. 6. a., displayed typical peaks for a monosubstituted aromatic ring (7.44–7.26 ppm) and the vinyl moieties (5.78 ppm and 5.27 ppm two doublets, and 6.74 ppm doublet of doublets).

In the ^{13}C NMR spectra (Figure 7) we have observed signals between 100 and 120 ppm, which corresponds to the alkene sp^2 hybridized carbon atoms. Signals corresponding to chemical shifts of 109, 111.3, 111.4, and 145.1 ppm could be assigned to the sp^2 hybridization carbon atoms. Also, we have concluded that the carbon atoms of the pyrolysis oils with chemical shifts from 14.4 to 46.0 ppm could be assigned to paraffinic carbon atoms, these signals are present in the PE, PP, and BOPP pyrolysis oils (Fig. 7. b, c, d).

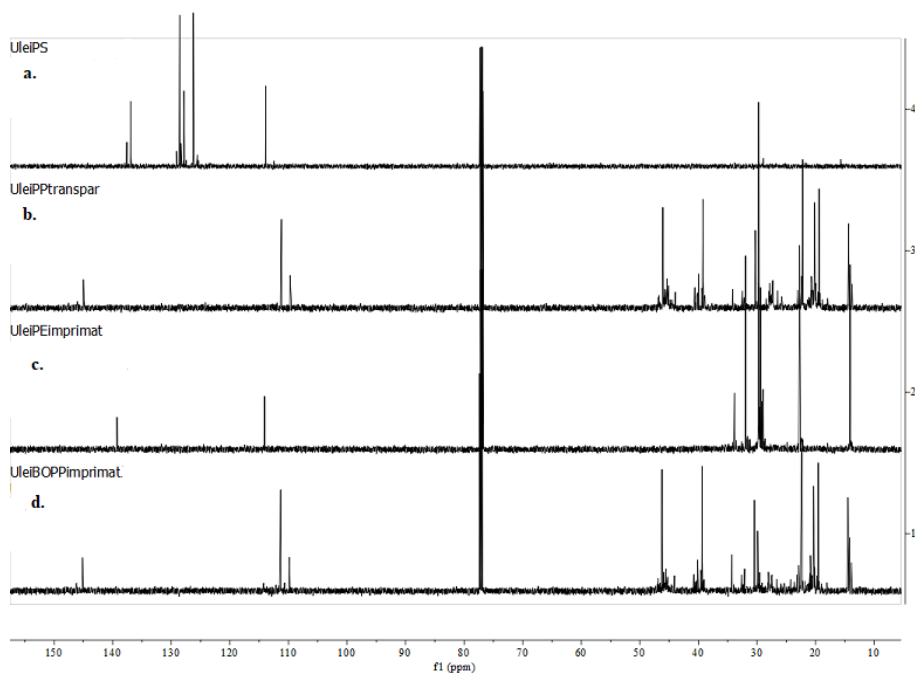


Figure 7. a-d Comparison of ^{13}C NMR (CDCl_3 , 150MHz) spectra of pyrolysis oil obtained from different raw materials: a - PS oil; b - transparent PP oil; c - white PE oil; d - BOPP with ink oil

The aliphatic carbon signals are absent in the PS sample, which is supported by previous analyses. In the case of the PS sample, the aromatic region of the spectra contains specific signals corresponding to styrene, ranging from 125 to 137 ppm and an alkene signal at 113 ppm for the sp^2 hybridized carbon atom (Fig. 7. a). The spectral data obtained show that the pyrolysis products contains unsaturated compounds. According to the literature [29], the signals between 100–150 ppm can be assigned to α -alkenes in the case of paraffinic samples.

CONCLUSIONS

Non-catalytic pyrolysis of various polyolefins (PE white, with ink, PP, PS) and multi-layer plastic (BOPP) waste samples were investigated experimentally, using plastic oil maker equipment, available on market. The quantities of oil, gas and char/ wax obtained from different plastics have been analyzed. Due to the waste plastic's inorganic content and the unconverted plastic left behind from insufficient pyrolysis, a solid yield was obtained. Pyrolysis oils have been physiochemically characterized, the calorific value of oil varies between 36- 45 KJ/g depending on the plastic quality, similar to conventional diesel. As a result, after further treatment and refining, pyrolysis oils have the potential to be used in a variety of energy and transportation applications. The flash point values of the pyrolysis oils are much lower than the diesel flash point, this property can be improved by removing lighter components from the pyrolysis oils. Hydrocarbon fingerprinting of pyrolysis oil has been determined using GC–MS, FT-IR, and 1H ^{13}C NMR respectively, in order to understand the feasibility of using it. The analysis of the composition of the oil fraction originating from PE and PP using gas chromatography/mass spectrometry (GC-MS) confirmed the formation of both linear alkanes and alkenes ranging from C_8 to C_{24} . Styrene can be obtained in a high yield (68%) from the PS pyrolysis, the obtained monomer after treatment can be reused for further polymerization and/ or to obtain other valuable chemicals.

The results of this study will contribute to develop more industrially feasible pyrolysis processes for the treatment of plastic waste.

EXPERIMENTAL SECTION

Materials and methods

Plastic waste, PE white, PE with ink, PP transparent, and BOPP with ink were collected from label printing equipment used at the Rottaprint company, a label printing leader in Romania.

Pyrolysis reactor and experimental setup

Batch pyrolysis experiments were carried out in a plastic oil maker, Be-j, equipment (Fig.1), manufactured in Japan, Nagata Shigyo Co., Ltd. 1 kg of polyolefin plastic waste was fed into the pyrolizer's inner chamber, which is surrounded by a stainless-steel outer compartment. The temperature measurement was performed using a thermocouple in the top and bottom of the pyrolizer inner chamber. The temperature range was maintained at 400-450 °C interval for the thermocatalytic depolymerization of different types of plastics. The equipment's processing ability is approximately 0.7- 1.0 kg/ a time in absence of oxygen. The cracked hydrocarbon vapors from the inner chamber were passed through the gas tube (Fig. 8) and bubbled in water, where the pyrolysis oil was collected. The noncondensable exhaust gases from the thermal oxidizer were passed on a filter and conducted to a fume hood. The pyrolysis experiments were repeated twice; in each case 1 kg of plastic waste was weighed, shredded into pieces of 2–5 cm size and was used without further treatments in the pyrolysis experiment, except polystyrene in which case only a smaller amount was introduced in the reactor due to its large volume. The obtained oil was collected from the oil collector tank (Fig. 8), and further characterization was carried out to reveal its chemical composition and

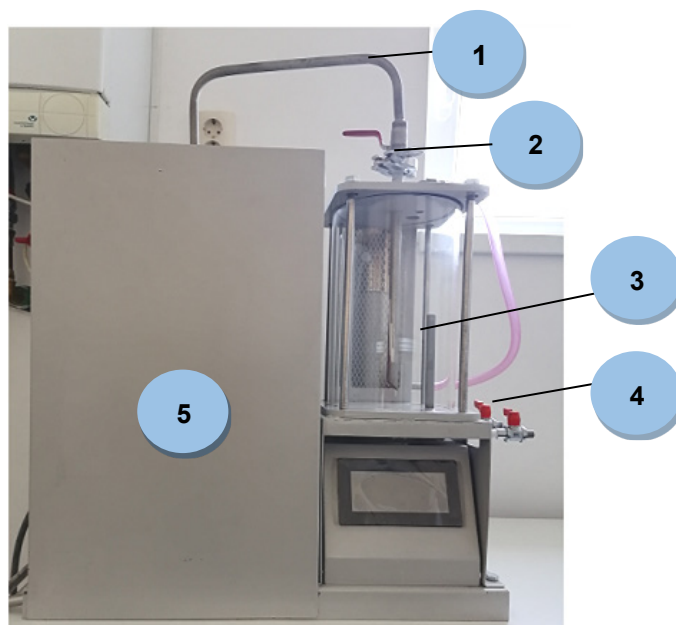


Figure 8. The used plastic oil maker, Be-j, equipment Components:
1. Gas tube; 2. Anti-counter current valve; 3. Water tank; 4. Oil taking valve;
5. Pyrolysis chamber, with stainless steel outer chamber.

characteristics for other potential applications. The obtained yield of each pyrolysis product (oil and wax) in wt % was calculated after the completion of each experiment. The produced liquid oil/ wax characterization was carried out in order to investigate the effect of feedstock composition on the quality of the obtained products.

Fig. 8 illustrates the pyrolysis equipment used in these experiments. The reactor is a 1000 ml bench-scale batch reactor. The waste plastics (non-printed and printed) were collected from the printing plant, 1 kg was used in each experiment, excepting the case of polystyrene, where was used 200 g of raw material. The equipment used does not permit to perform the experiment into an inert atmosphere. The water tank was filled up to the mark with water (2 L). After the raw material was loaded into the reactor, the top of the reactor was sealed using screws. The reactor was heated from room temperature (20 °C) to the target temperature of 450°C in each experiment. Subsequently, the reactor was maintained at the target temperature for 3.5 h, the condensed pyrolysis oil was drained from the tank. The reactor was cooled to 20 °C and the residue was collected and weighed.

The pyrolysis experiments were repeated twice. Following the completion of each experiment, the yield (wt%) of each pyrolysis product was calculated, the collected oil and the wax from each experiment were analyzed as it was described above.

REFERENCES

1. <https://www.grida.no/resources/15041>
2. <https://bioenergyinternational.com/plastic-pollution-rises-as-recycling-and-waste-management-fall-short-oecd/>
3. <https://doi.org/10.1787/aa1edf33-en>
4. L. Dai, N. Zhou, Y. Lv, Y. Cheng, Y. Wang, Y. Liu, K. Cobb, P. Chen, H. Lei, R. Ruan, *Prog. Energy Combust. Sci.*, **2022**, 93,101021
5. B. Kunwar, H. Cheng, S. Chandrashekar, B. Sharma, *Renew. Sust. Energ. Rev.*, **2016**, 54, 421–428
6. Z. Wang, J. Li, K. Burra, X. Liu, X. Li, M. Zhang, T. Lei, A. K. Gupta, *J. Energy Res. Technol.*, **2021**, 143, 031901
7. S. Al-Salem, P. Lettieri, J. Baeyens, *Waste Manage (Oxford)*, **2009**, 29, 2625–2643
8. P. Singh, N. Déparrois, K.G. Burra, S. Bhattacharya, A.K. Gupta, *Appl. Energy*, **2019**, 254, 113722
9. G. Lopez, M. Artetxe, M. Amutio, J. Bilbao, M. Olazar, *Renew. Sust. Energ. Rev.*, **2017**, 73, 346–368

10. S.D. Anuar Sharuddin, F. Abnisa, W. M. Ashri Wan Daud, M. K. Aroua, *Energy Convers. Manag.*, **2016**, *115*, 308–326
11. G. Elordi, M. Olazar, G. Lopez, P. Castaño, J. Bilbao, *Appl. Catal. B: Environmental*, **2011**, *102*, 1–2, 224–231
12. S.M. Al-Salem, P. Lettieri, J. Baeyens, *Prog. Energy Combust. Sci.*, **2010**, *36*, 1, 103–129
13. G. Elordi, M. Olazar, G. Lopez, M. Artetxe, J. Bilbao, *Ind. Eng. Chem. Res.* **2011**, *50*, 11, 6650–6659
14. M. A. Hossain, J. Jewaratnam, P. Ganesan, J. N. Sahu, S. Ramesh, S. C. Poh, *Energy Convers. Manag.* **2016**, *115*, 232–243
15. N. Lee, J. Joo, K.-Y. A. Lin, J. Lee, *Polymers*, **2021**, *13*, 1198
16. Y. Zhang, G. Ji, D. Ma, C. Chen, Y. Wang, W. Wang, A. Li, *Process Saf. Environ. Prot.* **2020**, *142*, 203–211
17. Y. Zhang, G. Ji, C. Chen, Y. Wang, W. Wang, A. Li, *Fuel Process Technol.* **2020**, *206*, 106455
18. S. Shah, Z. Khan, I. Raja, Q. Mahmood, Z. Bhatti, J. Khan, A. Farooq, N. Rashid, D. Wu, *J. Hazardous Mater.* **2010**, *179*, 15–20
19. <https://blest.co.jp/eng/service/be-h/>
20. K. Sivagami, G. Divyapriya, R. Selvaraj, P. Madhiyazhagan, N. Sriram, I. Nambi, *Process Saf. Environ. Prot.*, **2021**, *149*, 497–506
21. K. Sivagami, K.V. Kumar, P. Tamizhdurai, D. Govindarajan, M. Kumar, I. Nambi, *RSC Adv.*, **2022**, *12*, 7612–7620
22. O.Y. Yansaneh, S. H. Zein, *Processes*, **2022**, *10*, 683
23. I. Kalargaris, G. Tian, S. Gu, *Energy*, **2017**, *131*, 179–185
24. M. Sogancioglu, G. Ahmetli, E. Yel, *Energy Procedia*, **2017**, *118*, 221–226
25. C. Lu, H. Xiao, X. Chen, *e-Polymers*, **2021**, *21*, 428–432
26. Supriyanto, P. Ylivero, T. Richards, *J. Anal. Appl. Pyrolysis*, **2021**, *158*, 105248
27. P. Das, P. Tiwari, *Waste Manage*, **2018**, *79*, 615–624
28. E. Hajekova, L. Spodova, M. Bajus, B. Mlynkova, *Chem.Pap.*, **2007**, *61*, 262–270
29. J. Uebe, Z. Kryzevicius, R. Majauskeine, M. Dulevicius, L. Kosychova, A. Zukauskaitė, *Waste Manag. Res.*, **2022**, *40(8)* 1220 –1230
30. ASTM D240-19, Standard Test Method for Heat of Combustion of Liquid Hydrocarbon Fuels by Bomb Calorimeter, doi: 10.1520/D0240-19

RADIOCARBON DATING OF THE HISTORIC EMPEROR'S BEECH FROM MUNCCEL, BAIA DE ARIES, ROMANIA

Adrian PATRUT^{a,*}, Victor BOCOS-BINTINTAN^b,
Roxana T. PATRUT^a, Doriana PARTILA^c, Ileana-Andreea RATIU^{a,d},
Laszlo RAKOSY^e, Karl F. VON REDEN^f

ABSTRACT. The article reports the AMS (accelerator mass spectrometry) radiocarbon dating results of the historic Emperor's Beech (*Fagus Împăratului*) from Muncel, Baia de Arieș, Romania. Two wood samples were collected from the large tree, out of which four segments were extracted and analysed by AMS radiocarbon. The oldest dated sample segment had a radiocarbon date of 233 ± 18 BP, which corresponds to a calibrated age of 365 ± 5 years. This value suggests an age of 420 ± 20 years for the Emperor's Beech. Thus, the historic beech started growing around the year 1600.

Keywords: AMS radiocarbon dating, *Fagus sylvatica*, dendrochronology, age determination, Romania.

INTRODUCTION

The European beech (*Fagus sylvatica* L.), which belongs to the genus *Fagus* of the Fagaceae family, subfamily Fagoideae, is one of the most important and widespread broadleaved trees in Europe. It is typically 25–40 m tall, reaches

^a Babeș-Bolyai University, Faculty of Chemistry and Chemical Engineering, 11 Arany Janos, RO-400028, Cluj-Napoca, Romania.

^b Babeș-Bolyai University, Faculty of Environmental Science and Engineering, 30 Fantanele, RO-400294 Cluj-Napoca, Romania.

^c Dr. Lazar Chirila High School, 41 22 Decembrie 1989, RO-515300 Baia de Aries, Romania.

^d Babeș-Bolyai University, Raluca Ripan Institute for Research in Chemistry, 30 Fantanele, RO-400294 Cluj-Napoca, Romania.

^e Babeș-Bolyai University, Faculty of Biology and Geology, 44 Republicii, RO-400015, Cluj-Napoca, Romania.

^f NOSAMS Facility, Dept. of Geology & Geophysics, Woods Hole Oceanographic Institution, Woods Hole, MA 02543, U.S.A.

* Corresponding author: apatrut@gmail.com



up to 1.5 m trunk diameter and has a lifespan of 150-250 years. Its natural range extends from southern Scandinavia in the north to Sicily in the south and from Spain in the west to northwest Turkey in the east. High summer temperatures, drought and moisture availability are limiting factors for the distribution of beech in Europe. The European beech requires a humid atmosphere with precipitation well distributed throughout the year and a well-drained soil. It tolerates winter cold, but it is sensitive to spring frost [1-3].

Covering about 21×10^6 ha, *Fagus sylvatica* is the most widespread species of deciduous tree from Europe, representing 10% of the forests of the continent. Currently, around a third of the European beech forests are located in the Carpathian Mountains (6.9×10^6 ha), out of which over 2.1×10^6 are found in Romania [2,3].

Romania also hosts several monumental beech specimens, such as the Emperor's Beech from Muncel, Baia de Arieş (Alba county), the Princess' Beech from a forest near Breaza (Prahova county) and the giant beech of the Iezer Mountains, Aninoasa forest management unit (Argeş county). The latter is a giant specimen and by far the largest known European beech, with a height of 46 m, a circumference of 9.36 m and a wood volume over 100 m^3 [2]. On the other hand, the oldest dated European beech is Michele, a small tree growing at an altitude of 1,940 m in Pollino National Park, Italy. It has a height of 12 m, a diameter of only 0.62 m, a measured age of 622 yr (ring counting) and an incredible estimated age of 725 yr [4].

In 2005, we started an extended research project for elucidating several controversial problems of the architecture, growth and age of the African baobab and other baobab species. The research is based on an original approach which is not limited to deceased or fallen trees, but also allows to investigate and date live trees. The method consists of AMS radiocarbon dating of tiny wood samples extracted from different areas of such trees [5-12]. We extended our research by dating trees that belong to other angiosperm tree species, including specimens from Romania [13-19].

Here we present the investigation and AMS radiocarbon dating results of the historic Emperor's Beech of Muncel, Baia de Arieş.

RESULTS AND DISCUSSION

The Emperor's Beech and its area. The large historic beech is positioned in the area of Muncel village, which belongs to the Baia de Arieş mining town of the Western Carpathians in Alba county, Romania. The Muncel village is located on the National Road DN 75 Turda-Ştei, at 65 km west-southwest from Turda. The Emperor's Beech can be found next to a forest road, on a

RADIOCARBON DATING OF THE HISTORIC EMPEROR'S BEECH
FROM MUNCEL, BAIA DE ARIES, ROMANIA

hill at the height of around 40 m above the right shore of the Arieş river, near the Muncel village. The GPS coordinates are 46°22.327' N, 023°15.499' E and the altitude is 526 m. The mean annual rainfall is 1245 mm (Baia de Arieş station).



Figure 1. The Emperor's Beech, with its light brown foliage, can be observed on a hill, above the Arieş river and the Muncel village. The photograph was taken from the National Road DN 75, in February 2022.

The name of the historic tree comes from Franz Joseph I, the Emperor of Austria (1850 – 1918), who visited Transylvania in 1852 and would have even seen the beech.

The Emperor's Beech is also famous for its marcescent leaves which, although they dry up in the fall and turn brown, remain preserved during the winter. The leaves do not fall until the spring, when the new green leaves emerge (**Figure 2**). The cause of the marcescence is not yet sufficiently understood.



Figure 2. The impressive canopy of the Emperor's Beech, with marcescent leaves, in December 2009.

RADIOCARBON DATING OF THE HISTORIC EMPEROR'S BEECH
FROM MUNCEL, BAIA DE ARIES, ROMANIA

The Emperor's Beech was first mentioned in the scientific literature, as a monumental tree, in 1924, by the renowned botanist Alexandru Borza [20,21]. In 1995, the Emperor's Beech was declared a Natural Monument.

In fact, the beech grows at a distance of 3.5 m from the edge of the forest road, on a steep slope of over 50° toward the right bank of the Arieș river. The highest point of its base can be found at 3.2 m below the road, while the lowest point of the base is still 2.3 m below (**Figure 3**).



Figure 3. The Emperor's Beech grows very close to the forest road between Baia de Arieș and Muncel, on a steep slope toward the Arieș river. The photograph was taken in February 2022.

The Emperor's Beech has a maximum height $h = 23.2$ m. Its circumference at breast height (cbh; at 1.30 m above mean ground level), which was 5.33 m in 2009, decreased to 5.00 m in 2022. The cause of this decrease is the breaking of a large low branch around the year 2015, which also ruptured small pieces of the trunk. The tree forks at heights between 6.5 – 8 m into nine branches, out of which seven are still standing, while two are broken. The horizontal dimensions of the impressive canopy are 30.5 m (NS) x 24,6 m (SE). The current overall wood volume of the beech is 20 m³, out of which 16 m³ correspond to the trunk and 4 m³ to the canopy.

Wood samples. One wood sample, labelled EB-1, with the length of 0.51 m, was collected from the trunk with an increment borer, at the height of 1.70 m above the highest point from the ground (and 2.85 m above the mean point). Three pieces/segments, each 10⁻³ m long (marked a, b and c), were extracted from determined positions of sample EB-1.

Another tiny sample, labelled EB-2, was extracted with a sharp instrument from the centre of a branch with a base diametre of 0.54 m, which fell to the ground around the year 2015.

AMS results and calibrated ages. Radiocarbon dates of the four sample segments are presented in Table 1. The radiocarbon dates are expressed in ¹⁴C yr BP (radiocarbon years before present, i.e., before the reference year 1950). Radiocarbon dates and errors were rounded to the nearest year.

Table 1. AMS Radiocarbon dating results and calibrated ages of samples collected from the Emperor's Beech.

Sample code	Depth ¹ [height ²] (m)	Radiocarbon date [error] (¹⁴ C yr BP)	Cal CE range 1 σ [confidence interval]	Assigned year [error] (cal CE)	Sample age [error] (cal CE)
EB-1a	0.05 [2.85]	-	-	> 1950	> Modern
EB-1b	0.35 [2.85]	185 \pm 23	1666-1683 [14.2%] 1736-1784 [38.7%] 1794-1802 [5.5%] 1936-... [9.9%]	1760 \pm 24	260 \pm 25
EB-1c	0.51 [2.85]	233 \pm 18	1647-1664 [47.8%] 1785-1794 [20.4%]	1655 \pm 7	365 \pm 5
EB-2	- [-]	183 \pm 18	1667-1683 [14.2%] 1736-1782 [39.5%] 1796-1802 [4.0%] 1936-... [10.6%]	1759 \pm 23	255 \pm 25

¹ Depth in the wood from the sampling point.

² Height above ground level.

Calibrated (cal) ages, expressed in calendar years CE (CE, i.e., common era), are also listed in Table 1. The 1σ probability distribution (68.3%) was selected to derive calibrated age ranges. For one segment (EB-1c), the 1σ distribution is consistent with two ranges of calendar years, while for two sample segments (EB-1b, EB-2) it corresponds to four ranges of calendar years. In all these cases, the confidence interval of one range is considerably greater than that of the other(s); therefore, it was selected as the cal CE range of the segment for the purpose of this discussion.

For obtaining single calendar age values of sample segments, we derived a mean calendar age of each sample segment, called assigned year, from the selected range (marked in bold). Sample/segment ages represent the difference between the current year 2022 CE (for sample segments EB-1b and EB-1c) or the year 2015 CE, when the investigated low branch fell to the ground (for sample EB-2) and the assigned year, with the corresponding error. Sample ages and errors were rounded to the nearest 5 yr. We used this approach for selecting calibrated age ranges and single values for sample ages in our previous articles on AMS radiocarbon dating of large and old angiosperm trees [5-19,22-25].

Dating results of samples (segments). The oldest dated segment EB-1c, which represents the deepest sample end with a depth in wood of 0.51 m, had a radiocarbon date of 233 ± 18 BP, which corresponds to a calibrated age of 365 ± 5 calendar yr. The segment EB-1b, with a depth of 0.35 m, had a radiocarbon date of 185 ± 23 BP, corresponding to a calibrated age of 260 ± 25 calendar yr. The negative radiocarbon date and the age of segment EB-1a shows that the Emperor's Beech grew the last 0.05 m in radius in less than 72 years. The sample EB-2, extracted from the fallen branch, had a radiocarbon date 183 ± 18 BP, which corresponded in the year 2015 to a calibrated age of 255 ± 25 calendar yr. This value shows that the fallen branch did not belong to the first generation of branches.

Age of the Emperor's Beech. The oldest sample segment EB-1c corresponds to a depth in the wood of 0.51 m from the sampling point, at a height of 2.85 m above the mean ground level. At this sampling height, the diameter of the tree is 1.42 m, which corresponds to a radius of 0.71 m. Taking into account that young beeches grow fast, while old beeches grow much slower, we estimate that the Emperor's Beech grew its first 0.20 m in radius in around 50-60 years. Therefore, we consider that the Emperor's Beech is 420 ± 20 yr old and started growing around the year 1600.

CONCLUSIONS

Our research presents the AMS radiocarbon investigation results of the historic Emperor's Beech of Muncel, Baia de Arieș. Two wood samples were collected from the trunk and from a fallen branch, out of which four segments were extracted. The radiocarbon date of the oldest sample segment was 233 ± 18 BP, which corresponds to a calibrated age of 365 ± 5 years. This result, combined with the original position of the dated sample segment in the tree, indicates an age of 420 ± 20 years for the Emperor's Beech.

EXPERIMENTAL SECTION

Sample collection. The sample EB-1 was collected with a Haglöf CH 800 increment borer (0.80 m long, 0.0108 m inner diameter). A number of three tiny pieces/segments were extracted from predetermined positions along the sample. The small sample EB-2 was extracted with a sharp instrument from the centre of a fallen branch. The sample segments were processed and investigated by AMS radiocarbon dating.

Sample preparation. The α -cellulose pretreatment method was used for removing soluble and mobile organic components [26]. The resulting samples were combusted to CO_2 , which was next reduced to graphite on iron catalyst [27,28]. The resulting graphite samples were analysed by AMS.

AMS measurements. AMS radiocarbon measurements were performed at the NOSAMS Facility of the Woods Hole Oceanographic Institution (Woods Hole, MA, U.S.A.) by using the Pelletron® Tandem 500 kV AMS system [29]. The obtained fraction modern values, corrected for isotope fractionation with the normalized $\delta^{13}\text{C}$ value of -25 ‰, were ultimately converted to a radiocarbon date.

Calibration. Radiocarbon dates were calibrated and converted into calendar ages with the OxCal v4.4 for Windows [30], by using the IntCal20 atmospheric data set [31].

ACKNOWLEDGMENTS

The research was funded by the Romanian Ministry of Education CNCS-UEFISCDI under grant PN-III-P4-ID-PCE-2020-2567, No. 145/2021.

REFERENCES

1. T. Houston Durant, D. de Rigo, G. Caudullo, *Fagus sylvatica* and other beeches in Europe: distribution, habitat, usage and threats. In: "European Atlas of Forest Tree Species", **2016**, Publication Office of the European Union, Luxembourg, pp.94-95.
2. C.D. Stoiculescu, "Romanian beech forest in the European context under the influence of climate change" (in Romanian), Bucuresti, **2013**, 413 p.
3. I.A. Biris, *Bucovina Forestiera*, **2014**, *14(1)*, 77-85.
4. G. Piovesan, F. Biondi, M. Baliva, G. de Vivo, V. Marchian, A. Schettino, A. di Filippo, *Ecology*, **2019**, *0(0)*, e02737.
5. A. Patrut, K.F. von Reden, D.A. Lowy, A.H. Alberts, J.W. Pohlman, R. Wittmann, D. Gerlach, L. Xu, C. Mitchell, *Tree Phys.*, **2007**, *27*, 1569-1574.
6. A. Patrut, K.F. von Reden, R. Van Pelt, D.H. Mayne, D.A. Lowy, D. Margineanu, *Ann. Forest Sci.*, **2011**, *68*, 993-1003.
7. A. Patrut, S. Woodborne, K.F. von Reden, G. Hall, M. Hofmeyr, D. Lowy, R.T. Patrut, *PLoS ONE*, **2015**, *10(1)*, e0117193.
8. A. Patrut, S. Woodborne, K.F. von Reden, G. Hall, R.T. Patrut, L. Rakosy, P. Danthu, J-M. Leong Pock-Tsy, D.A. Lowy, D. Margineanu, *Radiocarbon*, **2017**, *59(2)*, 435-448.
9. A. Patrut, S. Woodborne, R.T. Patrut, L. Rakosy, D.A. Lowy, G. Hall, K.F. von Reden, *Nat. Plants*, **2018**, *4*, 423-426.
10. A. Patrut, R.T. Patrut, L. Rakosy, D.A. Lowy, D. Margineanu, K.F. von Reden, *Studia UBB Chemia*, **2019**, *LXIV*, *2 (II)*, 411-419.
11. A. Patrut, S. Woodborne, R.T. Patrut, G. Hall, L. Rakosy, C. Winterbach, K.F. von Reden, *Forests*, **2019**, *10*, 983-994.
12. A. Patrut, R.T. Patrut, L. Rakosy, I.A. Ratiu, D.A. Lowy, K.F. von Reden, *Dendrochronologia*, **2021**, *70*, 125898.
13. A. Patrut, K.F. von Reden, D.A. Lowy, S. Pasca, L. Kekedy-Nagy, I. Sovago, *Studia UBB Chemia*, **2010**, *LV*, *1*, 113-120.
14. A. Patrut, K.F. von Reden, V. Savu, D.A. Lowy, R. Mitea, I. Barbul, *Studia UBB Chemia*, **2011**, *LVI*, *1*, 145-155.
15. A. Patrut, N. Robu, V. Savu, R.T. Patrut, L. Rakosy, I.A. Ratiu, D.A. Lowy, D. Margineanu, K.F. von Reden, *Studia UBB Chemia*, **2018**, *LXIII*, *4*, 7-13.
16. A. Patrut, L. Rakosy, R.T. Patrut, V. Bocos-Bintintan, I.A. Ratiu, J. Bodis, S. Woodborne, *Studia UBB Chemia*, **2021**, *LXVI*, *3*, 255-263.
17. A. Patrut, K.F. von Reden, D.A. Lowy, R.T. Patrut, D.L. Vaida, D. Margineanu, *Nucl. Instrum. Methods Phys. Res. Sect. B.*, **2013**, *294*, 616-621.
18. A. Patrut, R.T. Patrut, L. Rakosy, I.A. Ratiu, D.A. Lowy, J. Bodis, K.F. von Reden, *Studia UBB Chemia*, **2018**, *LXIII*, *3*, 41-48.
19. A. Patrut, R.T. Patrut, V. Bocos-Bintintan, I.A. Ratiu, L. Rakosy, G. Zdrob, E. Vanca, K.F. von Reden, *Studia UBB Chemia*, **2022**, *LXVII*, *1*, 245-256.
20. Al. Borza, *Bul Grad. bot. Muz. Bot. Cluj*, **1924**, *4*, 1-24.

21. Al. Borza, *Apulum*, **1939-1942**, *I*, 248-256.
22. A. Patrut, D.H. Mayne, K.F. von Reden, D.A. Lowy, S. Venter, A.P. McNichol, M. L. Roberts, D. Margineanu, *Radiocarbon*, **2010**, *52(2-3)*, 727-734.
23. A. Patrut, K.F. von Reden, P. Danthu, J-M. Leong Pock-Tsy, L. Rakosy, R.T. Patrut, D.A. Lowy, D. Margineanu, *Nucl. Instrum. Methods Phys. Res. Sect. B*, **2015**, *361*, 591-598.
24. A. Patrut, R.T. Patrut, P. Danthu, J.M. Leong Pock-Tsy, L. Rakosy, D. Lowy, K.F. von Reden, *PLOS One*, **2016**, *11(1)*: e0146977.
25. A. Patrut, A. Garg, S. Woodborne, R.T. Patrut, L. Rakosy, I.A. Ratiu, *PLOS One*, **2020**, *15(1)*: e0227352.
26. N.J. Loader, I. Robertson, A.C. Barker, V.R. Switsur, J.S. Waterhouse, *Chem. Geol.*, **1997**, *136(3)*, 313–317.
27. Z. Sofer, *Anal. Chem.*, **1980**, *52(8)*, 1389-1391.
28. J.S. Vogel, J.R. Southon, D.E. Nelson, T.A. Brown, *Nucl. Instrum. Methods Phys. Res. Sect. B*, **1984**, *5*, 289-293.
29. M. L. Roberts, J. R. Burton, K. L. Elder, B. E. Longworth, C. P. McIntyre, K. F. von Reden, B. X. Han, B. E. Rosenheim, W. J. Jenkins, E. Galutschek, A. P. McNichol, *Radiocarbon*, **2010**, *52*, 228-235.
30. C. Bronk Ramsey, *Radiocarbon*, **2009**, *51*, 337-360.
31. P.J. Reimer, W.E.N. Austin, E. Bard, A. Bayliss, P.G. Blackwell, C. Bronk Ramsey, M. Butzin, H. Cheng, R. Lawrence Edwards, M. Friedrich, P.M. Grootes, T.P. Guilderson, I. Hajdas, T.J. Heaton, A. G. Hogg, K.A. Hughen, B. Kromer, S.W. Manning, R. Muscheler, J.G. Palmer, C. Pearson, J. van der Plicht, R.W. Reimer, D.A. Richards, E.M. Scott, J.R. Southon, C.S.M. Turney, L. Wacker, F. Adolphi, U. Büntgen, M. Capano, S.M. Fahrni, A. Fogtman-Schulz, R. Friedrich, P. Köhler, S. Kudsk, F. Miyake, J. Olsen, F. Reinig, M. Sakamoto, A. Sookdeo, S. Talamo, *Radiocarbon*, **2020**, *62(4)*, 727-757.

ICP-OES AND LC-ESI-MS/MS ANALYSES, ENZYME INHIBITION AND DNA PROTECTION POTENTIAL OF *PELARGONIUM QUERCETORUM* AGNEW

Ebru AKKEMİK^{a,c,*}, Mehmet FİDAN^b,
Merve BALABAN^c, Behcet İNAL^{d,*}

ABSTRACT. *Pelargonium quercetorum* Agnew extract affects activities of acetylcholinesterase (AChE) and carbonic anhydrase I-II enzymes (hCA I-II) was investigated under *in vitro* conditions. IC₅₀ values of *P. quercetorum* Agnew on hCA I-II and AChE activity were determined as 0.144±0.0720, 0.209±0.0593, and 0.062±0.0097 mg/mL, respectively. Rutin and shikimic acid was found to be the main phenolic component in *P. quercetorum* Agnew flower extract from the results of LC-ESI-MS/MS analysis. Rutin was found to be the main phenolic component in *P. quercetorum* Agnew leaf extract from the results of LC-ESI-MS/MS analysis. ICP-OES analysis showed that the leaves of *P. quercetorum* Agnew were rich in potassium. The DNA protective effect on plasmid DNA was demonstrated by using extracts obtained from leaf and flower tissues. Consequently, based on the findings of the current study, it could be anticipated that clinical trials related to *P. quercetorum* Agnew could be completed and the plant could be used pharmacologically.

Keywords: *Acetylcholinesterase; Carbonic anhydrase; DNA protection; ICP-OES; P. quercetorum Agnew*

INTRODUCTION

P. quercetorum Agnew is a species that belongs to *Pelargonium* genus of the Geraniaceae family in the Geraniales order. This species is distributed in Southeastern Anatolia Region of Türkiye [1]. *P. quercetorum*

^a Faculty of Engineering, Food Engineering, Siirt University, Kezer Campus, 56100, Siirt, Türkiye

^b Department of Biology, Faculty of Science and Literature, Siirt University, 56100, Siirt, Türkiye

^c Science and Technology Application and Research Center, Siirt University, Kezer Campus, 56100-Siirt, Türkiye

^d Department of Agricultural Biotechnology, Faculty of Agriculture, Siirt University, 56100, Siirt, Türkiye

* Corresponding authors: eakkemik@siirt.edu.tr, behcetinal@siirt.edu.tr



Agnew (Hakkari geranium), popularly known by the names Tolk or Tolik, is used for cooking and medical purposes [2]. There have been very few studies on *P. quercetorum* Agnew in the literature. Such as, chemical content of *P. quercetorum* Agnew was analyzed using GCxGC-TOF/MS, and 23 different compounds with different proportions were reported [3]. The main chemicals were found to be tetracosane, heneicosane, and 2-methyleicosane. Similarly, analysis of volatile components in oil extract of *P. quercetorum* Agnew using GC-MS revealed 26 compounds, and alpha pinene, alpha-fenchyl acetate, and limonene were found to be the dominant compounds [4]. Besides, different extracts of the plant showed antioxidant [5], anti-growth/cytotoxic activity on non-small cell lung cancer cells [3], human MCF-7, MDA-MB-231 breast cancer cells [6] and anthelmintic activity [5]. Despite all these studies, the research on *P. quercetorum* Agnew is limited. The fact that the plant grows only in a specific region limits its potential for use. Results obtain from current study will have contributed to many researchers recognize plant material and evaluate its potential uses in pharmacy, alternative medicine, and cosmetics. Therefore, the phenolic content, elemental analysis, DNA protective effect, and enzyme inhibitory effect of *P. quercetorum* Agnew were addressed.

Almost all mechanisms in the living system are coordinated through enzymes [7]. So, interfering with their activity is used in the diagnosis and treatment of many diseases [8]. Acetylcholinesterase and carbonic anhydrase enzymes used in the present study are some of these enzymes. Acetylcholinesterase (AChE, E.C.3.1.1.7) is a carboxylic ester hydrolase that catalyzes hydrolysis of choline esters called acetylcholine acetyl hydrolase [9]. Acetylcholinesterase inhibitors such as tacrine, donepezil, rivastigmine, and galantamine have been reported to be utilized in the treatment of Alzheimer's disease (AD) [10; 11]. The inhibitors of this enzyme were mentioned to stop the hydrolysis of acetylcholine, its usual substrate, thereby increasing cholinergic transmission [12]. In addition to AD inhibitors of the enzyme were reported to be used in myasthenia gravis and glaucoma diseases [13; 14]. That's why inhibition effects of many different plant extracts such as *Crinum moorei* Hook.f, *Galanthus ikariae* L., Narcissus 'Sir Winston Churchill', *Sarcococca coriacea* (Hook.f.) Sweet, *Corydalis bulbosa* DC., *Fritillaria imperialis* L., marigold [15] on AChE enzyme activity have been investigated. Besides, inhibitory effects of secondary metabolites from plant extracts on AChE enzyme have also been studied [16]. However, new and different inhibitors continue to be investigated because the existing inhibitors of the enzyme have a large number of side effects in the treatment of specified diseases [16] and cannot provide fully the desired effect. The other enzyme used in the present study was carbonic anhydrase, a clinically important enzyme similar to acetylcholinesterase. Carbonic anhydrase (CA,

E.C.4.2.1.1) is found in different cell types and encoded by different gene families. In mammals, this enzyme has 16 isoenzymes containing Zn^{2+} ion at its active site [17; 18]. Although the enzyme is known to catalyze many reactions, its major role in metabolism is to catalyze the conversion of CO_2 to HCO_3^- , thereby creating an important buffering in the living system as well as transporting CO_2 [7; 18]. Inhibitors and activators of carbonic anhydrase enzyme have potentials to be used as drugs. It was reported that the inhibitors of the enzyme can be used for the treatment of epilepsy, glaucoma, edema, obesity and cancer, while its activators can be used for the treatment of Alzheimer's disease [19; 20; 21]. However, it was also stated that the current inhibitors of the enzyme (sulfonamides, acetazolamides, dorzolamides, methazolamides and brinzolamide) used in the treatment of above-mentioned diseases have numerous side effects [22; 23]. For this reason, investigations have been going on to find natural or synthetic new inhibitors of the enzyme.

Exposure of DNA to hydrogen peroxide (H_2O_2) causes breakage of open-ended DNA and DNA breaks (chromatid and chromosome breaks) [24]. In the meantime, genetic disorders may occur as a result of breaks in the DNA chain. Irreversible DNA damage can lead to carcinogenesis, aging and other degenerative diseases [25]. Therefore, it is extremely important to investigate the effects of the active ingredients of plants on DNA protection. Since there is no study in the literature on how *P. quercetorum* Agnew influences genetic material, its DNA protective activity has been determined. The aim of this study was to determine the phenolic compound content, elemental analysis, antienzyme activity, and DNA protective activity of *P. quercetorum* Agnew to determine if it has potential for use in the medical, food, and cosmetic industries. Considering the aforementioned causes, in the current study, *in vitro* effect of *P. quercetorum* Agnew extract on the activities of acetylcholinesterase and carbonic anhydrase I-II, which play a critical role in metabolism, was evaluated for the first time. Furthermore, *P. quercetorum* Agnew was examined conducting phenolic compound analysis by LC-ESI-MS/MS and elemental analysis by ICP-OES. Additionally, the effect on DNA protection of *P. quercetorum* Agnew extract was evaluated by working in different concentrations in both flower and leaf tissue.

RESULTS AND DISCUSSION

In this study, *in vitro* effect, *P. quercetorum* Agnew on human erythrocyte carbonic anhydrase I-II and acetylcholinesterase enzymes were investigated to determine the being enzyme inhibitory properties. IC_{50} values calculated to determine the inhibition effect of *P. quercetorum* Agnew on hCA I-II and

AChE activities were 0.144 ± 0.0720 , 0.209 ± 0.0593 and 0.062 ± 0.0097 mg/mL, respectively. Thus, it was revealed that *P. quercetorum* Agnew has a better inhibition effect on AChE enzyme activity. On the other hand, carbonic anhydrase appeared to have a relatively similar inhibition effect on both isoenzymes, but it was more effective on hCA I enzyme activity (Figure 1, Table 1).

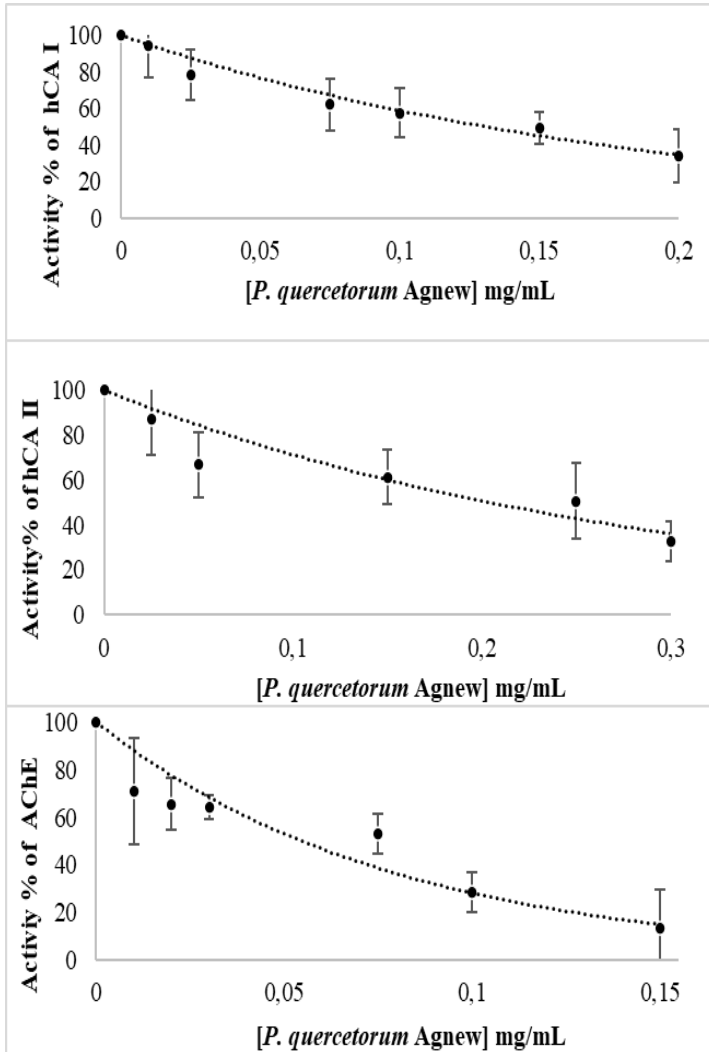


Figure 1. Effect of *P. quercetorum* Agnew on hCA I, II and AChE enzyme activity

Table 1. Anti-enzyme activity of *P. quercetorum* Agnew

	hCA I	hCA II	AChE
IC ₅₀ (mg/mL)	0.144±0.0720	0.209±0.0593	0.062±0.0097
K _i (mg/mL)	0.0363±0.0053	0.277±0.12880	0.0035±0.002

It was stated that phenolic compounds cause inhibition by forming hydrogen bonds with the water molecules around Zn²⁺ located at the active site of carbonic anhydrase enzyme [21; 26; 27; 28]. *P. quercetorum* Agnew appeared to exhibit a similarly powerful inhibition effect on both isoenzymes of carbonic anhydrase enzyme. The isoenzyme I and II of the carbonic anhydrase enzymes share about 60% similarity [29]. Therefore, although methanol extracts of *P. quercetorum* Agnew exhibit similar effects on activities of hCA I and hCA II enzymes, there was about two-fold difference in their IC₅₀ values. Consequently, due to similar inhibition effects, it is thought that the phenolic compounds in the extract interact with water molecules around Zn²⁺ in the active region of both isoenzymes by hydrogen bonding. A detailed analysis of the narrow groove-shaped active site of acetylcholinesterase (AChE), the other enzyme investigated in the present study, would reveal that its active region can be divided into several subregions: omega lobe (Cys69-Cys96), peripheral anionic subunit (Asp74, Tyr124, Ser125, Trp286, Tyr337, Tyr341), anionic subunit (Trp86, Tyr133, Glu202, Gly448, Ile451), oxyanion hole (Gly121, Gly122, Ala204), catalytic triad (Ser203, His447, Glu334) and acyl bonding pocket (Trp236, Phe295, Phe297, Phe338) [29]. Acetylcholinesterase enzyme has 14 aromatic amino acids at the active center [30; 31]. In this study, plant extract was used and it contained multiple phenolic compounds. Therefore, clamp formation by aromatic amino acid at the active center of the enzyme and multiple phenolic acids in plant extract of *P. quercetorum* Agnew through non-covalent interactions at different locations in the enzyme molecule at the same time, and thus increasing the effect of the inhibitor, is an expected situation. As a result, a low concentration of *P. quercetorum* Agnew had an inhibition effect on AChE.

In the LC-ESI-MS/MS analysis performed to the phenolic compound profile of the *P. quercetorum* Agnew extract was analyzed by using 45 different standards in-our-house library (48). Results showed that *P. quercetorum* Agnew leaf extract had 627.4441 ng/mL shikimic acid, 116.9617 ng/mL gallic acid, 4.7379 ng/mL hyperoside, 123.1750 ng/mL quercetin-3-glucoside, 1633.5768 ng/mL rutin, 473.4672 ng/mL hesperidine, 108.6753 ng/mL kaemerol-3-glucoside, and 66.7999 ng/mL fisetin while other standards could not be detected (Figure 2, Table 2). It was determined first time using LC-ESI-MS/MS analysis in the present study that dominant compound of *P. quercetorum* Agnew leaf extract is rutin (Table 2, Figure 2).

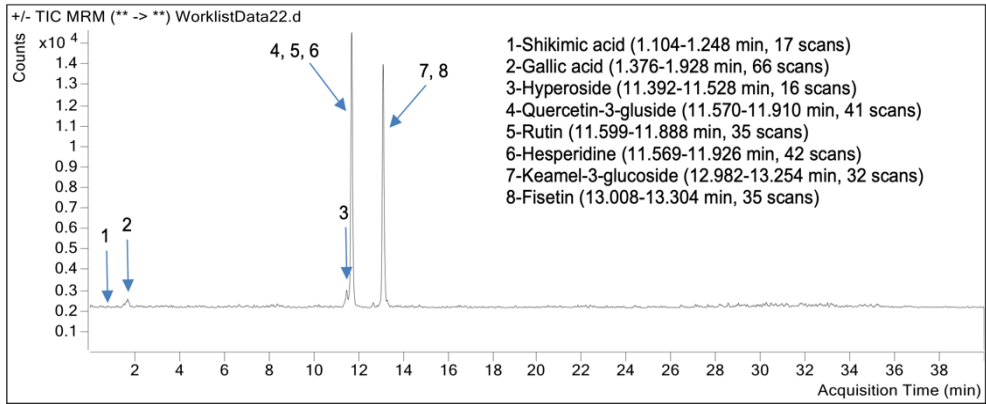


Figure 2. LC-ESI-MS/MS analysis of *P. quercetorum* Agnew leaf extract

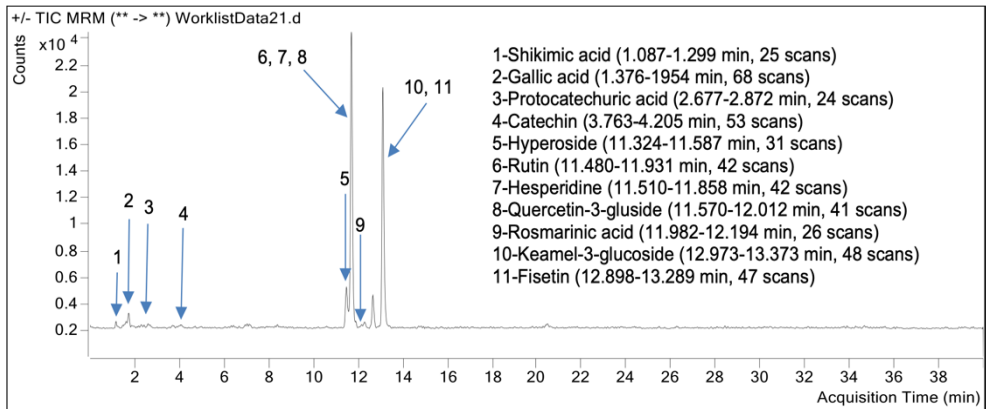


Figure 3. LC-ESI-MS/MS analysis of *P. quercetorum* Agnew flower extract

P. quercetorum Agnew flower extract had 3364.8076 ng/mL shikimic acid, 307.3271 ng/mL gallic acid, 6.2348 ng/mL protocatechuic acid, 379.4268 ng/mL catechin, 141.4570 ng/mL hyperoside, 252.6943 ng/mL quercetin-3-glucoside, 1787.7070 ng/mL rutin, 134.5509 ng/mL rosmarinic acid, 656.0438 ng/mL hesperidine, 181.2362 ng/mL kaemerol-3-glucoside, and 183.4773 ng/mL fisetin while other standards could not be detected (Figure 3, Table 2). It was determined first time using LC-ESI-MS/MS analysis in the present study that dominant compounds of *P. quercetorum* Agnew flower extract is rutin and shikimic acid (Figure 3, Table 2). Similarly, different extracts of *Pelargonium endlicherianum*, another *Pelargonium* species, prepared by different solvents contained apocynin and gallic acid, but apocynin was found

to be dominant. Moreover, it was stated in the same study that all extracts had vanillic acid in trace amounts, while only the ethyl acetate extract contained a low concentration of caffeic acid [5]. In *Pelargonium graveolens*, another *Pelargonium* species, flavonoid analysis was performed by library scanning using the LC MS device. It was reported that *P. graveolens* has nine flavonoids [32].

Table 2. Analysis of phenolic compounds in *P. quercetorum* Agnew by LC-ESI-MS/MS

	Compound name	RT	Flower ng/mL	Leaf ng/mL
1	Shikimic acid	1.155	3364.8	627.444
2	Gallic acid	1.733	307.33	116.962
3	Protocatechuic acid	2.736	6.2348	ND
4	Catechin	4.077	379.43	ND
5	Hyperoside	11.477	141.46	4.738
6	Quercetin-3-glucoside	11.706	252.69	123.175
7	Rutin	11.676	1787.7	1633.58
8	Rosmarinic acid	12.092	134.55	ND
9	Hesperidine	11.696	656.04	473.47
10	Kaempferol-3-glucoside	13.109	181.24	108.67
11	Fisetin	13.110	183.48	66.80

Mineral content of *P. quercetorum* Agnew was analyzed with ICP-OES. The mineral analysis of the leaf sample of *P. quercetorum* Agnew revealed that it is rich in potassium (3.21%), calcium (0.77%), phosphorus (0.23%) and magnesium (0.22%). Moreover, *P. quercetorum* Agnew was also found to contain 18 different minerals at low rates (Table 3). It was found that *P. quercetorum* Agnew contained alkaline metal, alkaline earth metals, 3A, 4A and 5A group and transition metals. In a related study examining mineral contents in different parts of *P. quercetorum* Agnew, a relative of *P. graveolens*, different parts of the plant were found to contain calcium (2.47 mg/100g), magnesium (0.35 mg/100g), sodium (1.34 mg/100 g), potassium (1.46 mg/100 g), phosphorus (0.18 mg/100g), nitrogen (1.06 mg/100g), chlorides (1.34 mg/100g) and sulphur (0.081 mg/100 g) based on analyses using flame photometer. Although both varieties seem to have similar minerals, it could be stated that *P. quercetorum* Agnew has a richer mineral content in terms of both quantity and variety of the minerals.

Table 3. Elemental analysis of *P. quercetorum* Agnew

Element	AVG (mg/kg)±SD	%
Al	193.7750±1.2468	0.0194
As	0.0000±0.0000	0
B	48.8165 ± 0.4232	0.0049
Ba	1.0374 ±0.0117	0.0001
Bi	0.0000±0.0000	0
Ca	7707.1867 ± 45.3395	0.77
Cd	0.0995 ± 0.0130	0.000001
Co	0.0640 ± 0.0377	0.000006
Cr	0.5635 ± 0.0215	0.000056
Cu	5.8670 ± 0.1360	0.00059
Fe	151.1622 ±1.8136	0.015
K	32098.3169 ± 154.1542	3.21
Zn	21.0820 ± 0.4345	0.0021
Mg	2192.8934±453.3947	0.22
Mn	35.9738±0.4798	0.0036
Mo	0.8862±0.0064	0.000089
Na	481.0847±0.7179	0.048
Ni	1.2680±0.0189	0.00013
P	2253.8071±42.3168	0.23
Pb	1.5450±0.1039	0.00015
Sb	0.3227 ±0.1095	0.000032
Se	0.0000±0.0000	0
Sn	0.7547 ±0.0117	0.000075
Sr	3.6554 ±0.0091	0.00036
Tl	0.0000±0.0000	0
Li	1.2642±0.0015	0.00013

There are diverse studies on the antioxidant capacity (5) and cancer activity (3; 6) of *P. quercetorum* but up to present, no study on plasmid DNA protection was found in the literature, we especially achieved the protective potential of total extract of *P. quercetorum* on plasmid DNA against the Fenton solvent DNA harmful effect. The DNA protective activity of ethanol-water extracts from *P. quercetorum* Agnew was achieved by using pBR322 plasmid DNA (Figure 4). In current study, the ability of extracts belongs to flower and leaf tissue at different concentrations to prevent DNA damage was handled. According to the obtained result, it was determined that H₂O₂ damaged form I of plasmid and transformed it into form II-form III (Figure 4-Line 9) and in Line 10 plasmid DNA without fenton solvent was observed

compact and only supercoil DNA was found. There was no found significantly DNA protecting effect of rosmarinic acid (Figure 4-Line 7) and tocopherol (Figure 4-Line 8) extract concentration (1 mg/mL) used at current study. However, when the two substances are compared, it can be said that rosmarinic acid has a slightly more protective effect.

On the other hand, it was observed that 2 and 3 mg/mL concentrations of both leaf and flower tissues have no DNA protective effect. Smear form was seeded and it was estimated that plant extracts almost destroyed the plasmid DNA (Figure 4). Hydrogen peroxide, a type of free radical, converts guanine to 8 hydroxy guanine and causes DNA damage (33; 34). However, it was observed that the concentrations of both tissues at 1 mg/mL preserved the form I and form III form of DNA. In this case, it can be said that the damage of OH radicals in the Fenton solution is significantly prevented (Figure 4). Under these circumstances, linear DNA bands were not formed in any 1 mg/mL of the extract's concentration of both tissues in both *P. quercetorum* Agnew. In other words, it has been determined that extracts protect DNA against the damaging effects of H₂O₂ on DNA. As a result of this study, it was concluded that extracts at different concentrations and solved in different solvents protect DNA at different levels. And it can be seen that extracts such as rosmarinic acid and tocopherol, which are some well-known DNA protective agents, do not protect DNA. Because the phytochemicals in plant extracts can also have an oxidative effect on DNA damage (35). It was observed that the extract obtained from *P. quercetorum* Agnew has a low effect on plasmid DNA protective activity. It was found that *P. quercetorum* Agnew extract in low concentration (1 mg/mL) in ethanol-water solvent mixture had a better protection effect.

P. quercetorum Agnew is widely used among the local population in the context of alternative medicine as a stomach stimulant or as a treatment for indigestion (2). However, studies on this plant in the literature are very limited. With this study, we aimed to reveal the important chemical metabolites of the plant. The secondary metabolites, such as shikimic acid, gallic acid, protocatechuic acid, catechin, hyperoside, quercetin-3-glucoside, rutin, hesperidine, kaemerol-3-glucoside, and fisetin are quite important chemical compounds in chosen plant in current study. Therefore, it is thought that the determined metabolites will help to clarify the relationship with the therapeutic disease. One of these chemicals or its mixture in the form of a mixture may have created the current effect. In addition, the secondary metabolites are important in the prevention of a variety of disease. The existence of the above-mentioned secondary metabolites is responsible for the antidiuretic, anti-inflammatory, antianalgesic, anticancer, antiviral, antimalarial, antibacterial, and anti-fungal properties (36). Usually, plants are utilized to find and test ionic

elements that are extremely useful in the development of novel medications. The elements that come out of the plant are very important for the functioning of the protein and especially the enzymes that serve in the metabolism. In this context, it can be said that the plant, which is the subject of the study, has an important nutritional element content. Moreover, in order to expand the potential for use of the plant in traditional medicine and ethnobotany, it was desired to investigate its effects on AChE and CA I-II enzyme activities and its potential for circular DNA protection. As a result of the study, it is thought that the plant may have an important potential effect in the treatments of Alzheimer's, glaucoma, epilepsy, gastric, spinal disorders, obesity and cancer. For the manufacture of important plants, phytochemical analysis is also significant and has commercial interest in both research institutes and pharmaceutical businesses.

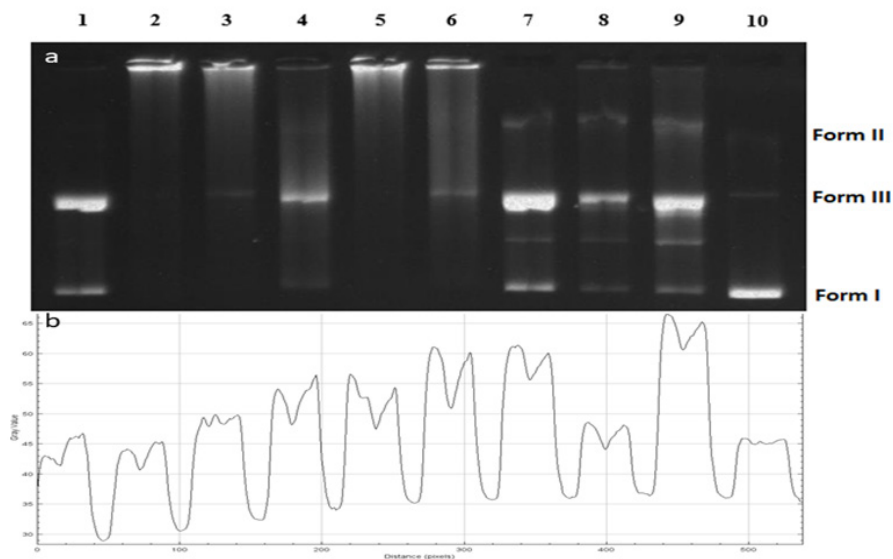


Figure 4. DNA protection gel image (a) and plot analysis (b) of flower and leaf extracts 1. DNA+Fenton Reagent+Flower extract (1 mg/mL), 2. DNA+Fenton Reagent+Flower extract (2 mg/mL), 3. DNA+Fenton Reagent+Flower extract (3 mg/mL), 4. DNA+Fenton Reagent+Leaf extract (1 mg/mL), 5. DNA+Fenton Reagent+Leaf extract (2 mg/mL), 6. DNA+Fenton Reagent+Leaf extract (3 mg/mL), 7. DNA+Fenton Reagent+Rosmarinic acid (1 mg/mL), 8. DNA+Fenton Reagent+alpha Tocopherol (1 mg/mL), 9. DNA+Fenton Reagent, 10. pBR322 DNA

CONCLUSIONS

P. quercetorum Agnew is rich in rutin, potassium (3.21%), calcium (0.77%), phosphorus (0.23%) and magnesium (0.22%). Thus, extracts can also be used as alternative natural sources for the treatment of different diseases. In the present study, methanol extract of *P. quercetorum* Agnew showed different effects on hCA I-II, AChE activity and also lower concentration of leaf and flower extract was found as a DNA protective effect. Synthetic drugs have fairly expensive synthesis and characterization even many side effects. Therefore, *P. quercetorum* Agnew may be preferred instead of synthetic drugs in diseases treatment such as glaucoma, epilepsy, gastric, neurological disorders, obesity, cancer, Alzheimer's treatment.

EXPERIMENTAL SECTION

Chemicals and standards

Human erythrocyte AChE was purchased from Sigma Aldrich. Methanol was obtained from Merck and all other reagents were purchased from Sigma Aldrich or Fluka. Shikimic acid, gallic acid, protocatechuic acid, gentisic acid, catechin, 4-hydroxybenzoic acid, chlorogenic acid, 4-hydroxybenzaldehyde, vanillic acid, caffeic acid, syringic acid, p-coumaric acid, salicylic acid, taxifolin, polydatine, trans-ferulic acid, sinapic acid, quercimeritrin, scutellarin, o-coumaric acid, cynarin, protocatechuic ethyl ester, hyperocide, quercetin 3- β -d-glucoside, rutin, resveratrol, naringin, rosmarinic acid, hesperidine, baicalin, kaempferol-3-glucoside, fisetin, oleuropein, trans-cinnamic acid, quercetin, naringenin, silibinin, hesperetin, kaempferol, tamarixetin, baicalein, biochanin a, chrysin, 5-hydroxyflavone, 6,2,4-trimethoxyflavone were obtained from sigma-aldrich (st. louis, mo, usa). HPLC grade methanol, ammonium formate and formic acid were purchased from Sigma-Aldrich (St. Louis, MO, USA). Ultra-pure water (18 M Ω) was obtained from a Milli-Q water purification system (Millipore Co., Ltd.). pBR322 plasmid DNA (catalog number SD0041) was obtained from ThermoFisher Scientific.

Plant sample and extraction process

P. quercetorum samples Agnew species were obtained in the rocky and stony regions of the Pervari province of Siirt city in Türkiye's south-east. Dr. Mehmet Fidan, Associate Professor at Siirt University's Faculty of Arts and Sciences' Biology Department, identified the species. For extraction, tissue samples were dried and crushed. Methods outlined in prior research were adapted for our laboratory circumstances for the extraction process [22; 37]

350 mL methanol was added to about 7 g of sample to prepare the extract, and the mixture was kept at room temperature and in the dark on the magnetic stirring over ten days. Then the solution was filtered through a filter paper. Methanol was evaporated by an evaporator device (Heidolph/Heizbad-hei-vap). Resulting samples were stored at -40°C until used.

Purification of human hCA I and II isoenzymes

As mentioned in our previous studies, hCA-I and hCA-II isozymes were purified with the help of sepharose-4B-tyrosine sulfanilamide affinity chromatography [20; 38; 39; 40; 41]. The erythrocyte solution used in the study was obtained from the blood bank in Siirt Ministry of Health Education and Research Hospital. A working temperature of 4°C was used throughout the study to maintain the stability of the enzymes. In purified enzymes and hemolysate, protein content was determined spectrophotometrically at 595 nm wavelength based on the method [42] Enzyme purity was determined by using SDS-polyacrylamide gel electrophoresis [43].

Determination of effect on carbonic anhydrase I-II and acetylcholinesterase enzymes of extracts of *P. quercetorum* Agnew

The activities of the carbonic anhydrase I-II isozymes were determined based on the method described by [44] Verpoorte et al. (1967). In this method, hCA I and II isozymes convert 4-nitrophenylacetate (NPA) to 4- nitrophenolate ion, and resulting product gives absorbance at 348 nm. The increase in absorbance was measured spectrophotometrically for three minutes (Shimadzu, UVmini-1280 UV-VI). The reaction medium without enzyme solution was used as a blank. For determination of the activity of AChE, a spectrophotometric method described by [45] Ellman et al. (1961) was used. In this method, acetylcholine iodine is used as substrate, the reaction was monitored spectrophotometrically at 412 nm. Enzymatic activity was assayed using at least five different inhibitor concentrations to determine IC₅₀ values. The enzyme activity medium which did not have any inhibitor was used as control and its activity was considered 100%. Then, the inhibitor concentration that halved the enzymatic activity was calculated by drawing graph against % activity [19; 40; 41]. K_i values were determined based on the method described by [46] Zhang et al. 2020. K_M and V_{max} values were calculated by drawing Lineweaver-Burk graphs [47].

$$V = \frac{V_{max} \times S}{K_M \times \left(1 + \frac{I}{K_i}\right) + S} \quad (1)$$

According to the equation (1), I is the concentration of the compound, K_i is the inhibition constant, S is the concentration of the substrate, Inhibition constant (K_i) values were calculated using nonlinear regression according to the above equation [46].

Analysis with LC-ESI-MS/MS of extracts of *P. quercetorum* Agnew

Method validation and LC-ESI-MS/MS analysis in study was carried out in Iğdır University Research Laboratory Application and Research Center (ALUM). The values used in Validation parameters (LOD, LOQ, R^2 and Linearity Range etc.) of compounds by LC-ESI-MS/MS method, Yılmaz et al., are partners with our study [48]. To determine the method and to perform the content analysis, 1 mg/mL stock solutions in methanol of 45 standard phenolic compounds were prepared. Generally, the stock solutions diluted to a concentration of 8 $\mu\text{g/mL}$ but scutellarin, hyperocide, quercetin-3- β -d-glucoside, kaempferol-3-glucoside, baicalein, baicalein, 5-hydroxyflavonen and flavone were diluted to 0.8 $\mu\text{g/mL}$ concentration with 50% methanol/water (v/v; 1:1). Nine calibration levels were prepared by serial dilution of the standard mixture containing 45 phenolic compounds to plot the calibration curve with 50% methanol/water (v/v; 1:1). 10 mg of *P. quercetorum* Agnew dry extract was dissolved in 2 mL methanol and the solution was diluted to 2 mg/mL 50% methanol/water (v/v; 1:1). Subsequently, the solution was filtered through 0.45 μm filters and transferred into vials before LC-ESI-MS/MS analysis.

An Agilent Technologies 1260 Infinity II liquid chromatography System combined to a 6460 Triple Quad mass spectrometer was used for quantitative and qualitative analysis of 45 phytochemical compounds. Poroshell 120 EC-C18 (100 mm \times 4.6 mm I.D., 2.7 μm) column was used for the chromatographic separation of the compounds [48]. Mobile phase flow rate, column temperature conditions and different mobile phases additives such as formic acid, ammonium acetate and acetic acid were applied together with acetonitrile, purified water, and methanol mobile phases to achieve the most ideal separation and ionization of the compounds. Thus, 0.1 % formic acid and 5 mM ammonium formate in water A mobile phase and 0.1 % formic acid and 5 mM ammonium formate in methanol B mobile phases were utilized in chromatographic separation. Using a flow rate of 0.4 mL/min, a gradient program of 15% for 1-12 min, 50% for 12-30 min, 90% for 30-32 min,

and 10% for 32-35 min was used in the B mobile phase, respectively. The injection volume was 4.0 μL , and the column temperature was maintained at 40°C [49]. An electrospray ionization (ESI) source operating in both negative and positive ionization modes was used to determine the mass-to-charge ratio (m/z) of the compounds. The ESI source parameters were set at capillary voltage to 4000 V, nebulizing gas (N_2) flow to 11 L/min, nebulizer pressure to 15 psi and gas temperature to 300°C to ensure ideal ionization of all compounds and achieve the ideal peak intensity. The precursor and product ions, collision energies and fragmentor voltage of each compound were determined for quantitative measurement as multiple reaction monitoring (MRM).

Mineral matter analysis with ICP-OES of *P. quercetorum* Agnew

This research was conducted out at Siirt University's Science and Technology Application and Research Center. The tests have been adjusted to our laboratory conditions. According to the Berghof microwave digestion speedwave MWS-2 device user manual V. 5.1, 0.3743 g of moisture-free ground material was weighed for the PTFE wet digestion system, and 6 mL nitric acid (65%) and 2 mL hydrogen peroxide (30%) were added to the sample. The sample was digested for 15+15 minutes at 180°C. After freezing, the samples were moved to volume containers with a final volume of 20 mL [50].

Two repetitive readings were performed with ICP-OES (device Perkin Elmer ICP-OES Optima 2100 DV) under the experimental conditions (Plasma power, 1300 W; nebulizer flow, 0.80 L/min; plasma flow, 15 L/min; auxiliary flow, 0.2 L/min; plasma view, axial; sample flow rate, 1.50 mL/min; delay time, 60 sec; source equilibration delay, 15 sec; plasma conditions, same for all elements; nebulizer start-up, Instant). Calibration solutions were prepared at five different concentrations ranging from 25.00 to 1000.00 ppb [51; 52].

DNA protective activity of extracts of different tissues of *P. quercetorum* Agnew

pBR322 plasmid DNA was used to measure the deleterious effects of Fenton's solution and protective effect of *P. quercetorum* Agnew extracts on DNA conformation. Extracts of leaf and flower tissues of the plant *P. quercetorum* Agnew were addressed to repair the DNA damage. Plant tissue extracts were prepared in a solution of a mixture of methanol (10%) and water (90%). Three different extract concentrations (1 mg/mL, 2 mg/mL, 3 mg/mL) were applied for each different tissue and for experimental design, negative (plasmid DNA only) and positive control (Fenton + plasmid DNA) groups were created. In addition, to compared results, a commercial extract with known

biological activities, antiviral, antibacterial, anti-inflammatory, antioxidant effects and DNA damage protective activity such as rosmarinic acid and alpha-tocopherol were used at a concentration of 1 mg/mL [53].

Accordingly, the reaction mixtures to be incubated was composed of 3 μ L of pBR322 plasmid DNA, 5 μ L of Fenton's solution (30 mM H₂O₂, 50 mM ascorbic acid and 80 mM FeCl₃) and 5 μ L from different concentrations (1 mg/mL, 2 mg/mL, 3 mg/mL) of plant extracts were taken and the final volume was completed to 20 μ L with distilled water. This mixture was then incubated at 37°C for 30 minutes. After incubation, 5 μ L of 6x loading dye was added to the reaction mixture. 10 μ L of the mixture was taken and loaded onto a 0.8% agarose gel stained with EtBr. The agarose gel was run at 100 volts for 60 minutes. Then the gel image was taken with the gel imaging device.

ACKNOWLEDGMENTS

We would also like to thank Siirt University, Science and Technology Application and Research Center for ICP-OES studies. Method validation and LC-ESI-MS/MS analysis in study was carried out in Iğdır University Research Laboratory Application and Research Center (ALUM).

REFERENCES

1. S. Alp, *Bagbahce J. Sci* **2017**, *4*(3), 14-19.
2. I. Uce, M. Tunçturk, *Res. J. Biol. Sci* **2014**, *7*(2), 21-25.
3. N. Aztopal, B. Cevatemre, M. Sarımahmut, F. Arı, E. Dere, M.Z. Ozel, M. Fırat M, E. Ulukaya, *Oncology Letters* **2016**, *12*, 1429-1437.
4. A. A. Taherpour, K. Kheradmand, *As. J. Chem* **2008**, *20*(8), 6335-6341.
5. G. S. Karatoprak, M. Fırat, M. Kosar, *Mersin University J. Health Sci* **2018** *11*(2), 174-183.
6. F. Arı, S. Celikler, D. Karakas, B. Cevatemre, M. Fırat. E. Ulukaya, *J. Clin. Exp. Invest* **2017**, *8*(1), 22-30.
7. O. I. Kufrevioglu, E. Keha, 'Biochemistry', ISBN: 9789758986200, Türkiye, **2018**.
8. O. D. Lopina, in 'Chapter 11: Enzyme inhibitors and activators' Intech, **2017**, p243-257.
9. K. A. Askar, A. C. Kudi, A. J. Moody, *Can. J. Vet. Res* **2011**, *75*(4), 261-270.
10. J. Grutzendler, J. C. Morris, *Drugs* **2001**, *61*(1), 41-52.
11. V. Zarotsky, J. J. Sramek, N. R. Cutler, *Am. J. Health Syst. Pharm* **2003**, *60*(5), 446-452.
12. K. Sharma, *Mol. Med. Reports* **2019**, *20*, 1479-1487.
13. D. M. Quinn, *Chem. Rev* **1987**, *87*, 955-979.
14. A. Rahman, M. I. Choudhary, *Pure Appl. Chem* **2009**, *73*(3), 555-560.
15. S. Lee, D. Lee, J. Baek, E. B. Jung, J. Y. Baek, I. K. Lee, T. S. Jang, K. S. Kang, K. H. Kim, *Pharm. Biol* **2017**, *55*(1), 2205-2210.

16. K. Hostettmann, A. Borloz, A. Urbain, A. Marston, *Cur. Org. Chem*, **2006**, *10*(8), 825-847.
17. D. Vullo, S. Del Prete, A. Nocentini, S. M. Osman, Z. Al Othman, C. Capasso, M. Bozdog, F. Carta, P. Gratteri, C. T. Supuran, *Bioorg. Med. Chem* **2017**, *25*(3), 1260-1265.
18. U. M. Kocyigit, Y. Budak, M. G. Gürdere, N. Duru, P. Taslimi, I. Gulcin, M. Ceylan, *Monatsh. Chem* **2019**, *150*, 721-731.
19. M. Boztas, Y. Cetinkaya, M. Topal, I. Gulcin, A. Menzek, E. Sahin, M. Tanc, C. T. Supuran, *J. Med. Chem* **2015**, *58*(2), 640-650.
20. H. Goksu, M. Topal, A. Keskin, M. S. Gultekin, M. Celik, I. Gulcin, M. Tanc, C. T. Supuran, *Arch. Pharm* **2016**, *349*(6), 466-74.
21. E. Akkemik, B. Cicek, Y. Camadan, U. Calisir, Z. Onbasioglu, *J. Biochem. Mol. Toxicol* **2018**, *32*(3), e22032.
22. S. U. Chon, Y. M. Kim, Y. J. Park, B. G. Heo, Y. S. Park, S. Gorinstein, *Eur. Food Res. Technol.* **2009**, *230*(2), 231-237.
23. M. Krasavin, M. Korsakov, Z. Zvonaryova, E. Semyonychev, T. Tuccinardi, S. Kalinin, M. Tanc, C. T. Supuran, *Bioorg. Med. Chem* **2017**, *25*(6), 1914-1925.
24. B. Tepe, S. Degerli, S. Arslan, E. Malatyali, C. Sarikurku, *Phytoter* **2011**, *82*(2), 237-246.
25. F. Tao, B. Gonzales-Flecha, L. Kobzik, *Free Rad. Biol. Med* **2003**, *35*(4), 327-340.
26. S. Durdagi, M. Senturk, D. Ekinci, H. T. Balaydin, S. Goksu, O. I. Kufrevioglu, A. Innocenti, A. Scozzafava, C. T. Supuran, *Bioorg. Med. Chem* **2011**, *19*(4), 1381-1389.
27. E. Akkemik, U. Calisir, B. Cicek, *J. BAUN Inst. Sci. Technol* **2017**, *19*(2), 192-199.
28. Y. Camadan, B. Cicek, S. Adem, U Calisir, E. Akkemik, *J. Biomol. Struct. Dyn.* **2021**, 1-10.
29. M. I. Hassan, B. Shajee, A. Waheed, F. Ahmad, W. S. Sly, *Bioorg Med Chem.* **2013**, *21*(6), 1570-1582.
30. J. Wiesner, Z. Kriz, K. Kuca, D. Jun, J. Koca J, *J. Enzyme Inhib. Med Chem.* **2007**, *22*, 417-424.
31. D. Szwajgier, *Annals Agri Env Med.* **2015**, *22*(4), 690-694.
32. M. Boukhris, M. S. J. Simmonds, S. Sayadi, M. Bouaziz, *Phytother. Res* **2013**, *27*(8), 1206-1213.
33. D. K. Bisset, R. A. Antonia, L. W. B. Browne, *J. Fluid Mech.* **1990**, *218*, 439-461.
34. A. B. Hashkavayi, S. Hashemnia, S. Osfouri, *Microchemical J.* **2020**, *159*, 105455.
35. S. M. Hadi, S. H. Bhat, A. S. Azmi, S. Hanif, U. Shamim, M. F. Ullah, *Semin. Cancer Biol* **2007** *17*(5), 370-376.
36. S. Kumar, S. Sharma, S. K. Chattopadhyay, *Fitoterapia* **2013**, *89*, 86-125.
37. A. S. Yaglioglu, F. Eser, S. Tekin, A. Onal, *Fron. Life Sci* **2016**, *9*(1), 69-74.
38. Y. Akbaba, E. Bastem, F. Topal, I. Gulcin, A. Maras, S. Goksu, *Arch. Pharm* **2014**, *347*, 950-957.

39. H. Gocer, A. Akıncıoğlu, S. Goksu, I. Gulcin, C. T. Supuran, *J. Enzyme Inhib. Med. Chem* **2015**, *30*(2), 316–320.
40. J. Smirnovienė, V. Smirnovas, D. Matulis, *Anal Biochem* **2017**, *522*, 61-72.
41. E. Akkemik, A. Aybek, I. Felek, *Appl. Ecol. Environ. Res.* **2019**, *17*(6), 14699-14713.
42. M. M. Bradford, *Anal Biochem* **1976**, *72*, 248-254.
43. U. K. Laemmli, *Nature* **1970**, *227*, 680-685.
44. J. A. Verpoorte, S. Mehta, J. T. Edsall, *J. Biol. Chem* **1967**, *242*(422), 1-9.
45. G. L. Ellman, K. D. Courtney, V. Andres, R. M. Featherston, *Biochem. Pharmacol* **1961**, *7*(2), 88-95.
46. X. Zhang, P. Feng, X. Gao, B. Wang, C. Gou, R. Bian, *Pharm. Biol* **2020**, *58*(1), 247-252.
47. H. Lineweaver, D. Burk, *J. Am. Chem. Soc.*, **1934**, *56*, 658.
48. Ü. Yırtıcı, A. Ergene, M.N. Atalar, & Ş. Adem, *South African Journal of Botany*, **2022**, *144*, 58-71.
49. M.A. Yılmaz, *Ind. Crops Prod.* **2020**, *149*, 112347.
50. http://www.onlinecas.com/Berghof/mWS3/Micronde%20MWS2/applications%20MWS2/AR_MWS-2_Food-Pharma-Cosmetics_140405.pdf, 14.07.20-15:30
51. K. W. Barnes, E. Debrah, *Atomic Spectroscopy* **1997**, *18*, 41-54.
52. https://www.perkinelmer.com/PDFs/downloads/ATL_BarnesFoodAtomicSpec.pdf, **2020b**, Accession date: 14.07.20-15:32.
53. C. Li, L. Chen, J. Chen, *Mol. Cell Biol* **2002**, *22*(21), 7562-7571.

THE INFLUENCE OF THE DISTILLATION PROCESS ON THE CONTENT OF METALS IN HOME- AND INDUSTRIALLY-BREWED ALCOHOLIC BEVERAGES – RISK ASSESSMENT TO HUMAN HEALTH

Norbert MUNTEAN^{a,b}, Tiberiu FRENȚIU^{a,b}, Gábor RÁKOS^a,
Enikő COVACI^{a,b,*}

ABSTRACT. The aim of this study was to assess the influence of the distillation processes on the content of Al, Ca, Cd, Co, Cr, Cu, Fe, Mg, Mn, Ni, Pb and Zn in 18 home-brewed fruit spirits, originating from different locations of Romania, and 3 industrially-brewed spirits and 19 cognacs. Metals quantification was achieved by inductively coupled plasma optical emission spectrometry (ICP-OES) after sample digestion. The study revealed higher metals concentration in the home-brewed spirits, compared to the industrially-brewed ones, with concentrations of Cu, Fe, Al and Zn in most of the samples above the Alcohol Measures for Public Health Research Alliance (AMPHORA) project set threshold in recorded alcoholic beverages. However, no risk to human health was found by a moderate consumption of the analyzed alcoholic beverages (100 mL/day) as respects to long-term non-carcinogenic health risk. The Principal Components Analysis (PCA) indicated a wide dispersion of the analyzed alcoholic beverages according to their elemental composition. The two-dimensional PCA representation after Varimax rotation indicated a group of elements of natural origin (Ca, Mg, Al, Cd, Mn, Pb), and another of trace elements (Co, Cr, Ni, Zn, Fe) originating from the distillation equipment. Copper however, was associated both with the raw material and the distillation equipment.

Keywords: *alcoholic beverage, human health risk assessment, Principal Component Analysis*

^a Babes-Bolyai University, Faculty of Chemistry and Chemical Engineering, 11 Arany Janos str., RO-400028, Cluj-Napoca, Romania

^b Research Center for Advanced Chemical Analysis, Instrumentation and Chemometrics, 11 Arany Janos str., RO-400028, Cluj-Napoca, Romania,

* Corresponding author: eniko.covaci@ubbcluj.ro



INTRODUCTION

According to the World Health Organization (WHO) the yearly average pure alcohol consumption in Romania is 12.6 L, from which 56%, 28% and 16% as beer, wine and spirits, respectively. In the same study it was revealed that of the 12.6 L alcohol consumed 10.4 L originates from recorded sources (store-bought) and 2.2 L from unrecorded ones (non-commercial alcohols), obtained in small scale distilleries or at home [1]. Moreover, until recently there were no legislation related to maximum admitted concentrations of metals in distilled beverages, except for wines, set by the International Organization of Vine and Wine (OIV) [2]. The maximum limits of metals in recorded alcohol were established for the first time in 2011 by the Alcohol Measures for Public Health Research Alliance (AMPHORA) project, funded by the European Community's Seventh Framework Programme [3].

Unrecorded alcoholic beverages may pose a great health risk concern as they could contain many toxic compounds, such as methanol, acetaldehyde, ethyl carbamate and even toxic metals [4]. The metals in alcoholic beverages may originate from the raw materials, substances added during brewing, the brewing equipment, bottling, aging and storage [4–6]. The metal concentration in raw materials is influenced by the soil [7], pollution of the environment and agrochemical treatments, like fungicides, pesticides and fertilizers [6]. These treatments contribute to the increase of Cd, Cu, Mn, Pb and Zn content in the final product [8]. In several studies it was pointed out that in industrially produced brandies Mn and Cu may also originate in higher quantities from the oak chips used for aging [9], or from the oak wood casks that they are stored in for aging [10].

Although Fe, Mn and Zn are essential for human health, in elevated concentrations they may be harmful, and thus, the United States Environmental Protection Agency (U.S. EPA) advises an oral reference dose (RfDo) of 0.7, 0.14 and 0.3 mg/kg body weight/day, respectively [11–13]. On the other hand, Cd and Pb are considered as priority hazardous metals with RfDo of 0.001 and 0.00015 mg/kg body weight/day [14, 15], which could cause kidney damage, anaemia, cancer and neurological disorders [16]. Cadmium is considered by the International Agency for Research and Cancer (IARC) group 1 carcinogen, while Pb group 2B carcinogen [17]. Elemental composition of alcoholic beverages, besides their verification from the point of view of human health risk, it can also be used to construct elemental fingerprints of different kinds of beverages, such as whiskies [18, 19], Spanish brandies [20] or *orujo* distillates [21], that could be used in their authentication and differentiation.

The study of metal content and health risk assessment by the consumption of unrecorded alcohol is of interest not only to the Romanian population, but also to the international ones, as they may be shipped across borders. Pantani *et al.* [22] reported that a large proportion of unrecorded alcohol, produced in Finland, Sweden and other northern Countries, is shipped across borders. In some countries home-made alcohol is even slowly transitioning to mass production. Furthermore, the recent trend of online shopping, which circumvents alcohol availability regulations, increases their availability and affordability, as they are sold at a much cheaper price [3,23]. Thus, the quality assessment of home or small scale brewed alcoholic beverages could be considered an issue at global level.

The aim of this study was to evaluate the influence of the distillation processes on the content of several elements, including priority hazardous metals (Cd, Pb), in home- and industrially-brewed spirits, and cognacs. The determinations were carried out by inductively coupled plasma optical emission spectrometry (ICP-OES) after bringing the samples to dryness and redissolving in nitric acid. The risk assessment to human health, especially of the priority hazardous metals, ingested with the alcoholic beverages under study, was evaluated according to the target hazard quotient (THQ) and total THQ (TTHQ) approach. Also, possible correlations between different metals in the analysed alcoholic beverages were investigated using Principal Component Analysis.

RESULTS AND DISCUSSION

Figures of merit and method validation

Table 1 presents the limits of detection (LODs) in alcoholic beverages obtained by the ICP-OES method for 12 metals. The LODs of elements were in the range 0.0003(Mg)–0.0055(Ni) mg L⁻¹. The LODs were 5 and 7 times lower than the maximum recommended concentration of Cd and Co in recorded alcohol, and more than 10 times lower for the other metals, set by the AMPHORA project [3]. Therefore, the ICP-OES method is adequate for the quantification of the 12 metals in distilled alcoholic beverages.

Table 1. Figures of merit of the ICP-OES method for the determination of 12 metals in alcoholic beverages

Element	Wavelength (nm)	Parameters of the calibration curve		LOD (mg L ⁻¹) ^a	LOQ (mg L ⁻¹) ^b
		Slope (L mg ⁻¹)	Correlation coefficient		
Al	396.152	0.0000129	0.9986	0.0014	0.0042
Ca	422.673	0.0000024	0.9996	0.0004	0.0012
Cd	214.438	0.0000375	0.9999	0.0014	0.0042
Co	237.862	0.0000752	0.9997	0.0021	0.0063
Cr	267.716	0.0000330	0.9999	0.0015	0.0045
Cu	324.754	0.0000054	0.9997	0.0030	0.0090
Fe	259.940	0.0000252	0.9999	0.0006	0.0018
Mg	285.213	0.0000244	0.9995	0.0003	0.0009
Mn	260.569	0.0000091	0.9998	0.0004	0.0012
Ni	341.476	0.0000281	0.9991	0.0055	0.0165
Pb	220.351	0.0000040	0.9994	0.0032	0.0096
Zn	213.856	0.0000179	1.0000	0.0042	0.0126

^a LOD was calculated using the 3 σ criterion and sample preparation protocol [24];

^b LOQ was considered as 3*LOD.

The accuracy of the ICP-OES method, was evaluated by fortifying the samples with the 12 metals. The recovery degrees were in the range 84–117% with a trueness of up to $\pm 20\%$. Thus, the ICP-OES method ensures accurate results in terms of metals determination in digested spirits and cognacs. The relative standard deviation was in the range 1.1–10.9%.

Content of major and trace metals in spirits and cognacs

Tables 2–5 presents the concentration of major and trace metals in home- and industrially-brewed spirits, and cognacs, respectively. It can be seen that the concentrations of metals were generally higher in home-brewed spirits compared to the industrially-brewed ones. The *t test* [24] revealed no significant differences in terms of major metals concentration (Ca, Mg, Cu, Fe, Al and Zn) in the home-brewed spirits from plums (samples 1–6), apples (samples 7–11) and grapes (samples 12–16), for 95% confidence level ($t_{\text{calc}} = 0.020\text{--}1.232 < t_{\text{tab}} = 2.32$). Also, it was revealed that there were no differences between beverages from different sources produced between 2016 and 2020. The concentrations of Ca and Mg in the home-brewed spirits were much higher (0.73–25.8 and 0.076–15.1 mg L⁻¹), compared to the industrially-brewed ones (0.13–0.65 and <0.0003(LOD)–0.11 mg L⁻¹). The difference could be attributed to the water used for the dilution of distillates.

THE INFLUENCE OF THE DISTILLATION PROCESS ON THE CONTENT OF METALS IN HOME- AND INDUSTRIALLY-BREWED ALCOHOLIC BEVERAGES - RISK ASSESSMENT TO HUMAN HEALTH

The concentration of Ca and Mg in the home-brewed spirits under study were similar to those reported by Iwegbue *et al.* [25] and Bora *et al.* [26] (0.62–21.74 mg L⁻¹ Ca and 0.09–11.26 mg L⁻¹ Mg) in distillates originating from Nigeria.

Table 2. Concentrations ± C.I.^a (mg L⁻¹) of major metals in home- and industrially-brewed spirits

	Sample nr.	Ca	Mg	Cu	Fe	Al	Zn	
Home-brewed	1	10.3 ± 0.4	2.90 ± 0.30	4.74 ± 0.58	7.55 ± 0.44	0.41 ± 0.04	0.22 ± 0.01	
	2	2.16 ± 0.18	0.66 ± 0.04	7.88 ± 0.46	1.57 ± 0.14	0.46 ± 0.05	0.073 ± 0.004	
	3	5.48 ± 0.54	2.27 ± 0.17	9.58 ± 1.09	1.80 ± 0.08	0.14 ± 0.01	2.69 ± 0.30	
	4	7.59 ± 0.61	0.93 ± 0.03	1.56 ± 0.18	22.06 ± 2.01	1.50 ± 0.05	0.64 ± 0.06	
	5	5.97 ± 0.39	1.96 ± 0.12	5.54 ± 0.86	2.87 ± 0.24	0.46 ± 0.05	2.30 ± 0.24	
	6	2.48 ± 0.14	0.35 ± 0.03	5.47 ± 0.41	1.68 ± 0.17	0.076 ± 0.008	0.048 ± 0.004	
	7	12.0 ± 0.7	3.84 ± 0.24	0.53 ± 0.10	21.03 ± 1.41	1.23 ± 0.15	0.46 ± 0.03	
	8	1.13 ± 0.09	0.15 ± 0.01	3.14 ± 0.31	2.42 ± 0.13	0.17 ± 0.02	0.17 ± 0.02	
	9	0.73 ± 0.06	0.076 ± 0.005	1.86 ± 0.16	0.066 ± 0.004	0.020 ± 0.001	0.061 ± 0.004	
	10	6.16 ± 0.57	1.13 ± 0.04	7.61 ± 0.35	16.7 ± 0.63	1.09 ± 0.04	0.96 ± 0.05	
	11	1.42 ± 0.10	0.19 ± 0.02	8.73 ± 0.73	0.18 ± 0.01	0.06 ± 0.01	0.18 ± 0.02	
	12	12.4 ± 0.9	1.89 ± 0.18	3.09 ± 0.15	3.97 ± 0.24	0.26 ± 0.04	0.20 ± 0.01	
	13	8.17 ± 0.40	0.53 ± 0.04	7.55 ± 0.53	21.7 ± 0.8	1.15 ± 0.10	2.57 ± 0.19	
	14	16.1 ± 1.8	2.19 ± 0.16	6.97 ± 0.47	5.65 ± 0.46	0.59 ± 0.03	0.38 ± 0.04	
	15	3.31 ± 0.12	0.61 ± 0.05	6.69 ± 0.46	7.19 ± 0.41	0.34 ± 0.03	0.28 ± 0.01	
	16	1.60 ± 0.16	0.27 ± 0.03	6.38 ± 0.63	0.030 ± 0.002	0.086 ± 0.005	0.20 ± 0.02	
	17	25.8 ± 1.8	15.1 ± 0.64	0.50 ± 0.07	4.64 ± 0.46	2.24 ± 0.17	0.76 ± 0.04	
	18	8.89 ± 0.37	2.38 ± 0.16	5.97 ± 0.24	22.1 ± 1.2	1.35 ± 0.07	0.78 ± 0.07	
		Conc. range	0.73–25.8	0.076–15.1	0.50–9.58	0.030–22.1	0.020–2.34	0.048–2.69
	Average	7.32	2.08	5.21	7.96	0.65	0.72	
	SD	6.41	3.43	2.82	8.50	0.63	0.87	
Industr.-brewed	19	0.13 ± 0.01	<0.0003	0.016 ± 0.002	<0.0006	0.055 ± 0.004	0.017 ± 0.003	
	20	0.30 ± 0.03	0.059 ± 0.005	0.022 ± 0.002	0.020 ± 0.003	0.088 ± 0.004	0.037 ± 0.005	
	21	0.65 ± 0.04	0.11 ± 0.01	0.061 ± 0.007	0.019 ± 0.003	0.116 ± 0.009	0.032 ± 0.004	
		Conc. range	0.13–0.65	<0.0003–0.11	0.016–0.061	<0.0006–0.020	0.055–0.116	0.017–0.037
		Average	0.36	0.086	0.033	0.020	0.086	0.028
	SD	0.26	0.038	0.024	0.001	0.031	0.010	

^aC.I. – is the confidence interval for n = 3 replicate measurements for 95% confidence level

Table 3. Concentrations \pm C.I.^a (mg L⁻¹) of trace metals in home- and industrially-brewed spirits

	Sample nr.	Cr	Cd	Co	Mn	Ni	Pb	
Home-brewed	1	<0.0015	0.012 \pm 0.001	<0.0021	0.13 \pm 0.01	<0.0055	<0.0032	
	2	0.070 \pm 0.10	<0.0014	<0.0021	0.026 \pm 0.001	<0.0055	<0.0032	
	3	<0.0015	<0.0014	<0.0021	0.032 \pm 0.002	<0.0055	<0.0032	
	4	0.008 \pm 0.002	0.005 \pm 0.001	0.015 \pm 0.003	0.44 \pm 0.04	0.008 \pm 0.002	0.038 \pm 0.004	
	5	<0.0015	0.004 \pm 0.001	<0.0021	0.058 \pm 0.003	<0.0055	<0.0032	
	6	0.025 \pm 0.002	<0.0014	0.020 \pm 0.002	0.015 \pm 0.001	0.051 \pm 0.004	0.065 \pm 0.008	
	7	0.067 \pm 0.006	0.008 \pm 0.001	0.008 \pm 0.002	0.18 \pm 0.01	<0.0055	<0.0032	
	8	<0.0015	<0.0014	<0.0021	0.029 \pm 0.002	<0.0055	<0.0032	
	9	<0.0015	<0.0014	<0.0021	0.014 \pm 0.001	0.007 \pm 0.001	<0.0032	
	10	0.016 \pm 0.002	<0.0014	0.015 \pm 0.001	0.29 \pm 0.02	0.017 \pm 0.004	0.064 \pm 0.005	
	11	<0.0015	<0.0014	<0.0021	0.032 \pm 0.003	<0.0055	<0.0032	
	12	<0.0015	<0.0014	<0.0021	0.030 \pm 0.001	<0.0055	<0.0032	
	13	0.019 \pm 0.003	0.005 \pm 0.001	0.017 \pm 0.004	0.17 \pm 0.01	0.018 \pm 0.002	0.43 \pm 0.03	
	14	0.022 \pm 0.004	0.005 \pm 0.001	<0.0021	0.16 \pm 0.01	<0.0055	0.042 \pm 0.006	
	15	<0.0015	<0.0014	<0.0021	0.059 \pm 0.005	<0.0055	<0.0032	
	16	0.008 \pm 0.005	<0.0014	0.010 \pm 0.001	0.016 \pm 0.002	0.024 \pm 0.002	<0.0032	
	17	<0.0015	0.042 \pm 0.003	<0.0021	0.65 \pm 0.06	<0.0055	0.67 \pm 0.07	
	18	<0.0015	0.009 \pm 0.002	0.010 \pm 0.002	0.26 \pm 0.02	<0.0055	0.038 \pm 0.007	
		<i>Conc. range</i>	<i><0.0015–0.070</i>	<i><0.0014–0.042</i>	<i><0.0021–0.020</i>	<i>0.014–0.65</i>	<i><0.0055–0.051</i>	<i><0.0032–0.67</i>
	<i>Average</i>	<i>0.029</i>	<i>0.011</i>	<i>0.014</i>	<i>0.14</i>	<i>0.020</i>	<i>0.19</i>	
	<i>SD</i>	<i>0.025</i>	<i>0.013</i>	<i>0.005</i>	<i>0.17</i>	<i>0.016</i>	<i>0.25</i>	
Industr.-brewed	19	<0.0015	<0.0014	0.012 \pm 0.002	<0.0004	0.027 \pm 0.003	<0.0032	
	20	<0.0015	<0.0014	<0.0021	<0.0004	0.025 \pm 0.003	<0.0032	
	21	0.108	<0.0014	<0.0021	<0.0004	0.033 \pm 0.002	<0.0032	
		<i>Conc. range</i>	<i><0.0015–0.108</i>	<i><0.0014</i>	<i><0.0021–0.012</i>	<i><0.0004</i>	<i>0.025–0.033</i>	<i><0.0032</i>
		<i>Average</i>	<i>-</i>	<i><0.0014</i>	<i>-</i>	<i>-</i>	<i>0.028</i>	<i><0.0032</i>
		<i>SD</i>	<i>-</i>	<i>-</i>	<i>-</i>	<i>-</i>	<i>0.004</i>	<i>-</i>

^aC.I. – is the confidence interval for n = 3 replicate measurements for 95% confidence level

Table 4. Concentrations \pm C.I.^a (mg L⁻¹) of major metals in industrially produced cognacs

Sample nr.	Ca	Mg	Cu	Fe	Al	Zn
22	0.67 \pm 0.07	0.11 \pm 0.01	7.65 \pm 0.40	1.21 \pm 0.11	0.046 \pm 0.004	0.078 \pm 0.009
23	1.19 \pm 0.10	2.59 \pm 0.33	11.1 \pm 1.1	1.52 \pm 0.14	0.079 \pm 0.006	0.11 \pm 0.01
24	0.59 \pm 0.07	0.21 \pm 0.03	8.66 \pm 0.61	6.29 \pm 0.49	0.038 \pm 0.002	0.18 \pm 0.02
25	0.59 \pm 0.05	0.066 \pm 0.010	7.88 \pm 0.42	0.96 \pm 0.10	0.032 \pm 0.003	0.10 \pm 0.01
26	0.36 \pm 0.02	0.072 \pm 0.006	11.9 \pm 1.3	3.76 \pm 0.41	0.030 \pm 0.003	0.15 \pm 0.01
27	0.20 \pm 0.01	0.020 \pm 0.003	11.6 \pm 0.8	7.08 \pm 0.50	0.032 \pm 0.004	0.14 \pm 0.01
28	0.57 \pm 0.05	0.086 \pm 0.013	12.5 \pm 1.0	11.4 \pm 0.65	0.19 \pm 0.02	0.25 \pm 0.02
29	1.09 \pm 0.09	0.17 \pm 0.02	10.0 \pm 0.6	9.58 \pm 1.13	0.078 \pm 0.005	0.24 \pm 0.02
30	0.25 \pm 0.01	0.081 \pm 0.009	7.29 \pm 0.60	0.81 \pm 0.11	0.029 \pm 0.003	0.26 \pm 0.01
31	0.89 \pm 0.09	0.071 \pm 0.008	11.4 \pm 0.6	1.20 \pm 0.10	0.028 \pm 0.004	0.15 \pm 0.02
32	0.57 \pm 0.06	0.11 \pm 0.01	11.1 \pm 1.0	3.10 \pm 0.30	0.060 \pm 0.008	0.14 \pm 0.01
33	0.73 \pm 0.09	0.12 \pm 0.01	50.6 \pm 3.2	0.31 \pm 0.03	0.041 \pm 0.003	0.36 \pm 0.04
34	0.46 \pm 0.04	0.16 \pm 0.01	51.3 \pm 2.7	1.94 \pm 0.18	0.054 \pm 0.007	0.38 \pm 0.03
35	4.65 \pm 0.30	2.57 \pm 0.19	21.5 \pm 2.0	2.75 \pm 0.31	0.072 \pm 0.003	0.24 \pm 0.02
36	4.88 \pm 0.43	2.48 \pm 0.27	20.3 \pm 1.6	1.01 \pm 0.09	0.11 \pm 0.01	0.20 \pm 0.02
37	4.25 \pm 0.27	2.38 \pm 0.23	14.0 \pm 1.4	0.20 \pm 0.02	0.081 \pm 0.011	0.11 \pm 0.01
38	5.03 \pm 0.20	2.64 \pm 0.21	22.1 \pm 2.0	1.31 \pm 0.11	0.11 \pm 0.01	0.25 \pm 0.02
39	4.91 \pm 0.39	2.35 \pm 0.24	35.2 \pm 2.5	0.38 \pm 0.03	0.080 \pm 0.013	0.29 \pm 0.04
40	5.07 \pm 0.34	2.52 \pm 0.28	23.3 \pm 3.3	0.32 \pm 0.03	0.13 \pm 0.01	0.32 \pm 0.04
<i>Conc. range</i>	<i>0.20–5.07</i>	<i>0.020–2.64</i>	<i>7.29–51.3</i>	<i>0.20–11.4</i>	<i>0.028–0.19</i>	<i>0.078–0.38</i>
<i>Average</i>	<i>1.94</i>	<i>0.99</i>	<i>18.4</i>	<i>2.90</i>	<i>0.070</i>	<i>0.21</i>
<i>SD</i>	<i>2.01</i>	<i>1.19</i>	<i>13.5</i>	<i>3.30</i>	<i>0.043</i>	<i>0.09</i>

^aC.I. – is the confidence interval for n = 3 replicate measurements for 95% confidence level

The content of Cu in home-brewed spirits was in the range 0.50–9.50 mg L⁻¹, higher than in store-bought alcoholic beverages (0.016–0.061 mg L⁻¹). According to OIV and Italian legislation the maximum permissible concentration of Cu in wine is set to 1 mg L⁻¹ [2] and 10 mg L⁻¹[27], respectively. The content of Cu in home-brewed spirits did not exceed the permissible level set by the Italian legislation, but was over the OIV level. The limit set by the AMPHORA project of 2 mg L⁻¹ [3] was also exceeded by the majority of home-brewed spirits.

Table 5. Concentrations \pm C.I.^a (mg L⁻¹) of trace metals in industrially produced cognacs

Sample nr.	Cr	Cd	Co	Mn	Ni	Pb
22	<0.0015	<0.0014	0.016 \pm 0.003	0.022 \pm 0.002	0.035 \pm 0.004	<0.0032
23	0.012 \pm 0.003	<0.0014	0.014 \pm 0.003	0.128 \pm 0.014	0.035 \pm 0.001	<0.0032
24	0.018 \pm 0.002	<0.0014	0.027 \pm 0.004	0.039 \pm 0.004	0.043 \pm 0.005	<0.0032
25	<0.0015	<0.0014	<0.0021	0.028 \pm 0.003	0.017 \pm 0.003	<0.0032
26	<0.0015	<0.0014	0.011 \pm 0.003	0.026 \pm 0.003	0.029 \pm 0.006	<0.0032
27	0.050 \pm 0.005	<0.0014	0.018 \pm 0.004	0.079 \pm 0.008	0.044 \pm 0.002	<0.0032
28	0.048 \pm 0.006	<0.0014	0.010 \pm 0.002	0.081 \pm 0.011	0.025 \pm 0.004	<0.0032
29	0.036 \pm 0.003	<0.0014	0.011 \pm 0.003	0.083 \pm 0.006	0.021 \pm 0.004	<0.0032
30	<0.0015	<0.0014	<0.0021	0.021 \pm 0.002	0.023 \pm 0.005	<0.0032
31	<0.0015	<0.0014	<0.0021	0.030 \pm 0.002	0.019 \pm 0.003	<0.0032
32	0.011 \pm 0.002	<0.0014	0.020 \pm 0.003	0.029 \pm 0.003	0.043 \pm 0.004	<0.0032
33	0.027 \pm 0.001	<0.0014	<0.0021	0.007 \pm 0.001	0.035 \pm 0.005	0.013 \pm 0.002
34	0.024 \pm 0.005	<0.0014	<0.0021	0.016 \pm 0.001	0.021 \pm 0.003	<0.0032
35	0.011 \pm 0.002	0.008 \pm 0.001	<0.0021	0.040 \pm 0.004	<0.0055	<0.0032
36	0.018 \pm 0.003	<0.0014	<0.0021	0.071 \pm 0.005	<0.0055	0.030 \pm 0.006
37	<0.0015	0.008 \pm 0.001	<0.0021	0.075 \pm 0.006	<0.0055	<0.0032
38	0.019 \pm 0.002	0.006 \pm 0.001	<0.0021	0.093 \pm 0.009	<0.0055	0.013 \pm 0.002
39	0.030 \pm 0.003	0.006 \pm 0.001	0.052 \pm 0.009	0.048 \pm 0.004	0.019 \pm 0.004	0.039 \pm 0.008
40	0.015 \pm 0.002	0.005 \pm 0.001	<0.0021	0.081 \pm 0.004	<0.0055	<0.0032
Conc. range	<0.0015–0.050	<0.0014–0.008	<0.0021–0.052	0.007–0.128	<0.0055–0.044	<0.0032–0.039
Average	0.024	0.007	0.020	0.052	0.029	0.023
SD	0.013	0.001	0.013	0.033	0.010	0.013

^aC.I. – is the confidence interval for n = 3 replicate measurements for 95% confidence level

The high Cu concentration could be explained by the fact that home brewers mainly use copper stills, while industrial distilleries use stainless steel. Adam *et al.* [19] found that the largest amount of Cu (97%) in whiskies originate from the copper stills, while a proportion of only 3% from the barley that is distilled from. Iwegbue *et al.* [25] and Bora *et al.* [26] found concentrations of Cu in store bought spirits in the range 0.71–1.33 and 0.56–1.89 mg L⁻¹, respectively. van Wyk *et al.* [28] found concentrations of Cu in pot stillled spirits up to 8.6 mg L⁻¹, attributed mainly to the distillation process. The Cu concentration in cognacs in our beverages was extremely high, between 7.29 and 51.3 mg L⁻¹.

Ibanez *et al.* [5] pointed out that besides the distillation equipment, Cu may originate from the metallic containers (low-quality steel or Cu alloys) in which the alcoholic beverages are stored, the bottling process, or from added Cu that improves their organoleptic properties.

The concentration of Fe, Al and Zn in the home-brewed spirits were between 0.030–22.1, 0.020–2.34 and 0.048–2.68 mg L⁻¹, respectively, while in those of commercially sold in stores were around 10 times lower. None of the three metals in the store-bought spirits surpassed the threshold of 2 mg L⁻¹, set by the AMPHORA project [3]. The values of Fe, Al, Zn in the majority of home-brewed spirits surpassed this threshold value. In the cognac samples, the concentration of Fe, Al and Zn was found to be up to 11.4 ± 0.65, 0.19 ± 0.02 and 0.38 ± 0.03 mg L⁻¹, respectively, similar to those found by Iwegbue *et al.* [25] and Bora *et al.* [26]. The content of Fe was above the AMPHORA set limit in seven cognac distillates, while the concentrations of Al and Zn were below the threshold values in all distillates of this type.

The concentration of Cd and Pb in the home-brewed spirit samples were in the range <0.0014–0.042 (mean 0.011) and <0.0032–0.67 (mean 0.19) mg L⁻¹. Cd concentration in the analyzed home- and industrially-brewed spirits were below the 0.010 mg L⁻¹ AMPHORA limit [3], with the exception of the home-brewed spirit from plums (sample 1, 0.012 ± 0.001 mg L⁻¹) and cherry (sample 17, 0.042 ± 0.003 mg L⁻¹). Pb concentrations were also below the 0.2 mg L⁻¹ AMPHORA limit [3], with the exception of the home-brewed spirit from grapes (sample 13, 0.43 ± 0.03 mg L⁻¹) and cherry (sample 17, 0.67 ± 0.07 mg L⁻¹). The elevated Pb concentrations in the two samples may originate from the soldering material used in the copper stills. Iwegbue *et al.* [25] found concentrations of Cd and Pb within the permissible levels in their spirit and cognac samples, 0.001–0.030 mg L⁻¹ Cd and 0.08–0.20 mg L⁻¹ Pb, respectively. On the other hand, Bora *et al.* [26] found, in average, Cd and Pb concentrations in their spirits of 0.03 ± 0.02 and 0.30 ± 0.13 mg L⁻¹, respectively, surpassing both the OIV [13] and AMPHORA [3] set limits.

The concentrations of Cr, Co, Mn and Ni were in the <0.0015–0.108, <0.0021–0.020, <0.0004–0.65 and <0.0055–0.051 mg L⁻¹ range, respectively, below the AMPHORA limits, with the exception of one home-brewed spirit (sample 17) in case of Mn (0.65 ± 0.06 mg L⁻¹). Our results were similar to those found by Iwegbue *et al.* [25] and Bora *et al.* [26].

Human health risk assessment

Table 6 presents a summary overview of the oral reference dose (RfDo), the recommended daily intake (RDA) and the maximum admitted concentrations (MACs) of the studied metals in wine, according to German,

Polish, Italian and Australian legislations, in recorded alcohol, according to the AMPHORA project, and in drinking water, set by the U.S. EPA, European Commission and European Food Safety Authority (EFSA).

Table 6. The oral reference dose (RfDo), the recommended daily intake (RDA) and the maximum admitted concentrations (MAC) of the studied elements in wine, recorded alcohol and drinking water

Metal	RfDo (mg/kg b.w./day)	RDA (mg/day)	MAC in wine (mg L ⁻¹)					MAC in recorded alcohol (mg L ⁻¹)	MAC in drinking water (mg L ⁻¹)
			OIV	DE	PL	IT	AU		
Ca	-	1000 [29]	-	-	-	-	-	-	50 [30]
Mg	-	220 in females [29] 260 in males [29]	-	-	-	-	-	-	12 [30]
Cu	0.04 [31]	1.3 in females [32] 1.6 in males [32]	1.00 [2]	5.00 [27]	-	10.00 [27]	5.00 [27]	2.00 [3]	2.0 [33] 0.02 [30]
Fe	0.7 [12]	19.6–58.8 in females [29] 9.1–27.4 in males [29]	-	-	-	-	-	2.00 [3]	0.3 [30,34]
Al	1.0 [35]	-	-	8.0 [27]	-	-	-	2.0 [3]	0.05–0.2 [34]
Zn	0.3 [11]	3.0–9.8 in females [29] 4.2–14.0 in males [29]	5.0 [2]	5.0 [27]	-	-	-	5.0 [3]	5.0 [34] 0.1 [30]
Cr	0.3 [36]	-	-	-	-	-	-	0.5 [3]	0.050 [33] 0.030 [30]
Cd	0.001 [14]	-	0.01 [2]	0.01 [27]	0.03 [27]	-	0.05 [27]	0.01 [3]	0.005 [33] 0.0005 [30]
Co	0.0016 [37]	0.12 [37]	-	-	-	-	-	-	0.01 [28]
Mn	0.14 [13]	3 [38]	-	-	-	-	-	0.50 [3]	0.05 [33,37]
Ni	0.013 [40]	-	-	-	-	-	-	0.20 [3]	0.020 [33] 0.010 [30]
Pb	0.00015 [15]	-	0.15 [2]	0.30 [27]	0.30 [27]	0.30 [27]	0.20 [27]	0.20 [3]	0.010 [33] 0.005 [33]

OIV - International Organization of Vine and Wine; DE – Germany; PL – Poland; IT – Italy; AU – Australia.

Table 7 presents the target hazard quotients (THQ) of each individual metal, and the total THQ (TTHQ) for the home- and industrially-brewed spirits. In terms of industrially-brewed alcohol, there were found no risk of exposure to metals by the consumption of these types of beverages, not even at a high consumption rate (300 mL/day), the highest TTHQ value being 0.0616. On the other hand, in case of the home-brewed spirits, at moderate consumption rate (100 mL/day) three home-brewed spirits were found to pose some health risk (TTHQ>1), samples 10, 13 and 17, due to the high

THE INFLUENCE OF THE DISTILLATION PROCESS ON THE CONTENT OF METALS IN HOME- AND INDUSTRIALLY-BREWED ALCOHOLIC BEVERAGES - RISK ASSESSMENT TO HUMAN HEALTH

content of Pb, which resulted in THQ values of 0.7144, 4.7611 and 7.4611, representing 65, 92 and 98% of TTHQ, respectively. Thus, with the exception of these three samples, there is no health concern by a moderate consumption of the home-brewed spirits for 365 days/year and an exposure period of 57 years.

Table 7. Estimated THQ and TTHQ values from metals exposure by the consumption of the home- and industrially-brewed spirits

	Sample nr.	THQ*										TTHQ*	
		Cu	Fe	Al	Zn	Cr	Cd	Co	Mn	Ni	Pb		
Home-brewed	1	0.1975	0.0180	0.0007	0.0012	0.0000	0.0198	0.0000	0.0015	0.0000	0.0000	0.2387	
	2	0.3281	0.0037	0.0008	0.0004	0.0004	0.0000	0.0000	0.0003	0.0000	0.0000	0.3337	
	3	0.3990	0.0043	0.0002	0.0149	0.0000	0.0000	0.0000	0.0004	0.0000	0.0000	0.4188	
	4	0.0651	0.0525	0.0025	0.0036	0.0000	0.0088	0.0158	0.0053	0.0010	0.4183	0.5730	
	5	0.2306	0.0068	0.0008	0.0128	0.0000	0.0065	0.0000	0.0007	0.0000	0.0000	0.2582	
	6	0.2277	0.0040	0.0001	0.0003	0.0001	0.0000	0.0213	0.0002	0.0065	0.7228	0.9830	
	7	0.0221	0.0501	0.0021	0.0026	0.0004	0.0127	0.0088	0.0022	0.0000	0.0000	0.1008	
	8	0.1306	0.0058	0.0003	0.0009	0.0000	0.0000	0.0000	0.0003	0.0000	0.0000	0.1379	
	9	0.0776	0.0002	0.0000	0.0003	0.0000	0.0000	0.0000	0.0002	0.0009	0.0000	0.0791	
	10	0.3171	0.0398	0.0018	0.0053	0.0001	0.0000	0.0152	0.0035	0.0022	0.7144	1.0994	
	11	0.3638	0.0004	0.0001	0.0010	0.0000	0.0000	0.0000	0.0004	0.0000	0.0000	0.3656	
	12	0.1288	0.0094	0.0004	0.0011	0.0000	0.0000	0.0000	0.0004	0.0000	0.0000	0.1401	
	13	0.3146	0.0517	0.0019	0.0143	0.0001	0.0083	0.0181	0.0020	0.0022	4.7611	5.1744	
	14	0.2902	0.0135	0.0010	0.0021	0.0001	0.0076	0.0000	0.0019	0.0000	0.4672	0.7836	
	15	0.2788	0.0171	0.0006	0.0016	0.0000	0.0000	0.0000	0.0007	0.0000	0.0000	0.2987	
	16	0.2658	0.0001	0.0001	0.0011	0.0000	0.0000	0.0101	0.0002	0.0030	0.0000	0.2805	
	17	0.0208	0.0110	0.0037	0.0042	0.0000	0.0705	0.0000	0.0077	0.0000	7.4611	7.5791	
	18	0.2485	0.0527	0.0023	0.0043	0.0000	0.0150	0.0102	0.0030	0.0000	0.4183	0.7544	
	<i>Min.</i>	<i>0.0208</i>	<i>0.0149</i>	<i>0.0008</i>	<i>0.0055</i>	<i>0.0000</i>	<i>0.0000</i>	<i>0.0000</i>	<i>0.0000</i>	<i>0.0000</i>	<i>0.0791</i>		
	<i>Max.</i>	<i>0.3990</i>	<i>0.0527</i>	<i>0.0037</i>	<i>0.0149</i>	<i>0.0004</i>	<i>0.0705</i>	<i>0.0213</i>	<i>0.0077</i>	<i>0.0065</i>	<i>7.4611</i>	<i>7.5791</i>	
	<i>Average</i>	<i>0.2170</i>	<i>0.0189</i>	<i>0.0011</i>	<i>0.0040</i>	<i>0.0001</i>	<i>0.0083</i>	<i>0.0055</i>	<i>0.0017</i>	<i>0.0009</i>	<i>0.8313</i>	<i>1.0888</i>	
Industrially-brewed	19	0.0007	0.0000	0.0001	0.0001	0.0000	0.0000	0.0127	0.0000	0.0034	0.0000	0.0170	
	20	0.0009	0.0000	0.0001	0.0002	0.0000	0.0000	0.0000	0.0000	0.0032	0.0000	0.0045	
	21	0.0025	0.0000	0.0002	0.0002	0.0006	0.0000	0.0000	0.0000	0.0043	0.0000	0.0078	
		<i>Min.</i>	<i>0.0007</i>	<i>0.0000</i>	<i>0.0001</i>	<i>0.0001</i>	<i>0.0000</i>	<i>0.0000</i>	<i>0.0000</i>	<i>0.0000</i>	<i>0.0032</i>	<i>0.0000</i>	<i>0.0041</i>
		<i>Max.</i>	<i>0.0025</i>	<i>0.0000</i>	<i>0.0002</i>	<i>0.0002</i>	<i>0.0006</i>	<i>0.0000</i>	<i>0.0127</i>	<i>0.0000</i>	<i>0.0043</i>	<i>0.0000</i>	<i>0.0205</i>
		<i>Average</i>	<i>0.0014</i>	<i>0.0000</i>	<i>0.0001</i>	<i>0.0002</i>	<i>0.0002</i>	<i>0.0000</i>	<i>0.0042</i>	<i>0.0000</i>	<i>0.0036</i>	<i>0.0000</i>	<i>0.0098</i>

*THQ and TTHQ values >1 are marked in bold face.

Figure 1 presents the exposure frequency to metals of the analyzed home-brewed spirits at moderate (100 mL/day), high (200 mL/day) and very high consumption (300 mL/day) rate. Exposure frequency was calculated as the number of samples in which THQ for Cu, Cd and Pb, and TTHQ value exceeded the limit value of 1 from the total number of samples. According to our analysis, at moderate consumption, 17% (3 samples) of the home brewed spirits present risk to human health, mainly due to the high content of Pb found in the samples. On the other hand, at high and very high consumption rate, the exposure frequency was 33 and 50%, respectively, due to the cumulative effects of the metals, where the main contribution was found to be Pb and Cu. At a high consumption rate of the home brewed spirits, TTHQ was found being up to 15.1048, while at very high consumption rate, up to 22.6571.

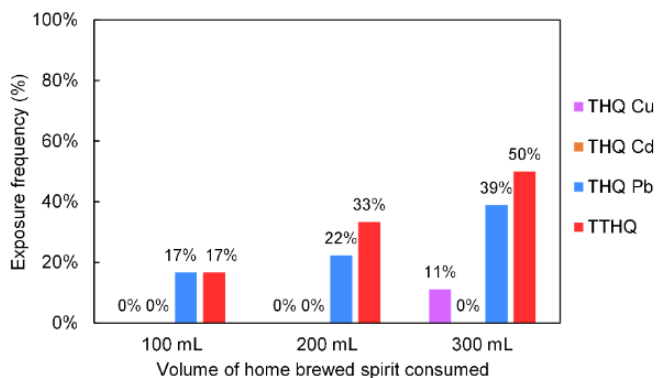


Figure 1. Exposure frequency to metals by consumption of home-brewed spirits in which the THQ and TTHQ values exceeded the value of 1

Elemental profiling of alcoholic beverages by PCA

Table 8 presents the results of the PCA analysis performed on the home- and industrially-brewed spirits and cognacs. The alcoholic beverages are characterized by four PCs, which explains ~79% of the elemental composition variability. The PC1 (45.5%), containing Ca, Mg, Al, Cd, Mn and Pb (0.75–0.95), was attributed to natural factors, such as water used in the distillation process. It can be observed the presence of the two priority hazardous elements (Cd, Pb), which leads to the idea that they could have a natural origin, but could also be associated with the fermentation and distillation conditions, considering that they were found in higher concentrations in the home-brewed spirits. The next 3 factors (PC2–PC4), describing 33.7% of the

variability, was associated with the distillation equipment material, because it contains Co and Ni (PC2, 14.1%), Fe, Cu and Al (PC3, 11.2%), and Zn and Cr (PC4, 8.4%). These three factors characterize primarily the industrially-brewed beverages, in which higher concentrations have been found, and which suggests that the distillation equipment was made of stainless steel. It is interesting to note that although Cu was found in high concentrations in the home-brewed spirits and in the industrially-brewed cognacs from wine, it has only an average influence on the characteristics of the alcoholic beverages analyzed (loading factor -0.61 in PC3, 11.2%). This demonstrates that the source of Cu is not well defined, and could be attributed to the raw material (wine) and the distillation equipment material. This is also supported by the fact that two of the elements (Fe and Al) in PC3 could be associated with their natural presence in wine.

Table 8. Principal components with eigenvalues > 1 and factor loadings of parameters after auto-scaling and Varimax rotation^a that describe the elements variability in the home- and industrially brewed spirits and cognacs

Element/Parameter	PC1	PC2	PC3	PC4
Ca	0.84	-0.29	0.25	0.14
Mg	0.95	-0.18	-0.06	0.01
Cu	-0.06	0.31	<i>-0.61</i>	0.18
Fe	0.20	0.21	0.85	0.29
Al	0.75	-0.02	<i>0.59</i>	0.17
Zn	0.15	0.03	0.31	0.80
Cr	-0.07	0.27	0.30	<i>-0.61</i>
Cd	0.97	-0.13	-0.02	0.00
Co	0.01	0.87	0.07	0.02
Mn	0.84	0.01	0.41	0.11
Ni	-0.27	0.75	-0.16	-0.30
Pb	0.85	0.13	0.09	0.19
Eigenvalue	5.45	1.69	1.35	1.01
Total variance (%)	45.5	14.1	11.2	8.4
Cumulative (%)	45.5	59.6	70.8	79.3

^a Strong relationship loading values > 0.70 are in bold face; moderate values between 0.50–0.70 are marked in italics; the values < 0.50 corresponding to a weak relationship are written with regular font [40]

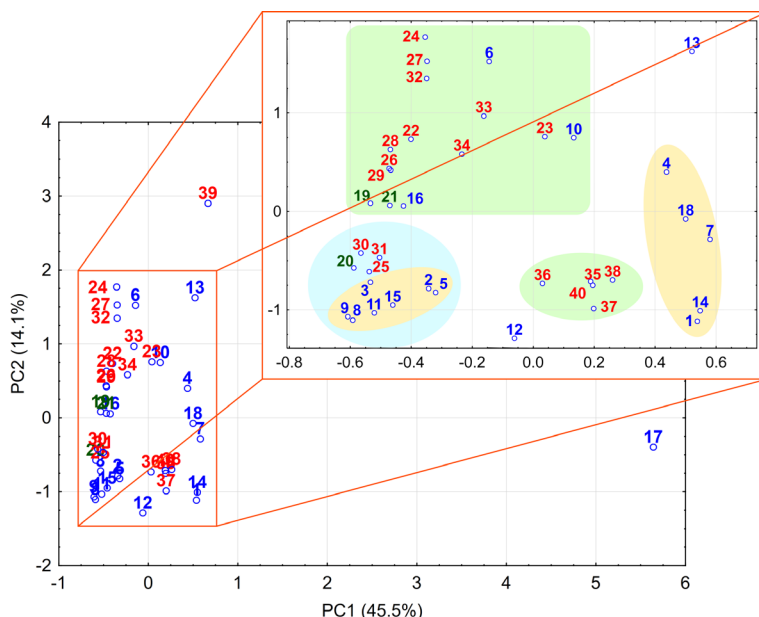


Figure 2. Two-dimensional PCA after auto-scaling and Varimax rotation of the analyzed home-brewed (marked in red) and industrially-brewed spirits (marked in green), and industrially-brewed cognacs (marked in blue)

Figure 2 shows the beverages clustering based on the two-dimensional Varimax rotated PCA after auto-scaling of the original data. According to Figure 1, there is a wide dispersion of alcoholic beverages, but can be observed a classification on clusters and sub-clusters according to their origin. Thus, a well-defined cluster of home-brewed spirits, and two of the industrially-brewed alcoholic beverages can be observed, one that groups cognacs and spirits, and another that groups only cognacs. A third group contains both industrially- and home-brewed beverages.

Figure 3 presents the two-dimensional PCA grouping of the parameters after auto-scaling and Varimax rotation, which characterize the analyzed alcoholic beverages. Two distinct groups could be observed, that of the elements of natural origin (Ca, Mg, Al, Mn, Cd, Pb), which have a great influence on the variability of alcoholic beverages based on the first factor (45.5%). The second group includes elements that show the influence of the distillation equipment material on the elemental content of the alcoholic beverages (Cu, Fe, Cr, Zn, Ni, Co). Of these elements, the greatest influence is observed for Ni and Co, while Cu present only a small influence in comparison. Its presence in alcoholic beverages, especially in the cognacs, is more influenced by the wine content, and less by the distillation equipment.

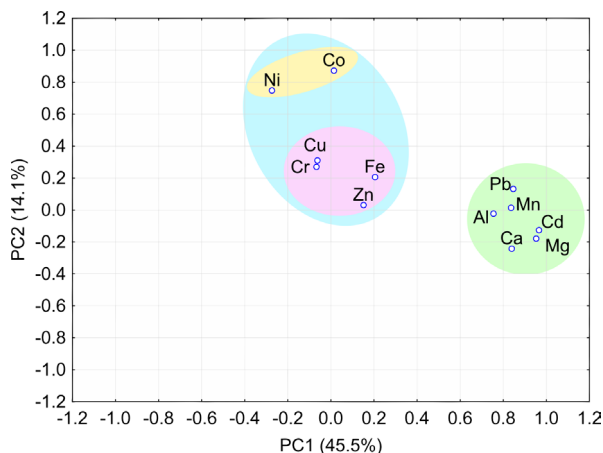


Figure 3. Two-dimensional PCA after auto-scaling and Varimax rotation of the analyzed alcoholic beverages

CONCLUSIONS

The results of the present study revealed that the concentrations of the 12 metals in the home-brewed spirits were significantly higher than in the industrially-brewed ones. In most of the analyzed samples the AMPHORA set threshold values for spirits were surpassed in case of Cu, which was attributed to the copper stills used by the home brewers. Nonetheless, health risk assessment by the THQ and TTHQ approach did not indicate non-carcinogenic long term health risk in case of moderate spirits consumption, with the exception of three home-brewed ones, that had very high Pb concentration. The results of this study also indicated no significant differences in terms of metals concentration in spirits home distilled from plums, apples and grapes. The statistical PCA analysis highlighted the fact that alcoholic beverages are characterized by a great variability of their elemental composition, the first four factors describing ~79% of the variability. However, a few groups of alcoholic beverages have been observed according to their origin (home- or industrially-brewed). Also, two clusters of the elements could be highlighted, one that includes elements of natural origin (Ca, Mg, Al, Mn, Cd, Pb), and the second, the trace elements, whose origin was associated with the material of the distillation equipment, or in the case of Cu, its presence in the cognacs was associated more with its content in wine, than the one resulting from the distillation equipment. However, it was observed that it has only an average influence, in proportion of around 11% on the variability of alcoholic beverages.

EXPERIMENTAL SECTION

Reagents and solutions

The ICP-OES instrument calibration was achieved using standard solutions obtained by dilution with 5% (v/v) HNO₃ of an ICP multi-elemental standard solution IV 1000 mg L⁻¹ produced by Merck (Darmstadt, Germany). Samples acidulation and preparation of the 5% (v/v) HNO₃ solution was prepared from 69% (w/w) HNO₃ for analysis (Merck, Germany). For the dilution of samples doubly distilled water was employed, obtained with the Fistream Cyclon Double (Bi-) Distiller (Cambridge, United Kingdom).

Samples and sample preparation

Samples consisted of 18 home- and 3 industrially-brewed spirits, and 19 industrially obtained cognacs. The home brewed spirits were distilled from plums (samples 1–6), apples (samples 7–11), grapes (samples 12–16), cherry (sample 17) and peach (sample 18) between 2016 and 2020 in small scale distilleries or in private homes. They originated from different locations across Romania, namely Tăutelec (Bihor County), Satu Mare (Satu Mare County), Carastelec (Sălaj County), Vama (Suceava County), Vaslui (Vaslui County), Sfântu Gheorghe (Covasna County), Viile Satu Mare (Satu Mare County), Viișoara (Cluj County) and Panciu (Vrancea County). The industrially-brewed spirits (samples 19–21) originated from local stores of Cluj-Napoca, while the cognacs (samples 22–40) were obtained industrially from an unadulterated producer, that were not intended for human consumption.

Samples preparation consisted in evaporation of aliquot volumes of 50 mL alcoholic beverage on a sand bath to dryness, retaking it in 10 mL HNO₃ 69% (w/w), boiling for 1 h in order to digest the organic compounds and dilution to 25 mL with doubly distilled water. Along with the samples, a blank solution was also prepared.

Instrumentation

The concentrations of metals in the alcoholic beverages were measured using the Spectro CIROS^{CCD} ICP-OES spectrometer (Spectro, Kleve, Germany) using the following conditions: 27.12 MHz radiofrequency, 1400 W plasma power, 12/0.6/1 L min⁻¹ outer/auxiliary/nebulaztion Ar flow rate, axial plasma viewing (X = -3.9 mm, Y = 3.6 mm, Z = +2.6 mm). The samples were pumped by a peristaltic pump, at a flow rate of 5 mL min⁻¹, into the cross-flow nebulizer (flushing time 40 s, delay time 20 s). The emission signals of the elements were separated by the double grating Paschen Runge polychromator with Ar filled chamber and were detected simultaneously by the 22 charge coupled devices (CCD). Signals were

processed as peak height with background correction in two-points. Quantitative determinations were realized after external calibration in the 0–10 mg L⁻¹ range (n = 8 points) for all elements.

Method validation

Method validation consisted of figures of merit (LOD, LOQ), accuracy and precision evaluation. LODs of the elements were calculated as the ratio of 3 times the standard deviation of 11 measurements of a blank sample and the slope of the calibration curve (3σ criterion), while LOQ was considered as 3*LOD [24]. Methods accuracy was verified by spike – recovery testing, using a concentration of 0.1 mg L⁻¹ ICP IV standard solution for elements in the <LOD–1 mg L⁻¹ concentration range, and 5 mg L⁻¹ ICP IV solution for 1–50 mg L⁻¹ concentration range. Methods precision was verified by relative standard deviation (RSD, %) calculation from samples replicate measurements.

Human health risk assessment

According to WHO, in Romania, the adult per capita consumption of pure alcohol is 12.6 L per year [1], which results in a consumption of 100 mL alcoholic beverage (40%, v/v) for a consumption frequency of 365 days/year.

The THQ values, for the assessment of non-carcinogenic health risk posed by the metals present in the alcoholic beverages, with the exception of Ca and Mg, was calculated using equation (1), while TTHQ was calculated as the sum of individual THQ values [14], taking into account 100 mL alcohol/day for moderate consumption, 200 mL for high consumption and 300 mL for very high alcohol consumption. If THQ and TTHQ are <1, then there is no health risk to non-carcinogenic diseases, while at THQ value >1, some detrimental health effects may appear due to exposure to metals in the analyzed alcoholic beverages. It can be considered that TTHQ is much more suitable for assessing the long-term risk exposure, because it reflects the cumulative effect of potentially toxic elements present in drinks or foods.

$$\text{THQ} = \frac{\text{Efr} \times \text{ED}_{\text{tot}} \times \text{Fir} \times c}{\text{RfDo} \times \text{Bwa} \times \text{ATn}} \times 10^{-3} \quad (1)$$

where, Efr – is the exposure frequency (365 days/year),

ED_{tot} – is the exposure duration (57 years, based on an average life expectancy in Romania of 75 years and consumption starting at age 18),

Fir – is the daily alcohol ingestion (100; 200; 300 mL/day),

c – is the concentration of the element in the alcoholic beverage (mg/L),

RfDo – is the oral reference dose (mg/kg/day),

B_{wa} – is the average body weight of an adult (60 kg),
AT_n – is the exposure time for non-carcinogens (20,805 days)
10⁻³ – is the unit conversion factor.

Elemental profiling of alcoholic beverages by PCA

The elemental profile of the studied alcoholic beverages was obtained by the unsupervised multivariate Principal Component Analysis (PCA) method after Varimax rotation of the auto-scaled data. In the PCA approach, a data set is transformed by combining the original parameters into a multidimensional space of new variables called principal components (PCs) or factors. Each PC contains a linear combination of the original variables. Only dominant PCs that have an eigenvalue greater than 1 according to the Kaiser criterion, that have the largest variance and describe the system's variability were considered in the Varimax rotation. Maximization of the variance of the retained PCs was achieved by Varimax rotation. The absolute loading values provided the influence of each parameter in a PC. A strong influence of a parameter was considered for loading values (> 0.70), while values in the range 0.50–0.70 or 0.30–0.50 indicate a moderate or weak influence [40]. The PCA analysis was performed considering all elements and all beverages. In the beverages in which the metals concentration was lower than the method LODs, the considered value was one half of LOD.

REFERENCES

1. World Health Organization (WHO), Global status on alcohol and health, **2018**, Geneva, License: CC BY-NC-SA 3.0 IGO
2. Organization International de la Vigne et du Vin (OIV), *Maximum acceptable limits*, **2015** (<https://www.oiv.int/public/medias/3741/e-code-annex-maximum-acceptable-limits.pdf>, accessed: 27 January 2021)
3. D.W. Lachenmeier; K. Schoeberl; F. Kanteres; T. Kuballa; E.M. Sohnus; J. Rehm. *Addiction*, **2011**, *106*, 20-30
4. L. Pal; T. Muhollari; O. Bujdoso; E. Baranyai; A. Nagy; E. Arnyas; R. Adany; J. Sandor; M. McKee; S. Szucs; *Regul. Toxicol. Pharmacol.*, **2020**, *116*, article number 104723
5. J.G. Ibanez; A. Carreon-Alvarez; M. Barcena-Soto; N. Casillas; *J. Food. Comp. Anal.*, **2008**, *21*, 672-683
6. A. Szymczycha-Madeja; M. Welna; P. Jamroz; A. Lesniewicz; P. Pohl; *Trends Anal. Chem.*, **2015**, *64*, 127-135
7. V.G. Mihucz; C.J. Done; E. Tatar, E. Virag; Gy. Zaray; E.G. Baiulescu; *Talanta*, **2006**, *70*, 984-990
8. P. Pohl; *TRAC-Trend. Anal. Chem.*, **2007**, *26*, 941-949
9. V. Ivanova-Petropulos; B. Balabanova; E. Bogeve; T. Frentiu; M. Ponta; M. Senila; R. Gulaboski, F.D. Irimie; *Food Anal. Methods*, **2017**, *10*, 459–468

10. M. Bonic; V. Tesevic; N. Nikicevic; J. Cvejic; S. Milosavljevic; V. Vajs; B. Mandic; I. Urosevic; M. Velickovic; S. Jovanic; *J. Serb. Chem. Soc.*, **2013**, 78, 933-945
11. U.S. Environmental Protection Agency (EPA). *Toxicological review of zinc and compounds*. **2005**. https://cfpub.epa.gov/ncea/iris/iris_documents/documents/toxreviews/0426tr.pdf (Accessed: 2 October 2022)
12. U.S. Environmental Protection Agency (EPA). *Provisional peer reviewed toxicity values for iron and compounds*. **2006**. <https://cfpub.epa.gov/ncea/pprtv/documents/IronandCompounds.pdf> (Accessed: 22 September 2022)
13. U.S. Environmental Protection Agency. National Center for Environmental Assessment. Integrated Risk Information System (IRIS). *Chemical Assessment Summary for Manganese*. https://cfpub.epa.gov/ncea/iris/iris_documents/documents/subst/0373_summary.pdf#nameddest=rfd (Accessed: 16 October 2022)
14. European Food Safety Authority (EFSA). Cadmium dietary exposure in the European population. *EFSA J.*, **2012**, 10:2551. <https://efsa.onlinelibrary.wiley.com/doi/pdf/10.2903/j.efsa.2012.2551> (Accessed: 10 October 2022)
15. Food and Drug Administration (FDA). *Lead in food, foodwares and dietary supplements*. <https://www.fda.gov/food/metals-and-your-food/lead-food-foodwares-and-dietary-supplements> (Accessed: 28 September 2022)
16. G. Nordberg; K. Nogawa; M. Nordberg; L.T. Friberg. *Handbook on the Toxicology of Metals*, third ed., **2007**, Elsevier, California
17. International Agency for Research and Cancer (IARC). *IARC Monographs on the Evaluation of Carcinogenic Risks to Humans*. **2009**. <http://monographs.iarc.fr> (Accessed: 16 October 2009)
18. H. Hopfer; G. Gilleland; S.E. Ebeler; J. Nelson; *Beverages*, **2017**, 3, article number 8
19. T. Adam; E. Duthie; J. Feldmann; *J. I. Brewing*, **2002**, 108, 459-464
20. A.M. Camean; I. Moreno; M. Lopez-Artiguez; M. Repetto; A.G. Gonzalez; *Talanta*, **2001**, 54, 53-59
21. R.I. Rodriguez; M.F. Delgado; J.B. Garcia; R.M.P. Crecente; S.G. Martin; C.H. Latorre; *Anal. Bioanal. Chem.*, **2010**, 397, 2603-2614
22. D. Pantani; Z.M. Sanchez; C. Greene; I. Pinsky; *Drug Alcohol Rev.*, **2021**, 40, 509-10
23. World Health Organization (WHO). Unrecorded alcohol: what the evidence tells us. Snapshot series on alcohol control policies and practice. Brief 2, 2 July **2021**
24. J.N Miller and J. Charlotte Miller; *Statistics and Chemometrics for Analytical Chemistry*, Pearson Education Ltd, Edinburgh Gate, England, **2005**.
25. C.M.A. Iwegbue; L.C. Overah; F.I. Bassey; B.S. Martincigh. *J. Inst. Brew.*, **2014**, 120, 521-528
26. F.D. Bora; A. Calugar; C.I. Bunea; V. Petrescu Mag; C. Cimpoi, V.R. Filimon; *Stud. Univ. Babeş-Bolyai Chem.*, **2019**, 64, 157-176
27. J. Plotka-Wasyłka; M. Frankowski; V. Simeonov; Z. Polkowska; J. Namiesnik; *Molecules*, **2018**, 23, article number 2886.
28. T.N. van Wyk; F. van Jaarsveld; O.J. Coleb. *S. Afr. J. Enol. Vitic.*, **2021**, 42, 36-43
29. World Health Organisation (WHO), *Vitamin and mineral requirements in human nutrition*, Second edition, Geneva, **2004** (<https://apps.who.int/iris/bitstream/handle/10665/42716/9291546123.pdf?ua=1>, Accessed: 27 January 2021)

30. Order number 511 bis from 13 June 2006 regarding the surface water quality in order to establish the ecological status of water bodies.
<https://legislatie.just.ro/Public/DetaliuDocumentAfis/74255?fbclid=IwAR2PyFH Xjme9c-e2cH-W3FJzmOHq4AqT1YlcKdYa9YG-ASK1ncfTuNUiuwQ>
 (Accessed: 22 September 2022)
31. A.A. Taylor; J.S. Tsuji; M.E. McArdle; W.J. Adams; W.L. Goodfellow Jr.; *Risk Analysis*, **2022**, 1–8. <https://doi.org/10.1111/risa.13906>
32. European Food Safety Authority (EFSA). Scientific opinion on dietary reference values for copper. *EFSA J.*, **2015**, *13*:4253. <https://efsa.onlinelibrary.wiley.com/doi/epdf/10.2903/j.efsa.2015.4253> (Accessed: 5 October 2022)
33. Directive (EU) 2020/2184 of the European Parliament and of the Council of 16 December 2020 on the quality of water intended for human consumption. *Off. J. Eur. U. L* 435/1.
<https://eur-lex.europa.eu/legal-content/EN/TXT/PDF/?uri=CELEX:32020L2184>
 (Accessed: 2 October 2022)
34. U.S. Environmental Protection Agency (EPA). *Drinking water regulations and contaminants*. <https://www.epa.gov/sdwa/drinking-water-regulations-and-contaminants>
 (Accessed: 10 October 2022)
35. European Food Safety Authority (EFSA). Safety of aluminium from dietary intake. *EFSA J.*, **2008**, *754*, 1–34. <https://efsa.onlinelibrary.wiley.com/doi/epdf/10.2903/j.efsa.2008.754> (Accessed: 11 September 2022)
36. European Food Safety Authority (EFSA). Scientific opinion on the risk to public health related to the presence of chromium in food and drinking water. *EFSA J.*, **2014**, *12*:3595. <https://efsa.onlinelibrary.wiley.com/doi/epdf/10.2903/j.efsa.2014.3595>
 (Accessed: 11 September 2022)
37. European Food Safety Authority (EFSA). *EFSA J.*, **2012**, *10*(6):2727. <https://efsa.onlinelibrary.wiley.com/doi/pdf/10.2903/j.efsa.2012.2727>
 (Accessed: 11 September 2022)
38. European Food Safety Authority (EFSA). Scientific opinion on dietary reference values for manganese. *EFSA J.*, **2013**, *11*:3419. <https://efsa.onlinelibrary.wiley.com/doi/epdf/10.2903/j.efsa.2013.3419> (Accessed 28 September 2022)
39. World Health Organization (WHO). *Guidelines for drinking-water quality*, 4th edition. **2017**. <https://www.who.int/publications/i/item/9789291549950> (Accessed 2 October 2022)
40. J.C. Davis, *Statistics and data analysis in geology*, 3rd edition, John Wiley & Sons, Hoboken, New Jersey, USA, **2002**, pp. 638

DEVELOPMENT OF A NEW MICRO-HPTLC PROTOCOL FOR TOTAL ANTIOXIDANT POTENTIAL DETERMINATION OF REDOX-ACTIVE DRUGS

Dorina CASONI^{a,b*}, Ileana Maria SIMION^a,
Simona Codruța Aurora COBZAC^{a,b}, Alexandra-Gabriela KIRALY^a

ABSTRACT. A new micro-HPTLC method assisted by image analysis technique was proposed for rapid evaluation of the total antioxidant potential (TAP) of redox-active drugs using 2,2-diphenyl-1-picrylhydrazyl (DPPH[•]) and 2,2'-azinobis-3 ethylbenzothiazoline-6-sulfonic acid (ABTS^{•+}) radicals. Colored compounds that can significantly influence the spectrophotometric and chromatographic measurements were revealed in case of selected drugs after their reaction with DPPH[•] and ABTS^{•+} radical respectively. The best chromatographic conditions were selected for accurate quantification of DPPH[•] and ABTS^{•+} radicals after their separation from the interfering compounds. The validation of the proposed method was performed in terms of linearity, limit of detection, limit of quantification, precision, and accuracy. Green and red color channel used for image processing were found to allow accurate quantification of DPPH[•]. For accurate quantification of ABTS^{•+} the red and gray channels were selected. A linear dependence of spot area/radical concentration was obtained in the range 0.78-2.76 $\mu\text{g}\cdot\text{spot}^{-1}$ and 0.21-2.49 $\mu\text{g}/\text{spot}$ for DPPH[•] and ABTS^{•+} radicals respectively. The developed method was found to be accurate and precise according to values higher than 92% for recovery and less than 3% for relative standard deviation parameters (RSD%). A statistical significant correlation was obtained comparing the spectrophotometric results with the chromatographic ones obtained for selected adrenergic drugs.

Keywords: *micro-HPTLC method; image analysis; total antioxidant potential; adrenergic drugs; DPPH[•] and ABTS^{•+} protocols*

^a Babeș-Bolyai University, Faculty of Chemistry and Chemical Engineering, 11 Arany Janos str., RO-400028, Cluj-Napoca, Romania

^b Research Center for Advanced Chemical Analysis, Instrumentation and Chemometrics – ANALYTICA, Babeș-Bolyai University 11 Arany Janos str., RO-400028, Cluj-Napoca, Romania

* Corresponding author: dorina.casoni@ubbcluj.ro



INTRODUCTION

The development of rapid protocols to measure the antioxidant activity of different classes of compounds is one of the topics with a great scientific interest in recent years [1-3]. High performance thin-layer chromatography combined with image analysis (HPTLC-IA) method is among the recently developed methods in the area of the antioxidant potential evaluation. Protocols based on scavenging the free-radicals 2,2-diphenyl-1-picrylhydrazyl (DPPH[•]) were found to be mostly used for the *in vitro* antioxidant activity evaluation purpose [4-9]. In the most popular approaches the typical planar chromatographic assay is used. In this approach developed plates are sprayed or immersed with/in DPPH[•] radical solution and the active antiradical constituents (appeared as yellowish white spots produced by bleaching the purple color of the DPPH[•] reagent) are quantified based on the integrated area of the chromatographic spot [5].

The HPTLC-IA methodology has the advantage of multiple parallel sample analysis on the same chromatographic plate, possibility to present results as a colorful image, multiple levels of visualization (in white light, UV 366 nm and/or UV 254 nm) and moreover the possibility of application of advanced image analysis techniques. The use of different color scale (channel) selection for image processing provides complementary information and allow an accurate quantification of compounds even if they are not separated with high resolution from the matrix constituents. Based on sensitive and accurate protocols developed until now, the HPTLC-IA method represents a promising, rapid and economic alternative for comprehensive evaluation of the antioxidant potential of classes of redox-active compounds. Results published in prestigious international journals [7-10] sustain the HPTLC-IA method as promising, rapid and economic alternative able to provide accurate evaluation/quantification of antioxidant potential of redox-active compounds and investigate/monitor the reaction mechanism with DPPH[•] radical.

In the micro-thin-layer chromatographic assay (micro-TLC) the antioxidant potential is evaluated by quantitative analysis of radical DPPH[•] and DPPH-H molecules after reaction with the sample [11], and then separated from the interfering compounds. So, the micro-TLC approach can offer the possibility of evaluation of total antioxidant potential (TAP) of redox-active compounds in free-of-interaction liquid medium. Combined with image analysis procedures by color scale selection, the micro-TLC method provides complementary information that may allow accurate quantification of radical molecules even if they are not well separated from the sample matrix constituents.

The objective of this study was to develop a micro-HPTLC method assisted by image analysis techniques (micro-HPTLC-IA method) for accurate determination of total antioxidant potential (TAP) of redox-active drugs

using both DPPH[•] and ABTS^{•+} radicals. During the method development, the chromatographic conditions were optimized and different image analysis techniques were evaluated for accurate determination of both DPPH[•] and ABTS^{•+} radicals. The method was validated in terms of linearity range, limit of determination and limit of quantification and the method advantages were highlighted for the determination of the antioxidant potential of selected adrenergic drugs.

RESULTS AND DISCUSSION

Optimization of the chromatographic parameters for the micro-HPTLC method

The preliminary investigations for selected adrenergic drugs using typical chromatographic method (TLC) revealed a considerable antiradical activity of these drugs against DPPH[•] and ABTS^{•+} radicals (Figure 1).

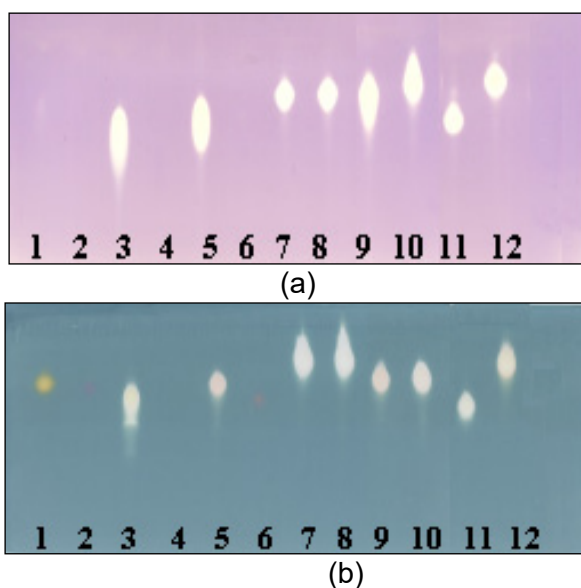


Figure 1. Image of the chromatographic plate (HPTLC Silica gel 60 F₂₅₄) after separation of selected adrenergic drugs (mobile phase methanol: water: formic acid, 60:40:0.5 v/v/v) and immersion in DPPH[•] solution (0.8x10⁻³ mol/L) (a) and ABTS^{•+} solution (0.7x10⁻³ mol/L) (b). (1-Terbutaline; 2-Albuterol; 3-Adrenalone; 4-Methoxamine; 5-Isoprenaline; 6-Ritodrine; 7-L-DOPA; 8-D-DOPA; 9-Epinephrine; 10-Norepinephrine; 11- Caffeic acid; 12-Trolox)

During our investigations, for some drugs as terbutaline (1), albuterol (2) and ritodrine (6) the reaction with $ABTS^{•+}$ radical on the chromatographic plate conducted to the formation of colored compounds (yellow-orange for terbutaline; purple-red for albuterol; pink-red for ritodrine) that can significantly influence the spectrophotometric and typical chromatographic measurements. Thus, for these drugs, the evaluation of the antioxidant potential using the classical spectrophotometric and typical chromatographic methods cannot be carried out with precision for the $ABTS^{•+}$ assay. For these situations the micro-TLC approach offer a promising alternative for rapid evaluation of total antioxidant potential (TAP) [11].

Development of the proposed micro-HPTLC protocol for quantitation of $DPPH^{•}$ and $ABTS^{•+}$ radicals started from optimization of the chromatographic conditions necessary for accurate determination of these radicals.

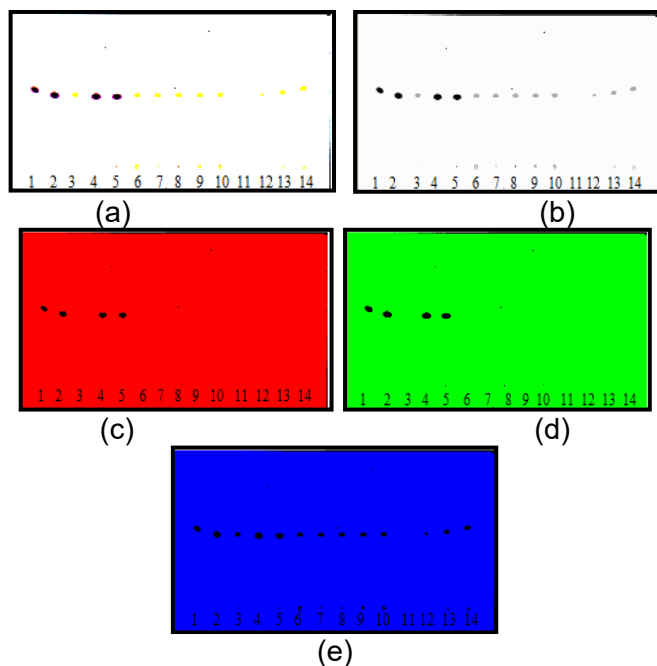


Figure 2. Image of the chromatographic plate (HPTLC Silica gel 60 F_{254s}) obtained after separation of $DPPH^{•}$ radical molecules and image processing using the ImageDecipher TLC software: (a) RGB (red, green and blue primary colors) color mode; (b) gray scale selection; (c) red scale selection; (d) green scale selection; (e) blue scale selection. (1-Terbutaline, 2-Albuterol, 3-Adrenalone, 4-Metoxamine, 5-Ritodrine, 6-Isoprenaline, 7-L-DOPA, 8-D-DOPA, 9-Epinephrine, 10-Norepinephrine, 11,12,13,14-Caffeic acid -2,4,6 and 8 μ L).

DEVELOPMENT OF A NEW MICRO-HPTLC PROTOCOL FOR TOTAL ANTIOXIDANT POTENTIAL DETERMINATION OF REDOX-ACTIVE DRUGS

In order to determine the optimal conditions of separation of DPPH• and DPPH-H, different stationary phases and mobile phases were tested. For the HPTLC Silica gel 60 F_{254s} plates mixtures of hexane and acetone (50:50; 60:40 and 70:30 v/v) and hexane, acetone and ethanol (60:30:10; 60:35:5 and 60:38:2 v/v/v) were used. Also different mixtures of methanol-water (from 40% to 70% methanol) were tested using the Silica gel 60 RP-18W F_{254s}, HPTLC Silica gel 60 RP-8 F_{254s} and HPTLC Silica gel 60 DIOL F_{254s} plates. The best results were obtained for HPTLC Silica gel 60 F_{254s} plates with mobile phase consisted of hexane: acetone: ethanol (60:38:2 v/v/v). In these conditions, both forms of DPPH (DPPH• and DPPH-H) were not completely separated but selective quantification of DPPH• molecules was performed in red and green channel respectively.

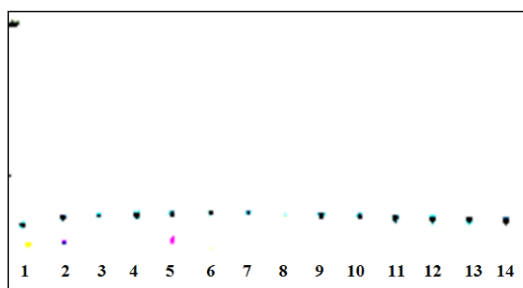


Figure 3. RGB (red, green and blue primary colors) image of the chromatographic plate (HPTLC silica gel RP-18W F_{254s}) obtained after separation of ABTS^{•+} radical molecules and image processing using the ImageDecipher TLC software. (1-Terbutaline; 2-Albuterol; 3-Adrenalone; 4-Metoxamine, 5-Ritodrine, 6-Isoprenaline, 7-L-DOPA, 8-D-DOPA, 9-Epinephrine; 10- Norepinephrine; 11, 12, 13, 14 - ABTS^{•+} sample).

For the ABTS assay the optimal condition for separation of ABTS^{•+} radical (green spots) from the colored interfering constituents (resulted from reaction of terbutaline, albuterol and ritodrine respectively with ABTS^{•+} radical) was targeted. The best results (Figure 3) were obtained for HPTLC silica gel RP-18W F_{254s} plates and mixture of methanol: water (40:60 v/v) as mobile phase. The gray and red channels provided the best sensitivity for ABTS^{•+} spots and both channel were selected to perform quantification of ABTS^{•+} molecules.

Method Validation

The method performance parameters expressed as linearity range, limit of detection (LOD) and limit of quantification (LOQ) for developed micro-HPTLC-DPPH• and micro-HPTLC-ABTS^{•+} protocols are presented in Table 1.

Table 1. Method performance parameters (linearity range, limit of detection - LOD and limit of quantification - LOQ) obtained for developed micro-HPTLC- DPPH[•] and micro-HPTLC-ABTS^{••} assays.

Metod performance parameters	micro-TLC- DPPH [•] assay		micro-TLC- ABTS ^{••} assay	
	Red channel	Green channel	Gray channel	Red channel
Calibration range	0.78 - 2.76 ($\mu\text{g}/\text{spot}$)		0.21 - 2.49 ($\mu\text{g}/\text{spot}$)	
Intercept	-1254.10	480.89	57.80	121.81
Slope	2412.60	2166.70	3884.30	5430
*R ²	0.9881	0.9918	0.9884	0.9946
LOD ($\mu\text{g}/\text{spot}$)*	0.24 \pm 0.01	0.22 \pm 0.01	0.03 \pm 0.01	0.02 \pm 0.01
LOQ ($\mu\text{g}/\text{spot}$)*	0.79 \pm 0.02	0.73 \pm 0.01	0.10 \pm 0.02	0.07 \pm 0.02

*regression determination coefficient ; *values \pm standard deviation (SD)

A good linear dependence ($0.9881 < R^2 < 0.9946$ for spot area of radical vs. radical concentration) was obtained for 0.78 - 2.76 ($\mu\text{g}/\text{spot}$) and for 0.21 - 2.49 $\mu\text{g}/\text{spot}$ in case of micro-HPTLC-DPPH[•] and micro-HPTLC-ABTS^{••} assay, respectively. Green channel selection was revealed to offers a better sensitivity (LOD = 0.22 $\mu\text{g}/\text{spot}$) for DPPH[•] quantification while the red channel selection conducted to beter sensitivity for ABTS^{••} determination (LOD = 0.02 $\mu\text{g}/\text{spot}$).

The accuracy of the micro-HPTLC method was evaluated by quantification of DPPH[•] and ABTS^{••} molecules on three concentration levels of radical /spot. Results, expressed by percent recovery ranged from 92% to 96% for DPPH[•] and from 0.93% to 95% for ABTS^{••} radical, respectively.

The relative standard deviation (RSD%) values less than 3% obtained by analysis of replicates of radical solution at three different concentrations (for both radicals) during three different time in one day revealed a good intraday precision and good repeatability of the method.

Application of the developed micro-HPTLC method for the determination of total antioxidant potential (TAP) of selected adrenergic drugs

Based on method development results, the total antioxidant potential for selected adrenergic drugs (Table 2) was determined by micro-HPTLC-DPPH[•] assay using red and green channels selection and by micro-HPTLC-ABTS^{••} assay using gray and red channels selection respectively. Results were expressed as caffeic acid equivalents for the DPPH[•] method and trolox equivalents for the ABTS^{••} method (calibration curves parameters for reference antioxidants caffeic acid in DPPH[•] assay and trolox in ABTS^{••} assay: $0.9990 < R^2 < 0.9996$).

DEVELOPMENT OF A NEW MICRO-HPTLC PROTOCOL FOR TOTAL ANTIOXIDANT POTENTIAL DETERMINATION OF REDOX-ACTIVE DRUGS

The obtained results revealed that catecholamine related drugs (L-DOPA, D-DOPA, adrenalone, epinephrine and isoprenaline) show a high antiradical potential against DPPH[•]. Ritodrine and terbutaline showed comparable activity with norepinephrine.

Similar results (expressed in trolox equivalents) were obtained by micro-HPTLC-ABTS^{•+} assay. L-DOPA, D-DOPA, adrenalone and isoprenaline (catecholamine related drugs) were revealed as drugs with highest antioxidant potential. They are followed by terbutaline, norepinephrine, albuterol and ritodrine.

Table 2. Total antioxidant potential (TAP) for selected adrenergic drugs determined by micro-HPTLC- DPPH[•] and micro-HPTLC-ABTS^{•+} assays.

Sample No.	Sample name	Total antioxidant potential (TAP)			
		micro-TLC-DPPH [•] (caffeic acid equivalents*) (μM)		micro-TLC-ABTS ^{•+} (trolox equivalents*) (μM)	
		Red channel	Green channel	Gray channel	Red channel
1	Terbutaline	71.46 \pm 0.16	71.99 \pm 0.58	58.28 \pm 1.01	55.99 \pm 1.02
2	Albuterol	25.63 \pm 0.27	24.74 \pm 2.82	44.28 \pm 0.98	43.66 \pm 1.51
3	Adrenalone	153.83 \pm 1.27	150.24 \pm 1.84	85.41 \pm 1.41	87.53 \pm 1.06
4	Metoxamine	6.43 \pm 0.04	7.09 \pm 0.12	0.72 \pm 0.20	0.88 \pm 0.08
5	Ritodrine	74.49 \pm 0.18	78.62 \pm 1.05	29.58 \pm 1.58	28.55 \pm 1.97
6	Isoprenaline	124.34 \pm 1.51	126.27 \pm 0.03	69.62 \pm 1.21	72.10 \pm 0.13
7	L-DOPA	168.39 \pm 1.27	163.69 \pm 0.88	142.06 \pm 1.44	144.69 \pm 0.78
8	D-DOPA	154.83 \pm 2.11	152.28 \pm 1.66	88.67 \pm 2.04	84.46 \pm 2.98
9	Epinephrine	136.72 \pm 0.20	134.94 \pm 1.44	18.51 \pm 0.76	17.38 \pm 1.26
10	Norepinephrine	73.14 \pm 1.10	75.05 \pm 1.31	48.21 \pm 1.08	50.80 \pm 1.54

* \pm SD - standard deviation determined for two replicate spots

Evaluation of the chromatographic results obtained by developed micro-HPTLC-DPPH[•] and micro-HPTLC-ABTS^{•+} assay respectively was made by comparison with results from classic spectrophotometric assay using DPPH[•] and ABTS^{•+} radicals. For this purpose, the antioxidant activity against DPPH[•] and ABTS^{•+} radicals was determined for the studied compounds using the spectrophotometric method. The spectrophotometric results expressed as caffeic acid equivalents (μM) for DPPH[•] assay and as trolox equivalents (μM) for ABTS^{•+} assay were calculated based on the calibration curves (% of consumed radical vs. concentration of the reference antioxidant) obtained for the reference antioxidants caffeic acid ($y = 204.86x + 1.9056$, $R^2 = 0,9999$) and trolox ($y = 3.3107x + 2.5715$, $R^2 = 0,9998$), respectively. The obtained results for the selected drugs are presented in Table 3.

Table 3. Total antioxidant potential (TAP) for selected adrenergic drugs determined by DPPH[•] and ABTS^{•+} spectrophotometric assays.

No.	Sample name	Total antioxidant potential (TAP)	
		DPPH [•] assay Caffeic acid equivalents* (μM)	ABTS ^{•+} assay Trolox equivalents* (μM)
1	Terbutaline	70.42 \pm 0.14	10.31 \pm 0.15
2	Albuterol	35.06 \pm 0.07	47.3 \pm 0.13
3	Adrenalone	140.17 \pm 0.15	85.81 \pm 0.18
4	Metoxamine	5.25 \pm 0.02	0.86 \pm 0.08
5	Ritodrine	83.40 \pm 0.12	14.81 \pm 0.13
6	Isoprenaline	116.41 \pm 0.13	74.22 \pm 0.14
7	L-DOPA	122.51 \pm 0.12	149.50 \pm 0.16
8	D-DOPA	125.24 \pm 0.16	86.36 \pm 0.15
9	Epinephrine	138.75 \pm 0.18	19.20 \pm 0.12
10	Norepinephrine	50.88 \pm 0.13	49.71 \pm 0.11

* \pm SD - standard deviation determined for three replicate measurements of absorbance

For L-DOPA, D-DOPA and adrenalone drugs, the spectrophotometric results showed a similar behavior as in the chromatographic assay, showing a high activity against both the DPPH[•] and the ABTS^{•+} radicals. Contrary to the chromatographic determinations, the spectrophotometric assay indicated a considerable activity for terbutaline and ritodrine against the ABTS^{•+} radical. These high values clearly highlight that the spectrophotometric determination is affected by the presence of intensely colored compounds formed from the reaction of these drugs with the ABTS^{•+} radical, compounds that were revealed by typical chromatographic investigations (Figure 1) and also by the developed micro-HPTLC method (Figure 3).

Table 4. The correlation parameters obtained between chromatographic and spectrophotometric results

Method *	DPPH (1)	DPPH (2)	ABTS (1)	ABTS (2)	DPPH (3)	ABTS (3)
DPPH (1)	1.00	1.00	0.73	0.72	0.96	0.72
DPPH (2)	1.00	1.00	0.72	0.71	0.96	0.71
ABTS (1)	0.73	0.72	1.00	1.00	0.57	0.94
ABTS (2)	0.72	0.71	1.00	1.00	0.56	0.94
DPPH (3)	0.96	0.96	0.57	0.56	1.00	0.55
ABTS (3)	0.72	0.71	0.94	0.94	0.55	1.00

* DPPH (1): micro-HPTLC-DPPH (red channel); DPPH (2): micro-HPTLC-DPPH (green channel); ABTS (1): micro-HPTLC-ABTS (gray channel); ABTS (2): micro-HPTLC-ABTS; DPPH (3): DPPH spectrophotometric assay; ABTS (3): ABTS spectrophotometric assay.

The comparison of the obtained results (Table 4) showed a significant correlation between the spectrophotometric and developed micro-HPTLC-DPPH[•] method on both red channel and green channel selection analysis ($r = 0.96$ in both cases).

Also in case of micro-HPTLC-ABTS^{•+} assay a significant correlation was observed with spectrophotometric results for both channel selected ($r = 0.94$) In this case a significant increasing of the correlation parameter was obtained ($r > 0.99$) when terbutaline and ritodrine were not considered for correlation study.

CONCLUSIONS

The micro-HPTLC method using the DPPH[•] and ABTS^{•+} radicals can be successfully applied for accurate determination of total antioxidant potential of redox-active drugs. The use of HPTLC Silica gel 60 F₂₅₄ plates with a mobile phase consisted of hexane: acetone: ethanol (60:38:2 v/v/v) and green channel selection allow an accurate quantification of DPPH[•] radical. New compounds were revealed after reaction of ABTS^{•+} radical with selected adrenergic drugs (terbutaline, albuterol and ritodrine respectively). The best separation of these compounds from the ABTS^{•+} molecules was obtained using the HPTLC silica gel RP-18W F₂₅₄ plates and mixture of methanol: water (40:60 v/v) as mobile phase. The validation of the micro-HPTLC-DPPH and micro-HPTLC-ABTS protocols performed in accordance with ICH guidelines indicates that the developed micro-HPTLC-IA method meets the criteria for linearity, precision and accuracy. In the above chromatographic conditions, a significant correlation ($r > 0.90$) was revealed between chromatographic and reference spectrophotometric results obtained for selected adrenergic drugs. It can be concluded that the proposed micro-HPTLC-IA method involving both DPPH[•] and ABTS^{•+} radicals is a powerful tool that allow a rapid evaluation of total antioxidant potential of redox-active drugs. The most significant advantage of the developed method is their accurate quantification of radicals even in presence of interfering compounds that can be formed by reaction of radicals with redox-active compounds.

EXPERIMENTAL SECTION

Reagents and samples

High purity standards of terbutaline, albuterol, adrenalone, methoxamine, ritodrine, isoprenaline, L-DOPA, D-DOPA, epinephrine and norepinephrine drugs and caffeic acid and trolox reference antioxidants were purchased from

Sigma-Aldrich company (Steinheim, Germany) and used for samples preparation in this study. Standards of 2,2-diphenyl-1-picrylhydrazyl (DPPH[•]), 2,2'-azinobis-(3-ethylbenzothiazole-6-sulfonic acid) (ABTS) and potassium persulfate (Sigma-Aldrich, Steinheim, Germany) were used for the preparation of the radical solutions.

Stock solutions of the samples were prepared in ethanol at concentrations of 5×10^{-3} mol/L.

Instrumentation and software programs

Linomat V TLC auto-sampler (CAMAG, Muttenz, Switzerland) and a Hamilton syringe (100 μ L) were used for sample application on the chromatographic plates. A specialized UV-Vis TLC scanner device (Thin Layer Chromatography Scanner TLC-2400S, BioDit Technology, Co.), the second-generation instrument for quantitative measurements in TLC, equipped with high qualified Micortek 3-linear color CCD camera was used for image acquisition.

Jasco V550 computer controlled spectrophotometer (Tokyo, Japan) equipped with double beam, single monochromator and quartz cuvettes of 1cm optical path was used for spectral measurements.

ImageDecipher software (BioDit Technology, Co.) was used for image processing and analysis.

Spectra Manager for Windows 95/ NT version 1.53.04 (1995–2002, Jasco Corporation) software package was used for the spectra acquisition control, smoothing process, storage and spectral data digitization.

Statistica 8.0 (StatSoft, Inc. 1984–2007, Tulsa, USA) software was used to perform correlation of the results obtained by the spectrophotometric and micro-HPTLC methods.

Solutions and samples preparation

The DPPH[•] radical stock solution (concentration 1×10^{-3} mol/L) was prepared by dissolving appropriate required amount of DPPH in methanol for both micro-TLC and spectrophotometric measurements. This solution was prepared daily and protected from light throughout the analysis time in order to minimize the loss of free radical activity. Working solutions of different concentrations were prepared by rigorous dilution from stock solution in all cases.

The ABTS^{•+} radical stock solution (concentration 1.25×10^{-3} mol/L) was produced according to the Ozcan protocol [12] by reacting equal volumes of the ABTS stock solution of 7 mmol/L concentration with solution of 2.45 mmol/l potassium persulfate (final concentration) and allowing the mixture to stand in the dark at room temperature for 12 – 16 h before use. The working solutions of ABTS^{•+} radical were prepared by required dilution in methanol.

Stock solutions (5×10^{-3} mol/L concentration) of reference antioxidants and drug samples were prepared by dissolving appropriate required amount of standard in methanol.

The method validation protocol

The proposed method was validated in terms of linearity, precision, accuracy, quantification limit (LOQ) and detection limit (LOD) in accordance with established International Conference on Harmonization (ICH) guideline [13].

Linearity test of developed micro-HPTLC method was made by the dilution of the stock solution of DPPH \cdot and ABTS $^{+\cdot}$ respectively to different required concentrations. For this aim a series of ten solutions from 1×10^{-4} to 2×10^{-3} mol/L concentration of DPPH \cdot and from 0.05×10^{-3} mol/L to 1.25×10^{-3} mol/L ($\epsilon = 1,6 \times 10^4 \text{ M}^{-1} \text{ cm}^{-1}$) ABTS $^{+\cdot}$ were prepared by appropriate dilution in methanol. Eight μL of each solution was spotted on HPTLC plate in all cases. The plates were developed using a mobile phase consisting hexane: acetone: ethanol (60: 38: 2 v/v) for DPPH \cdot and of methanol : water 40 : 60 v/v) for ABTS $^{+\cdot}$ separation. After separation, the plates were dried in dark conditions for ten minutes and scanned. All the process analysis was repeated three times. In both cases of radicals the calibration curve was plotted considering peak area versus concentration of radical ($\mu\text{g}/\text{spot}$). The linearity performance parameters for the calibration (coefficient of linear regression (R^2), slope, and intercept) were reported.

The limit of detection (LOD) and limit of quantification (LOQ) values were determined on the basis of specific calibration curves obtained for DPPH \cdot and for ABTS $^{+\cdot}$ respectively. The LOD was calculated as $\text{LOD} = 3\sigma/S$ and LOQ was calculated as $\text{LOQ} = 10\sigma/s$ where σ is the standard deviation of the spot area and S is the slope of the calibration curve.

The accuracy of the method was determined for DPPH \cdot and ABTS $^{+\cdot}$ assay on three concentration levels of radical/spot. Results were expressed as percent recovery calculated based on spot area of DPPH \cdot respectively ABTS $^{+\cdot}$. In case of micro-HPTLC-DPPH \cdot assay the percent recovery was calculated also for three concentration levels of DPPH \cdot in presence of DPPH-H molecules. These analyses were performed six times in each case.

Repeatability (intraday precision) of the method was determined by the analysis of three replicates of radical solution at three different concentrations of radicals in each case. All solutions were prepared independently and $8 \mu\text{L}$ of were applied on the chromatographic plate in each case. Precision was determined on the basis of measurements of spots area of three different concentration of radical and expressed as the relative standard deviation (RSD%) values.

Chromatographic protocol for TAP measurement

The total antioxidant potential (TAP values) of the drugs under study was determined by developed micro-HPTLC method.

For the DPPH[•] protocol, 5 mL of DPPH[•] solution (1×10^{-3} mol/L) were mixed with 50 μ L of drug sample (concentration 1×10^{-3} mol/L⁻¹) and kept in dark conditions for a 30 minutes reaction time. Spots of eight μ L from the each resulted sample were applied as spots on HPTLC Silica gel 60 F₂₅₄ plate (20 cm \times 10 cm, Merck, Darmstadt, Germany) with an application speed of 80 nL/s. Development of the plate was carried at room temperature over a distance of 8 cm in a normal chromatographic chamber using the mixture of hexane: acetone: ethanol in the ratio of 60: 38: 2 (v/v) as mobile phase. After separation the plates were dried in dark conditions at room temperature for 10 minutes. Plates were scanned and the quantification of DPPH[•] was performed based on spot area determined by gray, green, blue and red scales selection. Results were expressed as caffeic acid equivalents (μ g/spot) based on the equation of the calibration line obtained in the same chromatographic conditions for caffeic acid in the concentration range 0.01 - 0.1 μ g/spot.

For the ABTS^{•+} protocol, 2 mL ABTS^{•+} solution (concentration 1.25×10^{-3} mol/L) were mixed with 50 μ L of drug sample solution (concentration 1×10^{-3} mol/L) and kept in dark conditions for 30 minutes (reaction time). From each of the resulted samples, spots of 8 μ L were applied on the HPTLC silica gel RP-18W F₂₅₄ plates with an application speed of 60 nL/s. Development of the plate was carried at room temperature over a distance of 8 cm in a normal chromatographic chamber using mixture methanol: water in a various proportion (from 20% methanol to 60% methanol (v/v)) as mobile phase. After separation the plates were dried in dark conditions at room temperature for ten minutes and scanned. Quantification of ABTS^{•+} was performed based on spot area determined by gray, green, blue and red scales selection. Results were expressed as trolox equivalents (μ g/spot) based on the equation of the calibration curve obtained in the same chromatographic conditions for trolox in the concentration range 0.001 - 0.122 μ g/spot.

In all cases the samples were prepared in duplicate and from each sample duplicate spots were applied on the chromatographic plate.

The Spectrophotometric protocol for TAP measurements

For the spectrophotometric assay stock solutions of DPPH[•] (concentration 1×10^{-3} mol/L) and ABTS^{•+} (concentration 1.25×10^{-3} mol/L) radicals prepared as described above were used after appropriate dilution in methanol. Working solution of DPPH[•] of 0.15×10^{-3} mol/L was freshly prepared

for all determinations. 5 mL of working solution of DPPH[•] (concentration 0.15×10^{-3} mol/L) was mixed with 50 μ L of sample (concentration 1×10^{-3} mol/L) and the absorbance value was measured at $\lambda=518$ nm wavelength after a reaction time of 30 minutes (in dark conditions). Results were expressed as caffeic acid equivalents.

The ABTS^{•+} radical stock solution, prepared as described above, was diluted to an absorbance value of $A = 0.700$ (for $\lambda=734$ nm wavelength corresponding to the maximum of the absorbance; solution concentration 0.044×10^{-3} mol/L, calculated based on Lambert Beer's law for a value of the extinction coefficient $\epsilon = 1.6 \times 10^4$ M⁻¹ cm⁻¹) and used for the spectrophotometric assay. 3 mL of working ABTS^{•+} solution were mixed with 10 μ L of sample (concentration 1×10^{-3} mol/L) and the absorbance value was measured after a reaction time of 30 minutes at $\lambda=734$ nm wavelength corresponding to the maximum of the absorbance. Results were expressed as trolox equivalents. Three replicate samples were analysed in each case.

ACKNOWLEDGMENTS

This work was supported by a grant of the Ministry of Research, Innovation and Digitization, CNCS - UEFISCDI, project number PN-III-P1-1.1-TE-2021-0655, within PNCDI III.

REFERENCES

1. M. Antolovich; P.D. Prenzler; E. Patsalides; S. McDonald; K. Robards; *Analyst*, **2002**, *127*, 183-198
2. Z.Q. Liu; *Chem. Rev.*, **2010**, *110*, 5675-5691
3. Md. Nur Alam; N. J. Bristi; Md. Rafiquzzaman; *Saudi Pharm. J*, **2013**, *21*, 143-152
4. Ł. Cieřla; *Med. Chem.* **2012**, *8*, 102-111
5. Ł. Cieřla; J. Kryszewski; J. Kryszewski; A. Stochmal; W. Oleszek; M. Waksmundzka-Hajnos; *J. Pharm. Biomed. Anal.*, **2012**, *70*, 126-135
6. M. Olech; Ł. Komsta; R. Nowak; Ł. Cieřla; M. Waksmundzka-Hajnos; *Food Chem.*, **2012**, *132*, 549-553
7. I.A. Sima; D. Casoni; C. Sârbu; *Talanta*, **2013**, *114*, 117-123
8. D. Casoni; I.A. Sima; C. Sârbu; *J. Sep. Sci.*, **2014**, *37*, 2675-2681
9. D. Casoni; C. Sârbu; *J. Planar. Chromatogr. - Mod. TLC*, **2016**, *29*, 299-305
10. I.A. Sima; D. Casoni; C. Sârbu; *J. Liquid Chromatogr. Rel. Technol.*, **2013**, *36*, 2395-2404.
11. B.K. Głód; P.M. Wantusiak; P. Piszcz; P.K.Z. arzycki; *Food Chem.*, **2015**, *173*, 749-754.
12. E. Ozcan, *Clinical Biochem.*, **2004**, *37*, 277-285
13. C.H. Harmonised Tripartite Guideline: *Validation of analytical procedures: text and Methodology*, Q2(R1) Geneva, Switzerland, 2005, <http://www.ich.org>

DETERMINATION OF 2,4-DICHLOROPHENOXYACETIC ACID (2,4-D) FROM TOMATOES BY LC-MS/MS ANALYSIS

Liana Maria COSTEA^a, Raluca RAD^b, Claudia CIMPOIU^b,
Adela MEGHESAN^{b,*}

ABSTRACT. 2,4-D is a herbicide that in certain doses can be used as a growth stimulator for various crops. Although it is forbidden in our country to use it for such purposes, tomato growers use it to obtain large and fast harvests, but unfortunately of poor quality (the well-known tomatoes with tassel). In this work, we present a modified Miniluke extraction method and a LC-MS/MS analysis method of this pesticide from tomatoes. The method was validated both on tomatoes (presented in this paper) and strawberries, and its efficiency was demonstrated by participating to interlaboratory European tests where very good Z-scores were obtained.

Keywords: 2,4-D, growth plant stimulator, LC-MS/MS, Miniluke, QuEChERS

INTRODUCTION

2,4-dichlorophenoxyacetic acid (2,4-D) is the active ingredient in several formulation of herbicides recommended for the control of broadleaf weeds. Other uses include the control of aquatic weeds, some woody vegetation, and site preparation and conifer release in forests. [1]

2,4-D was used as herbicide in the herbicide Agent Orange, a 1:1 mixture of 2,4-D and 2,4,5-trichlorophenoxyacetic acid (2,4,5-T). Agent Orange was a herbicide widely used during the Vietnam war, and was often contaminated with 2,3,7,8-tetrachlorodibenzo-p-dioxin (2,3,7,8-TCDD), which

^a 1 Decembrie 1918 University, Faculty of Law and Social Sciences, Department of Physical Education and Sports, 15-17 Unirii str., Alba Iulia, Romania

^b Babeş-Bolyai University, Faculty of Chemistry and Chemical Engineering, 11 Arany Janos str., RO-400028, Cluj-Napoca, Romania

* Corresponding author: malleda@yahoo.com



result from the manufacture of 2,4,5-T, and this contaminant has high potential to be carcinogenic, teratogenic, and fetotoxic.[2]

The selective herbicide, 2,4-D, is used to protect grain crops against leafy weeds. It is also applied as a growth stimulator during the growth of plants (tomatoes), and post-harvest for the protection of fruits, especially citrus fruits.

After some experiments on various fruits and vegetables (lichi, pineapple, egg plant), Howell and Wittwer found that a single spray with 2,4-D on tomatoes (100 – 500 mg/L, somewhat dependent on the variety of herbicide) produced prompt flower formation. [3]

Many publications on the physiology of the tomato plant present that application of 2,4-D (2,4-dichlorophenoxyacetic acid), 4-CPA (4 chlorophenoxyacetic acid), and NOA (2-naphthoxyacetic acid) at recommended concentrations will increase fruit size and setting as well as accelerate fruit ripening. Even from 1953, was discovered that application of 2,4-D, NAA (Naphthaleneacetic acid), TIBA (2,3,5-triiodobenzoic acid), NOA (2-naphthoxyacetic acid) and IAA (Indole-3-acetic acid) inhibited Fusarium wilt in tomatoes. So, those plant growth regulators are important not only in increasing crops but also in controlling plant disease. [4, 5]

Today, 2,4-D is also applied as herbicide, a growth plant stimulator (but not approved in our country), and post-harvest protection of fruits, especially citrus fruits.

2,4-D mimics the effect of some natural plant growth regulating hormones (e.g. auxins), and thus stimulates growth, rejuvenates old cells, and overstimulates young cells leading to abnormal growth patterns and death in some plants. 2,4-D resistant plants convert the chemical into inactive, nontoxic carbohydrate conjugates, while susceptible plants convert it into amino acid conjugates which obstruct normal nucleic acid metabolism and protein synthesis. This obstruction affects the activity of enzymes, respiration, and cell division and therefore the plants treated with 2,4-D often exhibit malformed leaves, stems, and roots. [6]

Tomatoes are considered one of the most sensitive crops regarding 2,4-D and its derivatives. As a growth stimulator, it is applied in sublethal doses ranging between 0.42 - 13.44 g s.a /ha directly on the plants, in different stages of growth, from the beginning of flowering. For tomatoes, the tolerance to 2,4-D increases a lot with the age of the plant.

Due to the appearance on the Romanian market of some tomatoes of a abnormally shape (appearance of a tassel), with signs of phytotoxicity due to exposure to overdoses of the herbicide 2,4-D used as a growth regulator, the growth stimulation products based on 2,4-D were withdrawn from market.

DETERMINATION OF 2,4-DICHLOROPHENOXYACETIC ACID (2,4-D)
FROM TOMATOES BY LC-MS/MS ANALYSIS

Specialists in horticulture support that in our country are very few varieties of tomatoes (e.g. Prekos variety) that naturally produce this varietal character, that tassel, given by a gene, the B gene. Even in this cause, if that tassel is very pronounced, is a clear indication that growth plant stimulators were used, either for pollination (e.g. 2,4-D) or for forced fruit ripening (e.g. Ethrel). [8]

Ethrel is also withdrawn from the romanian market since 2013, but it is still used for various cultures (as well as 2,4-D), the source of supply of such products being the EU countries where they are still approved for their use and non-EU countries.

In our country are approved as growth plant stimulators sodium o-nitrophenolate, sodium 5-nitroguaiacolate and 1-methylcyclopropene - all of these just for fruits protection.

Few growers from all countries, including from us, follow the approved growth regulators and recommended application dosage, but many of them use unapproved products and high concentrations under the impression that a higher dose gave more effective results.

Many studies have already established that for tomato fruits exceeding recommended dosages (e.g. at twice the recommended concentration), produces deformed fruit (reduced fruit quality), increases fruit number and the appearance of a jelly tissue with immature seeds. Also, significant abnormalities with deformed shapes and poor pulp development were observed externally and in transverse sections. [4,5,9]

Other tests indicate that the fruits derived from the plants which were not treated with growth regulators were characterized by the smallest amount of jelly tissue while the fruits set under the influence of 0.001 % 2,4-D + 0.001 % BAP (benzylaminopurine) had the largest jelly tissue amount. The greatest differentiation was found in fertility which ranged from 7.5 seeds from the fruit derived from the plants treated with 0.005 % 2,4-D, to 75.7 seeds from the non-treated plants' fruit. [5,7,9]

In conditions without precipitation, 2,4-D is absorbed by the plant 4-6 hours after herbicide solution application, and if precipitation occurs, 2,4-D dissolves in rainwater and is absorbed by the plant through the vapors on the plant and from the soil.

So, when higher concentrations are used these substances can modify primary plant metabolisms and be unsafe to public health because these plant growth substances have an accumulative and residual effect. These products being synthetic substances, should be used only at recommended concentrations in order to preserve crop quality and not for obtaining large harvests in the shortest possible time, which can affect public health.

RESULTS AND DISCUSSION

In EU the residues of acidic pesticides (as 2,4-D) can be defined as free acids, esters or additionally conjugates. Conjugated residues are formed in crops as secondary products when acids was covalently bonded to different matrix components via ester-, glycoside- and other bonds.

In crop production acidic pesticides are applied either as free acids or esters linked to a variety of alcohol groups. Hydrolysis plays a key role in the mechanism of action of phenoxy-acid derivatives in plants and soil, and because of these reason most esters are reported as free acids. [9]

In analysis of acidic pesticides when residues definition include esters and/or conjugates is necessary to release acids by break-up of any covalent bonds between acidic pesticides and matrix-components, and this involves alkaline hydrolysis, enzymatic hydrolysis or a combination of both.

In 2007 the European Union Reference Laboratories (EURL) distributed on their site a Single Residues Method (SRM) that presented an extraction method of acidic pesticides, including 2,4-D, from wheat flour samples, where alkaline hydrolysis is performed at room temperature before QuEChERS extraction method. A few years ago, Anastassiades et al, presents a study with a new approach of hydrolysis that employs esterase enzymes in order to achieve full hydrolysis of sterically hindered esters, and similar to alkaline hydrolysis, this enzymatic hydrolysis is performed prior to QuEChERS. [10]

In our country, at the Directorate General for Health and Consumer Protection of the European Commission (DG SANCO) recommendation, the necessity to develop a single residues method for 2,4-D analysis appeared, when a problem was found, which actually persists even now, namely that of determining the 2,4-D residues in tomatoes, because there was more and more suspicion at the local level, that the tomatoes in the agro-food markets are treated with a product that gives them an unnatural appearance and are tasteless. The documentation for both the development of the analysis method and the development of the pesticide extraction method from tomatoes constituted a difficult process of finding information, as very few articles and books were found in the specialized literature dealing with this subject, the results were contradictory. [10,11]

Due to its polar nature 2,4-D is difficult to analyze; it is partially linked to the matrix compounds; a good increase in extractability can be achieved by alkaline hydrolysis (e.g. NaOH, K₂CO₃), but even in this situation the recovery rates are up to 65%. A European method (Alkaline hydrolysis preceding QuEChERS for breaking up conjugates (prior to adding acetonitrile)) has been developed for the determination of phenoxyacid pesticides in flour, including 2,4-D, which uses alkaline hydrolysis in the extraction method, whose part of the analysis method has many elements in common with the

DETERMINATION OF 2,4-DICHLOROPHENOXYACETIC ACID (2,4-D)
FROM TOMATOES BY LC-MS/MS ANALYSIS

one proposed in the present study, the significant difference being in the method of extraction. [10,11].

Also, the analysis method by LC-MS/MS QQQ was a challenge because in matrices of plant origin and animal origin 2,4-D expressed as 2,4-D contain a sum of 2,4-D, its salts, its esters and its conjugates.

In order to establish the most efficient method of extracting 2,4-D from tomatoes, we compared the QuEChERS method and the Miniluke method, with an alkaline hydrolysis previously applied for both.

Both qualitative (chromatographic) and quantitative results were against the QuEChERS method. In figures 1 and 2 were presented the differences between the shape, the amplitude and the areas of the chromatographic peaks obtained by the two extraction methods (HA QuEChERS - alkaline hydrolysis and HA MiniLuke- alkaline hydrolysis), the LCMS analysis method being the same.

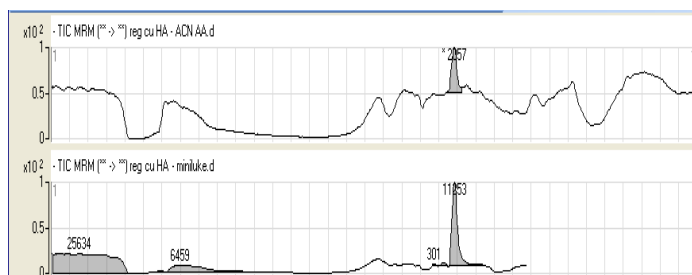


Figure 1. TIC chromatograms for QuEChERS HA - ACN AA) and HA Miniluke extraction method

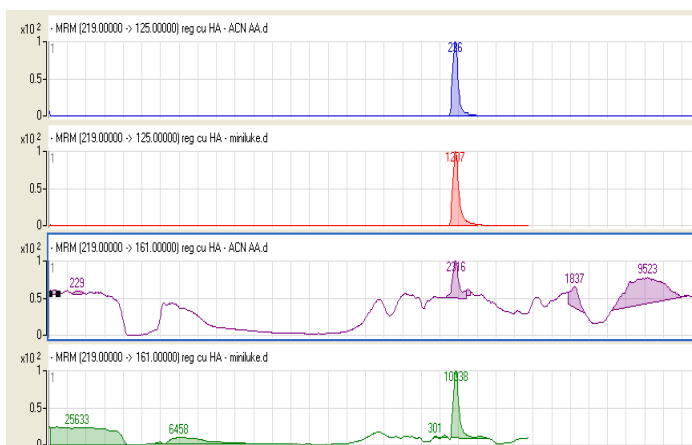


Figure 2. Peak areas for transitions 219→125 and 219→161 with HA Quechers (ACN AA) and HA Miniluke extraction method

The extraction method used by us is a combination of two known methods, namely in the first step an alkaline hydrolysis of the sample is performed, followed, 30 minutes after of the neutralization step, by a slightly modified MiniLuke method. This step is performed with the aim of breaking any covalent bonds between acidic pesticides and matrix components. The extraction procedure is shown schematically the following figure.

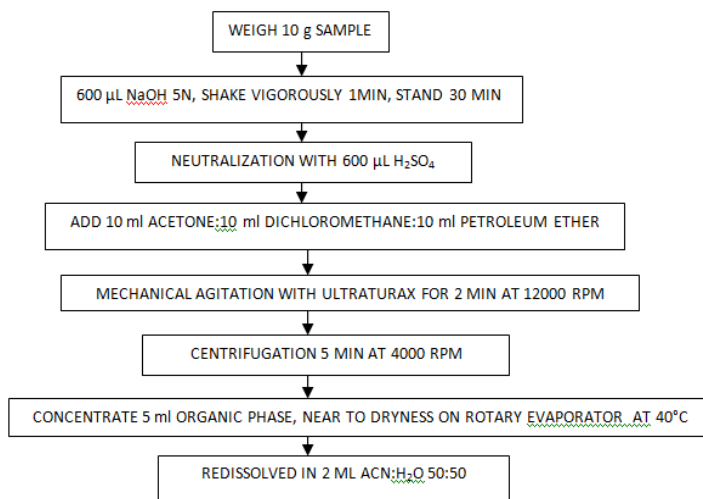


Figure 3. Extraction procedure of 2,4-D from tomatoes

CONCLUSIONS

The analysis method was validated on the matrix of tomatoes (matrix with high water content) and strawberries (matrix with high acidity content), and its efficiency was proven by participating in interlaboratory European tests organized by the European Reference Laboratory for the Analysis of Pesticide Residues from Almeria, Spain where very good Z scores were obtained.

The methods of analysis and extraction of 2,4-D proved effective for matrices with high water content (tomatoes) and those with high acidity (strawberries), but for samples with high starch content (cereals), the extraction method must be modified and adapted, by introducing a certain amount of cold water before the solvent extraction process. The amount of water varies depending on the type of sample (type of cereals) and its granulation after grinding.

The development and validation of 2,4-D extraction method from cereals will be the subject of a subsequent paper.

EXPERIMENTAL SECTION

LC-MS/MS QQQ analysis

For this LC-MS analysis, an AGILENT liquid chromatograph equipped with a quaternary pump model 1200, autosampler and a mass spectrometer triple quadrupole AGILENT 6410A, ionization source type Multi mode ionization (MMI), with electrospray ionization (ESI) in the negative mode.

All the solvents used for the development of the method were of HPLC purity, manufactured by Sigma Aldrich, and the analytical standard 2,4-D was also purchased from Sigma Aldrich. The other reagents were purchased from Merck, and the ultrapure water was produced with the TKA system consisting of two units, Lab Tower and GenPure.

The analytical column was a Zorbax Eclipse XDB-C18, 3.5 microns, 2.1x150mm, (Agilent) kept at 25 °C in the method. Injection volume was 5µL and flow rate of mobile phase was 0.35 ml /min. Mobile phase A was water and phase B was acetonitrile with 0.1% formic acid. Elution gradient was 50% B from the start ramped to the 100% B over the 1 minute, then was ramped at 0% B over the 6 minutes and ramped again at 50% B held until 7 minutes. Energy Fragmentation was established at 70V. Energy Collision for transition 219→161, was established at 10eV, and for transition 219→125 at 25eV. Capillary voltage was setting at 2500V, the temperature of the gas in the ion source at 350 ° C, nebulizer pressure at 60 psi and drying gas flow at 5 L / min. Nitrogen was used as nebulization, desolvation and collision gas.

Method validation

The modified Miniluke extraction method was validated for the tomato matrix, by the LC-MS/MS QQQ method developed in this work, in MRM (Multireaction Monitoring) mode, negative ESI.

Stock solutions of 1000 µg/mL were prepared in acetonitrile and kept in a freezer at -18°C. A 10 µg/mL concentration solution is obtained from the stock solution by dilution with acetonitrile: water 50:50, v/v, this solution being used to determine the optimal fragmentation and collision energies. Another 1µg/mL solution obtained from the 10 µg/mL solution by diluting with acetonitrile: water 50:50, v/v, is used to prepare the calibration standards, this solution if kept cold can be used for several months. The working standards (calibration levels) are obtained by diluting the mixture of pesticides with a concentration of 1 µg/mL, with acetonitrile: water 50:50, v/v, and are prepared whenever needed, being stable for several months if they are kept in optimal conditions (cold and in brown bottles).

In accordance with the guide DG SANCO 12495/2011 and DG SANCO 12571/2013, implemented on 01/01/2014, the following validation criteria are checked for the pesticide 2,4-D in the tomato matrix. [12]

Different types and modes of mass spectrometric detectors provide different degrees of selectivity and specificity, which relates to the confidence in identification. The DG SANCO requirements for LC-MS/MS identification are ≥ 2 product ions. For 2,4-D identification was used 2 transitions 219 \rightarrow 161, and 219 \rightarrow 125. According DG SANCO documents, the relative intensities or ratios of product ions (MS/MS), expressed as a ratio relative to the most intense (product) ion, should correspond to those of the calibration standard at comparable concentrations and measured under the same conditions. Matrix-matched calibration solutions may need to be used. For LC-MS/MS techniques, recommended maximum tolerances for ion ratio were $\pm 30\%$, this criteria has been achieved by proposed analysis method, ion ratio for the two transitions used, being between 8.9 % and 12.1%, depending on the pesticide concentration. (Figure 4)

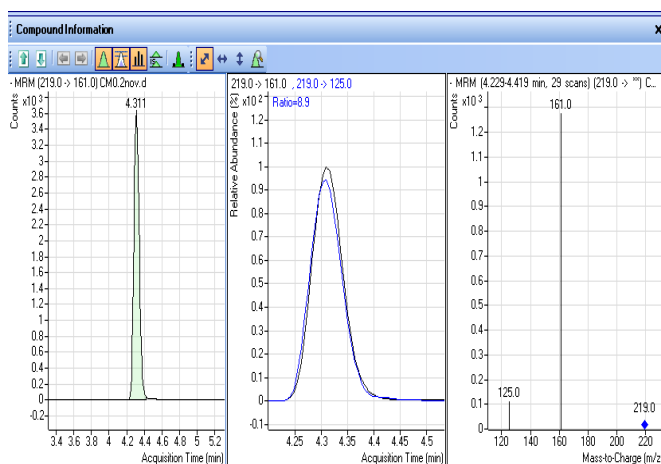


Figure 4. Selectivity and specificity and ion ratio for 2,4-D transitions

Linearity and LOQ

Linearity will be investigated for the pesticides of interest using a 4 point calibration curve (0.025; 0.05; 0.1; 0.2 $\mu\text{g/mL}$). Calibration levels are prepared in 100 ml volumetric flasks by diluting a standard solution of intermediate concentration of 1 $\mu\text{g/mL}$ with acetonitrile: water 50:50, v/v. We do not work with internal standard.

DETERMINATION OF 2,4-DICHLOROPHENOXYACETIC ACID (2,4-D)
FROM TOMATOES BY LC-MS/MS ANALYSIS

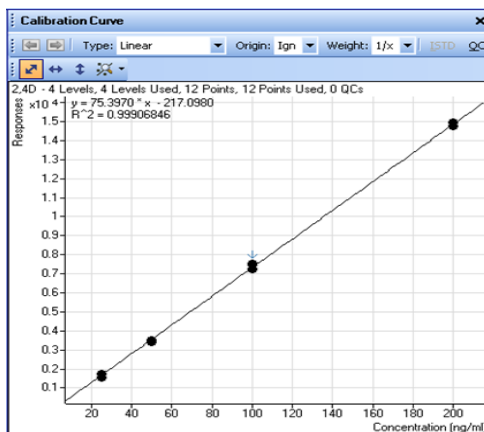


Figure 5. Calibration curve for 2,4-D in fortified blank matrix

The range of linearity is between 0.025-0.2 mg/kg. The linearity of the calibration curves was evaluated both in the solvent (acetonitrile: water 50:50, v/v) and in a blank matrix fortified at the levels of 0.025µg/mL, 0.05µg/mL, 0.1µg/mL and 0.2µg/mL. Each calibration solution was injected three times (n=3) and the relative standard deviation RSD, mean peak areas, calibration curve equation and correlation coefficient were specified. The correlation coefficient (r^2) must be greater than or equal to 0.98.

The LOQ was calculated by injecting lower pesticide concentration in spiked tomato extract that yielded a S/N equal to or slightly higher than 10. Also, by definition, LOQ was the lower concentration level of pesticide for which the acceptability criteria were demonstrated: the average recovery rate should be in the range of 70-120%, the standard deviation STDEV \leq 20%, the relative standard deviation RSD \leq 20% and the LOQ \leq MRL.

The LOQ (0.025 mg/kg) was much lower than the MRL's established by the EU legislations for tomatoes (0.05 mg/kg).

Retention time, regression coefficients (r^2), LOQ, recoveries, coefficient of variation RSD, matrix effects and MRL for 2,4-D in tomatoes are presented in the Table 1.

Table 1. Retention time, regression coefficients (r^2), LOQ, recoveries, coefficient of variation RSD (n= 5) %, matrix effects and MRL

R.T (min)	r^2	LOQ	Spiking level 0.05 mg/kg			Spiking level 0.15 mg/kg			MRL mg/kg
			Reco very %	RSD (n=5) %	Matrix effect	Reco very %	RSD (n=5) %	Matrix effect	
4.311	0.999068	0.025	110.5	5.6	- 4.5	95.8	3.29	-5.5	0.05

Matrix effect

Being a rather charged matrix due to the co-extractive compounds, especially lycopene, it was expected to observe a matrix effect.

The matrix effect was calculated on a control matrix that was fortified at 0.05 mg/kg (MRL level for 2,4-D in tomatoes) and 0.15 mg/kg, making an average of five injections from each fortification level, the analyte concentration was analyzed and calculated. (Table 1)

The extent of matrix effect can be measured in each analytical sequence by comparing calibration standards of the same concentration in solvent vs. those in matrix extracts.

The more different the slopes of the two curves are, the farther the curves are from each other, respectively the greater the matrix effect. (Figure 6)

The difference in the slopes of the calibration curves can be observed, which does not exceed 50%, so it can be argued that in this matrix the residual values of 2,4-D will not be debatable in the situation where the measurement uncertainty is estimated at $\pm 50\%$.

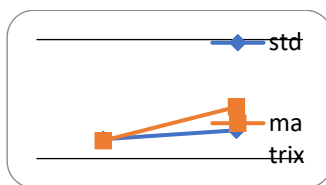


Figure 6. Matrix effect of 2,4-D calculated by the solvent calibration curve vs matrix calibration curve

The same conclusion is supported by the matrix effect calculation using a formula:

$$ME (\%) = \frac{\text{conc. of 2,4-D in matrix} - \text{conc of 2,4-D in solvent}}{\text{conc. of 2,4-D in matrix}} \times 100$$

Recovery and precision

Recovery studies were performed to examine the efficiency of extraction method. Blank samples was spiked at level 0.05 mg/kg and 0.15 mg/kg with five replicates at each level, by standard addition method, and then the recoveries were calculating. The obtained recoveries are shown in Table 1. The average recoveries were 110.5% and 95.8%, indicating that the criteria for this validation parameter was achieved.

DETERMINATION OF 2,4-DICHLOROPHENOXYACETIC ACID (2,4-D)
FROM TOMATOES BY LC-MS/MS ANALYSIS

Precision was evaluated by analyzing five fortified blank tomato samples for each level at the two concentration levels of the recovery studies. The precision was expressed as the RSD values, and the results is presented in Table 1. The obtained values for this validation parameter was according to DG SANCO criteria's. [12]

Measurement uncertainty

The uncertainty will be calculated taking into account both systematic errors (fidelity) and random errors (repeatability, reproducibility). The expanded uncertainty will be established using a 95% confidence interval.

Table 2. Components of measurement uncertainty

Pesticide	Sum of squares	Ucomb/c	Ucomb	U expand	U%
2.4D	4.6215E-03	6.80E-02	6.93E-03	0.01386	13.86

The measurement uncertainty is below 50%, so according to the DG SANCO 12495/2014 guide, in routine analysis, an uncertainty of $\pm 50\%$ can be attributed.

REFERENCES

1. J.J. Menn; *Environ. Health Persp.*, **1978**, Vol. 27, 113-124
2. D.E. Lilienfeld, M.A. Gallo - *Epidemiologic Reviews*, **1989** - hero.epa.gov
3. M.J. Howell, S.H. Wittwer; *Amer. Soc. Hort. Sci. Proc.*, **1954**, 66, 279-283
4. M. Gemici; B. Turkyilmaz, K. Tan; *JFS*, **2006**, Vol 29, 24-32
5. P. Nowaczyk; L. Nowaczyk; *Acta Physiologiae Plantarum*, **2000**, 22, 309–311
6. W.R. Mullison; *Environmental fate of phenoxy herbicides*, Biggar, J.W.Seiber, J.N. (eds.)- Oakland (USA): University of California, **1987**, p. 121-131
7. D. Gelmesa; B. Abebie; L. Desalegn; *Sci.Technol.Arts Res*, **2013**, 2, 25-34
8. C. Vîñătoru; B. Muşat; C. Bratu; *Tratat de legumicultură specială*, Editura ALPHA MDN, **2019**
9. M.R. Warmund; M.R. Ellersieck; R.J. Smeda; *Agriculture*, **2022**, 12, 1489
10. M. Anastassiades, CRL for Single Residue Methods, **2007**
11. EURL-SRM, Analytical Observations Report, *Analysis of Acidic Pesticides Entailing Conjugates and/or Esters in their Residue Definitions*, **2020**, 1
12. DGSANCO/12495/2014, *Method validation and quality control procedures for pesticides residues analysis in food and feed*, **2014**

STUDY ON THE CORROSION INHIBITION EFFICIENCY OF ALUMINUM TRIPOLYPHOSPHATE ON ZINC SUBSTRATE

Julia BOTH^a, Gabriella SZABÓ^{b*}, Liana-Maria MUREȘAN^a

ABSTRACT. The aim of the present study was the electrochemical investigation of the inhibition efficiency of aluminum-tripolyphosphate (ATPP) incorporated in silica (SiO₂) and chitosan (Chit) coatings prepared on zinc substrates. Coatings were prepared by dip-coating method. Electrochemical characterization of the coatings was performed by using electrochemical impedance spectroscopy (EIS) and potentiodynamic polarization curves (PDP). Effect of ATPP on Zn was also determined in 0.2g/L Na₂SO₄ solution and its adsorption on zinc was studied. Results concluded that the ATPP adsorption on Zn obeys Langmuir isotherm. The best corrosion resistance was reached when Zn was protected by SiO₂ coating, obtained from a precursor sol containing 10⁻³ M ATPP.

Keywords: zinc; silicon dioxide; chitosan; Al-tripolyphosphate; anti-corrosion coating; adsorption.

INTRODUCTION

Corrosion has been one of the main global issues of the century. With ever-advancing technologies, the most effective use and protection of all metal types and structures is of vital importance in order to obtain effective and lasting systems. The most common methods of corrosion prevention include the production of metal alloys, the use of inhibitors, or the application of anti-corrosive barrier coatings. Though highly effective, previously greatly

^a Babeș-Bolyai University, Faculty of Chemistry and Chemical Engineering Department of Chemical Engineering, 11 Arany Janos str., RO-400028, Cluj-Napoca, Romania.

^b Babeș-Bolyai University, Faculty of Chemistry and Chemical Engineering, Department of Chemistry and Chemical Engineering of Hungarian Line, 11 Arany Janos str., RO-400028, Cluj-Napoca, Romania.

* Corresponding author: gabriella.szabo@ubbcluj.ro.



demanding chromate inhibitors were excluded due to their high toxicity and carcinogenic nature [1], thus leaving the industry with a high demand for similarly effective alternatives. Developed for this sole purpose, both organic and inorganic coating systems have been previously reported in scientific literature.

Organic and hybrid polymer-based substances are the most commonly used as anti-corrosion barrier coatings, due to their versatility and resilience [2]. Examples of such studied organic coatings are paints [3], epoxy-[4], polystyrene-[5], —and a more environmentally friendly option— chitosan-[6, 7]. Chitosan, as a corrosion protective agent, was reported, along with its derivatives and composites for the corrosion protection of steel alloys [8], as self-healing barrier coating in the case of 2024 aluminum alloy [9], even as smart coating [10] and nanocontainers for antimicrobial applications [11]. Chitosan (Chit) is a great alternative for peelable and temporary coating systems for industrial use [12].

Inorganic materials, such as silica (SiO_2) [13, 14], were also thoroughly studied due to their durability and high resistance to the corrosive environment [15]. Silica nanoparticles were used as carriers for the encapsulation of corrosion inhibitors [16, 17] in different coating matrices for the development of smart coatings. The introduction of different functional groups *via* additives and inhibitors into the inorganic silica matrix was proven to aid corrosion resistance, while also enhancing mechanical and physical properties [18]. Thus, compact [19] and mesoporous [20] silica coatings loaded with a variety of organic inhibitors (e.g., tannic acid [21], benzotriazole, and cetyltrimethylammonium bromide [22, 23]) were rigorously investigated.

Aluminium-tripolyphosphate (ATPP) is a layered, inorganic compound with a wide application spectrum, due to its capacity to intercalate other compounds into its structure [24]. It is most commonly used as an anti-corrosion pigment or precursor for other corrosion inhibitors, due to its low toxicity [25] and low production costs [26]. ATPP also acts as a rust-converter, showing great compatibility with different resins [27]. Studies on ATPP were mostly conducted on steel substrates. Significant studies on the effects of ATPP on zinc plates are yet to be reported.

The aim of the current study was primarily the determination of the inhibition efficiency of ATPP in 0.2g/L Na_2SO_4 solution and after incorporation in two different coating types — an inorganic one, SiO_2 , and biopolymer, Chit — on zinc substrates. It is worth mentioning, that the mechanical properties (roughness, porosity, etc.) of the used metal substrates can potentially affect the behavior of the applied coatings. Based on previous studies, ATPP was introduced directly into the SiO_2 sol before the coating preparation [21], while for Chit coatings, ATPP was introduced *via* impregnation [6, 28]. The prepared coatings were characterized by electrochemical impedance spectroscopy (EIS)

and potentiodynamic polarization curves (PDP). A pre-assessment of the adsorption of different ATPP concentrations on the zinc wafer was determined by using Langmuir's isotherm, which was calculated with the use of R_p values deduced from EIS spectra [29].

RESULTS AND DISCUSSION

The inhibition effect of aluminum tripolyphosphate (ATPP) was studied either dissolved in Na_2SO_4 aqueous solutions, or after its incorporation in SiO_2 or Chitosan coatings. In all cases, Zn was the used substrate.

Effect of ATPP in aqueous solutions on Zn corrosion

In order to observe if the ATPP presents any corrosion inhibition efficiency, aqueous Na_2SO_4 solutions of pH 5 containing this compound were prepared in a wide concentration range. The effect of the different solutions on the Zn plates was studied by means of electrochemical methods, by both potentiodynamic polarization (PDP) and electrochemical impedance spectroscopy (EIS) measurements. First of all, the polarization curves of the different samples were recorded (**Figure 1**) and the corrosion current densities were determined by Tafel interpretation method (**Table 1**).

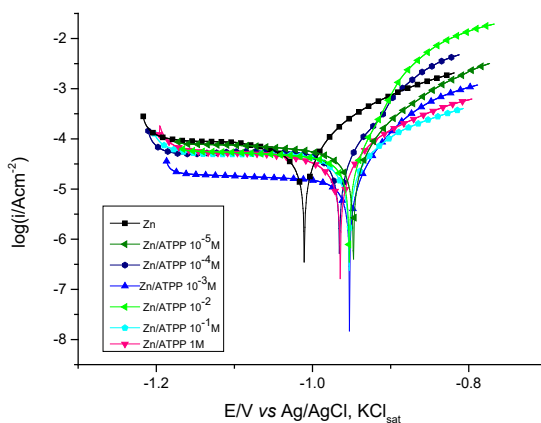


Figure 1. Anodic and cathodic polarization curves for Zn in 0.2 g/L Na_2SO_4 (pH=5) blank solution and in Al tripolyphosphate containing solution in 1M- 10^{-5}M concentration range.

It can be easily observed from the polarization curves, that in the case of extreme concentrations (1M, 10^{-1}M , and 10^{-5}M) the curves are very closely

situated one from another, and their position is only slightly lower than that corresponding to Zn in the solution without inhibitor. This fact is reflected in the values of the corrosion current densities too (**Table 1**). On the contrary, in solutions having the ATPP concentration in the middle of this interval, a greater inhibition effect was noticed, leading to the conclusion that there is an optimal concentration range for ATPP as a corrosion inhibitor. As it can be seen from **Figure 1**, mostly the anodic branches are affected by the inhibitor, due to the adsorption of the ATPP on zinc and blocking of the metal surface. The results are not spectacular but suggest clearly that ATPP acts mainly as an anodic inhibitor. Moreover, in all cases when the inhibitor was present in the solution, can be observed a shift of the E_{corr} toward positive values. This could be explained by the increased control degree of the anodic reaction— the metal dissolution, on the global process.

The efficiency of the inhibition (IE), determined from PDP measurements, was calculated with the following Equation (1):

$$IE\% = \frac{i_{corr}^0 - i_{corr}}{i_{corr}^0} \times 100 \quad (1)$$

where i_{corr}^0 and i_{corr} represent the corrosion current densities in solutions without and with ATPP content, respectively.

Table 1. Kinetic parameters obtained from the potentiodynamic polarization curves of the Zn samples immersed in ATPP aqueous solution

Sample	i_{corr} μAcm^{-2}	E_{corr} V vs Ag/AgCl, KCl _{sat}	b_c V/dec	b_a V/dec	IE %
Zn	62.18	-1.011	0.686	0.090	
Zn/ATPP-1M aq	40.68	-0.964	0.982	0.114	34.6
Zn/ATPP-10 ⁻¹ M aq	39.76	-0.953	0.724	0.127	36.1
Zn/ATPP-10 ⁻² M aq	34.51	-0.952	0.442	0.038	44.5
Zn/ATPP-10 ⁻³ M aq	13.24	-0.952	0.844	0.044	78.7
Zn/ATPP-10 ⁻⁴ M aq	33.37	-0.965	0.223	0.058	46.3
Zn/ATPP-10 ⁻⁵ M aq	50.68	-0.947	0.734	0.075	18.5

In order to get a more accurate image of this phenomenon and aiming to examine the inhibitor adsorption, EIS measurements were performed in a narrower concentration interval. The impedance spectra were recorded at open circuit potentials in the 10 kHz – 10 mHz frequency range. The obtained Nyquist diagrams are presented in **Figure 2**.

The capacitive loop of the Nyquist spectra is attributed to the polarization resistance, including a major contribution of the charge transfer resistance.

It can be observed, that at low concentrations (10^{-5} M) the spectrum is almost the same as that of Zn in absence of the inhibitor. With the increase of the ATPP concentration, the diameter of the loop is increasing, reaching the maximum at 10^{-3} M, and after that it decreases again.

It is worth mentioning that these results are in agreement with the polarization measurements, pointing out the optimal concentration of ATPP of 10^{-3} M. Also, the values of IE (calculated from the corrosion current densities) and z (the inhibition efficiency percentage) that indicates the effectiveness of the inhibition determined from the polarization resistance (equation 3 and 4), are very close to each other.

The possible mechanism reported in the literature is based on the capacity of aluminium triphosphate to release phosphates, which then form a protective layer on the metal substrate, impeding the access of the aggressive species and hindering metal corrosion [30].

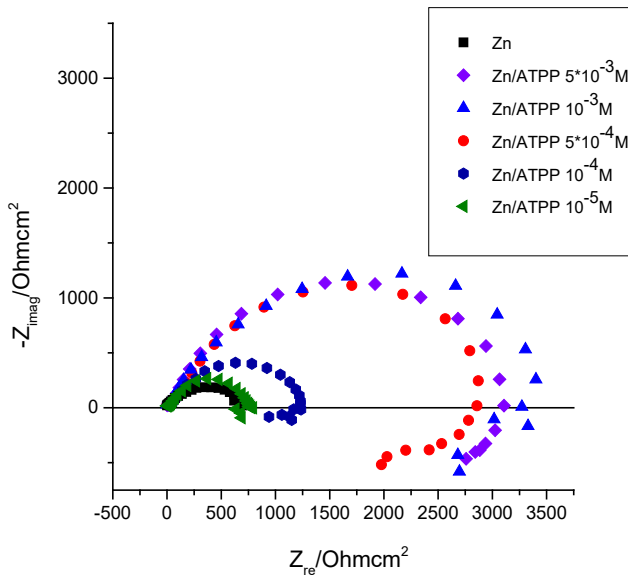


Figure 2. Nyquist spectra for Zn in 0.2 g/L Na_2SO_4 (pH=5) blank solution and in Al tripolyphosphate containing solution in $5 \cdot 10^{-3}$ - 10^{-5} M concentration range.

As already mentioned, the increase of the polarization resistance and, consequently, of the corrosion inhibition is due to the adsorption of the ATPP on Zn, therefore it is important to find the isotherm that fits the experimental data. The first isotherm that was taken into consideration was

the Langmuir isotherm. The linear form of the Langmuir isotherm is given by Equation (2):

$$\frac{c_{ATPP}}{\theta} = \frac{1}{K} + c_{ATPP} \quad (2)$$

where the θ represents the surface coverage, K is the adsorption constant, and c_{ATPP} is the concentration of the inhibitor. The surface coverage can be calculated from the impedance spectra with Equation (3):

$$\theta = \frac{R_p - R_p^0}{R_p} \quad (3)$$

The R_p and R_p^0 are the polarization resistance of solutions containing inhibitor and without it respectively. The inhibition efficiency percentage, calculated from EIS data, can be calculated with Equation (4):

$$z = 100 \times \theta \quad [\%] \quad (4)$$

The adsorption constant, K was calculated with Equation (5):

$$K = \frac{1}{55.5} \exp\left(\frac{-\Delta G_{ads}^0}{RT}\right) \quad (5)$$

In this equation, 55.5 stands for the molar concentration of water expressed in mol/dm³, R represents the universal gas constant, and T is the thermodynamic temperature. The determined adsorption parameters extracted from the impedance diagrams taking into account the Langmuir isotherm are summarized in **Table 2**.

Table 2. Adsorption parameters obtained from the Nyquist spectra of the Zn samples immersed in ATPP aqueous solution

C_{TPP}/M	$R_p/\Omega \cdot cm^2$	θ	$10^3 \cdot C_{TPP}/\theta$ M	z %	K M^{-1}	ΔG_{ads} kJ/mol
0	743	0	0		16.16 · 10 ³	-33.96
10 ⁻⁵	815	0.088	0.11	8.0		
10 ⁻⁴	1253	0.407	0.24	40.7		
5 · 10 ⁻⁴	2859	0.740	0.67	74.0		
10 ⁻³	3342	0.777	1.29	77.7		
5 · 10 ⁻³	3100	0.760	6.58	76.0		

The validity of Langmuir isotherm can be noticed on **Figure 3**, which fits the experimental data with high accuracy ($R^2 = 0.9995$).

STUDY ON THE CORROSION INHIBITION EFFICIENCY OF ALUMINUM TRIPOLYPHOSPHATE ON ZINC SUBSTRATE

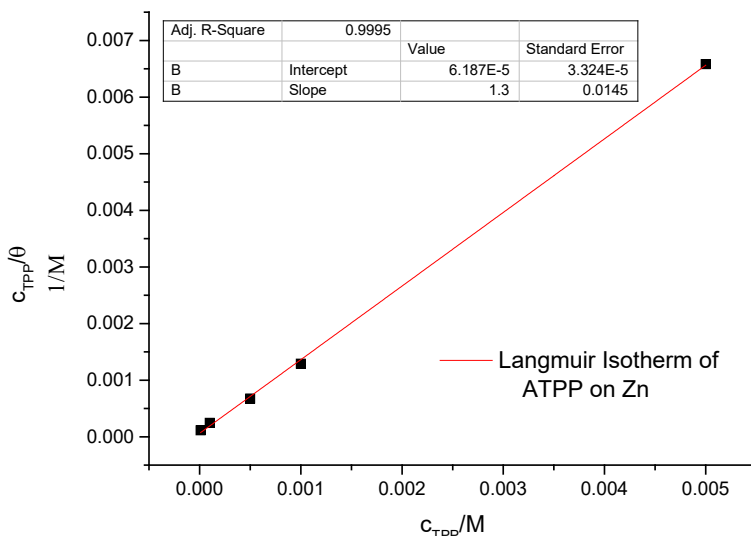


Figure 3. Aluminium tripolyphosphate adsorption from aqueous solutions on Zn substrate: Langmuir isotherm

In general terms, the free energy value determined from Equation (5) can inform about the nature of adsorption: whether it is only physical adsorption ($\Delta G_{ads.}^{\circ} > -20$ kJ/mol) or the process is accompanied by chemical bond formation (chemisorption) [31] when $\Delta G_{ads.}^{\circ} < -40$ kJ/mol. Taking into account the value obtained in our case, chemical bond formation between the inhibitor molecules and the substrate is unlikely.

Effect of ATPP incorporated in chitosan coating on Zn

Chitosan is a remarkable, wide used biopolymer in several industry branches because of its biodegradability, antibacterial properties, and bioavailability. Regardless of the many useful properties, its permeability is sometime inconvenient. Due to the pseudo-porosity of the chitosan thin layers the corrosive electrolyte species can easily reach the metal surface and consequently facilitate the dissolution process. Therefore, the remediation of this disadvantage is frequently obtained through chemical modification by impregnation technique. The positive charge of Chit and the negative charge of ATPP are a good starting point for creation of a consolidated coating with protective properties.

The Chit coated Zn samples were impregnated with 10^{-3} M ATPP aqueous solution, after this had proven to be the most effective incorporation method. The inhibitor was introduced in the layer by immersion for different time intervals. EIS measurements were performed on the chemically modified and dried coatings.

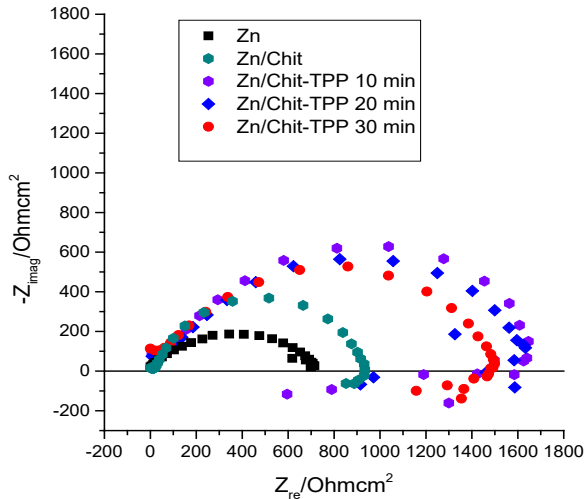


Figure 4. Nyquist spectra for Chit coated Zn impregnated for 10 min, 20 min and 30 min with 10^{-3} M Al tripolyphosphate aqueous solution, recorded in 0.2 g/L Na_2SO_4 (pH=5).

The recorded spectra are depicted in **Figure 4**. It can be observed, that: (i) in all cases the impregnation caused an increased polarization resistance; (ii) the optimal effect was reached with immersion for 10 min. An explanation of this inhibition effect can consist of the cross-linking of the Chit by the ATPP, due to the interaction between the protonated NH_2 groups of Chit and phosphate anions [32].

Effect of ATPP incorporated in SiO_2 coating on Zn

The beneficial effect of Aluminum-tripolyphosphate was also tested using an inorganic matrix, — silica coating.

In this case, the different amounts of ATPP were introduced in the precursor sol. EIS measurements were performed on the coated Zn samples. The obtained impedance spectra are presented in **Figure 5**.

The polarization resistance values are all larger than in the case of chitosan coatings, even without any inhibitor. This points out to better barrier properties of silica coatings, as compared with the chitosan ones. Moreover, even though both SiO_2 and ATPP are negatively charged, their combination led to a coating with higher resistance. This could be due to an insertion of phosphate ions in the silica network during the sol formation.

As it can be observed the best effect was provided by both coatings (SiO_2 and Chit) with 10^{-3} M ATPP content.

STUDY ON THE CORROSION INHIBITION EFFICIENCY OF ALUMINUM TRIPOLYPHOSPHATE
ON ZINC SUBSTRATE

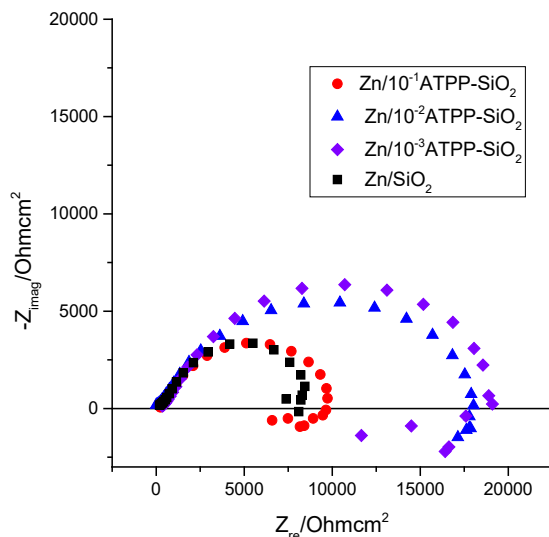


Figure 5. Nyquist spectra for SiO₂ coating doped with 10⁻¹M, 10⁻²M and 10⁻³ M Al tripolyphosphate on Zn, recorded in 0.2 g/L Na₂SO₄ (pH=5).

It is of great importance to mention, that SiO₂ and Chit coatings offer different uses and advantages: while SiO₂ has higher durability and resilience and thus can present as a permanent solution, Chit is also a great alternative for temporary systems. Both of these are of great use in the industry of corrosion protection, hence why, the fact that ATPP can be introduced in both coating systems offers a valuable information from a practical point of view.

CONCLUSIONS

ATPP inhibition effect was studied on Zn substrate. In aqueous solution containing ATPP, it was observed the existence of an optimal concentration (10⁻³M) that provides the highest corrosion current density decrease.

By examining the potentiodynamic polarization curves one can conclude, that the inhibition effect is visible mostly on the anodic branch and affects the metal dissolution process. The calculated standard free energy value allows us to conclude, that predominantly physical adsorption takes place.

ATPP kept its corrosion inhibitor properties even when it was introduced in two different types of coatings (inorganic or biopolymer), with different techniques (mixed in the precursor sol or impregnated from its solution).

The best corrosion resistance was reached when Zn was protected by SiO₂ coating prepared from a precursor containing 10⁻³ M ATPP.

EXPERIMENTAL SECTION

Materials

Natural zinc plates of 2x6x0.55 cm were used as the metal substrate for the applied coatings. Pre-treatment of the substrates was obtained with 0.1M HCl (37%, Merck) aqueous solution and 2-propanol (pure, Chempur).

Precursor sol of SiO₂ was prepared with ethanol (99.3%, Chemical Company), tetraethoxysilane (TEOS, 98%, Alfa-Aesar) and 0.1M HCl (37%, Merck) aqueous solution. Chit solution was prepared with medium molecular weight chitosan (Sigma-Aldrich) and 1% acetic acid (99.5%, Chemical Company) aqueous solution. ATPP (Bridgexim) inhibitor was introduced into both of the coating systems. 0.2 g/L Na₂SO₄ (99%, Sigma-Aldrich) aqueous solution was used as electrolyte medium to carry out electrochemical measurements.

Pretreatment of the zinc plates

Zinc substrates were subjected to a thorough pre-treatment process prior to the application of the prepared precursors. Firstly, the plates were carefully sanded with emery paper (P800, P1500, P2000, P3000, P5000), which was then followed by a surface treatment applied with 0.1M HCl solution, rinsed with distilled water and then degreased with 2-propanol.

Preparation of SiO₂ and Chit precursors

Different, sequential amounts of ATPP were introduced into the SiO₂ sols. The sols were prepared by blending of 20 mL ethanol and 7 mL TEOS with the addition of 10⁻³ M, 10⁻² M and 10⁻¹ M ATPP in a beaker. Concentrations were calculated with the total volume of a SiO₂ sol/batch. The mixture was stirred under standard conditions for 1 hour at 400 rpm. After 1 hour a mixture of 2ml ethanol, 2 mL TEOS and 4 mL .01M HCl was added to the beaker and left under agitation for an additional hour. Chit solution was prepared from the mixture of 1% aqueous acetic acid and 1g of medium molecular weight chitosan which was then agitated for 24 hours.

Preparation of the coatings

Coatings were prepared by dip-coating method with a home-made dip-coater. SiO₂ layers were prepared with a 12 cm/min dipping speed [21], while Chit layers were prepared with a 5 cm/min dipping speed [7]. SiO₂ coatings were thermally treated for 1 hour at 150°C. Chit layers were left to air-dry for 24 hours. After that the impregnation of the Chit coatings was performed by dip-coating technique. The Chit coated samples were immersed in 1mM

aqueous ATPP solution with 12 cm/min dipping speed, kept in solution for 10 min, 20 min and 30 min respectively, then withdrawn with the same 12 cm/min speed [28]. Finally, after withdrawal the excess of inhibitor was washed off with distilled water and the samples were dried.

Electrochemical evaluation of prepared coatings

Electrochemical characterization of the coatings was obtained by OCP, EIS and PDP measurements, which were performed in a three electrode cell on a PARSTAT-2273 potentiostat.

The three electrode cell contained a working electrode (WE- bare or coated zinc substrates), a counter electrode (CE- platinum wire) and a reference electrode (RE- Ag/AgCl/KCl_{sat}). 0.2g/L Na₂SO₄ aqueous solution was used as electrolyte solution.

OCP measurements were carried out for 1h each until the stabilisation of the coated and bare metal plates in the electrolyte solution, in order to obtain a E_{corr} (corrosion potential) as a reference value for further analyses. EIS measurements were carried out in a 10 mHz– 10 kHz frequency interval, with a sinusoidal current of 10 mV amplitude. PDP measurements were carried out at $E = \pm 200$ mV vs. OCP, at a scan rate of 1 mV/min.

ACKNOWLEDGMENTS

Julia Both thanks the Romanian Ministry of Education for the financial support of her doctoral studies.

REFERENCES

1. R.M. Park, J.F. Bena, L.T. Stayner, R.J. Smith, H.J. Gibb, P.S.J. Lees, *Risk Anal.*, **2004**, 24, 1099–1108
2. S.B. Lyon, R. Bingham, D.J. Mills, *Prog. Org. Coat.*, **2017**, 102(A), 2-7
3. J. Both, R. Mezei, G. Szabó, L. M. Mureşan, *Prot. Met. Phys. Chem.*, **2022**, 58(4), 822–833
4. K. Saravanan, S. Sathiyarayanan, S. Muralidharan, S. Syed Azim, G. Venkatachari, *Prog. Org. Coat.*, **2007**, 59(2), 160–167
5. J. Both, G. Szabó, G. Katona, L.M. Mureşan, *J. Electrochem. Sci.*, **2022**, 12(4)
6. Á.F. Szőke, G. Szabó, Z. Hórvölgyi, E. Albert, L. Gaina, L.M. Muresan, *Carbohydr. Polym.*, **2019**, 215, 63–72

7. Á.F. Szőke, G. Szabó, Z. Simó, Z. Hórvölgyi, E. Albert, A.G. Végh, L. Zimányi, L.M. Muresan, *Eur. Polym. J.*, **2019**, *118*, 205–212
8. H. Ashassi-Sorkhabi, A. Kazempour, *Carbohydr. Polym.*, **2020**, *237*, 116110
9. J. Carneiro, J. Tedim, S.C.M. Fernandes, C.S.R. Freire, A.J.D. Silvestre, A. Gandini, M.G.S. Ferreira, M.L. Zheludkevich, *Prog. Org. Coat.*, **2012**, *75(1–2)*, 8–13
10. J. Carneiro, J. Tedim, M.G.S. Ferreira, *Prog. Org. Coat.*, **2015**, *89*, 348–356
11. A.F. Bettencourt, C. Tomé, T. Oliveira, V. Martin, C. Santos, L. Gonçalves, M.H. Fernandes, P.S. Gomes, I.A.C. Ribeiro, *Carbohydr. Polym.*, **2021**, *254*, 117433
12. E. Luckachan, V. Mittal, *Corros. Sci. Technol.*, **2016**, *15(5)*, 209–216
13. W.J. van Ooij, D. Zhu, V. Palanivel, *et al.*, *Silicon Chem*, **2006**, *3*, 11–30.
14. T.R. Ovari, G. Katona, G. Szabo, L. M. Muresan, *Studia UBB Chemia*, **2022**, *67(1)*, 227–244
15. I.S. Bayer, *Coatings*, **2017**, *7*, 12
16. M Yeganeh, M. Omid, S.H.H. Mortazavi, A. Etemad, M.H. Nazari, S.M. Marashi, *MNT*, **2020**, 275–294
17. J.M. Falcón, F.F. Batista, I.V. Aoki, *Electrochim. Acta*, **2014**, *124*, 109–118
18. C.A. Milea, C. Bogatu, A. Duta, *Bull. Trans. Univer. Braşov ser. I Eng. Sci.*, **2011**, *4(53)*
19. E. Volentiru, M. Nyári, G. Szabó, Z. Hórvölgyi, L.M. Mureșan, *Period. Polytech. Chem. Eng.*, **2014**, *58(Supplement)*, 61–66
20. E. Albert, N. Cotolan, N. Nagy, Gy. Sáfrán, G. Szabó, L.M. Mureșan, Z. Hórvölgyi, *Micropor. Mesopor. Mater.*, **2015**, *206*, 102–113
21. J.Both, G. Szabó, G. Katona, L.M. Muresan, *Mater. Chem. Phys.*, **2022**, *282*, 125912
22. G. Szabó, E. Albert, J. Both, L. Kócs, Gy. Sáfrán, Á.F. Szőke, Z. Hórvölgyi, L.M. Mureșan, *Surf. Interfaces.*, **2019**, *15*, 216–223
23. N. Cotolan, S. Varvara, E. Albert, G. Szabó, Z. Hórvölgyi, L.M. Muresan, *Corros. Eng. Sci. Tech.*, **2016**, *51(5)*, 373–382
24. C. Hejjaj, A. Ait Aghzzaf, I. Bouali, R. Hakkou, M. Dahbi, C.B. Fischer, *Corros. Sci.*, **2021**, *181*, 109239
25. A. Khadiri, R. Saddik, K. Bekkouche, A. Aouniti, B. Hammouti, N. Benchat, M. Bouachrine, R. Solmaz, *J. Taiwan Inst. Chem. Eng.*, **2016**, *58*, 552–556
26. A. AitAghzzaf, B. Rhouta, E. Rocca, A. Khalil, J. Steinmetz, *Corros. Sci.*, **2014**, *80*, 46–52
27. W. Li, Z. Fan, X. Li, B. Jiang, F. Yan, Z. Zhang, X. Wang, *Prog. Org. Coat.*, **2019**, *135*, 483–489
28. P. Márton, E. Albert, N. Nagy, B. Tegze, G. Szabó, Z. Hórvölgyi, *Studia UBB Chemia*, **2020**, *65(3)*, 63–79
29. R. Bostan, S. Varvara, L. Găină, L.M.J. Mureșan, *Corros. Sci.*, **2012**, *63*, 275–286
30. D. Song, J. Gao, L. Shen, H. Wan, and X. Li, *J. Chem.*, **2015**, *2015*
31. D.Q. Zhang, Q.R. Cai, X.M. He, L.X. Gao, G.D.J. Zhou, *Mater. Chem.*, **2008**, *112(2)*, 353–358
32. Z. Cui, Y. Xiang, J. Si, M. Yang, Q. Zhang, T.J. Zhang, *Carbohydr. Polym.*, **2008**, *73(1)*, 111–116

GLYPHOSATE AND AMINOMETHYLPHOSPHONIC ACID LEVELS IN WATER AND SOIL SAMPLES FROM TRANSYLVANIAN ROMA COMMUNITY ANALYZED BY HPLC-FLD METHOD

Mihaela VLASSA^{a,*}, Miuța FILIP^a, Virginia COMAN^a, Vlad PĂNESCU^b,
Cătălina HERGHELEGIU^b, Simion BELDEAN-GALEA^b

ABSTRACT. This paper purpose was to develop a sensitive and selective method for the determination of glyphosate, and aminomethylphosphonic acid (AMPA) residues in water and glyphosate from soil samples. The method involves a derivatization step with 9-fluorenylmethylchloroformate in borate buffer of these compounds and liquid chromatography separation with fluorescence detection (HPLC-FLD). Separation of derivatized glyphosate and AMPA compounds was performed on an Agilent ZORBAX C18 reversed-phase column. The mobile phase consisted of a mixture of acetonitrile and 0.05 M KH_2PO_4 solution [30:70 v/v]. Limits of detection (LOD) was 0.28 $\mu\text{g L}^{-1}$ for glyphosate, and 0.35 $\mu\text{g L}^{-1}$ for AMPA, and limits of quantification (LOQ) was 0.84 $\mu\text{g L}^{-1}$ for glyphosate and 1.05 $\mu\text{g L}^{-1}$ for AMPA. The method has been validated for surface water and soil by recovery studies with samples spiked at 25 and 5 $\mu\text{g L}^{-1}$. In water samples, the mean recoveries values ranged between 86.44 - 103.9% for glyphosate, and 71.27 - 99.08% for AMPA. The mean recoveries values for glyphosate ranged from 57 - 81.5% in soil samples. The developed method has been applied for determination of these compounds in water and soil samples from agricultural and rural areas of Roma community from some Transylvania Counties.

Keywords: *Glyphosate, aminomethylphosphonic acid, water, soil, FMOC-Cl, RP-HPLC-FLD.*

^a Babeș-Bolyai University, Raluca Ripan Institute for Research in Chemistry, 30 Fântânele Str., RO-400294, Cluj-Napoca, Romania.

^b Babeș-Bolyai University, Faculty of Environmental Science and Engineering, 30 Fântânele Str., RO-400294, Cluj-Napoca, Romania.

* Corresponding author: mihaela.vlassa@chem.ubbcluj.ro, mihaela_cecilia@yahoo.com.



INTRODUCTION

Glyphosate, [N-(phosphonomethyl) glycine] (GLY), is a non-selective herbicide used primarily for weed and vegetation control [1]. GLY degradation in the environment is mainly due to biodegradation and its main metabolite in plants, water and soil is aminomethylphosphonic acid (AMPA) [2]. GLY low toxicity found to mammals and its rapid transport from plant leaves to their underground parts have contributed to the massive use of it, which has become one of the most widely used herbicides in the world [3]. The World Health Organization (WHO) reconsidered glyphosate in 2015 as potential carcinogenic to humans and the European Chemical Agency published in 2017 a scientific opinion as regards the harmonized classification of glyphosate [4,5,6,7].

GLY and AMPA are low molecular weight, low volatility, highly polar and exhibit insolubility in organic solvents and high solubility in water (12 g/L for GLY). Research studies have shown that both compounds, due to their functional groups, behaves as an amphoteric molecule [4], binding strongly to soil particles so that they persist for up to 170 days with a half-life of 45-60 days [8], this period being influenced by temperature and soil moisture [9]. Due to their physico-chemical properties, their analysis using liquid chromatography (LC) are most suitable than gas chromatography (GC) methods. Although, the lack of specific chemical groups of GLY and AMPA, like chromophores, UV absorption, fluorogenics, disturb their measurement by conventional detectors, being necessary pre-column or post-column derivatization procedures [10].

Direct analysis of GLY and AMPA, without the derivatization step, remain an open issue for the analysts. Marek and Koskinen developed a method for the straightforward analysis of GLY and AMPA in soil using for separation a Bio-Rad cation H exchange column coupled to LC-MS/MS [11] Pre-column methods are based mainly on derivatization with 9-fluorenylmethyl chloroformate (FMOC-Cl) (see Figure 1), fluorogenic labeling with o-phthalaldehyde (OPA) and mercaptoethanol with *N,N*-dimethyl-2-mercaptoethylamine. In post-column procedures, the most known reactions are ninhydrin derivatization followed by UV detection [12].

The HPLC methods coupled to a wide variety of detectors were used to analyze these pesticides: fluorescence (FLD) [13,14,15,16,17], ultraviolet (UV) [18]; reversed-phase liquid chromatography–heated electrospray ionization–tandem mass spectrometry (RP-LC-HESI-MS/MS) [19], HPLC coupled to mass spectrometry (MS) [20,21,22,23], HPLC tandem MS (MS/MS) [4,24,25,26], ultraperformance liquid chromatography–tandem mass spectrometry (UPLC-MS/MS) [27]; HPLC inductively coupled plasma MS (ICP-MS) [28,29] and time-of-flight MS (TOF-MS) [30].

The aim of this paper is to develop a sensitive and selective method for the determination of low concentrations of GLY and AMPA in surface water and GLY from soil samples, by RP-HPLC-FLD, after FMOCC-CL derivatization. The present study does constitute the first monitoring survey regarding the presence of GLY and AMPA in water sources, and GLY in soil, from the Roma community on the part of Transylvania territory. Samples were collected during the summer -autumn 2021 from agricultural as well as to rural areas, since GLY-containing products are also marketed for non-professional uses.

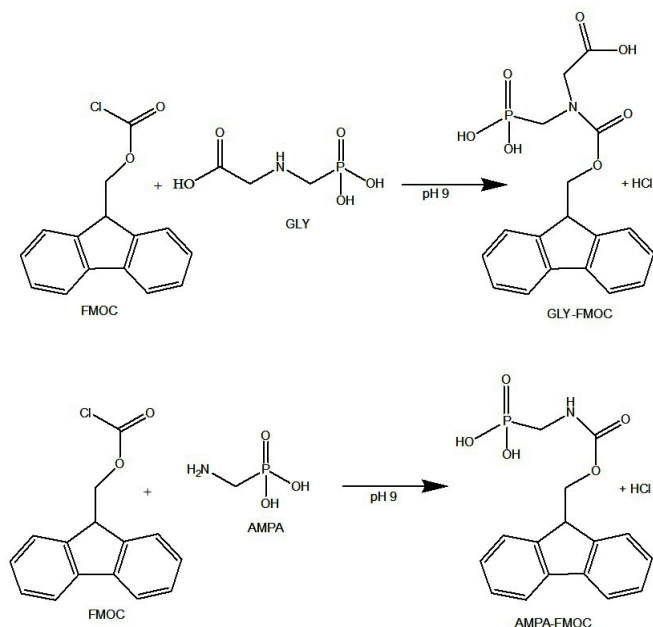


Figure 1. Derivatization reaction of GLY and AMPA with FMOCC-Cl

RESULTS AND DISCUSSION

Developing and validation of the RP-HPL-FLD method

An analytical procedure developed by the Garba et. al [17], based on pre-column derivatization with FMOCC-Cl followed by high-performance liquid chromatography with fluorometric detection was improved and optimized for the analysis of the GLY herbicide and its metabolite AMPA in water, and GLY in soil. The ultrasound-assisted extraction was used for the isolation of the target compound from soil samples, followed the above-mentioned procedure.

The RP-HPLC-FLD methods were validated on following parameters: selectivity, linearity, accuracy, precision, limits of detection (LOD) and quantification (LOQ) [31].

Selectivity was tested by comparing the chromatograms of a standard solution of mixture of GLY and AMPA, with those of a water and soil samples as presented in Figure 2. The chromatograms of the standard solution show the retention times of 2.820 and 4.961 min for GLY and AMPA, respectively. As can be seen from the chromatograms, alongside to the interest peaks, another large peak, which is attributed to FMOc -OH residual, appears at 35 min [17, 32].

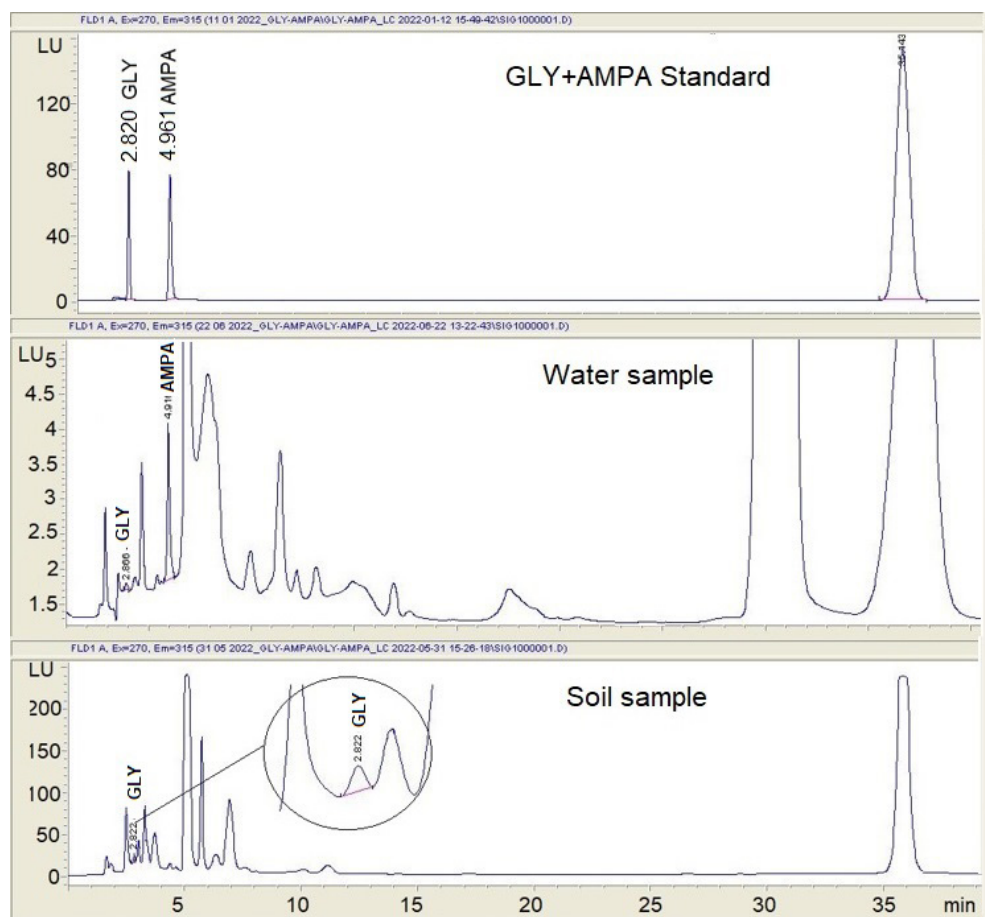


Figure 2. RP-HPLC-FLD chromatograms of GLY and AMPA in standard mixture, water sample and soil sample

Linearity is the method capacity to assure that the laboratory test results that are directly proportional to the concentration of the analyte in a sample. It was established by figured the analyte peak area versus the analyte concentration and was calculated on the basis of the calibration curve. To establish linearity, eight concentrations in the range of 0.195- 25 $\mu\text{g L}^{-1}$ of GLY and AMPA solutions were prepared from the stock solution and analysed in duplicate. The obtained results indicate correlation coefficients (R^2) of 0.99976 for GLY and 0.99945 for AMPA (Table 1). The limits of detection (LOD) reached were 0.28 $\mu\text{g L}^{-1}$ for GLY and for AMPA 0.35 $\mu\text{g L}^{-1}$ and the limits of quantification (LOQ) were 0.84 $\mu\text{g L}^{-1}$ for GLY and 1.05 $\mu\text{g L}^{-1}$ for AMPA respectively. These low values show a good sensitivity of the proposed method. The parameters of the calibration curve are presented in Table 1.

Table 1. Linear regression data, LOD and LOQ of GLY and AMPA compounds

Parameters	Compounds	
	GLY	AMPA
RT [min]	2.820	4.961
Equation of calibration	$Y=2.34289X-0.406231$	$Y=3.51385X-0.979488$
Linear range [$\mu\text{g L}^{-1}$]	0.195- 25	0.195- 25
R^2	0.99976	0.99945
RSD (%)	0.460	1.036
LOD $\mu\text{g L}^{-1}$	0.28	0.35
LOQ $\mu\text{g L}^{-1}$	0.84	1.05

RT retention time; R^2 regression coefficient of calibration curve (n=8, 21 points); LOD, the limit of detection (S/N = 3); LOQ, the limit of quantification (S/N = 10)

The data regarding *precision* of the method was determined by measuring repeatability for six independent measurements for each compound, carried out under the same conditions, and the results show there were no significant differences between the test results. The method precision was satisfactory, the data are showed in Table 2.

Table 2. Intra and inter day precision of GLY and AMPA compounds

Pesticide	Concentration [$\mu\text{g L}^{-1}$]	Intra-Day Precision (n=6)		Inter-Day Precision (n=9)	
		Concentration Mean \pm SD	RSD [%]	Concentration Mean \pm SD	RSD [%]
GLY	-	-	-	24.49 \pm 1.21	4.93
	12.5	12.31 \pm 0.26	2.08	12.21 \pm 0.62	5.08
	-	-	-	1.92 \pm 0.13	6.83
AMPA	-	-	--	24.24 \pm 1.14	4.72
	12.5	12.26 \pm 0.25	2.06	12.10 \pm 0.61	5.07
	-	-	-	1.96 \pm 0.12	6.02

Mean = Average of n determination; SD = Standard deviation;
RSD = Relative standard deviation;

Recovery parameter of the method was measured by addition of 25 and 5 $\mu\text{g L}^{-1}$ GLY and AMPA to a selected analyzed sample of water and 25 and 5 $\mu\text{g Kg}^{-1}$ of these compounds in soils, respectively. This step was taken before the extraction of GLY and AMPA and then the whole procedure was conducted. The obtained results show good accuracy for both compounds, the recoveries ranging between 82-103% for GLY and 71.27-99.08% for AMPA in water samples. In soil samples the recovery degrees were 47.5-81.5% (Table 3). Also, research studies report low recovery of GLY 34-74% from different type of soils in comparison with 80-110% from water samples [17], facts assigned due to high adsorption of GLY by the soil samples.

Table 3. Accuracy of the HPLC-FLD for GLY and AMPA method, recovery degree

Compound [water]	Amount [$\mu\text{g L}^{-1}$]			Recovery [%]	Mean \pm SD
	initial	added	found		
GLY	0	25	23.82	95.28	98.69 \pm 4.62
	0	25	25.99	103.96	
	0	25	24.21	96.84	
	0	5	4.51	90.20	91.80 \pm 9.90
	0	5	4.14	82.80	
	0	5	5.12	102.40	
AMPA	7.6	25	32.30	99.08	91.03 \pm 6.99
	7.6	25	28.55	87.58	
	7.6	25	28.18	86.44	
	7.6	5	11.01	87.38	78.76 \pm 8.11
	7.6	5	8.98	71.27	
	7.6	5	9.78	77.62	
<hr/>					
Compound [soil]	Amount [$\mu\text{g Kg}^{-1}$]			Recovery [%]	Mean \pm SD
GLY	45.92	25	40.42	57	68.5 \pm 12.32
	45.92	25	57.80	81.5	
	45.92	25	47.52	67	
	45.92	5	25.97	51	55.83 \pm 11.54
	45.92	5	35.13	69	
	45.92	5	24.19	47.5	

Mean = Average of three determination; SD = Standard deviation;

Aparicio et al., 2013, affirm that the GLY adsorbed into the soil is protected from biological degradation, due to a dynamic process of adsorption/desorption and only the microorganisms can degrade it to his metabolites [27]. Thus, can be a reason we found in almost half of the

GLYPHOSATE AND AMINOMETHYLPHOSPHONIC ACID LEVELS IN WATER AND SOIL SAMPLES
FROM TRANSYLVANIAN ROMA COMMUNITY ANALYZED BY HPLC-FLD METHOD

samples the presence of GLY in comparison with water samples where GLY was practical absent. The results obtained in studied surface water and soil samples were presented in Table 4.

Table 4. GLY and AMPA found in water and soil samples from localities took studied

Sampling point	County	Water samples			Soil samples	
		No	GLY range ($\mu\text{g L}^{-1}\pm\text{SD}$)	AMPA range ($\mu\text{g L}^{-1}\pm\text{SD}$)	No	GLY ($\mu\text{g Kg}^{-1}\pm\text{SD}$)
Roşia Montana	Alba	2	<LOD <LOD	<LOQ <LOQ	-	-
Diosig	Bihor	2	<LOD <LOD	<LOQ <LOQ	2	<LOD 2.47±0.02
Teţchea		2	<LOD <LOD	<LOQ <LOD	2	<LOD <LOD
Baţa	Bistriţa-Năsăud	2	<LOD <LOD	<LOQ <LOQ	-	
Reteag		2	<LOD <LOD	<LOD <LOQ	1	45.92±0.14
Bodoc	Covasna	1	<LOD	<LOQ	1	1.45±0.04
Boroşneu Mare		1	<LOD	<LOQ	2	25.60 ±0.07 14.00±0.09
Avrămeşti	Harghita	3	<LOD <LOD <LOD	<LOD <LOD 5.83±0.04	-	-
Atid		3	<LOD <LOD <LOD	<LOD <LOQ <LOQ	-	-
Zetea		2	<LOD <LOQ	<LOD <LOQ	-	-
Coltău	Maramureş	4	<LOD <LOD <LOD <LOD	<LOQ 1.02±0.06 <LOQ <LOQ	1	3.33±0.05
Băgaciu	Mureş	3	<LOD <LOD <LOD	<LOQ <LOQ <LOQ	2	18.42±0.09 29.45±0.09
Deda		-	-	-	1	2.74±0.03
Deleni		1	<LOD	<LOQ		
Gorneşti		2	<LOD <LOD	<LOD <LOD	-	-
Gurghiu		2	<LOD <LOD	<LOQ 1.844±0.05		
Saschiz		4	<LOD	<LOD	1	<LOD
			<LOD	5.09±0.04		
			<LOD	<LOD		

Sampling point	County	Water samples		Soil samples		
		No	GLY range ($\mu\text{g L}^{-1}\pm\text{SD}$)	AMPA range ($\mu\text{g L}^{-1}\pm\text{SD}$)	No	GLY ($\mu\text{g Kg}^{-1}\pm\text{SD}$)
			<LOD	<LOQ		
Șaeș		3	<LOD <LOD <LOD	<LOD 2.98±0.03 7.62±0.04	-	-
Terebești	Satu Mare	2	<LOD <LOD	<LOD <LOD	-	-
Tiream		4	<LOD <LOD <LOD <LOD	<LOQ <LOD 3.22±0.03 1.56±0.030	2	12.98±0.06 21.70 ±0.08
Turulung		2	<LOD <LOD	<LOD <LOQ	1	21.41±0.09
Almașu	Sălaj	3	<LOD <LOD <LOD	<LOQ <LOQ <LOQ	1	3.33±0.03
Racovița	Sibiu	2	<LOD <LOD	<LOQ 1.02±0.06	2	7.43±0.04 5.04±0.03
Sebeșu de sus		2	<LOD <LOD	<LOD <LOD	-	-

No - Number of analysed samples

In the studied surface waters, GLY was practically absent, while AMPA was found in almost all samples. In 15 % water samples the AMPA concentration ranging between 1.019 and 7.621 $\mu\text{g L}^{-1}$ and in 75 % samples the found values were under LOQ. In the 79 % of studied soil samples, GLY concentration found ranging between 1.449 and 45.925 $\mu\text{g Kg}^{-1}$. The studies conducted regarding the presence and concentration of GLY in soil samples by Aparicio et al., 2013 in farms from Buenos Aires, Argentina, presented glyphosate in concentrations between 35 and 1502 $\mu\text{g kg}^{-1}$. Primost et al., 2017 also from Argentina (Pampas area), measured concentrations of glyphosate between 530 and 4450 $\mu\text{g kg}^{-1}$ in soybean fields treated twice with glyphosate. In studied soils from a public garden in Spain, Ibañez et al., 2005, found concentrations of GLY between 170 and 730 $\mu\text{g kg}^{-1}$ and Karasali et al., 2019 had found in the major basins of the Greek territory GLY presence in concentration levels from 0.026 to 40.6 $\mu\text{g g}^{-1}$.

CONCLUSIONS

An analytical procedure, RP-HPLC-FLD based on FMOC-Cl derivatization have been developed, for the analysis of GLY pesticide and its AMPA metabolite in water and GLY in soil samples collected from rural Roma communities from 10 counties in Transylvania area.

The developed procedure showed good linearities and limits of detection and quantification, being applicable to the analysis of the selected pesticides in studied water and soil samples. The RP-HPLC-FLD procedure has been applied to monitor the target compounds in potable and non-potable surface water samples collected during 2 months in 2021 summer-autumn. The most found compound in water samples was the AMPA metabolite with values between 1.019 and 7.621 $\mu\text{g L}^{-1}$, while GLY were practical absent. Instead, the GLY was more present in the soil samples collected from agricultural and rural area. GLY concentration found ranging between 1.449 and 45.925 $\mu\text{g Kg}^{-1}$.

The presence of these compounds in surface water and soils is a current issue for environmental protection, therefore the periodical monitoring is recommended.

EXPERIMENTAL SECTION

Chemicals and reagents

All reagents were of analytical grade. Glyphosate (GLY, 99.7%) standard, amino phosphonic acid (AMPA, 99.0%) and 9-fluorenylmethyl chloroformate standard (FMOC-Cl, 98.0%) (Sigma-Aldrich USA, Germany), $\text{Na}_2\text{B}_4\text{O}_7 \cdot 10\text{H}_2\text{O}$ and KH_2PO_4 (AnalaR NORMAPUR, VWR Chemicals, Belgium), HPLC grade acetonitrile and KH_2PO_4 (HiperSolv CHROMANORM, Germany). Ultra-pure water, obtained with the Millipore water purification system (Millipore USA). Ethyl ether (AnalaR NORMAPUR, Germany).

Instruments and equipments

Analyzes were performed on an Agilent Technologies 1200 Series high-performance liquid chromatograph (Agilent, USA): Autosampler (Model ALS G 1329 A); Degasser (Model G 1322 A); Quaternary pump (Model G 1311 A); Thermostat (Model TCC SL G 1316 B); Detector FLD (Model FLD 60558084); Data collection and analyzes were performed using Software ChemStation. The samples were prepared using: analytical balance OHAUS (Switzerland), digital pH meter HANNA (Romania), ultrasound bath (ELMA Elmasonic P, Germany) and centrifuge (Eppendorf Centrifuge 5804 R, Germany). Analytical grade water was obtained from Milli-Q Ultrapure water purification system (Millipore, USA).

Chromatographic conditions for determination of GLY and AMPA by RP-HPLC-FLD

Separation of GLY and AMPA, FMOC-Cl derivatives was performed on an Agilent ZORBAX Eclipse Plus C18 reversed-phase column (5 μm particle size, 150 \times 4.6 mm i.d.). The fluorescence detector was set at 210 nm (excitation) and 315 nm (emission). The mobile phase consisted of a mixture of ACN and 0.05 M KH_2PO_4 solution [30:70 v/v]. Flow rate of the mobile phase has been selected of 0.7 mL / min, injection volume 20 μL , separation being done at a 40 $^\circ\text{C}$ of column temperature.

Samples collection and extraction conditions

The present study was performed on samples collected from 25 rural Roma communities from 10 counties in Transylvania (Figure 3).

Water sampling was done according to SR-ISO-5667-2007, in brown bottles. The soil sampling was performed according to STAS 7184/1-84. The soil samples were collected at a 5 - 20 cm depth, from two-three sampling points. All collected samples (water and soil) were transported in a cooling bag and stored in a freezer until analysis.

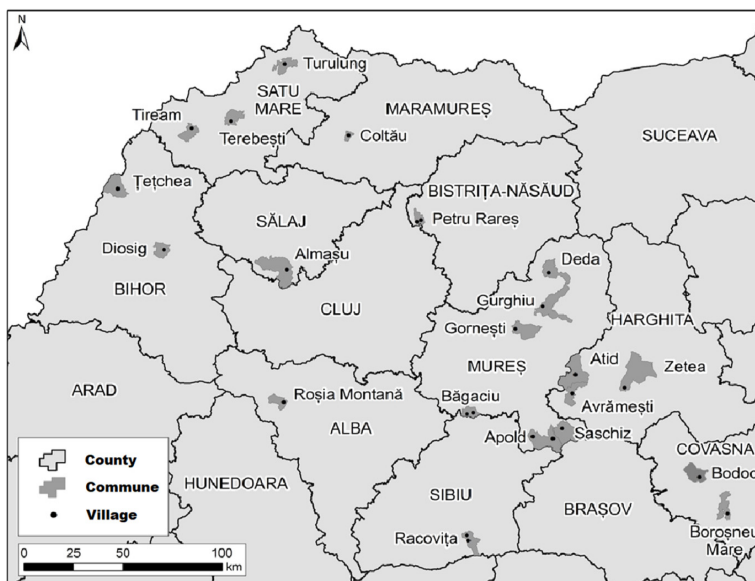


Figure 3. Geographic location of the studied area, regarding the locations of water and soil sampling from 10 counties in Transylvania.

Derivatization procedure of GLY and AMPA

Water samples were thawed, brought to room temperature, homogenized and filtered through a syringe 0.45 μm filter (Teknokroma, Spain)

To 500 μL aliquot of the water sample was added 500 μL of 0.02 M FMOCCl and 1 ml of 0.05 M borate buffer solutions. The mixture was vigorously stirred for 10 minutes, and then allowed to react in the darkness for 60 minutes. The excess FMOCCl reagent was extracted, by stirring for 3 minutes, with 1 mL of ethyl ether, twice. The upper layer of ether was removed by suction with a pipette. The aqueous layer was then transferred to a 1.5 ml vial for HPLC analysis. Samples were done in duplicate.

Soil samples were thawed, air dried, sieved for pebbles removal and weeds, and homogenized in a mortar. An approximately amount of 15 g of the soil sample was weighed and treated with 15 ml of 0.1 M KH_2PO_4 . The homogenized sample was ultra-sonicated for 30 minutes (100% power, 87 KHz), centrifuged for 15 min at 4000 rpm, and the supernatant was collected. The operation was repeated twice. The reunited supernatants were filtered by syringe 0.45 μm filter and further an aliquot of 0.5 mL was subjected to derivatization with FMOCCl as in the method described above. Samples were done in duplicate.

Preparation of the standard solution

The stock standard solution of 200 $\text{mg}\cdot\text{L}^{-1}$ GLY and AMPA each was prepared with Millipore water. Working standard solutions were prepared in water by appropriate dilution of stock solution, in the range of 0.192–25 $\mu\text{g}\cdot\text{mL}^{-1}$. Solutions of 0.05 M $\text{Na}_2\text{B}_4\text{O}_7\cdot 10\text{H}_2\text{O}$ (pH= 9), 0.1 M and 0.05 M KH_2PO_4 were prepared in water. The 0.02 M FMOCCl solution was prepared in acetonitrile. The solutions were kept in the refrigerator at 4°C and were stable for two weeks.

Method validation

The selectivity was tested by comparing the chromatogram of a standard solution of GLY and AMPA and the same compounds present in the studied samples. *Linearity* was assessed based on a plot of the analyte peak area against analyte concentration. Calibration range was between 0.192 – 25 $\mu\text{g}\cdot\text{L}^{-1}$ from each standard.

Accuracy of the method was studying the recovery degree. Three different concentration levels of 2 $\mu\text{g}\cdot\text{L}^{-1}$ (low level), 12.5 $\mu\text{g}\cdot\text{L}^{-1}$ (intermediate level) and 25 $\mu\text{g}\cdot\text{L}^{-1}$ (high level) of standard mixtures were added to the water

and soil sample. Spiked samples were prepared in triplicate. The recovery was calculated as follows equation:

$$\text{Recovery [\%]} = \text{found amount} - \text{initial amount} / \text{added amount} \times 100$$

The *intra-day precision* was obtained from the data of the 5 replicates analysis of 12.5 $\mu\text{g L}^{-1}$, standard solution;

Inter-day precision (three replicate for three consecutive days) determinations were performed on the three different standard solutions of 25, 12.5 and 2 $\mu\text{g L}^{-1}$; the precision was expressed as percentage of relative standard deviation (% RSD).

LOD and *LOQ* parameters were calculated as the concentration corresponding to three and ten times respectively, of the background noise of the blank (signal-to-noise ratio, S/N).

ACKNOWLEDGMENTS

The research leading to these results has received funding from the Norway Grants 2014-2021 under Project contract no. 23 / 2020 (RO-NO-2019-0463).

REFERENCES

1. P. J. Peruzzo; A. A. Porta; A. E. Ronco; *Environ. Pollut.*, **2008**, *156*, 61-66
2. I. Freuze; A Jadas-Hecart; A. Royer; P-Y. Communal; *J. Chromatogr. A*, **2007**, *1175*, 197-206
3. M. P. García de Llasera; L. Gómez-Almaraz; L. E. Vera-Avila; A. Peña-Alvarez; *J. Chromatogr. A*, **2005**, *1093*, 139-146
4. H. Karasali; G. Pavlidis; A. Marousopoulou; *Environ. Sci. Pollut. Res.*, **2019**, *26*, 36308-36321
5. J. P. Muñoz; T. C. Bleak; G. M. Calaf; *Chemosphere*, **2021**, *270*, 128619
6. L. Battisti; M. Potrich; A. R. Sampaio; N. de Castilhos Ghisi; F. M. Costa-Maia; R Abati; C.B. Dos Reis Martinez; S.H.Sofia; *Sci. Total Environ.*, **2021**, *767*, 145397
7. Y. Sang; J.-C. Mejuto; J. Xiao; J. Simal-Gandara; *Plants*, **2021**, *10*, 405-427
8. H. Vereecken; *Pest Manag. Sci.*, **2005**, *61*, 1139-1151
9. C. P. Bento; X. Yang; G. Gort; S. Xue; R. van Dam; P. Zomer; H. G. J. Mol; C. J. Ristema; V. Geissen; *Sci. Total Environ.*, **2016**, *572*, 301-311
10. T. Arkan; I. Molnár-Perl; *Microchem. J.*, **2015**, *121*, 99-106
11. L. J. Marek; W. C Koskinen; *Pest Manag. Sci.*, **2014**, *70*, 1158-1164
12. L. B. Bhaskara; P. Nagaraja; *Helv. Chim. Acta*, **2006**, *89*, 2686-2693
13. M. E. Baez; E. Fuentes; M. J. Espina; J. Espinoza; *J. Sep. Sci.* **2014**, *37*, 3125-3132

GLYPHOSATE AND AMINOMETHYLPHOSPHONIC ACID LEVELS IN WATER AND SOIL SAMPLES
FROM TRANSYLVANIAN ROMA COMMUNITY ANALYZED BY HPLC-FLD METHOD

14. K. Mardian-Jansar; B. S. Ismail; *AIP Conference Proceedings*, **2014**, 1614, 795-802
15. S. Wang; B. Liu, D. Yuan; J. Ma; *Talanta*, **2016**, 161, 700–706
16. L. Sun; D. Kong; W. Gu; X. Guo; W. Tao; Z. Shan; Y. Wang; N. Wang; *J. Chromatogr. A*, **2017**, 1502, 8–13
17. J. Garba; A. W. Samsuri; R. Othman; M. S. A. Hamdani; *Environ. Sci. Technol.*, **2018**, 1, 19-30
18. T. C. P. G. Catrinck; A. Dias; M. C. S. Aguiar; F. O. Silvério; P. H. Fidêncio; G. P. Pinho; *Braz. Chem. Soc.*, **2014**, 25, 1194–1199
19. W. Skeff; C. Recknagel; D. E. Schulz-Bull; *J. Chromatogr. A*, **2016**, 1475, 64–7310-11.
20. A. M. Botero-Coy; M. Ibanez; J. V. Sancho; F. Hernandez; *J. Chromatogr. A*, **2013**; 1292, 132-141
21. L. J. Marek; W. C. Koskinen; *Pest Manag. Sci.*, **2014**, 70(7), 1158-1164
22. L. L. Alonso; P. M. Demetrio; M. A. Etchegoyen; D. J. Marino; *Sci. Total Environ.*, **2018**, 645, 89-96
23. T. Erban; M. Stehlik; B. Sopko; M. Markovic; M. Seifrtova; T. Halesova; P. Kovaricek; *Chemosphere*, **2018**, 207, 78-83
24. M. Ibáñez; Ó. J. Pozo; J. V. Sancho; F. J. López; F. Hernández; *J. Chromatogr. A*, **2005**, 1081, 145-1557
25. A. Ghanem; P. Bados; L. Kerhoas; J. Dubroca; J. Einhorn; *Anal. Chem.* **2007**; 79, 3794-3801
26. T. Ohara; T. Yoshimoto; Y. Natori; A. Ishii; *Nagoya J. Med. Sci.*, **2021**, 83, 567-587
27. V. C. Aparicio; E. De Gerónimo, D. Marino; J. Primost; P. Carriquiriborde; J. L. Costa; *Chemosphere*, **2013**, 93, 1866–1873
28. M. Popp; S. Hann; A. Mentler; M. Fuerhacker; G. Stingereder; G. Koellensperger; *Anal. Bioanal. Chem.*, **2008**, 391, 695–699
29. J. P. F. Tiago; L. C. Sicupira; R. E. Barros; G. P. de Pinho; F. O. Silvério; *J. Environ. Sci. Health - B Pestic. Food Contam. Agric. Wastes*, **2020**, 1532-4109
30. V. G. Amelina; A. M. Andoralov; *J. Anal. Chem.*, **2016**, 71, 82–93
31. ICH harmonised tripartite guideline. Validation of analytical procedures: Text and methodology Q2 (R1). 2005.
http://www.ich.org/fileadmin/Public_Web_Site/ICH_Products/Guidelines/Quality/Q2_R1/Step4/Q2_R1_Guideline.pdf, pp. 1-17.]
32. T. V. Nedelkoska; G. K-C. Low; *Anal. Chim. Acta*, **2004**, 511, 145–153
33. J. E. Primost; D. J. Marino; V. C. Aparicio; J. L. Costa; P. Carriquiriborde; *Environ Pollut.* **2017**, 229, 771–779.

HISTORICAL ASSESSMENT OF ATMOSPHERIC PERSISTENT ORGANIC POLLUTANTS DEPOSITIONS IN MUNTINU GLACIAL LAKE, SOUTHERN ROMANIAN CARPATHIANS, BASED ON RADIONUCLIDE-DATED SEDIMENTS

Vlad Alexandru PĂNESCU^a, Robert BEGY^a,
Gheorghe ROȘIAN^a, Maria Concetta BRUZZONITI^b,
Mihail Simion BELDEAN-GALEA^{a*}

ABSTRACT. This study aims to assess the pollution history of persistent organic pollutants (POP) in lake Muntinu, Carpathian Mountains, Romania. Gamma spectrometry was used to measure ²¹⁰Pb and ¹³⁷Cs radionuclides in order to determine the age of sediment layers. The target compounds were isolated from sediment samples by ultrasound-assisted extraction method, followed by purification of extracts using open-column chromatography. 16 polycyclic aromatic hydrocarbons (PAHs), 20 organochlorine pesticides (OCPs) and 12 polychlorinated biphenyls (PCBs) were analysed in each dated sediment layer using gas chromatography coupled with mass spectrometry or electron capture detector. The results show that, over the past 100 years, POP concentrations from sediment samples ranged from 2.53 to 156.27 ng/g for PAHs, from 1.78 to 71.12 ng/g for OCPs, and from not detected to 76.03 ng/g for PCBs. PAHs diagnostic ratios such as Σ LMW/ Σ HMW, ANT/(ANT+PHE) and FLT/(FLT+PYR) show that the main source of PAHs in the sediment is of pyrogenic nature, especially from biomass and coal combustion. The sources of OCPs and PCBs could not be determined due to the lack of data obtained. However, the study demonstrates that the analysis of POP residues in sediments is a suitable method for reconstructing the history of surface water pollution.

Keywords: *Historical pollution, Polycyclic aromatic hydrocarbon, Organochlorine Pesticide, Polychlorinated biphenyl, radionuclides dated sediment.*

^a Babeș-Bolyai University, Faculty of Environmental Science and Engineering, 30 Fântânele str., RO-400294 Cluj-Napoca, Romania.

^b Department of Chemistry, University of Turin, via P. Giuria 7, Torino, Italy.

* Corresponding author: simion.beldean@ubbcluj.ro.



INTRODUCTION

Persistent organic pollutants (POPs) are chemical compounds considered of high interest in environmental studies due to their high persistency and high toxicity. These pollutants are the main subject of the Stockholm Convention, in which all the partners involved have reached a conclusion that these pollutants possess toxic properties, they have long half-lives, are very resistant to degradation, they can bioaccumulate, they can volatilize and be transported over long distances. Given the fact that they are very toxic, these compounds represent a health risk to both human and other beings. Thus, in 2001, with the initiation of the Stockholm Convention, a number of 12 compounds and classes of compounds were banned. The so called “dirty dozens” were the following: Aldrin, Chlordane, DDT, Dieldrin, Endrin, Heptachlor, Hexachlorobenzene (HCB), Mirex, Toxaphene, polychlorinated biphenyls (PCBs), polychlorinated dibenzo-p-dioxins (PCDD) and polychlorinated dibenzofurans (PCDF). As of 2022, a number of 28 compounds and classes of compounds complete the list of prohibited substances [1].

Among persistent organic pollutants, Organochlorine pesticides (OCPs) and Polychlorobiphenyls (PCBs) are prohibited to be used in most countries, but there are exceptions and they are still being used locally in underdeveloped or developing countries. In the category of OCPs, the most frequently mentioned are: HCHs, DDTs, and chlorinated cyclodienes.

HCH (hexachlorocyclohexane) is solid white chemicals of synthetic nature having four common isomers: α -, β -, γ -, δ -HCH. The most used and well known from them is the γ -HCH isomer, also known as Lindan, which was considered a very potent insecticide for the protection of crops. Although HCH have been banned for decades, they are still used in some countries for treatment against scabies and body lice [2]. Given the fact that γ -HCH isomer is considered the most toxic of class, most of the studies focus only on its detection, neglecting the other isomers. The appropriate way would be to focus on each of them, since they are all found in the environment. From the acute exposure point of view, γ -HCH isomer is the most toxic for mammals, followed by α -, δ - and β - isomers. In terms of chronic exposure, β -isomer has the highest level of toxicity, followed by α -, γ - and δ -HCH isomers [3].

DDT 1,1,1-Trichloro-2,2-bis(4-chlorophenyl)ethane was developed at the end of the 1930s and it is one of the most well-known modern synthetic insecticides. This compound is better known as p,p'-DDT (4,4' DDT) and it is used together with its accompanied substitution isomer 1,1,1-Trichloro-2-(2-chlorophenyl)-2-(4-chlorophenyl)ethane, or o,p'-DDT (2,4' DDT). Due to its effectiveness, it was once heavily used for pest control in agriculture, forestry and to control mosquito-borne malaria in the 20th century. Like the other

categories of persistent organic pollutants, DDT has persistent stability, high capacity of bioaccumulation, strong toxicity, and it can be carried at long distances from the application areas [4], representing a major concern on human health. Common DDT metabolites are DDE (2, 4'- and 4,4' DDE) and DDD (2, 4'- and 4,4' DDD). 4,4' DDT, was considered to be the most important chlorinated insecticide ever marketed [5]. 4,4' DDE and 4,4' DDD are metabolites of DDT, which share the same characteristics but are considered to be less toxic than its parent.

Methoxychlor has been widely used as a replacement of DDT, due to its lower persistence level in the environment [6].

Endosulfan is an organochlorine insecticide, composed out of α - and β - isomers. It is often produced as a mixture of α - and β - isomers in ratios of 2:1 or 7:3. It has been used worldwide to control leaf-eating pests such as bollworms and aphids. [7].

Chlordane and chlordane related compounds have been heavily used in the past in order control termite and cutworm populations. Due to its persistence and distribution in environment, it has been classified as persistent organic pollutant and as active endocrine disruptor organochlorine pesticide [8]. Technical chlordane is classified as cyclopentadiene pesticide and is a mixture of 140 compounds, the most abundant of its components being *cis*-chlordane and *trans*-chlordane. The peak of its production was in the 1970s and it is estimated that almost 50% of the technical chlordane ever produced is unaltered in the environment [9].

Aldrin and dieldrin are two very common insecticides used for protection against soil insects like worms, beetles and termites. They were used heavily between 1950s and 1970s. Dieldrin is a metabolite of aldrin, it shares the same toxicity as its father being found in environment and human tissues, but is easier metabolized by animal and plants [10]. Endrin and endrin aldehyde are OCPs from the same class like aldrin, mainly used against insects, rodents and some species of birds. It was heavily produced and used from the 1950s to 1970s, very toxic, with a half-life that can range up to 12 years [11]. Endrin aldehyde is a degradation product of endrin and little is known about its properties.

Heptachlor is chlorinated cyclodiene, class which derives from cyclopentadiene, mainly used to control insect pests like termites and soil borne insects. It was intensely used from the early 1950s until the end of 1970s, very soon getting banned in most countries. Heptachlor can be oxidized to heptachlor epoxide, which is considered more toxic and persistent than its parent, and even after decades since its banning, heptachlor and its residue can still be found in the environment [12, 13].

Polychlorobiphenyls (PCBs) are chemicals of organic nature consisting of 209 chlorinated compounds discovered in the 19th century and first

synthesized in 1929. They are divided into groups and are based on the number of chlorines atoms. Each group has a number of isomers: mono-chlorobiphenyl 3, di- 12, tri- 24, tetra- 42, penta- 46, hexa- 42, hepta- 24, octa- 12, nona- 3, and decachlorobiphenyl 1. The most commonly used form of referring to PCBs is by using the numbering system and lists PCBs from PCB 1 (mono-Cl) to PCB 209 (deca-Cl) [14].

These types of compounds have most often been used in production of industrial oils, plastic additives and different types of paint. Like OCPs, PCBs are considered a danger for the environment being very persistent and toxic, so their production has been stopped from the late 1970s. They were included in the first list of the Stockholm convention from 2001, the so called "dirty dozen" [14].

Polycyclic aromatic hydrocarbons (PAHs) are organic compounds which consist in two or more aromatic fused rings. In the environment, the most common PAHs compounds that are found contain two to seven fused benzene rings [15].

They are present in the environment since prehistoric times from naturally produced activities such as fires and volcanoes [16], but also derive from other industrial activities, indicating anthropogenic pollution such as incomplete combustion of fossil fuels [17].

These compounds are subjected to degradation mechanisms such as oxidative and photolytic reactions. PAHs that derive from anthropogenic sources reach the atmosphere either by adsorption onto particles or by gaseous state, so they can be easily transported over long distances by wind and air currents, where they deposit on water or solid materials like soils and sediments [18].

The analysis of POPs in sediment and soil samples involves their extraction and analysis by chromatographic methods. The most used techniques for extraction is Soxhlet extraction [19, 20], ultrasound assisted extraction [19, 21, 22] or accelerated solvent extraction (ASE) [20]. For the analysis, gas chromatography coupled with mass spectrometry [17, 19-21] or selective detectors like electron capture detector (ECD) for halogenated compounds [20, 21] are the most used techniques. High performance liquid chromatography coupled with fluorescence detector is also used for PAHs analysis [22].

Due to the high persistency of POPs in environmental factors such as water, soil, and sediments, these compounds are used as tracers of historical pollution from the last hundred years, and this kind of study is combined with the analysis of river and lake sediments using radionuclides for the dating process. Using this methodology, information can be obtained about the incidence and intensity of the use of these compounds in agriculture and industry.

The aim of this study was to evaluate the historical pollution with POPs of an alpine lake (Lake Muntinu, located in the Southern Carpathian Mountains), as well as to identify the sources of POPs pollution. To the best of our knowledge, this is one of the first studies carried out in Romanian alpine lakes on this subject.

RESULTS AND DISCUSSION

POPs concentration in sediment layers

A number of 20 sediment layers samples with a thickness ranged between 0.5 and 1.5 cm resulted from the sectioning of 60 cm of collected sediment were selected. For our study we took into account only the first 18 centimeter which corresponds to a period from 2018 in the first centimetre to 1905 along 18th centimeter. Bellow the 18th centimeters are layers of sediments older than the 20th century, which can be hundreds, maybe thousands of years old. These layers were not included in this study because their age exceeds 100 years. Each layer was subjected to the radionuclides dating method previously described by Begy et al. [23] in order to establish the age of the layer.

Subsequent, each sediment layer was subjected to GC analysis in order to determine the variation of the concentration of each class of POPs over the last 100 years.

The obtained results show that the concentration of POPs in the sediment layers varied during the last century, the layers with the highest POP concentration correspond to the period between 1945 and 1990, known as the period of greatest industrialization in Romania (Figure 1).

Different maxima can be identified for each class of compounds that can be associated taking into account the errors of sediment dating with some events or with the development of Romanian society in the last hundred years. Thus, for PAHs, four maxima can be identified corresponding to the years 1920, 1942, 1965 and after 1987. If we look at the past, 1920 corresponds to the period of the First World War, 1942 to the Second World War, 1965 to the beginning of coal mining in the Jiu Valley and after 1987, the period of the opening of the Transalpina road.

If we take into account that at a distance of approximately 30 km is the city of Petroșani, which has a very rich history in the mining industry, and at a distance of approximately 60 km is the city of Hunedoara, one of the most important steel centres in Romania, we can consider that along with the few other small industrial towns and villages in this region are the main contributors to the high levels of PAHs in the sediment of Lake Muntinu.

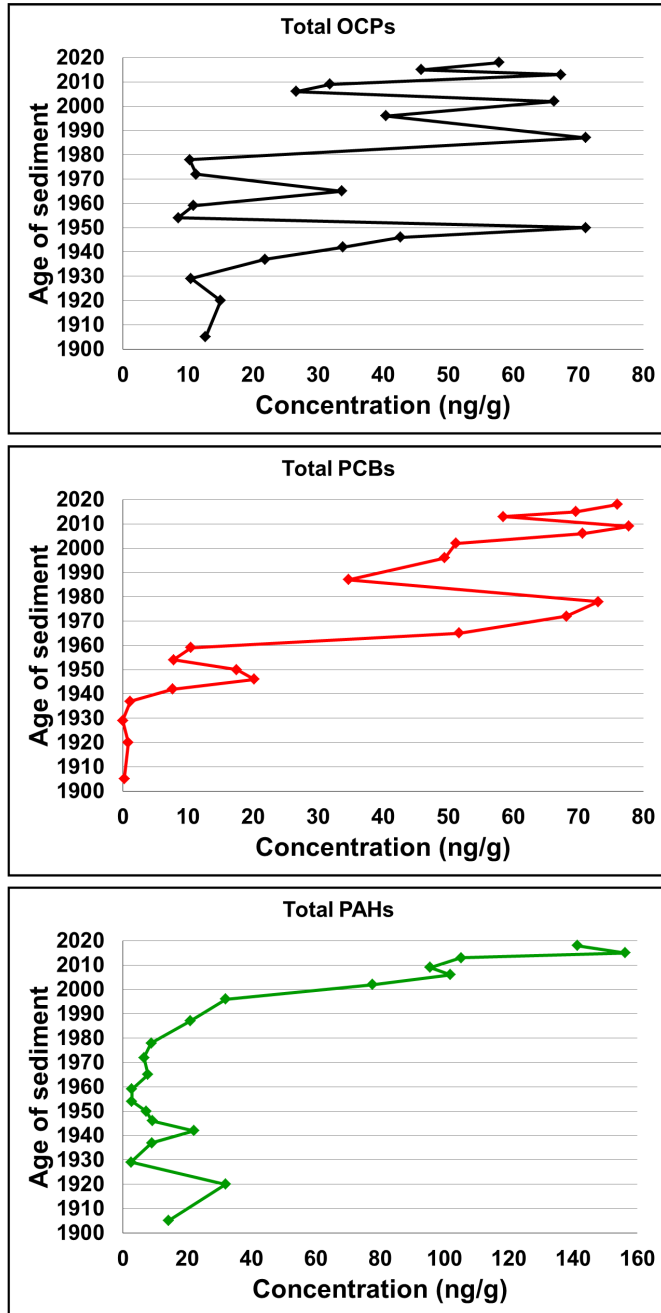


Figure 1. Variation of OCPs, PCBs and PAHs concentration, in the core sediment of Lake Muntinu over the past 100 years

HISTORICAL ASSESSMENT OF ATMOSPHERIC PERSISTENT ORGANIC POLLUTANTS
DEPOSITIONS IN MUNTINU GLACIAL LAKE...

For OCPs the highest peaks correspond to the period 1950, 1965, 1987, 2013, while for PBCs the period 1946, 1978, 2009. The period from 1950 to 1990 is known as the period of intensive development of agriculture and heavy industry in Romania which could be an explanation of the higher amount of OCPs and PCBs found in the analysed layers sediment.

On the other hand, the peaks in 2009 and 2013 could be correlated with the increase in human activity in the area with the start of the rehabilitation works of the transalpine road and implicitly with the opening of the ski resorts.

PAHs distribution and sources

The total PAH concentration in sediment core ranged from 2.53 to 156.27 ng/g, the highest levels being in the upper layers, 2015 layer (156.27 ng/g) and 2018 layer (141.34 ng/g) (Table 1).

Table 1. Concentrations of OCPs, PCBs, PAHs and PAHs isomeric ratios Σ LMW/ Σ HMW, ANT/(ANT+PHE), FLT/(FLT+PYR) according to the ages of sediment layers.

Age of sediments	Total OCPs*	Total PCBs*	Total PAHs*	Σ LMW/ Σ HMW	ANT/(ANT+PHE)	FLT/(FLT+PYR)
2018	57.86	76	141.3	0.69	0.4	0.79
2015	45.90	69.6	156.2	0.75	0.45	0.64
2013	67.30	58.5	105.1	0.45	0.55	0.79
2009	31.84	77.8	95.61	0.24	0.52	0.61
2006	26.65	70.7	101.8	0.13	0.35	0.77
2002	66.28	51.2	77.67	1.26	0.41	0.7
1996	40.47	49.5	32	1.32	0.39	0.7
1987	71.12	34.7	20.95	0.78	0.3	0.65
1978	10.28	73.1	8.89	0.66	0.5	0.86
1972	11.28	68.2	6.61	0.02	-	-
1965	33.64	51.7	7.79	1.29	0.29	1
1959	10.85	10.5	2.81	0.06	-	-
1954	8.52	7.8	2.81	0.04	-	-
1950	71.12	17.5	7.26	0.99	0.46	-
1946	42.66	20.2	9.15	0.98	0.24	0.61
1942	33.81	7.65	22.11	2.51	0.46	1
1937	21.89	1.13	9.02	1.48	0.2	-
1929	10.48	nd	2.53	0.04	-	-
1920	15.04	0.83	31.9	1.44	0.48	0.68
1905	12.71	0.24	14.19	3.09	0.36	1

*ng/g dry sediment, "-" not estimated, nd – not detected

Several diagnostic ratios were used in order to have a better estimation of the sources of PAHs from sediment cores. One of them was the ratio between low molecular weight PAHs (Σ LMW) which represent the ones with 2 or 3 rings and with high molecular weight PAH, (Σ HMW) which are the PAHs that have between 4 and 6 rings (Σ LMW / Σ HMW). A ratio lower than or equal to 1 it indicates a pyrogenic source (combustion processes and volcanoes), while a value greater than 1 indicates a petrogenic source (fossil fuels, oil and coal) [17, 22].

Other isomeric ratios used were Anthracene/ (Anthracene+ Phenanthrene), [ANT/(ANT+PHE)]; and Fluoranthene/ (Fluoranthene+ Pyrene), [FLT/(FLT)+PYR)] [17, 22]. A ratio ANT/(ANT+PHE), less than or equal to 0.1, indicates a petrogenic source, and greater than 0.1, a pyrogenic nature. A ratio of FLT/(FLT+PYR) less than 0.4, it indicates PAHs deriving from oil products, between 0.4 and 0.5 attests a source of PAHs from fossil fuels burning, and higher than 0.5 are a characteristic of natural sources such as biomass and coal burning [17, 22].

According to our results the values of the Σ LMW/ Σ HMW ratio from Lake Muntinu ranged between 0.02 and 3.09. 13 out of 20 samples were below 1, which indicates that sources are mostly of pyrogenic nature (Figure 2).

From the ratios of ANT/(ANT+PHE) and FLT/(FLT+PYR) the results suggest that the PAHs present are of biomass and coal combustion (Figure 3). The results confirm our hypothesis that the sources of PAHs in the sediments of Lake Muntinu are the result of atmospheric deposition from the coal and steel industry in the neighboring cities. Moreover, with the opening of the Transalpina road, PAHs resulted from the combustion of fossil fuels are also an important source of PAHs.

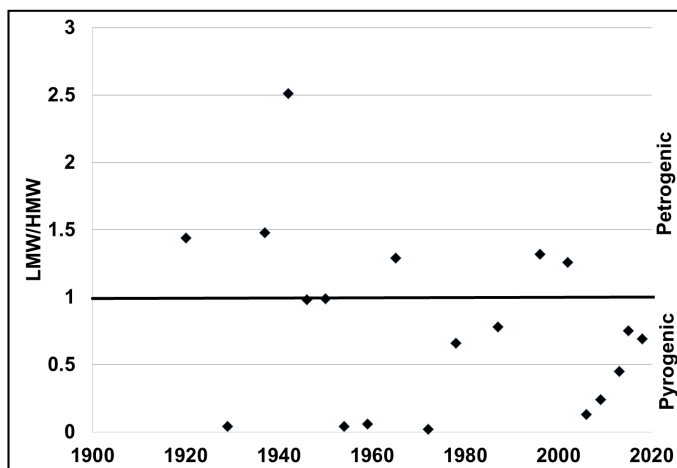


Figure 2. Isomeric ratios of Σ LMW/ Σ HMW versus the age of sediment

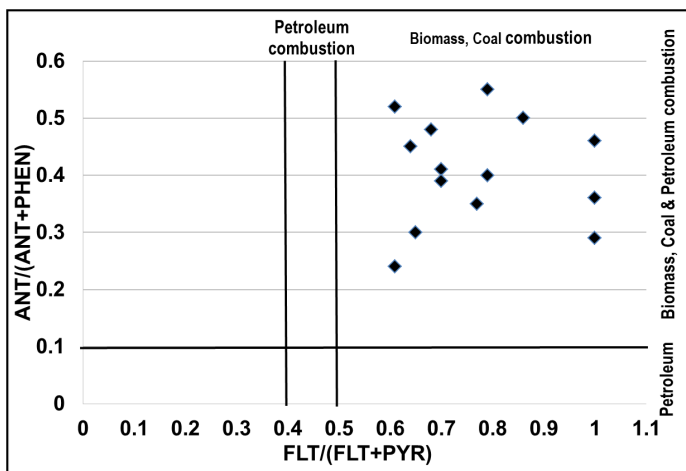


Figure 3. Isomeric ratios of ANT / (ANT + PHE) versus FLT / (FLT + PYR) in the sediment layers of Lake Muntinu

Organochlorines (OCs) distribution and sources

The concentration of OCPs ranged from 8.52 to 71.12 ng/g. The identified compounds were Heptachlor (<loq (0.01) to 19.75 ng/g), α -HCH (<loq to 62.93 ng/g) and Heptachlore exo-epoxide (<loq to 95.08 ng/g), which was the most common out of all the OCPs. Tecnazene, Hexachlorobenzene, γ -HCH, Quintozene, Aldrin, Heptachlor endo-epoxide, *trans*-Chlordane, 2,4'-DDE, α -Endosulfan, *cis*-Chlordane, Dieldrin, 4,4'-DDE, 2,4'-DDD, Endrin, β -Endosulfan, 2,4'-DDT, 4,4'-DDT were not detected in any of the samples. Unfortunately, due to the lack of data on individual OCPs, an estimate of their provenance cannot be made.

PCBs concentration tend to be at the same range as OCPs, the total concentration ranging from <loq (0.01) to 77.8 ng/g. The highest concentration detected was for PCB 52 with concentrations from <loq to 73 ng/g, and the lowest were for PCBs 138 with concentrations from <loq to 5.6 ng/g, and for PCB 194 with concentrations from <loq to 11.78 ng/g. PCBs -18, -28, -31, -44, -101, -114, -149, -153 and -180 were not detectable.

By comparing the total concentration of OCPs with the total concentration of PCBs it can be observed that the PCBs started to be used in 1965 while the use of OCPs stopped to be used in 1950 (Figure 4). The high concentration of OCPs from 1987 to 2018 can be explained by their high retention in environmental factors and their transport through air currents, but in the absence of data on the movement of air currents and precipitation in the studied area, this connection cannot be established.

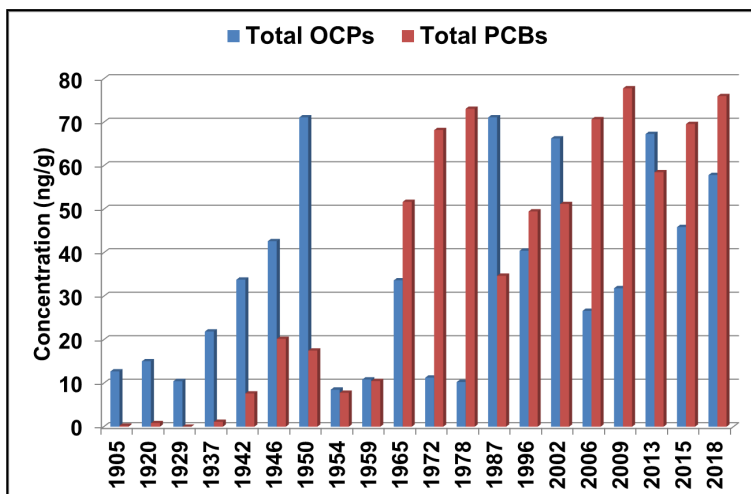


Figure 4. Comparison between total OCPs concentration and total PCBs concentration in sediment layers over the past 100 years

CONCLUSIONS

The lack of monitoring data for POPs in the environment over the last century makes it quite difficult to establish policies to reduce these pollutants in the environment, respectively to assess the health risk due to its exposure. This study provides valuable information about pollution with three classes of POPs of a region of Romania in the last 100 years through their analysis in the aquatic core sediments of an alpine lake.

The results of the study show that the concentrations of these pollutants are directly related to human activities in the studied area and even if human settlements are relatively far away, pollutant emissions can affect areas at high altitudes. Thus, PAHs (range 2.53 - 156.27 ng/g) have pyrogenic pattern showing that they are generated by combustion and not by the spills of petroleum products. The OCPs (range 1.78 - 71.12 ng/g) could be connected with agriculture, while PCBs (range not detected - 76.03 ng/g) with industrial activities.

Moreover, even if the sources of POPs could be identified through the use of isomeric ratios, more studies are needed for a clearer understanding of the anthropogenic contribution to environmental pollution. In summary, this method is a good way to determine a historical deposition of POPs, and also to evaluate toxicological potential and their distribution in the environment.

EXPERIMENTAL SECTION

Area of study and samples collection

The glacial lake Muntinu is situated in Vâlcea county at an altitude of over 1900 meters, very near Transalpina road, at approximately 2 km away, and the nearest urban area of the city of Petrosani at about 30 km away (Figure 5). The maps presented in figure 5 were built using the ArcMap 10.8 software starting from the information from the database and created by vectorization and downloading information from GPS. The coordinates of the sampling point are 45°21'58"N and 23°39'14"E. This lake has no any tributaries, and it was formed naturally by precipitation and by the melting of glaciers.

Sediment sample was collected at the point of the lake discharge using a gravity corer of stainless steel material, with a sampling tube of 60 cm. Before the analysis, the samples were pre-treated and prepared in accordance with Begy et al. study [23].

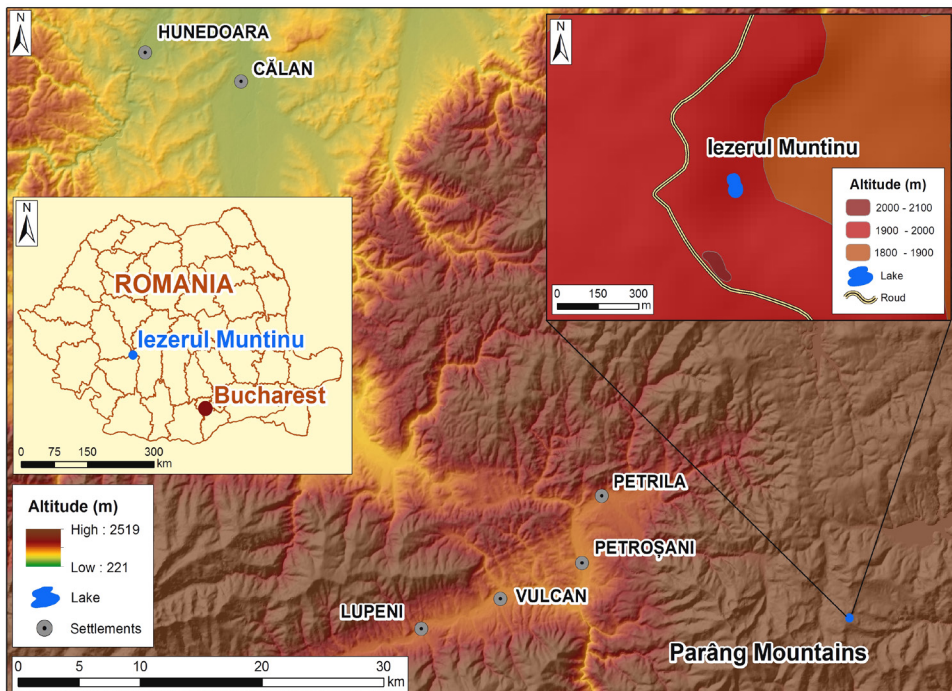


Figure 5. Map illustrating the geographical position of Lake Muntinu (Iezerul Muntinu)

Chemicals and reagents

For the qualitative and quantitative analysis, standard mixtures of different types of POPs were used. OCPs standard solution in concentration of 2000 µg/mL in hexane:toluene (1:1 v/v) (EPA CLP Organochlorine Pesticide Mix), and containing 20 compounds: Tecnazene, α-HCH, Hexachlorobenzene, γ-HCH, Quintozene, Heptachlor, Aldrin, Heptachlor exo-epoxide, Heptachlor endo-epoxide, Trans-Chlordane, 2,4'-DDE, α-Endosulfan, Cis-Chlordane, Dieldrin, 4,4'-DDE, 2,4'-DDD, Endrin, β-Endosulfan, 2,4'-DDT, 4,4'-DDT was provided by Supelco (Merck Romania SRL, Bucharest, Romania). PCBs mix congeners in concentration of 10 µg/mL, in heptane, containing a number of 12 PCBs: -18, -28, -31, -52, -44, -101, -114, -149, -153, -138, -180, -194 was obtained from Supelco (Merck Romania SRL, Bucharest, Romania). For PAHs, the standard solution with a concentration of 500 µg/mL, in acetonitrile:toluene mixture (92:8 v/v) was purchased from Restek (Restek Corporation, Bellefonte, United States), The mixture certified as CRM EPA Method 8310 PAH Mixture, contains a number of 16 compounds such as: Naphthalene, Acenaphthylene, Acenaphthene, Fluorene, Phenanthrene, Anthracene, Fluoranthene, Pyrene, Benz[a]anthracene, Chrysene, Benzo[b]fluoranthene, Benzo[k]fluoranthene, Benzo[a]pyrene, Dibenz[a,h]anthracene, Benzo[g,h,i]perylene, and Indeno[1,2,3-cd]pyrene.

For the quantification of OCs and PCBs, PCB-30 and PCB-155 were used as internal standards. As for PAHs, a surrogate standard (IS1) containing 4 deuterated compounds such as: Naphthalene-d8, Anthracene-d10, Fluoranthene-d10 and Perylene-d12, was used to assess the extraction recovery and another one (IS2) containing 3 deuterated compounds: Acenaphthene-d10, Phenanthrene-d10 and Chrysene-d12 for quantitative analysis of PAHs respectively.

For the extract purification step a purification open column containing from bottom to top silica, alumina and granular anhydrous sodium sulphate (200-300 mesh, Merck, Germany), activated at 450°C in a furnace for 6 h was used. For extract desulphurization, copper of < 425 µm size and 99.5% purity (Sigma-Aldrich, Merck, Germany), activated with hydrochloric acid (1 N) was used. The reagents used in the analysis were acetone, acetonitrile, dichloromethane, and hexane, acquired from Merck (Germany) and were all HPLC purity graded.

The Milli-Q water prepared using a Milli-Q-Plus ultra-pure water system from Millipore (Milford, MA, USA) was also used.

Instrumentation

The analysis of POPs was carried using Gas Chromatography, and depending on the nature of the compounds of interest, two types of analysis were carried-out. Gas chromatography-mass spectrometry (GC-MS) was used for the analysis of PAHs and gas chromatography – electron capture detector (GC-ECD) for OCPs and PCBs.

For PAHs analysis a Focus gas chromatograph equipped with a DSQII mass spectrometer operating in electron impact ionisation (EI) mode (70 eV), and a TriPlus Autosampler (Thermo Electron Corporation) was used. A capillary column model TR-5 MS (30 m x 0.25 mm i.d., 0.25 µm film thickness, Thermo) was used for the separation of the compounds, using a gradient temperature program of 60°C with holding time of 1 min, from 60 to 130°C with 10°C/min, from 130 to 300°C using 3°C/min and a holding time of 5 min at 300°C. Helium (99.999%) was used as a carrier gas with a flow rate of 1.2 mL/min. The identification of PAH compounds was achieved using the selected ion monitoring (SIM) mode and the comparison of relative retention times between sample and the standard solution. X-Calibur software was used for the acquisition of data.

As for OCPs and PCBs, the analysis process was performed by GC-ECD, using a gas chromatograph model Trace GC equipped with a ⁶³Ni electron capture detector, and a TriPlus Autosampler (Thermo Electron Corporation). For separation, a capillary column model HP-5MS (30 m × 0.25 mm i.d., 1.0 µm film thickness, Agilent) was used. The gradient temperature program was 70°C to 180°C at a rate of 25°C/min, from 180 to 200°C at 1°C/min, from 200 to 260°C at a rate of 2°C/min, and from 260 to 300°C at 5°C/min with a holding time of 5 min at 300°C. The carrier gas was nitrogen (99.99%) with a constant flow rate of 2 mL/min. The temperatures of the injector and detector were set at 270°C and 300°C. Identification of OCPs and PCBs compounds was based on the retention time of the standard mixtures. Acquisition of data was performed using Chrom-Card software.

Dating of sediments

Sediment samples have been collected using a gravity corer of stainless steel material, with a sampling tube of 60 cm. Before the analysis, the samples were pre-treated and prepared in accordance with Begy et al. study [23].

Using The CRS (Constant Rate of ²¹⁰Pb Supply) mathematical method by Appleby, 2001 [24], we determined the age and depth of the sediment column.

Gamma spectrometry was used for the analysis of radionuclides, using a HPGe detector from ORTEC, model GWL-120-15 type with a resolution of 2.08 keV for 1.33 MeV ⁶⁰Co and 1.1 keV for 122 keV ⁵⁷Co gamma lines. The detection limits for the radionuclides were the following: 7 Bq/kg for ²¹⁰Pb,

0.3 Bq/kg for ^{137}Cs and 0.5 Bq/kg for ^{226}Ra [25]. The associated dating errors are: one year for the period 2006-2015, two years for 1996 – 2006, three years for 1972 – 1996, four years for 1954 – 1972, five years for 1942 – 1954 and six years before 1942.

Extraction and purification of POPs

Extraction and clean-up procedure for POPs was performed in accordance to Barhoumi et al. [21], but with small modifications. Approximately 4 g of homogenized dry sediment samples were placed into a 50 mL centrifuge tube and spiked with 100 ng each of multistandard mixture PAHs (IS1) and 20 ng PCB-30. 20 mL of acetone: hexane mixture (1:1, v/v) was added; the tube was capped and sonicated for 20 min in an ultrasonic bath. The mixture was centrifuged for 5 min at 4400 rpm and the solvent extract was transferred in a glass round flask of 100 mL. This procedure was repeated for two more times with 20 mL fresh solvent mixture. The final extract which contained all three extracts combined was concentrated to approximately 2 mL via rotary evaporation, mixed with 1 g of activated copper and left overnight for desulphurization. The following day, 10 mL of *n*-hexane was added, the copper was decanted away from the flask, and the extract was concentrated to approximately 2 mL with rotary evaporator and subjected to purification procedure.

For the purification step, a silica-alumina chromatograph column (15 mm i.d., made of glass) which contained from bottom to top, 3 g activated silica, 3 g activated alumina, and 1 g dehydrated Na_2SO_4 was used. This column was washed with 20 mL of *n*-hexane before use.

The ~2 mL concentrated extract was loaded onto the purification column and the target compounds have been eluted with 20 mL of *n*-hexane and 40 mL of *n*-hexane: dichloromethane (DCM) solution (80:20, v/v), concentrated to approximately 2 mL, dry evaporated under nitrogen stream and redissolved with 0.2 mL *n*-hexane:DCM solution (80:20, v/v). Before analysis, each sample was spiked with 100 ng each PAHs multistandard mixture (IS2) and 20 ng PCB-155.

The extraction and analyses procedure were validated in our previous study [21] using certified reference materials EC-3 (PAHs, PCBs and OCPs in marine sediments from Niagara River in Lake Ontario). The obtained recoveries ranging from $68.8 \pm 5.6\%$ to $110.1 \pm 2.9\%$ for PAHs, and from $89.8 \pm 10.7\%$ to $117.2 \pm 14.1\%$ for POCs and PCBs respectively [21].

ACKNOWLEDGMENTS

This work was supported by the PhD Student Program of Babeș-Bolyai University, Faculty of Environmental Science and Engineering, Cluj Napoca.

REFERENCES

1. United Nations Environmental Program, Stockholm Convention. <http://chm.pops.int/TheConvention/ThePOPs/ListingofPOPs/tabid/2509/Default.aspx>, Accessed on October 12, 2022.
2. G. Chen; Hexachlorocyclohexanes Including Lindane, In *Encyclopedia of Toxicology*, 3rd ed, P. Wexler, Elsevier, Amsterdam, **2014**, pp. 874-876A.
3. A. M. Jackovitz; R. M. Herbert; Wildlife Toxicity Assessment for Hexachlorocyclohexane (HCH), In *Wildlife Toxicity Assessments for Chemicals of Military Concern*, M. Williams, G. Reddy, M. Quinn, M. Johnson, Elsevier, Amsterdam, **2015**, Chapter 27, pp. 473-497.
4. H. J. Xu; J. Bai; W. Y. Li; L. X. Zhao; Y. T. Li; *J. Hazard. Mater.*, **2019**, *365*, 622–631.
5. J. Kim; Q. Sun; Y. Yue; K. S. Yoon; K. Y. Whang; J. Marshall Clark; Y. Park; *Pesticide Biochemistry and Physiology*, **2016**, *131*, 40–45.
6. R. K. Gupta; R. A. Schuh; G. Fiskum; J. A. Flaws; *Toxicol. Appl. Pharmacol.*, **2006**, *216*, 436–445.
7. Y. Zhang; Z. Dong; Z. Peng; J. Zhu; F. Zhuo; Y. Li, Z. Ma; *Environ. Pollut.*, **2022**, *309*, 119725
8. Q. Wu; X. Du; X. Feng; H. Cheng; Y. Chen; C. Lu; M. Wu; H. Tong; *Ecotoxicol. Environ. Saf.*, **2021**, *225*, 112739.
9. A. M. Dearth; R. A. Hites; *Environ. Sci. Technol.* **1991**, *25*, 245-254.
10. M. H. G. Berntssen; A. Maage; A. K. Lundebye; Contamination of finfish with persistent organic pollutants and metals, In *Chemical Contaminants and Residues in Food*, Schrenk. D., Woodhead Publishing Ltd: Cambridge, United Kingdom, **2012**, pp. 498–534.
11. M. Honeycutt; L. Jones; Endrin, In *Encyclopedia of Toxicology*, 3rd ed.; P. Wexler, Academic Press, Elsevier, Amsterdam, 2014, **2014**, pp. 344–347.
12. N. R. Reed, S. Koshlukova; Heptachlor, In *Encyclopedia of Toxicology*, 3rd ed.; P. Wexler, Academic Press, Elsevier, Amsterdam, **2014**, pp. 840–844.
13. A. S. Purnomo; T. Mori; S. R. Putra; R. Kondo; *Int. Biodeterior. Biodegradation*, **2013**, *82*, 40–44.
14. D. Megson; Polychlorinated Biphenyls, In *Encyclopedia of Analytical Science*, 3rd ed, P. Worsfold, A. Townshend, C. F. Poole, M. Miro; Elsevier, Amsterdam, **2019**, pp. 318-328.
15. P. D. Boehm; Polycyclic Aromatic Hydrocarbons (PAHs), *Environmental Forensic*, 1st ed.; R. Morrison, B. Murphy, Elsevier, Amsterdam, **2005**, pp. 313-337.
16. K. Kozak; M. Ruman; K. Kosek; G. Karasinski; Ł. Stachnik; Z. Polkowska; *Water*, **2017**, *9*, 42.
17. W. Zhang, S. Zhang, C. Wan, D. Yue, Y. Ye, X. Wang, *Environ. Pollut.*, **2008**, *153*, 594-601.
18. A. N. Gachanga; Polycyclic Aromatic Hydrocarbons, In *Encyclopedia of Analytical Science*, 3rd ed., P. Worsfold, A. Townshend, C. F. Poole, Elsevier, Amsterdam, **2005**, pp. 234-242.

19. P. Wang, Q. Zhang, Y. Wang, T. Wang, X. Li, L. Ding, G. Jiang, *Anal. Chim. Acta*, **2010**, *663*, 43–48.
20. W. Wang, B. Meng, X. Lu, Y. Liu, S. Tao, *Anal. Chim. Acta*, **2007**, *602*, 211–222.
21. B. Barhoumi, M. S. Beldean-Galea; A. M. Al-Rawabdeh; C. Roba; I. M. Martonos; R. Bălc; M. Kahlaoui; S. Touil; M. Tedetti; M. R. Driss; C. Baciuc; *Sci. Total Environ.*, **2019**, *660*, 660-676.
22. L. Zhu, Y. Chen, R. Zhou; *J. Hazard. Mater.*, **2008**, *150(2)*, 308-316.
23. R.C. Begy; S. Kelemen; H. Simon; C. Tănăsolia; *Geochronometria*, **2018**, *45*, 97-106.
24. P.G. Appleby; Chronostratigraphic Techniques in Recent Sediments, in *Tracking Environmental Change Using Lake Sediments*, Smol, J.P. (eds). Developments in Paleoenvironmental Research, vol 1. Springer, Dordrecht, Netherlands, **2002**, pp. 171-203.
25. R.C. Begy; C. F. Savin; S. Kelemen; D. Vereș; O. L. Munteanu; C. V. Maloș; T. Kovacs; *PLoS One*, **2021**, *16(6)*, e0251603.

ALTERNATIVE PROCEDURES FOR THE GREEN SYNTHESIS OF 3,7-BIS(*N,N*-(2- HYDROXYETHYL)AMINO)PHENOTHIAZINIUM DYE

Melinda GAL^{a*}, Alexandru TURZA^b, Bianca STOEAN^a, Luiza GAINA^a,
Castelia CRISTEA^a, Emese GAL^a, Tamas LOVASZ^a, Dan PORUMB^a,
Luminita SILAGHI-DUMITRESCU^a

ABSTRACT. Two experimental procedures implying mechanochemical and ultrasounds assisted protocols were assessed as alternatives to the classical synthesis of the title MB analogue, based on the substitution of the phenothiazinium tetraiodide with diethanolamine nucleophile. These greener alternatives required a much shorter reaction time and consequently less energy consumption. The sonochemical procedure gave a crystalline reaction product demanding a facile purification. UV-vis spectroscopic analysis emphasized the optical properties of the 3,7-bis(*N,N*-(2-hydroxyethyl)amino)phenothiazinium dye characterized by an intense absorption maxima situated at 663 nm and weak fluorescence emission in aqueous solution (quantum yield 0.7% relative to methylene blue standard) with the emission maxima situated at 685 nm (Stokes shift 484 cm⁻¹). The solid state structure of the dye was determined by X-ray diffraction.

Keywords: *Phenothiazinium dye, mechanochemistry, sonochemistry, XRD, UV-vis absorption spectroscopy*

^a Babeş-Bolyai University, Faculty of Chemistry and Chemical Engineering, 11 Arany Janos str., RO-400028, Cluj-Napoca, Romania.

^b Department of Mass Spectrometry, Chromatography and Applied Physics, National Institute for Research and Development of Isotopic and Molecular Technologies, 67-103 Donat str., RO-400293 Cluj-Napoca, România.

* Corresponding author: melinda.gal@ubbcluj.ro.



INTRODUCTION

Many synthetic compounds containing the phenothiazine heterocycle core exhibited *in vitro* or *in vivo* biological activities modulated by the introduction of structural appendages such as N-alkyl chains and/or (hetero)aromatic rings which may cause substantial amendments of the pharmacological properties (e.g. anti-microbial, anti-viral, anti-inflammatory, anti-oxidant, anti-tumour properties) [1]. Methylene blue (MB) is a phenothiazine derived cationic dye (3,7-*bis*(dimethylamino)phenothiazin-5-ium, figure 1) which display distinct photophysical, electrochemical, and biological properties and it is considered as the model compound for analogues series encompassing various substituents attached at the carbon atoms of the peripheral aromatic rings. [2]. A large number of MB analogues were designed by the systematic variation of the amino-auxochromes grafted in position C3 and C7 of the phenothiazinium chromophore (the oxidized state of the phenothiazine nucleus), thus paving the way towards MB dye congeners useful in modern biomedicine for selective staining, chemotherapeutics or photosensitizers for photoantimicrobial and photo dynamic therapy (PDT) applications [3-5]. By the way of illustration, in figure 1 are depicted the chemical structures of symmetrical (Figure 1a, 1b) or unsymmetrical (Figure 1c) 3,7-disubstituted phenothiazinium dyes bearing symmetrical (Figure 1a, 1c) or non-symmetrical (Figure 1b) secondary amino-auxochrome units comprising short C₁-C₃ alkyl and/or hydroxyalkyl chains imparting higher hydrophilicity.

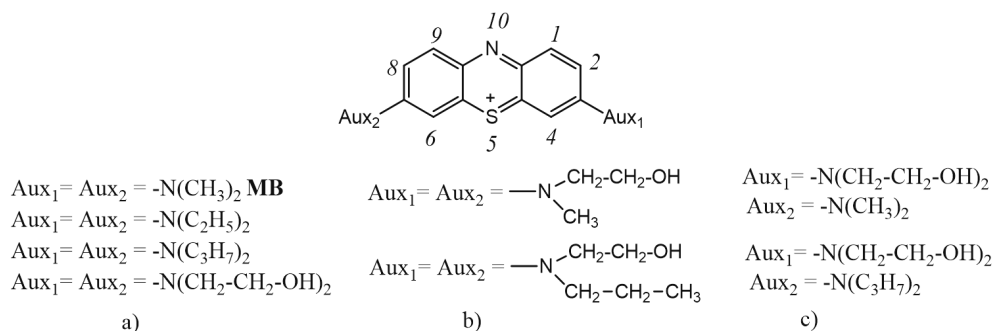
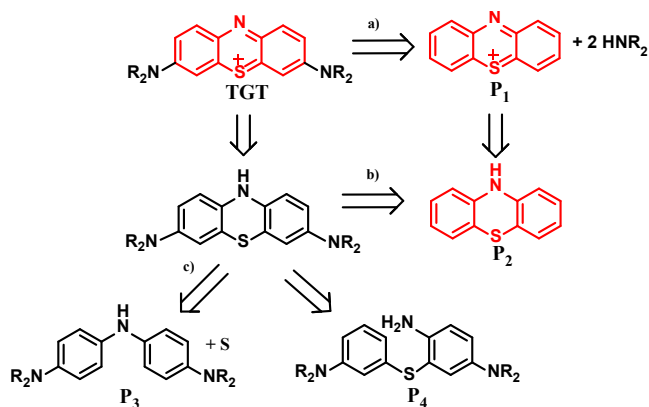


Figure 1. MB analogues: a) symmetrical 3,7-*bis*(dimethylamino)-, 3,7-*bis*(diethylamino)-, 3,7-*bis*(dipropylamino)- 3,7-*bis*(*bis*(2-hydroxyethyl)amino)- [6], b) 3,7-*bis*(2-hydroxyethyl)(methyl)amino)-, 3,7-*bis*(2-hydroxyethyl)(propyl)amino)- [7] c) unsymmetrical 3-dipropylamino-7-(*bis*(2-hydroxyethyl)amino)- [8] phenothiazinium dyes.

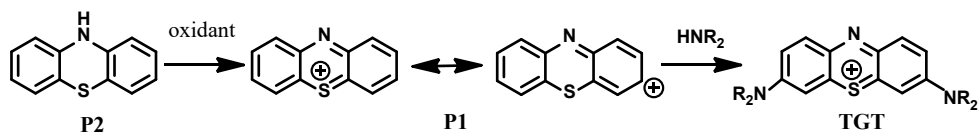
ALTERNATIVE PROCEDURES FOR THE GREEN SYNTHESIS OF
3,7-BIS(*N,N*-(2-HYDROXYETHYL)AMINO)PHENOTHIAZINIUM DYE

A retrosynthetic analysis of target MB analogues (**TGT**) summarized in **Scheme 1** proposes the molecular simplification by C-heteroatom bonds disconnection based on reliable transforms such as: path a) nucleophilic substitution of a phenothiazinium precursor **P1** with amines, path b) coupling of a phenothiazine precursor **P2** with amines path c) ring closure of diphenylamine **P3** or diphenyl sulphide **P4** precursors.



Scheme 1

A literature data survey indicate that the vast majority of the synthetic strategies applied in the preparation of MB analogues are based on the retrosynthetic path a) depicted in scheme 1, following the most straightforward reaction pathway shown in **Scheme 2**.



Scheme 2

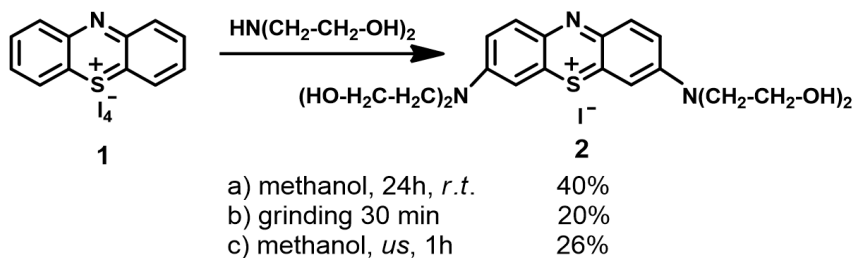
In the first reaction step, phenothiazine precursor **P2** is oxidized to the phenothiazinium cation **P1** which in the second step is subjected to substitution reaction using secondary amine nucleophiles. The success of this strategy is ensured on one hand by the high reactivity of the electron rich phenothiazine core toward oxidation and on the other hand by the regioselectivity of the nucleophilic substitution of the phenothiazinium cation in positions C3 and C7 oriented by the electron withdrawing effect of the thionium salt. The oxidation of the phenothiazine substrate can be achieved by using different reagents, the most widely employed being iodine (generating the phenothiazin-5-ium tetraiodide) followed by bromine (producing phenothiazin-5-ium perbromide). Symmetrical 3,7-disubstituted phenothiazinium dyes were obtained by using an excess of amine nucleophile, while non-symmetrical 3,7-disubstituted phenothiazinium dyes were prepared by a two stages methodology implying successive substitutions using two different amines [2]

The green chemistry philosophy recommends synthetic plans based on environmentally friendly strategies built on a careful selection of reagents and auxiliaries (e.g. minimal waste generation, reduced organic solvent use, sustainable feedstocks, effective catalytic processes) and reaction conditions for improved process efficiency. Improved energy efficiency can be attained by switching from a thermal source of energy (which partially dissipate energy in the surrounding area) towards more specific alternative energy inputs which may be beneficially applied (e.g. photochemical, microwaves, ultrasounds irradiation) [9] Over the years our research group accumulated knowledge and contributed to the design of new efficient green protocols for the preparation of phenothiazine derivatives by microwaves assisted synthesis (e.g. amino- [10], 1,3-dioxanyl- [11], or imino-phenothiazines [12] and sonochemistry [13]); the relevance of ultrasound irradiation and mechanochemical synthesis *versus* classical convective heating procedures was emphasized in the preparation of novel dyes such as (phenothiazinyl)vinyl-pyridinium [14] and MB analogues [15].

In this work, we examine the benefits brought by ultrasound assisted and mechanochemical synthetic procedures recently elaborated by our group, in comparison with classical procedures previously reported for the preparation of 3,7-*bis*(*N,N*-(2-hydroxyethyl)amino)phenothiazinium dye [6, 16], a MB analogue useful as direct dyestuff constituent of hair dye compositions [17]. The optical properties of this dye and its solid-state structure were investigated by UV-vis absorption/fluorescence emission in solution and X-ray diffraction respectively.

RESULTS AND DISCUSSION

The preparation of the symmetrical disubstituted MB analogue **2** is depicted in Scheme 3.

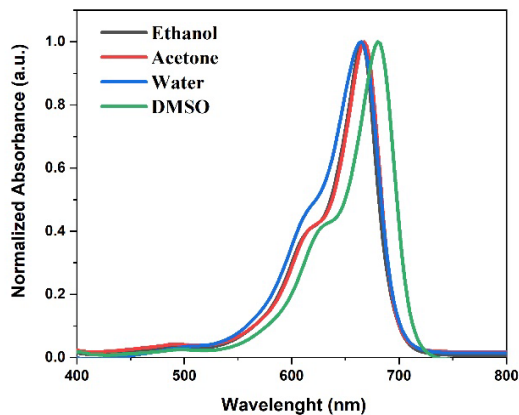


Scheme 3

The target 3,7-*bis*(*bis*(2-hydroxyethyl)amino)-phenothiazinium iodide **2** was obtained by subjecting phenothiazinium tetraiodide substrate **1** to a substitution reaction using an excess of diethanolamine nucleophile. Aiming the optimization of the reaction conditions, three alternative experimental procedures were applied: a) classical conditions in homogeneous methanol solution, b) solvent free mechanochemical conditions and c) ultrasound irradiation conditions. Even though the reaction yields obtained by applying mechano- and sonochemical conditions (20-26%) were not superior to the ones afforded by the classical ones (40%), these alternative procedures may be considered “greener” because they require a much shorter reaction time (30-60 minutes in comparison with 24hours) and consequently less energy consumption; moreover, the ultrasounds assisted procedure provided a crystalline reaction product demanding facile purification.

The optical UV-vis absorption properties of **2** recorded in four different solvents (figure 2) show a weak solvatochromism (376 cm^{-1}) upon switching from water to dimethylsulfoxide (DMSO), a solvent with known ability for stabilization by hydrogen bonding.

In aqueous solution, upon excitation of **2** with its longest absorption maxima ($\lambda_{\text{max}}=664\text{ nm}$) was recorded a fluorescence emission band situated at $\lambda_{\text{max,em}}=685\text{ nm}$ with 484 cm^{-1} Stokes shift and fluorescence quantum yield 0.7% relative to MB standard ($\phi_F 2\%$.[18])



Solvent	λ [nm] (ϵ [$\text{cm}^{-1} \text{M}^{-1}$])
Ethanol	667 (13272)
Acetone	667 (32202)
Water	664 (56058)
DMSO	681 (35896)

Figure 2. UV-vis absorption bands of **2** in various solvents.

Based on the crystal structure determination by X-ray diffraction, **2** was found to crystallize in the centrosymmetric orthorhombic *Pbcn* space group. The asymmetric unit is comprised by one 3,7-bis(dietanolamino)phenothiazinium cation, one recrystallization water molecule and one iodide anion (Figure 3a). Unit cell is packing eight such asymmetric units which are generated via symmetry operations (Figure 3b).

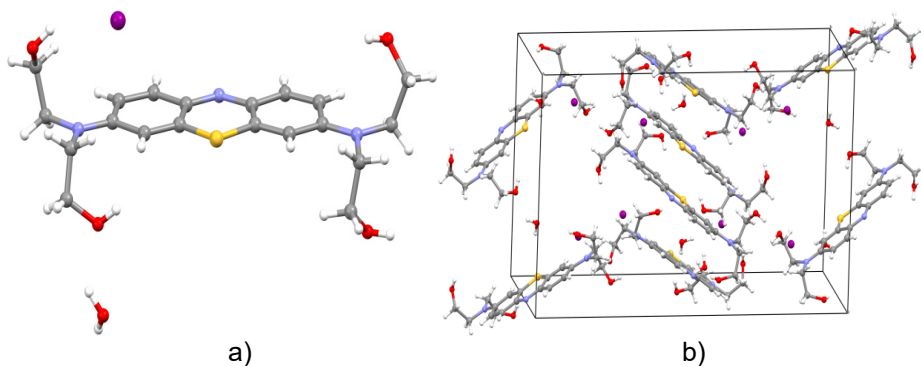


Figure 3. Crystal structure of **2**: a) asymmetric unit; b) unit cell packing

The folding angle between the two aromatic rings of the phenothiazinium core is 178.48° depicting a planar conformation. Such almost planar geometries were reported in literature by single crystal X-ray diffraction on various derivatives which belong to phenothiazine group [19-21].

The supramolecular self-assembled layers of molecules are shaped in a zig-zag fashion with the recrystallization water located between and connecting these layers via O-H···O interactions while the iodide anion is located roughly on the layers (Figure 4). It is worth mentioning that the adjacent molecules (related by a glide plane) are interacting via O-H···N (hydroxyl···thiazine) hydrogen bonds and phenyl···phenyl interactions as well (π ··· π interactions with a contact distance of 3.292 Å and 3.366 Å respectively) which are contributing to the stabilization of zig-zag layout.

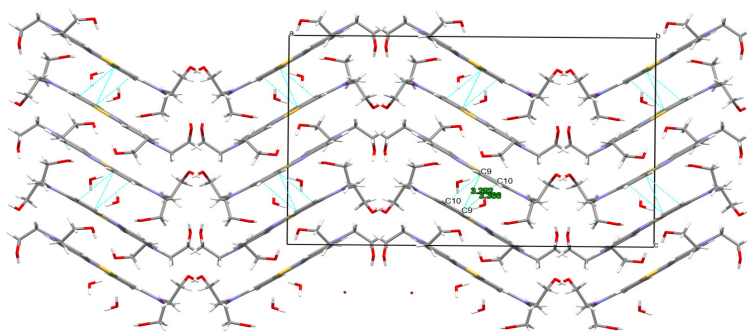


Figure 4. Overall packing perspective seen along *a*-axis displaying zig-zag molecular arrangements

CONCLUSIONS

The 3,7-*bis*(*N,N*-(2-hydroxyethyl)amino)phenothiazinium iodide **2** is a blue dye displaying an intense absorption maxima situated at 663 nm, a weak fluorescence with the emission maxima situated at 685 nm, which crystallize in the centrosymmetric orthorhombic *Pbcn* space group. The classical synthetic procedures requiring a long reaction time could be amended by greener alternatives such as the hereby described mechanochemical or ultrasounds assisted procedures.

EXPERIMENTAL SECTION

NMR spectra were recorded on Bruker NEO-1 400 MHz instrument. UV-vis absorption spectra were recorded with Perkin Elmer Lambda 35 spectrophotometer. UV-vis emission spectra were recorded on Perkin Elmer LS55 spectrophotometer. HRMS spectra were recorded on Thermo LTQ Orbitrap XL instrument. The powder X-Ray diffraction pattern was recorded on a Bruker D8 Advance diffractometer (X-ray tube operates at 40 kV, 40 mA) which is equipped with a germanium (1 1 1) monochromator and LYNXEYE detector using monochromatic CuK α 1 radiation ($\lambda=1.54056 \text{ \AA}$).

All chemicals used were of reagent grade.

Starting material Phenazathionium tetraiodide **1** was prepared by the oxidation of phenothiazine with iodine in DCM solution according to the previously reported procedure [22].

Experimental procedures for the synthesis of

3,7-bis(N,N-(2-hydroxyethyl)amino)phenothiazinium iodide 2

a) Classical synthesis

In a round-bottom flask with a magnetic stirrer and a reflux condenser were introduced 1.5 g (0.002 mol) of phenothiazinium tetraiodide **1** and 40 ml of methanol and then diethanolamine (3ml, 3.27g, 0.03 mol) was added dropwise over 30 minutes. The reaction mixture was stirred for 24 hours at room temperature. After the completion of the reaction, the solvent was removed by vacuum distillation. The solid product was purified by reprecipitation from methanol solution with diethyl ether. The dark precipitate was filtered affording the pure product (yield of 40 %).

b) Mechanochemical synthesis

In a mortar, phenothiazinium tetraiodide **1** (1.5g, 0,002 mol) and diethanolamine (3ml, 3.27g, 0.03 mol) were added and the mixture was grounded with a pestle for 30 minutes. The reaction product was dissolved in methanol and reprecipitated with diethyl ether. The dark precipitate was filtered affording the pure product (yield of 20%).

c) Sonochemical synthesis

Phenothiazinium tetraiodide **1** (1.5 g, 0.002mol) and diethanolamine (3ml, 3.27g, 0.03 mol) were dissolved in ethanol and were introduced into a pear-shaped flask. The flask was equipped with a septum with a syringe needle for degasing the volatile products. After 1 hour of ultrasonating the

solvent was recovered and the product was purified by reprecipitation with methanol and diethyl ether. The dark precipitate was filtered affording the pure product (yield of 26%).

$^1\text{H-NMR}$ (400 MHz, DMSO-d_6) δ (ppm): 7.81 (d, $^3\text{J}= 8\text{Hz}$, 2H), 7.51 (m, 4H), 5.03 (t, $^3\text{J}= 7\text{Hz}$, 4H), 3.85 (m, 8H), 3.72 (m, 8H).

$^{13}\text{C-NMR}$ (100 MHz, DMSO-d_6) δ (ppm): 154.42, 137.96, 135.44, 133.88, 120.05, 107.5, 59.12, 54.43.

HRMS: calculated for $\text{C}_{20}\text{H}_{26}\text{NO}_4\text{S}^+$ 404.13865, found 404.157.

X-Ray powder diffraction

The powder X-Ray diffraction pattern was recorded on a Bruker D8 Advance diffractometer (X-ray tube operates at 40 kV, 40 mA) which is equipped with a germanium (1 1 1) monochromator and LYNXEYE detector using monochromatic $\text{CuK}\alpha 1$ radiation ($\lambda=1.54056 \text{ \AA}$). The CIF file of **2** has been deposited with the Cambridge Crystallographic Data Centre, having the associated deposition number 2225437.

The crystal structure determination for **2** was carried out from a high-resolution X-ray powder diffraction pattern. The method implies the determination of a structural model by direct-space Monte-Carlo with parallel tempering methods.

The procedure of crystal structure determination from a powder diffraction pattern is a multi-step procedure and requires the use of several computation methods: diffraction pattern indexing; Pawley refinement; space group determination; the search for a structural model and the final Rietveld refinement [23].

Reflex module implemented in Materials Studio software [24] was used for pattern indexing via multiple programs such as TREOR90 [25], DICVOL96 [26], X-cell [27]. The indexing offers multiple possible solutions of unit cells but based on the figure of merit, a common solution of lattice parameters was obtained in all three programs, which belongs to the orthorhombic crystal system and possess the following lattice constants: $a=25.49 \text{ \AA}$, $b=10.91 \text{ \AA}$, $c=16.28 \text{ \AA}$, $\alpha=\beta=\gamma=90^\circ$, $V=4531 \text{ \AA}^3$. Further the solution was subjected to Pawley refinement, the orthorhombic crystal system being confirmed and the unit cell was found to belong to the Pbcn space group. Based on the molecular composition of the analysed compound, the asymmetric unit would consist of one 3,7-*bis*(diethanolamino)phenothiazinium molecule ($\text{C}_{20}\text{H}_{26}\text{N}_3\text{O}_4\text{S}$), one water molecule and a iodine anion such that the calculated density is roughly 1.60 g/cm^3 . As a next step, the search of structural model was accomplished via Powder Solve module employing

Monte Carlo and parallel tempering optimization. The method is based on molecular translations, rotations and changes in torsion angles in the unit cell. A few million trials per cycle are verified and a comparison between simulated and experimental pattern after each change is carried out such as the match to be as good as possible. Rietveld refinement technique is used in order to refine the structural solution obtained by parallel tempering optimization. A Pseudo-Voigt function was used to approximate the diffraction peaks profiles along with the U, V, W parameters of Caglioti's equation [6] were refined. Bragg-Brentano instrument geometry was considered with profile parameters, shift parameters, zero point refined as well. The asymmetry of diffraction lines was refined in a Berar-Baldinozzi approximation. The background was approximated by a polynomial function of order 20 and the preferred orientation parameters were refined considering the March-Dollase correction. As a result, a final comparison between calculated (theoretical) and experimental powder X-ray pattern is shown in Figure 5 and crystallographic details are presented in Table 1.

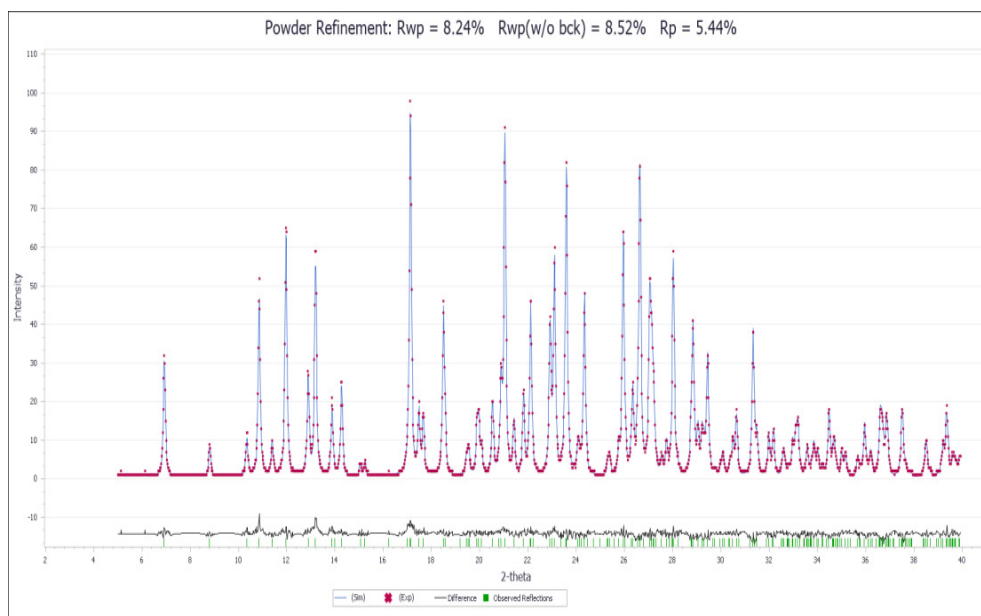


Figure 5. Rietveld refinement highlighting the match between simulated and experimental pattern

Table 1. Crystallographic details for **2** obtained
by powder X-ray diffraction analysis

Chemical formula	C₂₀H₂₈IN₃O₅S
Formula weight (g/mol)	548.40
Crystal system	Orthorhombic
Space group	Pbcn (No. 60)
Z	8
a (Å)	25.50
b (Å)	10.91
c (Å)	16.28
α (°)	90
β (°)	90
γ (°)	90
V (Å ³)	4532
R _w p (%)	8.24
ρ _{calc} g/cm ³	1.60

ACKNOWLEDGMENTS

This work was supported by a grant of Romanian Ministry of Research and Innovation, CNCS–UEFISCDI, project number PN-III-P4-ID-PCCF-2016-0142, within PNCDI III.

REFERENCES

1. C. Gopi, M. D. Dhanaraju, *Rev. J. Chem.*, **2019**, 9(2), 95–126.
2. P.L. Padnya, A.I. Khadieva, I.I. Stoikov, *Dyes Pigm.*, **2022**, 208, 110806.
3. M. Wainwright, *Biotechn. Histochem.*, **2003**, 78(3-4), 147-155.
4. C. M. L. Francisco, J. M. L. A. Gonçalves, B. S. Brum, T. P. C. Santos, A. Lino-dos-Santos-Franco, D. F. T. Silva, C Pavani, *New J. Chem.*, **2017**, 41, 14438-14443.
5. M Wainwright, *Photodiagnosis Photodyn. Ther.*, **2005**, 2, 263-272.
6. G. De Crozals, C. Farre, M. Sigaud, P. Fortgang, C. Sanglar, C. Chaix, *Chem. Commun.*, **2015**, 51, 4458-4461.

7. A. Gollmer, A. Felgentrager, W. Baumler, T. Maisch, A. Spath, *Photochem. Photobiol. Sci.*, **2015**, *14*, 335-351.
8. S. A. Gorman, A. L. Bell, J. Griffiths, D Roberts, S. B. Brown, *Dyes Pigm.*, **2006**, *71* 153-160.
9. P. Anastas, J. Warner, "Green Chemistry Theory and Practice", Oxford Univ. Press, **1998**.
10. L.I. Găină, L.N. Mătarângă-Popa, E. Gal, P. Boar, P. Lönnecke, E. Hey-Hawkins, C. Bischin, R. Silaghi-Dumitrescu, I. Lupan, C. Cristea, L. Silaghi-Dumitrescu, *Eur. J. Org. Chem.*, **2013**, *24*, 5500–5508.
11. L. Gaina, E. Gal, L. Matarânga-Popa, D. Porumb, A. Nicolescu, C. Cristea, L. Silaghi-Dumitrescu, *Tetrahedron*, **2012**, *68(11)*, 2465 – 2470.
12. L. Gaina, T. Lovasz, I. A. Silberg, C. Cristea, S. Udrea, *Het. Commun.*, **2001**, *7(6)*, 549–554.
13. E. Gal, L. Gaina, H. Petkes, A. Pop, C. Cristea, G. Barta, D. C. Vodnar, L. Silaghi-Dumitrescu, *Beilstein J. Org. Chem.*, **2020**, *16*, 2929–2936.
14. B. Stoean, D. Rugina, M. Focsan, A.-M. Craciun, M. Nistor, T. Lovasz, A. Turza, D.I. Porumb, E. Gál, C. Cristea, L. Silaghi-Dumitrescu, S. Astilean, L. Gaina, *Int. J. Mol. Sci.*, **2021**, *22*, 2985.
15. B. Stoean, L. Gaina, C. Cristea, R. Silaghi-Dumitrescu, A. M. V. Branzanic, M. Focsan, E. Fischer-Fodor, B. Tigu, C. Moldovan, A. D. Cecan, P. Achimas-Cadariu, S. Astilean, L. Silaghi-Dumitrescu, *Dyes Pigm.*, **2022**, *205*, 110460.
16. D. Creed, Willie C. Burton, and Newton C. Fawcett, *J. Chem. Soc., Chem. Commun.* **1983**, 1521-1523.
17. A. Lagrange, EP1607393, **2005**.
18. P.T.K. Chin, M.M. Welling, S.C.J Meskers, R.A. Valdes Olmos, H. Tanke, F.W.B. Van Leeuwen *Eur J Nucl Med Mol Imaging*, **2013**, *40*, 1283–1291.
19. W. Li, Q. Huang, Z. Mao, J. Zhao, H. Wu, J. Chen, Z. Yang, Y. Li, Z. Yang, Y. Zhang, M.P. Aldred, Z. Chi, *Angew.Chem., Int. Ed.*, **2020**, *59*, 3739.
20. L. Marin, A. Bejan, S. Shova, *Dyes Pigm.*, **2020**, *175*, 108164.
21. R.B. Von Dreele, J. Harris, *Acta Crystallogr., Sect. C: Cryst. Struct. Commun.*, **1983**, *39*, 170.
22. J. A. Cody, C.S. Larrabee, M. D. Clarck, S. Hlynchuk, J. A. Tatum, *Tet Lett.*, **2012**, *53*, 4896-4899.
23. A. Meden, *Croat. Chem. Acta*, **1998**, *71*, 615–633.
24. Dassault Systèmes BIOVIA, **2014** [Materials Studio], [v8.0.0.843], San Diego: Dassault Systèmes.
25. P-E. Werner, L. Eriksson, M. Westdahl, *J Appl. Cryst.*, **1985**, *18*, 367–370.
26. A. Boultif, D. Louer, *J. Appl. Cryst.*, **2004**, *37*, 724-731.
27. M. A. Neumann, *J. Appl. Cryst.*, **2003**, *36*, 356-365.

SYNTHESIS OF Pt(II)-COMPLEXES WITH SYMMETRICAL AND UNSYMMETRICAL GLYOXIMES, THEIR PHYSICAL-CHEMICAL AND BIOLOGICAL STUDY

Csaba VÁRHELYI Jr.^{a*}, Roland SZALAY^b, György POKOL^c,
János MADARÁSZ^c, Laura MARINCAS^a, Raluca-Anca MEREU^a,
Judith MIHÁLY^d, Judit PAPP^e, Melinda SIMON-VÁRHELYI^a,
Róbert TÖTÖS^a, Maria TOMOAI-COTIȘEL^a

ABSTRACT. A series of Pt-complexes of the type [Pt(DioxH)₂L₂], (DioxH= deprotonated diethyl-glyoxime, methyl-pentyl-glyoxime, methyl-propyl-glioxime, L=amine) were synthesized, described and characterized with thermoanalytical (TG-DTG-DTA), spectroscopical (FTIR, ESI-MS, UV-VIS and NMR), powder XRD and AFM methods. The biological activity, especially the antibacterial effect, was also studied. The complexes were tested against selected Gram-positive and Gram-negative bacteria. The thermoanalytical measurements revealed the stability of complexes until 200 °C, which then loose characteristic fragments of their ligands. The spectroscopic data are in accordance with the thermal properties of the samples, confirming their composition. The compounds exhibited antibacterial effect against the bacterial strain studied.

Keywords: Pt(II)-complexes, α -dioxime, amine ligand, thermal properties, spectroscopy, AFM, antimicrobial activity

^a Babeş-Bolyai University, Faculty of Chemistry and Chemical Engineering, Arany J. str. 11, RO-400 028, Cluj-Napoca, Romania.

^b Eötvös Loránd University, Institute of Chemistry, Pázmány Péter sétány 1/A, H-1117, Budapest, Hungary.

^c Budapest University of Technology and Economics, Faculty of Chemical Technology and Biotechnology, Műegyetem rkp. 3, H-1111 Budapest, Hungary.

^d Research Centre for Natural Sciences, Institute of Materials and Environmental Chemistry, Magyar tudósok körútja 2, H-1117 Budapest, Hungary.

^e Babeş-Bolyai University, Faculty of Biology and Geology, Mihail Kogălniceanu str. 1, RO-400084, Cluj-Napoca, Romania.

* Corresponding author: csaba.varhelyi@ubbcluj.ro.



INTRODUCTION

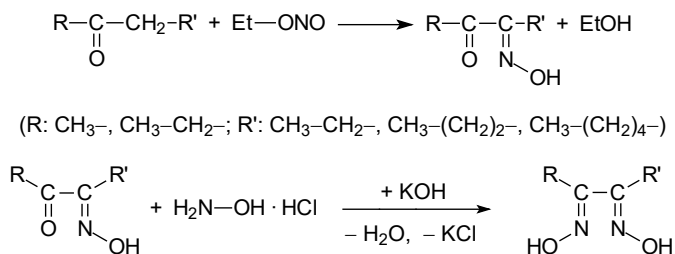
After the discovery of anticancer activity of cisplatin by Barnett Rosenberg, platinum coordination complexes became a very important class of drugs [1]. In recent years other platinum-based drugs have entered in clinical trials, and high efforts have been made to find more active and less toxic agents for cancer treatment in humans [2-5]. The mode of action of platinum based antitumor drugs, such as cisplatin and its analogues, is that they bind to the DNA in cancer cells [6-9]. Many pathogenic bacteria show resistance toward antibiotics, therefore it is necessary to find new compounds to control the multidrug-resistant microorganisms [10-13]. For example, some tetracyclines coordinated to Pt(II) showed improved antimicrobial activity [14]. In order to obtain new Pt(II) metallodrugs as good candidates for anticancer or antimicrobial agents, N donor ligands, such as Schiff-bases [15, 16], aliphatic or aromatic amines, are often used [17-20].

Platinum group metal complexes with α -diimine ligands have been used as photosensitizers in energy conversion and electron transfer, in chemi- and electroluminescent systems, and as probes for heterogeneous binding and dynamics of macromolecular structure [21-24]. Other platinum coordination and organometallic complexes have demonstrated applications in homogeneous catalysis, such as the oxidation of ethanol to acetic acid or acetaldehyde, the oxidation of sulfur dioxide to sulfuric acid and, furthermore, in catalytic combustion, hydrogenation reactions. The rationale in utilization is their ability to catalyze reactions under milder conditions with higher selectivity, compared to other metals, their high stability in various oxidation states, functional-group tolerance, and their highly understood synthetic chemistry [25, 26].

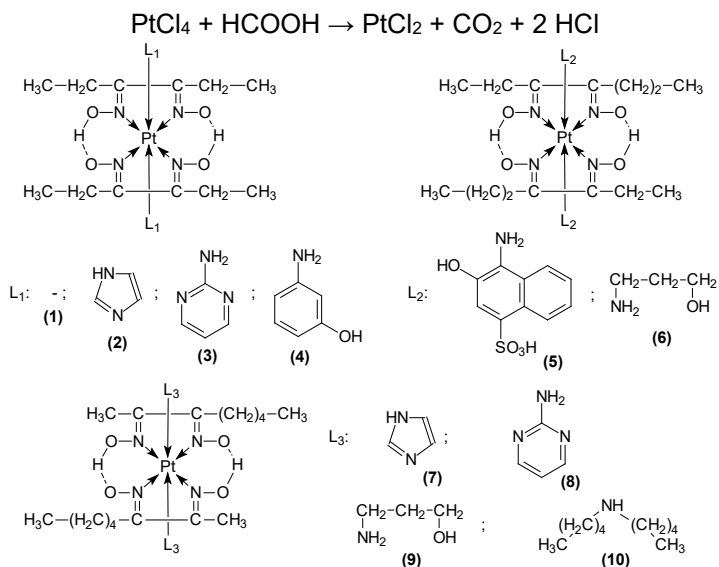
Thermal properties of bioactive compounds are relevant to their future usage, therefore thermal analysis is an appropriate technique to characterize the complexes with biological activity [27-30]. Thermoanalytical methods provide important informations on thermal stability, polymorphic forms or structural changes [31-34], as well as purity of potential new drugs [35-36]. The aim of this study was the synthesis, physical-chemical and antimicrobial characterization of some compounds with general formula $[\text{Pt}(\text{DioxH})_2\text{L}_2]$. Since the thermal properties of biological active compounds are crucial for their future applications, another aim of this work was the detailed thermal analysis of the synthesized coordination compounds.

RESULTS AND DISCUSSION

For the synthesis of [Pt(DioxH)₂L₂] type complexes three different glyoximes were used as primary ligand sources. In the first step platinum(IV) chloride was reduced by formic acid to give PtCl₂, then reacted with the selected glyoxime and amine ligands. The dioximes as precursors were prepared by the isonitroso method, namely, from the corresponding monoketones acidified with HCl upon continuous bubbling of gaseous ethyl-nitrite into the cooled mixture. The dione-monoximes obtained as intermediate products were converted with hydroxyl-amine to the corresponding α-dioxime. The general reaction scheme of glyoximes is shown in Scheme 1, and the structures of complexes are presented in Scheme 2.



Scheme 1. The general reaction scheme of glyoxime syntheses



Scheme 2. The reduction step and structures of selected complexes

IR-spectral measurements

We recorded the mid- and far-IR spectra for our compounds, and the results are summarized in the experimental part. Strong bands related to $\nu_{C=N}$ (1519–1535 cm^{-1}) and ν_{Pt-N} (414–518 cm^{-1}) vibrations appear for all studied compounds, which demonstrate the formation of complexes.

If we compare the spectrum of compounds containing symmetrical and unsymmetrical glyoxime ligands we can observe generally a small shift to smaller values of ν_{Pt-N} , $\nu_{C=N}$ bands in case of the unsymmetrical complexes, which can be explained by electronic effects. For example, in Figures 1 and 2 two IR spectra are presented with the only difference in the dioxime moiety. In case of the symmetrical compound the ν_{Pt-N} band appears at 512 cm^{-1} and in the unsymmetrical one does at 508 cm^{-1} . This difference can be explained with the distortion of the molecule, and the increasing Pt–N distance in case of the unsymmetrical complexes.

In the far-IR range (400–100 cm^{-1}) several deformation vibrations appeared, mostly for the heterocyclic amines and for the N–Pt–N groups (δ_{N-Pt-N} : 324–358 cm^{-1}) [37].

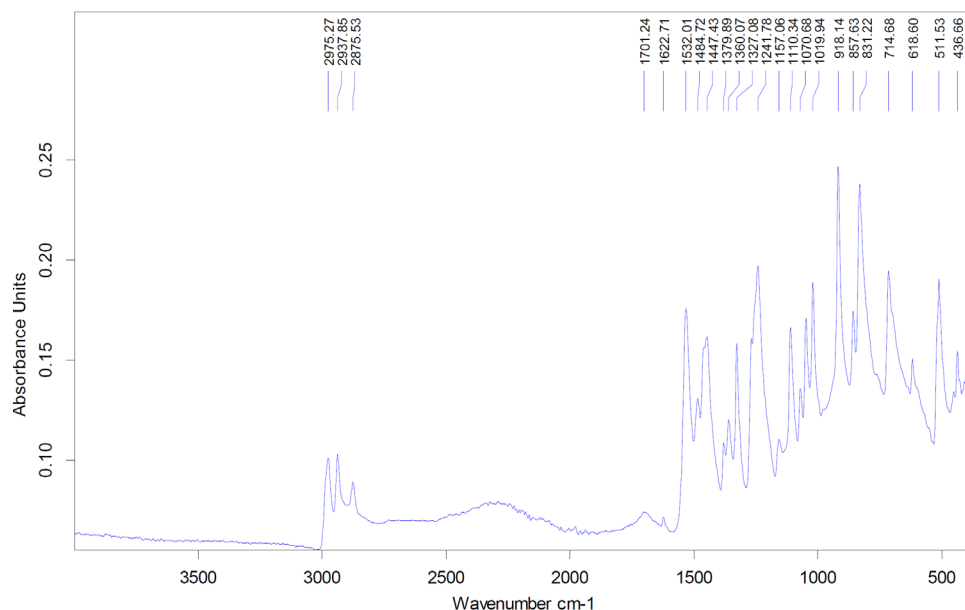


Figure 1. IR spectrum of $[Pt(\text{Diehyl-DioxH})_2(\text{imidazole})_2]$

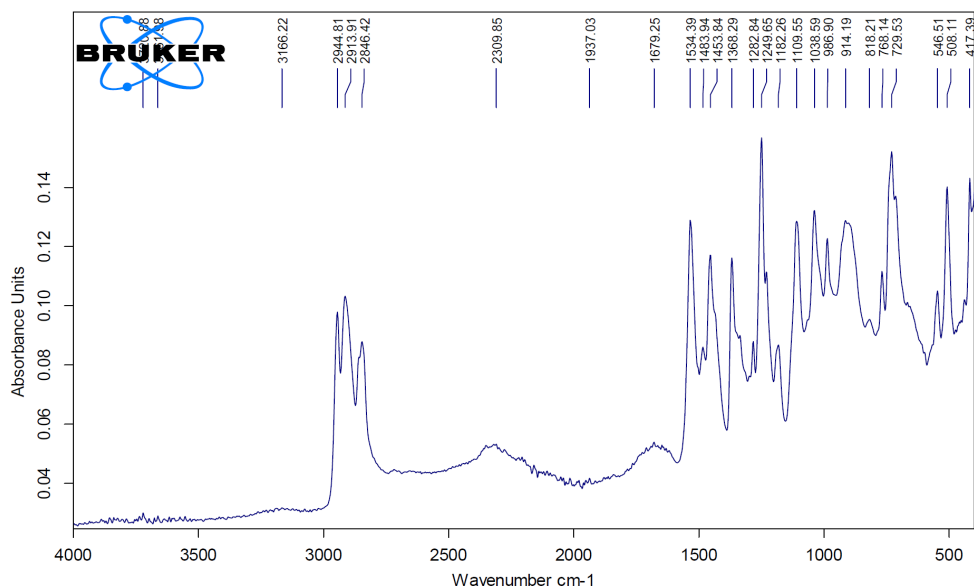


Figure 2. IR spectrum of $[Pt(Me-Pentyl-DioxH)_2(imidazole)_2]$

Raman-spectral measurements

The Raman spectra were recorded in the range of 4000–50 cm⁻¹ for a few complexes exhibiting less dark color. The most important bands appear at the same positions like in the IR spectra but with lower intensities. Due to selection rules in Raman spectroscopy the symmetric vibrations are also detectable which, as a result, can aid the proper assignation of vibrational bands.

Electronic spectra (UV–VIS)

The electronic spectra of some $[Pt(DioxH)_2L_2]$ type complexes were recorded. The free ligand absorption bands appear between 212–286 nm and 320–324 nm which can be assigned to $\pi \rightarrow \pi^*$ transitions of the aromatic rings and $n \rightarrow \pi^*$ transitions of the C=N groups, respectively. A weak band can also be observed between 470–623 nm corresponding to a $d-d$ electron transition that demonstrates a rectangle-planar geometry of glyoxime groups around the metal ion [22]. The calculation of the acidity constants shows that our complexes are weakly acidic due to the deprotonation of the dioximes in basic buffer solutions.

Mass spectrometric measurements

In the mass spectra the molecular ions were successfully detected for all complexes. Table 1 presents the characteristic fragments of complexes. The base peak is generally $[Pt(DioxH)_2]^+$ which indicates the stability of this planar moiety and a weak bonding of Pt to the amines [38].

Table 1. Electrospray mass spectrometric data for $[Pt(DioxH)_2L_2]$ type complexes

Compound	Fragments (m/z)
$[Pt(\text{Diethyl-DioxH})_2]$ (1)	480.9 $[M]^+$, 338.4 $[Pt(\text{Diethyl-DioxH})]^+$, 100.9 $[CH_3-CH_2-C=N-O-O-N]^+$, 60.0 $[N_2O_2]^+$
$[Pt(\text{Diethyl-DioxH})_2(\text{imidazole})_2]$ (2)	617.2 $[M]^+$, 550.9 $[Pt(\text{Diethyl-DioxH})_2(\text{imidazole})]^+$, 480.9 $[Pt(\text{Diethyl-DioxH})_2]^+$, 100.9 $[CH_3-CH_2-C=N-O-O-N]^+$, 60.0 $[N_2O_2]^+$
$[Pt(\text{Diethyl-DioxH})_2(2\text{-amino-pyrimidine})_2]$ (3)	694.8 $[M+Na]^+$, 671.2 $[M]^+$, 481.0 $[Pt(\text{Diethyl-DioxH})_2]^+$, 100.9 $[CH_3-CH_2-C=N-O-O-N]^+$, 60.0 $[N_2O_2]^+$
$[Pt(\text{Diethyl-DioxH})_2(3\text{-aminophenol})_2]$ (4)	722.0 $[M+Na]^+$, 699.0 $[M]^+$, 681.9 $[M-OH]^+$, 665.6 $[M-2OH]^+$, 480.9 $[Pt(\text{Diethyl-DioxH})_2]^+$, 100.9 $[CH_3-CH_2-C=N-O-O-N]^+$, 60.0 $[N_2O_2]^+$
$[Pt(\text{Et-Pr-DioxH})_2(4\text{-amino-3-hydroxynaphthalene-1-sulfonic acid})_2]$ (5)	990.7 $[MH_2]^+$, 830.6 $[Pt(\text{Et-Pr-DioxH})(4\text{-am.-3-hydr.-naph.-1-sulfonic acid})_2]^+$, 510.2 $[Pt(\text{Et-Pr-DioxH})_2]^+$, 434.4 $[Pt(4\text{-am.-3-hydr.-naph.-1-sulfonic acid})]^+$
$[Pt(\text{Et-Pr-DioxH})_2(3\text{-amino-1-propanol})_2]$ (6)	659.7 $[M]^+$, 582.9 $[Pt(\text{Et-Pr-DioxH})_2(3\text{-am.-1-prop})]^+$, 509.3 $[Pt(\text{Et-Pr-DioxH})_2]^+$
$[Pt(\text{Me-Pentyl-DioxH})_2(\text{imidazole})_2]$ (7)	712.6 $[M+K]^+$, 673.4 $[M]^+$, 657.4 $[M-O]^+$, 605.3 $[Pt(\text{Me-Pentyl-DioxH})_2(\text{imidazole})]^+$, 538.2 $[Pt(\text{Me-Pentyl-DioxH})_2]^+$
$[Pt(\text{Me-Pentyl-DioxH})_2(3\text{-amino-1-propanol})_2]$ (9)	727.6 $[M+K]^+$, 688.5 $[M]^+$, 576.2 $[M-DioxH_2]^+$, 538.2 $[Pt(\text{Me-Pentyl-DioxH})_2]^+$, 428.3 $[Pt(\text{Me-Pentyl-DioxH})_2N_2O_2]^+$
$[Pt(\text{Me-Pentyl-DioxH})_2((n\text{-Bu})_2NH)_2]$ (10)	795.4 $[M]^+$, 779.4 $[M-OH]^+$, 763.4 $[M-OHO]^+$, 538.2 $[Pt(\text{Me-Pentyl-DioxH})_2]^+$, 130.2 $[(n\text{-Bu})_2NH_2]^+$

Thermoanalytical study

The TG, DTG, DTA curves were recorded for the obtained complexes. One example is presented in Fig. 3, and the results for all studied complexes are included in Table 2.

SYNTHESIS OF Pt(II)-COMPLEXES WITH SYMMETRICAL AND UNSYMMETRICAL GLYOXIMES,
THEIR PHYSICAL-CHEMICAL AND BIOLOGICAL STUDY

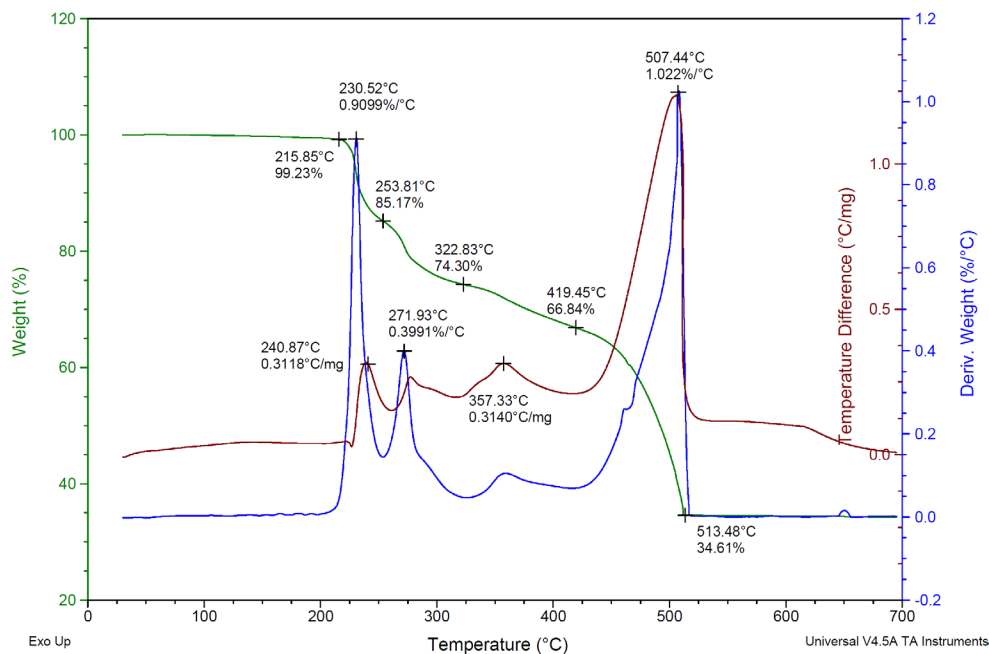


Figure 3. Thermal decomposition curves of $[Pt(DiehyI-DioxH)_2(imidazole)_2]$

The first observation from the thermal decomposition study is the stability of complexes between the temperatures of 115–223 °C. The stability is influenced by the nature of glyoximes and the coordinated amines. Complexes containing symmetrical glyoxime are usually more stable than the unsymmetrical ones (206–223 °C), however, the nature of amines has also influence on the stability. Amines with electron-releasing groups enhance the stability of complexes. The mechanism of the thermal decomposition of complexes was established as well. In the first step the amine elimination takes place until 350 °C, and then the glyoxime groups are leaving until 550 °C which is demonstrated with a big exothermic peak on the DTA curve.

The general decomposition mechanism of $[Pt(DioxH)_2L_2]$ type complexes is shown below:

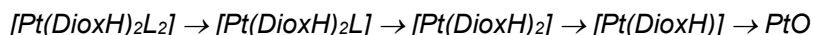


Table 2. Thermoanalytical data of $[Pt(DioxH)_2L_2]$ type complexes

No.	Fragment	t (°C)	m; $-\Delta m$ (%)	DTG (°C)	DTA (°C)
1.	-	206	99.86; 0.14	233.83	238.07 (ex.)
	Diethyl-DioxH	304	66.3; 33.56	274.08	297.39 (ex.)
	Diethyl-DioxH	557	35.96; 30.34	501.48	501.48 (ex.)
	PtO (rest)	695	35.06		
2.	-	216	99.23; 0.77		
	imidazole	254	85.17; 14.06	230.52	240.87 (ex.)
	imidazole	323	74.30; 10.87	271.93	357.33 (ex.)
	2 (Diethyl-DioxH) PtO (rest)	513 513	34.61; 39.69 34.61	507.44	507.44 (ex.)
3.	-	223	99.76; 0.24		
	2 (2-am.-pyrimidine)	293	72.54; 27.22	279.69	302.98 (ex.)
	2 (Diethyl-DioxH)	351	38.11; 34.33	340.94	340.94 (ex.)
	PtO (rest)	689	36.23		
4.	-	223	99.44; 0.56		
	2 (3-hydroxy-aniline)	307	67.84; 31.6	279.69	292.63 (ex.)
	2 (Diethyl-DioxH)	366	40.41; 27.43	349.57	350.43 (ex.)
	PtO (rest)	693	37.75		
5.	-	219	100; 0		
	-SO ₃ H	266	92.35; 7.65	243.79	247.02 (ex.)
	1-amino-2-HO- naphthalene	350	80.15; 12.2	307.54	314.8 (end.)
	2 (Et-Pr-DioxH) + am.	450	29.79; 50.36	442.3	441.5 (ex.)
	PtO (rest)	992	29.24		
6.	-	154	100; 0	197.8	261.54 (ex.)
	2 (3-am.-1-propanol)	284	79.07; 20.93	259.93	359.19 (ex.)
	2 (Et-Pr-DioxH)	395	35.98; 43.09	358.38	
	PtO (rest)	991	33.8		
7.	-	222	98.94; 1.06		
	2 imidazole	282	85.87; 13.07	260.74	263.97 (ex.)
	2 (Me-Pentyl-DioxH)	382	38.6; 47.27	354.34	355.15 (ex.)
	PtO (rest)	990	35.96		
8.	-	115	99.49; 0.51	205.86	174.39 (end.)
	2(2-am.-Py- midine+Me+pentyl)	239	50.49; 49	257.51	260.74 (ex.)
	2 (DioxH)	386	15.68; 34.81	353.54	351.92 (ex.)
	PtO (rest)	991	13.38		
9.	-	200	97.67; 2.33		
	2 (3-am.-1-propanol)	277	83.67; 14	259.93	260.74 (ex.)
	2 (Me-Pentyl-DioxH)	545	38.07; 45.6	338.21	335.78 (ex.)
	PtO (rest)	990	36.76		
10.	-	217	100; 0		
	2 [(n-Bu) ₂ NH] ₂]	310	84.47; 15.53	259.12	262.35 (ex.)
	2 (Me-Pentyl-DioxH)	387	44.98; 39.49	363.22	362.41 (ex.)
	PtO (rest)	990	42.48		

(See the numbering of complexes in the experimental part or scheme 2!)

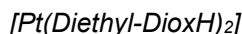
Abbreviations: ex. = exothermic, end. = endothermic

Powder-XRD measurements

The powder-XRD measurements revealed that complexes with symmetrical glyoxime groups show crystalline form with many peaks. However, samples containing unsymmetrical glyoxime groups precipitated out in an amorphous state displaying only some peaks therefore their structure has to be characterized by other methods. The crystalline complexes XRD structures can not be found in the Cambridge Structural Database.

AFM investigations

Two complexes, namely, $[Pt(\text{Diethyl-DioxH})_2]$ and $[Pt(\text{Diethyl-DioxH})_2(2\text{-aminopyrimidine})_2]$ were investigated by atomic force microscopy, and results are presented below.



The film resulting from adsorption is of very good quality, well structured to AFM investigation. The most representative images resulting from the scanning area of $1\ \mu\text{m} \times 1\ \mu\text{m}$ are presented in Figure 4.

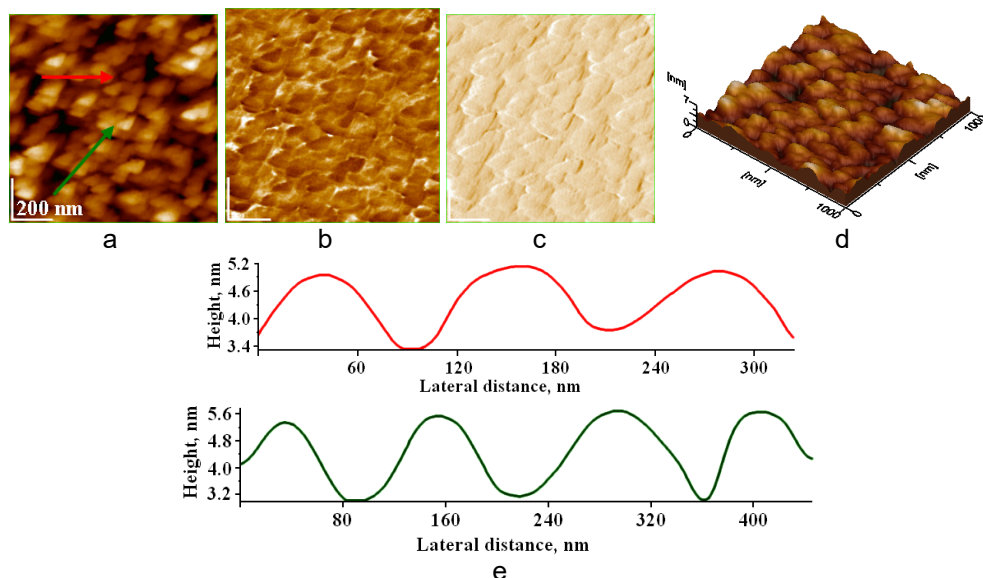
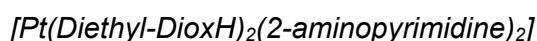


Figure 4. AFM images for $[Pt(\text{Diethyl-DioxH})_2]$: a) topographic image, b) phase image, c) amplitude image, d) 3D image, e) profiles along the arrows in image (a). Scanning area $1\ \mu\text{m} \times 1\ \mu\text{m}$

The topography of the surface highlights an uniform deposition with very well individualized nanoparticles. Their shape is partially equiaxial, enough to allow us to speak about their diameter, but edges appear under sharp angle what foreshadow the formation of corners. The fact correlates with a high crystalline aspect of the interior of these nanoparticles. Their appearance would correlate with well-developed and slender XRD maxima.

The phase and amplitude images, Figures 4b and c, highlight with special clarity the individualization of nanoparticles in the deposition film. Its three-dimensional aspect is shown in Figure 4d. The profiles in Figure 4e indicate a middle diameter of the nanoparticles to be 60 nm.



The deposition film resulting from adsorption has a very good quality too, and lent itself to AFM investigation. The most representative images resulting from the scanning area of $1\ \mu\text{m} \times 1\ \mu\text{m}$ are presented in figure 5.

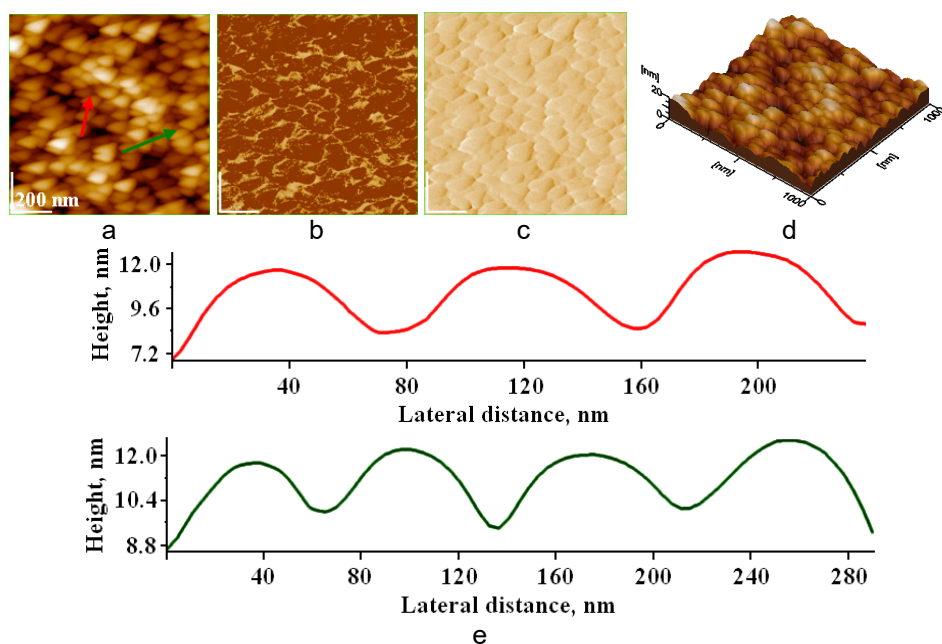


Figure 5. AFM images for $[Pt(\text{Diethyl-DioxH})_2(2\text{-aminopyrimidine})_2]$: a) topographic image, b) phase image, c) amplitude image, d) 3D image, e) profiles along the arrows in image (a). Scanning area $1\ \mu\text{m} \times 1\ \mu\text{m}$

The topographic image, Figure 5a, allows us to visualize the nanoparticles with great clarity. In this way their shape and dimensional aspects, such as the diameter of the nanoparticles can be observed, and the roughness of the deposition can be measured. In the present case we have a fairly uniform film of well-individualized nanoparticles with an equiaxial shape (approximately the same radius in any direction starting from the center of the nanoparticle). Although the observed nanoparticles have a rounded appearance, they are not perfectly spherical due to the fact that their internal crystalline structure leaves its mark to some extent on the external appearance.

In the phase image, Figure 5b, the limit between the nanoparticles appears with a light yellow shade while they have a brown appearance. The fact supports the good individualization of the nanoparticles in the deposition film. The amplitude image, Figure 5c, shows that the sample was scanned under optimal conditions, and the nanoparticles stand out clearly. AFM imaging has the advantage to produce real three-dimensional images due to the scaling in metric units of the Z axis. Therefore, Figure 5d clearly shows the three-dimensional aspect of the deposition and the nanoparticles can be clearly seen how they adsorbed on the glass surface. This deposition is very smooth with a roughness of only 3.18 nm (Table 3). Last but not least, the profiles drawn in Figure 5e allow us to observe the rounded equiaxial aspect of the nanoparticles and thus to determine their diameter accurately. We found that the sample has nanoparticles with a diameter of 40 nm.

Table 3. AFM measured values

Compound	Height (nm)	Rugosity RMS (nm)			Nanopart. diameter (nm)
		Area	Red profile	Green profile	
[Pt(Diethyl-DioxH) ₂] (1)	7	1.09	0.50	0.81	60
[Pt(Diethyl-DioxH) ₂ (2-aminopyrimidine) ₂] (3)	20	3.18	1.37	0.96	40

It is observed that samples with small diameter of nanoparticles lead to the formation of films with lower roughness, while samples with nanoparticles with larger diameters and a very good individualization led to higher values of roughness.

NMR measurements

The NMR spectra of some complexes containing symmetrical and unsymmetrical glyoxime were recorded. In case of the symmetrical glyoximes, in the ¹H NMR spectra the aliphatic protons from the glyoxime

groups appear at 1.1–2.8 ppm in all complexes, and the aromatic protons from the amines appear between 7.7–8.3 ppm. In the ^{13}C NMR spectra the aliphatic carbons appear at 10–20 ppm, and the double bonded carbons appear at 158 ppm. In case of unsymmetrical glyoximes in the ^1H NMR spectra the aliphatic protons from the glyoxime groups appear at 0.8 ppm up to 2,6 ppm on the longer chain. The glyoxime OH protons appear at 11.3–11.4 ppm, the aliphatic amine protons appear between 0.85–2.5 ppm, the amino group protons values are 2.6–8.2 ppm. In case of imidazole group the shift is 8.1 ppm.

Making a comparison between the free ligand and the complex, for example Et-Pr-DioxH₂ and $[\text{Pt}(\text{Et-Pr-DioxH})_2(3\text{-amino-1-propanol})_2]$, a small shift to higher ppm values can be observed in case of the complex (e. g.: from 0.85 ppm to 0.88 ppm – methyl group, from 11.30 ppm to 11.32 ppm – glyoxime OH group). This can be explained with the electron attracting effect of Pt. This effect is reduced by the electron-donor property of the aliphatic amino groups. In case when the amine ligand is aromatic the first peak of methyl group appears at higher value, 1.1 ppm (complexes **1 – 4**).

Adsorption test

The adsorption of $[\text{Pt}(\text{Me-Pentyl-DioxH})_2(\text{imidazole})_2]$ was tested on hydroxyapatite. The adsorption efficiency was 90.5 % and the adsorption capacity 226.36 mg/g, calculated from the calibration straight equation. The OH group of hydroxyapatite and the calcium center serve as active sites for the formation of H-bridge bonds.

Biological assay

The antimicrobial effects of the Pt-complexes were tested against Gram-negative *Serratia marcescens* and Gram-positive *Bacillus subtilis* bacteria. The complexes were dissolved in DMSO, and the concentration was 2 mmol/l. In case of $[\text{Pt}(\text{diethyl-DioxH})_2(\text{imidazole})_2]$ and $[\text{Pt}(\text{diethyl-DioxH})_2(3\text{-hydroxy-aniline})_2]$ the Kirby-Bauer disk diffusion method, while in case of $[\text{Pt}(\text{Et-Pr-DioxH})_2(4\text{-amino-3-hydroxynaphthalene-1-sulfonic acid})_2]$, $[\text{Pt}(\text{Me-Pentyl-DioxH})_2(2\text{-aminopyrimidine})_2]$, $[\text{Pt}(\text{Me-Pentyl-DioxH})_2(3\text{-amino-1-propanol})_2]$ the fluorescein-diacetate (FDA) hydrolysis assay were used for the evaluation of the antibacterial potential. The inhibitory effect of compounds on the development of bacteria was determined by measuring the inhibition zone around the paper discs containing 5 μl , 10 μl , 20 μl or 30 μl of the tested complexes. The spectrophotometrically determined FDA hydrolysis

rate reflect the biofilm-inhibiting effect of the complexes added in different quantities (5 μ l, 10 μ l or 20 μ l) to the nutrient media used for the cultivation of bacteria. The antibacterial effect can be deduced from the absorbance values at 490 nm: the smaller absorbance values indicate a bigger inhibition of the enzyme activity of biofilm-forming bacteria. The degree of inhibition can be calculated in relation to the control sample, which was prepared without Pt-complexes, so the enzyme activity and the biofilm formation was considered 100 %. Each value obtained represents the average of 5 different measurements. The results are included in Table 4 and 5.

Table 4. The dimensions of inhibition zones as a function of the quantity of complexes applied

Compound	5 μ l	10 μ l	20 μ l	30 μ l
[Pt(diethyl-DioxH) ₂ (imidazole) ₂] (2)	-	9 mm	12,7 mm	16,33 mm
[Pt(diethyl-DioxH) ₂ (3-hydroxy-aniline) ₂] (4)	-	7,83 mm	13,66 mm	14,66 mm

Table 5. The inhibition degree of bacterial biofilm-forming capacity ($A_{control} = 1.575$)

Compound	5 μ l/ml		10 μ l/ml		20 μ l/ml	
	A	Inhibition degree (%)	A	Inhibition degree (%)	A	Inhibition degree (%)
[Pt(Et-Pr-DioxH) ₂ (4-amino-3-hydroxynaphthalene-1-sulfonic acid) ₂] (5)	1.235	21.587	1.124	28.635	0.500	68.254
[Pt(Me-Pentyl-DioxH) ₂ (2-amino-pyrimidine) ₂] (8)	1.468	6.794	1.352	14.159	1.327	15.746
[Pt(Me-Pentyl-DioxH) ₂ (3-amino-1-propanol) ₂] (9)	1.458	7.429	1.430	9.206	1.320	16.190

(5, 10 or 20 μ l complex solution was added to 1 ml nutrient broth)

Conclusions

Platinum complexes containing novel N-donor ligands were synthesized, and their structure was characterized by different spectroscopic and diffraction methods. According to the thermoanalytical studies the samples show good thermic stability below 125 °C and their stepwise decomposition mechanism

was also determined. The antibacterial activity of the synthesized compounds was tested against selected bacteria by two microbiological methods providing good inhibition results. In future we also wish to extend our researches to investigate their anti-tumor effect.

EXPERIMENTAL SECTION

The IR spectra of the complexes were recorded with a Bruker Alpha FTIR spectrometer (Platinum single reflection diamond ATR), at room temperature, in the mid-IR (4000–400 cm^{-1}) and far-IR (650–150 cm^{-1}) range, respectively, on a Perkin–Elmer System 2000 FTIR spectrometer, operating with a resolution of 4 cm^{-1} . Raman spectra were measured with a Bio-Rad (Digilab) FT-Raman spectrometer (1064 nm NdYAG laser excitation, 250 mW laser power per sample, 4 cm^{-1} resolution, 512 scan). The electronic-spectra were recorded in aqueous solution of 10^{-4} mol/l concentration with Jasco V-670 Spectrophotometer.

Thermal measurements were performed with a 951 TG and 910 DSC calorimeter (TA Instruments), in Ar or N_2 atmosphere, at a heating rate of 10 $\text{K}\cdot\text{min}^{-1}$ (sample mass 4–10 mg). Mass spectrometric (MS) measurements were carried out by a PE Sciex API 2000 triple quadrupole mass spectrometer, using electrospray ionization (ESI) in the 200–1200 m/z region. By ESI-MS, ionization takes place at milder conditions as compared with classical mass spectrometry, therefore it is more sensible for the detection of single and associated dimer molecular ions and their fragment ions.

The NMR spectra were recorded in DMSO-d^6 in 5 mm tubes at RT on a Bruker DRX 500 spectrometer at 500MHz using TMS as internal reference. The AFM measurements were carried out with a JEOL JSPM 4210 atomic force microscope using NSC 15 Hard cantilevers manufactured by Micromasch Co. Phase and amplitude topographic images were recorded simultaneously.

Synthesis of glyoximes

Diethyl-glyoxime was prepared from 3,4-hexanedione (0.1 mol, 13 ml) reacting with hydroxyl-amine hydrochloride (0.2 mol, 13.9 g) dissolved in 50 ml water. The solution was neutralized with KOH (0.2 mol, 11.2 g). The reaction mixture was heated for 2–3 hours (70–80°C), and then the precipitated product was filtered off. After re-crystallization from EtOH or MeOH, it was dried on air.

Ethyl-propyl-glyoxime and methyl-pentyl-glyoxime were prepared from 3-heptanone and 2-octanone, respectively, by the isonitroso method.

Accordingly, upon cooling (ice + NaCl + H₂O) gaseous ethyl-nitrite was bubbled into a mixture containing 0.5 mol monoketone acidified with 2.5 ml HCl for 2–3 hours. The dion-monoximes as intermediate products were converted to the corresponding dioxime with hydroxyl-amine hydrochloride in the same way as in the diethyl-glyoxime preparation. The crude products were recrystallized from ethyl or methyl alcohol. Yield: 80–90%.

Synthesis of [Pt(DioxH)₂L₂] type complexes

The platinum salt was reduced with formic acid (1 ml for 1.0 mmol PtCl₄) before its use in the complex synthesis (Scheme. 2). 2.0 mmol glyoxime dissolved in EtOH or MeOH (20 ml) was added to the aqueous solution of the reduced platinum salt (PtCl₂, 1.0 mmol). The mixture was heated for 1 hour, and then the corresponding amine (2.0 mmol) was added, and heated further for 2–3 hours. After cooling, the formed complexes were filtered, washed with EtOH–water mixture (1:1), and dried on air. Details of the preparations, yields are given in Table 6.

Table 6. Preparation data for [Pt(DioxH)₂L₂] type derivatives

No.	Starting materials (g; mol)			Product	Yield (g; %)
	PtCl ₄	DioxH ₂	Amine		
1.	0.34; 0.001	diethyl-DioxH ₂ 0.3; 0.002	-	[Pt(di-Et-DioxH) ₂]	0.3; 59
2.	0.34; 0.001	diethyl-DioxH ₂ 0.3; 0.002	imidazole 0.14; 0.002	[Pt(di-Et-DioxH) ₂ (imidazole) ₂]	0.36; 56
3.	0.34; 0.001	diethyl-DioxH ₂ 0.3; 0.002	2-amino-pyrimidine 0.19; 0.002	[Pt(di-Et-DioxH) ₂ (2-aminopyrimidine) ₂]	0.38; 54
4.	0.34; 0.001	diethyl-DioxH ₂ 0.3; 0.002	3-am.-phenol 0.22; 0.002	[Pt(di-Et-DioxH) ₂ (3-aminophenol) ₂]	0.31; 42
5.	0.34; 0.001	Et-Pr-DioxH ₂ 0.32; 0.002	4-amino-3-HO-napht.- 1-sulfonic acid 0.48; 0.002	[Pt(Et-Pr-DioxH) ₂ (4- amino-3-HO-napht.- 1-sulfonic acid) ₂]	0.25; 25
6.	0.34; 0.001	Et-Pr-DioxH ₂ 0.32; 0.002	3-am.-1-propanol 0.15; 0.002	[Pt(Et-Pr-DioxH) ₂ (3- amino-1-propanol) ₂]	0.34; 51
7.	0.34; 0.001	Me-Pent.-DioxH ₂ 0.34; 0.002	imidazole 0.14; 0.002	[Pt(Me-Pentyl- DioxH) ₂ (imidazole) ₂]	0.27; 41
8.	0.34; 0.001	Me-Pent.-DioxH ₂ 0.34; 0.002	2-amino-pyrimidine 0.19; 0.002	[Pt(Me-Pent.-DioxH) ₂ (2-aminopyrimidine) ₂]	0.29; 43
9.	0.34; 0.001	Me-Pent.-DioxH ₂ 0.34; 0.002	3-am.-1-propanol 0.15; 0.002	[Pt(Me-Pent.-DioxH) ₂ (3-am.-1-propanol) ₂]	0.29; 43
10.	0.34; 0.001	Me-Pent.-DioxH ₂ 0.34; 0.002	(n-Bu) ₂ NH 0.26; 0.002	[Pt(Me-Pentil- DioxH) ₂ ((n-Bu) ₂ NH) ₂]	0.41; 52

Analysis

The microscopic appearance studied with an optical microscope and IR-spectral measurement results for the synthesized compounds are given in Tables 7, 8.

Table 7. Microscopic aspect, color and molar mass for $[Pt(DioxH)_2L_2]$ type derivatives

No.	Compound	Molar mass	Color	Microscopic aspect
1.	$[Pt(di-Et-DioxH)_2]$	481.41	Brown	triangle-based prisms
2.	$[Pt(di-Et-DioxH)_2(imidazole)_2]$	617.56	Brown	square-based long crystals
3.	$[Pt(di-Et-DioxH)_2(2-aminopyrimidine)_2]$	671.61	Brown	long needles, triangle-based prisms
4.	$[Pt(di-Et-DioxH)_2(3-aminophenol)_2]$	699.66	Black	shining, triangle-based prisms
5.	$[Pt(Et-Pr-DioxH)_2(4-amino-3-HO-napht.-1-sulfonic\ acid)_2]$	987,95	Purple	smaller triangle-based prisms
6.	$[Pt(Et-Pr-DioxH)_2(3-amino-1-propanol)_2]$	687,73	Dark purple	triangle-based prisms
7.	$[Pt(Me-Pentyl-DioxH)_2(imidazole)_2]$	673,67	Reddish-brown	needle-like triangle-based prisms
8.	$[Pt(Me-Pent.-DioxH)_2(2-aminopyrimidine)_2]$	727,72	Dark purple	bigger triangle-based prisms
9.	$[Pt(Me-Pent.-DioxH)_2(3-am.-1-propanol)_2]$	687,73	Dark purple	triangle-based prisms
10.	$[Pt(Me-Pentil-DioxH)_2((n-Bu)_2NH)_2]$	796,00	Reddish-brown	thin needle-shaped triangle-based prisms

Electronic spectra (UV–VIS)

As having similar absorption wavelengths and acidity constants the electronic spectra of only some representative $[Pt(DioxH)_2L_2]$ complexes were recorded in aqueous solution containing 10% EtOH. Making a comparison between the free ligand and the complex, for example Et-Pr-DioxH₂ and $[Pt(Et-Pr-DioxH)_2(3-amino-1-propanol)_2]$, a small shift to higher ppm values can be observed in case of the complex (e. g.: from 0.85 ppm to 0.88ppm – methyl group, from 11.30 ppm to 11.32 ppm – glyoxime OH group). This can be explained with the electron attracting effect of Pt. This effect is

reduced by the electron-donor property of the aliphatic amino groups. In case when the amine ligand is aromatic the first peak of methyl group appears at higher value, 1.1 ppm (complexes **1 – 4**). The observed absorption bands are summarized in Table 7. The spectra in Sørensen buffer solution in basic domain [39] were also recorded, and the acidity constants were calculated. The concentration of complexes was $2.8 \cdot 10^{-5}$ mol/l, and the used formula:

$$pK_a = pH + \lg \frac{A - A_{max}}{A_{min} - A}, K_a = 10^{-pK_a},$$

where A – absorbance for the selected pH value, A_{max} – maximum absorbance, A_{min} – minimum absorbance. The acidity constants are summarized in Table 9.

Table 8. FTIR-spectroscopic data

Vibration (cm ⁻¹)	1	2	3	4	5	6	7	8	9	10
ν_{N-H}	-	-	-	3223 w	3196 3098 w	3184 w	3166 w	3188 m	3142 w	3165 w
ν_{C-H}	2975 2938 2876 m	2975 2938 2876 m	2975 2937 2875 m	2974 2937 2876 w	2944 2908 m	3030 2948 2862 m	2945 2914 2846 m	2943 2918 2860 s	2945 2914 2847 m	2944 2916 2848 s
$\nu_{C=C}$	-	1623 w	1670 w	1610 m	1647 m	-	1679 w	1683 w	-	-
$\nu_{C=N}$	1535 s	1532 vs	1535 s	1534 s	1519 vs	1528 vs	1534 vs	1531 s	1534 vs	1527 s
δ_{CH_2}	1459 s	1447 s	1459 s	1448 s	1427 s	1451 vs	1454 s	1442 s	1453 s	1451 s
δ_{CH_3}	1360 m	1360 s	1359 m	1358 w	1347 s	1371 vs	1368 s	1371 s	1369 s	1372 s
ν_{N-O}	1241 vs	1242 vs	1241 vs	1240 vs	1221 s	1238 vs	1250 vs	1247 s	1249 vs	1258 vs
ν_{N-OH}	1107 s	1110 s	1106 s	1106 s	1104 s	1109 vs	1110 vs	1112 m	1110 s	1112 s
τ_{O-H}	916 vs	918 vs	916 vs	915 vs	1044 vs	913 vs	1039 vs	974 vs	1039 s	919 s
γ_{C-H}	712 s	715 s	712 s	710 s	655 vs	739 s	730 vs	726 vs	730 vs	732 vs
ν_{Pt-N}	518 s	515 509 s	518 515 s	513 501 s	519 s	506 434 s	508 417 vs	508 420 m	507 417 vs	511 414 vs
δ_{N-Pt-N}	358 vs	356 vs	328 vs	324 vs	-	-	-	-	-	-

s = strong; vs = very strong; m = medium; w = weak

AFM investigations

In a first phase, an attempt was made to display the samples on a solid support by dispersion in ultrapure water and transfer to the glass surface by vertical adsorption from the aqueous dispersion, but the results obtained were not satisfactory. For this reason, the powdery material was dispersed in DMSO, followed by vertical adsorption on glass slides. Sample drying has been shown to be a primary factor in the success of the AFM investigation. In this sense, we opted for natural drying in a vertical position to facilitate the draining of DMSO excess from the slide before solidification of the deposited film. The adsorption time was 5 s.

Several macroscopically different areas (minimum 5 areas) were scanned on each sample at several scanning areas such as for example 2.5 μm x 2.5 μm to 1 μm x 1 μm . Upon detailed examination of the resulting images, it was observed that the structures on the samples are best highlighted at the 1 μm x 1 μm scan area, revealing the nanostructural aspects of the samples. With the help of the image processing software, JEOL Win SPM Processing 2.0, measurements of surface roughness and profilometry associated with the measurement of the diameters of the nanoparticles in the composition of the samples were performed.

Table 9. Electronic spectral data

Compound	Absorption band (nm)	K_a
[Pt(Diethyl-DioxH) ₂] (1)	271 vs 320 m 470 w	$2.30 \cdot 10^{-10}$
[Pt(Diethyl-DioxH) ₂ (2-aminopyrimidine) ₂] (3)	198 vs 286 m	$3.24 \cdot 10^{-10}$
[Pt(Et-Pr-DioxH) ₂ (3-amino-1-propanol) ₂] (6)	215vs 284 s 324 s 520 m	$7.98 \cdot 10^{-11}$
[Pt(Me-Pentyl-DioxH) ₂ (imidazole) ₂] (7)	212 s 282 s 324 s 623 w	$8.39 \cdot 10^{-12}$

vs = very strong; s = strong; m = medium; w = weak

Adsorption test

For the adsorption test 0.1 g hydroxyapatite was measured and added 5 ml of $[Pt(Me-Pentyl-DioxH)_2(imidazole)_2]$ solution with a concentration of 2 g/l. The mixture was stirred for 24 hours on a magnetic stirrer. At the end of the adsorption time, the solution was centrifuged to ensure that the solid and liquid phases were well separated. After centrifugation, the two phases were separated by decantation, and the liquid phase was analyzed spectrophotometrically.

The measurements were performed with a Jasco V-650 two-way spectrometer. The adsorption was carried out in ethanol, ethanol was also used as a reference solution. Calibration series were prepared. The non-adsorbed complex quantity was calculated from the equation of the calibration line, and from here, knowing the initial concentration, the exact quantity of the adsorbed complex was calculated. The measurements were carried out at wavelength of $\lambda = 330$ nm. The adsorption capacity was determined by using the following formula:

$$q_t = \frac{m_{ads}}{m_{ad}} \left(\frac{mg}{g} \right)$$

where, q – adsorption capacity, m_{ads} – adsorbed quantity of $[Pt(Me-Pentyl-DioxH)_2(imidazole)_2]$ (mg), m_{ad} – quantity of support material (g).

The adsorption efficiency was determined using the following formula:

$$\eta = \frac{c_i - c_f}{c_i} \cdot 100 (\%)$$

where, c_i – initial concentration of $[Pt(Me-Pentyl-DioxH)_2(imidazole)_2]$ (mol/l) and c_f – the $[Pt(Me-Pentyl-DioxH)_2(imidazole)_2]$ concentration at a specific time (mol/l). Using these equations, were obtained the values of adsorption efficiency: 90.5 % and adsorption capacity: 226.36 mg/g [40].

Biological probes

The antimicrobial effects for two complexes were tested by the Kirby-Bauer disk diffusion method, for a Gram-negative (*Serratia marcescens*) bacteria. The tested bacterial suspension was spread on nutrient agar medium, then sterile filter paper disks, containing 5 μ l, 10 μ l, 20 μ l or 30 μ l of the sample solution (2 mmol/l) were added. After incubation (24 hour at 37 °C) the diameter of inhibition zones were measured.

Other complexes were studied for biofilm-inhibiting effect in case of the Gram-positive bacterium (*Bacillus subtilis*). The antibacterial properties were evaluated spectrophotometrically, based on the fluorescein-diacetate hydrolysis assay.

ACKNOWLEDGEMENT

The authors wish to express their thankfulness to the “Domus Hungarica Foundation” of Hungary for the several fellowships provided to Csaba Várhelyi jr.

REFERENCES

1. N.J. Wheate; S. Walker; G.E. Craig; R. Oun; *Dalton Trans.*, **2010**, *39*, 8113-8127
2. W.A. Wani; S. Prashar; S. Shreaz; S.Gómez-Ruiz; *Coord. Chem. Rev.*, **2016**, *312*, 67-98
3. Z. Wang; M. Wua; S. Gou; *J. Inorg. Biochem.*, **2016**, *157*, 1-7
4. M. Benedetti; F. De Castro; A. Romano; D. Migoni; B. Piccinni; T. Verri; M. Lelli; N. Roveri; F.P. Fanizzi; *J. Inorg. Biochem.*, **2016**, *157*, 73-79
5. B. Mavroidi; M. Sagnou; K. Stamatakis; M. Paravatou-Petsotas; M. Pelecanou; C. Methenitis; *Inorg. Chim. Acta*, **2016**, *444*, 63-75
6. L. Kelland; *Nature Reviews Cancer*, **2007**, *7*, 573-584
7. J. Chen; K. Li; S. Swavey; K.M. Church; *Inorg. Chim. Acta*, **2016**, *444*, 76-80
8. M. Gaber; H.A. El-Ghamry; S.K. Fathalla; *Spectrochim. Acta, Part A*, **2015**, *139*, 396-404
9. E.O. Gulumsek; E.E. Baykal; C. Kucukpolat; E. Onal; P. Balcik-Ercin; T. Yagci; V. Ahsen; A.G. Gurek; *J. Coord. Chem.*, **2022**, *75(1-2)*, 197-210
10. A.R. Timerbaev; C.G. Hartinger; S.S. Aleksenko; B.K. Keppler; *Chem. Rev.*, **2006**, *106*, 2224-2248
11. N.T. Zanvettor; D.H. Nakahata; R.E.F. de Paiva; M.A. Ribeiro; A. Cuin; P.P. Corbi; A.L.B. Formiga; *Inorg. Chim. Acta*, **2016**, *443*, 304-315
12. W. Saenger; P. Orth; C. Kisker; W. Hillen; W. Hinrichs; *Angew. Chem. Int. Ed. Engl.*, **2000**, *39*, 2042-2052
13. B.S. Speer; N.B. Shoemaker; A.A. Salyers; *Clinical Microbiol. Rev.*, **1992**, *5*, 387-399
14. W. Guerra; I.R. Silva; E.A. Azevedo; A.R. de S. Monteiro; M. Bucciarelli-Rodriguez; E. Chartone-Souza; J.N. Silveira; A.P.S. Fontes; E.C. Pereira-Maia; *J. Braz. Chem. Soc.*, **2006**, *17*, 1627-1633
15. C. Shiju; D. Arish; N. Bhuvanesh; S. Kumaresan; *Spectrochim. Acta, Part A*, **2015**, *145*, 213-222
16. F.U. Rahman; A. Ali; I. Khan; R. Guo; L. Chen; H. Wang; Z.T. Li; Y. Lin; D.W. Zhang; *Polyhedron*, **2015**, *100*, 264-270

17. A.M. Mansour; N.T. Abdel-Ghani; *Inorg. Chimica Acta*, **2015**, 438, 76-84
18. N.T. Abdel-Ghani; A.M. Mansour; *J. Mol. Struct.*, **2011**, 991, 108-126
19. S.J. Sabounchei; P. Shahriary; S. Salehzadeh; Y. Gholiee; A. Chehregani; *Comptes Rendus Chimie*, **2015**, 18, 564-572
20. S.J. Sabounchei; P. Shahriary; S. Salehzadeh; Y. Gholiee; D. Nematollahi; A. Chehregani; A. Amani; Z. Afsartala; *Spectrochim. Acta, Part A*, **2015**, 135, 1019-1031
21. J.N. Demas; B.A. DeGraff; *Coord. Chem. Rev.*, **2001**, 211, 317-351
22. P. Deveci; B. Taner; Z. Kilic; A. O. Solak; U. Arslan; E. Ozcan; *Polyhedron*, **2011**, 30, 1726-1731
23. M.Z. Shafikov; A.F. Suleymanova; R.J. Kutta; F. Brandl; A. Gorski; R. Czerwiec; *J. Mater. Chem. C*, **2021**, 9, 5808-5818
24. H.Y. Ku; B. Tong; Y. Chi; Y. Chi; C.C. Yeh; C.H. Chang; G.H. Lee; *Dalton Transactions*, **2015**, 44(18), 8552-8563
25. P.B. Kettler; *Org. Proc. Res. Develop.*, **2003**, 7, 342-354
26. J.M. Gichumbi. H.B. Friedrich; *J. Organomet. Chem.*, **2018**, 866, 123-143
27. A.M. Mansour; *J. Thermal Anal. Calorim.*, **2016**, 123, 571-581
28. M.H. Soliman; A.M.M. Hindy. G.G. Mohamed; *J. Thermal Anal. Calorim.*, **2014**, 115, 987-1001
29. E.M. Zayed; M.A. Zayed; A.M.M. Hindy; *J. Thermal Anal. Calorim.*, **2014**, 116, 391-400
30. S. Arora; D. K. Aneja; M. Kumar; C. Sharma; O. Prakash; *J. Thermal Anal. Calorim.*, **2013**, 111, 17-25.
31. D. Giron; *J. Thermal Anal. Calorimetry*, **2001**, 64, 37-60
32. C. Schmidt; N. Senfter; U. J. Griesser; *J. Thermal Anal. Calorimetry*, **2003**, 73, 397-408
33. M.I. Noordin; L.Y. Chung; *J. Thermal Anal. Calorimetry*, **2009**, 95, 891-894
34. B. Holló; J. Magyari; V. Živković-Radovanović; G. Vučković; Z. D. Tomić; I. M. Szilágyi; G. Pokol; K. Mészáros-Szécsényi; *Polyhedron*, **2014**, 80, 142-150
35. D. Giron; C. Goldbronn; *J. Thermal Anal. Calorimetry*, **1995**, 47, 217-251
36. V. Todeschini; P.R. de Oliveira; L.S. Bernardi; R.L. Pereira; C.E.M. de Campos; M.A.S. Silva; N.M. Volpato; *J. Thermal Anal. Calorimetry*, **2014**, 115, 2295-2301
37. K. Nakamoto; *Infrared and Raman spectra of inorganic and coordination compounds*, Part B, 5th Ed. J. Wiley, New York, **1997**
38. J.T. Watson; *Introduction to Mass Spectrometry*, Ed. Racon, New York, **1985**
39. L. Mázor; *Analitikai zsebkönyv*, Műszaki könyvkiadó. Budapest, **1971**, pp. 394
40. R. Barabás; N.I. Farkas; Cs. L. Nagy; O. Cadar; C. Moisa; L. Bizo; *Ceramics International*, **2021**, 47 (6), 8584-8592

SYNTHESIS AND INVESTIGATIONS OF γ -L-GLUTAMYL-CYCLOHEXYL AMIDE AND ITS TRANSITION METAL COMPLEXES

Carmen SACALIS^{a,*}, Sara JAHJI^b, Alexandra AVRAM^a

ABSTRACT. A new route to obtain by regioselective acylation of cyclohexyl amine using N-phthaloyl-L-glutamic anhydride, followed by hydrolysis of phthaloyl group with hydrazine hydrate was performed in order to prepare γ -L-glutamyl-cyclohexyl amide. This one was used as ligand for a novel series of metal transition complexation like Cu(II), Co(II) and Ni(II). The ligand and its metal complexes were characterized *via* their spectral and thermogravimetric analysis. The thermal stability of the compounds was discussed in the 20-800°C temperature range. In all these complexes, the γ -L-glutamyl amide act as a bidentate ligand with coordination involving the carboxylate group and the nitrogen atom belonging to the amino group of glutamic acid fragment. The results indicate that their stability range obeys the Irving-Williams series.

Keywords: *L-glutamic acid, glutamyl amides, metal complexes, thermal behavior*

INTRODUCTION

L-Glutamic acid is one of the most important amino acid, presents as a key intermediate in the biosynthesis of other amino acids by as transamination process, as a flavor-enhancing component for food, as an excitatory neurotransmitter in the vertebrate nervous system and so on. Diagnosis of some pancreatic and liver diseases are based on determination of enzymatic activity of γ -glutamyl transpeptidase (GGT) [1].

^a Babeş-Bolyai University, Faculty of Chemistry and Chemical Engineering, 11 Arany Janos str., RO-400028, Cluj-Napoca, Romania.

^b University of Tetova, Faculty of Natural Sciences and Mathematics, Bldv.Illinden, nn, 1200 Tetova, Republic of North Macedonia.

* Corresponding author: carmen.sacalis@ubbcluj.ro.



Starting from these results, other glutamyl amides were tested for this purpose with satisfactory results [2,3]. Other glutamyl derivatives were tested as substrate for γ -Glutamylamine cyclotransferase (gGACT) or glutamate carboxypeptidase II (GCPII) [4,5].

Recently, novel lanthanide coordination compounds like Tb(III) and Eu(III) based on amino acid derivative ligands such as N-benzamido-L-Glutamic acid which exhibits fluorescent properties were synthesized [6]. The amino acids derivatives have both amino and carboxyl functional groups, which exhibit excellent coordination capabilities [7,8]. L-Glutamyl amide derivatives were also tested as a low-molecular weight organogelator and showed thixotropic property [9]. Different peptides containing glutamyl rest complexations with metal such as Zn(II) or Cu(II) showed antimicrobial activity [10]. Recently, the results of a spectrophotometric research of the complexation of Mg(II) with L-Glutamic acid can be used in studies of biomineralization process in human body, as well in the creation of medications intended for targeted exposure [11].

A theoretical study provides the amino acids including L-Glutamic acid or L-Glutamine and its derivatives as a chelating agent to remove metals cations such as Cd^{2+} , Cu^{2+} , Fe^{3+} , Hg^{2+} , Mn^{2+} , Ni^{2+} , and Zn^{2+} . The removal methods can reduce the heavy metal pollution in water and soil environments [12].

Taking into account the important biochemical application of L-Glutamic acid and its derivatives, including its metal complexes, this paper presents a new route for the synthesis of the γ -L-Cyclohexyl glutamyl amide, analog to the synthesis of other γ -L-Glutamyl amides that we have reported [13]. This one we have used as a ligand for complexations with some transition metal ions like Cu(II), Co(II) and Ni(II). All these compounds were analyzed by spectral and thermal investigations. The literature mentioned synthesis of this ligand from *N*-(Benzyloxycarbonyl)-L-Glutamic acid, Benzyl bromide, Dicyclohexylamine and Cyclohexylamine to another route with a 50% yield in the last step. After recrystallization from 50% hot ethanol/water mixture overall yield was 27% [4,15]. We obtained the ligand with 62% yield in the last step *via* a mild phthaloylation. The new synthesis method of the ligand (**4**) is more advantageous, as because after purifications, the overall yield increased to 41%.

RESULTS AND DISCUSSION

The ligand synthesis

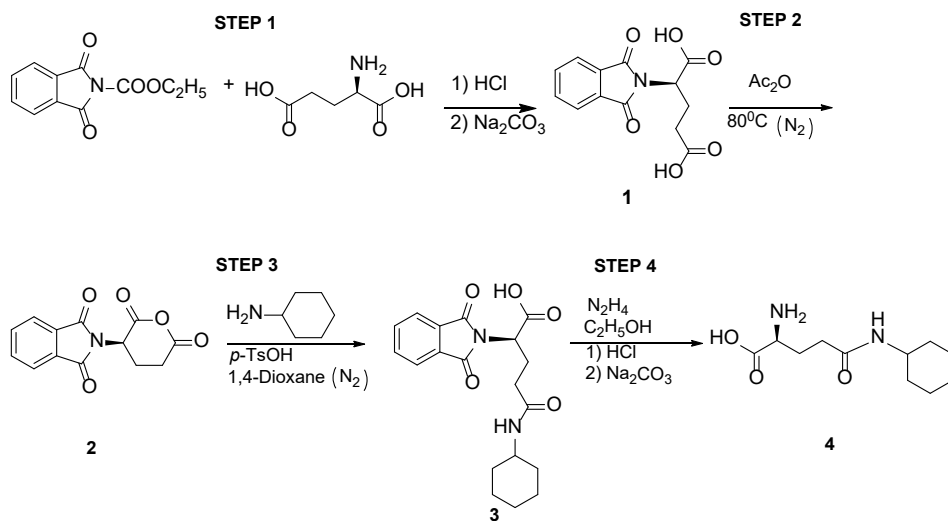
The ligand (**4**) γ -L-Cyclohexyl glutamyl amide, namely (*S*)-2-amino-5-(Cyclohexylamino)-5-oxopentanoic acid, was obtained in four steps, analog to the peptide synthesis, under mild conditions.

SYNTHESIS AND INVESTIGATIONS OF γ -L-GLUTAMYL-CYCLOHEXYL AMIDE
AND ITS TRANSITION METAL COMPLEXES

A convenient method for the preparation of the γ -L-Glutamyl amides consists of the use of the phthaloyl rest as an amino protective group in the first synthesis step (Scheme 1). In our previous research, we identified *N*-ethoxycarbonylphthalimide as an easy-to-use reagent, with good yields, in the protection stage [13,14]. Our investigation has shown that, when *N*-protected amino acid (**1**) is treated with acetic anhydride by heating, under nitrogen atmosphere, the Phthaloyl-L-glutamic anhydride (**2**) was obtained as an activation form for the carboxylic group, in the second synthesis step.

The third step consists of a condensation of the *N*-protected anhydride (**2**) with Cyclohexylamine, under inert atmosphere (nitrogen), in 1,4 -Dioxan and *p*-Toluenesulphonic acid as catalysator, to obtain the *N*-protected L-Glutamic amide. The first three steps were monitored by TLC in ethanol:acetone = 3:1 (v/v) (visualization in UV at $\lambda=245$ nm).

After this, in the last step, we have easily removed the phthaloyl group with hydrazine hydrate 100% in ethanol under reflux. The free amide (**4**) was obtained at the pH 6-6.5 as a white solid. The process was monitored by TLC in 1-propanol:acetic acid:water = 8:1:1 and visualisation in ninhydrin or I_2 vapor. The *N*-Cyclohexyl-L-glutamine (**4**) was characterized by NMR and HRMS to confirm its structure.



Scheme 1. Synthesis of γ -L-Cyclohexyl glutamyl amide (**4**) by phthaloylation method

The identity of the ligand was confirmed by routine analysis such as $^1\text{H-NMR}$, $^{13}\text{C-NMR}$ and HRMS spectra (Figure 1a-b). All the complexes are paramagnetic, therefore the NMR spectra of them could not be recorded. The NMR spectra for the compound (**4**) were recorded in Acetic acid- d_4 , at 600 MHz. The multisignals within 1.29-1.51 ppm range are assigned to five

protons of the cyclohexyl rest. The overlapped signals within 1.72-2.01 ppm are assigned to the other five protons belonging to the cyclohexyl rest. The signals at 2.40 ppm were assigned to protons H₃, at 2.71 ppm to protons H₄, at 3.79 ppm a triplet to proton H₂, at 4.23 ppm to proton H₆. In the ¹³C-NMR spectra, both the presence of the signals of the compound and of the solvent can be identified, sometimes, as overlapping's (see Experimental Section). HRMS spectrum (ESI) of γ -L-Cyclohexyl glutamyl amide (**4**) confirm the presence of the [M+1] peak, as a molecular peak, at 229.1557 value.

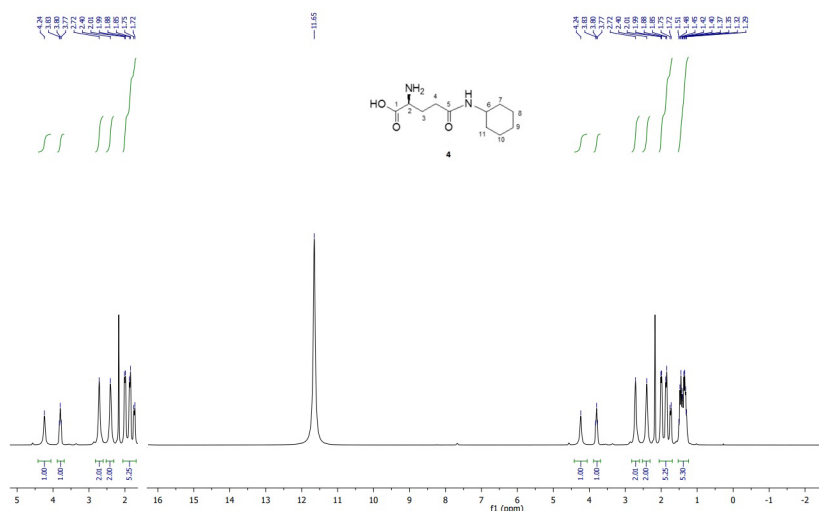


Figure 1a. ¹H-NMR spectrum of γ -L-Cyclohexyl glutamyl amide (**4**)

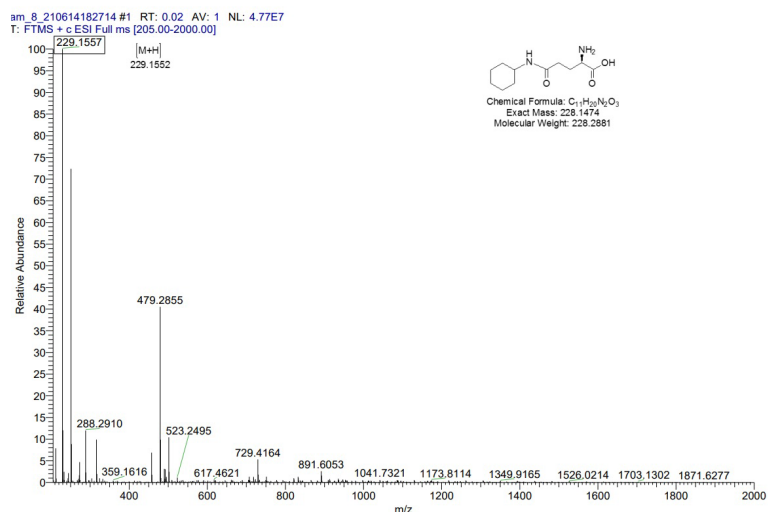


Figure 1b. HRMS spectrum (ESI) of γ -L-Cyclohexyl glutamyl amide (**4**)

The structure of the metal complexes

In continuation of our effort in a similar direction, new coordination compounds of γ -L-Cyclohexyl glutamyl amide (**4**) as ligand with 3d transition metal ions such as Cu(II), Co(II) and Ni(II) were synthesized by a standard procedure, like other metal complexes, with various amino acid derivatives [16-19]. The complexation reaction of metal salts occurs in mild conditions and, in each case, yields a solid-colored product. Higher melting points of these products compared of the ligand (**4**) indicate the formation of metal complexes (see Experimental Section). Their elemental analysis data is in good agreement with the molar ratio Metal:Ligand=1:2, that indicate the glutamyl amide acts as a bidentate ligand, its coordination involving the carboxyl group and the nitrogen atom belonging to the amino group of the glutamic acid fragment [20,21]. In exchange, the elemental analysis data indicate also that the ligand is anhydrous, the copper complex is hydrated with one molecule of water within the sphere of coordination, but de nickel and cobalt complexes are hydrated with three molecules of water: one outside and two inside the sphere of coordination, fact proven by thermal analysis data too.

On the other hand, the HRMS spectrum for the metal complexes proves the complexation process (Figure 2a-c). The [M+1] peak supports the complexation idea with the metal ions, for each of them.

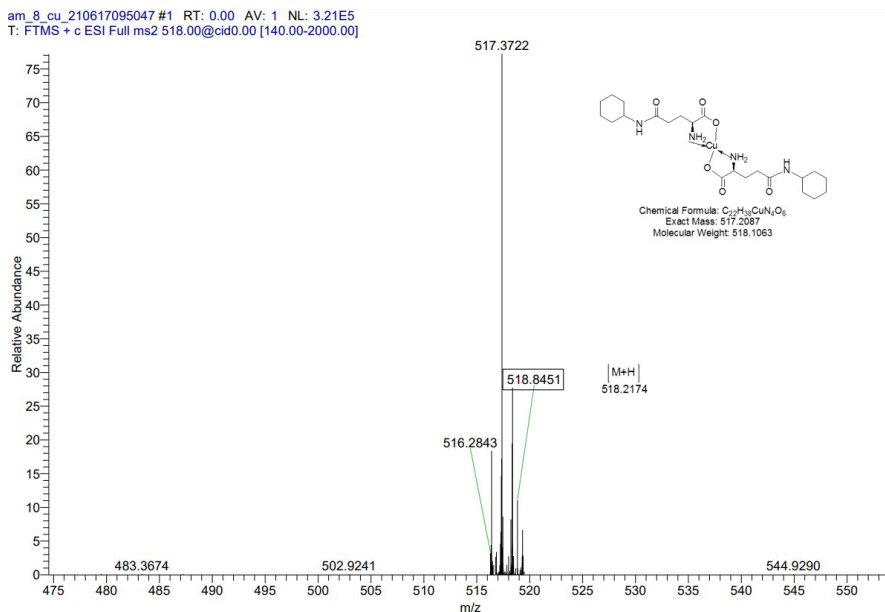


Figure 2a. HRMS spectrum (ESI) of copper complex (**5**)

am_8_co_210617092117 #1 RT: 0.01 AV: 1 NL: 1.50E6
T: FTMS + c ESI Full ms2 513.00@cid0.00 [140.00-2000.00]

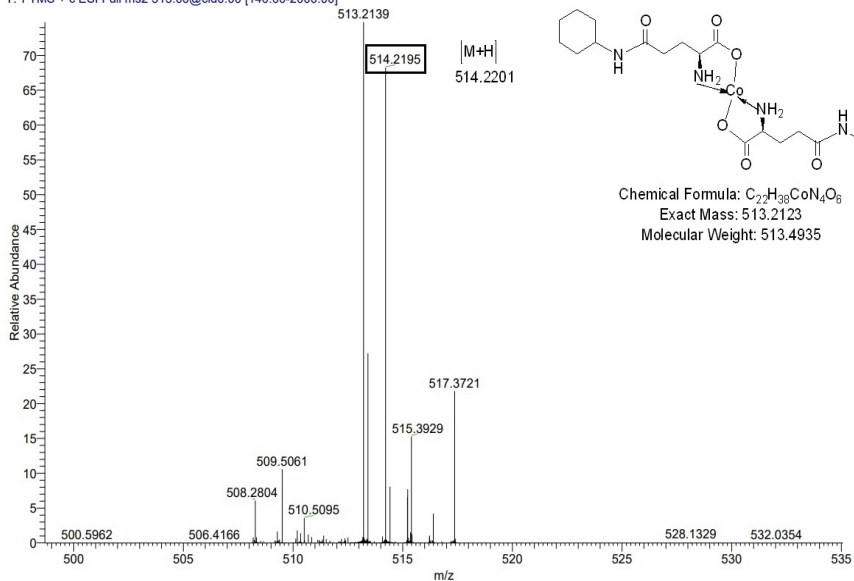


Figure 2b. HRMS spectrum (ESI) of cobalt complex (6)

am_8_ni_210617092117 #1 RT: 0.00 AV: 1 NL: 2.31E6
T: FTMS + c ESI Full ms [100.00-2000.00]

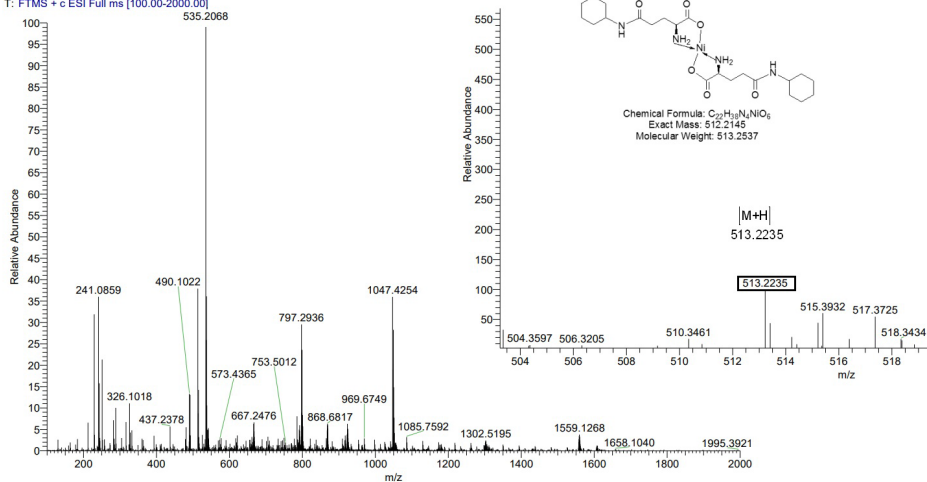


Figure 2c. HRMS spectrum (ESI) of nickel complex (7)

Thermal investigation

The thermal decomposition of the ligand (**4**) and its transition metal complexes was investigated by means of a derivatograph in air atmosphere, in the temperature range of 20-800°C. Thermal stability domains, decomposition phenomena and their assignments are summarized in Table 1 and Figure 3a-d.

For the ligand (**4**) in the temperature range of 20-200°C two small endothermic peaks at 30°C and 100°C with a mass loss of 0.31%, respectively 0.91%, could be assigned to the loss of residual water present in the pores. This phenomenon could be explained by the general synthesis of the ligand from aqueous solution, but the thermogravimetric analysis indicated that the ligand (**4**) is anhydrous. Between 200-400°C, a strong exothermic peak at 220°C correspond to the melting, cleavage of the organic rest $-C_2H_4NO_2$, provided from the amino acid accompanied by oxidation process. This violent burning process of organic rest is generally specific to compounds with a high nitrogen and oxygen content [22].

Another exo peak at 270°C, probably correspond to the split of the $>C_3H_4O$ rest from the amidic bond. Finally, in the domain of 400-800°C an exothermic peak at 523°C indicate the slowly pyrolysis of cyclohexyl rest. As we can see in the Figure 3a, the organic compound is completely pyrolyzed until 586°C, finally some ash remaining in the crucible.

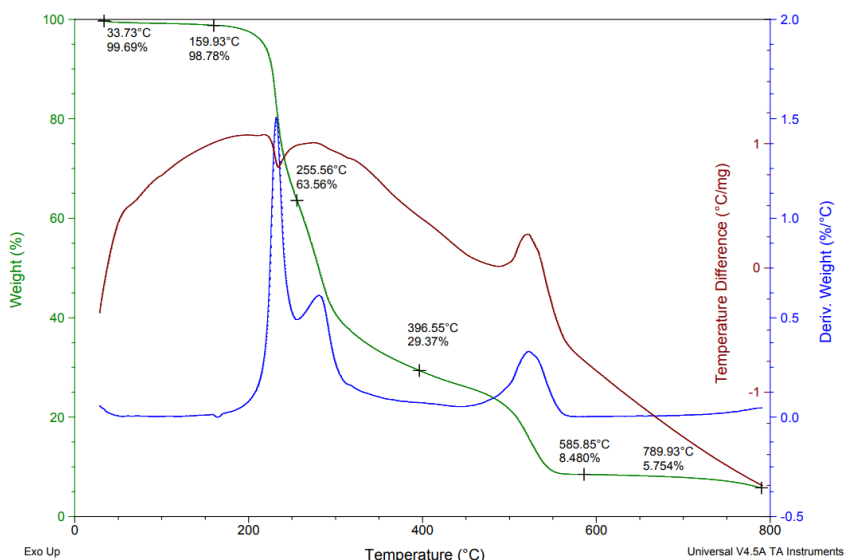


Figure 3a. TG-DTG-DTA diagram for the ligand (**4**)

The aim of the thermal analysis of the metal complexes is to obtain information concerning their thermal stability of them and to decide whether the water molecules are inside or outside the coordination sphere.

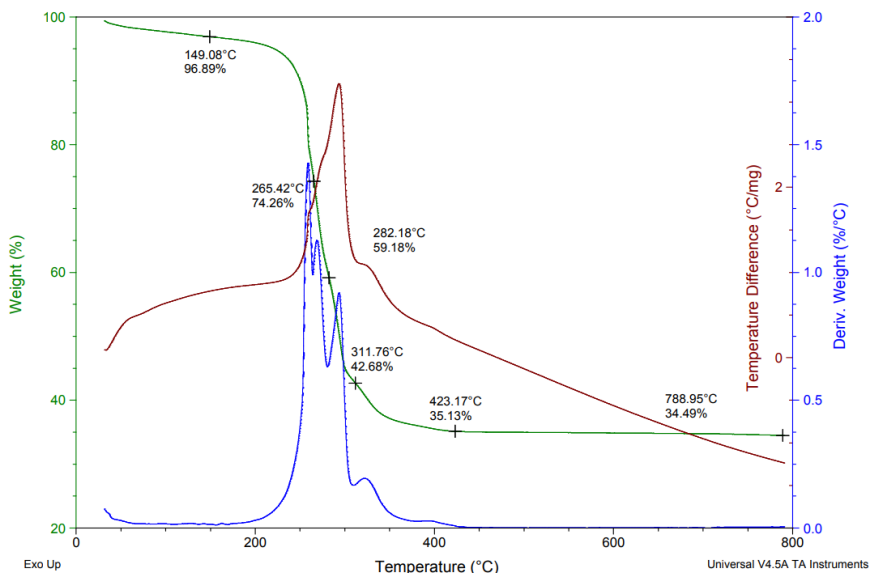


Figure 3b. TG-DTG-DTA diagram for the copper complex (**5**)

For the copper complex (**5**), the first step of the decomposes process starts with an endo peak at 100°C and a mass loss of 3.11% (calcd. 3.36%) corresponding to the loss of one molecule of water, fact that indicated it belongs to the inside of coordination sphere of copper complex. In the temperature range of 200-400°C, one endo peak at 275°C and two exo peaks at 260°C, respectively at 294°C were assigned to the simultaneous process of melting process accompanied by organic rest fragmentations. The experimental value of 54.21% and calculated data of 55.23% are similar. The last temperature domain presents an exo peak at 326°C corresponding to the pyrolysis of organic rests. The recorded mass loss of 42.68% is in good agreement to the calculated data (41.41%). Finally, the copper oxide and ash remain in the crucible.

For the cobalt complex (**6**) the first stage decomposition starts with an endothermic peak 80°C which corresponds to the loss of one molecule of water located outside the coordination sphere and some residual water present in the metal complex pores (experim. 4.37%, calcd. 3.18%). Another endo peak at 142°C indicate the loss of two molecules of water located inside the coordination sphere. In the domain 200-400°C two strong exothermic

SYNTHESIS AND INVESTIGATIONS OF γ -L-GLUTAMYL-CYCLOHEXYL AMIDE
AND ITS TRANSITION METAL COMPLEXES

effect marks by two sharp peaks at 266^oC, respectively at 300^oC, were assigned to the total pyrolysis of the organic fragments. The cobalt complex (**6**) is completely decomposed at 311^oC, in the crucible remain ash and metal oxide.

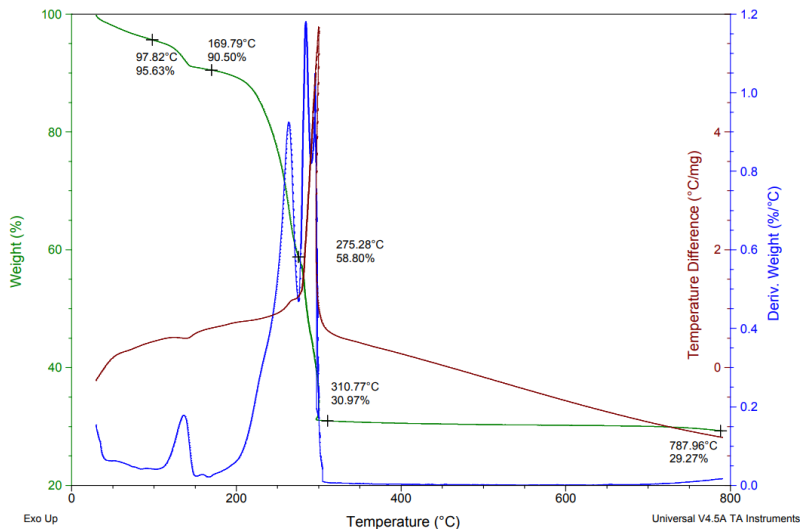


Figure 3c. TG-DTG-DTA diagram for the cobalt complex (**6**)

The thermal investigation of the nickel metal complex (**7**) behaves similarly to the copper and cobalt studied compounds.

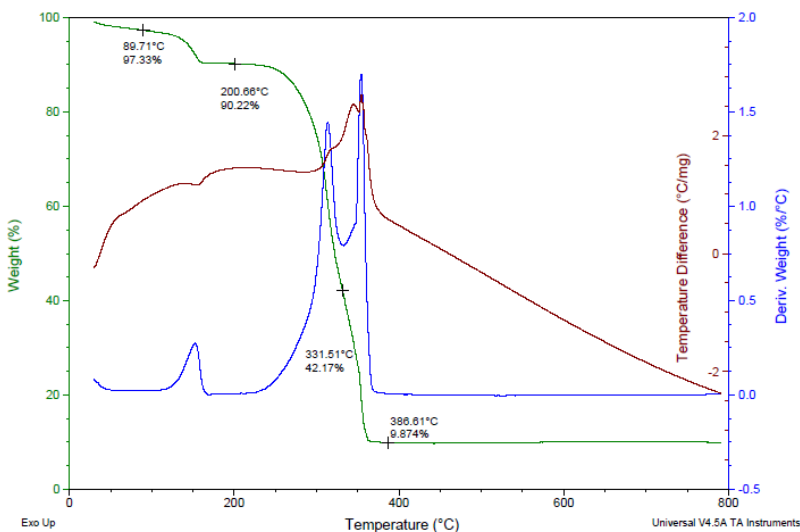


Figure 3d. TG-DTG-DTA diagram for the nickel complex (**7**)

Table 1. Thermal analysis data of the ligand (4) and its metal complexes (5-7)

Compound	Temperature range (°C)	DTA peak(°C)		Mass loss TG(%)		Assignment
		ENDO	EXO	Calcd.	Experim.	
C₁₁H₂₀N₂O₃ L or (4)	20-200 20-34 34-160	30 100	- -	- -	0.31 0.91	-residual water present inside pores
	200-400 160-256	-	220	32.44	35.22	-melting, cleavage the -C ₂ H ₄ NO ₂ rest, oxidation process
	256-397	-	270	36.35	34.19	-cleavage the >C ₃ H ₄ O rest
	400-800 397-790	- -	523 -	31.21 -	23.62 5.75	-pyrolysis of organic rest
C₂₂H₄₀CuN₄O₇ [Cu(L)₂•H₂O] or (5)	20-200 20-149	100	-	3.36	3.11	-1 molecule of hydrating water
	200-400 149-282	275	260	37.82	37.71	-melting, quickly cleavage of 2-C ₆ H ₅ NH- rest
	282-312	-	294	17.41	16.50	-loss of 2 -CO- rest from the amidic bond
	200-400 312-423	-	326	41.41	7.54	-quickly pyrolysis of organic rest
	400-800 423-788		-	-	0.65 34.49	CuO and ash
C₂₂H₄₄CoN₄O₉ [Co(L)₂•(H₂O)₂]•H₂O or (6)	20-200 20-98	80	-	3.18	4.37	-1 molecule water outside coordination sphere and residual water inside pores
	98-170	142	-	6.56	5.13	-2 molecules of water inside coordination sphere
	200-400 140-275	-	266	38.25	31.70	-quickly cleavage of 2-C ₆ H ₅ NH- rest

SYNTHESIS AND INVESTIGATIONS OF γ -L-GLUTAMYL-CYCLOHEXYL AMIDE
AND ITS TRANSITION METAL COMPLEXES

Compound	Temperature range ($^{\circ}\text{C}$)	DTA peak($^{\circ}\text{C}$)		Mass loss TG(%)		Assignment
		ENDO	EXO	Calcd.	Experim.	
	275-311	-	300	23.37	27.83	-pyrolysis of organic rest and oxidation process
	400-800 311-788			28.64	1.7 29.27	CoO and ash
$\text{C}_{22}\text{H}_{44}\text{N}_4\text{NiO}_9$ $[\text{Ni}(\text{L})_2 \cdot (\text{H}_2\text{O})_2] \cdot \text{H}_2\text{O}$ or (7)	20-200 20-90	80	-	3.17	2.68	-1molecule of hydrating water
	90-200	156	-	6.56	7.10	-2 molecules of water inside coordination sphere
	200-400 200-331	-	316	49.16	48.02	-loss of 2 - $\text{C}_6\text{H}_5\text{NHCO}$ - rest
	331-386	-	354	29.52	32.33	-pyrolysis of organic rest and oxidation process
	400-800	-	-	11.59	9.87	NiO and ash

First, the nickel complex (7) loses at 80°C one molecule of hydrating water and humidity, marked by a small endo peak and a loss of 2.68% (calcd. 3.17%). An endo peak slightly more intense at 156°C and a mass loss of 7.10% (calcd. 6.56%), was assigned to the loss of two water molecules inside the coordination sphere of the metal complex.

Obviously, the next two strongly exothermic peaks at 316°C , respectively at 354°C , correspond to the total pyrolysis of the metal complex. Finally, only ash and metal oxide remain in the crucible.

A comparison between the thermal behavior of the free ligand and of the metal complexes reveals that the melting point of the free ligand is lower than those of its complexation products (see Table 1). This phenomenon proves that the thermal stability is increased by the formation of coordination compounds with M-N and M-O bonds.

On the other hand, the copper complex is completely pyrolyzed at 423°C , followed by the nickel complex at 387°C and the cobalt complex at 311°C , which would be in good agreement to the relative stabilities of complexes formed by transition metals ions predicted by H. Irving and R. Williams [23].

CONCLUSIONS

The γ -L-Cyclohexyl glutamyl amide (**4**) has been alluded to the literature but not by *via* a mild phthaloylation [4]. For this purpose, the amide bond formation protocol was used, from the peptide synthesis starting from an *N*-terminal amino acid. The overall yield beginning from L-Glutamic acid increased to 41% under this route compared to synthesis started from *N*-(Benzyloxycarbonyl)-L-Glutamic acid (overall yield 27% [4]). The identity of the compound was confirmed by elemental and spectral analysis, and this one was used as a ligand in metal transition complexation like Cu(II), Co(II) and Ni(II).

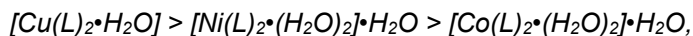
The new metal complexes (**5-7**) were analyzed by elemental, spectral and thermogravimetric studies. Mass spectra indicated the $[M+1]$ peak corresponding for each of investigated compounds (**4-7**).

Elemental and thermal analysis lead to the idea that all the transition metal complexes are hydrating with molecules of water inside coordination sphere. As expected, the organic compound acts as a bidentate ligand, its coordination involving the carboxylate oxygen and the nitrogen atom belonging to the free amino group of the L-Glutamic acid rest.

During heating in air atmosphere in the 20-800°C temperature range, both the ligand and its metal complexes, decompose in multistage, some of stage are weakly separated one from another. The final products of pyrolysis are ash for the ligand or ash and metal oxide from the metal complexes.

The results are in good agreement with the corresponding formulae: $C_{11}H_{20}N_2O_3$ (**4**), $[Cu(C_{11}H_{19}N_2O_3)_2 \cdot H_2O]$ (**5**), $[Co(C_{11}H_{19}N_2O_3)_2 \cdot 2H_2O] \cdot H_2O$ (**6**), and $[Ni(C_{11}H_{19}N_2O_3)_2 \cdot 2H_2O] \cdot H_2O$ (**7**) respectively.

The copper complex (**5**) is completely pyrolyzed at 423°C, the nickel complex (**7**) at 387°C and the cobalt complex (**6**) at 311°C. The thermal behaviors of the synthesized metal complexes indicated that their stability sequence:



conforms with the Irving-Williams series [16, 23].

The obtained data allows us to propose the following structural formulas for the studied metal complexes (Figure 4).

SYNTHESIS AND INVESTIGATIONS OF γ -L-GLUTAMYL-CYCLOHEXYL AMIDE
AND ITS TRANSITION METAL COMPLEXES

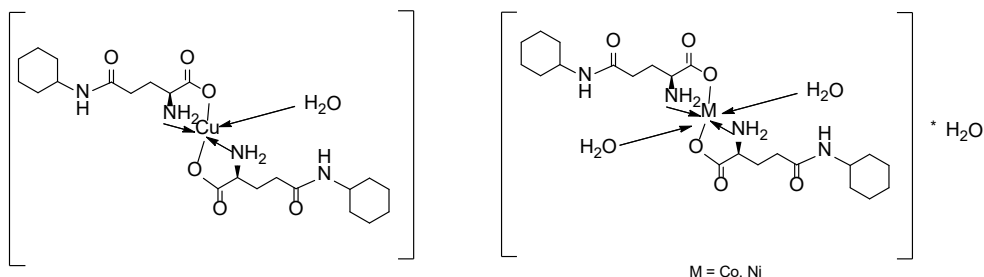


Figure 4. Suggested structure for the metal complexes

EXPERIMENTAL SECTION

Materials and instrumentation

All reagents and chemicals were purchased from commercial sources and used as received. TLC monitoring was performed by using aluminum sheets with silica gel 60 F₂₅₄ (Merck® (visualization in UV at $\lambda=254$ nm; I₂ bath or ninhydrin). NMR spectra were recorded on Bruker® AM 600 instruments operating at 600 and 150 MHz for ¹H and ¹³C nuclei, respectively. All chemical shifts (δ value) are given in ppm without TMS added. The chemical shifts were measured against the solvent residual peak. Elemental analyses were determined on Thermo Scientific Flash EA 1112 Elemental Analyzer. Melting points were measured on an ELECTROTHERMAL® instrument and were not corrected. Mass spectra were carried out on a LTQ ORBITRAP® XL (Thermo Scientific) instrument which was externally calibrated using the manufacturer's APCI or ESI(+) calibration mix. The samples were introduced into the spectrometer by direct infusion.

Thermogravimetry and differential thermal analysis (TG-DTG-DTA) curves were recorded with a Thermal Analyzer TA Instruments SDT Q600 V20.9 Build 20 on an interval of 20-800°C, at a heating rate of 10°C/min, in alumina crucibles and a dynamic air atmosphere.

Synthesis of the ligand γ -L-Cyclohexyl glutamyl amide (4) and its metal complexes (5-7)

The ligand (4) was obtained by a literature procedure and investigated by spectroscopic and thermal methods [11,12].

Cu(II), Co(II) and Ni(II) complexes of the ligand (**4**) were prepared by following a general method. The metal salt [$\text{CuSO}_4 \cdot 5\text{H}_2\text{O}$, $\text{CoSO}_4 \cdot 7\text{H}_2\text{O}$ $\text{NiSO}_4 \cdot 7\text{H}_2\text{O}$] (1.25mmol) was dissolved in 8 mL distilled water. The ligand (**4**) (2mmol) was solved in a solution of Na_2CO_3 1M until pH =11. To a solution of ligand was added slowly, dropwise during 30 min, a solution of the metal salt, at room temperature. The mixture was let to stir at the room temperature overnight. By adding a solution of metal ions to a solution of ligand, immediate color change was observed depending on the metal ion. Also, the final pH change to 7.5-8.0 for all the compounds. The isolated solid complexes were obtained by vacuum filtration, washed with distilled water and finally dried in a vacuum desiccator for 48h. The dried complexes were subjected to elemental, spectroscopic and thermal analysis.

$\text{C}_{13}\text{H}_{11}\text{NO}_6$ (**1**), White solid; MW = 277.2295; Yield 89%, mp = 158-160°C (Lit. [14]160°C); TLC analysis yielded a single spot ($R_f = 0.49$) (ethanol:acetone = 3 :1 (v/v) (visualization in UV at $\lambda=245$ nm); Elemental Analysis (%) Calcd.(Found) C: 56.32(56.18), H: 4.00(4.19), N: 5.05(5.38); $^1\text{H-NMR}$ (DMSO, 600MHz, δ (ppm)): 12.03 (1H, from COOH group); 7.25-7.92 (overlapped signals, 4H from aromatic rest); 5.31 (1H, s, NH); 2.71 (2H, m); 2.32 (2H, t); $^{13}\text{C-NMR}$ (DMSO, 150MHz, δ (ppm)): 180.5; 177.1; 158.9; 137.2; 129.5; 117.8; 56.5; 41.4; 32.3

$\text{C}_{13}\text{H}_9\text{NO}_5$ (**2**), White solid; MW = 259.2143; Yield 93%, mp = 198-200°C; (Lit. [14]199-201°C); TLC analysis yielded a single spot ($R_f = 0.53$) (ethanol:acetone = 3 :1 (v/v) (visualization in UV at $\lambda=245$ nm); Elemental Analysis (%) Calcd.(Found) C: 60.24(60.13), H: 3.50(3.78), N: 5.40(5.82); $^1\text{H-NMR}$ (DMSO, 600MHz, δ (ppm)): 7.99-7.81 (4H, m); 3.41 (2H, t); 3.17(1H, t); 2.96 (2H, m); $^{13}\text{C-NMR}$ (DMSO, 150MHz, δ (ppm)): 167.2; 166.8; 135.3; 131.6; 123.9; 48.1; 29.9; 20.8

$\text{C}_{19}\text{H}_{22}\text{N}_2\text{O}_5$ (**3**), Beige solid; MW = 358.3884; Yield: 79%; mp = 172-174°C; TLC analysis yielded a single spot ($R_f = 0.76$) (ethanol:acetone = 3 :1 (v/v) (visualization in UV at $\lambda=245$ nm); Elemental Analysis (%) Calcd.(Found) C: 63.67(63.81), H: 6.19(6.77), N: 7.82(8.01); $^1\text{H-NMR}$ (Acetic acid-d4 600MHz, δ (ppm)): 8.11 (1H,NH); 7.78-7.57 (4H, m); 3.81 (1H, t); 2.16 (1H, s); 1.90 (2H t); 1.57-1.43 (2H, q), 1.38-1.27 (2H, q); $^{13}\text{C-NMR}$ (Acetic acid-d4, 150MHz, δ (ppm)): 175.1; 158.3; 142.8; 53.4; 38.5; 29.6; 23.2

$\text{C}_{11}\text{H}_{20}\text{N}_2\text{O}_3$ (**4**) White solid; MW = 228.2881; Yield: 62% (Overall yield 41%); mp. = 219-221°C (Lit. [4] 220-222°C); TLC analysis yielded a single spot ($R_f = 0.53$) (1-propanole:acetic acid:water = 8:1:1 (v/v) visualization

with ninhydrin); Elemental Analysis (%) Calcd.(Found) C: 57.87(57.13), H: 8.83(8.11), N: 12.27(11.93); MS (ESI, CH₃OH) [M+1]: 229.1552; Exact Mass: 228.1474; ¹H-NMR (Acetic acid-d₄, 600MHz, δ (ppm)): 4.23 (s, 1H, H₆). 3.79 (t, J=8.2Hz, 1H, H₂); 2.71 (s, 2H, H₄); 2.40 (s, 2H, H₃); 1.72-2.01 (overlapped signals, 5H from cyclohexyl rest); 1.29-1.51 (m, 5H from cyclohexyl rest); ¹³C-NMR (Acetic acid-d₄, 150MHz, δ (ppm)): C₁ overlapped with solvent (178.9) C₅ (175.1). C₆ (50.7); C₂ (33.9); C₇, C₁₁ (33.8); C₄ (33.5); C₃ (27.7); C₈, C₁₀ (26.9); C₉ (26.3). Thermal Analysis: 30°C (Endo) (TG_{exp.} = 0.31%); 100°C (Endo) (TG_{exp.} = 0.91%); 220°C (Exo) (TG_{calcd.} = 32.44%, TG_{exp.} = 35.22%); 270°C (Exo) (TG_{calcd.} = 36.35%, TG_{exp.} = 34.19%); 523°C (Exo) (TG_{calcd.} = 31.21%, TG_{exp.} = 29.37%).

C₂₂H₄₀CuN₄O₇ (**5**) Dark-blue solid; MW = 536.1216; Yield: 87%; mp. = 282-284°C (desc.); Elemental Analysis (%) Calcd.(Found) C: 49.29(48.17), H: 7.52(7.16), N: 10.45(10.82); MS (ESI, CH₃OH, without coordination water) [M+1]: 518.8451, Exact Mass: 517.2087; Thermal Analysis: 100°C (Endo) (TG_{calcd.} = 3.36%, TG_{exp.} = 3.11%); 260°C (Exo) (TG_{calcd.} = 37.82%, TG_{exp.} = 37.71%); 275°C (Endo) and 294°C (Exo) (TG_{calcd.} = 17.41%, TG_{exp.} = 16.50%); 326°C (Exo) (TG_{calcd.} = 41.41%, TG_{exp.} = 42.68%); Molar Ratio M:L:H₂O = 1:2:1.

C₂₂H₄₄CoN₄O₉ (**6**) Fuchsia solid; MW = 567.5394; Yield: 83%; mp. = 273-275°C (desc.); Elemental Analysis (%) Calcd.(Found) C: 46.56(47.03), H: 7.81(8.11), N: 9.87(10.03); MS (ESI, CH₃OH, without coordination water) [M+1]: 514.2195, Exact Mass: 513.2123; Thermal Analysis: 80°C (Endo) (TG_{calcd.} = 3.18%, TG_{exp.} = 4.37%); 142°C (Endo) (TG_{calcd.} = 6.56%, TG_{exp.} = 5.13%); 266°C (Exo) (TG_{calcd.} = 38.25%, TG_{exp.} = 31.70%); 300°C (Exo) (TG_{calcd.} = 23.37%, TG_{exp.} = 27.83%); Molar Ratio M:L:H₂O = 1:2:3.

C₂₂H₄₄N₄NiO₉ (**7**) White-greenish solid; MW = 567.2996; Yield: 72%; mp. = 293-295°C (desc.); Elemental Analysis (%) Calcd.(Found) C: 46.58(46.19), H: 7.82(7.53), N: 9.88(10.25); MS (ESI, CH₃OH, without coordination water) [M+1]: 513.2235, Exact Mass: 512.2145; Thermal Analysis: 80°C (Endo) (TG_{calcd.} = 3.17%, TG_{exp.} = 2.68%); 156°C (Endo) (TG_{calcd.} = 6.56%, TG_{exp.} = 7.10%); 316°C (Exo) (TG_{calcd.} = 49.16%, TG_{exp.} = 48.02%); 354°C (Exo) (TG_{calcd.} = 29.52%, TG_{exp.} = 32.33%); Molar Ratio M:L:H₂O = 1:2:3.

REFERENCES

1. M. Orlowski; A. Meister; *Biochim. Biophys. Acta*, **1963**, 73(4), 679-681
2. N.I. White; N. Razvi; R.M. Lawrence, M.M. Manson; *Anal. Biochem.*, **1996**, 233(1), 71-75
3. A. Menard; R. Castonguay; C. Lherbet; C. Rivard; Y. Roupioz; J.W. Keillor; *Biochemistry*, **2001**, 40, 12678-12685
4. T.E. Bowser; M.L. Trawick; *Amino Acids*, **2013**, 44, 143-150
5. M. Kriegelstein; A. Marek; *J. Label Compd. Radiopharm.*, **2022**, 65, 244-253
6. Q. Deng; K. Deng; M. Yan; Y. Shen; J. Wang; L. Ma; S. Shi; H. Song; *J. Lumi.*, **2022**, 248, 118934
7. H.H. Song; M.L. Li; *J. Solid State Chem.*, **2013**, 206, 182-191
8. H.H. Song; Q. Feng; M.J. Yan; S.K. Shi; *Inorganica Chim. Acta*, 415, 75-80
9. T. Shirosaki; S. Chowdhury; M. Takafuji; D. Alekperov; G. Popova; H. Hachisako; H. Ihara; *J. Mater. Res.*, **2006**, 21(5), 1274-1278
10. A. Miller; A. Matera-Witkiewicz; A. Mikolajczyk; J. Watly; D. Wilcox; D. Witkowska; M. Rowinska-Zyrek; *Int. J. Mol. Sci.*, **2021**, 22(13), 6971
11. I.A. Tomashevskii; O.A. Golovanova; S.V. Anisina; *Russ. J. Gen. Chem.*, **2021**, 91(12), 2621-2626
12. X. Liu; M. Wu; C. Li; P. Yu; S. Feng; Y. Li; Q. Zhang; *Molecules*, **2022**, 27, 2407
13. I. Cristea; S. Mager; C. Batiu; G. Ple; *Rev. Roum. Chim.*, **1994**, 39(12), 1435-1441
14. G.H.L. Nefkens; G.I. Tesser; R.J. Nivard; *Recl. Trav. Chim. Pays-Bas*, **1960**, 79(7), 688-698
15. A.A. Hassoni; M.L. Chen; R. Sharma; R.J. Walker; *Comp. Biochem. Physiol. C. Toxicol. Pharmacol.*, **1992**, 101(2), 409-414
16. L. Ghizdavu; C. Balan; L. David; C. Batiu; O. Cozar; D. Ristoiu; *J. Thermal. Anal. Calorim.*, **2000**, 62, 729-736
17. L. David; C. Craciun; C. Balan; O. Cozar; L. Ghizdavu; C. Batiu; *Acta Chim. Slov.*, **2001**, 48, 407-415
18. C. Batiu; C. Jelic; N. Leopold; O. Cozar; L. David; *J. Mol. Struct.*, **2005**, 744-747, 325-330
19. C. Batiu; L. Ghizdavu; L. David; O. Cozar; *Synthesis and Reactivity in Inorganic and Metal-Organic Chemistry*, **2003**, 33(8), 1391-1403
20. A. Chilwal; P. Malhotra; A. K. Narula; *J. Thermal. Anal. Calorim.*, **2013**, 114, 345-351
21. J. Wang; J.G. Wang; X.H. Li; H.P. Xiao; *Trans. Met. Chem.*, **2013**, 765-770
22. C.A. Terraza; L.H. Tagle; D. Munoz; A. Tundidor-Camba; P.A. Ortiz; D. Coll; C.M. Gonzalez-Henriquez; I.A. Jessop; *Polym. Bull.*, **2016**, 73, 1103-1117
23. H. Irving; R.J.P. Williams; *J. Chem. Soc.*, **1953**, 3192-3210

CARACTERISATION OF ORIGANUM VULGARE EXTRACTS

Sorin HODISAN^a, Ramona POP MAGHIAR^b, Alina GROZE^a,
Mariana GANEA^c, Oana STANASEL^{a*}

ABSTRACT. *Origanum vulgare* L., commonly known as oregano, is a woody, rhizomatous perennial plant. Oregano extracts are a complex mixture of different compounds, in which major constituents are terpenes (mono- and sesquiterpenes). The flavor of oregano oil is generally due to the presence of thymol and carvacrol. Carvacrol has multiple properties: antioxidant, antimicrobial, antitumor, antimutagenic, antigenotoxic, analgesic, antispasmodic, anti-inflammatory, angiogenic, antiparasitic, antiplatelet, insecticidal, antihepatotoxic and neuroprotective. The oregano extract was characterized by analyzing, the antioxidant activity, the total polyphenols content (obtaining 2.4 - 3 mg gallic acid/g), the content of phenolic acids and flavonols by HPLC chromatography, the content of carvacrol (21, 29% in essential oil and 19.78% in ethanolic extract) and thymol (2.59% in essential oil and 2.67% in alcoholic extract) by GC-MS chromatography. Oregano extracts were tested for antimicrobial activity against *Staphylococcus aureus*. The test results demonstrate the significant antimicrobial activity of these preparations.

Keywords: *Oregano vulgare*, antioxidant activity, polyphenols, HPLC, GC-MS

INTRODUCTION

Phytotherapy is the science that studies the use of plant products for therapeutic purposes. Herbs and products extracted from them are used to treat various infectious diseases in traditional medicine because of their

^a University of Oradea, Faculty of Informatics and Science, 1st Universitații str., RO-410087, Oradea, Romania

^b National College "Mihai Eminescu", 18 Roman Ciorogariu str., RO-410017, Oradea, Romania

^c University of Oradea, Faculty of Medicine and Pharmacy, Department of Pharmacy, 1st December Square, RO-410068, Oradea, Romania

* Corresponding author: ostanasel@uoradea.ro



properties. It is also important to note that, according to the World Health Organisation, about 80% of the world's population currently uses herbs and medicinal plants as traditional remedies. However, although these products are natural, they are slower acting in the acute phase of the disease compared to synthetic

Oreganum vulgare L has beneficial properties due to the presence of essential oils, which contain volatile aromatic compounds that function as secondary metabolites of the plant, while the primary metabolites are responsible for the survival of the plant. Essential oils provide the plant with protection from hazards, predators or other threats, promoting healthy reproduction and helping to attract pollinators. [1]

Origanum vulgare L., commonly known as oregano, is a woody, rhizomatous perennial plant, with stems up to 90 cm or more, usually branched at the top, pubescent, hirsute or velvety, rarely glabrous. The name oregano can be translated as 'mountain delight' and comes from the Greek 'oros' meaning mountain and 'ganos', joy. Oregano belongs to the *Lamiaceae* family of the order *Lamiales*. The genus *Origanum* includes more than 70 species, 49 taxa (species and subspecies) and natural hybrids found throughout most of the Mediterranean area, including northern Africa, but also in temperate Asia and Central America. Wild oregano species can grow at different altitudes, from coastal to mountainous areas, on different soils and are able to withstand quite low temperatures.

An average of 1-2% essential oil is extracted from a plant, but the amount depends on the species grown. In *Origanum vulgare L* oil was found terpenes (limonene, α -pinene, γ -terpinene, p-cymen, α -myrcene), alcohols (thymol, carvacrol, eugenol, linalool, 2-phenyl-ethanol, 3-hexen-1-ol, mimosquinone, thymoquinone, octen-3-ol, 1,8-cineole, cis-p-ment-2-en-1-ol, terpinen-4-ol, α -terpineol, spatulenol and benzyl alcohol). [2]

The essential oil content, as well as the ratio of carvacrol and thymol to the total amount of oil, is quite variable depending on the species of oregano, the soil and terrain of origin, the time of harvesting, and the method of distillation.

While thymol is antibacterial, anti-inflammatory, antiprotozoal it also has antioxidant, cytotoxic, and pesticidal activities and is a good allelopathic agent. Carvacrol has multiple properties: antioxidant, antimicrobial, antitumor, antimutagenic, antigenotoxic, analgesic, antispasmodic, anti-inflammatory, angiogenic, antiparasitic, antiplatelet, insecticidal, antihepatotoxic and neuroprotective. [3]

GC-MS chromatographic analysis identified the following components in oregano essential oil: 27% monoterpene hydrocarbons (α -pinen, camphen, β -pinen, myrcen, α -phellandren, α -terpinen, p-cymen, limonen, γ -terpinen),

66% oxygenated monoterpenes (1,8-cineole, linalool, α -thujone, camphor, borneol, terpinen-4-ol, α -terpineol, geranial, thymol, carvacrol), 6% sesquiterpene hydrocarbons (α -copaen, β -caryophyllene, α -humulene), 0.5% oxygenated sesquiterpenes (caryophyllene oxide) and 0.5% aromatic compounds (phenylpropanoids: 1-octen-3-ol), listed according to the Kovat index retention (RI), C8-C32 n-alkane, calculated by gas chromatograph on an apolar HP-5MS column. [4]

The oregano plant is also very rich in minerals such as Ca (1043 mg/kg), Fe (159 mg/kg), K (19625 mg/kg), Cr (7.43 mg/kg), and Ba (79.8 mg/kg), which are important structural components of tissues and could influence water and acid-base balance. [5]

In vitro studies, the antioxidant activity of the oregano plant was found to be 12 times higher than in oranges, 30 times higher than in potatoes and 42 times higher than in apples. The beneficial health effects of extracts (ethanolic, methanolic and in acetone) of oregano are attributed to its high antioxidant activity, determined by carvacrol and thymol. Several studies demonstrate that a high content of polyphenols in oregano leads to a major antioxidant potential, which is determined by organic acids with biological effects mostly related to remarkable antioxidant, antimutagenic, anticarcinogenic and anti-inflammatory activities. Polyphenolic acids have a high capacity to scavenge reactive oxygen radicals. These polyphenols are able to inhibit inflammatory processes and tumor propagation by deactivating pro-oxidative enzymes, described below. In some *in vivo* animal studies, *Origanum* plants have been shown to be a dietary supplement *and* have been used in animal diets for weight gain, infection control and immune enhancement. [6,7,8]

Various studies using *Origanum* plants have shown good results, showing that its inclusion in the diet increases the weight of animals; helps fight parasite infections and increases the animals' innate immune response. These important effects on farm animals are due to the presence in the essential oils of the polyphenols: carvacrol, linalool, borneol, α -terpinene, γ -terpinene, α -pinen and β -pinen.[9,10,11]

RESULTS AND DISCUSSIONS

Extraction methods are based on the distribution of the components of a mixture in a polar solvent. Maceration was carried out using polar solvents with different polarities: methanol, ethanol, acetone.

The Folin-Ciocalteu test is the most common procedure used to determine the total polyphenol content of different extracts. The amount of polyphenols with antioxidant properties is expressed in gallic acid equivalents

(mg/ml). In the concentration range of 0.05 - 2.0 mg/ml (gallic acid) a strong dependence of concentration on absorbance is obtained. The line obtained has the equation $y = 4.3916x + 0.1236$, the correlation coefficient $R^2 = 0.9975$ showing a good correlation of the results.

The extracts obtained by maceration and essential oils of DoTERRA and Purarom were analyzed and the results are presented in table 1.

It is observed that in the case of extractions in methanol and acetone the amount of polyphenols extracted is higher than in ethanolic solutions and in essential oils 0.61 mg/ml.

The health benefits of oregano extracts are explained by the high antioxidant activity due to the polyphenols they contain. In order to determine antioxidant activity, the analysis is based on the measurement of free radical neutralizing capacity. The unpaired electron of the nitrogen atom in DPPH is reduced by accepting a hydrogen atom from the antioxidants at the corresponding hydrazine.

Table 1. Amount of polyphenols and absorbances of samples analysed

No.	Type of extract used	Absorbance (nm)	Polyphenol content in the test solution (mg gallic acid/ml)
1	Purarom essential oregano oil	1.1935	0.48±0.02
2	doTERRA® Oregano essential oil	1.2095	0.49±0.03
A	Methanolic extract	1.4713	0.61±0.018
B	Acetone extract	1.4731	0.61±0.02
C	Ethanolic extract	1.2003	0.49±0.017

The total polyphenol content of extracts ranged from 0,48 mg GA/ml to 0,61 mg GA/ml. These results were like previous oregano powder findings [xx]. Ethanolic extract of oregano powder is rich in rosmarinic acid quercetin coumarinic acid, caffeic acid [12] demonstrated by HPLC analysis of the extracts.

DPPH is a stable paramagnetic radical. The unpaired electron from the nitrogen atom is delocalized, belonging to the whole molecule. The solution is dark purple, showing an absorption maximum at a wavelength of 517 nm. The antioxidant activity of the three extracts and the essential oils of oregano was determined. Table 2 shows the results of the determinations.

From the analysis of the experimental results obtained, it is observed that doTERRA oregano essential oil shows the highest free radical neutralizing activity. In the case of extraction by the maceration method, the ethanolic

sample shows the highest free radical neutralizing activity. This is due to the higher solubility of compounds with antioxidant activity in ethyl alcohol. Licina [13] reported the DPPH radical scavenging activity of different extracts of *O. vulgare* L. in terms of IC50 values and found that ethanol extract was the most active with an IC50 value of 34.5 μ g/ml, while acetone extract was the least active with an IC50 value of 86 μ g/ml.

Table 2. Antioxidant activity results of analyzed samples

No	Type of extract used	Absorbance (nm) after 60 minutes	Antioxidant activity (%) neutralizing free radicals
1	Purarom essential oil of oregano	0.0884	89.89%
2	doTERRA® Oregano essential oil	0.0363	95.84%
A	Methanolic extract	0.7067	19.17%
B	Acetone extract	0.1283	85.32%
C	Ethanolic extract	0.0840	90.39%

By HPLC chromatographic analysis the polyphenol content was determined. Initially, the calibration curves of some polyphenols that were determined in extracts were determined. The calibration curves obtained with analytical standards are shown in Table 3.

Table 3. Results obtained by HPLC chromatographic analysis

Compound	Retention time (min.)	Equation of the calibration line	R ²
Gallic acid	2.2	Y=28572x + 457.97	0.9943
Caffeic acid	4.6	Y=42330x - 157.55	0.9960
Kaempferol	15.1	Y=207.88x - 4.5454	0.9966
Quercetin	22.1	Y=19277x-1233.2	0.9998
Umbelliferone	6.4	Y=1739.9x + 2751.8	0.9988

After HPLC chromatographic analysis of the extracts, the polyphenol content was determined and quantification was carried out using calibration curves for each compound. In Table 4, the results of the experimental determinations obtained from the analysis of oregano extracts/essential oils by the chromatographic method are presented.

Table 4. Amount of polyphenols in the analyzed samples

Sample	Gallic acid	Caffeic acid	Umbelliferone	Kaempferol	Quercetin
Methanolic extract (mg/ml)	0.5	0.8	0.06	0.9	0.16
Ethanol extract (mg/ml)	0.4	0.2	0.5	0.21	1.1
Acetone extract (mg/ml)	29	1.1	0.4	-	5.5
Purarom essential oil (mg/ml)	0.09	0.072	0.015	0.42	0.16
doTerra oil (mg/ml)	0.015	0.08	0.025	Cannot quantify	

From the experimental results obtained it can be seen that gallic acid, caffeic acid, and umbelliferone were identified in all samples. Along with these compounds, the flavonols kaempferol and quercetin were identified. In the extract made with an aqueous acetone solution, the highest amounts of these compounds were obtained. The analyses of volatile oil were carried out by GC-MS chromatography. The results are shown in Table 5.

Table 5. Results obtained by GC-MS chromatographic analysis

Compound	Rt (min)	Earth Oil	Ethanolic extract
		Conc (%)	Conc(%)
Izobutilacetat		1.37	1.24
α -Phellandren	5.949	0.25	0.28
3,6,6-trimethyl-2-norpinene	6.078	1.54	1.62
β -Mircen	6.972	3.53	2.97
(+)-2-Carene	7.377	2.74	2.58
A-Cimene	7.513	5.52	5.73
D-Limonen	7.574	1.12	0.98
2-Thujen	8.040	6.24	6.61
Beta-cis-Terpincol	8.180	0.41	0.49
Linalool	8.663	10.18	11.12
Endo-Borneol	9.734	1.48	1.55
Carvona	11.098	0.42	0.39
Thymol	11.438	2.59	2.67
Carvacrol	11.620	21.29	19.78
Cariophilen	13.356	1.94	2.11
β -Bisabolen	14.353	3.15	3.67

The results show a high concentration of carvacrol and thymol, compounds that have antibacterial activity, 21.29%, and 2.59% respectively in the essential oil and 18.78% and 2.67% in the hydroalcoholic extract.

In studies carried out on oregano extracts, it was determined a carvacrol content of 17-27%, depending on the country of origin. [14] The results obtained are comparable to others from the literature. [15] Antimicrobial activity was tested using the *Staphylococcus aureus* reference strain. In parallel, four antibiotics were tested: azithromycin, erythromycin, levofloxacin, and tetracycline. Different volumes of essential oil and oregano extract were tested. If in the case of antibiotics the diameters obtained were between 25 mm (azithromycin) and 32 mm (erythromycin) in the case of oregano preparations the diameter was 32 mm even at 0.2 µl extract respectively oil essence. The test results demonstrate the significant antimicrobial activity of oregano extracts. In the literature, a correlation between carvacrol content and antimicrobial activity is shown [16]

In addition, in agreement with literature data [17] terpenoids show analgesic, antitumoral, and antinociceptive activity. These data explain the free radical neutralizing activity and antimicrobial activity of oregano extracts.

Considering the obtained experimental results, oregano extracts are potential candidates for antimicrobial agents. At the same time, the combination of marked antioxidant properties with antibacterial action makes extracts of oregano a good candidate to be used in medicine, pharmaceutical, and cosmetic industry, as an antimicrobial, analgesic, antioxidant, and skin whitening agent. Being a widely used spice and having above mentioned biological activities, oregano could also be used as a food preservative.

CONCLUSIONS

Oregano is a widely used medicinal herb due to its special phenolic compounds and medicinal properties. In this study, we characterized the extracts of *Oregano vulgare*. In this study, we characterized the extracts of oregano... and essential oils. In ethanol: water extract, obtained by maceration, a polyphenol content of 0,48 mg GA/ml was determined. The ethanolic extract is rich in quercetin, and caffeic acid, which also explains the neutralization activity of free radicals at 90.3% in 60 minutes. The GC-MS analysis determined the content of 19.78% carvacrol and 2.67% thymol in the ethanolic extract, respectively. These compounds have antioxidant and antibacterial activity.

Oregano is a common spice and can be important in the prevention and treatment of many diseases, including bacterial infections. As a rich source of phenolic compounds and other secondary metabolites with

antioxidant and antimicrobial activity, oregano extracts could be used as nutritional supplements for the prevention of degenerative diseases. The potential of these extracts should be further evaluated for their application in modern medicine, the food industry, and cosmetics due to their antioxidant and antibacterial properties.

EXPERIMENTAL SECTION

Materials

All chemicals (methanol, acetic acid, sodium carbonate) used for assays were of analytical grade. 2,2-diphenyl-1-picrylhydrazyl (DPPH), gallic acid, vallinic acid, synaptic acid, quercetin, catechin, caffeic acid, umbelliferone, kaempferol were procured from Sigma-Aldrich Company. Folin- Ciocalteau reagent were procured from Merck Co.

The oregano plants used were grown from selected seeds, under organic conditions. When the plant reached maturity, the leaves were harvested, washed in order to remove impurities, then dried in the air current. The dry plant was further processed.

Equipment

A UV-visible spectrophotometer from Analitic-Jena was used for measuring the absorbance.

Determination of phenols by HPLC was performed on a HPLC ACME 3000 Younglin Instrument, equipped with SP 930 D module and UV730D detector module.

Thermo GC-MS (Model Trace 1310 ISQ7000) equipped with an HP-5MS capillary column (30 m length x 0.32 mm internal diameter x 0.25 μ m film thickness). GC-MS spectroscopic detection, an electron ionization system with an ionization energy of 70eV was used.

Extract sample preparation

Dried plants were ground into a fine powder and then subjected to phytochemical extraction. We performed extraction by maceration, using several solvents: methanol: water 1:1, ethanol: water 1:1, and acetone: water 1:1. Plant powder (1 gram) was macerated with 10 ml solvent at room temperature for 2 days with shaking from time to time. The suspension

obtained was filtered. The extract is filtered by a Millipore filter with a 0,45 µm and diluted with the same solvent at 10 ml. The solution was stored at 4° C in the refrigerator until analyzed.

1. *Determination of Total Phenolic Content*

The total phenols content of each extract was evaluated using the Folin-Ciocalteu reagent described by [39] with slight modifications. It is a colorimetric method based on the transfer of electrons, in an alkaline medium, from phenolic compounds to form a blue chromophore consisting of a phospho- and phosphomolybdenum complex in which the maximum absorption is proportional to the total concentration of polyphenolic compounds. The reduced forms of Folin-Ciocalteu reagent are detectable with a spectrophotometer in the 690 to 750 nm range. The reaction temperature was used to reduce the time to reach maximum color, $t = 37^{\circ}\text{C}$. Gallic acid was used as the standard reference compound according to the method described by the International Organization for Standardization ISO 14502-1. A calibration curve is initially constructed using a compound with significant antioxidant properties as a reference.

In a test tube, was introduced 8 ml distilled water, 1 ml standard working solution or analysis solution and 1 ml Foline-Ciocateau reagent (diluted 1:10). It was shaken and left to rest 1 minute, then 2 ml Na_2CO_3 20% solution was added and was maintained at 40° C for 1 hour. The absorbance of the resulting blue color was measured at 765 nm with a UV-VIS spectrophotometer.

Quantification was done on the basis of the standard curve of gallic acid concentration range between 0.05-0.25 mg/ml ($y = 4.3916x + 0.1236$; $R^2 = 0.9975$). The amount of total phenolic compounds was expressed as mg gallic acid equivalent (GAE)/ml extract.

2. *DPPH scavenging assay*

The hydrogen donating or the radical-scavenging ability of the extraction solution was measured using the stable radical DPPH-. DPPH radical scavenging assay of each sample was carried out by using a DPPH method with modification [40].

DPPH solution was prepared by dissolving 2 mg DPPH in 50 ml methanol (about 3 mM). 0.2 ml of each extracted sample was mixed with 2.8 ml DPPH solution. The mixture was incubated at room temperature in the dark. After 60 minutes, the absorbance was determined at 517 nm and gallic acid

was used as a positive control. The DPPH radical scavenging ability of each extracted sample was calculated using the following equation:

$$\text{DPPH radical scavenging rate (\%)} = (A_{\text{control}} - A_{\text{sample}}) \times 100 / A_{\text{control}}$$

where A_{control} is the absorbance of DPPH solution (without extract sample), A_{sample} is the absorbance of the extract sample.

Analysis of phenols by reverse-phase high-performance liquid chromatography(HPLC)

Determination of phenols was performed on a HPLC, under the following chromatographic conditions: isocratic conditions, mobile phase methanol: water: acetic acid 300:700:2, flow 1 ml/min. Chromatographic separation of the constituents of the sample was obtained using a reverse-phase YMC-Pack ODS AQ column, 150 cm long and with an internal diameter of 4.6 mm. A volume of 0.2 μl of each sample was injected into the chromatograph at room temperature.

GC-MS analysis

The GC-MS analysis of various organic crude extract leaves of *Origanum vulgare L.* was performed using a Thermo GC-MS GC-MS spectroscopic detection, and an electron ionization system with an ionization energy of 70eV was used. Helium was used as a carrier gas at 30 cm s^{-1} and the injection volume was 1 μl . The mass transfer line and injector temperature were set at 220° C and respectively 290° C. The oven temperature was programmed at 45° C for 1 min, raised to 250° C at 5 C/min, and maintained at 250° C for 5 min. Diluted samples of 1 μl were injected in the split mode with a split ratio of 120:1. The relative percentage of the chemical constituents in the dried extracts was expressed as the percentage by peak area normalization.

Determination of antimicrobial activity

To test the antimicrobial activity of the extract, agar-type Mueller-Hinton plates with a layer thickness of 90 mm were used and the test method was the diffusion method. Testing of the antimicrobial activity of the extract was performed on Gram-positive bacteria (*Staphylococcus aureus*) compared to the different antibiotics. The oregano extract was applied at different concentrations and after 24 H at 37° C, the diameter of the inhibition zone was compared to that produced by the antibiotics.

REFERENCES

1. E. Skoufogianni, A.D. Solomou, N.G. Danalatos, *Naturae Botanicae Horti Agrobotanici*, **2019**, 47(3), 545-552.
2. L. Pizzale, R. Bortolomeazzi, S. Vichi, E. Überegger, L.S. Conte, *J. Sci. Food Agriculture*, **2002**, 82, 1645–1651.
3. M. Moradi, A. Hassani, A. Ehsani, M. Hashemi, M. Raeisi, S.S. Naghibi, *J. Food Qual. Hazards Control*, **2014**, 1, 120-124.
4. M.D. Ibanez, M. Amparo Blazquez, *Food Agric. Immunol.*, **2017**, 28(6), 1168-1180.
5. M.S. Chiş, S. Muste, A. Păucean, S. Man, A. Sturza, G.S. Petruţ, A.C. Mureşan, *Hop and Medicinal Plants*, **2017**, XXV, no. 1-2: 17-27.
6. I. Giannenas, P. Florou-Paneri, M. Papazahariadou, E. Christaki, N.A. Botsoglou, A.B. Spais, *Arch. Anim. Nutr.*, **2003**, 57(4), 99-106.
7. P. Nosal, D. Kowalska, P. Bielański, J. Kowal, S. Kornaś, *Annals Parasitol*, **2014**, 60(1), 65-69.
8. M.P. Franciosini, P. Casagrande-Proietti, C. Forte, D. Beghelli, G. Acuti, D. Zanichelli, A. Dal Bosco, C. Castellini, M. Trabalza-Marinucci, *J. Appl. Animal Res.*, **2016**; 44(1), 474-479.
9. M.J.B. Fernandes, A.V. Barros, M.S. Melo, I.C. Simoni, *J. Med. Plants Res.*, **2012**, 6(12), 2261-2265.
10. M. Ranim, R. Mussa, S.N. Suslina, *J Adv Pharm Technol Res.*, **2021**, 12(4), 340–344.
11. M. Viuda-Martos, A.N. El Gendy, E. Sendra, J. Fernández-López, A.K. El Razik, E.A. Omer, *J. Agric. Food Chem.*, **2010**, 58(16), 9063-9070.
12. S.S. Chun, D.A. Watem, Y.T. Lin, P. Shetty. *Process Biochem*, **2005**, 40, 809–816.
13. B.Z. Licina, O.D. Stefanovic, S.M. Vasic, I.D. Radojevic, M.S. Dekic, L.R. Comic, *Food Control*, **2013**, 33, 498–504.
14. C.H. Chen, H.C. Chan, Y.T. Chu, *Molecules*, **2009**; 14(8), 2947-58.
15. M. Farhat., J. Toth, B. Hethelyi, Sz. Szarka, *Acta Facultatis Pharmaceuticae Universitatis Comeniana*, Tomus LIX, **2012**, 6-14.
16. L. Vernon, R. Orthofer, R. M. Lamuela-Raventos, *Methods in enzymology*, Academic Press, **1999**, 152-177.
17. P. Molyneux, *J. Agric. Food. Chem.*, **2004**, 62, 4251-4260.